Universidade de Aveiro Departamento de Física

2016

Maria Rosa
Nunes Soares

Desenvolvimento de materiais luminescentes à base de Zircónia para aplicação em iluminação e como biomarcadores

Development of Zirconia based phosphors for application in lighting and as luminescent bioprobes

Universidade de Aveiro

2016

Departamento de Física

Maria Rosa Nunes Soares

Desenvolvimento de materiais luminescentes à base de Zircónia para aplicação em iluminação e como biomarcadores

Development of Zirconia based phosphors for application in lighting and as luminescent bioprobes

Dissertação apresentada à Universidade de Aveiro para cumprimento dos requisitos necessários à obtenção do grau de Doutoramento em Nanociências e Nanotecnologia, realizada sob a orientação científica da Doutora Teresa Maria Fernandes Rodrigues Cabral Monteiro, Professora Associada com Agregação, do Departamento de Física da Universidade de Aveiro, e coorientação da Doutora Florinda Mendes da Costa, Professora Associada, do Departamento de Física da Universidade de Aveiro.

Por me ensinar a pescar em vez de me dar o peixe e pelo enorme esforço que fez para me fornecer as ferramentas necessárias para tal,

dedico este trabalho ao meu Pai.

o júri / the jury

president / president

Doutor Eduardo Anselmo Ferreira da Silva
Professor Catedrático, Universidade de Aveiro

vogais / examiners committee

Doutor Eduardo Jorge da Costa Alves
Investigador Coordenador, Instituto de Plasmas e Fusão Nuclear, Instituto Superior Técnico, Universidade de Lisboa

Doutora Teresa Maria Fernandes Rodrigues Cabral Monteiro
Professora Associada com Agregação, Universidade de Aveiro (orientadora)

Doutora Regina da Conceição Corredeira Monteiro
Professora Associada, Faculdade de Ciências e Tecnologia, Universidade Nova de Lisboa

Doutor Manuel Jorge e Araújo Pereira Soares
Professor Auxiliar, Universidade de Aveiro

Doutora Maria de Fátima Guimarães Cerqueira
Professora Auxiliar, Universidade do Minho

agradecimentos /
acknowledgements

palavras-chave   Zircónia, iões lantanídeos, monocristais, nanopartículas, ablação laser em meio líquido, fusão de zona com laser, combustão em solução, luminescência, *upconversion*, espectroscopia.

resumo   O progresso observado nas últimas décadas na área da fotónica e optoelectrónica, acompanhado de um desenvolvimento exponencial nas áreas da nanociência e nanotecnologia, resulta numa constante procura por materiais luminescentes eficientes com características cada vez mais exigentes.

Matrizes de largo hiato energético dopadas com iões lantanídeos assumem-se, atualmente, como uma classe de materiais luminescentes de elevada importância tecnológica. Dentro destas, a zircónia apresenta uma combinação de propriedades químicas e físicas que a potenciam como matriz para a incorporação dos iões mencionados, tendo em vista o seu uso em diversas áreas, destacando-se as aplicações em iluminação e sensores óticos, entre os quais sensores de pressão e biossensores. Associada à necessidade de materiais luminescentes com características superiores, encontra-se a necessidade de técnicas de produção rápidas, económicas e com potencial para produção em larga escala.

Tendo em conta estas necessidades, técnicas como a fusão de zona com laser, combustão em solução e ablação laser em meio líquido são exploradas neste trabalho para a produção de monocristais, nanopós e nanopartículas de matrizes à base de zircónia intencionalmente dopadas com lantanídeos. Em simultâneo, é realizado um estudo detalhado das propriedades morfológicas, estruturais e óticas dos materiais produzidos. São estudadas as características luminescentes de matrizes de zircónia (ZrO_2) e zircónia estabilizada com ítrio (YSZ) dopadas com vários iões lantanídeos (Ce^{3+} ($4f^1$), Pr^{3+} ($4f^2$), Sm^{3+} ($4f^5$), Eu^{3+} ($4f^6$), Tb^{3+} ($4f^8$), Dy^{3+} ($4f^9$), Er^{3+} ($4f^{11}$), Tm^{3+} ($4f^{12}$), Yb^{3+} ($4f^{13}$)) e co-dopadas com Er^{3+},Yb^{3+} e Tm^{3+},Yb^{3+}. Para além da luminescência de Stokes, foi avaliada e discutida a emissão anti-Stokes (*upconversion* e radiação de corpo negro) sob excitação no infravermelho. A comparação da luminescência em materiais com diferentes dimensões permitiu analisar o efeito do tamanho nas propriedades luminescentes dos iões dopantes. A discussão do trabalho é acompanhada por uma integração dos resultados visando as aplicações destes materiais luminescentes em emissores do estado sólido, biossensores e sensores de pressão.

keywords

Zirconia, lanthanide ions, single crystals, nanoparticles, pulsed laser ablation in liquids, laser floating zone, solution combustion synthesis, luminescence, upconversion, spectroscopy.

abstract

The strong progress evidenced in photonic and optoelectronic areas, accompanied by an exponential development in the nanoscience and nanotechnology, gave rise to an increasing demand for efficient luminescent materials with more and more exigent characteristics.

In this field, wide band gap hosts doped with lanthanide ions represent a class of luminescent materials with a strong technological importance. Within wide band gap material, zirconia owns a combination of physical and chemical properties that potentiate it as an excellent host for the aforementioned ions, envisaging its use in different areas, including in lighting and optical sensors applications, such as pressure sensors and biosensors. Following the demand for outstanding luminescent materials, there is also a request for fast, economic and an easy scale-up process for their production.

Regarding these demands, laser floating zone, solution combustion synthesis and pulsed laser ablation in liquid techniques are explored in this thesis for the production of single crystals, nanopowders and nanoparticles of lanthanides doped zirconia based hosts. Simultaneously, a detailed study of the morphological, structural and optical properties of the produced materials is made. The luminescent characteristics of zirconia and yttria stabilized zirconia (YSZ) doped with different lanthanide ions (Ce^{3+} ($4f^1$), Pr^{3+} ($4f^2$), Sm^{3+} ($4f^5$), Eu^{3+} ($4f^6$), Tb^{3+} ($4f^8$), Dy^{3+} ($4f^9$), Er^{3+} ($4f^{11}$), Tm^{3+} ($4f^{12}$), Yb^{3+} ($4f^{13}$)) and co-doped with Er^{3+},Yb^{3+} and Tm^{3+},Yb^{3+} are analysed. Besides the Stokes luminescence, the anti-Stokes emission upon infrared excitation (upconversion and black body radiation) is also analysed and discussed. The comparison of the luminescence characteristics in materials with different dimensions allowed to analyse the effect of size in the luminescent properties of the dopant lanthanide ions. The potentialities of application of the produced luminescent materials in solid state light, biosensors and pressure sensors are explored taking into account their studied characteristics.

Table of Contents

Acronyms list

Acronym	Definition
AFM	Atomic force microscope
ATF	Amino-terminal fragment
BF	Bright field
Bio-BPE	Biotinylated phycobiliprotein
CB	Conduction band
CCD	Charge-coupled device
CCT	Colour correlated temperature
CEES	Combined excitation–emission spectroscopy
CIE	Commission Internationale de l'Eclairage
CN	Coordination number
CR	Cross-relaxation
CRI	Colour rendering index
CSU	Cooperative sensitization upconversion
CT	Charge transfer
DC	Downconversion
DF	Dark field
DNA	Deoxyribonucleic acid
DS	Downshifting
DSL	Downshifted luminescence
ED	Electric dipole
EDS	Energy dispersive X-ray spectroscopy
EMU	Energy migration mediated upconversion
ESA	Excited state absorption
ETU	Energy transfer upconversion
FITC	Fluorescein isothiocyanate
FRET	Fluorescence resonance energy transfer
FSZ	Fully stabilized zirconia
FTIR	Fourier transform infrared
FWHM	Full width at half maximum
GSA	Ground state absorption
HRTEM	High resolution transmission electron microscopy

Acronym	Definition
IBM	International Business Machines
ICDD	International Centre for Diffraction Data
IL	Ionoluminescence
IR	Infrared
LCD	Liquid crystal display
LDA	Lithium diisopropylamide
LED	Light emitting diode
LFZ	Laser floating zone
LHPG	Laser heated pedestal growth
Ln	Lanthanides
LOD	Limit of detection
MD	Magnetic dipole
MEEAA	2-[2(2-methoxyethoxy)ethoxy]acetic acid
MRI	Magnetic resonance imaging
NIR	Near-infrared
NPs	Nanoparticles
OH	Hydroxyl group
PA	Photon avalanche
pc-LED	Phosphor converted light emitting diode
PIXE	Particle Induced X-ray Emission
PL	Photoluminescence
PLA	Pulsed laser ablation
PLAL	Pulsed laser ablation in liquids
PLE	Photoluminescence excitation
PMT	Photomultiplier tube
PSZ	Partial stabilized zirconia
PVA	polyvinyl alcohol
QW	Quantum wells
RGB	Red-green-blue
RT	Room temperature
SCS	Solution combustion synthesis
SDS	Sodium dodecyl sulfate
SEM	Scanning electron microscopy
SHG	Second harmonic generation
SHS	Self-propagating high temperature synthesis

Acronym	Definition
SOFC	Solid oxide fuel cells
SSR	Solid state reaction
STEM	Scanning transmission electron microscopy
STM	Scanning tunnelling microscopy
STPA	Simultaneous two photon absorption
TBC	Thermal barrier coatings
TEM	Transmission electron microscopy
TM	Transition metals
TR	Time resolved
TR-PL	Time resolved photoluminescence
TR-FRET	Time resolved fluorescence resonance energy transfer
TT	Thermal treatment
TZP	Tetragonal zirconia polycrystals
UC	Upconversion
UC-FRET	Upconversion fluorescence resonance energy transfer
UCL	Upconversion luminescence
UV	Ultraviolet
VB	Valence band
VUV	Vacuum ultraviolet
XRD	X-ray diffraction
YAG	Yttrium aluminium garnet
YSZ	Yttria stabilized zirconia
ZPL	Zero phonon lines

Chapter 1.

Introduction and motivation

In this chapter a general introduction to N&N field and the motivation behind the realization of this work is presented.

Nanomaterials have been used for centuries, with relevant facts indicating their use during the Archaic and Classical periods (620–300 BC) [1]. Nonetheless, the first concept of nanotechnology occurred for the first time in 1959, in one talk given by the physicist Richard Feynman entitled "*There is plenty of room at the bottom*", in which he suggested that it should be possible to construct tiny machines that can specifically arrange atoms and manipulate chemical synthesis [2,3]. Richard Feynman envisioned several aspects of *nanoscience and nanotechnology* field *(N&N* field*)*, which at that time for many seems as science fiction, but today are a major constant. Within other ideas, this physicist suggested that it would be possible to use focused electron beams to write nanoscale features on materials surface or that it would be possible to improve microscopes resolution to an atomic level. Both previsions are nowadays a reality, the first one expressed by the electron beam lithography, and the second one by the development of scanning tunnelling microscope (STM), and its derivatives such as the atomic force microscope (AFM) [2]. It was only in 1974, fifteen years after the famous talk of Richard Feynman, that the actual term *nanotechnology* was employed by the first time by Professor Norio Taniguchi from the Tokyo Science University. In a conference paper he wrote: *"Nanotechnology mainly consists of the processing of separation, consolidation, and deformation of materials by one atom or by one molecule"* [2,3]. Further divulgation of the concept of nanotechnology was promoted by Dr. K. Eric Drexler who wrote two books in the field of nanotechnology entitled *Engines of Creation: The Coming Era of Nanotechnology* in 1987 [4] and *Nanosystems: Molecular Machinery, Manufacturing and Computation* in 1992 [5]. The first book is currently considered the first one published in the field of nanotechnology [2]. In the 80's decade important milestones that strongly contributed for the progress in *N&N* took place. Such include, on one hand, the development in cluster science and, on the other hand, the aforementioned progresses of microscopes with atomic resolution (invention of STM in 1981 and AFM six year after [2,3]). These developments opened the door for the discovery of many nanomaterials, such as the well-known carbon nanotubes, and to the controlled manipulation of materials at an atomic level as well. In 1989, Don Eigler (who shared the 2010 Kavli Prize in Nanoscience with Nadrian Seeman) was the first to manipulate individual atoms in the production of nanostructures. Using the STM, this physicist from the International Business Machines (IBM) manipulated 35 individual Xenon atoms on a surface of Nickel to write the letters "IBM" [2,3]. The possibility to observe, measure and manipulate objects at nanoscale using these and other developed equipments boosted a strong research in *N&N* leading to a wide number of methods for the synthesis, characterization, computer simulation and theoretical modelling, manufacturing, and applications of nanomaterials [6]. It was only in *2000s* that the use of nanotechnology started to be implemented in

commercial products. Nowadays, nanomaterials are commonly present in several products of our daily use, from cosmetics to electronic devices. Figure 1.1 depicts a schematic diagram with the main research categories at nanoscale level along with their principal field of applications [3].
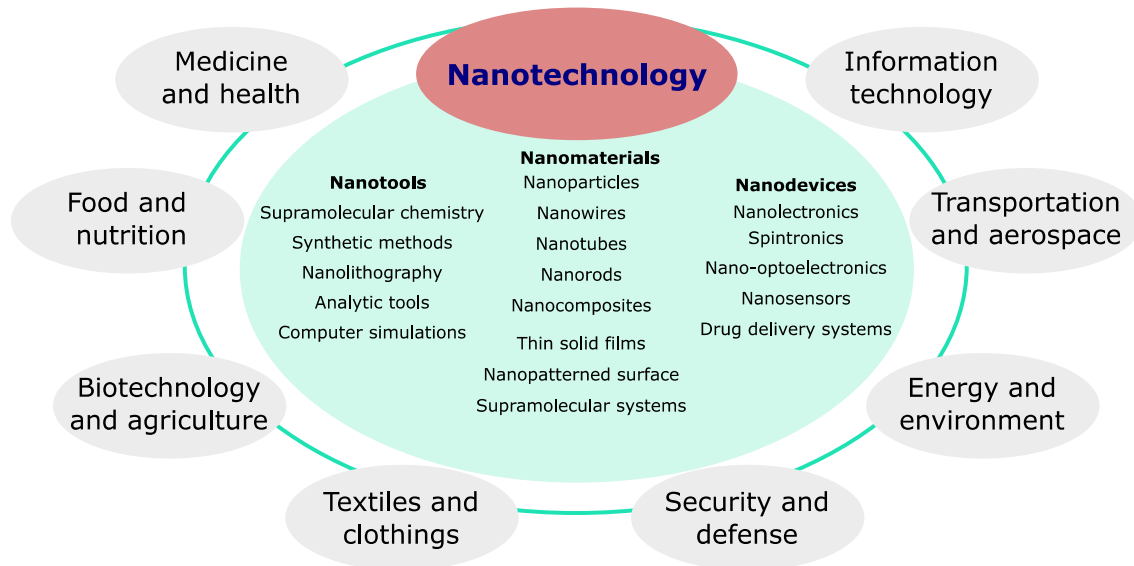
Figure 1.1. The three current categories of research in nanotechnology: examples and application fields (adapted from [3]).

The rapid development of *N&N* field verified in the last decades opened the door for a large variety of nanomaterials and nanodevices with new and/or improved properties [3]. The current research in *N&N* field is essentially focused in three main categories: *nanotools*, *nanomaterials*, and *nanodevices* [3]. Nanotools refer to a group of methods and techniques that allow the production and evaluation of nanostructured materials and nanodevices. Nanodevices are devices formed by nanostructured materials with specific functionalities, improved performance and/or new properties [3]. On the other hand, nanomaterials (or nanostructured materials) are materials in which at least one of their structural dimensions is at the nanoscale (usually considered <100 nm), showing different properties or functionalities from the same material in bulk form. Nanomaterials cover a large range of materials with different sizes and shapes including nanoparticles (NPs), nanorods, nanowires, nanofibers, nanotubes, nanocomposites, nanostructured surfaces, and thin solid films (Figure 1.1).

Within nanomaterials, inorganic NPs such as metal NPs [7–9], metal oxide NPs [10,11], semiconductor quantum dots (QDs) [1,12], and many others, are currently under an intense research worldwide, due to their potential applicability in different technological fields.

3

Inorganic NPs are commonly used in practical technological applications in different areas, from catalysis to medical science [9,13]. Due to their high surface/volume ratio and quantum-confinement effect, NPs can present unique and novel electrical, mechanical, chemical, optical, magnetic, thermal, and/or biological properties, as well as surface reactivity, different from their bulk counterparts [3,14].

A high number of techniques are now available for the production of these inorganic NPs. These are usually categorized as *physical* and *chemical* routes [1]. Physical routes includes the pulsed laser ablation (PLA), vapour condensation methods and other methods in which chemical reactions are not involved, and the NPs are generated by the vaporization/ablation and condensation of species from a solid material [15,16]. In contrast, in chemical routes, chemical reactions are involved in the formation of NPs. Examples of chemical processes are the chemical precipitation and chemical decomposition. The synthesis processes are also grouped in *top-down* and *bottom-up* approaches. *Top-down* approaches comprise the synthesis methods that involves the thermal, mechanical, or chemical disintegration of bulk materials into NPs [9,17]. In contrast, *bottom-up* approaches include synthesis techniques in which single atoms and/or molecules are assembled into larger NPs. *Bottom-up* include most of the chemical processes used nowadays. In addition, the synthesis processes are typically categorized according with the reactive medium as vapour phase, solution phase and solid phase synthesis. In particular solution-phase colloidal chemistry routes, which includes sol-gel process, hot-injection, coprecipitation, hydrothermal and solvothermal methods, template synthesis, biomimetic approaches, within others [13] have been widely studied in the preparation of inorganic NPs. Chemical synthesis in liquid phase typically allow a better control over particle size and shape. However, the amount of material produced by these chemical routes is usually limited to milligrams, which hinders its use in a large scale production. In addition, this type of approaches, frequently give rise to nanoparticle colloids with low purity due to the presence of residual unreacted chemical precursors. On the other hand, vapour-phase methods are continuous processes that allow high product yield and the production of NPs with high purity and thermal stability. Such characteristics contributes to the predominance of vapour-phase techniques in industrial production [17]. Currently, research in NPs synthesis is focused in the development of new or optimized techniques that combine both the benefits of chemical and physical approaches, in order to achieve more efficient, reproducible and economic, large scale manufacturing [2].

The progress in *N&N* field had a strong impact on the field of luminescent materials, allowing to extend the range of their technological applications. Luminescent inorganic NPs can now be used in applications where materials with higher dimensions cannot be used.

This is the case of luminescent NPs used as nanoprobes for bioapplications, including in biodetection, bioimaging, diagnosis and therapy. In fact, the study of luminescent nanomaterials for biomedicine applications is today one of the strongest focuses of research in *N&N*, attempting to unravel the cure for several societal needs. The spectral features and dynamics of luminescence in nanomaterials can be strongly modified by the size reduction to the nanoscale, allowing design luminescent biosensors and biomarkers for specific disease targets after an appropriate surface functionalization. Understand how these properties change with size is crucial for further manipulation and technological application of NPs.

An important class of luminescent materials that have received special attention in the last decade are the wide band gap inorganic host doped with lanthanide (Ln) ions. The luminescent features of Ln ions combined with the intrinsic properties of such hosts (in particular oxides) can result in materials with outstanding properties that can be used to overcome the current needs in photonics and optoelectronics (including solid state lighting), biosensors and theranostics. On one hand, the fast development in lighting technologies based on solid state materials leads to a strong demand for alternative luminescent materials with high performance. On the other hand, the need of high sensitive and less harmful bioassays results in an intense search for alternative luminescent bioprobes.

Zirconia (ZrO_2) is an oxide material with a high potential as host for the incorporation of Ln ions to produce high performance luminescent materials. Besides its appropriated optical properties, including wide band gap energy (4-6 eV, depending on crystalline phase nature [18]) and relatively low cut-off phonon energy (with reported energy of stretching mode around 470 cm^{-1} [19]), this oxide has a high chemical, thermal and photostability and is also bio-inert. All these characteristics make zirconia an appropriated choice for application in harsh environments. For example, thanks to the high photostability, zirconia can resist long times to high levels of UV radiation without deteriorate its properties.

Motivated by the current demands for luminescent materials with improved characteristics, and by the huge expectation in the application of inorganic luminescent nanomaterials, this work aims to:

- Explore alternative synthesis technique that allow a simple, rapid and reproducible large scale production of Ln-doped zirconia;
- Produce Ln-doped zirconia materials in different scales (millimetric, micrometric and nanometric crystals);

- Explore the luminescent properties of zirconia hosts doped with different lanthanide ions;
- Investigate the nano-size effect on the luminescence characteristics of Ln-doped zirconia nanomaterials;
- Explore the potential applications of the produced materials in lighting and bioapplications.

Two achieve these goals, luminescent materials based on zirconia doped with different lanthanide ions were produced using three different techniques: laser floating zone (LFZ), solution combustion synthesis (SCS) and pulsed laser ablation in liquids (PLAL), which allow the production of bulk crystals, nanocrystalline powders and NPs, respectively. Among other reasons, these techniques where selected based on their simplicity and potentiality for scale-up. LFZ exhibit advantageous over other crystal growth techniques, since it allows the growth of crystals with high purity at higher growth rates, and of materials with high melt temperature [20]. SCS allows the rapid and economic production of large quantities of nanocrystalline powders [21,22]. PLAL consists in a simple and green technique to produce NPs colloids. Before the work herein presented, reports related with the production of zirconia NPs by PLAL were limited to a few published data related with undoped NPs [23,24]. The work developed in this thesis also intends to contribute for a higher comprehension of the benefits and limitations of the studied synthesis processes and to evaluate the viability of each one in the production of lanthanide based luminescent materials. In addition to the exploitation of the fundamental properties of different lanthanide ions incorporated into zirconia based lattices, this work also aims to contribute to the comprehension of the size effect on the optical properties of these materials, by comparing the properties of the single crystals, powders and NPs. Besides, the downshifted luminescence of Ln ions in the trivalent charge state embedded in zirconia host, the upconversion luminescence of some of these ions was also explored under different ambient environments, upon infrared excitation. The latter is suitable for the development of specific devices based on such excitation/luminescence phenomena.

1.1 Structure of the thesis

This thesis is organized in 10 chapters. In first chapter, a general introduction to *N&N* field and the motivation behind the realization of this work is presented. A brief introduction to the role of the inorganic luminescent materials, with special attention to the luminescence based on lanthanide ions embedded in inorganic hosts is given in Chapter 2. At the end of

this chapter, the main applications of such luminescent materials are explored, with the emphasis placed in solid state lighting and luminescent bioprobes. In Chapter 3 an overview of zirconia material properties is presented. The distinct zirconia polymorphs and the mechanisms for the stabilization at room temperature (RT) of the high temperature crystalline phases are explored. In addition, since in this thesis yttrium was used as stabilizer, a brief revision of the ZrO_2-Y_2O_3 phase diagram is also presented. The properties and technological applications of stabilized zirconia are also revised. At the end, the potentialities of zirconia as an effective host for the incorporation of optically active Ln ions are also explored. In Chapter 4, the characterization techniques used to evaluate the morphology, structure and luminescent properties of the produced samples are described.

Chapters 5, 6 and 7 are dedicated to the growth/synthesis of bulk crystals by LFZ, nanocrystalline powders by SCS and nanoparticles colloids by PLAL, respectively. These chapters follow identical structure and can be dived in two main parts. In the first part, the fundaments of respective growth/synthesis technique (LFZ, SCS and PLAL) are explained and the used experimental setup is described. In the second part, the results obtained of morphological, structural and optical characterization of the produced samples (bulk crystals, nanocrystalline powders, and nanoparticles colloids) are presented and discussed.

Chapter 8 consists in a special section dedicated to the upconversion luminescence. In the first part of this chapter the fundaments and mechanisms behind the upconversion luminescence are revised. After, the upconversion luminescence of bulk crystal, nanocrystalline powders and nanoparticles are detailed and explored.

In Chapter 9, the perspectives of applications of the produced luminescent materials are envisaged. An overview of the work undertaken in this thesis and final conclusions followed with new ideas for further developments are presented in Chapter 10.

References

[1]   C. Altavilla, C. Enrico, *Inorganic Nanoparticles: Synthesis, Applications, and Perspectives*; 1 edition.; CRC Press: Boca Raton, FL, 2010.

[2]   Z. P. Aguilar, *Nanomaterials for Medical Applications*; 1 edition.; Elsevier: Amsterdam ; Boston, 2012.

[3]   P. Iqbal, J. A. Preece, P. M. Mendes, In *Supramolecular Chemistry*; John Wiley & Sons, Ltd, 2012.

[4]   E. Drexler, *Engines of Creation: The Coming Era of Nanotechnology*; Reprint edition.; Anchor, 1987.

[5]   K. Eric Drexler, *Nanosystems: Molecular Machinery, Manufacturing, and Computation*; 1 edition.; Wiley: New York, 1992.

[6]   J. Li, N. Wu, *Biosensors Based on Nanomaterials and Nanodevices*; 1 edition.; CRC Press: Boca Raton, 2013.

[7]   V. V. Mody, R. Siwale, A. Singh, H. R. Mody, *J. Pharm. Bioallied Sci.* **2010**, *2*, 282.

[8]   T. S. Sreeprasad, T. Pradeep, In *Springer Handbook of Nanomaterials*; Vajtai, R., Ed.; Springer Berlin Heidelberg, 2013; pp. 303–388.

[9]   M. Zahmakıran, S. Özkar, *Nanoscale* **2011**, *3*, 3462.

[10]   R. Shukla, D. P. Dutta, J. Ramkumar, B. P. Mandal, A. K. Tyagi, In *Springer Handbook of Nanomaterials*; Vajtai, R., Ed.; Springer Berlin Heidelberg, 2013; pp. 517–552.

[11]   J. A. Rodriguez, M. Fernández-García, *Synthesis, Properties, and Applications of Oxide Nanomaterials*; John Wiley & Sons, 2007.

[12]   B. A. Kairdolf, A. M. Smith, T. H. Stokes, M. D. Wang, A. N. Young, S. Nie, *Annu. Rev. Anal. Chem.* **2013**, *6*, 143.

[13]   M. Niederberger, N. Pinna, *Metal Oxide Nanoparticles in Organic Solvents*; Engineering Materials and Processes; Springer London: London, 2009.

[14]   J. Z. Zhang, *Optical Properties and Spectroscopy of Nanomaterials*; World Scientific, 2009.

[15]   S. Iravani, H. Korbekandi, S. V. Mirmohammadi, B. Zolfaghari, *Res. Pharm. Sci.* **2014**, *9*, 385.

[16]   M. Singh, S. Manikandan, A. K. Kumaraguru, *Res. J. Nanosci. Nanotechnol.* **2011**, *1*, 1.

[17]   W. H. Zhong, *Nanoscience and Nanomaterials: Synthesis, Manufacturing and Industry Impacts*; DEStech Publications, Inc, 2012.

[18]   F. Gallino, C. Di Valentin, G. Pacchioni, *Phys. Chem. Chem. Phys.* **2011**, *13*, 17667.

[19]   G. Cabello, L. Lillo, C. Caro, G. E. Buono-Core, B. Chornik, M. A. Soto, *J. Non-Cryst. Solids* **2008**, *354*, 3919.

[20]   M. R. B. Andreeta, A. C. Hernandes, In *Springer Handbook of Crystal Growth*; Dhanaraj, G.; Byrappa, K.; Prasad, V.; Dudley, M., Eds.; Springer Berlin Heidelberg, 2010; pp. 393–432.

[21]   F.-T. Li, R. J. Ran, M. Jaroniec, S. Qiao, *Nanoscale* **2015**, *7*, 17590.

[22]   T. Mimani, K. C. Patil, *Mater. Phys. Mech.* **2001**, *4*, 134.

[23]   H. Zeng, X.-W. Du, S. C. Singh, S. A. Kulinich, S. Yang, J. He, W. Cai, *Adv. Funct. Mater.* **2012**, *22*, 1333.

[24]   S. C. Singh, H. B. Zeng, C. Guo, W. Cai, *Nanomaterials: Processing and Characterization with Lasers*; John Wiley & Sons, 2012.

Chapter 2.

Luminescent inorganic materials

A brief introduction to the role of the inorganic luminescent materials, with special attention to the luminescence based on lanthanide ions embedded in inorganic hosts is given in this chapter.

The main applications of such luminescent materials are explored, with the emphasis placed in solid state lighting and luminescent bioprobes.

As light is essential for the existence of life in a fundamental sense, the development of light technologies is also crucial to promote life quality and to revolutionize the society through the development of different areas such as medicine, communications, entertainments and culture [1]. With such high potentialities, *photonics* (the science and technology for understanding, controlling and exploiting the interaction of light/photons and matter [2]), is considered one the most important technologies of the future. Nowadays, the advancements in the photonic-based technologies are focused in solving important challenges in our society, such as energy generation and energy efficiency, healthy ageing of the population, climate changes, and security [1].

Photonic technologies represent an economically strong industry (Figure 2.1), with a huge impact on the world's economy with a global market of 300 billion euros in 2011 and the roadmap project values over 600 billion euros in 2020, according with the Photonics Industry Report 2013, released by photonics21.org [1,3].
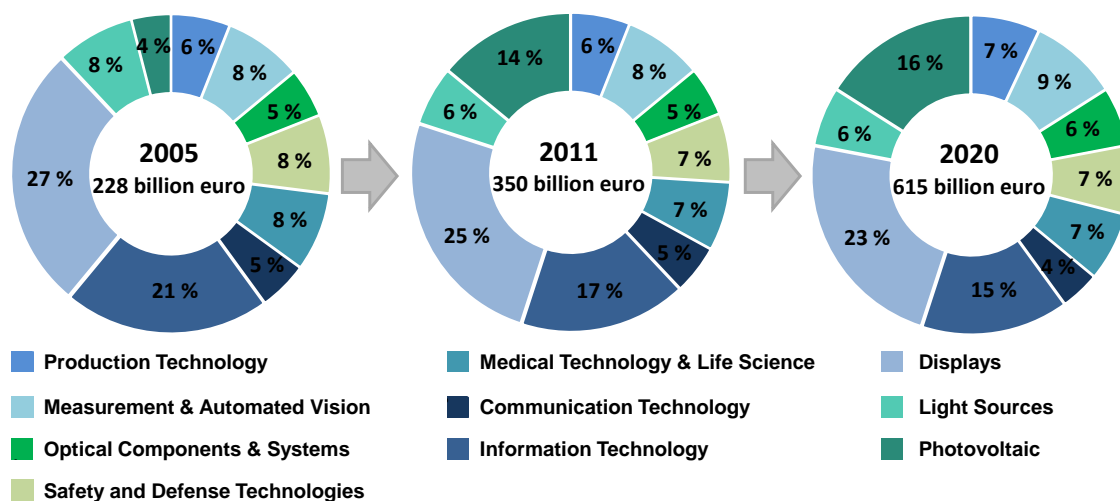
Figure 2.1. World market in photonic in the years 2005 and 2011 and expectations for 2020 [1,3].

Luminescent materials, defined as solid materials that convert absorbed energy into electromagnetic radiation rather than thermal radiation [4,5], are key components in several photonics applications, mainly in the ones which aim the generation and amplification of light [4,5]. These materials, sometimes also named as phosphors, are known from a long time and their development and of their technological applications was marked by several important landmarks over the years. The luminescence phenomena was first identified in natural crystals such as willemite, a zinc silicate mineral (Zn_2SiO_4), scheelite, a calcium tungstate mineral ($CaWO_4$) and calcite, a calcium carbonate mineral ($CaCO_3$) [6]. For a long

time, the luminescent materials were only used for decoration purposes [6]. It was in the end of nineteenth century that one first important milestone for the development of luminescent materials and devices took place. This development was driven by the first realization of gas discharge and electron beams in evacuated gas tubes by Geissler and Braun, as well by the discovery of the X-rays by Röntgen [6]. The first luminescent devices, including cathode ray tubes (CRTs), fluorescent lamps and X-ray intensified screens, were developed only few years after these discoveries. An important phosphor used in these applications was the $CaWO_4$ that has an efficient blue emission [6]. Further developments in luminescent materials and devices were strongly stimulated during the Second World War, with the intense research in luminescent materials for CRTs due to the demand for radar screens development. Later, in the first half of twentieth century, luminescence materials development was motivated by the quick and successful application of fluorescent lamps in lighting and of X-rays in medical imaging [6]. The first luminescent devices contained only one luminescent material and typically presented a coloured emission. Lamps with white luminescence, using only one phosphor, were firstly invented in 1926 by Meyer and *et al.* [7]. These lamps used a doped halophosphate ($Ca_5(PO_4)_3(Cl,F):Sb^{3+},Mn^{3+}$) as luminescent material, with the perceived white emission provided by a broad luminescence band extended over all the visible spectral region. Other important landmark in the development of luminescent materials and devices occurred when Koedam and Opstelten [8] suggested in 1971 the use of Ln ions for improving the emission characteristics of such materials. This was particularly important to the evolution of lighting technologies. In 1972, phosphors using a combination of three Ln ions, $Sr_3(PO_4)_5Cl:Eu^{2+}$, $LaPO_4:Ce^{3+},Tb^{3+}$ and $Y_2O_3:Eu^{3+}$ with light emission in blue, green and red regions, respectively, were used in fluorescent lamp to produce white light with higher efficiency and lumen equivalency [6]. Since then, the increase demand for efficient light sources has driven the worldwide research in undoped and doped wide band gap hosts with different dimensionalities, among which are, for instance, the nitrides hosts responsible for the efficient blue InGaN light emitting diode (LEDs) used in our daily life. The latter, combined with a phosphor ($Y_2O_3:Ce$) leads to the white light sources currently used in illumination purposes [9].

Luminescence, i.e. the phenomena in which a material emits light after energy absorption, is categorized according with the type of radiation used as excitation [4,10,11]. In Figure 2.2 are indicated some of luminescence categories according with the type of absorbed energy. *Electro-*, *cathode-*, *radio-* and *photo*luminescence, in which the material is excited, respectively, by an electric field, electron beam, ionizing radiation and photons are nowadays highly explored techniques to produce different types of luminescent devices. In

this thesis, the emphasis will be placed in the analysis of luminescent materials using photons as excitation, the above designated photoluminescence (PL).

	Energy source	Applications
Electroluminescence	Electric field	LEDs; EL panels; Semiconductor Laser.
Cathodoluminescence	Electrons	CRT for TVs; displays and measurements; field emission display.
Radioluminescence	Ionizing radiation	Fluoroscopic screens; scintilators; radiographic imaging plates; dosimeters
Photoluminescence	Electromagnetic radiation/photons	White LEDs; fluorescent pigments and marking; luminous paints; solid state laser materials; high pressure mercury lamps; fluorescent lamps; plasma displays; bioapplications.
Ionoluminescence	High energetic accelerated particles or ion beams	
Chemiluminescence	Chemical and electrochemical reactions	
Thermoluminescence	Heat	
Mechanoluminescence	Mechanical action	
Crystalloluminescence	Crystallization	

Bioluminescence from mushrooms (http://www.sciencenutshellcom)

White LED (https://www.adafruit.com)

Figure 2.2. Overview of several luminescence phenomena according with the type of absorbed energy (drawn based in [10]).

Over the years, a wide variety of both inorganic and organic luminescent materials have been explored for photonic applications. Organic luminescent materials, which consist in polymers or low molecular weight materials applied as thin films or solid solutions, show usually intense luminescence. However, these materials are characterized by low chemical, thermal and photostability [12]. In contrast, inorganic luminescent materials can show a high stability meaning that they are much more suitable and reliable for practical applications.

Regarding the inorganic hosts, several types of semiconductor materials, such as SiC, GaN, ZnSe, CdS, GaAs, InGaN, AlGaAsP and others, can be found in many light emitting technologies taking advantage of their direct band gap and efficient recombination from an electron in conduction band (CB) with a hole in the valence band (VB), the so-called band-to-band transitions. In addition, intrinsic lattice defects and intentionally introduced dopants in a given host, can lead to optically active centres, inducing remarkable luminescence properties in semiconductors and insulator materials for the above

mentioned applications (Figure 2.3) [13]. In particular, inorganic wide band gap materials intentionally modified with a controlled and reproducible doping emerged as a new class of luminescent materials with high technological importance for lighting and biomedical applications [4,14]. The large band gap of the host lattice makes it transparent to ultraviolet (UV) and visible radiation and prevents any electrons from bridging the forbidden gap thermally, in such way that the undoped host is expected to be optically and electrically inert [13]. The incorporation of the dopant ions on the lattice leads to the introduction of electronic energy levels of the ion within the energy gap of the host. In the end, the luminescent properties of the doped materials are dependent on the intrinsic properties of the host and the dopant ion [13]. In some cases, sensitizer ions, with high absorption cross section of the excitation energy, are also intentionally incorporated in the lattice (co-doping process) in order to increase the emission intensity of a given activator ion, after energy transfer processes (Figure 2.3).
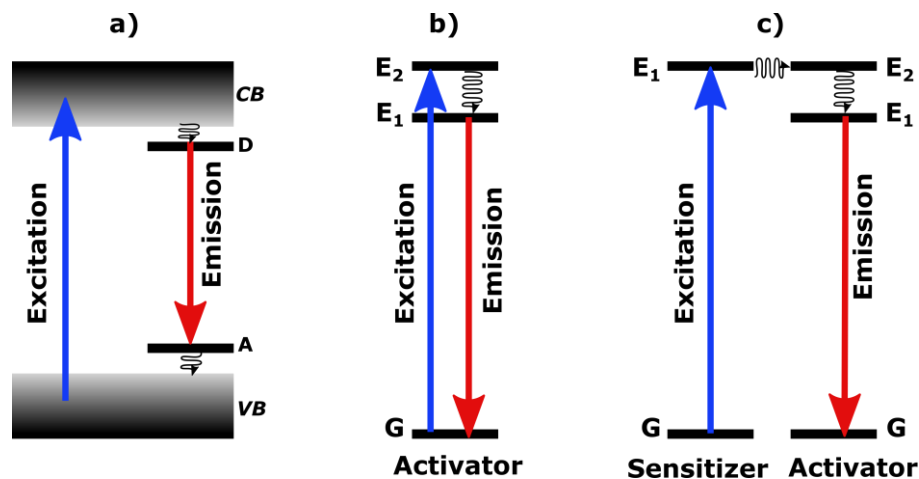
Figure 2.3. Simplified schemes of the luminescence in inorganic materials: a) example of an emission in a semiconductor after band to band absorption (VB and CB represent the valence and conduction bands, respectively, and A and D the acceptor and donor energy levels); b) and c) corresponds to the emission from an activator ion after absorption of the excitation energy by itself and after absorption of the excitation energy by a sensitizer ion, respectively. In the latter case energy transfer from the sensitizer to the activator occurs. G represents the ground state energy level and E_1 and E_2 excited states of the ions. In a general way, these schemes can also be applied to other optically active defects (adapted from [15]).

Transition metals (TM) and Ln ions are the most common dopants that are deliberately incorporated into wide band gap materials to confer specific luminescence characteristics to the host material [13]. Within the TM ions, the ones with an $1s^2\,2s^2\,2p^6\,3s^2\,3p^6\,3d^n$ (n=1 to 9) electronic distribution, called the 3d elements, are the most used as optically active dopants. The positive valence of these ions in solid materials depends on the host nature. Additionally, since the electrons involved in the optical transitions are the 3d electrons

placed in the outer shell, the electronic energy levels are strongly influenced by the surrounding crystal field. [11]. Typically, absorption and emission spectra of TM ions in crystalline hosts are characterized by broad emission bands due to the strong electron-phonon coupling to the lattice phonons, even though sharp lines (zero phonon lines, ZPL) are sometimes observed. Additionally, TM optically activated ions are characterized by a large Stokes shift between the absorption and emission bands [11].

Despite the interest of the properties of TM ions as activators, the main research on phosphors for photonics and bioapplications has been placed on Ln ions, considering such ions in different charge states. In particular, the trivalent Ln ions (Ln^{3+}) show particular photophysical properties which give rise to peculiar luminescent features, as will be described in next subsection. The dopant Ln ions are known to frequently substitute some of the lattice cations. As a result of the incorporation of Ln^{3+} in the host lattice, well-localized energy levels belonging to the $4f^n$ ground state configuration and $4f^{n-1}5d$ excited state configuration of the Ln^{3+} dopant (see next subsection) are introduced between the valence and the conduction bands of the hosts [13,16]. Therefore, under proper excitation, and depending on the used Ln^{3+}, the materials can emit a widespread of photons covering all the electromagnetic spectrum, from UV, visible and infrared.

Besides the transparency in the UV and visible spectral range, effective inorganic hosts for the incorporation of optically active Ln^{3+}, should have a low phonon cut-off energy in order to achieve intraionic efficient luminescence by minimizing the nonradiative deexcitation through multiphonon relaxations. In addition, materials with high photostability that can resist to high energy photon irradiation by a long period of time are also advantageous. Moreover, for many photonic applications, materials with high chemical and thermal stability, and in some cases with high mechanical resistance, are also required. Intraionic luminescence of Ln^{3+} embedded in several inorganic hosts, including fluorides, oxides, oxynitrides, sulphides, selenides, halides or silicate alkaline halides, chlorides, tungstates, phosphates, and others have been reported [13,14]. Within these materials, doped fluorides and oxides are among the most promising hosts for phosphors and bioapplications. In a general way, fluorides hosts usually lead to a higher efficiency of the dopants luminescence, mainly due to their lower vibrational energy which decreases the probability of the nonradiative paths. On the other hand, oxides, including zirconia, generally have a better photo and chemical stability, which is a major issue for phosphor technologies. In addition, oxides are usually synthesised by more simple, fast and less expensive techniques [17]. These issues strongly motivated the study of the luminescence of Ln ions in wide band gap oxides.

2.1 Luminescence of Ln ions

The lanthanides are constituted by 15 consecutive chemical elements of the sixth row in the periodic table, starting in lanthanum (La), with atomic number 57, until lutetium (Lu), with atomic number 71 [18]. As aforementioned, when incorporated in solid state materials, these elements can be found in the trivalent (Ln^{3+}), divalent (Ln^{2+}), or either in a tetravalent charge state (Ln^{4+}) [4,19]. Both the trivalent and divalent lanthanide ions are important optically activators used nowadays in several photonic applications.

Table 2.1. Electronic configuration of lanthanide elements and respective trivalent ions. The ionic radius of the ions is also indicated [20].

Ln atom	Atomic number	Ln electronic configuration	Ln^{3+} ion	Ln^{3+} electronic configuration (Ground state)	Ln^{3+} ionic radius (Å)
La	57	[Xe] $5d^1 6s^2$	La^{3+}	[Xe]	-
Ce	58	[Xe] $4f^1 5d^1 6s^2$	Ce^{3+}	[Xe] $4f^1$ ($^4F_{5/2}$)	1.034
Pr	59	[Xe] $4f^3 6s^2$	Pr^{3+}	[Xe] $4f^2$ ($^3H_4$)	1.013
Nd	60	[Xe] $4f^4 6s^2$	Nd^{3+}	[Xe] $4f^3$ ($^4I_{9/2}$)	0.995
Pm	61	[Xe] $4f^5 6s^2$	Pm^{3+}	[Xe] $4f^4$ ($^5I_4$)	0.980
Sm	62	[Xe] $4f^6 6s^2$	Sm^{3+}	[Xe] $4f^5$ ($^6H_{5/2}$)	0.964
Eu	63	[Xe] $4f^7 6s^2$	Eu^{3+}	[Xe] $4f^6$ ($^7F_0$)	0.950
Gd	64	[Xe] $4f^7 5d^1 6s^2$	Gd^{3+}	[Xe] $4f^7$ ($^8S_{7/2}$)	0.938
Tb	65	[Xe] $4f^9 6s^2$	Tb^{3+}	[Xe] $4f^8$ ($^7F_6$)	0.923
Dy	66	[Xe] $4f^{10} 6s^2$	Dy^{3+}	[Xe] $4f^9$ ($^6H_{15/2}$)	0.908
Ho	67	[Xe] $4f^{11} 6s^2$	Ho^{3+}	[Xe] $4f^{10}$ ($^5I_8$)	0.894
Er	68	[Xe] $4f^{12} 6s^2$	Er^{3+}	[Xe] $4f^{11}$ ($^4I_{15/2}$)	0.881
Tm	69	[Xe] $4f^{13} 6s^2$	Tm^{3+}	[Xe] $4f^{12}$ ($^3H_6$)	0.869
Yb	70	[Xe] $4f^{14} 6s^2$	Yb^{3+}	[Xe] $4f^{13}$ ($^2F_{7/2}$)	0.858
Lu	71	[Xe] $4f^{14} 5d^1 6s^2$	Lu^{3+}	[Xe] $4f^{14}$ ($^1S_0$)	0.848

Ln^{3+} and Ln^{2+} have very different spectroscopic features, which are particularly related with their electronic configurations. In both oxidation states, the ions have an $4f^n$ ground state electronic configuration, in which n is the number of electrons and includes one more electron for the Ln^{2+} when compared with the Ln^{3+} based on the same element [11]. However, while for the divalent lanthanide ions the $4f^{(n-1)} 5d$ excited configuration is not far in energy from the $4f^n$ ground state configuration, in the case of Ln^{3+} the energy separation between the excited configuration and the ground state configuration is high. As result, typically $4f^n \rightarrow 4f^{(n-1)} 5d$ interconfigurational transitions of Ln^{2+} ions occur in the visible range of the electromagnetic spectrum [11]. On the other hand, in Ln^{3+} the $4f^n \rightarrow 4f^{(n-1)} 5d$ interconfigurational transitions typically occur at higher energies, in the UV or vacuum

ultraviolet (VUV) spectral regions [11]. Nevertheless, for Ln^{3+} a wide range of electronic states are incorporated in the material forbidden band gap. Therefore UV, visible and near-infrared (NIR) emissions are usually observed and commonly assigned to electronic transitions between the energy levels within the $4f^n$ configuration. The dominance of the intraconfigurational electronic transitions in the case of Ln^{3+} and of the interconfigurational electronic transition in the case of Ln^{2+} leads to very distinct spectroscopic properties when the material is excited with UV or visible radiation, as it will be explored in the following sections.

2.1.1 Effect of crystal field on the dynamics of Ln^{3+} luminescence

The number of electrons in the unfilled $4f^n$ shell in Ln^{3+} increases between 0 and 14 from La^{3+} to Lu^{3+} (see Table 2.1). In these ions, the filled $5s^2$ and $5p^6$ subshells are located farther from the nucleus than the incomplete $4f^n$ shell [13]. This displacement is schematic illustrated in Figure 2.4 a) for a Ln^{3+} embedded in a given crystal and by the radial probability distribution functions of the $4f$ valence and core electrons for Nd^{3+}, shown in Figure 2.4 b). As a result of this displacement the electrons in the incomplete $4f^n$ shell are shield from the surrounding environment by the electrons of the outer $5s^2$ e $5p^6$ subshells and there is little or no overlap between their wavefunctions with those of the electrons of ligand ions [11,21]. As a consequence, when a Ln^{3+} is incorporated in a solid state material, the energy levels of the free ion are weakly disturbed by the local crystalline field. Therefore, the optical intra-$4f$ transitions maintain almost its atomic character, resulting in absorption and emission spectra with well-defined and narrow lines, very similar to the ones expected for the free ions [2,20,21]. In addition, due to the weak interaction between the ion and the surrounding medium, the energy positions of the intra-$4f$ transitions are practically independent of the host in which the ion is embedded. Such means that the absorption and emission bands assigned to a specific intra-$4f$ electronic transition appear almost at the same wavelength for a given ion incorporated in different matrixes. In addition, since the intra-$4f$ electronic transitions are forbidden by parity in accordance with Laporte rule [22], the intra-$4f$ emissions of Ln^{3+} are characterized by long lifetimes. In contrast, the energy levels of the electron in the $5d$ shell are significantly affected by the crystalline field generated by the surrounding environment. Hence, the spectral positions of the $4f^n \rightarrow 4f^{(n-1)} 5d$ electronic transitions in Ln^{2+} ions are very sensitive to the type of crystalline lattice and, therefore to the local crystalline field in which the ion is inserted. As a result, the same ion inserted in different hosts can show very distinct energy emission colours. For example, Eu^{2+} incorporated into Sr$_2$P$_2$O$_7$ shows intense emission in the violet region, while the same ion inserted in SrAl$_2$O$_4$ emits in the green spectral region [11]. In general, Ln^{2+} visible emission is

characterized by broad and intense bands, associated to the electric dipole (ED) allowed $4f^n \rightarrow 4f^{(n-1)}5d$ electronic transitions, while the intra-$4f$ transition in Ln^{3+} give rise to sharp emission lines and to low Stokes shifts.
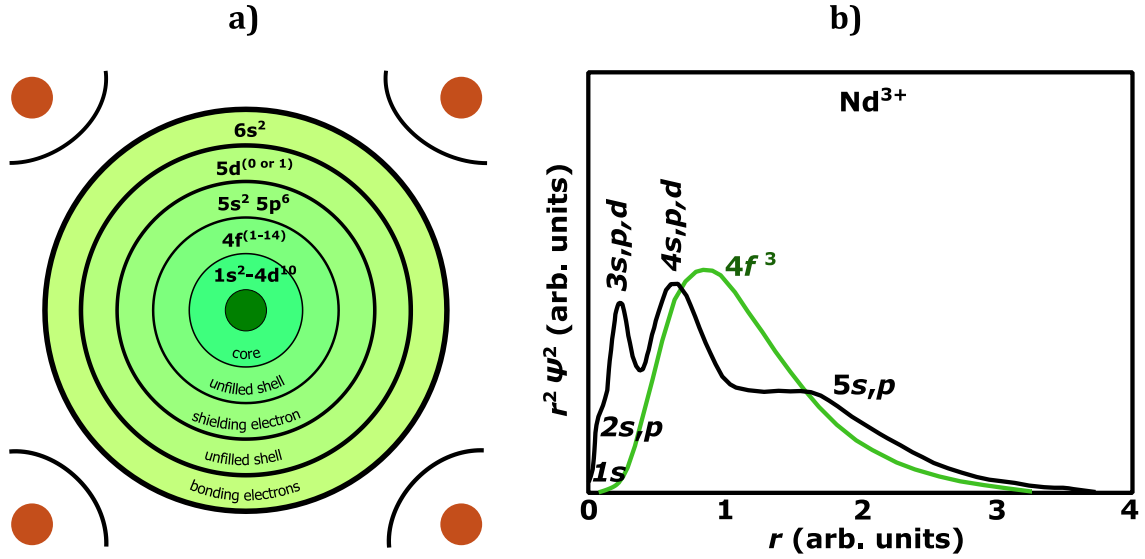
Figure 2.4. a) Schematic representation of the electronic structure of a Ln³⁺ when incorporated in a crystalline lattice (adapted from [21]). b) Radial probability distribution functions of valence 4f electrons (green line) and core electrons (black line) of Nd³⁺ (adapted from [23]).

When compared with the free ion, the effect of the local crystalline field in the electron energy levels of the Ln^{3+} incorporated in a solid host, can be summarized by a slight shift in energy with further level splitting due to the decrease of the ions local symmetry [2]. For a Ln^{3+} incorporated in a solid material the Hamiltonian H that describes all the electron interactions in the ion is given by *Eq.* 2.1, in which H_{FI}, H_L and H_{CF} are the Hamiltonian for the free ion, lattice and crystal field, respectively [13].

$$H = H_{FI} + H_L + H_{CF} \qquad\qquad Eq.\,2.1$$

The free ion Hamiltonian, H_{FI}, describes all the electric and magnetic interactions in the ion. In the case of ions with high number of electrons, as is the case of Ln^{3+}, the most important terms of the interactions can be described by [13]

$$H_{FI} = H_O + H_C + H_{SO.} \qquad\qquad Eq.\,2.2$$

H_O includes the kinetic energy of the electrons and the electrostatic interaction of each electron with an average potential due to the nucleus and the other electrons in the inner and outer shells. As the all valence electron are under the same potential, for a particular electron configuration, the eigenstates of H_O are degenerated [13]. For the free ion, the degenerated states in an electron configuration are further splitted as a result of Coulombic

17

interaction (described by the H_C) and spin-orbit coupling (described by the H_{SO}). The splitting of the energy levels of the electrons in the $4f$ configurations, due to different electronic interactions, is schematically represented in Figure 2.5, where the [Xe] $4f^6$ configuration of Eu^{3+} is taken as an example. The stronger electronic interaction is the Coulombic interaction that represents the electron-electron repulsion within the $4f$ orbitals. These interactions lead to different ^{2S+1}L terms, separated between them by energies in the order of 10^4 cm^{-1}, in which 2S+1 represents the total spin multiplicity and L the total angular orbital momentum [2]. Each one of these terms is further unfolded into several energy J-levels due to the spin-orbit coupling. As a result of the heavy nucleus of Ln^{3+}, the spin-orbit coupling splitting is relatively large, leading to energy separations between J-levels in the order of 10^3 cm^{-1}. Each one of these J-levels is represented by the symbols $^{2S+1}L_J$, in each J is the total angular momentum of the $4f$ electrons, and these are the free Ln^{3+} energy levels [2]. When the ion is inserted in a crystalline environment an additional splitting of the $^{2S+1}L_J$ levels, due to the interaction of the $4f$ electron with the neighbouring ions (generating a local crystalline field in the Ln^{3+} place) is observed. As explained above, the latter interaction is weak due the shielding of the valence electrons, giving rise to sublevels with energy separations in the order 10^2 cm^{-1} [2]. The result of the crystalline field splitting in the absorption/emission spectra of a Ln^{3+} in a crystal is identified by the presence of a fine structure in the individual band of the $^{2S+1}L_J \rightarrow {}^{2S'+1}L'_{J'}$ transitions.

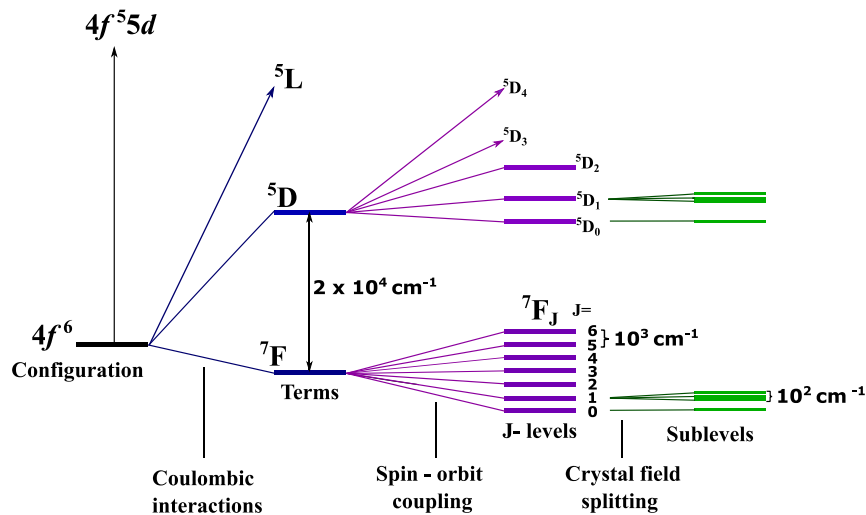**Figure 2.5. Partial representation of the splitting of the electron energy levels, due to different interactions in Ln^{3+}. The [Xe] $4f^6$ configuration of Eu^{3+} was taken as example (adapted from [2]).**

The maximum number of split sublevels for each $^{2S+1}L_J$ multiplet is given by (2J+1) for an integer J and by $(J+\frac{1}{2})$ for a half integer J [24]. In fact, the number of unfolded components is

determined by the local symmetry around the Ln^{3+} in the crystal. The maximum number of sub-levels splitted by the crystalline field as a function of J quantum number and for different lattice symmetries is indicated in Table 2.2 [22]. A complete split of the $^{2S+1}L_J$ in its maximum components is only observed when the ion is placed in an environment with very low symmetry. On the other hand, when the ions are placed in high symmetry environments the number of unfolded components is low. As such, important information about the symmetry of the coordination environment of the Ln^{3+} can be obtained by the analysis of the number of splitted components observed in the emission or absorption spectra [2]. However, the identification of the local symmetry of the ion taking into account the number of splitted components observed in a spectrum is not always easy. First, a high resolution spectrum, with all the lines well resolved should be considered. Second, the mixing of splitted components due to the Ln^{3+} in different local symmetries (e.g. different site locations in the host) will difficult the analysis.

Table 2.2. Maximum number of sub-levels splitted by the crystalline field as a function of J quantum number [22].

Symmetry	Site symmetry	Integer J							
		1	2	3	4	5	6	7	8
cubic	T, T_d, T_h, O, O_h	1	1	3	4	4	6	6	7
hexagonal	C_{3h}, D_{3h}, C_6, C_{6h}, C_{6v}, D_6, D_{6h}	1	2	5	6	7	9	10	11
trigonal	C_3, S_6, C_{3v}, D_3, D_{3d}	1	2	5	6	7	9	10	11
tetragonal	C_4, S_4, C_{4h}, D_4, D_{2d}, D_{4h}	1	2	5	7	8	10	11	13
low	C_1, C_s, C_2, C_{2h}, C_{2v}, D_2, D_{2h}	1	3	7	9	11	13	15	17
Symmetry	Site symmetry	Half-integer J							
		1/2	3/2	5/2	7/2	9/2	11/2	13/2	15/2	17/2
cubic	T, T_d, T_h, O, O_h	1	1	2	3	3	4	5	6	6
All others*	--	1	2	3	4	5	6	7	8	9

*All ligand-field sub-levels are doubly degenerated

In the 1960s, Dieke and co-workers reported a first overview of the $4f^n$ energy levels for all the Ln^{3+} [25]. The energy level diagram, known as the Dieke diagram, was built based on systematic measurements of the optical spectra of the different Ln^{3+} incorporated in a particular lattice, the lanthanum chloride ($LaCl_3$). The diagram shows the $^{2S+1}L_J$ energy states of the Ln^{3+} in this host, in the near UV, visible and NIR spectral regions. Figure 2.6 shows an adaptation of the Dieke diagram for the ions between Ce^{3+} and Yb^{3+}. The width of each energy state indicates the magnitude of the crystal field splitting and the energy states that are marked with a semicircle or triangle correspond to light emitting levels, in other words, to levels for each the direct depopulation originates luminescence [11]. Due to the weak influence of the crystal filed in the energy levels, the Dieke diagram is currently used to extrapolate the energy levels of Ln^{3+} in other lattices. As such, the Dieke diagram remains

nowadays an important guide to predict, in a roughly way, the energy location of the Ln^{3+} multiplets and to help for a proper assignment of the emission spectra corresponding to the Ln^{3+} in crystals [11]. The most intense radiative intra-$4f^n$ transition of each Ln^{3+} in $LaCl_3$ host is highlighted in the Dieke diagram shown in Figure 2.6. The widespread of the Ln^{3+} electronic energy levels allows tuning the emission from the UV (Gd^{3+}), visible (Eu^{3+}, Tb^{3+}, Dy^{3+}, Pr^{3+}, Sm^{3+}, Tm^{3+}, etc.) to the NIR (Pr^{3+}, Nd^{3+}, Ho^{3+}, Er^{3+}, Yb^{3+}), by a proper choice of the dopant ion or mixture of ions [22].
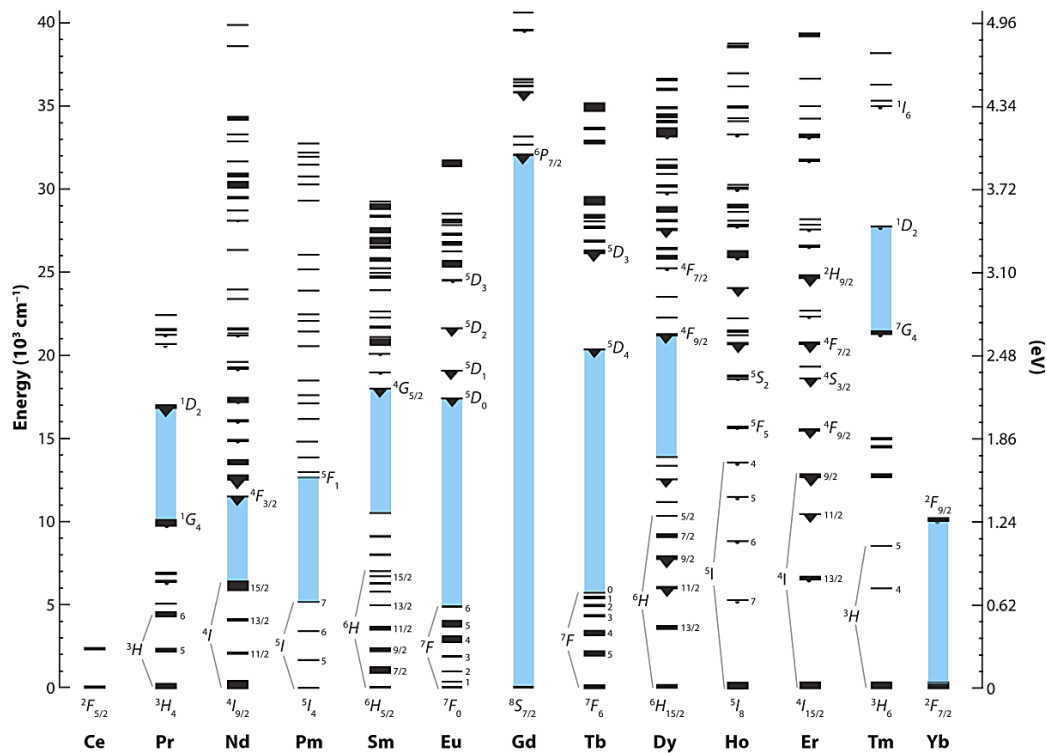
Figure 2.6. Dieke energy levels diagram of trivalent lanthanide ions from cerium to ytterbium [26].

Even though the Dieke diagram is an extremely useful tool for the assignment of the emission lines in an emission spectrum, no information regarding the relative intensity (and exact energy) of the emission lines of the ion in a specific material can be obtained from these diagrams. Theoretical works developed independently by Judd and Ofelt in 1962 were an important contribution in this subject. The so-called Judd-Ofelt [27,28] theory allows the calculation of the intensity of the ED induced transitions between the multiplets of the Ln^{3+}, often used to forecast the luminescent properties of Ln^{3+} in crystals or glasses using well resolved absorption spectra [21].

While the crystal field interaction has a weak effect on the energy states of the system, the dynamic of the luminescence processes can be strongly affected when the ions are placed in a given host [13]. The relative intensity between different intra-$4f$ transitions and also the overall intensity of the emission is strongly dependent on the local symmetry in which the Ln^{3+} is placed. In an hypothetical free Ln^{3+} ion, only magnetic dipole (MD) intra-$4f$ transition are allowed. As mentioned above, the ED transitions are forbidden by parity (Laporte rule). However, when the Ln^{3+} is placed in a coordinated environment a relaxation of the selection rules occurs and induced ED transitions can be observed as the ligand field mixes odd-parity wavefunctions [2]. While the strength (probability) of the allowed MD transitions are practically independent of the crystalline environment where the ions are inserted, in the case of the ED transitions, since these are induced by the ligand fields, their probabilities are very sensitive to the crystal field interaction. Strong and asymmetric ligand fields lead to ED transitions with relatively high intensities [2]. In fact, some transitions are extremely sensitive to the Ln^{3+} coordinating environment, called the hypersensitive transitions. In this case, depending on the ligand field the transitions can be either completely absent or very intense [2]. One example of these hypersensitive transitions is the emission line assigned to the $^5D_0 \rightarrow {}^7F_2$ transition of Eu^{3+}. Comparatively to the completely allowed transitions of other luminescent materials, the probability of both MD and the induced ED transitions of Ln^{3+} ions are weak. This is reflected in long radiative lifetimes, usually in the order of milliseconds, depending on the Ln^{3+} and on the host where the ions are inserted. As it will be explored further, emission with long lifetimes are of particular interest in some applications, including those related with bioimaging and biodetection.

A negative consequence of the induced ED nature of intra-$4f$ transitions in solid materials is the weak absorption of Ln^{3+}, usually with extinction coefficient (ability for a material to absorb light of a specific wavelength) in the order of 1 $M^{-1}cm^{-1}$ and bandwidths lower than 0.2 nm [2]. As such, the Ln^{3+} emission upon resonant excitation in their excited multiplets is not a very efficient process. The emission efficiency of these ions can be improved by increasing the absorption of the excitation light, which can be made using different approaches. For example, a second dopant ion, a sensitizer, with high cross section absorption, which efficiently absorbs the excitation energy and transfers it to the Ln^{3+} activator, can be used. Other alternative for efficient excitation into the intra-$4f$ energy levels of Ln^{3+} is via parity allowed absorption, either by $4f \rightarrow 5d$ transitions or by charge transfer (CT) transition. In comparison with intra-$4f$ transitions, the parity allowed $4f \rightarrow 5d$ absorption are much more intense, with extinction coefficients in the range of 200-1000 $M^{-1}cm^{-1}$, which in principle can be seen as an efficient alternative to excite the trivalent

lanthanide ions [22]. However, besides their strongly dependence of the surrounding coordination environment, $4f{\rightarrow}5d$ transitions of Ln^{3+} have large energies, usually above 6.2 eV ($\lambda < 200$ nm), with the exception of Ce^{3+} (> 4 eV, $\lambda < 312$ nm), Pr^{3+} and Tb^{3+} (> 5 eV, $\lambda < 250$ nm) [22]. As such, $4f{\rightarrow}5d$ transitions of Ln^{3+} are rarely observed in coordinated compounds. These high energies invalidate, in most of the cases, the practical applications of Ln^{3+} doped phosphors excited via $4f{\rightarrow}5d$ transitions. As for the $4f{\rightarrow}5d$ transitions, ligand-metal ion CT transitions also have huge energies that, with the exception of Eu^{3+}, Tb^{3+}, Sm^{3+} and Tm^{3+}, usually appear at wavelengths lower than 200 nm [22].

Beyond an efficient route for Ln^{3+} excitation, the intensity of the Ln^{3+} emission spectra depends on the competition between the radiative and nonradiative mechanisms for the electron deexcitation. The high number of the electronic energy levels within the $4f$ configuration, allows for multiple sequential (cascade) radiative and nonradiative relaxation in the excited ion [2]. The knowledge of the radiative and nonradiative pathways for the ions relaxation is important to understand the emission of the lanthanide ions and to optimize the luminescent properties of the materials. The direct radiative emission probability of an excited energy level of Ln^{3+} is strongly related with the energy mismatch between this level and the next lower multiplet. Usually, a low energy gap between an excited state and the next lower energy level results in a nonradiative deexcitation of the excited state. In contrast, excited levels with wide energy gap next to the lower multiplet are usually light emitting levels [11]. In solid materials, the nonradiative deexcitation occurs typically by the dissipation of energy through lattice vibrations/phonons, in a process called multiphonon relaxation. The phonons involved in this process, the effective phonons, are the ones with higher energy and with high density of states. The multiphonon emission rate (A_{nr}) of a specific excited energy level decreases exponentially with the energy gap between the excited state and the energy of the level below. This dependence is expressed by the *Eq.* 2.3, in which A_{nr} *(0)* and *a* are constants that depend on the host lattice and ΔE is the energy gap between the two electronic states [13].

$$A_{nr} = A_{nr}(0) \times e^{-a\Delta E} \qquad\qquad Eq.\,2.3$$

This equation represents the experimentally known *energy gap law* that gives the nonradiative deexcitation rate of each energy level of a Ln^{3+} in a solid lattice, only through the knowledge of the energy gap, independently of the ion or the nature of the electronic emitting level [13]. As such, only knowing the energy level diagram of the Ln^{3+} ion it is possible to have a prevision of the nonradiative deexcitation rates of the energy levels of different trivalent lanthanide ions. The exponential decrease in the nonradiative relaxation

with increase in the forbidden energy between the multiplets is strictly related with the number of lattice phonons that are necessary to overpass the energy gap between the two levels. In the case of a high energy difference a high number of phonons will be required to overpass such gap, and consequently the probability of nonradiative deexcitation is low. The number of phonons (p) involved in a multiphonon emission process of a specific energy level can be calculated by dividing the energy gap (ΔE) by the energy of the effective phonon ($\hbar\omega_0$). Thus, the nonradiative deexcitation rate in *Eq.* 2.3 can be rewritten as a function of the number of phonons (*Eq.* 2.4) [11].

$$A_{nr} = A_{nr}(0) \times e^{-(ah\omega_0)p} \qquad\qquad Eq.\, 2.4$$

Results from experience shows that, if energy of more than five effective phonons are required to overpass the energy gap between the two multiplets, the deexcitation from the high energy level occurs radiatively [11]. In Ln^{3+}, as a result of the nonradiative deexcitation mediated by multiphonons, the emission originates preferentially from the excited energy level with the higher energy separation to the next lower energy level. Once again, the coordinated environment of the Ln^{3+} plays an important role in the emission spectra of the Ln^{3+} [2]. The development of efficient luminescent materials doped with Ln^{3+} requires an appropriated selection of the host lattices. As mentioned before, hosts with low effective phonons energies are essential to achieve efficient emissions.

Other important aspect that should be taken into account during the engineering of efficient Ln^{3+}–doped inorganic phosphors is the solubility of a specific Ln^{3+} in a given host. Above a critical concentration value, the ions tend to form precipitates in the solid matrix [19]. These can be ions clusters or compounds and alloys formed with a component of the host. Aggregates formation usually induce a quenching in the luminescence, which can be originated by the formation of optical inactive lanthanide compounds or due to ion-ion interactions [19]. As such, the establishing of ion concentration limits is important to improve the intraionic luminescence intensity. Ion-ion interactions can occur between ions of the same species, for example in a cluster, or between different ions, for example in co-doped hosts with sensitizers. Usually, the interaction between ions of the same nature constitutes a loss mechanism, since it leads to an increase in the nonradiative deexcitation channels or in luminescence from unwanted transitions. Such interactions are dependent on the ion concentration, since high concentrations lead to shorter distances between the ions embedded in a given host. A high number of ion–ion interactions can occur. Figure 2.7 shows a schematic representation of two different ion-ion interactions between ions of the same species, Er^{3+} is taken as an example. The first example, energy migration (Figure 2.7 a)

is strongly dependent on the ion concentration, and occurs when one ion in an intermediate excited state (ion 1 in the example) interacts with a neighbour ion in the ground state (ion 2) promoting this to an intermediate excited state. Even though radiative deexcitation can occur for the ion 2, this process consists in a loss mechanism, since the probability of nonradiative deexcitation increases with each successive energy transfer [19].

a) Energy migration   b) Cross-relaxation
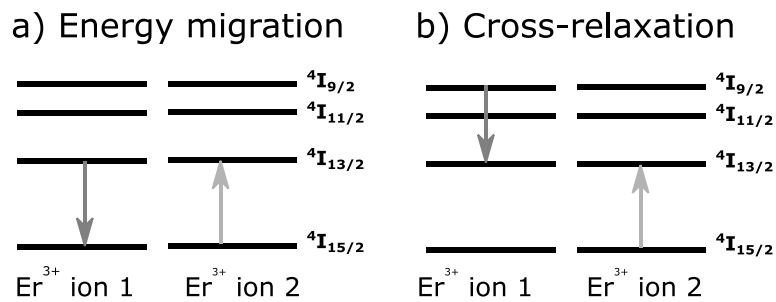
Figure 2.7. Schematic representation of energy migration and cross-relaxation processes between Er [3+] ions (adapted from [19]).

In the cross-relaxation process (Figure 2.7 b) the deexcitation energy from an ion (ion 1 in the example) decaying from a high energy level promotes the excitation of a neighbour ion (ion 2) from the ground state to an intermediate excited state. In order to observe this process, the energy difference between the upper excited state and the intermediate one, of the ion 1, should be close to the energy difference between the two energy levels involved in the energy absorption of the second ion [19]. This is for instance the case of the Er^{3+} ions indicated in Figure 2.7 where the energy difference between the $^4I_{9/2}$ and $^4I_{13/2}$ levels is similar to the energy difference between $^4I_{13/2}$ and $^4I_{15/2}$ levels. Therefore, the population of the intermediate excited state may be increased by the cross-relaxation process, namely in samples with high ion concentrations. Although cross-relaxation is a loss mechanisms, in some cases this process is induced purposely. For example in Er^{3+} doped materials the cross-relaxation processes can be used to tune the emission colour from green to red as will be discussed latter on in Chapters 7 and 8 with the presentation of the experimental results in erbium doped zirconia samples.

The interaction between ions of different elements can be used to promote new excitation schemes of Ln^{3+} ions. In such cases, the host needs to be intentionally doped, in a controllable way, with two or more different ions. As introduced in the beginning of the current chapter, assuming a simple co-doping (considering two distinct ions), one of the ions - the sensitizer - which can be a Ln^{3+} or other type of ion, absorbs the energy of the excitation radiation. The absorbed energy is transferred to the activator, in this case the

Ln[3+], which is promoted to an excited state. This type of interaction allows, on one hand, the use of a wide range of excitation energies while, by the other hand, leads to the improvement of the luminescence efficiency of the Ln[3+] ion [13,20].

The luminescence of trivalent lanthanide ions in inorganic materials is frequently classified into three categories, named downshifting (DS), downconversion (DC) and upconversion (UC) luminescence, according with the relative energy of excitation and emission light [15,18,29]. In DS luminescence, an absorbed photon with high energy gives rise to one emitting photon with a lower energy (Stokes emission) [18]. The DS luminescence, which is maybe the most common process, is usually simply called as luminescence and, typically, the conversion efficiency is lower than the unit due to the occurrence of nonradiative relaxations. Even if in theory, visible DS luminescence is expected for the most of Ln[3+] ions due to their high abundant energy level diagrams, usually strong visible emission at RT is only observed for a few Ln[3+] in solid state hosts. As already stated, typically, intense emission at RT can be achieved in phosphors doped with Eu^{3+}, Tb^{3+} or Dy^{3+} activators, which possess a high energy gap between the emitting energy level and the next low-lying state [18]. As such, practical applications of DS luminescence from Ln-doped phosphors are mainly restricted to phosphors doped with these ions. In addition, the characteristic long lifetime of DS emissions of Ln[3+] is particularly important for specific practical applications, including in biodetection assays, as it will be explored in the section 2.2.2.

The downconversion (DC) luminescence is a similar mechanism to the DS. However, in the DC process the high energy excitation photon is converted into two or more low energy photons. This phenomenon is commonly termed as *quantum cutting* and in some materials, leads to a conversion efficiency higher than 100% [30].
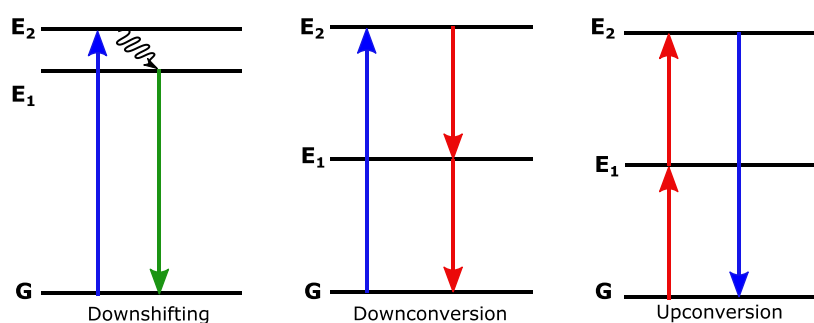

Figure 2.8. Schematic diagram illustrating the processes downshifting, downconversion and upconversion luminescence (adapted from [31]).

UC is a luminescence phenomenon in which two or more low energy excitation photons are sequentially absorbed to give rise to an emission photon with a higher energy (anti-Stokes emission), via long lived intermediate states [18]. Efficient UC luminescence is mostly produced in inorganic hosts doped with specific trivalent Ln ions, in particular Er^{3+}, Tm^{3+} and Ho^{3+} [18]. The high UC luminescence efficiency in these Ln^{3+} is related with their ladder-like energy level configuration together with the long lifetime of the emission of the intermediate states which allows the promotion of the electron to a superior high energy level by the successive absorption of the excitation photons. The mechanism involved in UC luminescence will be further explored in Chapter 8 where a detailed analysis of this phenomena in the co-doped samples prepared in this work will be presented and discussed. Taking advantage of their UC luminescence, Ln^{3+}-doped inorganic materials are currently a challenge in several light-based technological fields (e.g. lighting and displays, photovoltaics, solid state laser, infrared quantum counters and optical telecommunications [32,33]). As a consequence of the advances and development in nanoscience and nanotechnology, UC NPs with improved properties can be produced by new strategies of nanomaterials synthesis. Nowadays, inorganic UC NPs are among the most promising candidates as luminescent bioprobes for biomedical applications, including in optical biodetection and bioimaging (see section 2.2.2), being one of the greater worldwide research topic in this field.

As referred above, nanomaterials frequently present different physical properties from the ones observed in its bulk counterparts [4,20]. In the particular case of luminescence, the decrease of the materials particle size to a nanometric scale can strongly modify their luminescence properties. A concrete and well-known example is the high energy shift of the band edge emission in semiconductors QDs, when the particle size is reduced bellow a critical value (the exciton Bohr radius) due to quantum confinement effects. In such case, a three dimensional spatial confinement of the electron and hole carriers arises in the CB and VB, respectively, breaking the translational symmetry. This leads to size-dependent discrete electronic energy levels in a similar way to the atomic systems with enhanced band to band transition probabilities due to an higher overlap of the electron and hole wavefunctions.

In the particular case of Ln^{3+}-doped nanophosphors, no quantum confinement effect is expected to the intra-4f transitions, due to the localized nature of the electronic states of the lanthanide ions [29]. However, the high surface to volume ratio, structural disorder and surface defects in NPs play an important role in the luminescence dynamic of these materials, as well as the local environment in which the Ln^{3+} is inserted in the matrix [20,34]. Luminescence quantum efficiency, radiative lifetimes, nonradiative relaxation or excitation energy transfer processes in Ln^{3+}-phosphors have been reported to be dependent on

particle size [20]. A proper understand of the size effects in the luminescence properties of Ln^{3+}-doped nanomaterials is essential for the use of efficient nanophosphors in the aforementioned applications [34].

2.2 Applications of Ln^{3+} phosphors

Ln^{3+} doped inorganic hosts constitute a class of luminescence materials with an important role in photonics. Since the early applications of luminescent Ln ions in lighting at the end of 19th century, followed by the discovery of the efficient red emitting Y_2O_3:Eu^{3+} phosphors in the beginning of 20th century, the discovery of YAG:Nd^{3+} laser in 1964 and the use of Er^{3+} doped optical fibres for telecommunications in 1987, the number of applications of luminescent materials based on Ln^{3+} increased significantly [22,35]. Today, luminescent Ln^{3+}-doped inorganic materials in the form of bulk crystals, glasses, films, powders or NPs are used in daily applications from lighting and displays, lasers, optical amplifiers and waveguides for optical telecommunications, photovoltaics, sensors, luminescent coatings, security ink, night vision, guiding systems, counterfeiting tags, and others, by making use of both downshifting and upconversion luminescence of these ions (Figure 2.9) [35]. In addition, Ln^{3+}-doped phosphors show a high potential as bioprobes for high sensitive bioassays. An increasing research is this field has been observed in the last decade.
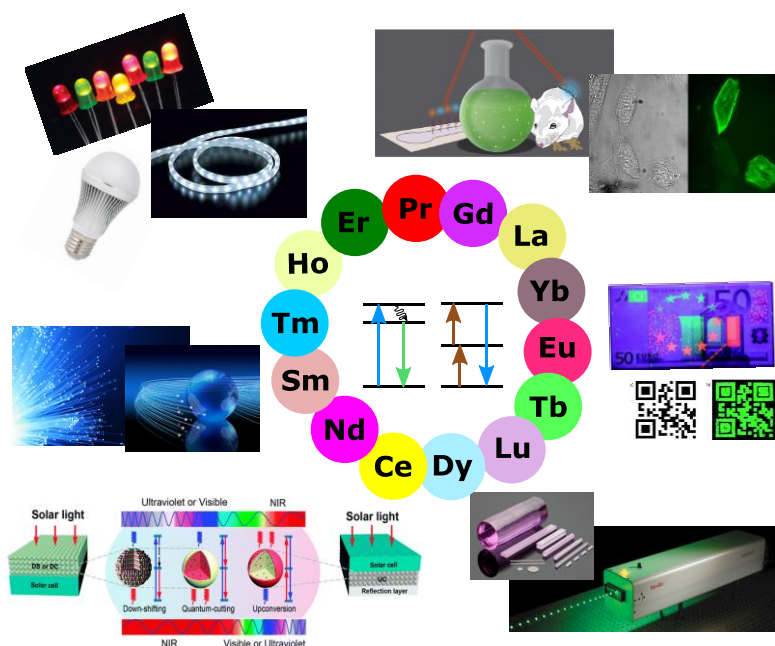
Figure 2.9. Some examples of the applications of Ln^{3+}-doped luminescent materials.

2.2.1 Lighting applications

One of the most important and explored applications of Ln^{3+}-doped phosphors is in lighting technologies. Artificial light sources are indispensable in our daily life, not only for lighting purposes when illumination by natural sun light is not possible, but also for other aspects including health and security. Over the years, a great effort has been applied in the development of light sources with high efficiencies that can contribute for the decrease in global electric energy consumption, which constitutes a huge challenge faced by our society [36]. Ln^{3+}-doped phosphors strongly contributed for the development of more efficient lighting sources, firstly in fluorescent lamps and more recently in LEDs [36].

White light based on the emissions of Ln^{3+} was firstly achieved in the fluorescent lamps, where a mixture of phosphor powders, with emission at different wavelengths in the visible spectrum, is deposited in the inner wall of the lamp glass. The phosphor layer converts the UV light, generated by electric discharge of the gas inside the tube (mercury in the case of typical compact fluorescent lamps) into visible radiation (Figure 2.10 a). The emission spectrum of mercury is non-continuous being characterized by several narrow emission bands, wherein one of the strongest emissions occurs in the UV spectral region at 254 nm (Figure 2.10 b). Phosphors usually used in fluorescent lamps efficiently absorb this light. This type of light technology, emerged as efficient alternative to the incandescent lamps that are now almost completely removed from the market due to its very low efficiency [36]. However, the used mercury gas is very toxic, therefore their use in fluorescent lamps represents an environmental and public health problem [12]. Moreover, an additional problem assigned to this type of lamps, is the possible emission of UV radiation, mostly if the phosphors do not absorb all the UV excitation, which can be dangerous for our eyes and skin.
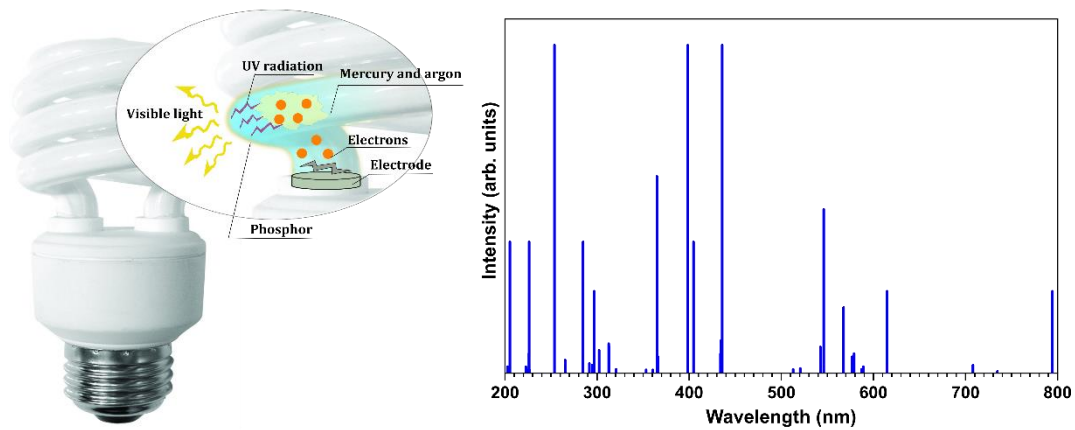
Figure 2.10. Photo of a fluorescent compact lamp and schematically representation of the process of white light generation on this type of lighting technology (left) (adapted from [37]). Discrete emission spectrum of a mercury gas discharge (right) [38].

Recently, LEDs emerged as an alternative lighting technology already in use in our daily life. This technology is now under fast progress and is considered the light technology of future [39,40]. Solid state light technology, which is based in electroluminescence, results from the high development in semiconductors field in the middle of 20th century. In a LED, the light is emitted as result of electron-hole recombination at the semiconductor p-n junction when a forward bias is applied. Under this bias condition, electrons flow into the p-type part of the junction while holes flow into the n-type, allowing the electron-hole recombination process in the depletion zone (Figure 2.11 a). Typically, the emitted radiation of a LED is characterized by a narrow bandwidth (few dozens of nanometres) and the emission wavelength is dependent of the semiconductor materials used in the device [41]. Single and multiple quantum wells (QW) based on thin films of gallium nitride (GaN) and their alloys, namely the InGaN (which constitutes the LED active layer), are nowadays the most used materials for the production of visible LED.

Over the years, the development of LED technology was marked by several important contributions. One of the most important was given by Isamu Akasaki, Hiroshi Amano, and Shuji Nakamura, between 1980s and 1990s, who solved the problem related with the p-type doping in GaN allowing the further developments for the production of efficient blue LEDs [42]. After that, an exponential progress in solid state light technology occurred and still persists. The achievements of the mentioned researchers were crucial to the actual state of the art in lighting technologies and their work was worldwide recognized through their nomination and award to the Nobel Prize in Physics in 2014. Currently LEDs with different shapes and characteristics are available on the market and found different lighting applications, ranging from backlight units for liquid crystal displays (LCD), general outdoor

and indoor illumination, automobile lighting or even for illumination of special places such as museums [41,43,44]. Figure 2.11 b) shows a representation of a typical LED and Figure 2.11 c) shows a photograph of several LEDs emitting different light colours and a photo of a white LED strip.
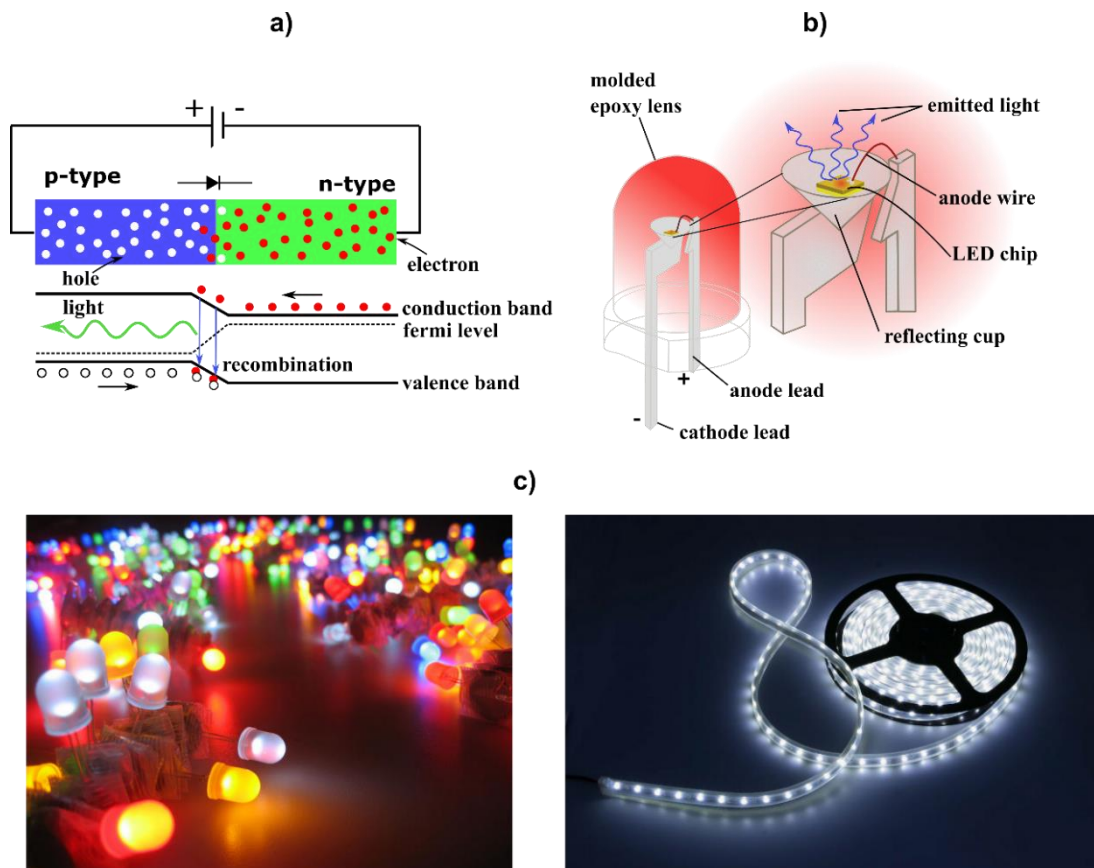
Figure 2.11. a) The p-n junction in a diode (adapted from [45]). b) Schematic representation of a LED (adapted from [46]). c) Photography of LEDs emitting different light colours (left) and white LEDs strip (right) [47].

As each semiconductor material in a LED chip emits light in a narrow region of the visible electromagnetic spectrum, the most used approach to the generation of the perceived white light in LEDs is based on strategies that involve the combination of different colours. The first strategy considers the combination of multiple LED chips emitting at different wavelengths in a single device, frequently in the blue, green and red and so denominated a RGB LED (Figure 2.12. a). Other possible strategy, is the use of a phosphor or mixture of phosphors emitting in different wavelengths, on the top of a LED chip (Figure 2.12. b). The light emitted by the LED chip can be totally or partially absorbed by the phosphor(s) and converted into light with a higher wavelength (downconversion). The combination of the light colours emitted by the LED chip and the phosphor(s), is perceived as white light. These type of white-LEDs are called phosphor converted LED (pc-LEDs). The third approach is a

combination between the first and second ones, in which a combination between the emissions from a LED chip and a pc-LEDs is used to produce white light (Figure 2.12.c) [48,49].

The evolution of lighting technologies from the incandescent lamps to fluorescent lamps and more recently to LEDs constituted a major breakthrough to decrease the global electrical energy consumption. In an incandescent lamp only around 10% of the emitted radiation is in the visible range and 90% of electric energy is loss as heat [50]. In contrast, phosphors used in LEDs and fluorescent lamps emit predominantly in the visible range and high luminance efficiency can be achieved in these light technologies. In addition, LEDs bulbs are characterized by much longer lifetimes. In Table 2.3 the characteristics of a conventional halogen incandescent lamp, a compact fluorescent lamp and a white LED bulb, used in domestic illumination are compared. The information was obtained from the data sheet specifications of three commercial products from OSRAM GmbH [51]. White LEDs show a combination of characteristics, including high brightness, long durability, good colour rendition, low power consumption, mercury-free composition and easy manufacturability, which make them very attractive over other white light sources [43].
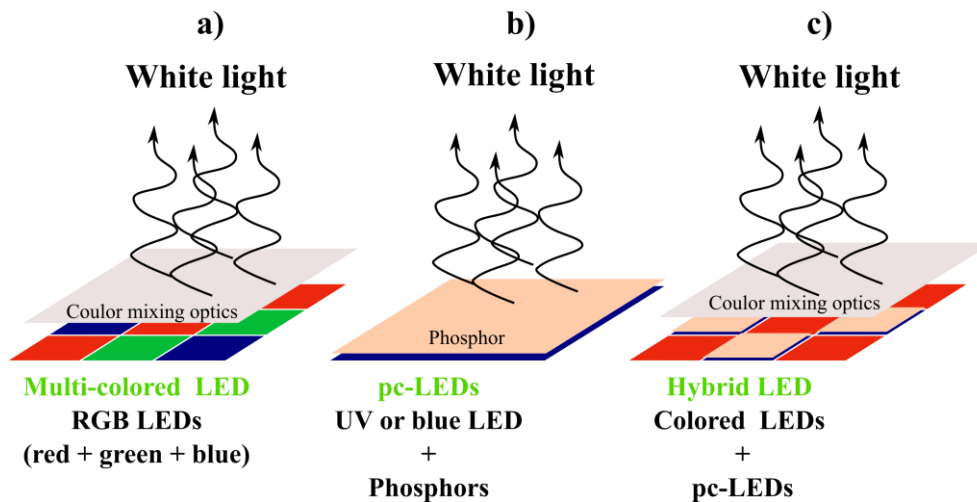
Figure 2.12. Different approaches to achieve white light using LEDs (adapted from [48]).

The white light generated by a light source is mainly characterized by its chromaticity coordinates, colour correlated temperature (CCT), colour rendering index (CRI) and luminous efficiency. The chromaticity coordinates (x,y) are defined based on the Commission Internationale de l'Eclairage (CIE) system, which is the most common method to describe the composition of any colour in terms of tristimulus values (X,Y,Z) [49]. In the CIE system any colour is characterized by a luminance parameter Y and two colour coordinates

(x, y), which locate the emission colour in the chromaticity diagram. In this diagram the perfect white light has CIE coordinates (0.33, 0.33) [45].

The CCT of a light source is defined as the absolute temperature at which a blackbody radiator (such as the tungsten filament of an incandescent lamps) should be operated in order to have a chromaticity equal to that of the test light source [49]. The blackbody radiation consists in a continuum emission spectrum that can cover all the visible range. As is well known, the increase of the temperature in a blackbody radiator induces a shift of the maximum of the emission for higher energies. As such, as the temperature of a blackbody radiator is raised from 2000 K to 10000 K, the emitted white light moves from reddish (warm) to bluish (cold) [52]. In the same way, a luminescent light source (fluorescent lamp or white LEDs) can produce a cold or warm white light depending on the intensity ratio between the blue and yellow/red emission components. In fluorescent lamps and white pc-LEDs, the used phosphor(s) strongly define the CCT of the light source [52]. Therefore, the choice of an appropriated combination of phosphors emitting in different parts of visible electromagnetic spectrum allows to manipulate the colour temperature of the white light, according with the envisaged applications and in order to create the desirable atmospheres.

Other important parameter of a light source is its colour rendering index. The CRI expresses the ability of a light source in reproduce the colours of an object in the same way as they are seen under an ideal white light source, such as the sun light [52]. The CRI of a white-light source is determined by comparing the deviation in the reflection spectra of eight standard coloured reference samples illuminated first with an ideal white light source and then with the tested white light source. Both the reference and the test light sources should have the same CCT. Due to its continuum emissions spectra, the colour of any object can be well reproduced when irradiated with sunlight or an incandescent lamp. As such, the CRI has a maximum value of 100 for this type of light sources. Since the emission spectrum of the combination of phosphors used in fluorescent lamps and white pc-LEDs, is hardly a continuous spectrum in all the visible range, the CRI value of these light sources are lower than 100 [49]. As it will be further explored, the CRI of a pc-LEDs can be improved by the use of a mixture of phosphors that emits in a wide range of wavelengths in the visible spectrum.

Table 2.3. Comparison of the characteristics of three commercial white light lamps used in domestic illumination (halogen incandescent bulb, fluorescent compact bulb and a white-LED bulb) with the same CCT [51].

Features	Incandescent	Fluorescent	LEDs
Wattage	20 W	11 W	5 W
Luminous flux	235 lm	600 lm	470 lm
Luminous efficacy	12 lm/W	55 lm/W	94 lm/W
CCT	2700 K	2700 K	2700 K
Light colour designation	Warm white	Warm white	Warm white
CRI	100	≥ 80	≥ 80
Starting time	0.0 s	< 0.3 s	≤ 0.5 s
Warm-up time	0.0 s	< 40.0 s	≤ 1.0 s
Lamp lifetime	2 000 h	6 000 h	15 000 h
Nº of switching cycles	50 000	6 000	10 000
Lamp mercury content	0 mg	0.9 mg	0.0 mg
Energy efficiency class	D	A	A+
Energy consumption	20 kWh/1000 h	11 kWh/1000 h	5 kWh/1000 h

2.2.1.1 White phosphor converted LEDs

In principle, the best strategy to produce white light in LEDs is by the combination of RGB LEDs chips, since the energy conversion of the light emitted by an LED through a pc-LED consists in an energy loss mechanism due to the Stokes shift [45]. However, the low efficiency of green and yellow LEDs chips limits the high efficiency of a multi-chip white-LEDs. Moreover, even though the CCT of a multi chip-LED can be tuned by varying the power of each individual component, such requires additional costs and complexity. This type of white LEDs are also characterized by a low CRI due to the narrow emission bands of each component. In addition, the different response of each individual chip of the RGB LED to variations in voltage and temperature, together with their differential aging can lead to a low stability of the white colour [45,53]. As such, white pc-LEDs are nowadays considered best alternatives for the white light generation. Nowadays, through a proper LEDs design, luminous efficacy as high as 150 lumens/W operated at 1 W can be reached in pc-LEDs [39]. Even so, some limitations are also associated to this type of white LEDs, which includes the non-tuneable emission and absorption, inflexibility of form (since the phosphors need to be placed in the emission path of the LED chip), and the necessity to guide the light emitted by the phosphor in the desired direction. In addition, the high reflectivity of the powder

phosphors can induce significant reflected light back-toward the LED chip. Such causes a significant increase in the temperature of the chip and a demand for complex and rigorous heat dissipation designs [45].

White light can be generated in pc-LEDs using different combinations of LED chip and phosphor emissions. Next it will be discussed the most usual approaches explored to produce white light in a pc-LED. The most popular approach consists in a blue LED chip (440-470 nm [45]) covered with a yellow phosphor layer. Part of blue light that is emitted by the LED chip (usually with a InGaN active layer) is absorbed by the phosphor layer and converted into yellow light. The phosphor layer must be semi-transparent to the blue light emitted by the LED chip. For that, the phosphor layer thickness and density should be carefully selected [45]. The combination of blue and yellow complementary emissions colours is perceived as white light to our eyes. A typical yellow phosphor used in this kind of LEDs is the yttrium aluminium garnet doped with trivalent cerium (YAG:Ce^{3+}) [12,45,49]. Figure 2.13 a) presents a schematic representation and a typical emission spectrum of such pc-LEDs. Due to the intense emission in the blue region, these pc-LEDs are characterized by a cool-white light, with high CCT (CT > 4000 K). Moreover, this type of solid state light sources present a low CRI (< 80%), since only the yellow and blue colours of objects are properly reproduced when exposed to such source of light [45]. Even so, these are currently the most produced white LEDs, since it is the most inexpensive and simple approach to produce solid state white light and due to the high efficiency of the blue LEDs and the YAG:Ce phosphors currently available in the market. Therefore, these LEDs are used as white light sources in a wide range of applications, that does not require high CRI, including traffic lights, cycle lights, car headlights, outdoor lighting, flashlights and marking lamps in tunnels [12]. However, sophisticated applications, as indoor lighting, require white light with excellent CRI. Moreover a warm-white light, with a lower CCT, is desired to create a comfortable atmosphere.

Warm white light can be achieved in pc-LEDs if the emission in the red spectral region is enhanced. A second approach to generate white light in a pc-LED consists in a LED emitting blue light covered with two phosphors emitting in the red and green/yellow regions (Figure 2.13. b). Due to the higher emission in the red region, comparatively to blue LED covered with a yellow phosphor, this has lower CCT, a warmer white light and a higher CRI. However, comparatively to the white LED constituted by the blue chip and yellow phosphor, these LEDs are characterized by a low luminous efficacy [45].
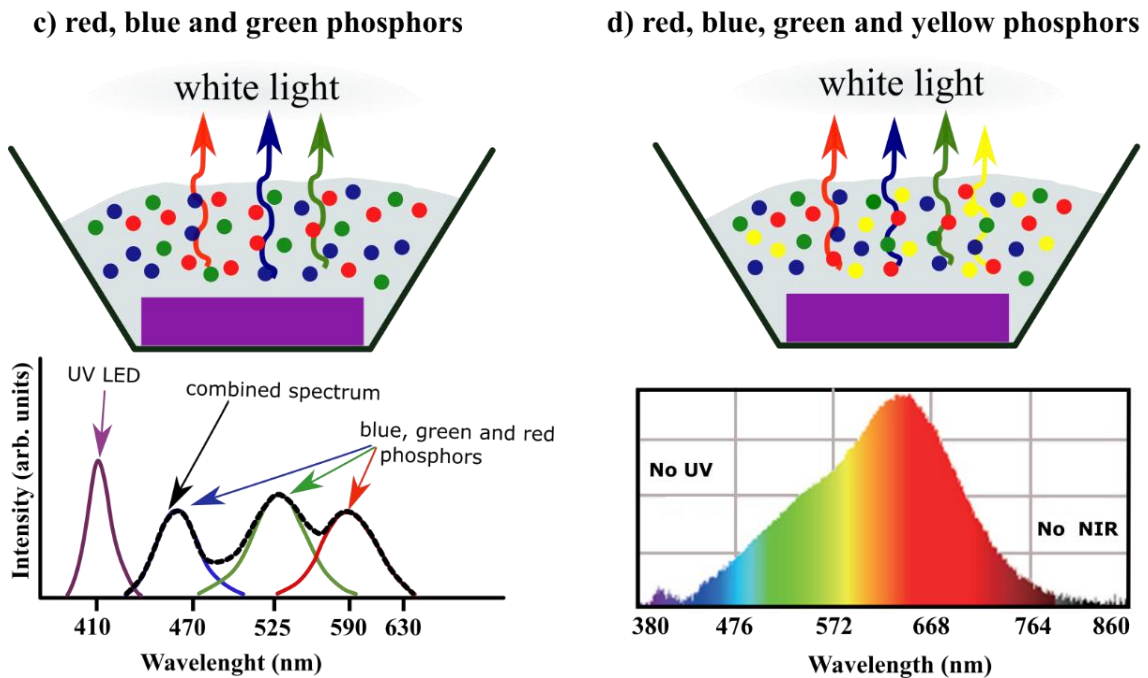
34
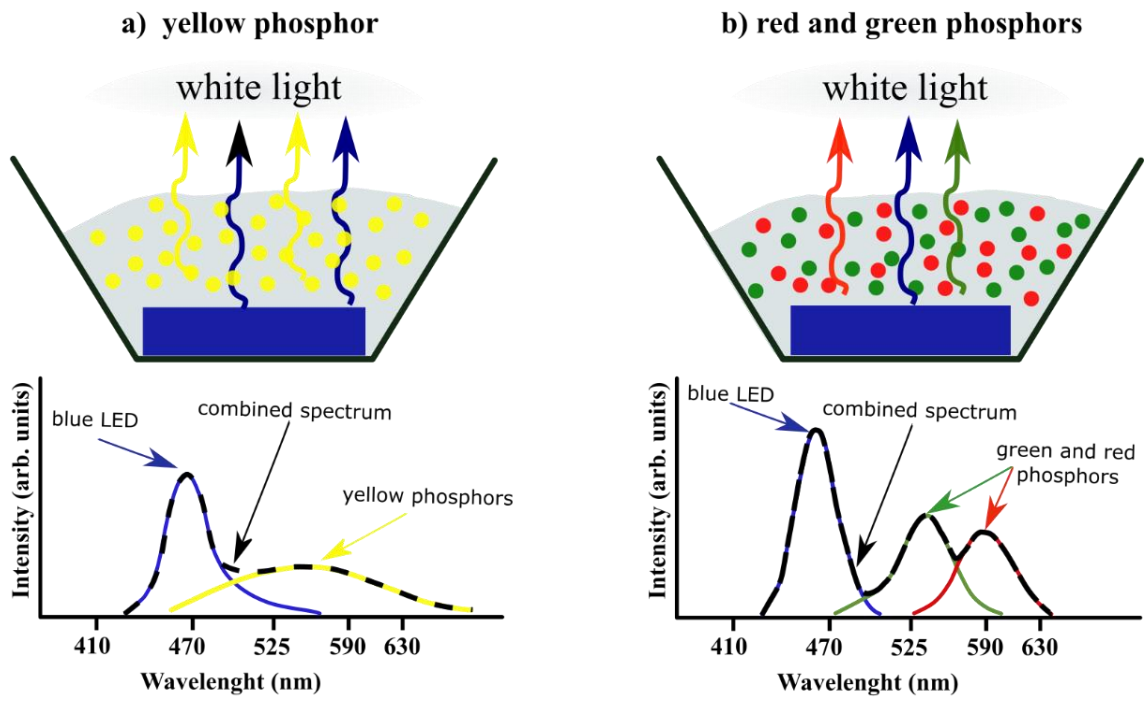
Figure 2.13. Different strategies to produce white light in pc-LEDs (adapted from [49,54]) .

Other possibility is the use of a UV LED chip (350-410 nm [45]) combined with RGB phosphors. In this case, the white light is produced by the combination of blue, green and red light emitted by three phosphors that are excited by the UV radiation of the LED chip [45].

The emission of the LED chip does not contribute to the white light and, as a result, higher colour stability can be achieved since changes in the UV emission wavelength will not affect the colour output of the pc-LEDs. This type of LEDs can be advantageous if both the efficiency of the UV LEDs chip, as well as efficiency of the energy conversion in the phosphor, overpass the efficiency of the blue LEDs. Nevertheless, the use of multiple phosphors can reduce the efficiency of the LEDs if the emission of one phosphor is reabsorbed by the other ones, which consist in an energy loss mechanism [45].

Besides the approaches mentioned above, other combinations of LEDs chips and phosphors have been studied in order to obtain white light with higher CRI value and luminous efficacy and desirable CCT. One example is the white pc-LED registered and produced by ALLIX Company with the name XENOLED™ 400 [54]. This pc-LED uses a combination of RGB phosphors plus a yellow one to convert the light from a monochromatic near-UV LED (399-400 nm) into visible light (Figure 2.13 d). The idea is to broad the emission spectrum along all visible range in order to obtain a more continuum spectrum. White light with CRI between 90-99 % and wide range of CCT, between 2700 and 6700 K, can be produced using this approach. These pc-LEDs can be used as light sources for biological and medical applications such as stereomicroscope, endoscope, medical examination rooms, production line of pharmaceutical factory, and museum applications including art gallery shops, art drawing rooms and any other application which needs enhanced spectrum characteristics with ultra-high CRI [54].

Phosphors used in a pc-LED should fulfil several requirements in order to produce efficient white light with appropriated colour characteristics according with the envisaged applications [41]. A first request to have into consideration in the selection of a phosphor is its luminescence features, including the emission and excitation spectrum. On the other hand, intrinsic properties of the phosphor such as the emission quantum efficiency, the phosphor absorption cross section at the same wavelength range as the light emitted by the LED chip (blue and near UV) and the thermal stability of the luminescence will determine the phosphor performance [41]. At least part of this light should be absorbed by the phosphors, which is valid in the case of blue LEDs. In the case of UV LEDs, all the emitted light must be absorbed. It is also advantageous if the material absorption spectra correspond to wide absorption bands rather than narrow lines in order to compensate small variations on the emission wavelengths of the LED chips. In addition, emission saturation for high excitation powers is also undesirable since it will contribute for the decrease in the quantum efficiency. This phenomenon is especially important in the case of phosphors with high absorption strength and relatively large decay time. As such, the absence of saturation

requires an appropriated balance between the two characteristics. During the working time of a LED, the phosphor layer can easily reach temperatures above 150 ^{0}C. Whereby phosphors with stable luminescence, which do not suffer thermal quenching in this range of temperature, are mandatory. Phosphors with high thermal stability of the luminescence at higher temperatures with a lumen maintenance higher than 90% of its value at room temperature are usually required [41]. To meet this requirement, refractory and high melting temperature phosphor host materials should be selected [41]. The phosphors should also present a high chemical, photo and thermal stability. During the working time, the phosphor material is subjected to high levels of radiation and temperature variations. Taking into account the long projected lifetimes of a LEDs that can reach 100000 hours, it is important that the phosphor material present a long term stability and does not deteriorate during this time in order to ensure the colour stability. Furthermore, the usage of inexpensive materials is also an important requirement that should be taken into account as it will reduce the overall production cost of the pc-LED and enabling further implementation of solid state lighting. In addition, environmentally benign composition should be selected. Materials that contain toxic elements in its composition should be ruled out [41]. Some of the current phosphors used in pc-LEDs are indicated in Table 2.4.

Table 2.4. Some phosphors used in pc-LEDs.

Phosphor	Emission colour	Ref	Phosphor	Emission colour	Ref
YAG:Ce^{3+}	Yellow	[55]	Na_2SnF_6:Mn^{4+}	Red	[56]
$BaMgAl_{10}O_{17}$:Eu^{2+}	Blue	[14]	Cs_2SnF_6:Mn^{4+}	Red	[56]
$(Ce,Gd)MgB_5O_{10}$:Tb^{3+}	Green	[14]	Na_2SiF_6:Mn^{4+}	Red	[57]
Y_2O_2S:Eu^{3+}	Red	[14]	Na_2GeF_6:Mn^{4+}	Red	[57]
K_2SiF_6:Mn^{4+}	Red	[58]	β-sialon:Pr^{3+}	Red	[59]
$CaAlSiN_3$:Eu^{3+}	Red	[60]	β-sialon:Ce^{3+}	Green	[61]
$Br_2Si_5N_8$:Eu^{3+}	Red	[62,63]	$SrSi_2N_2O_2$:Eu^{2+}	Green	[64]
Ca-α–sialon:Eu^{2+}	Yellow	[65,66]	K_2TiF_6:Mn^{4+}	Red	[58]
$La_3Si_6N_{11}$:Ce^{3+}	Yellow	[67]	$Sr_3Y_2(BO_3)_4$:Dy^{3+}	Yellow/white	[49]

Phosphors used in pc-LEDs are frequently applied in the form of powders. These powders have been produced by different synthesis techniques including solid state reaction, sol-gel, solution combustion synthesis and many others [49]. The simplicity, cost effectiveness and time saving characteristics of the SCS combined with the possibility to produce powders in large scale, results in an attractive and effective technique to produce phosphors for pc-LEDs [68–70]. The SCS technique was used in this thesis to produce zirconia based phosphors powders as will be discussed in the Chapter 6.

Nowadays a number of pc-LEDs products are available on the market with different package designs. The efficiency, durability and colour homogeneity of white pc-LED are strongly determined by the features of the used phosphor, including their optical properties, grain size, morphology, density, among other properties, as well as by the way how these powders are applied in the top of LED chip [50,71]. Usually, phosphors are placed on the top of the LED chip using two different configurations: proximity or contact layer and a remote layer. In the contact layer configuration, the phosphor particles are in direct contact with the LEDs chip. In this configuration, the phosphors can be either randomly dispersed or conformably dispersed in the LED chip surface. Figure 2.14 shows some of the configurations explored to apply phosphors in the LED chips [72].
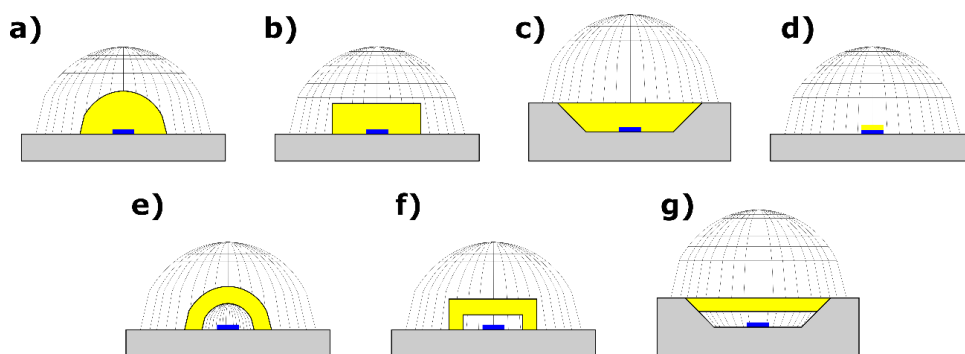
Figure 2.14. Examples of approaches studied for the application of the phosphor layer (represented in yellow) on the top of LEDs chip (represented in blue), placed in the substrate (grey component): a)-d) different contact layer configurations; e)-g) different remote layer configurations (adapted from [72]).

A contact layer with phosphor particles randomly dispersed is, in a simple way, prepared by mixing phosphors powders with a transparent encapsulating resin (usually epoxy resin or silicon, depending on the LED power). The mixture is then dump on the top of a LED chip and baked to harden encapsulates [71]. This type of approach has been widely used in mass production since, beyond its simplicity, it offers high conversion efficiency. However, the resulting phosphor layer thickness is usually inhomogeneous relatively to the surface of the LEDs that can lead to problems in angle colour uniformity. A strong research has been dedicated to the increase of light extraction and improvement of colour homogeneity in white pc-LEDs by the development of new designs for the phosphor layer. The use of conformal phosphor coating, in which a phosphor layer with uniform thickness is applied on the top surface and sidewalk of the LED chip, revealed to improve the colour uniformity. An additional problem of the use of contact layer is the high percentage of light that is directed backward and reabsorbed by the chip or the package, leading to a reduction in the device

efficiency and contributing to the heating of the LED chip. The application of a remote, which means non-contact phosphor layer, demonstrated to increase the light extraction and colour uniformity [71].

The use of LEDs in lighting applications, including general illumination, automotive illumination, or in backside illumination in LCDs, requires the combination of multiples white LEDs to achieve the required lumen intensity. Regarding the general illumination, and as mentioned above, several bulbs with different designs are now commercially available. Figure 2.15 a) and b) shows a photo of a typical white pc-LEDs lamp constituted by 24 LEDs chips and a schematic illustration with the indication of their constituents, respectively.
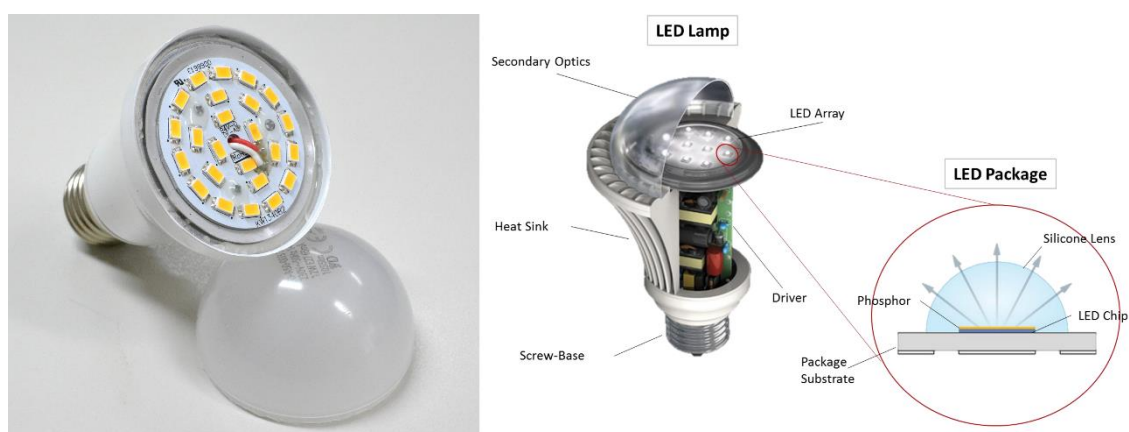
Figure 2.15. Photo of a common white LED lamp (left). Schematic representation of a pc-LED lamp and their constituents (right) (adapted from [73]).

Even if until nowadays very interesting results were already achieved in field of solid state light technology, with the currently available phosphors allowing the production of pc-LEDs with luminous efficacy exceeding that of fluorescent lamps, there is still a long way to go in order to fully realizing the expected potential benefits of LED lighting technology [41,74]. The colour performance, light output, luminous efficacy, reliability, cost, lifetime, and manufacturability are pc-LEDs characteristics that need be further improved in order to achieve an attractive value in the marketplace [41]. The enhancement of many of these characteristics is strictly dependent on the performance and availability of phosphors, which leads to a continuum research for phosphor materials with outstanding characteristics for pc-LEDs. Zirconia, as it will explored in the next chapter, shows a set of physical and chemical properties that foster it as an effective host for the incorporation of Ln ions to be used as phosphors in pc-LEDs [75]. On the other hand, simple, fast and low cost techniques are required for large scale phosphor production. As already mentioned, SCS,

which can fulfil these requirements, is a powerful technique to produce high quality phosphors.

2.2.2 Bioapplications: biodetection, bioimaging and therapy

The rapid advance in nanoscience and nanotechnology strongly contributed to the exploration of simple, cheap and more sensitive analytical biological techniques through the use of luminescent nano-bioprobes. Particularly, Ln^{3+}-doped inorganic NPs are seen of huge importance for several bioapplications [20]. These NPs constitute an interesting alternative to the conventional materials used nowadays as luminescent bioprobes for sensitive biodetection, high-contrast bioimaging, as well as effective treatment of diseases like cancer [76]. Conventional bioprobes, which includes organic dyes, lanthanide chelates and semiconductor QDs show a set of drawbacks which limit their use as bioprobes. In particular, organic dyes, besides their poor photostability, show broad absorption and emission bands that limit the use of different coloured dyes to monitor different biological processes at the same time (multiplexing) [18,29]. On the other hand, lanthanide chelates, have as a major disadvantage, low photostability and low resistance to photobleaching. As already stated, semiconductor QDs have high photostability and enhanced optical characteristics, however, the use of UV light as QDs excitation results in a strong limitation to their applicability in live cells. By one side, UV light can causes deoxyribonucleic acid (DNA) damage and cell death and, on the other hand, induce significant auto-fluorescence from the biological tissues, resulting in a high background signal. In addition, UV light has limited penetration depth on the biological organisms limiting the use of QDs for *in vivo* bioimaging [29]. Moreover, some semiconductor QDs as the ones with Cd element in their composition, show long-term toxicity [18,32].

In contrast to these materials, luminescent Ln^{3+}-doped inorganic NPs (mainly based on fluorides and oxide hosts) have higher chemical stability, excellent photostability, high resistance to photobleaching and low toxicity [76,77]. Additionally, as aforesaid, these materials show superior optical characteristics, such as the narrow intra-4f lines, large Stokes and/or anti-Stokes shifts, long-lived luminescence and emission colour that can be tuned by the change of lanthanide ion and its concentration, as well as the proper selection of host lattice [77,78]. Such characteristics are advantageous for the envisaged bioapplications [79]. The characteristic long lifetimes (μs-ms range) of the intra-4f emission of Ln^{3+} ions can be used to avoid the background noise from the auto-fluorescence of biological tissues by applying time resolved photoluminescence (TR-PL) measurements. As it will be discussed, the use of TR-PL assays leads to an increase of the signal-to-noise ratio and consequently in

a higher sensitivity of the assay. In particular, upconversion luminescent Ln^{3+}-doped inorganic NPs emerged recently as a very promising class of bioprobes for biodetection, bioimaging, therapeutics and diagnostics (theranostics) [32,80,81]. The use of NIR radiation as excitation source of UC luminescence in nano-bioprobes constitutes a strong advantage over UV or visible excitation [22,29,32,33]. In comparison with UV light excitation, NIR light excitation, with wavelength within the biological optical window (from 650 to 1000 nm), is less absorbed by the biological medium. As such, NIR light induces weak auto-fluorescence of the biological tissues promoting a better signal-to-noise ratio and consequently an improved sensitivity of the assay. Moreover, NIR light can penetrate tissues more deeply than light with lower wavelength which is beneficial for the *in vivo* applications [18]. In addition, the photodamage induced by NIR light irradiation is negligible [76,82]. Due to the negligible background signal together with the large wavelength separation between the excitation and emission, there is no need for time-resolved detection. In addition, the possibility to excite simultaneously UC NPs emitting different visible colours, by using the same NIR excitation laser, allows a simultaneous detection of multiple analytes [83]. All these advantages make the UC NPs highly promising for *in vitro* and *in vivo* bioapplications, resulting in a worldwide search for UC NPs with enhanced characteristics.

In order to be used in bioapplications the Ln^{3+}-doped inorganic luminescent NPs should fulfil a set of characteristics. First, the NPs must exhibit intense luminescence, biocompatibility and low toxicity and have a good colloid stability in water and biological solutions [18,20]. In addition, NPs with small size and narrow size distribution which can be easily functionalized with specific functional groups for posterior conjugation with biomolecules, are also required [20,29].

Several synthesis techniques have been explored in order to prepare luminescent Ln-doped inorganic NPs with controlled crystalline phase, shape and size. Within the synthesis methods available for the preparation of NPs, wet chemical approach revealed to be more appropriated for the production of inorganic NPs for bioapplications. Several chemical methods, including thermal decomposition [84], high temperature co-precipitation, hydro(solvo)thermal, sol-gel, combustion synthesis, cation exchange, and other techniques, have been used in the production of Ln^{3+}-doped inorganic nano-bioprobes [18,29]. In particular, since stable liquid suspension of NPs is required for the most of bioapplications, chemical synthesis methods that lead to the production of stable colloidal suspensions are preferred [85].

Typically, in the majority of these chemical synthesis processes, capping ligands with hydrophobic nature are used during the process to control crystal growth, leading to NPs with hydrophobic surface. These as-synthesised NPs, which are not soluble in water or in biological solutions, cannot be directly applied in bioapplications in which hydrophilicity is a prerequisite [20]. Additionally, the surface of as-synthesised NPs is free of biocompatible groups that are required for further bioconjugation. As such, before the use of these luminescent NPs in any one of these applications, steps of surface modification and bioconjugation need to be usually performed [20].

Surface modification and functionalization of hydrophobic NPs allows on one hand, the production of water soluble NPs, and on the other hand provides reactive groups (e.g. carboxylic acids, amines, etc.) on NPs surface, that are necessary for further bioconjugation with specific biomolecules including peptides, proteins or DNA [20,32,76,79]. Several strategies for the modification and functionalization of the surface of luminescence NPs have been developed and extensively applied [20,32,76,79]. These include ligand exchange, ligand oxidation, ligand-free synthesis, ligand attraction, electrostatic layer-by-layer assembly or surface silanization strategies (Figure 2.16). Additional information about each one of these surface modification strategies can be found in the works of Chen and DaCosta [20,32]. Within these strategies, ligand exchange is the most frequently applied. In this approach the NPs shape, morphology or composition are unaffected during the process. The original capping ligand linked to NPs surface is replaced by a bifunctional organic molecule or polymer. One of the functional groups of the new ligand should bind to the NPs surface while the other functional group, in the other end of the molecule, needs to be hydrophobic and appropriate for further conjugation with specific capture biomolecules or analytes molecules [20].

It should be referred that, in some cases, surface modification of NPs leads to a decrease in the emission intensity of NPs due to the presence of some functional groups with high vibrational frequencies, such as OH and NH_2. Additionally, surface modification steps are complicated and time consuming. As such, high efforts have been applied in the developing of one-step processes for production of monodisperse, water-soluble, surface-functionalized, and biocompatible Ln^{3+}-doped luminescent NPs. Some chemical synthesis methods, including hydrothermal microemulsion synthesis [86,87] or one-pot hydrothermal synthesis assisted by hydrophilic and/or binary cooperative ligands [88–98], have been successfully used for the production of water soluble and functionalized luminescent NPs.
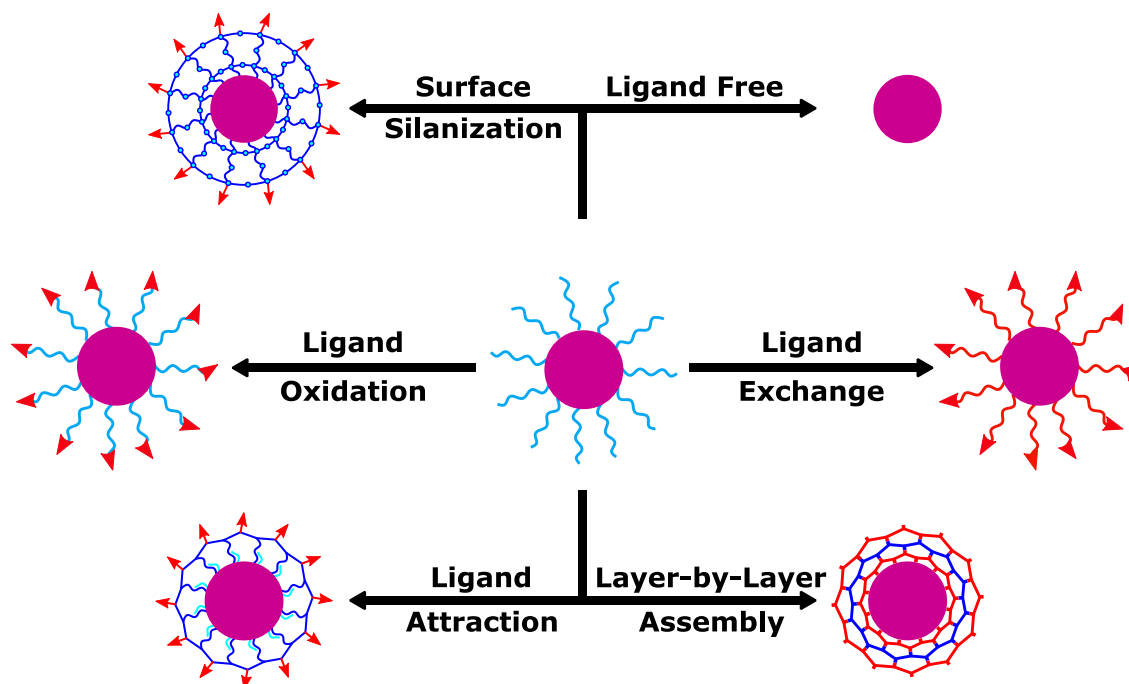
Figure 2.16. Different strategies for NPs surface modification (adapted from [20]).

2.2.2.1 Ln³⁺-doped inorganic nanoprobes for biodetection

Regarding the biodetection using luminescent Ln^{3+}-doped nanoprobes for *in vitro* biological analysis and clinical diagnosis different assay protocols have been proposed and explored. In general, these protocols can be divided in two categories according to signal detection format: the heterogeneous PL and homogeneous PL assays [18,20,76]. Both these types of assays involve the attachment of biomolecules on the NPs surface for probing target molecules (analytes) through highly specific binding affinity between biological molecules, such as an antigen and an antibody [76].

Heterogeneous PL consists in high sensitivity assay methods that has been highly explored for biological and clinical analyses [18]. In heterogeneous PL assays trace amounts of a target analyte are detected by taking the advantage of the specific recognition and high binding affinity between the analyte and a capture molecule anchored to a solid substrate. Two different types of heterogeneous assays have been proposed: the sandwich-type assay and the competitive assay, which differ in the way how the analyte is connected to the bioprobes and consequently in the way how it is quantified. The procedure used in these two types of assays is schematically represented in Figure 2.17.

Figure 2.17. Schematic representation of two types of heterogeneous assays based on Ln³⁺-doped nanoprobes: a) sandwich assay, and b) competitive assay (adapted from [33,79]).
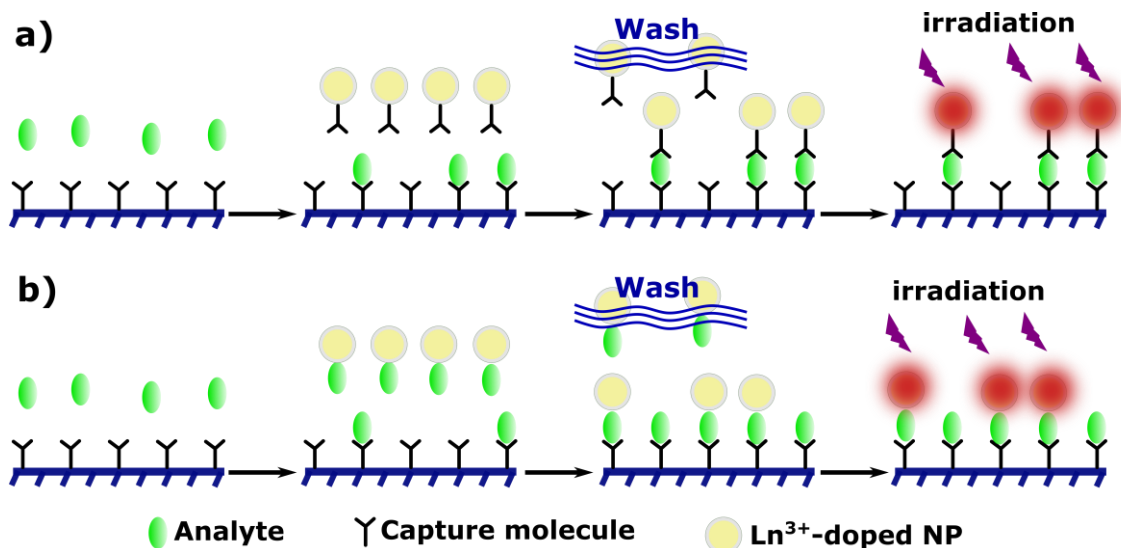
In the sandwich-like assay (Figure 2.17 a), capture molecules previously immobilized in a solid substrate by incubation, are conjugated with the analyte solution. In order to prevent negative effects from other biological species the sample is washed. After, a solution containing NPs-labelled/capture molecules is added in order to mark the analyte. The analyte is then captured between the molecules immobilized in the substrate and labelled to the NPs. Further separation and washing steps are needed to remove the excess of unbounded NPs-labelled/capture molecules before the PL measurement [18,76]. The analyte concentration can be quantified by the direct measurement of NPs luminescence, since this is directly proportional to the analyte concentration. In the case of heterogeneous competitive assays (Figure 2.17 b), instead of the addition of a solution of NPs-labelled/capture molecules, it is added a solution of NPs-labelled/analyte. The NPs-labelled/analyte will compete with the free analyte to bind to the capture molecules in the substrate. In this case the measured luminescence intensity of NPs varies inversely with the analyte concentration [20].

Heterogeneous PL assay based on both downshifting and upconversion luminescence have been explored for biomolecules detection. Conventional DS luminescence based heterogeneous assays were explored for the detection of several biomolecules using different types of inorganic bioprobes [20,79]. However, in this assay UV light is used as excitation source. As stated before, the use of UV light in bioassays constitutes a limitation since it induces light scattering and auto-fluorescence of cells and biological tissues. The recent development of assay methods based on DS time-resolved PL measurements, called heterogeneous TR-PL bioassay (Figure 2.18 a), contributed to the minimization of the

44

negative effects associated with UV light excitation. Since the lifetimes of Ln^{3+} transitions is much longer than those of the scattered light and the tissue auto-fluorescence (in the order of ns), a TR-PL signal free of short–lived background noise can be acquired by setting a proper delay time after the excitation pulse and proper gate time, during which the PL signal is acquired. Comparatively to the conventional DS heterogeneous assays, TR-PL heterogeneous assays offer higher detection sensitivity together with a better signal-to-noise ratio. Other effective strategy that leads to an high suppression of the background noise consists in the use of lanthanides doped NPs with upconversion luminescence that are excited by NIR light. In a UC-PL bioassay (Figure 2.18 b), as discussed above, the measured PL signal is free of background noise since the NIR light does not induce light scattering and auto-fluorescence from the biological sample.

Even if in general, heterogeneous TR-PL and UC-PL constitute high sensitive assays for biodetection, the separation and washing steps required in the processes before the PL measurement are complicated and time consuming, hampering a rapid biodetection, especially in clinical applications [18,20,76]. Moreover, this restricts this type of protocols to be used only in high-affinity binding system where the probe-analyte are not destroyed during the separation and washing steps [18].

Contrary to the heterogeneous PL assays, homogeneous PL assays can be easily performed in one step without the need of complicated and prolonged periods of time for the separation and washing steps. Homogeneous PL assays are directly performed in a biological solution and are usually based on fluorescence resonance energy transfer (FRET) mechanism [18]. FRET based assays, make use of the distance dependent energy transfer between an excited donor and a neighbour acceptor molecule to detect analyte biomolecules in a solution. The donor excitation by irradiation with a light source with appropriated energy triggers the energy transfer to the acceptor promoting this to an excited energy state. The deexcitation of the acceptor results in the emission of light. The energy transfer will, apparently, lengthen the emission lifetime of acceptor, which is intrinsically short-lived. In this system, Ln^{3+}-doped NPs act as donors and the most common used acceptor are organic dyes, however other type of materials including metallic NPs [78,82], graphene, graphene oxide or carbon NPs have been explored as acceptors in FRET assays [20]. Ln^{3+}-doped inorganic NPs are considered ideal donors for FRET assays due to its long-lived luminescence.
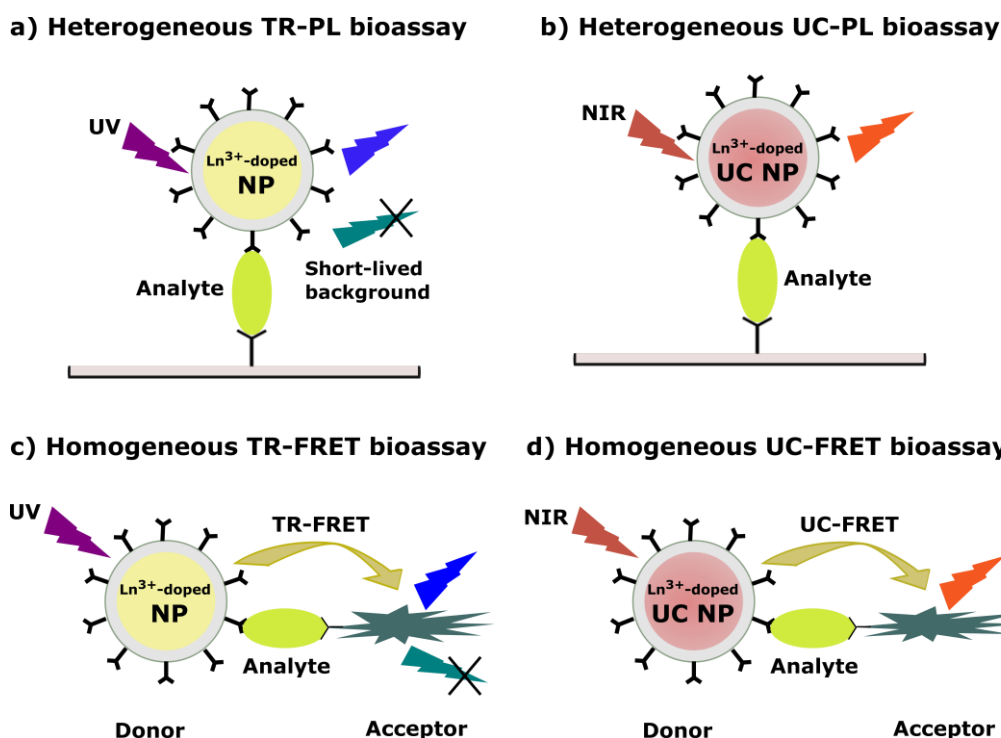
Figure 2.18. Schematic representation of different proposed detection protocols based on Ln^{3+}-doped luminescent bioprobes: heterogeneous TR-PL (a) and UC PL (b) bioassays and homogeneous TR-FRET (c) and UC-FRET (d) bioassays (adapted from [18]).

A careful selection of the pair donor-acceptor should be made in order to obtain efficient FRET detection. A spectral overlap between the absorption of the acceptor and the emission of the donor is essential. In a homogeneous FRET assay the quantification of an analyte biomolecule in a solution is performed taking into account the PL intensity of the acceptor and the PL intensity of the donor. Both donor and acceptor are labelled to capture molecules, which easily link to the specific analyte. As such, if the target analyte is present in the solution, it will bound to the capture molecule linked to the donor and capture molecules linked to the acceptor. In this case, the distance between acceptor and donor will be enough short and FRET will occurs. As a result, the emission intensity of the acceptor at the expense of the donor emission intensity it will be strictly dependent on analyte concentration, constituting an effective strategy to its quantification [77].

Recently, different FRET homogeneous assays methods based on Ln^{3+}-doped NPs have been proposed and extensively explored in the detection of biomolecules. Comparatively to heterogeneous assays, homogeneous FRET allows simple, rapid, reliable and sensitive biodetection [18]. Following the previous discussion, conventional FRET assays with steady-state detection mode, in which DS luminescent bioprobes excited with UV light are used, show limited practical applications due to the low sensitivity of PL detection imposed by the autofluorescence interference. In order to improve the detection sensitivity, novel

46

FRET assay techniques have emerged [77]. Two well explored homogeneous protocols are the TR-FRET assays and UC-FRET assays. In homogeneous TR-FRET assays, Figure 2.18 c), like in the heterogeneous TR-PL assays discussed above, the PL signal is acquired after an appropriated time delay after the pulse excitation leading to a high suppression of the short-lived background signal (see Figure 2.19 a). Homogeneous UC-FRET bioassays concept, Figure 2.18 d), was firstly validated by Kuningas et $al.$ [99]. In this work the authors used streptavidin-conjugated La_2O_2S:Yb^{3+}, Er^{3+} or Y_2O_2S:Yb^{3+}, Er^{3+} UC luminescent probes, as energy donors, for the sensitive detection of biotin by using biotinylated phycobiliprotein (bio-BPE) as acceptor. In both these protocols the background noise from the scattered light and the auto-fluorescence from biological tissues were minimized, in the first case by time resolved PL measurements and in the second one by using UC NPs that were excited with NIR light.

Both TR-FRET and UC-FRET assays have been increasingly explored in the last few years for the detection and quantification of different types of analyte biomolecules, using several Ln^{3+}-doped inorganic NPs as bioprobes. An high effort has been applied in order to decrease the limit of detection (LOD) of these analytes by using bio-conjugated luminescent nanoprobes with proper properties. Table 2.5 shows some examples of the homogeneous FRET assays based on Ln^{3+}-doped inorganic NPs reported in literature for the detection of several analytes, such as avidin [77,97,100], glucose [101], immunoglobulin G (IgG) [82], DNA [102] and others [103].

Concerning the bioprobes used in downshifted luminescence assays, including the homogeneous TR-FRET or heterogeneous TR-PL assays, different types of inorganic NPs, including fluorides and oxides doped mostly with Tb^{3+} and Eu^{3+} ions have been used [20]. The preferential choice of these two ions is related with the long lifetimes of the intra-4f emission together with the high quantum efficiency of the Tb^{3+} and Eu^{3+} luminescence in different inorganic lattices. Relatively to upconversion nanoprobes used in biodetection assays based on upconversion luminescence of Ln^{3+}-doped inorganic NPs, such as the heterogeneous UC-PL and homogeneous UC-FRET assays, co-doped NPs with Tm^{3+} or Er^{3+} and Yb^{3+} are the most explored [20]. This is explained by an intense UC emission of Tm^{3+} and Er^{3+} ions, when sensitized by Yb^{3+} ions, when excited with NIR light (~980 nm). Particularly, Er^{3+},Yb^{3+} co-doped fluoride NPs show efficient UC luminescence, which leads to a strong research of these materials as UC bioprobes. However, as aforementioned, comparatively to oxides NPs, fluorides exhibit low photo, chemical and thermal stability that in some cases can be limitative for practical applications [17].
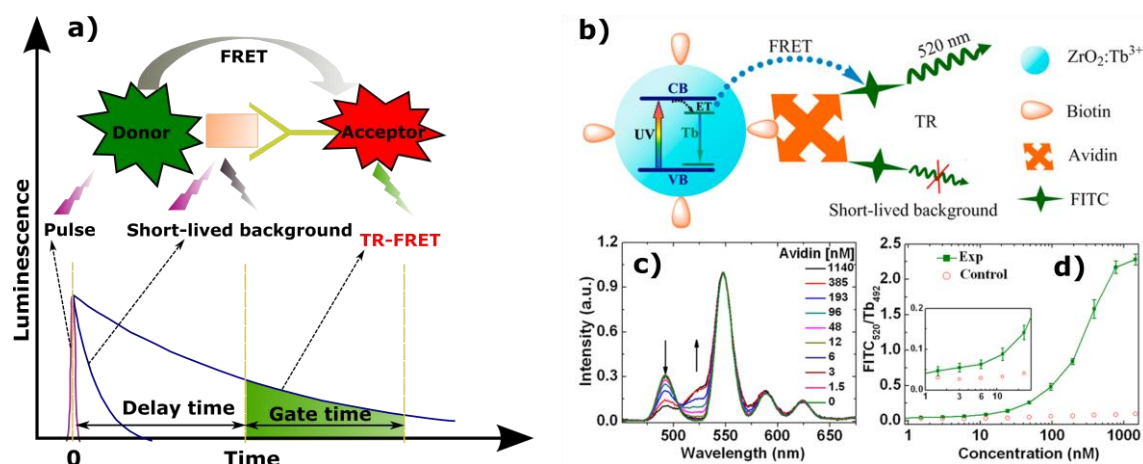
Figure 2.19. a) and b) Schematic illustration showing the principle of TR-FRET detection of avidin by employing biotinylated ZrO$_2$:Tb^{3+} NPs as donor and FITC-labelled avidin as acceptor. c) TR-FRET spectra of the bioassays as a function of avidin concentration. All the spectra were normalized to unity at the maximum emission peaked at 547 nm corresponding to the most intense line of the Tb^{3+} emission (^{5}D$_4$→^{7}F$_5$ transition), and each data point represents average of triplicate measurements. (d) Calibration curve of TR-FRET detection for the integrated PL intensity ratio FITC (520 nm)/Tb (492 nm) versus avidin concentration [100].

Regarding the application of Ln^{3+}-doped zirconia luminescence nanoprobes in biodetection, the work reported in literature is very limited. Nevertheless, in a recent published work, Y. Liu and co-workers [100] reported interesting and promising results that validate the use of Ln^{3+}-doped zirconia NPs in biodetection. In that work, amine-functionalized Tb^{3+} doped zirconia NPs (size < 5 nm) were conjugated with biotin molecules for avidin detection by using a TR-FRET bioassays. Tb^{3+} NPs were used as energy donors, while FITC dyes were used as energy acceptors in FRET (Figure 2.19 b, c and d). A limit of detection of avidin molecules of 3 nM was achieved by using the zirconia bioprobes in the FRET assay. In addition, the same amine-functionalized NPs, when bioconjugated with amino-terminal fragment (ATF), exhibit a high specific recognition of uPAR (urokinase-type plasminogen activator receptor), highly expressed on the membrane of many types of cancer cells such as human lung cancer. These results show the high potential of these zirconia NPs for targeted bioimaging and biodetection applications.

Table 2.5. Some examples of homogeneous FRET assays reported in literature using various bioprobes for the detection of different analyte.

Bioprobe	Size (nm)	Assay type	Analyte	LOD	Refs.
$YVO_4:Eu^{3+}$	20	Sandwich DS-PL	IgG*	0.01 g/mL	[92]
$LaF_3:Ce^{3+},Tb^{3+}$	15-20	FRET	Glucose	~0.5 mM	[101]
$CaF_2:Ce^{3+},Tb^{3+}$	~5	TR-FRET	Avidin/SuPAR	0.164/0.328 nM	[103]
$ZrO_2:Tb^{3+}$	< 5	TR-FRET	Avidin	3 nM	[100]
$NaYF_4:Ce^{3+},Tb^{3+}$	20-40	TR-FRET	Avidin	4.8 nM	[77]
$KGdF_4:Tb^{3+}$	20-30	TR-FRET	Avidin	5.5 nM	[97]
$NaYF_4:Yb^{3+},Er^{3+}$	14	UC-FRET	DNA	~10 nM	[102]
$Na(Y_{1.5}Na_{0.5})F_6:Er^{3+},Yb^{3+}$	50	UC-FRET	Avidin	~0.5 nM	[78]
$NaYF_4:Er^{3+},Yb^{3+}$	30-70	UC-FRET	IgG*	~5nM	[82]

*IgG- immunoglobulin G antibody

2.2.2.2 Ln³⁺-doped nanoprobes in bioimaging and therapy

Luminescent bioimaging is a powerful non-invasive strategy to visualize morphological details in biological tissues. Ln³⁺-doped inorganic NPs also play an important role in this field of biomedicine and appeared recently as ideal candidates for optical imaging due to their particular optical characteristics referred above. In the particular case of *in vivo* applications, the use of an inorganic host for the incorporation of Ln ions is special beneficial since its rigid crystalline structure decrease the chance of release of toxic ions.

Both downshifted and UC luminescent Ln³⁺-doped inorganic NPs have been explored as potential bioprobes for bioimaging [104]. However, as happens in the case of biodetection, bioimaging using the DS luminescence of NPs with efficient absorption in the UV spectral range, results in a high background signal due to the auto-fluorescence of biological tissues. TR luminescence imaging, UC luminescence imaging, NIR-NIR luminescence imaging and persistent luminescent imaging emerged as new alternative techniques to the conventional DS luminescence bioimaging, in which better signal-to-noise ratio can be achieved [20].

Time resolved luminescence imaging was firstly demonstrated in 1990 by Beverloo [105], using $Y_2O_2S:Eu^{3+}$ luminescent probes conjugated with proteins. Since then TR-PL imaging has been explored using different Ln³⁺-doped NPs. As in the case described in the previous subsection, higher sensitivity is achieved due to the minimization of the short lived background. Additionally, as exposed before, the use of UV light as excitation should be ruled out for bioimaging. Therefore, in order to overpass the stated limitations, alternative

bioimaging modes, including persistent luminescence and UC luminescence (including NIR-to-NIR UC) bioimaging have been explored [20].

Persistent luminescence is an interesting phenomenon in which the long-lasting emission of the material persists for a long time (from several minutes to several hours) after the removal of the excitation source, the so called afterglow [106–108]. Ln-doped inorganic NP with persistent luminescence are very promising bioprobes for bioimaging. Even if UV light is used for excitation, in persistent luminescence bioimaging the negative effects caused by the use of this radiation are avoided since the bioprobes luminescence can be excited before their injection in the biological organism. Several Ln-doped inorganic probes have been studied for this proposes, including $Ca_2Si_5N_8:Eu^{2+},Tm^{3+}$ [106], $Ca_{1.86}Mg_{0.14}ZnSi_2O_7:Eu^{2+},Dy^{3+}$ [109], $SrMgSi_2O_{16}:Eu^{2+},Dy^{3+}$ [110], and $CaMgSi_2O_6:Mn^{2+},Eu^{2+},Pr^{3+}$ [111] (see Table 2.6). In particular, persistent luminescent materials with emission in the biological spectral window (red/NIR region) are of special interest for bioimaging [107,108]. Despite its high potential, the practical use of this type of bioprobes in clinical application is uncommon, which could be related with the need of high temperature synthesis methods for the preparation of these materials that make difficult to obtain small sized NPs [20]. The pulsed laser ablation in liquid techniques, studied in this work, can be an effective alternative to the high temperature synthesis routes for the production of inorganic NPs with persistent luminescence and small particle size, as already confirmed by Maldiney and co-workers [106].
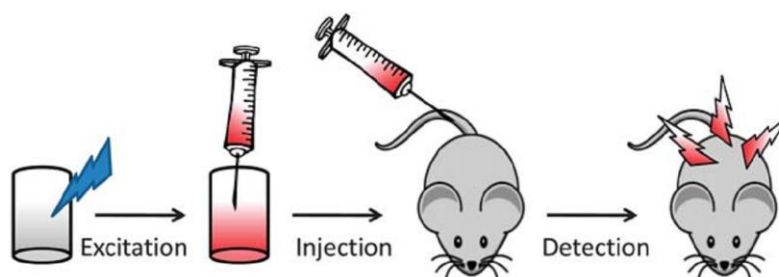
Figure 2.20. a) Schematic illustration of *in vivo* bioimaging experiments based on persistent luminescence NPs (adapted from [35]).

Ln^{3+}-doped inorganic NPs with UC luminescence show also a high potential for bioimaging. The use of NIR light excitation constitutes a great advantage over UV or visible excitation for *in vivo* applications [20]. As stated, reduced damage of cells and tissues, minimization of short-lived background signal and improved penetration deep can be achieved using the NIR light excitation. Furthermore, UC NPs are not sensitive to photobleaching simplifying long-time PL microscopy [20]. UC luminescence bioimaging was firstly reported in 1999 by

Zijlmans and co-workers [112] in the system $Y_2O_3S:Yb^{3+},Tm^{3+}$, using as excitation 980 nm wavelength photons. Since then, other inorganic hosts have been employed including oxysulphides, oxides and fluorides (Table 2.6). For such purposes, the inorganic hosts are frequently co-doped with distinct lanthanide ions (e.g. Er^{3+}, Tm^{3+} and Ho^{3+}) with the Yb^{3+} as a common sensitizer [84,113,114].

Other interesting inorganic bioprobes for bioimaging are the ones in which both the excitation and emission light occurs in the NIR region, within the optical transmission biological window. Visible light emitted by the bioprobes can be absorbed by the biological sample resulting in a low detection signal [20]. In NIR-to–NIR luminescence imaging, since both excitation and emission are in the NIR range, the light absorbed by the biological sample is minimized leading to high contrast PL imaging in *in vitro* and *in vivo* assays [20]. For this propose, Tm^{3+} ions are frequently selected due to the intense NIR intraionic transitions occurring between 750-850 nm under 980 nm wavelength laser excitation [20,84]. An example of high contrast NIR-to-NIR bioimaging of pancreatic cancer cells by using $NaYF_4:Tm^{3+},Yb^{3+}$ nanoprobes is shown in Figure 2.21 [84].

Single band emission of UC NPs, preferentially with emission maximum shifted to the red spectral regions revealed to be more efficient for optical imaging than the ones with multiband luminescence. Usually, single band emission in the red spectral regions can be detected at higher depth than multiband emission, for example than multiple green and red emissions of Er^{3+} in the some crystalline hosts [20]. Moreover, the emission colour of UC NPs with multiple emission bands can change with image depth due to different attenuation levels of the different colour by the biological organisms [20]. Therefore, the development of UC NPs with single band emission in the red/NIR spectral region can be very important for efficient bioimaging applications.
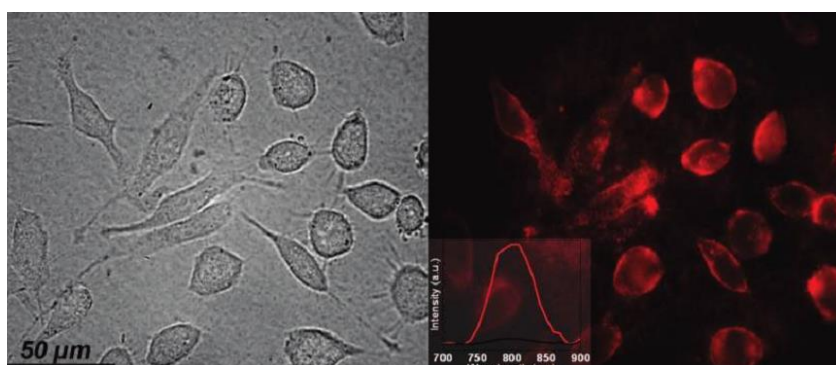

Figure 2.21. *In vitro* transmission (left) and PL (right) images of human pancreatic cancer cells obtained with $NaYF_4:Tm^{3+},Yb^{3+}$ NPs with NIR emission, following excitation at 975 nm. Inset shows localized PL spectra taken from cells (red) and background (black) (adapted from [84]).

In addition to the single modal bioprobes applications discussed above, Ln^{3+}-doped inorganic NPs have been also indicated as a promising new class of multi-modal bioprobes. Multimodal bioprobes combines two or more functionalities in one single particle that can be used at the same time to get more information in clinic diagnostics. For example, it is expected that Ln^{3+}-doped optical/magnetic multi-modal probes can be guided, through the application of an external magnetic field, into a specific place in the organism, while the luminescence from Ln^{3+} can be used for real-time tracking [20]. This type of magnetically guided delivery, which combines the high sensitivity from the PL detection together with the excellent spatial resolution of magnetic resonance imaging (MRI), has a high potential for applications in bioimaging, bio-separation, target anti-cancer drug delivery, clinical theranostics [20]. Due to its high potentialities, a growing interest in the synthesis of inorganic bioprobes with both optical and magnetic properties has been observed in the last years. Multimodal bioprobes have been essentially achieved by using core-shell NPs with a magnetic core and a luminescent shell or vice-versa or by using single phase NPs doped with optically active ions, also active under the application of external magnetic fields. Core-shell NPs are mostly prepared by a layer by layer coating process and iron oxide is frequently used as a magnetic unit, while several Ln^{3+}-doped inorganic nanoparticles are used as the luminescent unit [115,116]. Multi-modal bioprobes based on single phase NPs are typically constructed using Gd^{3+} ions together with other luminescent Ln^{3+} ions. Gd^{3+} not only acts as a paramagnetic relaxation agent but also as luminescence sensitizer. Example of single phase NPs with optical and magnetic properties studied for multimodal bioprobes includes $KGdF4$: Tb^{3+} [97] $KGdF_4$: Tm^{3+},Yb^{3+} [117] and $NaGdF_4$:Er^{3+},Yb^{3+} [118] NPs.

Table 2.6. Example of Ln^{3+}-doped inorganic luminescent bioprobes used in bioimaging.

Probe	Synthesis method	Size (nm)	assay	ref
ZrO_2:Tb^{3+}	Solvothermal	< 5	DSL bioimaging	[100]
Y_2O_3S:Tm^{3+},Yb^{3+} Y_2O_3S:Er^{3+},Yb^{3+}	Superheating of precursor oxides	200-400	UCL bioimaging	[112]
$NaYF_4$: Er^{3+},Yb^{3+}	Hydrothermal microemulsion	20-40	UCL bioimaging	[86]
Y_2O_3: Er^{3+},Yb^{3+}	Homogeneous precipitation	50-250	UCL bioimaging	[119]
$NaYF_4$:Er^{3+},Yb^{3+}	--	~30	UCL bioimaging and targeted drug delivery	[120]
$NaYF_4$:Tm^{3+},Yb^{3+}	Thermal decomposition	20-30	NIR-NIR UCL bioimaging	[84]
$Ca_2Si_5N_8$:Eu^{2+},Tm^{3+}	PLAL	3-5	Persistent lum. bioimaging	[106]
$CaMgSi_2O_6$:Eu^{2+},Mg^{2+},Pr^{3+}	Sol-Gel	140	Persistent lum. bioimaging	[111]
$SrMgSi2O6$:Eu^{2+},Dy^{3+}	Template method	50-500	Persistent lum. bioimaging	[110]
$(CaMg)_2ZnSi_2O_7$:Eu^{2+},Dy^{3+}	Sol-Gel	--	Persistent lum. bioimaging	[109]

Furthermore, silica shells have been used to encapsulate luminescent Ln^{3+}-doped inorganic NPs in order to promote enhanced chemical stability and biocompatibility, easy

functionalization of NPs, and to decrease the quenching of luminescence of NPs in aqueous medium. In addition, mesoporous silica shell can be used to the loading of drugs, which is impossible to do in the rigid inorganic NPs [20,121]. For instance, magnetic and luminescent multimodal NPs coated with a mesoporous silica shell are important systems for target drug delivery. By application of a magnetic field the NPs can be guided to the site of interest, and there the drug release amount can be monitored by the change in emission intensity [20]. Furthermore, Ln[3+]-doped UC NPs coated with silica shells are very promising for photodynamic therapy [20,121]. In photodynamic therapy, a chemical photosensitizer, when activated under the light irradiation, generates short-lived toxic oxygen radicals from water that will kill cancer cells, see Figure 2.22. Since the sensitizer is usually excited with visible light, it could not be used in tissues beyond a limited depth [29]. The depth limit can be improved by using UC NPs coated with a mesoporous silica shell, where the photosensitizer can be loaded. Under NIR excitation, which has a high penetration depth in tissues, the UC NPs emits visible light that will activate the photosensitizer to the reactive oxygen species. In this experiments, UC NPs performs different functions: help to solubilize the sensitizer, convert low energy photons into higher energy photons and help to target the sensitizer to cancer cells [29].
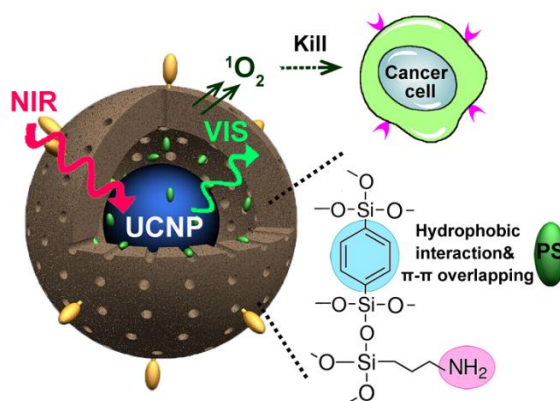
Figure 2.22. Illustration of photodynamic therapy by using UC NPs coated with mesoporous silica shell in which photosensitizers are loaded (adapted [121]).

As shown, Ln[3+]-doped inorganic NPs consist of a new class of luminescent bioprobes with a strong potential for *in vitro* and *in vivo* bioapplications. In particular, NPs with UC luminescence are of special importance. The high photo, thermal and chemical stability of Ln[3+]-doped oxide NPs, resulting from their more rigid crystalline environment and higher lattice-binding energy, together with its enhanced optical properties, makes them highly promising for bioapplications [20]. Even so, the difficulty in the preparation of water soluble,

biocompatible, oxide NPs having at the same time small size, high purity and intense emission limits their practical use. To overpass these issues, new synthesis techniques, as well as new surface modification strategies should be studied in order to achieve NPs with such requirements dispersed in biocompatible liquid media. Pulsed laser ablation in liquids, as it will be explored in Chapter 7, could consist in an alternative strategy to produce oxide NPs that fulfil these essential requirements.

References

[1]   International Year of Light, http://www.light2015.org (accessed: June 26, 2015).

[2]   M. H. V. Werts, *Sci. Prog.* **2005**, *88*, 101.

[3]   Photonics21, http://www.photonics21.org (accessed: June 26, 2015).

[4]   G. Blasse, B. C. Grabmaier, *Luminescent materials*; Springer-Verlag, Berlin, 1994.

[5]   W. M. Yen, S. Shionoya, H. Yamamoto, *Phosphor handbook*; CRC Press/Taylor and Francis, 2007.

[6]   T. J. C. Feldmann, *Adv. Funct. Mater.* **2003**, *13*, 511.

[7]   E. Germer, F. Meyer, H. J. Spanner, Metal vapor lamp (US 2182732 A) **1926**.

[8]   M. Koedam, J. J. Opstelten, *Light. Res. Technol.* **1971**, *3*, 205.

[9]   S. Nakamura, T. Mukai, M. Senoh, *Appl. Phys. Lett.* **1994**, *64*, 1687.

[10]   T. Jüstel, H. Nikol, C. Ronda, *Angew. Chem. Int. Ed.* **1998**, *37*, 3084.

[11]   J. Solé, L. Bausa, D. Jaque, *An Introduction to the Optical Spectroscopy of Inorganic Solids*; John Wiley and Sons, 2005.

[12]   H. A. Höppe, *Angew. Chem. Int. Ed.* **2009**, *48*, 3572.

[13]   B. Di Bartolo, J. Collins, In *Handbook of Applied Solid State Spectroscopy*; Vij, D. R., Ed.; Springer US, 2006; pp. 509–575.

[14]   D. P. Dutta, A. K. Tyagi, *Solid State Phenom.* **2009**, *155*, 113.

[15]   X. Huang, S. Han, W. Huang, X. Liu, *Chem. Soc. Rev.* **2012**, *42*, 173.

[16]   J. C. Krupa, M. Queffelec, *J. Alloys Compd.* **1997**, *250*, 287.

[17]   F. Gonell, M. Haro, R. S. Sánchez, P. Negro, I. Mora-Seró, J. Bisquert, B. Julián-López, S. Gimenez, *J. Phys. Chem. C* **2014**, *118*, 11279.

[18]   D. Tu, W. Zheng, Y. Liu, H. Zhu, X. Chen, *Coord. Chem. Rev.* **2014**, *273–274*, 13.

[19]   A. J. Kenyon, *Prog. Quantum Electron.* **2002**, *26*, 225.

[20]   X. Chen, Y. Liu, D. Tu, *Lanthanide-Doped Luminescent Nanomaterials: From Fundamentals to Bioapplications*; Springer Science & Business Media, 2013.

[21]   B. Walsh, In *Advances in Spectroscopy for Lasers and Sensing*; Bartolo, B.; Forte, O., Eds.; Springer Netherlands, 2006; pp. 403–433.

[22]   S. V. Eliseeva, J.-C. G. Bünzli, *Chem. Soc. Rev.* **2009**, *39*, 189.

[23]   G. Liu, B. Jacquier, *Spectroscopic Properties of Rare Earths in Optical Materials*; Springer, 2006.

[24]   G. Ehrhart, M. Bouazaoui, B. Capoen, V. Ferreiro, R. Mahiou, O. Robbe, S. Turrell, *Opt. Mater.* **2007**, *29*, 1723.

[25]   G. H. Dieke, *Spectra and Energy Levels of Rare Earth Ions in Crystals*; Interscience Publishers: New York, 1968.

[26]   M. D. Chambers, D. R. Clarke, *Annu. Rev. Mater. Res.* **2009**, *39*, 325.

[27]   B. Judd, *Phys. Rev.* **1962**, *127*, 750.

[28]   G. S. Ofelt, *J. Chem. Phys.* **1962**, *37*, 511.

[29]   D. K. Chatterjee, M. K. Gnanasammandhan, Y. Zhang, *Small* **2010**, *6*, 2781.

[30]   Q. Y. Zhang, X. Y. Huang, *Prog. Mater. Sci.* **2010**, *55*, 353.

[31]   H. Dong, L.-D. Sun, C.-H. Yan, *Chem. Soc. Rev.* **2015**, *44*, 1608.

[32]   M. V. DaCosta, S. Doughan, Y. Han, U. J. Krull, *Anal. Chim. Acta* **2014**, *832*, 1.

[33]   W. Zheng, P. Huang, D. Tu, E. Ma, H. Zhu, X. Chen, *Chem. Soc. Rev.* **2014**.

[34]   T. Anh, P. Benalloul, C. Barthou, L. thiKieu Giang, N. Vu, L. Minh, *J. Nanomater.* **2008**, *2007*, e48247.

[35]   J.-C. G. Bünzli, S. V. Eliseeva, *Chem. Sci.* **2013**, *4*, 1939.

[36]   S. Kitsinelis, *Light Sources: Technologies and Applications*; CRC Press, 2010.

[37]   Electron Configurations in the Environment-ChemPRIME, http://wiki.chemprime.chemeddl.org/index.php/Electron_Configurations_in_the_Environment (accessed: June 27, 2015).

[38]   National Institute of Standards and Technology, http://www.nist.gov/pml/data/handbook/index.cfm (accessed: October 6, 2015).

[39]   C.-C. Sun, Y. Chang, T.-H. Yang, *SPIE Newsroom* **2015**.

[40]   E. F. Schubert, J. K. Kim, *Science* **2005**, *308*, 1274.

[41]   Y. Tian, *J. Solid State Light.* **2014**, *1*, 1.

[42]   S. Nakamura, *The blue laser diode : the complete story*; 2nd updated and extended ed.; Springer: Berlin; New York, 2000.

[43]   J. H. Oh, J. R. Oh, H. K. Park, Y.-G. Sung, Y. R. Do, *Opt. Express* **2011**, *19 Suppl 3*, A270.

[44]   Z. Liu, S. Liu, K. Wang, X. Luo, *Front. Optoelectron. China* **2009**, *2*, 119.

[45]   V. K. Khanna, *Fundamentals of solid-state lighting : LEDs, OLEDs, and their applications in illumination and displays /*; CRC Press: Boca Raton, FL, 2014.

[46]   LED | electronics, http://www.britannica.com/technology/LED (accessed: September 20, 2015).

[47]   LEDs, http://www.instructables.com/id/LEDs (accessed: September 20, 2015).

[48]   T. Lougheed, *Environ. Health Perspect.* **2014**, *122*, A81.

[49]   S. Ye, F. Xiao, Y. X. Pan, Y. Y. Ma, Q. Y. Zhang, *Mater. Sci. Eng. R Rep.* **2010**, *71*, 1.

[50]   D. A. Steigerwald, J. C. Bhat, D. Collins, R. M. Fletcher, M. O. Holcomb, M. J. Ludowise, P. S. Martin, S. L. Rudaz, *IEEE J. Sel. Top. Quantum Electron.* **2002**, *8*, 310.

[51]   Light is OSRAM|OSRAM, http://www.osram.com/osram_com (accessed: October 1, 2015).

[52]   S. Pimputkar, J. S. Speck, S. P. DenBaars, S. Nakamura, *Nat. Photonics* **2009**, *3*, 180.

[53]   N. C. George, K. A. Denault, R. Seshadri, *Annu. Rev. Mater. Res.* **2013**, *43*, 481.

[54]   ALLIX - XENOLED™ Ⅱ , http://www.allixs.com (accessed: October 18, 2015).

[55]   V. Bachmann, C. Ronda, A. Meijerink, *Chem. Mater.* **2009**, *21*, 2077.

[56]   Y. Arai, S. Adachi, *J. Lumin.* **2011**, *131*, 2652.

[57]   Y. K. Xu, S. Adachi, *J. Appl. Phys.* **2009**, *105*, 013525.

[58]   A. A. Setlur, E. V. Radkov, C. S. Henderson, J.-H. Her, A. M. Srivastava, N. Karkada, M. S. Kishore, N. P. Kumar, D. Aesram, A. Deshpande, B. Kolodin, L. S. Grigorov, U. Happek, *Chem. Mater.* **2010**, *22*, 4076.

[59]   T.-C. Liu, B.-M. Cheng, S.-F. Hu, R.-S. Liu, *Chem. Mater.* **2011**, *23*, 3698.

[60]   K. Uheda, N. Hirosaki, H. Yamamoto, *Phys. Status Solidi A* **2006**, *203*, 2712.

[61]   N. Hirosaki, R.-J. Xie, K. Kimoto, T. Sekiguchi, Y. Yamamoto, T. Suehiro, M. Mitomo, *Appl. Phys. Lett.* **2005**, *86*, 211905.

[62]   Y. Q. Li, J. E. J. van Steen, J. W. H. van Krevel, G. Botty, A. C. A. Delsing, F. J. DiSalvo, G. de With, H. T. Hintzen, *J. Alloys Compd.* **2006**, *417*, 273.

[63]   H. A. Höppe, H. Lutz, P. Morys, W. Schnick, A. Seilmeier, *J. Phys. Chem. Solids* **2000**, *61*, 2001.

[64]   Y. Q. Li, A. C. A. Delsing, G. de With, H. T. Hintzen, *Chem. Mater.* **2005**, *17*, 3242.

[65]   R.-J. Xie, M. Mitomo, K. Uheda, F.-F. Xu, Y. Akimune, *J. Am. Ceram. Soc.* **2002**, *85*, 1229.

[66]   J. W. H. van Krevel, J. W. T. van Rutten, H. Mandal, H. T. Hintzen, R. Metselaar, *J. Solid State Chem.* **2002**, *165*, 19.

[67]   N. Kijima, T. Seto, N. Hirosaki, *ECS Trans.* **2009**, *25*, 247.

[68]   S. Ekambaram, K. C. Patil, M. Maaza, *J. Alloys Compd.* **2005**, *393*, 81.

[69]   P. K. Jisha, R. Naik, S. C. Prashantha, H. Nagabhushana, S. C. Sharma, H. P. Nagaswarupa, K. S. Anantharaju, B. D. Prasad, H. B. Premkumar, *J. Lumin.* **2015**, *163*, 47.

[70]   H. B. Premkumar, B. S. Ravikumar, D. V. Sunitha, H. Nagabhushana, S. C. Sharma, M. B. Savitha, S. Mohandas Bhat, B. M. Nagabhushana, R. P. S. Chakradhar, *Spectrochim. Acta. A. Mol. Biomol. Spectrosc.* **2013**, *115*, 234.

[71]   H. Rao, C. Li, Q. Zhang, C. Zhou, W. Zhang, K. Zhang, D. Zhou, Q. Lei, X. Wang, *Opt. Express* **2015**, *23*, A949.

[72] C.-C. Sun, Y.-Y. Chang, T.-H. Yang, T.-Y. Chung, C.-C. Chen, T.-X. Lee, D.-R. Li, C.-Y. Lu, Z.-Y. Ting, B. Glorieux, Y.-C. Chen, K.-Y. Lai, C.-Y. Liu, *J. Solid State Light.* **2014**, *1*, 19.

[73] How do LED light bulbs work? - Electrical Engineering Stack Exchange, http://electronics.stackexchange.com (accessed November 11, 2015).

[74] P. T. Chung, C. T. Yang, S. H. Wang, C. W. Chen, A. S. T. Chiang, C.-Y. Liu, *Mater. Chem. Phys.* **2012**, *136*, 868.

[75] F. Ramos-Brito, C. Alejo-Armenta, M. García-Hipólito, E. Camarillo, J. Hernández A, H. Murrieta S, C. Falcony, *Opt. Mater.* **2008**, *30*, 1840.

[76] H. Wen, F. Wang, In *Nanocrystalline Materials (Second Edition)*; Tjong, S.-C., Ed.; Elsevier: Oxford, 2014; pp. 121–160.

[77] D. Tu, L. Liu, Q. Ju, Y. Liu, H. Zhu, R. Li, X. Chen, *Angew. Chem. Int. Ed.* **2011**, *50*, 6306.

[78] L. Wang, R. Yan, Z. Huo, L. Wang, J. Zeng, J. Bao, X. Wang, Q. Peng, Y. Li, *Angew. Chem. Int. Ed.* **2005**, *44*, 6054.

[79] Y. Liu, D. Tu, H. Zhu, E. Ma, X. Chen, *Nanoscale* **2013**, *5*, 1369.

[80] F. Wang, D. Banerjee, Y. Liu, X. Chen, X. Liu, *Analyst* **2010**, *135*, 1839.

[81] M. Bettinelli, L. Carlos, X. Liu, *Phys. Today* **2015**, *68*, 38.

[82] M. Wang, W. Hou, C.-C. Mi, W.-X. Wang, Z.-R. Xu, H.-H. Teng, C.-B. Mao, S.-K. Xu, *Anal. Chem.* **2009**, *81*, 8783.

[83] F. Wang, W. B. Tan, Y. Zhang, X. Fan, M. Wang, *Nanotechnology* **2006**, *17*, R1.

[84] M. Nyk, R. Kumar, T. Y. Ohulchanskyy, E. J. Bergey, P. N. Prasad, *Nano Lett.* **2008**, *8*, 3834.

[85] F. Zhang, *Photon Upconversion Nanomaterials*; Springer: Ottawa, Ontario, Canada, 2015.

[86] L.-Q. Xiong, Z.-G. Chen, M.-X. Yu, F.-Y. Li, C. Liu, C.-H. Huang, *Biomaterials* **2009**, *30*, 5592.

[87] J. Zhou, X. Zhu, M. Chen, Y. Sun, F. Li, *Biomaterials* **2012**, *33*, 6201.

[88] D. K. Chatteriee, A. J. Rufalhah, Y. Zhang, *Biomaterials* **2008**, *29*, 937.

[89] J.-Q. Gu, J. Shen, L.-D. Sun, C.-H. Yan, *J. Phys. Chem. C* **2008**, *112*, 6589.

[90] F. Wang, X. Liu, *J. Am. Chem. Soc.* **2008**, *130*, 5642.

[91] M. Wang, C.-C. Mi, J.-L. Liu, X.-L. Wu, Y.-X. Zhang, W. Hou, F. Li, S.-K. Xu, *J. Alloys Compd.* **2009**, *485*, L24.

[92] J. Shen, L.-D. Sun, J.-D. Zhu, L.-H. Wei, H.-F. Sun, C.-H. Yan, *Adv. Funct. Mater.* **2010**, *20*, 3708.

[93] Q. Ju, W. Luo, Y. Liu, H. Zhu, R. Li, X. Chen, *Nanoscale* **2010**, *2*, 1208.

[94] X.-F. Yu, Z. Sun, M. Li, Y. Xiang, Q.-Q. Wang, F. Tang, Y. Wu, Z. Cao, W. Li, *Biomaterials* **2010**, *31*, 8724.

[95] Z.-L. Wang, J. Hao, H. L. W. Chan, G.-L. Law, W.-T. Wong, K.-L. Wong, M. B. Murphy, T. Su, Z. H. Zhang, S. Q. Zeng, *Nanoscale* **2011**, *3*, 2175.

[96] Q. Ju, Y. Liu, D. Tu, H. Zhu, R. Li, X. Chen, *Chem. – Eur. J.* **2011**, *17*, 8549.

[97] Q. Ju, D. Tu, Y. Liu, R. Li, H. Zhu, J. Chen, Z. Chen, M. Huang, X. Chen, *J. Am. Chem. Soc.* **2012**, *134*, 1323.

[98] G. Gao, C. Zhang, Z. Zhou, X. Zhang, J. Ma, C. Li, W. Jin, D. Cui, *Nanoscale* **2013**, *5*, 351.

[99] K. Kuningas, T. Rantanen, T. Ukonaho, T. Lövgren, T. Soukka, *Anal. Chem.* **2005**, *77*, 7348.

[100] Y. Liu, S. Zhou, D. Tu, Z. Chen, M. Huang, H. Zhu, E. Ma, X. Chen, *J. Am. Chem. Soc.* **2012**, *134*, 15083.

[101] L. Wang, Y. Li, *Chem. Weinh. Bergstr. Ger.* **2007**, *13*, 4203.

[102] Z. Chen, H. Chen, H. Hu, M. Yu, F. Li, Q. Zhang, Z. Zhou, T. Yi, C. Huang, *J. Am. Chem. Soc.* **2008**, *130*, 3023.

[103] W. Zheng, S. Zhou, Z. Chen, P. Hu, Y. Liu, D. Tu, H. Zhu, R. Li, M. Huang, X. Chen, *Angew. Chem. Int. Ed.* **2013**, *52*, 6671.

[104] Y. Zhang, W. Wei, G. K. Das, T. T. Yang Tan, *J. Photochem. Photobiol. C Photochem. Rev.* **2014**, *20*, 71.

[105]   H. B. Beverloo, A. van Schadewijk, S. van Gelderen-Boele, H. J. Tanke, *Cytometry* **1990**, *11*, 784.

[106]   T. Maldiney, G. Sraiki, B. Viana, D. Gourier, C. Richard, D. Scherman, M. Bessodes, K. Van den Eeckhout, D. Poelman, P. F. Smet, *Opt. Mater. Express* **2012**, *2*, 261.

[107]   S. K. Singh, *RSC Adv.* **2014**, *4*, 58674.

[108]   V. Caratto, F. Locardi, G. A. Costa, R. Masini, M. Fasoli, L. Panzeri, M. Martini, E. Bottinelli, E. Gianotti, I. Miletto, *ACS Appl. Mater. Interfaces* **2014**, *6*, 17346.

[109]   B.-Y. Wu, H.-F. Wang, J.-T. Chen, X.-P. Yan, *J. Am. Chem. Soc.* **2011**, *133*, 686.

[110]   L. Zhan-Jun, Z. Hong-Wu, S. Meng, S. Jiang-Shan, F. Hai-Xia, *J. Mater. Chem.* **2012**, *22*, 24713.

[111]   T. Maldiney, A. Lecointre, B. Viana, A. Bessière, M. Bessodes, D. Gourier, C. Richard, D. Scherman, *J. Am. Chem. Soc.* **2011**, *133*, 11810.

[112]   H. J. M. A. A. Zijlmans, J. Bonnet, J. Burton, K. Kardos, T. Vail, R. S. Niedbala, H. J. Tanke, *Anal. Biochem.* **1999**, *267*, 30.

[113]   J.-C. Zhou, Z.-L. Yang, W. Dong, R.-J. Tang, L.-D. Sun, C.-H. Yan, *Biomaterials* **2011**, *32*, 9059.

[114]   Q. Zhan, J. Qian, H. Liang, G. Somesfalean, D. Wang, S. He, Z. Zhang, S. Andersson-Engels, *Acs Nano* **2011**, *5*, 3744.

[115]   X. Zhu, J. Zhou, M. Chen, M. Shi, W. Feng, F. Li, *Biomaterials* **2012**, *33*, 4618.

[116]   L. Zhang, Y.-S. Wang, Y. Yang, F. Zhang, W.-F. Dong, S.-Y. Zhou, W.-H. Pei, H.-D. Chen, H.-B. Sun, *Chem. Commun.* **2012**, *48*, 11238.

[117]   H.-T. Wong, F. Vetrone, R. Naccache, H. L. W. Chan, J. Hao, J. A. Capobianco, *J. Mater. Chem.* **2011**, *21*, 16589.

[118]   Z.-L. Wang, J. H. Hao, H. L. W. Chan, *J. Mater. Chem.* **2010**, *20*, 3178.

[119]   S. F. Lim, R. Riehn, W. S. Ryu, N. Khanarian, C. Tung, D. Tank, R. H. Austin, *Nano Lett.* **2006**, *6*, 169.

[120]   C. Wang, L. Cheng, Z. Liu, *Biomaterials* **2011**, *32*, 1110.

[121]   S. Lu, D. Tu, P. Hu, J. Xu, R. Li, M. Wang, Z. Chen, M. Huang, X. Chen, *Angew. Chem. Int. Ed.* **2015**, *54*, 7915.

Chapter 3.

Zirconia overview

An overview of zirconia material properties is presented. The distinct zirconia polymorphs and the mechanisms for the stabilization at room temperature of the high temperature crystalline phases are explored. A brief revision of the ZrO_2-Y_2O_3 phase diagram is also presented.

The properties and technological applications of stabilized zirconia are also revised. At the end, the potentialities of zirconia as an effective host for the incorporation of optically active Ln ions are also explored.

Zirconia or zirconium dioxide, ZrO_2, is one of the most important technical ceramics materials used nowadays. This very versatile material offers an interesting combination of thermal, chemical, electrical, mechanical and optical properties, which are uncommon to find in ceramic materials [1]. Therefore, besides its importance as a structural material, zirconia also found several advanced applications in different areas, including in energy, thermal barrier coatings and biomaterials. However, pure zirconia, which has three different polymorphic phases (monoclinic, tetragonal and cubic with increasing temperature, respectively), at atmospheric pressure, has limited applications [2]. This is due to a destructive tetragonal to monoclinic phase transformation during the material cooling that occurs with a strong variation of dimensions resulting in the development and propagation of cracks in the bulk material [2–4]. Fortunately, the introduction of some cations in the lattice of pure zirconia allows the stabilization of the high temperature phases at RT, avoiding phase transformation during materials cooling [1,3–6]. Stabilized zirconia ceramics can show a high diversity of morphologies depending on dopant concentration and dopant nature, leading to materials with distinct properties and applications [1,7]. Moreover, it was reported that in pure zirconia the high temperature phases can be stabilized at RT as an effect of size reduction [2,8,9]. The decrease of particle size below a critical value can avoid phase transformation and the stabilization of cubic and/or tetragonal phases at RT [2,8,9].

3.1 ZrO_2 crystalline structures

Figure 3.1 a) shows the equilibrium phase diagram of the binary zirconium (Zr)-oxygen (O), at atmospheric pressure. As can be observed in the diagram, there is only one stable phase, the zirconium oxide. This oxide starts to be formed when a molar percentage of oxygen around 30% is introduced in zirconium lattice and the stoichiometric composition is achieved for a percentage of oxygen around 67%.
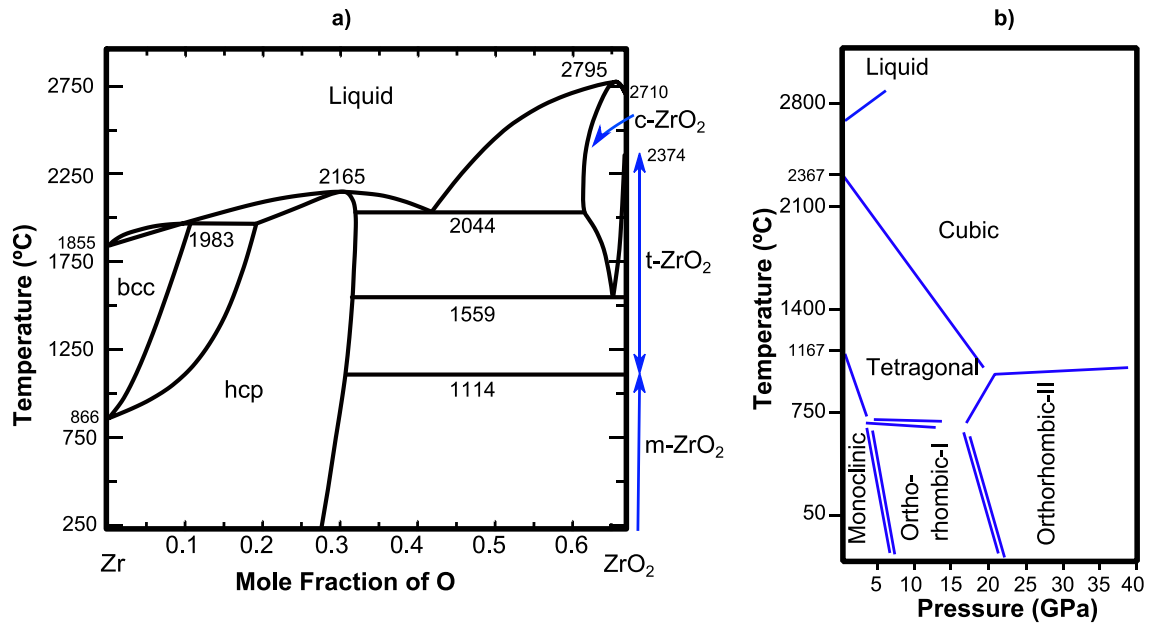
Figure 3.1. a) Equilibrium phase diagram of the binary system Zr-O at atmospheric pressure (adapted from [10]). Bcc and hcp indicate the body-centred cubic and hexagonal closest packed unit cells, respectively. b) Temperature-pressure phase diagram of pure zirconia (adapted form [5]).

At atmospheric pressure, pure zirconia has three crystalline phases, which are stable at different ranges of temperatures (see Figure 3.1). At RT, zirconia is monoclinic (m), being this the only stable polymorph at this condition. With the increase in temperature, zirconia undergoes two crystalline phase transformations. At around 1170 ⁰C the monoclinic phase is transformed into the tetragonal (t) phase, which is thermally stable until around 2370 ⁰C, from which zirconia becomes cubic (c). The cubic phase remains until the melting temperature (~2700 ⁰C) [5,4,1,3]. These phase transitions are reversible during material cooling.

The cubic phase of zirconia has a face-centred cubic fluorite-type structure, belonging to the space group *Fm3m* with a theoretical lattice parameter *a*= 5.12 Å [11]. The primitive cell, with one formula unit (Z= 1), contains one zirconium ion located at (0,0,0) coordinated (CN) to eight equidistant oxygen ions, placed at the same distances and occupying the (¼, ¼, ¼) positions on the cell [1,4,5]. A representation of the cubic face-centred arrangement is illustrated in Figure 3.2. In this structure, each zirconium ion has eightfold symmetry against the oxygen atoms, which are arranged in two ideal tetrahedra [11].
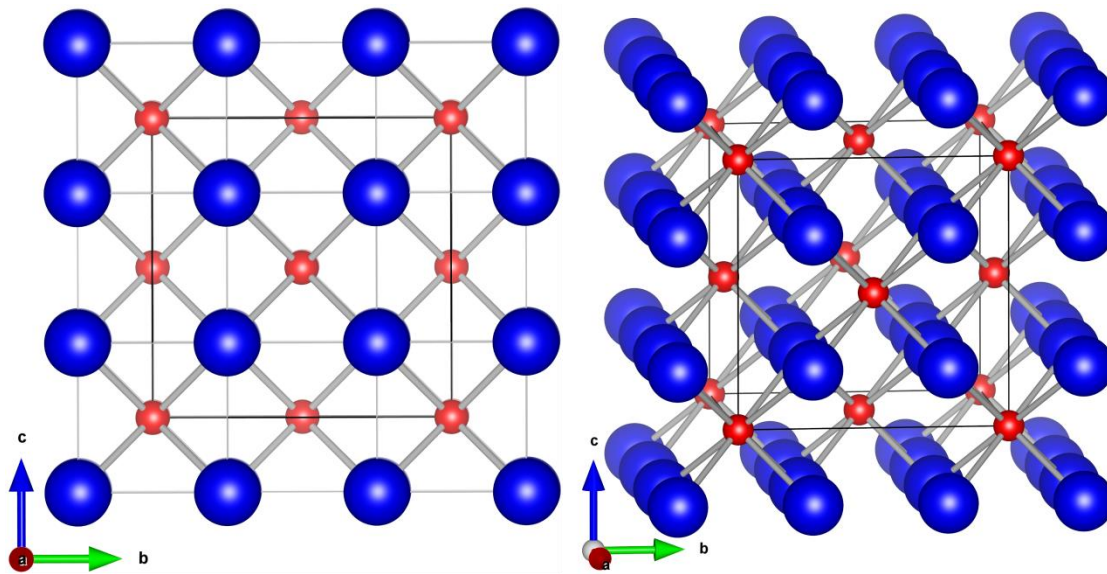
61

Figure 3.2. Cubic structure of zirconia in which Zr and O atoms are represented in red and blue, respectively (illustrated using *Vesta* software [12]).
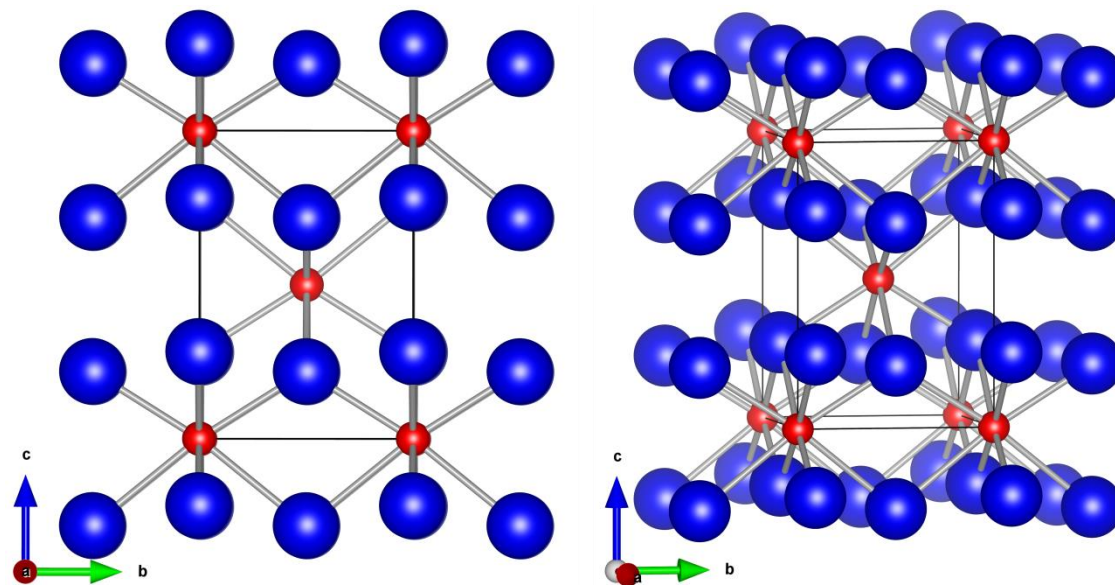

Figure 3.3. Tetragonal structure of zirconia in which Zr and O atoms are represented in red and blue, respectively (illustrated using *Vesta* software [12]).

The tetragonal zirconia phase has a slightly distorted fluorite structure designed by body centred tetragonal structure, belonging to the *P4$_2$/nmc* space group and with lattice parameters $a=b=$ 3.64 Å and $c=$ 5.27 Å, for a body centred tetragonal representation [13]. However, other lattice parameters are also commonly reported in literature for the same tetragonal zirconia phase [4,11]. The exact same structure, considering a pseudofluorite structural representation, can be described by lattice parameters: $a^*=a\cdot\sqrt{2}$, as illustrated in Figure 3.4. Comparatively to the cubic structure, the tetragonal structure presents an

elongation along one of the axis. For the cell represented in Figure 3.3 the elongation is along the *c*-axis. In this structure, the Zr atoms maintained the same eightfold coordination with the oxygens, as in the cubic structure. However, in this case, the oxygen atoms are not equidistant [1]. Four oxygen ions surround the zirconium ions in a flattened tetrahedron arrangement at a distance of 206.5 pm, while the other four oxygen ions are placed at a distance of 245.5 pm at the vertices of an elongated tetrahedron rotated against the former by 90 ^{0} [11].
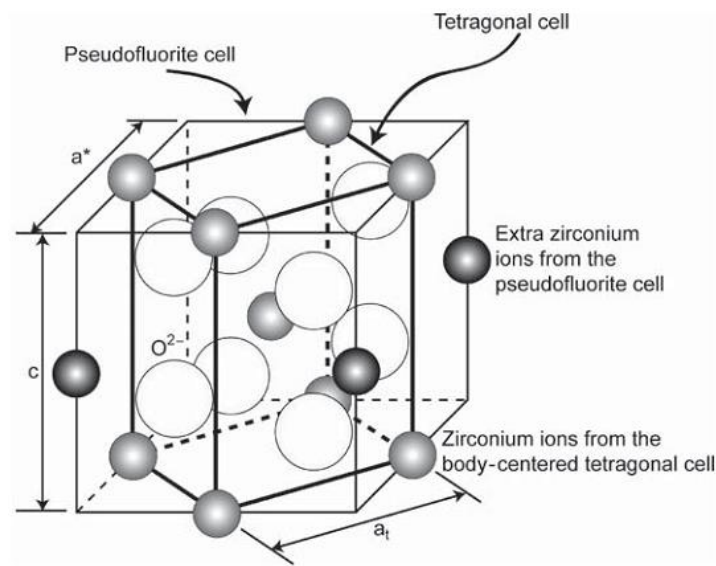
Figure 3.4. Tetragonal zirconia unit cell in both the body-centred tetragonal and pseudofluorite descriptions [5].

The monoclinic structure (Figure 3.5), belonging to the *P2$_1$/c* space group and with lattice parameters *a*= 5.16 Å, *b*= 5.19 Å, *c*= 5.30 Å and β = 98 ^{0} 9', is known as Baddeleyite, an abundant mineral present in the earth's crust [4,11]. This mineral is very stable under natural conditions and its structure could be seen as a result of a high distortion of the cubic structure. As shown in Figure 3.5 the coordination number of Zr is 7, lower than in the other two structures, and half of the oxygen anions are connected to 4 Zr cations (CN=4) while other half are connected to 3 Zr cations (CN=3) [4]. Table 3.1 summarize the structural characteristics of monoclinic, tetragonal and cubic zirconia phases.

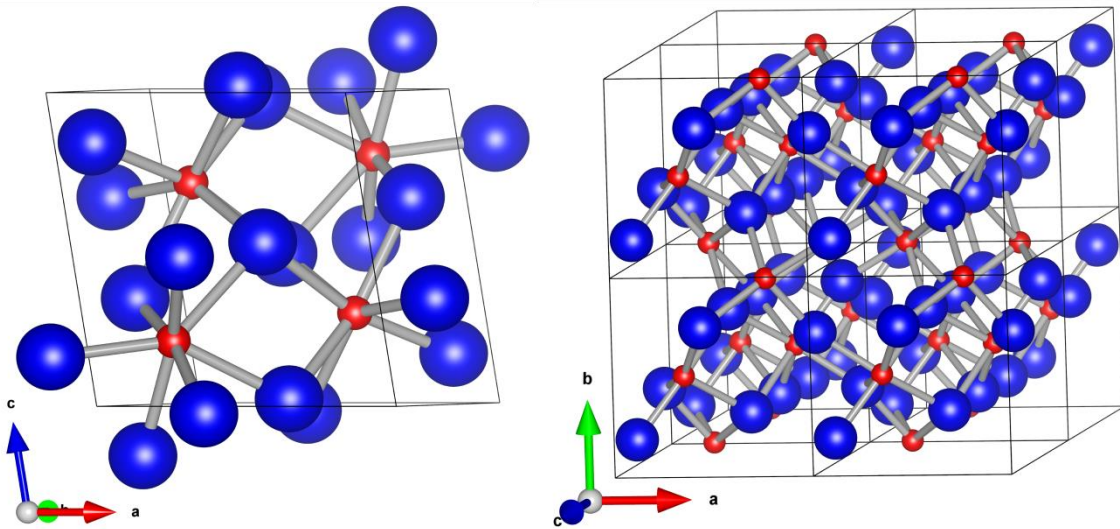**Figure 3.5. Monoclinic structure of zirconia, in which Zr and O atoms are represented in red and blue, respectively (illustrated using *Vesta* software [12]).**

Table 3.1. Summary of the structural characteristics of ZrO$_2$ phases at atmospheric pressure [11,13].

ZrO$_2$ phase	Space group	Lattice parameters				Zr coordination number	Density (Mg/m^3)
M	*P2$_1$/c*	*a*= 5.16 Å	*b*= 5.19 Å	*c*= 5.30 Å	β = 98^{0}9'	7	5.83
T	*P4$_2$/nmc*	*a=b*= 3.64 Å		*c*= 5.27 Å		8	6.10
C	*Fm3m*	*a*= 5.12 Å				8	6.09

Additionally to these three atmospheric pressure phases, other zirconia phases were reported for high pressure and temperature conditions. When subjected to high pressures, monoclinic zirconia undergoes two phase transformations to orthorhombic phases [5], as can be observed by the temperature-pressure phase diagram of pure zirconia shown in Figure 3.1 b). The first orthorhombic phase, denominated O-I, starts to appear at an applied pressure of around 3.5 GPa, depending on the crystallite size. Typically, a lower crystallite size slows the starting pressure transformation. This phase transformation is only completed for an applied pressure around 10 GPa and is stable until ~25 GPa. The O-I phase belongs to the *Pbca* space group, with a coordination number of 7 [5]. Above 25 GPa, a second orthorhombic phase, O-II, appears. This phase is stable, at RT, until an applied pressure of at least 70 GPa. The O-II phase belongs to *Pnma* space group, with Z= 4 and CN of 9 [5]. A high temperature and high pressure hexagonal phase was also reported for pure zirconia. This phase was first reported by Ohtaka *et al.* [14] after the quenching of pure zirconia powders exposed at temperatures above 1000 ^{0}C and a pressure of 20 GPa. When the pressure is released, the material returns to the monoclinic structure for a pressure below 1 GPa [5].

As mentioned above, at RT and atmospheric pressure the monoclinic phase is the only stable phase of pure zirconia. Thermodynamically, it is very difficult to retain the cubic and tetragonal phases at RT, even by a rapid thermal quenching of the structure. Since the driving force for the transformation is high (the free energy of the t-phase, G_t, is much higher than the free energy of the c-phase, G_c, and the free energy of the m-phase, G_m, is much higher than the free energy of the t-phase) these transformations occur spontaneously [1]. These crystalline phase transformations are martensitic, occurring without diffusion and involving only a cooperative shift of the ions from its starting positions. Furthermore, t ⟶ m transformation is accompanied by a significant volume expansion (t ⟶ m: ~5%) that exceeds the limit of elastic deformation of the material, leading to cracking and break of the bulk material [3]. This implies that, if a bulk pure zirconia is submitted to a temperature above the m ↔ t transformations, the material will crack during the cooling due to the drastic volume expansion. Such invalidate the use of the pure zirconia in applications where a solid intact structure is required. In fact, technological applications of pure zirconia are very limited due to its mechanical behaviour.

3.2 Stabilization of high temperature phases

The thermodynamic stability of the monoclinic structure of zirconia at RT is related with the strong covalent nature of the Zr-O bond which favours a sevenfold coordination number [2]. Due to the low ionic radius of Zr^{4+}, the distances between the oxygen ions in the zirconia lattice are small and electrostatic repulsion forces induce the distortion of dense ion package and the consequent formation of more distorted crystalline structures (monoclinic) [2]. With an increase in the temperature, the tetragonal and cubic structures of pure zirconia are stabilized due to the generation of oxygen ion vacancies in the lattice. To accommodate these thermally generated oxygen ion vacancies, the structure of zirconia changes to one having eightfold coordination. First, the tetragonal structure is stabilized in the temperature range from 1170 to 2370 ^{0}C, for which the concentration of oxygen ion vacancies is low. For high temperatures (> 2370 ^{0}C), the concentration of oxygen ion vacancies increases and the cubic phase is stabilized [2]. It is also reported that the tetragonal and cubic structures can be stabilized at low temperature in atmospheres of low oxygen partial pressure. Once again the stabilization is associated with the generation of oxygen ion vacancies in zirconia lattice. However, either during material cooling or when it is exposed to air, reversible monoclinic phase transformation occurs due to the diffusion of surrounding oxygen into the zirconia lattice [2,15].

The high potential for RT applications of the high temperatures phases of zirconia and the impossibility to produce intact dense products of pure zirconia promoted an intense search for solutions to stabilize the tetragonal and cubic phases of zirconia at RT and under atmospheric pressure. Nowadays, it is well known that the two high temperature phases of zirconia can be successfully stabilized at RT and atmospheric pressure by different stabilization processes. However, there is still no full agreement about the mechanics behind these stabilization processes [2].

The most common process used in the stabilization of tetragonal and cubic phases of zirconia at RT is based in the doping of pure zirconia with some aliovalent cations or, in some cases, with cations with the same valence as the Zr^{4+}, called stabilizers. The stabilizer cations, that can have lower, the same or even higher valence than Zr ions, will replace some of the Zr^{4+} ions in the zirconia lattice. The replacement of Zr^{4+} by cations with lower valence, usually trivalent cations, results in the generation of oxygen ion vacancies due to charge balance. As happens in high temperature condition, depending on the oxygen ion vacancies concentration, which can be controlled by the dopant amount, both tetragonal and cubic phases can be stabilized at RT by this mechanism [2]. Typical oxides used in the stabilization of the high temperature phases by this process include Y_2O_3, CaO, MgO, Ga_2O_3 and Gd_2O_3. Figure 3.6 shows a schematic representation of the cubic stabilized zirconia structure obtained by doping pure cubic zirconia with yttria.
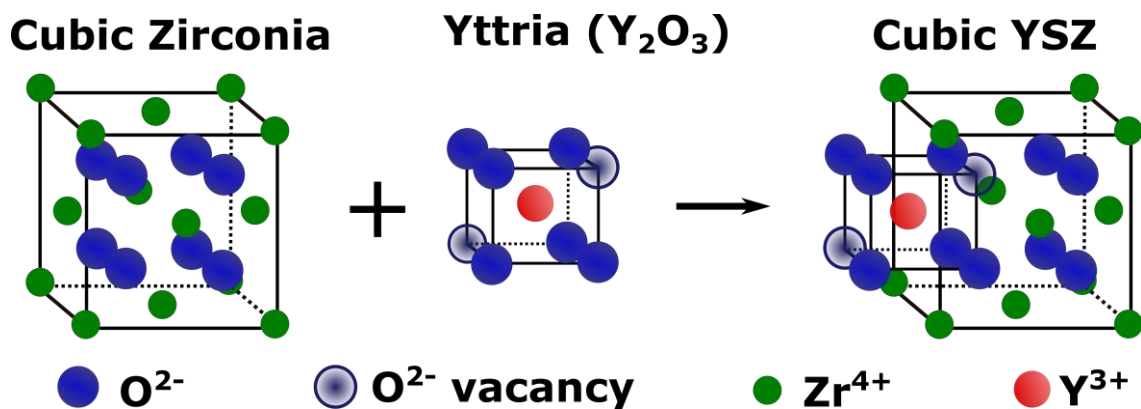
Figure 3.6. Yttria stabilized zirconia cubic structure [16].

The stabilization of tetragonal and cubic phases of zirconia by high concentration of oxygen vacancies generated either in high temperature conditions, or in an atmosphere with low partial oxygen pressure or even by doping with divalent and trivalent cations, suggests that the stability is only governed by oxygen vacancies. However, some experimental results reported along the years contradict this idea, as they show that it is possible to stabilize

66

tetragonal and cubic phase of zirconia by other mechanisms in which the oxygen ion vacancies are not involved [2]. One example is the stabilization of tetragonal and cubic zirconia phases at RT by doping pure zirconia with tetravalent cations, such as Ce^{4+}, Ti^{4+} and Ge^{4+} ions. In this case, the replacement of Zr^{4+} cation by other cation with the same valence, do not generate oxygen vacancies, being the stabilization of metastable phases of zirconia at RT explained as an effect of cation size. The replacement of some of the Zr^{4+} by cations with a higher ionic radius induces an increase in the ratio between cation and anion radius. Consequently an higher average distance between the ions results in a decrease of their electrostatic repulsion which is responsible for the distortion of the more symmetric crystalline structures of pure zirconia [4]. The doping of pure zirconia with pentavalent cations, such as Nb^{5+}, is also an effective approach for the stabilization of the tetragonal and cubic zirconia phases at RT. In this case the stabilization is explained as a result of combination of the oxygen vacancies and cation size stabilization mechanisms [2].

Additionally to the RT stabilization of tetragonal and cubic zirconia phases by the doping with stabilizer cations, it was reported in literature that these phases can be stabilized at RT in undoped nanocrystalline zirconia below a critical size, due to a reduced size effect [2,8,9,17]. This mechanism is not yet completely understood. Different mechanisms based on thermodynamic, strain energy or kinetic, involving the diffusion of oxygen vacancies in the zirconia lattice, have been explored in several works [2].

A proper selection of the type and concentration of stabilizer and the adjustment of processing parameters, allows the manipulation of crystalline phases and microstructures and, by this way, the optimization of some properties over others, taking into accounting specific applications. Some of the most explored zirconia microstructures include the partial stabilized zirconia (PSZ), tetragonal zirconia polycrystals (TZP) and fully stabilized zirconia (FSZ). PSZ materials are constituted by coarse tetragonal precipitates dispersed in a cubic zirconia matrix. TZP ceramics contains around 100% of tetragonal stabilized zirconia with grain sizes between 0.2-1 μm. FSZ refers to a zirconia material that is completely stabilized in the cubic phase [1,3].

The doping with trivalent ions is one of the most frequent approaches used in the stabilization of metastable phase of zirconia at RT due to the high technological importance of the products. Within this, yttria is particularly effective in the stabilization of tetragonal and cubic zirconia phases due to its cubic lattice structure similar to the cubic structure of zirconia [18]. In this thesis work, yttria was selected as the zirconia high temperature phase

stabilizer and therefore it is fundamental to understand the ZrO_2-Y_2O_3 system in order to predict and control the obtained phases and microstructures in the produced samples.

3.3 ZrO_2-Y_2O_3 system

Among all the cations added to zirconia to stabilize the high temperature phases at RT, Y^{3+} is one of the most used in industrial applications. As such, the ZrO_2-Y_2O_3 system is of enormous technological importance. Even though the first diagram of the ZrO_2-Y_2O_3 system was reported a long time ago in 1951 by Duwez *et al.* [19] and since then extensive research has been done in this system, the experimental data obtained are often contradictory and some parts of the diagram are still not completely understood [4,10]. The most reliable and accepted phase diagram of the ZrO_2-Y_2O_3 system is the one proposed by Scott in 1975 [20]. Special attention has been added to the zirconia-rich composition of this diagram in which solid solutions are produced, due to their high interest for practical applications [4]. This part of the phase diagram, reproduced based on the phase diagram reported by Scott, is presented in Figure 3.7.

Comparatively to the phase diagrams of other systems including ZrO_2-CaO and ZrO_2-MgO used to stabilize zirconia, the phase diagram of the ZrO_2-Y_2O_3 system has a much larger tetragonal solid solution field and the temperature of transformation from t-phase to the m-phase is lower [1]. Moreover, solubility of yttrium in the zirconia lattice is much higher than the solubility of other ions typically used in the stabilization [1]. As a consequence, it is possible to produce zirconia ceramics that are essentially 100% tetragonal or 100% cubic by the stabilization with Y^{3+} [1]. The zirconia-rich part of the ZrO_2-Y_2O_3 phase diagram is a complex system, in which several complicated phase transition occurs. The conditions under which these phase transitions take place are dependent on several factors including the sample preparation process, thermal history and grain size. Moreover, the presence of metastable phases in this region of the diagram is also common [4].
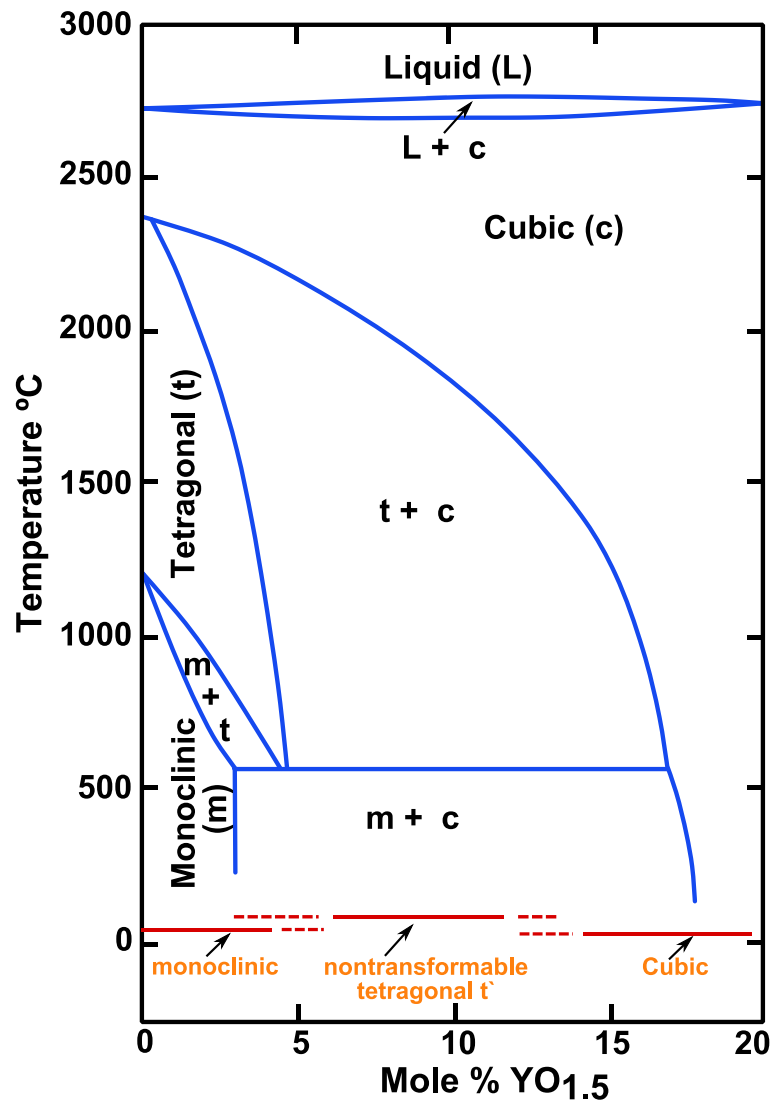
Figure 3.7. Zirconia-rich end of the zirconia-yttria equilibrium phase diagram (drawn based on reference [20]).

As shown in diagram presented in Figure 3.7, for low content of $YO_{1.5}$ (between 0-5 mol.%) there is a narrow two-phases (m + t) region for a range of temperatures above the temperature in which monoclinic phases exists. For the same range of $YO_{1.5}$ content, during heating, this two-phase region is followed by a tetragonal phase region (t-phase). One important feature of this system is the decrease in the temperature of t→m transformation with increase in yttrium content [4]. This t-phase, which exists in a range of $YO_{1.5}$ content between 0-5 mol.%, is typically called as transformable tetragonal phase, since upon material cooling it undergoes phase transition to monoclinic [4]. However, this phase transformation can be avoided for t-phases with $YO_{1.5}$ content around 3-4 mol.% if the grain size is small enough (from 0.2 to 1 µm) [4]. In this case the transformation to the m–phase does not occur spontaneously and the t-phase is preserved at RT. Even so, the t → m transformation can be induced by a significant mechanical loading. This t → m phase

transition upon mechanical loading is responsible for one of the most important characteristics of zirconia, the transformation toughness that will be discussed later. For higher contents of $YO_{1.5}$ there is other two-phase region containing a mixture of cubic phase (c-phase) and an untransformable tetragonal phase (t'-phase). The rapid cooling starting from temperatures in a range of cubic solid solution, of samples with $YO_{1.5}$ content between 4-13 mol.% undergo a phase transformation to the t'-phase. This untransformable t'-phase does not undergo phase transition into monoclinic. Further increase in $YO_{1.5}$ content above 15 mol.% leads to a decrease in the distortion of tetragonal structure resulting in a region where a fully stabilized cubic solid solution exists [4]. The limit of $YO_{1.5}$ contents in each metastable tetragonal and cubic phase that it is possible to retain at RT is indicated in a red colour in the Figure 3.7.

3.4 Properties and technological applications

As mentioned above, the practical applications of pure zirconia are very limited due to the destructive t $\rightarrow$ m phase transformation [2]. As such, the stabilization of tetragonal and cubic phases at RT, avoiding phase transformation during cooling, is determinant for the use of zirconia in industrial applications. At the beginning, the stabilization of high temperatures phases at RT by doping the pure zirconia aimed only to avoid martensitic phase transformation and consequent material cracking. Meanwhile, it was realized that, materials with new and/or improved properties are produced as side effect of RT phase stabilization. The stabilization of metastable phases of zirconia at RT paved the way for a wide range of engineering applications. Nowadays, zirconia is one of the most important industrial ceramic materials for both structural and functional advanced applications, by making use of their superior mechanical and unique functional properties [11]. The resultant properties of zirconia based materials are strictly dependent on the phases and microstructure of the material that, in turn, can be manipulated by a proper selection of the nature and concentration of the stabilizing cations and processing condition [4,5]. As such, specific properties can be optimized over others, regarding specific applications.

The two most important effects of the stabilization of zirconia in its physical properties is, on one hand, the great improvement in the strength of zirconia ceramics with particular microstructures and, on the other hand, the oxygen ion conductivity achieved at elevated temperatures [5,7]. The same martensitic tetragonal to monoclinic phase transformation that is responsible for the degradation of the mechanical properties of pure zirconia is also responsible for a high improvement in the mechanical properties of stabilized zirconia by a

mechanism called transformation toughening [7,11,21,22]. Transformation toughening is especially effective in materials in which transformable tetragonal (t-phase) zirconia particles, with appropriated size, are homogeneously dispersed in a matrix that can be cubic zirconia (in the case of PSZ) or even other ceramic that needs to be mechanically reinforced (for example an Al_2O_3 matrix). When submitted to an external stress induced by a growing crack, the t-phase particles undergo martensitic transformation to the monoclinic phase. The volume expansion occurred in $t \rightarrow m$ transformation produces a compressive field in the surrounding particles, preventing crack propagation or even close the cracks, resulting in a mechanically stronger material [22]. This mechanism of transformation toughening is illustrated in Figure 3.8. The magnitude of the resulting enhanced mechanical strength depends on the transformation potential of the metastable tetragonal particles, which is governed by the size and structure of the metastable precipitates and the structure of the matrix. The latter, is influenced by the nature and concentration of the stabilizer, the particle size and residual impurities in the precursor zirconia and the temperature control during heating, sintering and cooling [22]. The strong influence of these parameters in the final mechanical characteristics of zirconia results in properties within wide range of values.
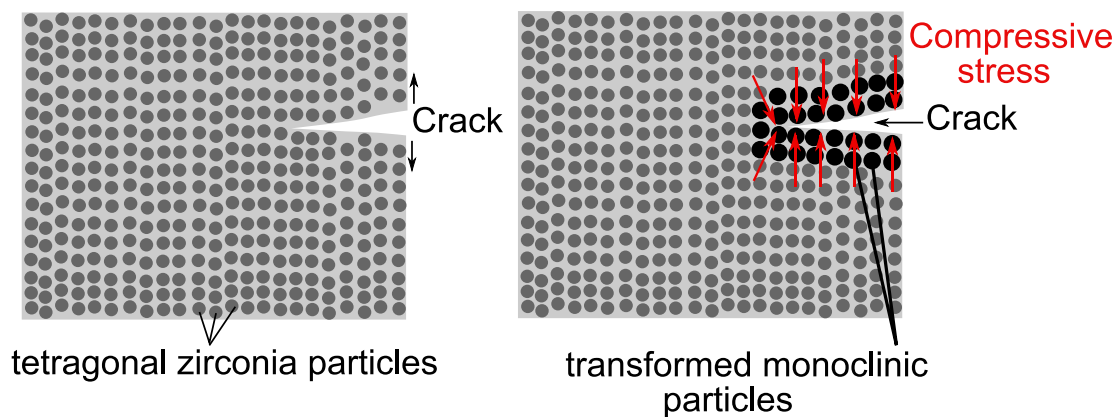

Figure 3.8. Process of fracture toughening promoted by $t \rightarrow m$ martensitic phase transformation induced by an external stress, resulting from crack propagation in a PSZ material (adapted from [7]).

Other important consequence of the zirconia stabilization with aliovalent cations, in particular trivalent cations as Y^{3+}, is the production of oxygen ion vacancies in the zirconia lattice, as discussed above [22]. At high temperature, oxygen ions diffuse through the vacancies generating new vacancies and giving rise to solid electrolytes with oxygen ion conductivity [23]. The ionic conductivity is strongly dependent on the amount of oxygen vacancies in the materials, which in turn is controlled by the dopant concentration. The best ionic conductivity is achieved in fully stabilized material, 100% cubic phase. However, cubic

zirconia typically presents lower mechanical strength and resistance to temperatures changes, comparatively to the partially stabilized zirconia or tetragonal zirconia, which can be limitative in some applications [23]. As such, an appropriated compromise between mechanical properties and ionic conductivity should be achieved according with specific needs. High values of ionic conductivity are only required in some specific cases, while for most of zirconia solid electrolytes applications, the ionic conductivity achieved in partially stabilized is sufficient [23].

As mentioned, zirconia is an outstanding material that shows a combination of properties that are uncommon in ceramic materials. In this oxide material, the typical characteristics of a ceramic are combined with other physical properties that usually are associated to metals. As a general result, zirconia is characterized by a high refractive index (2.15 to 2.18 for cubic zirconia [11]), high melting temperature ($\sim$2700 ^{0}C [11]), low thermal conductivity, high thermal expansion coefficient (around 10×10^{-6} K^{-1}, in the same order as steel [11]), superior corrosion resistance at elevated temperatures, good chemical, thermal and photostability, high fracture toughness and tensile strength, high hardness, high resistance to wear and oxygen ion conductivity at elevated temperatures (600 ^{0}C) [11,24]. Depending on the dopant nature and concentration, thermal history and resultant material microstructure, as well as crystalline phases, these properties can be optimized within a wide range of values according with the desired applications. Table 3.2 displays a summary of the properties of three different zirconia ceramic commercial products from Dynamic-Ceramics Ltd: magnesium partial stabilized zirconia (Mg-PSZ), tetragonal zirconia polycrystals stabilized with yttrium (3Y-TZP) and yttrium fully stabilized zirconia (8Y-FSZ) [25].

Table 3.2. Properties of different zirconia ceramic products from Dynamic-Ceramics Ltd [25].

Properties		Material		
Composition		Mg-PSZ	3Y-TZP	8Y-FSZ
Density	g/cm^3	5.60	6.05	5.7
Flexural strength (20^{0}C/800 ^{0}C)	MPa	545/354	1400/270	180/270
Compressive strength	MPa	1700	2000	1500
Modulus of elasticity	GPa	205	205	160
Poisson ratio		0.31	0.30	0.3
Hardness	Hv$_{0.3}$	1120	1350	700
Fracture toughness	MPa.m$^{1/2}$	6.0	10	3.5
Thermal expansion coefficient	$\times 10^{-6}$ K^{-1}	10	10	11
Thermal conductivity	W/mK	2.5	2	2.5
Thermal shock resistance	ΔT ^{0}C	375	250	200
Specific heat capacity	J/kgK	400	400	-

As a consequence of these unique properties, zirconia materials are nowadays used in a wide range of applications in different areas. Due to its high thermal and chemical stability, zirconia is currently employed as refractory materials, for instance in crucibles for the melt of metals and as separators in aerospace batteries [25]. Additionally, taking advantage of its low thermal conductivity and high thermal expansion coefficient, zirconia is used as thermal barrier coating (TBC), for example for aeroplane turbines [11,26,27]. Zirconia is also currently used in different cutting and metal forming tools, as milling media and in combustion engines due to its high strength, fracture toughness, hardness and resistance to thermal shock [11]. This oxide host also found applications in electronics, as electric insulator material, and telecommunications as ceramic ferrules and ceramic sleeves for connecting fibre optic cables [28,29]. Moreover, due its high ionic conductivity at high temperature, zirconia is used as solid electrolyte in solid oxide fuel cells (SOFC) and in oxygen sensors [2,11,30]. Additionally, zirconia has been considered as a ceramic biomaterial [31–33]. By taking advantage of its superior chemical and dimensional stability, high mechanical strength and toughness and Young´s modulus in the same order of magnitude as stainless steel alloys, zirconia has been used to produce ball heads for total heap replacement [34]. Additionally, zirconia has been used in dental implants in alternative to titanium, because of its proximity to the tooth-like colour, biocompatibility, and low plaque affinity [35]. Cubic zirconia finds also applications in jewellery, due to its transparency and refractive index close to the diamond [2,11].

In addition, zirconia is considered a wide band gap semiconductor, with reported band gap energies between 4-6 eV (depending on crystalline phase [36]), transparent from the NIR to the UV spectral region (< 300 nm to 8 µm [37]). These characteristics, combined with the aforementioned properties, makes it suitable for different applications in optics and photonics. Namely, considering the high refractive index, transparency, high radiation hardness, and photostability, zirconia is used as anti-reflection coatings for lasers in optical industry, as well as in coatings for high refractive mirrors and broad band interference filters [30].

Furthermore, the wide band gap of zirconia together with its relative low phonon cut-off energy (energy of stretching mode around 470 cm^{-1} [38]), potentiate it as a host for the incorporation of Ln ions with visible intense emission at room temperature [38]. The wide band gap of zirconia host allows the introduction in the forbidden band of several well-localized energy states belonging to the $4f^n$ ground configuration and $4f^{n-1}5d$ excited configuration of the trivalent Ln ions. With several of these energy states localized in the visible spectral range, under proper energy excitation, the material can emit visible light.

The relatively low phonon cut-off energy of zirconia host, decreases the probability of nonradiative deexcitation of the excited Ln ion that can lead to relatively intense luminescence at RT [39].

When added to zirconia, Ln^{3+} usually occupy the Zr^{4+} cations lattice sites and oxygen vacancies are formed for charge compensation [40]. Therefore, the stabilization of tetragonal and cubic phase of zirconia at RT can be achieved by the doping with trivalent lanthanide ions, which, in turn, are of upmost importance for the already discussed lighting technologies and bioapplications.

Since the pioneer works of Dexpert-Ghys *et al.* [41] and van der Voort *et al*. [42], the interesting properties of zirconia and yttrium stabilized zirconia (YSZ) as hosts for the incorporation of lanthanides ions have attracted the attention of several research groups over the world [24,30,38,40]. Different synthesis techniques have been used to produce zirconia and YSZ doped with distinct lanthanide ions, including bulk polycrystalline and single crystals, films, powders and ceramics, and NPs. Table 3.3 shows a representative summary of the used synthesis techniques to produce luminescent materials based on zirconia and YSZ reported in literature. Techniques such as the skull method and the laser heated pedestal growth (LHPG) have been used to produce single crystals of YSZ doped with different lanthanide ions. Regarding the production of the doped hosts with Ln ions several techniques have been used including sol-gel/deep coating and atomic layer deposition. Solid state reaction and sol-gel techniques are the most frequent methods used to produce micro-sized powders phosphors. The production of nanophosphors of zirconia and YSZ doped with different lanthanides were also reported, as indicated in Table 3.3. For the preparation of these nanophosphors mostly chemical approaches have been applied, including hydrothermal synthesis, co-precipitation, solvothermal reaction, sol-gel, solution combustion synthesis and water-oil emulsion processes. The huge potential of zirconia-based luminescent materials was already recognized by the international scientific community (see Table 3.3). However, a deep knowledge is needed to enhance the materials luminescence properties. Particularly, those related with the role of the optically activated lanthanides in zirconia and YSZ hosts which are of upmost interest to the development of new solid state light strategies and bioapplications. In such regard, it should be mentioned that the industrial applications of these phosphors requires, besides the knowledge of the materials fundamental properties, synthesis strategies that can be scalable for manufacturing.

Table 3.3. Zirconia based phosphor and respective synthesis techniques found in literature.

Ln³⁺-doped ZrO₂	**Bulk crystals** Single crystals and polycrystalline crystals	**Skull method**	-Bulk polycrystalline ZrO_2:Sm^{3+} [43]; -Single crystals YSZ:Er^{3+} [44–46], YSZ:Pr^{3+} [47], YSZ:Ho^{3+} [48], YSZ:Dy^{3+} [49];
		LHPG	-Single crystals YSZ:Er^{3+}, YSZ:Pr^{3+}, YSZ:(Er^{3+}, Pr^{3+}) [50];
		Arc image furnace	-Transparent polycrystalline YSZ:Eu^{3+} [51];
	Films	**Sol-gel/Deep coating**	-ZrO_2:Eu^{3+} thin films [30,52]; -ZrO_2:Tb^{3+} thin films [52–54]; -ZrO_2:Er^{3+} thin films [55,56]; -ZrO_2:Sm^{3+} thin films [52];
		Atomic layer deposition	-ZrO_2:Sm^{3+} thin films [43]; -ZrO_2:Dy^{3+} thin films [57];
		Others	-ZrO_2:Eu^{3+} mesoporous films [58]; -ZrO_2:Eu^{3+} [38]; ZrO_2:(Tb^{3+}, Eu^{3+})[59] films; -ZrO_2:Tb^{3+} [60–62], YSZ:Tb^{3+} [63] films; -ZrO_2:Dy^{3+}[64,65], ZrO_2:(Dy^{3+}, Li^+) [64], ZrO_2:(Dy^{3+}, Gd^{3+}) [65] films; -ZrO_2:Er^{3+} thin film [38,66]; -YSZ:(Tm^{3+}, Dy^{3+}) coatings [67];
	Phosphors Powders, particles, ceramics	**Solid state reaction**	-ZrO_2:Eu^{3+} powders [68–70]; -ZrO_2:(Sm^{3+}, Sn^{4+}) powders [71]; -ZrO_2:(Dy^{3+}, Eu^{3+}) powders [72]; -ZrO_2:Er^{3+}, (Er^{3+}, Yb^{3+}), (Er^{3+}, Mo^{6+}), (Er^{3+}, Yb^{3+}, Mo^{6+}) powders [73];
		Sol-Gel	-ZrO_2:Eu^{3+}, ZrO_2:Er^{3+} sub-micron particle [74]; -YSZ:Eu^{3+} microtubes [75]; -ZrO_2:Pr^{3+} powders [76]; -YSZ:Ce^{3+} fibres [77];
		Others	-ZrO_2:Eu^{3+} submicrometer particles [78]; -ZrO_2:Tb^{3+} ceramics [79]; -ZrO_2:Pr^{3+} micro-spheres [80], powders [39];
	Nanophosphors Nanocrystals, NPs, nanotubes, etc	**Hydrothermal synthesis**	-ZrO_2:Eu^{3+} nanocrystals [24,40,81–85]; -ZrO_2:Tb^{3+} NPs [85]; -ZrO_2:Pr^{3+} nanocrystals [86–88]; -YSZ:Pr^{3+} nanocrystals [89]; -ZrO_2:Yb^{3+} NPs [90];
		Co-precipitation	-ZrO_2:Eu^{3+} nanopowders [91–94]; -YSZ:Eu^{3+} nanopowders [41]; -ZrO_2:Pr^{3+} nanocrystals [95–97]; -ZrO_2:(Pr^{3+}, Sm^{3+}) nanocrystals [95]; -ZrO_2:Dy^{3+} NPs [98]; -ZrO_2:(Mn^{2+}, Er^{3+}) nanocrystals [99]; -YSZ:(Ho^{3+}, Yb^{3+}) nanocrystals [100];

Ln³⁺-doped ZrO₂	**Solvothermal reaction**	-ZrO₂:Eu³⁺ NPs [101,102]; -ZrO₂:Tb³⁺ NPs [102,103]; -ZrO₂:Ho³⁺ NPs [104]; -ZrO₂:(Ho³⁺, Yb³⁺) NPs [104];
	Sol-gel	-ZrO₂:Eu³⁺ nanopowders [105], nanocrystals [106,107]; -YSZ:(Eu³⁺, Yb³⁺) nanocrystals [108]; -YSZ:Eu³⁺ nanophosphors [109]; -ZrO₂:Sm³⁺ nanocrystals [110], nanophosphors [111,112]; -ZrO₂:Dy³⁺ nanocrystals [113]; -YSZ:Dy³⁺ nanocrystals [114]; -ZrO2:Er³⁺ [115–122]; ZrO₂:(Er³⁺,Yb³⁺) [116,118,119,123–127], ZrO₂:(Er³⁺, Li⁺) [119], ZrO₂:(Er³⁺, Yb³⁺, Li⁺) [119] nanophosphors; -ZrO₂:Ho³⁺ nanocrystals [128]; -ZrO₂:(Ho³⁺, Yb³⁺) nanocrystals [129,130]; -ZrO₂: (Tm³⁺, Yb³⁺, Er³⁺, Ho³⁺) nanocrystals [131]; -ZrO2:Tm³⁺ [132,133], ZrO₂:(Tm³⁺, Yb³⁺)[134] nanocrystals;
	Combustion synthesis	-ZrO₂:Eu³⁺ nanophosphors [135–137]; -ZrO₂:Tb³⁺ nanophosphors [138–140]; -ZrO₂:(Er³⁺,Yb³⁺) nanomaterials [124]; -ZrO₂:Yb³⁺ nanophosphors [141];
	Water-oil-emulsion	-ZrO₂:Tb³⁺ NPs [142]; -ZrO₂:Pr³⁺ nanocrystals [143]; -ZrO₂:Ce³⁺ NPs [144];
	Others	-ZrO₂:Eu³⁺ nanopowders [145] -ZrO₂:Tb³⁺ nanofibers [146], NPs [147]; -ZrO₂:Ce³⁺ nanophosphors [148]; -ZrO₂:(Ho³⁺, Yb³⁺) nanopowders [149]; -ZrO₂:(Dy³⁺, Eu³⁺) nanocrystals [150]; -ZrO₂:(Gd³⁺, Eu³⁺) nanocrystals [151] -ZrO₂:Sm³⁺, Nd³ nanocrystals [152]; -ZrO₂:Er³⁺ nanotubes [153], nanophosphors [154,155].

References

[1]   J. J. Swab, *Role of Oxide Additives in Stabilizing Zirconia for Coating Applications*; Defense Technical Information Center- Army research laboratory: US, 2001.
[2]   S. Shukla, S. Seal, *Int. Mater. Rev.* **2005**, *50*, 45.
[3]   J. R. Kelly, I. Denry, *Dent. Mater.* **2008**, *24*, 289.
[4]   V. V. Osiko, M. A. Borik, E. E. Lomonova, In *Springer Handbook of Crystal Growth*; Dhanaraj, G.; Byrappa, K.; Prasad, V.; Dudley, M., Eds.; Springer Berlin Heidelberg, 2010; pp. 433–477.
[5]   O. A. Graeve, In *Ceramic and Glass Materials*; Shackelford, J. F.; Doremus, R. H., Eds.; Springer US, 2008; pp. 169–197.
[6]   H. J. Scheel, T. Fukuda, *Crystal growth technology*; J. Wiley, 2003.
[7]   J. Park, *Bioceramics: Properties, Characterizations, and Applications*; Springer Science & Business Media, 2009.
[8]   S. Shukla, S. Seal, R. Vij, S. Bandyopadhyay, Z. Rahman, *Nano Lett* **2002**, *2*, 989.
[9]   S. Shukla, S. Seal, *Rev. Adv. Mater. Sci.* **2003**, *4*, 123.
[10]   M. Chen, B. Hallstedt, L. J. Gauckler, *Solid State Ion.* **2004**, *170*, 255.
[11]   R. B. Heimann, *Classic and advanced ceramics: from fundamentals to applications*; Wiley-VCH-Verl: Weinheim, 2010.
[12]   K. Momma, F. Izumi, *J. Appl. Crystallogr.* **2011**, *44*, 1272.
[13]   G. Teufer, *Acta Crystallogr.* **1962**, *15*, 1187.
[14]   O. Ohtaka, T. Yamanaka, T. Yagi, *Phys. Rev. B* **1994**, *49*, 9295.
[15]   N. Mommer, T. Lee, J. A. Gardner, *J. Mater. Res.* **2000**, *15*, 377.
[16]   J.-P. Brog, C.-L. Chanez, A. Crochet, K. M. Fromm, *RSC Adv.* **2013**, *3*, 16905.
[17]   I. G. Tredici, F. Maglia, M. Dapiaggi, G. Spinolo, U. Anselmi-Tamburini, *J. Eur. Ceram. Soc.* **2012**, *32*, 343.
[18]   M. Ghatee, M. H. Shariat, J. T. S. Irvine, *Solid State Ion.* **2009**, *180*, 57.
[19]   P. Duwez, F. H. Brown, F. Odell, *J. Electrochem. Soc.* **1951**, *98*, 356.
[20]   H. G. Scott, *J. Mater. Sci.* **1975**, *10*, 1527.
[21]   R. H. J. Hannink, P. M. Kelly, B. C. Muddle, *J. Am. Ceram. Soc.* **2000**, *83*, 461.
[22]   B. Basu, *Int. Mater. Rev.* **2005**, *50*, 239.
[23]   A. Reckziegel, *Properties and applications of high-performance ceramics made of zirconia*; Friatec AG Technical paper: Mannheim, 2015.
[24]   L. Chen, Y. Liu, Y. Li, *J. Alloys Compd.* **2004**, *381*, 266.
[25]   Zirconia | Dynamic Ceramic, http://www.dynacer.com/data-sheets/zirconia (accessed: December 7, 2015).
[26]   L. B. Chen, *Surf. Rev. Lett.* **2006**, *13*, 535.
[27]   J. Chevalier, L. Gremillard, A. V. Virkar, D. R. Clarke, *J. Am. Ceram. Soc.* **2009**, *92*, 1901.
[28]   M. J. Lance, E. M. Vogel, L. A. Reith, W. R. Cannon, *J. Am. Ceram. Soc.* **2001**, *84*, 2731.
[29]   C.-L. Yang, H.-I. Hsiang, C.-C. Chen, *Ceram. Int.* **2005**, *31*, 297.
[30]   G. Ehrhart, M. Bouazaoui, B. Capoen, V. Ferreiro, R. Mahiou, O. Robbe, S. Turrell, *Opt. Mater.* **2007**, *29*, 1723.
[31]   C. Piconi, G. Maccauro, *Biomaterials* **1999**, *20*, 1.
[32]   J. Chevalier, *Biomaterials* **2006**, *27*, 535.
[33]   P. F. Manicone, P. Rossi Iommetti, L. Raffaelli, *J. Dent.* **2007**, *35*, 819.
[34]   C. Piconi, W. Burger, H. G. Richter, A. Cittadini, G. Maccauro, V. Covacci, N. Bruzzese, G. A. Ricci, E. Marmo, *Biomaterials* **1998**, *19*, 1489.
[35]   Z. Özkurt, E. Kazazoğlu, *J. Oral Implantol.* **2010**, *37*, 367.
[36]   F. Gallino, C. Di Valentin, G. Pacchioni, *Phys. Chem. Chem. Phys.* **2011**, *13*, 17667.
[37]   R. R. Gonçalves, Y. Messaddeq, A. Chiasera, Y. Jestin, M. Ferrari, S. J. L. Ribeiro, *Thin Solid Films* **2008**, *516*, 3094.

[38]   G. Cabello, L. Lillo, C. Caro, G. E. Buono-Core, B. Chornik, M. A. Soto, *J. Non-Cryst. Solids* **2008**, *354*, 3919.

[39]   F. Ramos-Brito, C. Alejo-Armenta, M. García-Hipólito, E. Camarillo, J. Hernández A, H. Murrieta S, C. Falcony, *Opt. Mater.* **2008**, *30*, 1840.

[40]   K. Smits, L. Grigorjeva, D. Millers, A. Sarakovskis, A. Opalinska, J. D. Fidelus, W. Lojkowski, *Opt. Mater.* **2010**, *32*, 827.

[41]   J. Dexpert-Ghys, M. Faucher, P. Caro, *J. Solid State Chem.* **1984**, *54*, 179.

[42]   D. Van der Voort, G. Blasse, *Chem. Mater.* **1991**, *3*, 1041.

[43]   S. Lange, I. Sildos, M. Hartmanova, J. Aarik, V. Kiisk, *J. Non-Cryst. Solids* **2008**, *354*, 4380.

[44]   E. Greenberg, G. Katz, R. Reisfeld, N. Spector, R. C. Marshall, B. Bendow, R. N. Brown, *J. Chem. Phys.* **1982**, *77*, 4797.

[45]   R. I. Merino, V. M. Orera, R. Cases, M. A. Chamarro, *J. Phys. Condens. Matter* **1991**, *3*, 8491.

[46]   B. Savoini, J. E. Muñoz-Santiuste, R. González, G. K. Cruz, C. Bonardi, R. A. Carvalho, *J. Alloys Compd.* **2001**, *323–324*, 748.

[47]   J. E. Muñoz-Santiuste, B. Savoini, R. González, *J. Alloys Compd.* **2001**, *323-324*, 768.

[48]   S. Gutzov, W. Assmus, *J. Mater. Sci. Lett.* **2000**, *19*, 275.

[49]   R. I. Merino, V. M. Orera, O. Povill, W. Assmus, E. E. Lomonova, *J. Phys. Chem. Solids* **1997**, *58*, 1579.

[50]   F. S. De Vicente, A. C. Hernandes, A. C. De Castro, M. F. De Souza, M. R. B. Andreeta, M. S. Li, *Radiat. Eff. Defects Solids Inc. Plasma Sci. Plasma Technol.* **1999**, *149*, 153.

[51]   H. Yugami, A. Koike, M. Ishigame, T. Suemoto, *Phys. Rev. B* **1991**, *44*, 9214.

[52]   R. Reisfeld, M. Zelner, A. Patra, *J. Alloys Compd.* **2000**, *300–301*, 147.

[53]   E. Pereyra-Perea, M. R. Estrada-Yañez, M. García, *J. Phys. Appl. Phys.* **1998**, *31*, L7.

[54]   K. Joy, *Thin Solid Films* **2014**, *556*, 99.

[55]   C. Urlacher, C. Marco de Lucas, E. Bernstein, B. Jacquier, J. Mugnier, *Opt. Mater.* **1999**, *12*, 19.

[56]   L.-J. Lai, T.-C. Chu, M.-I. Lin, Y.-K. Lin, *Solid State Commun.* **2007**, *144*, 181.

[57]   V. Kiisk, A. Tamm, K. Utt, J. Kozlova, H. Mändar, L. Puust, J. Aarik, I. Sildos, *Thin Solid Films* **2015**, *583*, 70.

[58]   C. M. Leroy, T. Cardinal, V. Jubera, C. Aymonier, M. Treguer-Delapierre, C. Boissière, D. Grosso, C. Sanchez, B. Viana, F. Pellé, *Microporous Mesoporous Mater.* **2013**, *170*, 123.

[59]   A. I. Ramos-Guerra, J. Guzmán-Mendoza, M. García-Hipólito, O. Alvarez-Fregoso, C. Falcony, *Ceram. Int.* **2015**, *41*, 11279.

[60]   T. Rivera, J. Azorín, C. Falcony, E. Martínez, M. García, *Radiat. Phys. Chem.* **2001**, *61*, 421.

[61]   M. García-Hipólito, R. Martínez, O. Alvarez-Fregoso, E. Martínez, C. Falcony, *J. Lumin.* **2001**, *93*, 9.

[62]   J. C. Pivin, N. V. Gaponenko, I. Molchan, R. Kudrawiec, J. Misiewicz, L. Bryja, G. E. Thompson, P. Skeldon, *J. Alloys Compd.* **2002**, *341*, 272.

[63]   N. H. J. Stelzer, J. Schoonman, *J. Mater. Synth. Process.* **1996**, *4*, 429.

[64]   A. Baéz-Rodríguez, O. Alvarez-Fragoso, M. García-Hipólito, J. Guzmán-Mendoza, C. Falcony, *Ceram. Int.* **2015**, *41*, 7197.

[65]   R. C. Martínez-Olmos, J. Guzmán-Mendoza, A. Báez-Rodríguez, O. Álvarez-Fragoso, M. García-Hipólito, C. Falcony, *Opt. Mater.* **2015**, *46*, 168.

[66]   F. S. De Vicente, A. C. De Castro, M. F. De Souza, M. Siu Li, *Thin Solid Films* **2002**, *418*, 222.

[67]   W. Wang, J. Wei, H. Hong, F. Xuan, Y. Shan, *J. Alloys Compd.* **2014**, *584*, 136.

[68]   X. Yin, Y. Wang, D. Wan, F. Huang, J. Yao, *Opt. Mater.* **2012**, *34*, 1353.

[69]   R. K. Tamrakar, D. P. Bisen, K. Upadhyay, *J. Radiat. Res. Appl. Sci.* **2015**, *8*, 11.

[70]   R. K. Tamrakar, D. P. Bisen, K. Upadhyay, S. Tiwari, *J. Radiat. Res. Appl. Sci.* **2014**, *7*, 486.

[71]   Z. Zhao, Y. Wang, *J. Lumin.* **2012**, *132*, 2842.
[72]   J. Kaur, Y. Parganiha, V. Dubey, D. Singh, D. Chandrakar, *Superlattices Microstruct.* **2014**, *73*, 38.
[73]   Y. Cong, D. Liu, N. Yu, Y. Xiao, Q. Yang, Y. Fu, *Mater. Chem. Phys.* **2014**, *144*, 440.
[74]   I. Freris, P. Riello, F. Enrichi, D. Cristofori, A. Benedetti, *Opt. Mater.* **2011**, *33*, 1745.
[75]   K. Utt, M. Part, T. Tätte, V. Kiisk, M. G. Brik, A. A. Chaykin, I. Sildos, *J. Lumin.* **2014**, *152*, 125.
[76]   J. Isasi-Marín, M. Pérez-Estébanez, C. Díaz-Guerra, J. F. Castillo, V. Correcher, M. R. Cuervo-Rodríguez, *J. Phys. Appl. Phys.* **2009**, *42*, 075418.
[77]   L. Y. Zhu, X. Q. Wang, G. Yu, X. Q. Hou, G. H. Zhang, J. Sun, X. J. Liu, D. Xu, *Mater. Res. Bull.* **2008**, *43*, 1032.
[78]   Z. W. Quan, L. S. Wang, J. Lin, *Mater. Res. Bull.* **2005**, *40*, 810.
[79]   C. L. Hardin, Y. Kodera, S. A. Basun, D. R. Evans, J. E. Garay, *Opt. Mater. Express* **2013**, *3*, 893.
[80]   F. Ramos-Brito, M. García-Hipólito, C. A. Alejo-Armenta, E. Camarillo, J. M. Hernández, H. O. Murrieta, C. Falcony, *J. Mater. Sci.* **2008**, *43*, 4527.
[81]   E. Hemmer, K. Soga, T. Konishi, T. Watanabe, T. Taniguchi, S. Mathur, *J. Am. Ceram. Soc.* **2010**, *93*, 3873.
[82]   Y. Hui, B. Zou, S. Liu, S. Zhao, J. Xu, Y. Zhao, X. Fan, L. Zhu, Y. Wang, X. Cao, *Ceram. Int.* **2015**, *41*, 2760.
[83]   S. D. Meetei, S. D. Singh, *J. Alloys Compd.* **2014**, *587*, 143.
[84]   L. Yu, H. Liu, M. Nogami, *Opt. Mater.* **2010**, *32*, 1139.
[85]   Y. Hakuta, K. Sue, Y. Takebayashi, S. Yoda, T. Furuya, H. Takashima, *Key Eng. Mater.* **2012**, *512-515*, 59.
[86]   S. Möller, J. D. Fidelus, W. Łojkowski, *Solid State Phenom.* **2007**, *128*, 97.
[87]   A. Opalińska, D. Hreniak, W. Łojkowski, W. Stręk, A. Presz, E. Grzanka, *Solid State Phenom.* **2003**, *94*, 141.
[88]   A. Opalinska, C. Leonelli, W. Lojkowski, R. Pielaszek, E. Grzanka, T. Chudoba, H. Matysiak, T. Wejrzanowski, K. J. Kurzydlowski, *J. Nanomater.* **2007**, *2006*, e98769.
[89]   J. D. Fidelus, S. Yatsunenko, M. Godlewski, W. Paszkowicz, E. Werner-Malento, W. Łojkowski, *Scr. Mater.* **2009**, *61*, 415.
[90]   Y.-W. Zhang, X. Sun, G. Xu, C.-H. Yan, *Solid State Sci.* **2004**, *6*, 523.
[91]   S. Gutzov, M. Bredol, F. Wasgestian, *J. Phys. Chem. Solids* **1998**, *59*, 69.
[92]   A. Parma, I. Freris, P. Riello, F. Enrichi, D. Cristofori, A. Benedetti, *J. Lumin.* **2010**, *130*, 2429.
[93]   S. Dhiren Meetei, S. Dorendrajit Singh, N. Shanta Singh, V. Sudarsan, R. S. Ningthoujam, M. Tyagi, S. C. Gadkari, R. Tewari, R. K. Vatsa, *J. Lumin.* **2012**, *132*, 537.
[94]   H. Q. Liu, L. L. Wang, S. G. Chen, B. S. Zou, *J. Alloys Compd.* **2008**, *448*, 336.
[95]   L. Jx, L. Sc, L. Xm, *Guang Pu Xue Yu Guang Pu Fen Xi Guang Pu* **2006**, *26*, 605.
[96]   F. Ramos-Brito, H. M. S, J. H. A, E. Camarillo, M. García-Hipólito, R. Martínez-Martínez, O. Álvarez-Fragoso, C. Falcony, *J. Phys. Appl. Phys.* **2006**, *39*, 2079.
[97]   F. Ramos-Brito, M. García-Hipólito, R. Martínez-Martínez, E. Martínez-Sánchez, C. Falcony, *J. Phys. Appl. Phys.* **2004**, *37*, L13.
[98]   F. Gu, S. F. Wang, M. K. Lü, G. J. Zhou, S. W. Liu, D. Xu, D. R. Yuan, *Chem. Phys. Lett.* **2003**, *380*, 185.
[99]   S. F. Wang, F. Gu, M. K. Lü, G. J. Zhou, Z. P. Ai, D. Xu, D. R. Yuan, *J. Cryst. Growth* **2003**, *257*, 84.
[100]   Y. Zhou, H. Wang, B. Xu, L. Cao, *J. Lumin.* **2015**, *161*, 288.
[101]   T. Ninjbadgar, G. Garnweitner, A. Börger, L. M. Goldenberg, O. V. Sakhno, J. Stumpe, *Adv. Funct. Mater.* **2009**, *19*, 1819.
[102]   Y. Liu, S. Zhou, D. Tu, Z. Chen, M. Huang, H. Zhu, E. Ma, X. Chen, *J. Am. Chem. Soc.* **2012**, *134*, 15083.

[103] B. K. Moon, J. H. Jeong, S. Yi, S. E. Choi, P. S. Kim, H. Choi, J. H. Kim, *J. Lumin.* **2007**, *122-123*, 873.

[104] H. M. Noh, H. K. Yang, B. K. Moon, B. C. Choi, J. H. Jeong, H. Choi, J. H. Kim, *J. Nanosci. Nanotechnol.* **2013**, *13*, 4006.

[105] A. Speghini, M. Bettinelli, P. Riello, S. Bucella, A. Benedetti, *J. Mater. Res.* **2005**, *20*, 2780.

[106] P. Ghosh, A. Patra, *Langmuir* **2006**, *22*, 6321.

[107] H. Zhang, X. Fu, S. Niu, G. Sun, Q. Xin, *Mater. Chem. Phys.* **2005**, *91*, 361.

[108] J. Liao, D. Zhou, S. Liu, H.-R. Wen, X. Qiu, J. Chen, *Phys. B Condens. Matter* **2014**, *436*, 59.

[109] J. Liao, D. Zhou, B. Yang, R. Liu, Q. Zhang, *Opt. Mater.* **2012**, *35*, 274.

[110] E. De la Rosa-Cruz, L. A. Diaz-Torres, P. Salas, R. A. Rodríguez, G. A. Kumar, M. A. Meneses, J. F. Mosiño, J. M. Hernández, O. Barbosa-García, *J. Appl. Phys.* **2003**, *94*, 3509.

[111] E. De la Rosa, L. A. Diaz-Torres, P. Salas, R. A. Rodríguez, *Opt. Mater.* **2005**, *27*, 1320.

[112] E. De la Rosa-Cruz, L. A. Díaz-Torres, P. Salas, D. Mendoza, J. M. Hernández, Castaño, V. N., *Opt. Mater.* **2002**, *19*, 195.

[113] L. A. Diaz-Torres, E. De la Rosa, P. Salas, V. H. Romero, C. Angeles-Chávez, *J. Solid State Chem.* **2008**, *181*, 75.

[114] X. Fu, S. Niu, H. Zhang, Q. Xin, *Mater. Sci. Eng. B* **2006**, *129*, 14.

[115] E. D. la Rosa-Cruz, L. A. Díaz-Torres, R. A. Rodríguez-Rojas, M. A. Meneses-Nava, O. Barbosa-García, P. Salas, *Appl. Phys. Lett.* **2003**, *83*, 4903.

[116] D. Solís, T. López-Luke, E. De la Rosa, P. Salas, C. Angeles-Chavez, *J. Lumin.* **2009**, *129*, 449.

[117] T. López-Luke, E. De la Rosa, D. Sólis, P. Salas, C. Angeles-Chavez, A. Montoya, L. A. Díaz-Torres, S. Bribiesca, *Opt. Mater.* **2006**, *29*, 31.

[118] L. Liu, Y. Wang, Y. Bai, X. Zhang, K. Yang, C. Huang, Y. Song, *Opt. Commun.* **2012**, *285*, 1528.

[119] L. Liu, Y. Wang, X. Zhang, K. Yang, Y. Bai, C. Huang, W. Han, C. Li, Y. Song, *Opt. Mater.* **2011**, *33*, 1234.

[120] L. Liu, C. Li, X. Zhang, Y. Chen, L. Li, Z. Zhang, Y. Wang, *Opt. Commun.* **2013**, *287*, 228.

[121] A. Patra, C. S. Friend, R. Kapoor, P. N. Prasad, *J. Phys. Chem. B* **2002**, *106*, 1909.

[122] A. Patra, *Chem. Phys. Lett.* **2004**, *387*, 35.

[123] O. Meza, L. A. Diaz-Torres, P. Salas, E. De la Rosa, D. Solis., *Mater. Sci. Eng. B* **2010**, *174*, 177.

[124] L. Pihlgren, T. Laihinen, L. C. V. Rodrigues, S. Carlson, K. O. Eskola, A. Kotlov, M. Lastusaari, T. Soukka, H. F. Brito, J. Hölsä, *Opt. Mater.* **2014**, *36*, 1698.

[125] L. A. Diaz-Torres, O. Meza, D. Solis, P. Salas, E. De la Rosa, *Opt. Lasers Eng.* **2011**, *49*, 703.

[126] Luis A. Gómez, L. de S. Menezes, C. B. de Araújo, R. R. Gonçalves, S. J. L. Ribeiro, Y. Messaddeq, *J. Appl. Phys.* **2010**, *107*, 113508.

[127] P. Salas, C. Angeles-Chávez, J. A. Montoya, E. De la Rosa, L. A. Diaz-Torres, H. Desirena, A. Martínez, M. A. Romero-Romo, J. Morales, *Opt. Mater.* **2005**, *27*, 1295.

[128] D. Patel, N. King, C. Mingo, *Proc. SPIE* **2009**, 72121E.

[129] E. De la Rosa, P. Salas, H. Desirena, C. Angeles, R. A. Rodríguez, *Appl. Phys. Lett.* **2005**, *87*, 241912.

[130] D. Solís, E. D. la Rosa, P. Salas, C. Angeles-Chávez, *J. Phys. Appl. Phys.* **2009**, *42*, 235105.

[131] D. Solís, T. López-Luke, E. De La Rosa, O. Meza, S. Anderson, *SPIE Proc.* **2010**, *7617*, 76171Q.

[132] H. Zhang, X. Fu, S. Niu, Q. Xin, *J. Non-Cryst. Solids* **2008**, *354*, 1559.

[133] A. Patra, P. Ghosh, P. S. Chowdhury, M. A. R. C. Alencar, W. Lozano B., N. Rakov, G. S. Maciel, *J. Phys. Chem. B* **2005**, *109*, 10142.

[134] A. Patra, S. Saha, M. A. R. C. Alencar, N. Rakov, G. S. Maciel, *Chem. Phys. Lett.* **2005**, *407*, 477.

[135] Y. S. Vidya, K. S. Anantharaju, H. Nagabhushana, S. C. Sharma, H. P. Nagaswarupa, S. C. Prashantha, C. Shivakumara, Danithkumar, *Spectrochim. Acta. A. Mol. Biomol. Spectrosc.* **2015**, *135*, 241.

[136] N. Tiwari, R. K. Kuraria, S. R. Kuraria, *Mater. Sci. Semicond. Process.* **2015**, *31*, 214.

[137] S. F. Wang, F. Gu, M. K. Lü, Z. S. Yang, G. J. Zhou, H. P. Zhang, Y. Zhou, S. M. Wang, *Opt. Mater.* **2006**, *28*, 1222.

[138] B. Marí, K. C. Singh, M. Sahal, S. P. Khatkar, V. B. Taxak, M. Kumar, *J. Lumin.* **2010**, *130*, 2128.

[139] S. J. Yoon, K. Park, *Int. J. Hydrog. Energy* **2015**, *40*, 825.

[140] Y. S. Vidya, K. Gurushantha, H. Nagabhushana, S. C. Sharma, K. S. Anantharaju, C. Shivakumara, D. Suresh, H. P. Nagaswarupa, S. C. Prashantha, M. R. Anilkumar, *J. Alloys Compd.* **2015**, *622*, 86.

[141] R. K. Tamrakar, N. Tiwari, V. Dubey, K. Upadhyay, *J. Radiat. Res. Appl. Sci.* **2015**, *8*, 399.

[142] Z. Ye, M. Tan, G. Wang, J. Yuan, *J. Fluoresc.* **2005**, *15*, 499.

[143] C. Tiseanu, V. Parvulescu, D. Avram, B. Cojocaru, N. Apostol, A. V. Vela-Gonzalez, M. Sanchez-Dominguez, *Phys. Chem. Chem. Phys.* **2014**, *16*, 5793.

[144] S. Das, C.-C. Chang, C.-Y. Yang, S. Som, C.-H. Lu, *Mater. Charact.* **2015**, *106*, 20.

[145] T. Myint, R. Gunawidjaja, H. Eilers, *J. Phys. Chem. C* **2012**, *116*, 21629.

[146] Y. Xie, Z. Ma, L. Liu, Y. Su, H. Zhao, Y. Liu, Z. Zhang, H. Duan, J. Li, E. Xie, *Appl. Phys. Lett.* **2010**, *97*, 141916.

[147] P. Riello, S. Bucella, D. Cristofori, A. Benedetti, R. Polloni, E. Trave, P. Mazzoldi, *Chem. Phys. Lett.* **2006**, *431*, 326.

[148] C.-M. Lee, Y.-H. Pai, T.-P. Tang, C.-C. Kao, G.-R. Lin, F.-S. Shieu, *Mater. Chem. Phys.* **2010**, *119*, 15.

[149] C. Ming, F. Song, Y. Yu, Q. Wang, *J. Alloys Compd.* **2012**, *512*, 121.

[150] S. Das, C.-Y. Yang, C.-H. Lu, *J. Am. Ceram. Soc.* **2013**, *96*, 1602.

[151] E. G. Villabona-Leal, L. A. Diaz-Torres, H. Desirena, J. L. Rodríguez-López, E. Pérez, O. Meza, *J. Lumin.* **2014**, *146*, 398.

[152] Z. Assefa, R. G. Haire, P. E. Raison, *Spectrochim. Acta. A. Mol. Biomol. Spectrosc.* **2004**, *60*, 89.

[153] X. Wang, J. Zhao, P. Du, L. Guo, X. Xu, C. Tang, *Mater. Res. Bull.* **2012**, *47*, 3916.

[154] R. Jia, W. Yang, Y. Bai, T. Li, *Opt. Mater.* **2006**, *28*, 246.

[155] L. A. Díaz-Torres, E. D. la Rosa-Cruz, P. Salas, C. Angeles-Chavez, *J. Phys. Appl. Phys.* **2004**, *37*, 2489.

Chapter 4.

Characterization techniques

In this chapter the characterization techniques used to evaluate the morphology, structure and luminescent properties of the produced phosphor materials are described.

An appropriated characterization of the produced luminescent materials (phosphors) is crucial to evaluate its potential for a specific aim, i.e. to determine if the material has the requested characteristics needed for the envisaged applications. On other hand, a suitable characterization is important to understand how the properties of the phosphors can be improved. A correlation between structure, morphology, particle size and luminescence features of the produced materials is essential for further optimization of phosphors performance.

In this thesis, the morphology and crystal/particle size of zirconia based phosphors were analysed by electron microscopy while the structural analyses were carried out by X-ray diffraction (XRD) and Raman spectroscopy techniques. The luminescent properties of the produced phosphors were accomplished via optical spectroscopic techniques including, steady state photoluminescence (PL), PL excitation (PLE), time resolved PL spectroscopy (TR-PL), and lifetimes measurements.

Next, a brief revision of the principles and experimental setup of each one of these techniques will be presented. The importance of the use of electron microscopy, XRD, Raman and PL spectroscopy in the characterization of the zirconia phosphors will be also discussed.

4.1 Electron microscopy

Electron microscopy is one of the most powerful tools available for the microstructural characterization of materials. In particular, electron microscopy techniques are fundamental tools in the characterization of nanomaterials, allowing to acquire morphological, structural, compositional, and other relevant information that could be very hard to be obtained by other characterization techniques. In fact, the advancing in the electron microscopy strongly contributed for the development in nanoscience.

The use of high energy electrons instead of visible light employed in the traditional optical microscopes opened the door to imaging objects with very low dimensions. Optical microscopes are known to be inappropriate systems to imaging objects, and their details, with dimensions below the micro scale due to their low depth of field and low spatial resolution (in the best cases around 0.2 μm), conditioned by the wavelength of visible light [1–3]. In contrast, electrons, with energy that can be increased simply by accelerating them across a high voltage [1], can be used to produce microscope images with high spatial resolution and high depth of field.
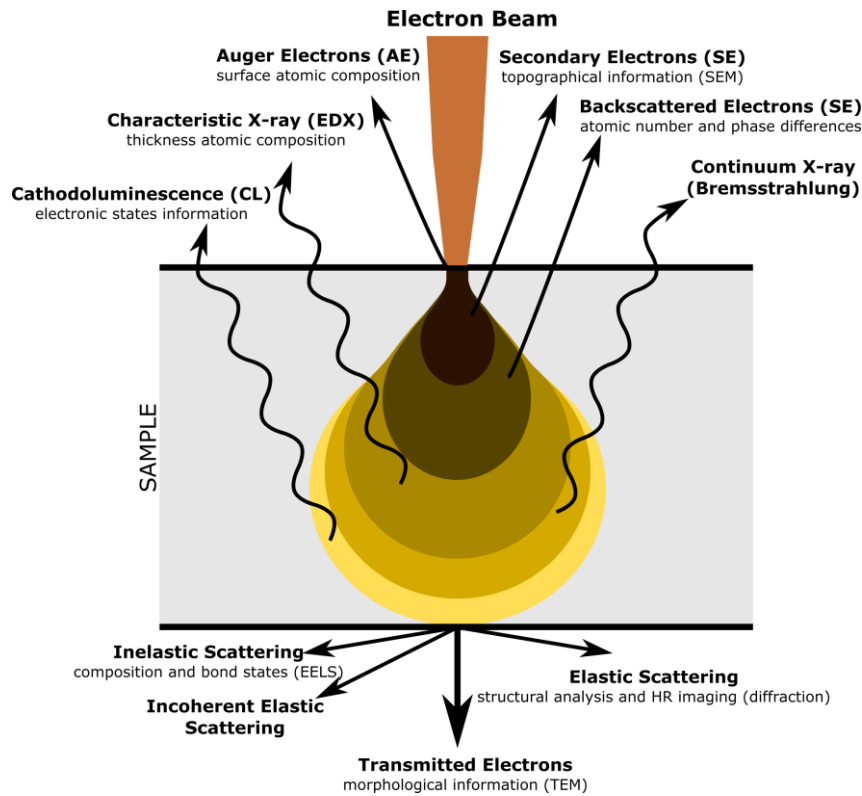
Figure 4.1. Various signals produced from the interaction between the electron beam and the sample (adapted from [4]).

Other strong advantage of the use of electrons is related with the high number of different signals that are generated from the interaction between the materials and the electrons beam (Figure 4.1). Each one of these signals can give different type of information about the material under study, including chemical composition, surface topography, crystallography, atomic number distribution, electric conductivity and others [3]. Using the appropriated detectors, the different signals can be acquired and analysed in the same equipment. Therefore, electron image can be combined with other characterization techniques in order to get information from a specific and localized region of the sample. As an example, energy dispersive X-ray spectroscopy (EDS) is often associated with electron microscopes, to identify specific chemical elements in the sample by the analysis of the emitted X-ray radiation [2]. This technique allows not only to identify the chemical elements, but also to analyse the distribution of specific elements by mapping a specific region of the sample.

In this work both scanning electron microscopy (SEM) and transmission electron microscopy (TEM) were used for microstructural characterization of the produced samples. In both types of microscopes, the monochromatic electrons are accelerated by the application of an acceleration voltage (kV) in the electron gun. A set of electromagnetic lens are used to focus the electrons into a small, coherent beam and to direct the beam onto the

surface of the sample. Figure 4.2 shows a schematic illustration of the principal components of the image formation in a typical SEM and TEM microscopes.
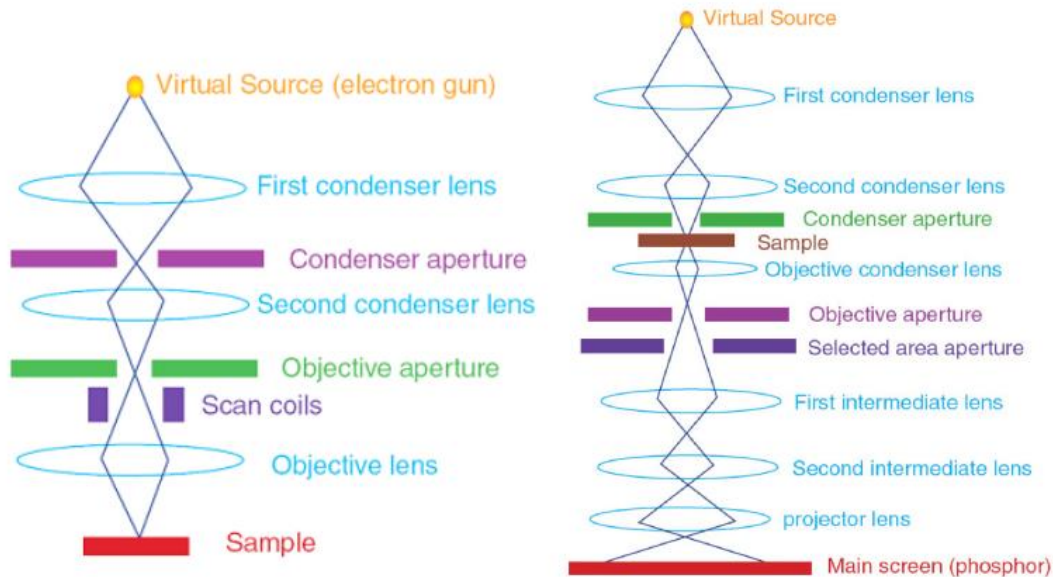

Figure 4.2. Schematic representation of the principal components in a typical SEM (left) and TEM (right) microscopes (adapted from [2]).

In a SEM, the secondary electrons generated by the interaction of the electron beam and the materials, are used to imaging the surface of the samples [2]. Since the emission efficiency of the secondary electrons is very sensitive to the geometry and chemical characteristics of the surface as well as to the bulk chemical composition, the SEM can provide important information about surface topography and morphology of the samples [2]. Typically, acceleration voltages in the range between 5-30 kV are used in the SEM and spatial resolutions in the order of 1 nm can be achieved. In this work two SEM equipments were used: a S4100 Hitachi and a HR-FESEM HitachiSU-70. SEM was used to analyse the bulk crystals produced by LFZ, including the existence of grain boundaries, segregations or defects, such as bubbles and cracks. For such experiments, the crystals were cut and impregnated in an epoxy resin for further polishing of the crystal surface. Since zirconia is not a conductor material, before observation in SEM it was necessary to deposit a thin conductor film (carbon) on the surface of the sample in order to avoid charge concentration. Charge accumulation prevents the interaction of the electron beam with the samples surface hindering the image formation. EDS analyses were performed during the SEM to investigate the distribution of the dopant ions along the length and diameter of the crystals.

In the TEM technique, the electrons transmitted by a very thin sample are used to create the image. TEM is a powerful tool to investigate the morphology, crystalline structure and orientation of nanomaterials at a very high spatial resolutions [1]. This type of electronic microscope typically works at an acceleration voltage in the order of 100-300 kV and resolutions around 0.10 nm can be achieved. In addition to the lower magnification images that give access to nanocrystals/nanoparticles size and shape and interface between particles, high resolution (HRTEM) images can be used to get structural information of the samples, including those of individual particles. Moreover, in TEM electron diffraction patterns, which also contain important crystallographic information of the samples, can be detected and analysed. Due to the small diameter in which the electron beam can be focused (~0.3 nm), electron diffraction, HRTEM images or other complementary analysis, including quantitative chemical analysis, can be performed in a single nanocrystal [2]. In this work, the NPs produced by PLAL and the nanocrystalline powders produced by SCS were analysed by TEM. Two different equipments were used, a HR-(EF) TEM-JEOL 2200FS and a Hitachi H-900 equipment. In contrast to other type of samples, including thin films or bulk samples, the preparation of the nanocrystalline powders or nanoparticles for observation in TEM is much simpler. In the case of dried SCS powders, a very small amount of powders were dispersed in distillate water under ultrasonic agitation. In the case of NPs colloids produced by PLAL, a small volume of the colloidal solution was diluted in distilled water and was ultrasonically agitated. In both cases, a drop of the diluted suspension was released in the top of a copper TEM grid with carbon support film and was dried at RT. TEM and HRTEM images allowed to observe crystallinity, particle shape and to determine average particle size of the SCS and PLAL samples.

4.2 X-ray diffraction (XRD)

The knowledge of the crystalline structure and microstructure of a material is one of the most fundamental steps to understand its properties. As referred above, in Ln-doped phosphors the luminescence features are strongly related with the materials crystalline structure. As such, a proper structural characterization of phosphor materials is an important initial characterization to understand and improve their properties. XRD is one of the most powerful and widely used techniques for identification of crystalline phases and analysis of their unit cell dimensions [5,6].

In crystalline materials, the crystallographic information obtained by XRD is strictly related with the distance between crystalline planes, which can be measured through the diffraction

phenomena. XRD makes use of the Huygens–Fresnel principle since that the wavelength of X-rays radiation is in the same order of magnitude as the distance between atoms placed in a periodic array, with inter-planar distance d, in a crystalline lattice (angstrom (Å)) [7]. In this condition, when a crystalline material is irradiated by a monochromatic beam, each atom in the periodic array act as a scattering element, in which the electromagnetic waves are scattered in all directions by the scatters centres [6]. Waves scattered from different atoms can interact constructively at certain angles if the waves are in phase, giving rise to diffraction maxima [5,6]. In a solid material, the condition in which XRD occurs is schematically illustrated in Figure 4.3.
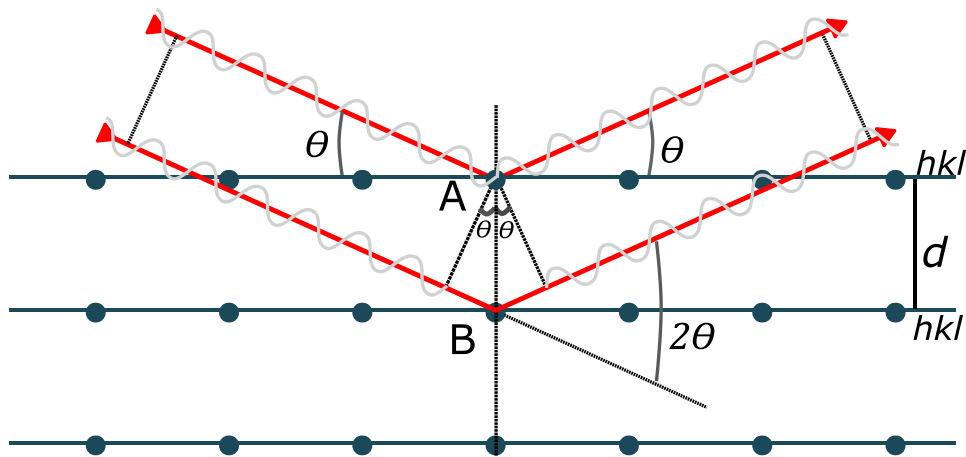

Figure 4.3. Illustration diagram of the X-rays diffraction by a crystal (Bragg condition) (adapted from [6]).

When an arbitrary group of parallel planes described by the Miller indexes (*hkl*) in a crystal, with an inter-planar distance d, is irradiated at an angle θ with a monochromatic beam of X-rays, the waves scattered by each crystalline plane (which have the same phase of the wave scattered by an arbitrary atom in these planes) will interfere constructively if the path difference between the incident and scattered waves in the two planes is a integer multiple of the wavelength. Considering the two atoms A and B in the Figure 4.3, the path difference between the incident and scattered waves by these two atoms is equal to $2d \sin θ$, in which θ is the angle between the incident beam and the diffracting plane and d is the inter-planar distance. Therefore, the phenomenon of X-ray diffraction in a crystal occurs in the scattering directions that satisfy Bragg's law, expressed by the *Eq.* 4.1 (where *n* is the diffraction order) and which is a consequence of the periodicity arrangement of the crystalline planes [5].

$$n\lambda = 2d \, \sin\theta \qquad\qquad Eq. 4.1$$

Since monochromatic X-ray radiation is used, only one first order diffraction maximum is produced by each set of parallel planes, detected at a specific angle between the incident and the diffracted waves, called the diffraction angle (2θ). Therefore, by scanning the diffraction angle, the diffractogram composed by the diffraction maxima associated to each crystalline plane in the crystal can be constructed. Since each material has a unique arrangement and number of atoms, its diffraction pattern is also unique [7]. Hence, X-ray diffraction is a valuable technique to identify the crystalline phases present in a sample, which could be a single crystal, polycrystalline powder or even thin films.

In this work, powder XRD technique was used to identify the zirconia crystalline phases in the powders produced by SCS. The measurements were performed in a Philips X'Pert MPD system at RT, using the K_α emission line of Cu with 1.5418 Å wavelength. In this system, the X-ray source is in a fixed position, while the sample and the detector are rotated θ and 2θ, respectively, in order to change the incidence and detection angles.

In addition to the identification of crystalline phases, XRD was used to analyse the crystallinity of the bulk crystals produced by LFZ. In a random oriented powder, independently on the orientation of the sample, there is always a considerable number of crystals in which the crystalline planes have the proper orientation to diffract for a certain Bragg angle θ and, as a result, the diffraction maxima of all the crystalline planes appear in the diffractogram. On the other hand, in the case of a single crystal or preferentially oriented polycrystals the situation is different. In a single crystal, the crystalline planes are oriented, and therefore the diffraction maxima associated to these planes will be more spatially localized. Therefore, the planes can be aligned in such way that the diffraction direction is aligned with the detector. Hence, while the diffraction maxima of all the planes can be detected along only one axis of rotation in randomly oriented samples, in single crystalline samples two axis of rotation are necessary to record all the diffraction maxima. These differences in the diffraction pattern of a polycrystalline and single crystal samples is very useful to analyse the crystallinity of the sample with resource to X-ray diffraction techniques. In this work, single crystal XRD technique was of particular importance to analyse in which experimental conditions zirconia based single crystals can be grown by LFZ technique.

The identification of the crystalline phases using the diffractograms obtained by X-ray diffraction was performed by comparison with other diffractograms obtained for reference materials registered in the ICDD (International Centre for Diffraction Data) database. In this

search for a match, information about the position of the diffraction maxima, peak intensity and intensity distribution as a function of diffraction angles was compared.

Additional crystallographic information, including the lattice parameters or quantitative determination of crystalline phases, can be extracted from the acquired diffractograms using more advanced analyses. For example, after indexation of the crystalline phases, the lattice parameters of the unit cell can be calculated using the inter-planar distance *d* (determined by the Bragg's law (*Eq.* 4.1) of an indexed *hkl* plane. Depending on the symmetry of the crystalline lattice, 1, 2 or 3 planes are need to determine the lattice parameter *a, b* and *c. Eq*. 4.2 shows the relation between the inter-planar distance *d* of the plane (*hkl*) and the lattice parameter *a* for a cubic lattice [7].

$$\frac{1}{d^2} = \frac{1}{a^2} \, (h^2 + k^2 + l^2) \qquad\qquad Eq. \, 4.2$$

As explored in Chapter 3, zirconia can crystallize in three different structures, monoclinic, tetragonal and cubic, at atmospheric pressure, by increasing the temperature. The tetragonal and cubic phases are of high technological importance and can be stabilized at RT by different processes. While the tetragonal and cubic phases of zirconia can be well distinguished from the monoclinic phase by XRD, the same does not happen, between the cubic and tetragonal phase. The diffraction pattern of the monoclinic phase of zirconia can be well distinguished from the diffractogram of other two phases, by the analysis of the diffraction maxima in the 2θ range between 26 ^{0} and 33 ^{0} [8]. This is evidenced in Figure 4.4, which shows the diffraction patterns of a monoclinic (A), tetragonal (B) and cubic (C) zirconia in such 2θ region. For the monoclinic phase there are two diffraction maxima with high intensity associated to the (111) and (11$\bar{1}$) crystalline planes, while in the tetragonal and cubic phases there is only one diffraction maxima associated to the (111) crystalline plane, also with high intensity and which are not overlapped with any of the other two [8]. Therefore, it is easy to distinguish the monoclinic phase from the tetragonal or cubic ones. However, due to the high similarity of the tetragonal and cubic structures of zirconia, which results in very similar diffraction patterns, the assignment of these two phases based on X-ray diffraction can be ambiguous [8]. One reported way used to distinguish these two phases using XRD, is by comparing their diffractograms in the 2θ range of 71-76 ^{0}. In this 2θ range the tetragonal structure can be distinguished from the cubic one by the presence of (004)(400) doublets, whereas cubic phase exhibit only one maximum of diffraction [8]. However, the identification of tetragonal and cubic phases using these low intensity and highly overlapped diffraction maxima is very difficult. In the particular case of samples with small crystallite sizes, including the nanoparticles produced by PLAL, due to the

enlargement of the diffraction peaks, it is difficult to spectrally resolve the doublets of the tetragonal phase and consequently it is very hard to distinguish the two phases. To overpass this limitation XRD should be used together with other complementary techniques, for example with Raman spectroscopy.
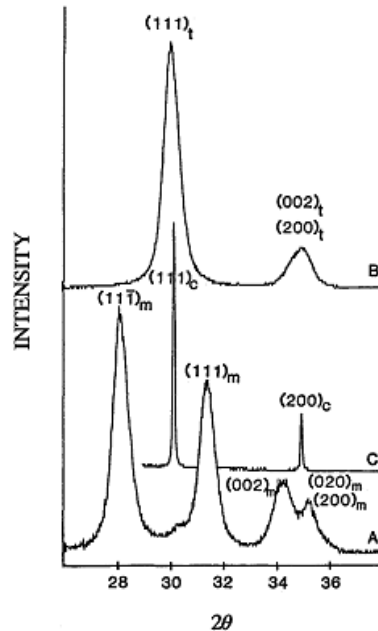

Figure 4.4. XRD patterns of a monoclinic (A), tetragonal (B), and cubic (C) zirconia acquired between 26-38 ^{0} [8].

4.3 Raman spectroscopy

Raman spectroscopy is an optical technique that relies in the phenomenon of inelastic scattering, or Raman scattering, which provides information about the collective vibrational modes of atoms in a crystalline lattice. The Raman scattering or Raman effect, is the phenomenon in which an incident monochromatic electromagnetic radiation (with frequency ω_i) interacts with the vibrating atoms in crystals, resulting in a small fraction of scattered radiation with frequencies ($\omega_i \pm \omega_0$), i.e. inelastic scattering [9]. The difference between the frequencies of the incident radiation and the inelastic scattered light ($\pm\omega_0$) corresponds to the energy of the normal vibrational modes of the crystalline lattice.

From a physical point of view, the Raman scattering can be interpreted as the result of the modulation of the material's electric polarization *P (r,t)* by the lattice vibrations, which results in scattered light with frequencies that differ from the frequency of the incident light [10]. In the following we will consider the simplest case of an isotropic material, in which its electric susceptibility, χ, can be represented by a scalar. When the material is irradiated by a

monochromatic electromagnetic light, the electrons in the material are driven away from their equilibrium position by the sinusoidal plane electromagnetic field F *(r,t)* of the incident light, with wavevector k_i and frequency ω_i, described by the wave function in *Eq.* 4.3. Such, induces an electric polarization *P(r,t)* in the material, that varies in time with the same frequency *(ω_i)* as the applied electrical field (described by the wave function shown in *Eq.* 4.4) and with an amplitude *P(k_i ω_i)*, given by the *Eq.* 4.5, which depends on the electric susceptibility of the material, χ [10]. In such case, the light scattered by the material has the same frequency as the incident light (elastic scattering, Rayleigh scattering).

$$F(r,t) = F_i(k_i\omega_i)\cos(k_i \cdot r - \omega_i t) \qquad\qquad Eq.\,4.3$$

$$P(r,t) = P(k_i\omega_i)\cos(k_i \cdot r - \omega_i t) \qquad\qquad Eq.\,4.4$$

$$P(k_i, \omega_i) = \chi(k_i, \omega_i) \cdot F_i(k_i, \omega_i) \qquad\qquad Eq.\,4.5$$

The time-dependent nuclear displacements, i.e. the thermally excited atomic vibrations will, however, contribute to the time-dependent electric polarization of the host, as it will induce fluctuations in the electric susceptibility of the host. The nuclear displacement is expressed as a plane wave *Q(r,t)* (*Eq.* 4.6) with wavevector q and frequency ω_0.

$$Q(r,t) = Q(q\omega_0)\cos(q \cdot r - \omega_0 t) \qquad\qquad Eq.\,4.6$$

Assuming that the electronic frequencies that characterized χ are much larger than the frequency ω_0 of the phonons, a quasi-static approximation can be considered, and the χ can be expressed as a function of *Q(r,t)*. On the other hand, since the amplitude of the vibrations at RT are small comparatively to the lattice constants, the χ can be expanded as a Taylor series in *Q(r,t)*. [10]. The χ is then composed by a static term, represented by the susceptibility of the medium without fluctuations (χ_0) and by a dynamic term that represents the oscillating susceptibility induced by the nuclear displacements (*Q(r,t)*) [10].

$$\chi(k_i, \omega_i, Q) = \chi_0(k_i, \omega_i) + \left(\frac{\partial\chi}{\partial Q}\right)_0 Q(r,t) \qquad\qquad Eq.\,4.7$$

Therefore, material's polarization can be also expressed by the two terms expression in *Eq.* 4.8, in which P_0, in the first term, is the oscillating polarization in phase with the incident electromagnetic field, and P_{ind}, in the second term, is the polarization induced by the lattice vibrations (phonons).

$$P(r, t) = P_0(r, t) + P_{ind}(r, t, Q) \qquad\qquad Eq. 4.8$$

$$= \chi_0(\boldsymbol{k}_i, \omega_i)\boldsymbol{F}_i(k_i, \omega_i)\cos(\boldsymbol{k}_i \cdot \boldsymbol{r} - \omega_i t) + \left(\frac{\partial \chi}{\partial \boldsymbol{Q}}\right)_0 \boldsymbol{Q}(r, t)\boldsymbol{F}_i(\boldsymbol{k}_i, \omega_i)\cos(\boldsymbol{k}_i \cdot \boldsymbol{r} - \omega_i t)$$

By rewriting the second term in *Eq.* 4.8, the frequency and wavevector of the polarization induced by phonons (P_{ind}) can be determined. As expressed in *Eq.* 4.9, the polarization induced by the lattice vibrations (P_{ind}) is composed by two sinusoidal waves in which their wavevectors (k_s and k_{as}) and frequencies (ω_s and ω_{as}) are shifted from the k_i and ω_i of the incident electromagnetic radiation, by ± q (wavevector associated to lattice vibrations) and ± ω_0 (frequency of lattice vibrations), respectively (*Eq.* 4.10) [10]. This shift is known as the Raman shift.

$$\boldsymbol{P}_{ind}(r, t, \boldsymbol{Q}) = \left(\frac{\partial \chi}{\partial \boldsymbol{Q}}\right)_0 \boldsymbol{Q}(q, \omega_0)\cos(\boldsymbol{q} \cdot \boldsymbol{r} - \omega_0 t) \times \boldsymbol{F}_i(\boldsymbol{k}_i, \omega_i)\cos(\boldsymbol{k}_i \cdot \boldsymbol{r} - \omega_i t) \qquad Eq. 4.9$$

$$= \frac{1}{2}\left(\frac{\partial \chi}{\partial \boldsymbol{Q}}\right)_0 \boldsymbol{Q}(q, \omega_0)\boldsymbol{F}_i(\boldsymbol{k}_i, \omega_i t)$$

$$\times \{\cos[(\boldsymbol{k}_i + \boldsymbol{q}) \cdot \boldsymbol{r} - (\omega_i + \omega_0)t] + \cos[(\boldsymbol{k}_i - \boldsymbol{q}) \cdot \boldsymbol{r} - (\omega_i - \omega_0)t]\}$$

As a result, the scattered light is composed by three frequency components, one with the frequency ω_i equal to the frequency of incident light and known, as aforementioned, as Rayleigh scattering, and other two with frequencies slightly higher ($\omega_{as} = \omega_i + \omega_0$) and slightly lower ($\omega_s = \omega_i - \omega_0$) than the frequency of incident light, which constitutes the anti-Stokes and Stokes components of the Raman scattered light, respectively. The difference in frequency between the incident electromagnetic radiation (ω_i) and the Raman scattered radiation (ω_s or ω_{as}), known as Raman shift, corresponds to the frequency of the lattice vibrations. The intensity of the elastic scattered light is much higher than the intensity of the inelastic scattered components [10].

$$Stokes\ scattering: \ \boldsymbol{k}_s = (\boldsymbol{k}_i - \boldsymbol{q}) \ and\ \omega_s = (\omega_i - \omega_0) \qquad\qquad Eq. 4.10$$

$$Anti-Stokes\ scattering: \ \boldsymbol{k}_{as} = (\boldsymbol{k}_i + \boldsymbol{q}) \ and\ \omega_{as} = (\omega_i + \omega_0)$$

The phenomenon of Raman scattering can be interpreted based on energy transitions between the vibrational energy levels of the lattice and virtual energy states, where the interaction of the incident electromagnetic radiation (with energy $\hbar\omega_i$) with the material, can give rise to anti-Stokes scattering ($\hbar(\omega_i+\omega_0)$), Rayleigh scattering ($\hbar\omega_i$) and Stokes scattering ($\hbar(\omega_i-\omega_0)$), as represented in the top image of Figure 4.5. Considering the fundamental vibrational state of a given electronic state with energy v_0 and the energy level described by v_1 in the figure, a schematic overview of the scattered phenomena can be given.

In the Stokes scattering, the incident monochromatic radiation with energy $\hbar\,\omega_i$ is scattered with energy $(\hbar\,(\omega_i-\omega_0))$ by the material. Particularly, in this case, the system is in its fundamental vibrational state of energy (v_o) and upon the scattering of the incident radiation the system is left in a higher vibrational state of energy (v_1). However, if the material is already in an excited vibrational state of energy (v_1) due to thermal population, the light is scattered with an energy $\hbar\,(\omega_i+\omega_0)$, higher than the energy of the incident light (anti-Stokes scattering), due to the vibrational energy transferred from the material to the radiation [11]. The energy shift in anti-Stokes and Stokes scattered light, relatively to the energy of the elastic scattered light (Rayleigh scattering) corresponds to the $\pm\hbar\,\omega_0$, to the energy of the vibrational state *(v_1)*.
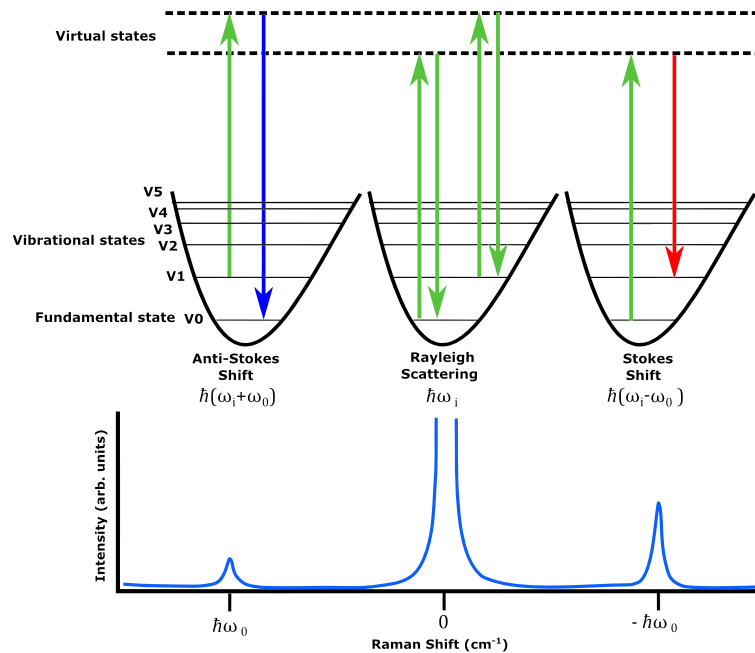

Figure 4.5. Schematic representation of the phenomena of anti-Stokes shift, Rayleigh scattering and Stokes shift (top) and example of a Raman spectrum corresponding to these processes (down) (adapted from [4]).

The normal vibrational modes show characteristic energies which are dependent on the type of chemical elements and bounding states, the lattice structural defects and tension and on the local symmetry and neighbour atoms [9]. As such, the analysis of the energy of the vibrational modes provides information about the lattice structure and composition. Therefore, Raman spectroscopy is a powerful technique used to identify the structure of materials based on their characteristic fingerprints vibrational energies. This non-destructive and non-contact technique, which does not require any pre-preparation of the samples, is a very versatile technique that can be applied not only to study crystalline

solid materials, but also materials with a short range-order structure, including amorphous materials, liquids or gases [9]. In addition, Raman spectroscopy also allows the study of adsorbed molecules in the surface of materials [9].

In this work it was used a Horiba Jobin Yvon HR800 Raman spectrometer that works in a backscattering configuration. A simple schematic representation of the system is shown in Figure 4.6. The main components of the Raman spectrometer are an excitation source (laser), optical components (including filters, lenses, mirrors and beam splitter), a microscope, the grating and the detector (CCD). In the used system, various lasers with different wavelengths (UV, blue, red and green) are available as excitation sources. The accessibility of different wavelengths of excitation is important on one hand because light with different wavelengths has different penetration depths on the material and, consequently, it is possible to study the material at different penetration depths. On the other hand, the possibility to select the most appropriated excitation wavelength for a specific sample, prevents the detection of other types of light such as thermal or luminescence radiation that can lead to invalid interpretation of the results [9]. This is especially important in the case of luminescent samples as the ones studied in this work. In order to prevent the interference with the luminescence signal from the doped samples with the Raman scattered light, the Raman spectra were acquired under excitation of a He-Cd UV laser with 325 nm wavelength (Kimmon IK Series). The laser beam pass through a band pass filter, which improves its monochromaticity. The beam is directed into the microscope by the mirrors and the beam splitter and focused in the sample through the objective lenses. The notch filter is an essential component to work in a backscattering configuration, since it reflects the laser beam but transmits the radiation with other wavelengths to the grating. The coupled microscope, besides constitutes a simple and versatile way to focus the laser beam on the samples and capture the scattered light from the sample to the detector, is also a powerful tool which allows to perform micro Raman spectroscopy. Micro Raman analysis can be very useful to analyse the phase homogeneity of the samples as well as for phase identification in small specific areas of the sample [9].
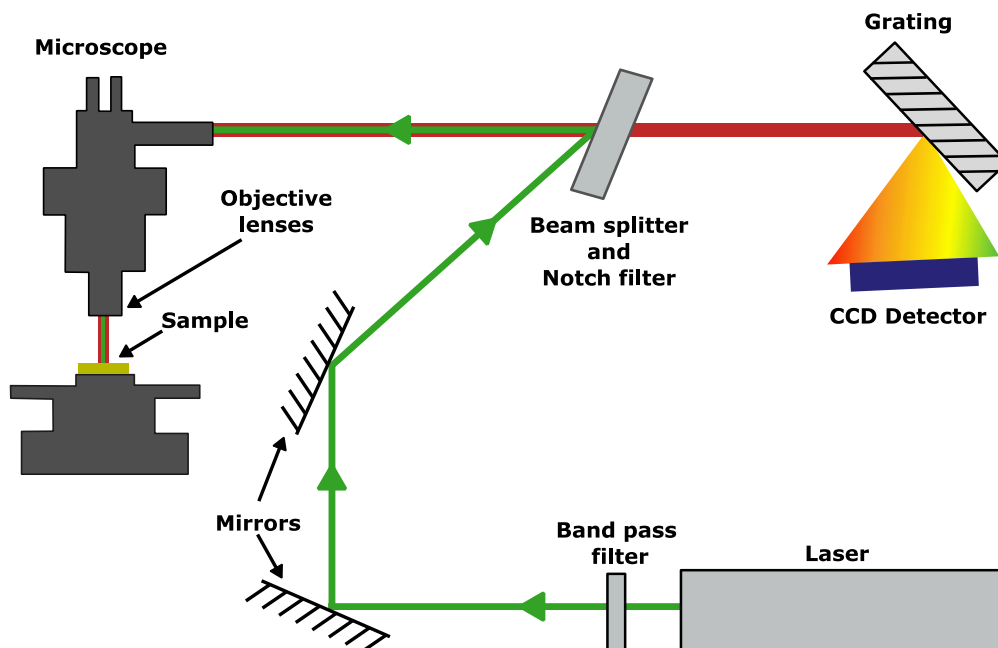
Figure 4.6. Schematic representation of the main components in a Raman spectrometer in a backscattering geometry.

In contrast to XRD technique, Raman spectroscopy allows to identify and distinguish the different crystalline phases of zirconia, one from the others, without ambiguities [9]. This technique has been used as a current and useful technique to assess the zirconia crystalline phase identification since the spectra of the correspondent vibrational modes of each one of zirconia polymorphs (monoclinic, tetragonal and cubic) are very well distinguishable. For the monoclinic crystalline phase (point group: C_{2h}), the one stable at room temperature and ambient pressure for pure zirconia, according to group theory predictions 18 Raman active vibrational modes are expected ($9A_g$ + 9 B_g) to occur [12]. The number of Raman active modes is expected to decrease with the increase in the crystal symmetry with the phase transformation from monoclinic to tetragonal and to cubic. For zirconia tetragonal phase (point group: D_{4h}) 6 fundamental Raman active vibrational modes ($1A_{1g}$ + $2B_{1g}$ + $3E_g$) are predicted, whereas in the case of cubic zirconia (point group: O_h) only one Raman active vibrational mode (T_{2g}) is expected [12]. However, in the case of the cubic fluorite-type structure, which is stabilized at RT by doping with cations as substitutional solid solutions, a continuum Raman spectra with more than one band are frequently reported. This is attributed to the presence of substitutional cations and to the oxygen vacancies that induce lattice distortions, leading to a decrease in the crystal symmetry.
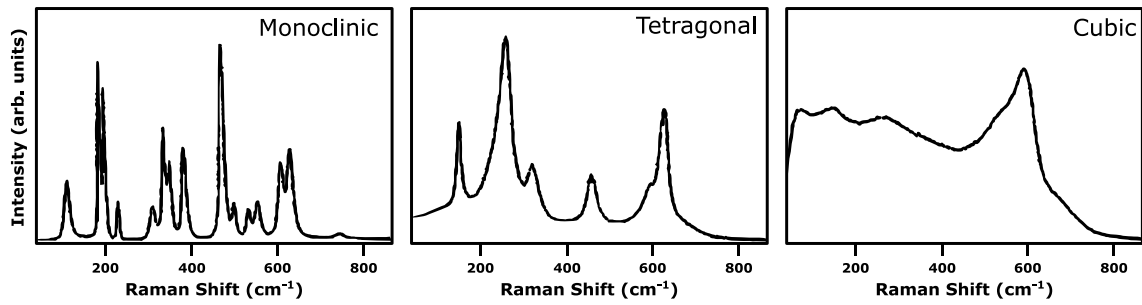
Figure 4.7. Raman spectra of monoclinic, tetragonal and cubic phases of zirconia [9].

4.4 Luminescence spectroscopy

A proper luminescence spectroscopic characterization of the produced phosphors is essential to understand the excitation and emission mechanisms and, by this way, be able to evaluate and improve the luminescent features of the materials and consequently the performance of the devices where they are inserted. As referred above, important parameters characterizing the luminescence, which determines the viability of a particular phosphor for a specific application, includes their emission and excitation spectra, luminescence lifetime and quantum efficiency. Therefore, from a technological point view, spectroscopic data that provides this information is fundamental. In addition, from a scientific point of view, these spectroscopic data together with temperature and power excitation dependence of the luminescence intensity, as well as time resolved luminescence measurements are essential for the understanding of the physical behaviour of the optically active centres in luminescent materials.

In other to understand the mechanisms behind the emission of light in a luminescent material, one should first understand how electromagnetic radiation and matter interact. Considering a beam of electromagnetic radiation, with intensity I_0, incident in a solid material, the interaction of the incoming light with atoms and/or defects in the solid results in different emerging light beams [13,14]. This interaction is illustrated in a simple way in Figure 4.8, in which it is represented the beams reflected at the material surface (I_r), the inelastically or elastically scattered (I_s) beams, the transmitted radiation (I_t) and the emitted light of intensity I_e. The analysis of the different signals resulting from the interaction of the incoming radiation, through optical spectroscopy techniques, allow us to get information on the electronic structure of an emitting centre, their lattice location and their environment [14].
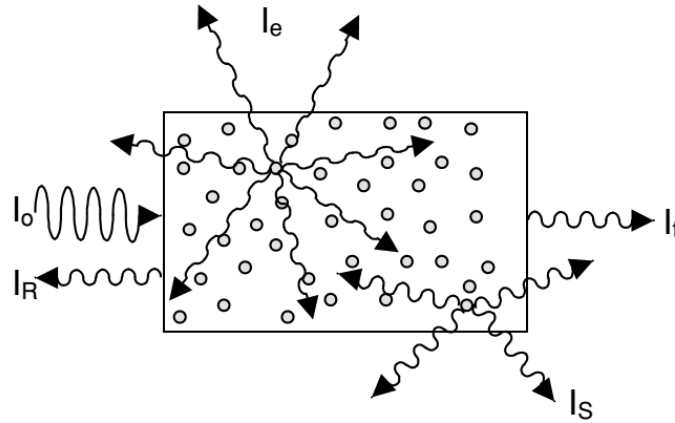
Figure 4.8. Possible emerging light beams from a material after light irradiation with intensity I_0. The points represent atoms or defects in the solid material which are interacting with the incoming light (adapted from [14]).

The emission of light from the materials can occur after absorption of the excitation radiation. Light absorption will occurs if the energy of the excitation radiation is resonant with the energy of an electronic excited state of the atoms/defect in the solid material [14]. i.e., when the energy difference between a fundamental and the excited electronic levels equals the energy of the incoming photons. The absorbed energy can be then dissipated radiatively, i.e. with the emission of light, or nonradiatively, through thermal dissipation to the lattice. The interpretation of absorption/emission spectra requires the previous understanding of the atomic/defect and lattice electronic structures. As mentioned in Chapter 3, in Ln-doped zirconia phosphors the visible emission results from the electronic transitions between the energy levels within the $4f^n$ configuration of the Ln^{3+} ions. As well known, the energy levels of the free dopant ion are modified (splitted and shifted) when the ion is inserted in the crystalline lattice, due to the influence of the electric field that the ligand ions of the lattice produced in the dopant ion. The determination of the electronic energy levels, E_i, of a certain Ln^{3+} ion inserted into a crystalline field requires solving the Schrödinger equation in *Eq.* 4.11, in which ψ_i represents the eigenfunction of the optical centre and H is the Hamiltonian that, as described in section 2.1, represents the different interactions of the valence electrons [14].

$$H\psi_i = E_i\psi_i \qquad\qquad Eq.\,4.11$$

In a real crystal the lattice is not static, as the constituent ions are vibrating around the equilibrium positions. The optical centre should be considered an integrated part of a vibrating lattice, in which the ions are surrounded by a dynamic ambient, and can participate in the collective lattice vibrations. It is then assumed that the dopant ion is

98

coupled to the vibrating lattice, i.e. the vibrations of the ligand ions around an average position affect the electronic states of the optically activator dopant and, on the other hand, the ion environment can also be affected by changes in the electronic states of the dopant ion. Taking into account this ion-lattice coupling, the crystalline field Hamiltonian term (H_{CF}) couples the electronic and ionic motions and, therefore is dependent on both the coordinates of the valence electrons ($\mathbf{r}_i$) and the coordinates of the ligand ions ($\mathbf{R}_l$) ($H_{CF} \equiv H_{CF}$ ($\mathbf{r}_i$, $\mathbf{R}_l$)). In the same way, the eigenfunction are also functions of $\mathbf{r}_i$, $\mathbf{R}_l$ ($\psi \equiv \psi$ ($\mathbf{r}_i$, $\mathbf{R}_l$)) [14]. As a result, the solution of the Schrödinger equation is quite complex and several approaches are considered in order to clarify the experimental observed absorption and emission spectra. Since the nucleus of the constituent atoms is much heavy than electrons, the motion of the ions is very slow in comparison with the motion of valence electron (adiabatic approximation). Therefore, it could be considered that electron motion occurs at a given nuclear coordinate and, consequently, the motion of electrons can be treated independently. In addition, it could be considered that the lattice vibrations can be represented by a single vibrational mode, the *breathing mode*, in which the ligand atoms pulsate radially "in and out" [14]. In this case the radial vibrations of the ligand ions can be described by only one nuclear coordinated, Q, which corresponds to the distance between the dopant ion and the ligand ions and is known as *configurational coordinate* [14] (this approach was already assumed in the description of the Raman effect). Following these two approximations, the solution of the Schrödinger equation for a dynamic optical active centre with one coordinate can be represented in a *configurational coordinate diagram*, as the one shown in Figure 4.9 for a centre with two electronic energy levels. In this diagram, the curves represent the interionic interaction potential energy and the horizontal lines represent the discrete phonon states, as also pointed out in Figure 4.5.

The electronic transitions occurring in an optical centre incorporated in a solid host can be described based on the configurational coordinate diagram. Considering an optical centre with two electronic energy states (E_i and E_f), represented by the diagram in Figure 4.9, when the material is irradiated with light having energy resonant with the energy difference between the two electronic states, the excitation light is absorbed (ν_{abs}) promoting an electron from the fundamental energy state to a higher energy state. This transition is very fast and occurs without any change in the equilibrium position of the fundamental state (Q_0). In the excited state, the electron relaxes to the equilibrium position ($Q_0`$) that corresponds to the minimum energy. This process occurs nonradiatively with the emission of phonons. From the equilibrium position of the excited state, the electron relaxes to the fundamental one, radiatively, i.e. with emission of light, without any change in the

configurational coordinate. Then, the electron relaxes again to the minimum energy of the ground state, once again with the emission of phonons [14].
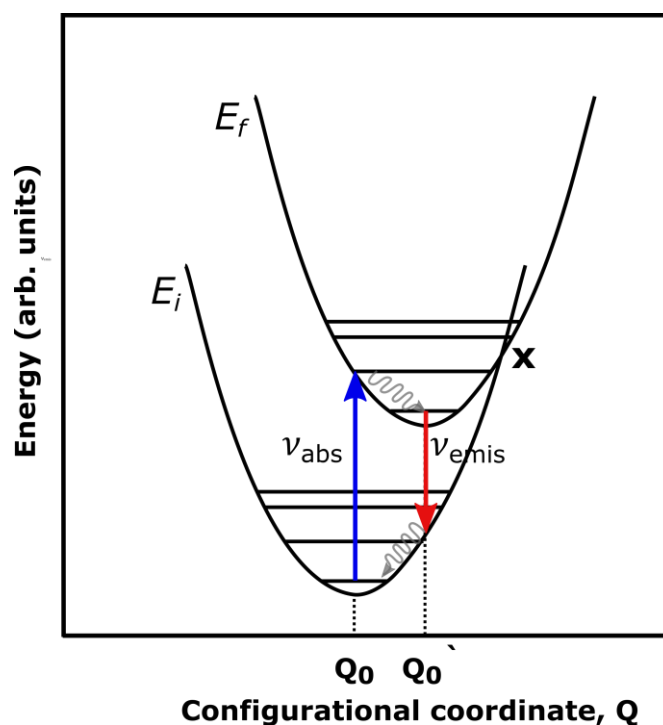

Figure 4.9. Configurational coordinate diagram of an optical centre described by two electronic energy states. Straight arrows represent radiative transitions, while sinusoidal arrows indicate the nonradiative pathways. *X* represents the crossover point (adapted from [14]).

From the example discussed above, once can easily understand that the frequency of the emitted light (ν_{emis}) is lower than the frequency of the absorbed light (ν_{abs}), due to the occurrence of nonradiative relaxations within each electronic state. This difference in energy is called the Stokes shift (already mentioned in Chapter 2) and the resultant emission is classified as Stokes emission [14]. The amplitude of the Stokes shift depends on the distance separation between the equilibrium configurational coordinates of the two states involved in the electronic transition, which in turn is related with the strength of the electron-lattice coupling. In the particular case of Ln^{3+} ions, the weak electron-lattice coupling results in a small separation between the equilibrium configurational coordinates of the electronic levels, which leads to small Stokes shifts.

The analysis of the configurational coordinate diagram can be very useful to explain multiphonon deexcitation processes in an optically active centre. Considering the two configurational coordinate diagrams shown in Figure 4.10, which represents two cases of strong electron-lattice coupling. In both cases there is a point where the two parabolas

intercept, named the crossover point (X) [14]. In the first case (a), the crossover point is placed above the populated vibrational level of the excited state. Therefore, the electron deexcitation occurs radiatively following the same process described above for the example in Figure 4.9. However, in the situation shown in Figure 4.10 b), due to a higher separation between the equilibrium coordinates of the two electronic states, the crossover point appears below the populated vibrational level of the excited state. In this situation, the crossover point corresponds to an energy degenerated vibrational state belonging to both parabolas of the fundamental and excited states As a result, the probability of the system to return to the ground state through nonradiative multiphonon relaxation is high [14]. The increase in temperature induces an increase in the nonradiative deexcitation probability, since it promotes the thermal population of high energy vibrational states, thus increasing the probability to reach the crossover point. The process of energy transfer between closer spaced optically active centres can be interpreted in a similar way. If the centres are close enough, in such way that an overlapping between the electronic wavefunctions occurs, then energy transfer between the centres can occurs without the emission of light, depending on the crossover point [14].
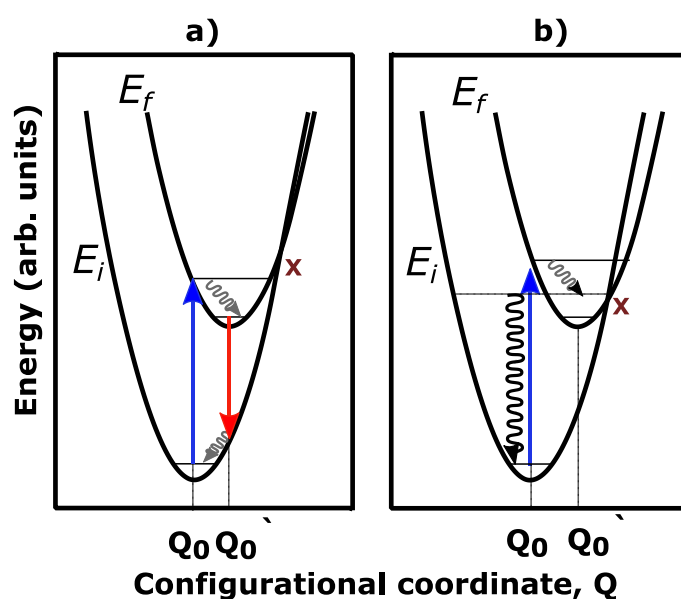

Figure 4.10. Configurational coordinate diagrams to illustrate (a) radiative and (b) nonradiative (multiphonon emission) deexcitation processes. Straight arrows represent radiative transitions, while sinusoidal arrows indicate the nonradiative pathways. *X* represents the crossover point (adapted from [14]).

The spectral features of an optical centre are determined by both the radiative and nonradiative processes [13]. In particular, the nonradiative processes, which includes the absorption and emission of phonons, strongly affects the luminescent characteristics,

including intensity, line shape and width, lifetime and quantum efficiency, of an optical active centre including the ones that are weakly coupled to the lattice, as is the case of Ln^{3+} ions [13]. As mentioned above, a proper knowledge of the electronic states involved in the population and deexcitation processes accompanied with the discussion/interpretation of the mechanisms responsible for the defects luminescence and their quantum efficiency are of upmost importance to understand and improve the emission features of a given optical active centre. All this information can be extracted from photoluminescence, photoluminescence excitation and response to pulsed excitation measurements that will be explored below.

4.4.1 Steady state PL and PLE

Steady state photoluminescence spectroscopy deals with the light emitted by a given sample upon a continuous excitation energy (typically with monochromatic electromagnetic radiation) resulting in a steady state population condition. The so emitted light is further detected and analysed. Two types of spectra can be acquired: the photoluminescence (PL) spectra and the photoluminescence excitation spectra (PLE). In this type of measurements, steady state, the excitation intensity is maintained constant for each excitation wavelength. In this situation, the feeding of the excited states equals the rate of depopulation for the fundamental state and, as a result, the intensity of the emission is usually constant in time [14].

A PL spectrum consists in an emission spectrum of the irradiated sample and plots the intensity of the emitted light as function of the wavelength or energy. The spectrum is acquired by set the monochromatic excitation energy and through the scan of the emission monochromator within a predefined wavelength range. For a given excitation energy, an emission spectrum provides information about the optically active defects in a given sample, helping to identify the electronic energy levels involved in the recombination process. The latter can be related either with band to band recombination, band to defect recombination or, as will be discussed in this thesis work, intra-defect transitions. This is the case of the Ln^{3+} in zirconia hosts, as PL measurements are relevant to their energy characterization and evaluation of their potentialities as phosphors.

Considering an excitation beam with intensity I_0 and energy resonant with an absorbing electronic energy level, in such way that part of the incident radiation is absorbed by the material (I_{abs}), resulting in the emission of light with intensity I_{emis}, the emission of a phosphor can be typified via the definition of the emission quantum yield. The quantum efficiency (luminescence efficiency or quantum yield), η, is defined as the ratio between the

number of emitted photons and absorbed photons, and can be determined by the ratio between the intensity of the emitted and absorbed radiation, (*Eq.* 4.12). The η varies between 0 and 1 and is linearly proportional to the emitted light that depends on the intensity of the excitation light [14].

$$\eta = \frac{number\ of\ emitted\ photons}{number\ of\ absorbed\ photons} = \frac{I_{emis}}{I_{abs}} \qquad\qquad Eq.\ 4.12$$

Due to the Stokes shift discussed above, usually the emission band assigned to a specific radiative electronic transition between an excited and the fundamental states ($E_e \rightarrow E_f$) occurs at lower energy (high wavelength) then the absorption band assigned to the inverse transition ($E_f \rightarrow E_e$). Therefore, it is possible to have a system with $\eta = 1$ that shows, however, a loss of energy between absorbed and emitted radiation (dissipated by phonons). This process constitutes a loss energy mechanism and the energy of the emitted and absorbed photons should be considered when the quantum efficiency is analysed. As mentioned, Ln^{3+} ions shows relatively small Stokes shift given rise to low losses of energy by this process. In the particular case of anti-Stokes radiation, as is the case of upconversion luminescence, a contrary situation occurs. In this case, as will be explored in Chapter 8, the energy of the emitted radiation is higher than the energy of the absorbed radiation, though usually one emission photon is generated per at least two excitation photons.

In the analysis of Ln^{3+} emission spectra, the effect of the Ln dopant concentration in their emission intensity can give important information about the threshold of concentration quenching. In addition, the study of the emission spectra at low temperature and as a function of temperature allows to understand the nonradiative mechanisms in the optical centre and how these affect the luminescence efficiency. The quantum efficiency of a certain radiative transition, η_i, can be defined as the ratio between the radiative probability (A_r) and the total deexcitation probability (A_T) (that includes the radiative (A_r) and nonradiative probability (A_{nr}), i.e $A_T = A_r + A_{nr}$) as expressed in *Eq.* 4.13 [9].

$$\eta_i = \frac{A_r}{A_T} = \frac{A_r}{A_r + A_{nr}} \qquad\qquad Eq.\ 4.13$$

The probability of nonradiative deexcitation follows a Boltzmann dependence with temperature in a classical approximation and, consequently, the quantum efficiency can be also expressed as a function of temperature as shown in *Eq.* 4.14, in which C is assumed as a constant independent of temperature (related with the degeneracy of the emitting levels), k_B is the Boltzmann constant and E_a is the activation energy of the thermal assisted nonradiative process which compete with the luminescence [14].

$$\eta_i(T) = \frac{A_r}{A_r + C.e^{-\frac{E_a}{k_B T}}} \qquad\qquad Eq.\,4.14$$

Considering that the emission intensity at a given temperature (I (T)), is proportional to the radiative transition probability and that at low temperature the nonradiative transitions are negligible ($A_{nr}\equiv 0 \rightarrow \eta_i = 1$), the intensity of the emission can be expressed as a function of the sample temperature as described by *Eq.* 4.15 [14].

$$\frac{I(T)}{I_0} = \frac{1}{1 + C.e^{-\frac{E_a}{k_B T}}} \qquad\qquad Eq.\,4.15$$

Therefore, the activation energy involved in the thermal quenching of the luminescence process can be determined based on the PL spectra acquired as a function of the sample temperature.

A photoluminescence excitation spectrum (PLE), simple named excitation spectrum, is acquired by monitoring the intensity of a specific emission while the wavelength of the excitation light is changed within a selected wavelength range. The excitation spectrum shows us in which spectral range the sample should be pumped in order to favours the electronic transition responsible for the monitored emission. A PLE spectrum is of upmost importance to identify the electronic energy levels of a given optically active defect, including the higher excited energy levels of a Ln^{3+} ion, and the population mechanisms of the emitting state [13]. Additionally, such technique is also an important tool for the identification of reliable energy transfer processes between different optical centres. The energy transfer from a centre A to a centre B can occur if an overlapping between the excitation spectra of B and the emission spectra of A occurs [13]. Therefore, knowing the emission and excitation spectra of distinct optical centres allows us to predict and engineer the probability of energy transfer between two optical centres for a desired application. This is for instance the case of the use of lanthanides for bioapplications.

The setup for photoluminescence measurements is essentially composed by an excitation source that irradiates the sample with photons, optical components including lenses, filters and slits to collect and select the intensity of the emitted light, a emission monochromator in which the emitted light is dispersed in their different wavelength components by the gratings, a detector and a computer with the specific software to control, monitoring and acquire the spectral data [13]. Despite the existence of different configurations, the main components are always the same. For the PL spectra acquisition, the excitation sources can be either a lamp, with a continuum wide spectrum, or a monochromatic laser beam. In the

first case, a monochromator (excitation monochromator) is used to select the excitation wavelength. For PLE spectra acquisition the continuum lamp with an excitation monochromator is used.

In this work, luminescence characterization was mainly performed in two different equipments. The first one, a Fluorolog®-3 spectrometer from Horiba Scientific was used for acquisition of RT PL and PLE spectra. The main components of this system are illustrated in Figure 4.11. In this system a 450 W Xe arc lamp coupled to a double-grating excitation monochromator, which provides an optimum wavelength excitation range between 220 and 660 nm (1200 gr/mm), is available as excitation source for PL and PLE spectra acquisition. In addition, external sources, including lasers, can be also coupled to the system. The light emitted by the samples, is dispersed by a double-grating emission monochromator. The detection gratings can be selected from a set of three gratings, with different optimum working range (330 nm-1000 nm (1200 gr/mm), 620 nm-2000 nm (600 gr/mm) and 520 nm-1560 nm (600 gr/mm)). The system contains two photomultiplier tube (PMT) detectors that allow to work in different spectral ranges, one in the near UV-visible range (200 nm-850 nm) and the other one in the NIR region (900 nm-1700 nm). In addition to these principal constituents, the system is equipped with several accessories, including a microscope that allows to performed micro-PL analyses, an integrated sphere for quantum efficiency measurements and the required components (such as a pulsed lamp and LEDs) to perform lifetime measurements.
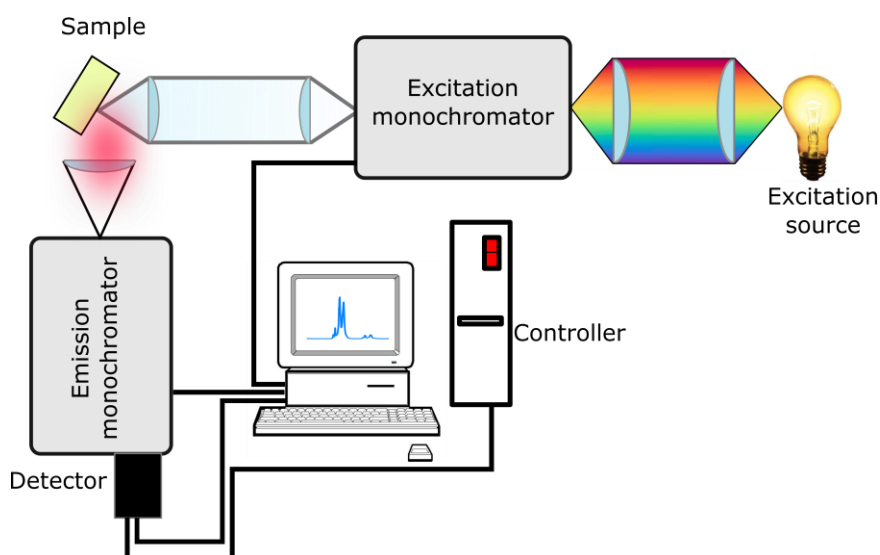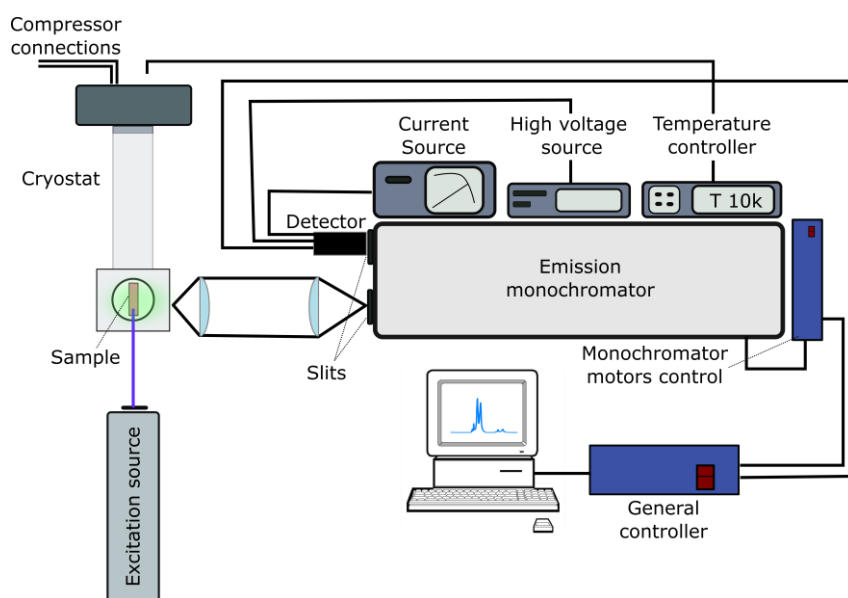

Figure 4.11. Main components of the system used for PL/PLE spectra acquisition.

In addition to the Fluorolog system, other experimental setup, which includes a SPEX 1074 emission monochromator to disperse the emitted light and a cooled Hamamatsu R928 photomultiplier detector, was widely used in the acquisition of the PL spectra of the Ln-doped samples. The principal components of this system are shown in Figure 4.12. The SPEX 1074 emission monochromator, with a high optical length (1 meter) and a grating with 1200 gr/mm, allows the acquisition of spectra at high resolution (below 0.5 Å). Therefore, the use of this system is advantageous to distinguish between narrow and close emission lines in Ln^{3+} emission spectra, for example to resolve the different Stark splitted components. In addition, this system is equipped with different excitation sources, in particular lasers with different wavelengths, which have higher excitation density then the Xenon lamp in Fluorolog ® system. Therefore, samples with lower emission intensity can be studied at different wavelength excitations. Moreover, this system is also equipped with a cold finger of a closed cycle helium cryostat that allows to decrease the sample temperature up to ~14 K and, therefore, to perform temperature dependent luminescence measurements (typically between 14 K and RT). For both systems used for PL, the acquired spectra were corrected to the optics and detector response. In addition, the PLE spectra acquired in the Fluorolog system were corrected to the wavelength dependent lamp intensity.

Figure 4.12. Main components of the system used for temperature dependent PL spectra acquisition.

4.4.2 Lifetimes and TR-PL measurements

In addition to the important information obtained based on steady state photoluminescence, time dependent photoluminescence studies are also an important source of relevant information.

In contrast to a continuum excitation source that leads to a stationary density of the centre population in an electronic excited state, the irradiation of a luminescent material with a pulsed excitation source promotes a nonstationary density of centres N in the excited state. The subsequent radiative and nonradiative decay to the fundamental state give rise to a decay-time intensity signal [14]. The time evolution of the population $N(t)$ of the excited state is expressed in *Eq.* 4.16, where N_0 is the density of the excited centres for $t= 0$, i.e. for the instant just after the pulse of light be absorbed, and A_T , as referred above, is the total deexcitation rate or total transition probability [14].

$$N(t) = N_0 \, e^{-A_T t} \qquad\qquad Eq.\,4.16$$

Since the intensity of the emitted light at a given time t after pulse excitation ($I_{emis}(t)$) is proportional to the depopulation rate of the optical centres, the intensity of the emission can be expressed as a function of time after pulse, expressed in *Eq.* 4.17. The variation of the emission intensity with time typically follows an exponential decay (I_0 is the emission intensity for $t= 0$) [13,14].

$$I_{emis}(t) = I_0 \, e^{-A_T t} \qquad\qquad Eq.\,4.17$$

This depopulation process can be experimentally observed trough the temporal decay of the emitted light. Such measurements are known as lifetime measurements, since the analysis of the experimental curve allows finding the luminescence lifetime, τ, which is given by the inverse of the total decay rate (A_T). This lifetime represents the time at which the emission intensity decreased to I_0/e. Although, τ is called luminescence lifetime (since it is obtained through luminescence experiments) it includes both the radiative (τ_{rad}) and nonradiative ($\tau_{non\text{-}rad}(T)$) part, as expressed in *Eq.* 4.18 [13,14].

$$\frac{1}{\tau} = \frac{1}{\tau_{rad}} + \frac{1}{\tau_{non-rad}(T)} \qquad\qquad Eq.\,4.18$$

The radiative lifetime, τ_{rad} ($\tau_{rad} = 1/A_r$) can be determined by combining lifetimes and quantum efficiency measurements. As such, the quantum efficiency described above in *Eq.* 4.12 can be defined in terms of lifetimes by *Eq.* 4.19.

$$\eta_i = \frac{A_r}{A_r + A_{nr}} = \frac{\tau}{\tau_{rad}} \qquad\qquad Eq.\,4.19$$

Lifetime measurements can be performed by fixing the emission monochromator at a specific wavelength (correspondent to the emitting excited state under study) and by integrating the emission signal, during a selected temporal window, starting at different delay times after the excitation pulse (see Figure 4.13). The experimental setup is very similar to the one used for steady state PL measurements however, in this case, a pulsed excitation source is used. In this work, the luminescence lifetimes were measured in the Fluorolog ®-3 spectrometer described above, coupled to a phosphorimeter that includes a pulsed xenon lamp and electronics to control the size and temporal displacement of the detection window.
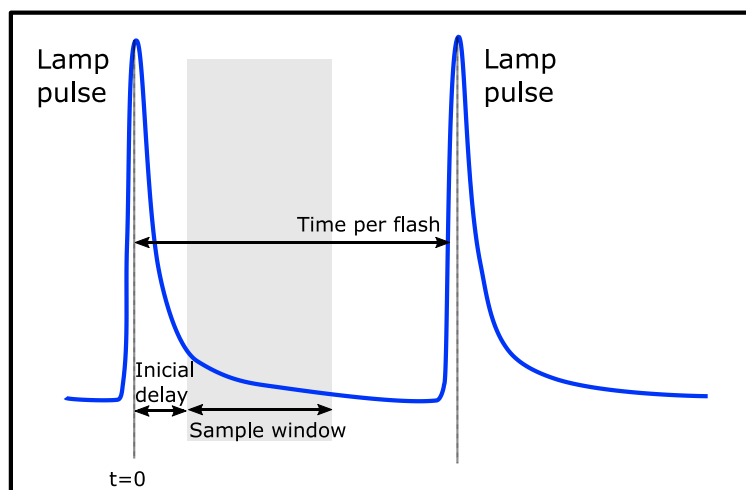
Figure 4.13. Representation of the initial delay and sample window parameters in lifetime measurements

In addition to time-decay emission curves, pulsed sources can be used to acquire emission spectra at different time delays after the absorption of the pulsed light. These measurements, known as time resolved photoluminescence (TR-PL), can be very useful to analyse complex luminescence systems and to distinguish overlapped emission bands with different decay times by an appropriate choice of the delay time and time window parameters [13,14]. TR-PL spectra help to identify transitions with origin in different excited states. In addition, it also helps to identify additional emitting centres with low emission intensity, that could not be observed in a steady state emission spectra (masked by the intense emissions), if the luminescence lifetime of this centre is higher than the one of the centre with higher emission intensity [13,14]. In this thesis work, TR-PL spectra were also

acquired using a Surelite II/10 pulsed Nd:YAG laser (1064 nm, 10 Hz repetition rate) coupled to a fourth harmonic generator crystal (Surelite SLD-II and SLF) in order to achieve 266 nm pulsed excitation with a ~5 ns pulse width and 60 mJ of energy. The detection was performed by diffracting the collected emission in an ORIEL MS-125 monochromator, with a 400 gr/mm grating and acquired in an ANDOR iccd (model DH-520, P46 phosphor coated). The emission spectra acquired in this system were not corrected to the detector and optics.

References

[1]   M. Niederberger, N. Pinna, *Metal Oxide Nanoparticles in Organic Solvents*; Engineering Materials and Processes; Springer London: London, 2009.

[2]   J. Z. Zhang, *Optical Properties and Spectroscopy of Nanomaterials*; World Scientific, 2009.

[3]   D. B. Williams, C. B. Carter, *Transmission Electron Microscopy: A Textbook for Materials Science*; Springer Science & Business Media, 2009.

[4]   C. Nico, Niobium oxides and niobates physical properties. Doutoramento em Nanociências e Nanotecnologia, Universidade de Aveiro: Aveiro, 2015.

[5]   R. Jenkins, In *Encyclopedia of Analytical Chemistry*; John Wiley & Sons, Ltd, 2006.

[6]   R. Jenkins, R. Snyder, *Introduction to X-Ray Powder Diffractometry*; Wiley, 1996.

[7]   *Principles and Applications of Powder Diffraction*; Clearfield, A.; Reibenspies, J. H.; Bhuvanesh, N., Eds.; John Wiley & Sons.; 2009.

[8]   R. Srinivasan, R. J. De Angelis, G. Ice, B. H. Davis, *J. Mater. Res.* **1991**, *6*, 1287.

[9]   K. Nogi, M. Naito, T. Yokoyama, *Nanoparticle Technology Handbook*; Elsevier, 2012.

[10]   P. Y. Yu, M. Cardona, *Fundamentals of Semiconductors*; Graduate Texts in Physics; Springer Berlin Heidelberg: Berlin, Heidelberg, 2010.

[11]   E. Smith, G. Dent, *Modern Raman Spectroscopy - A Practical Approach*; John Wiley & Sons, Ltd: Chichester, UK, 2004.

[12]   E. F. López, V. S. Escribano, M. Panizza, M. M. Carnasciali, G. Busca, *J. Mater. Chem.* **2001**, *11*, 1891.

[13]   B. Di Bartolo, J. Collins, In *Handbook of Applied Solid State Spectroscopy*; Vij, D. R., Ed.; Springer US, 2006; pp. 509–575.

[14]   J. Solé, L. Bausa, D. Jaque, *An Introduction to the Optical Spectroscopy of Inorganic Solids*; John Wiley and Sons, 2005.

Chapter 5.

Crystals growth by Laser Floating Zone

In the first part of this chapter, the fundaments of the LFZ are explained and the used experimental setup is described.

In the second part, the results obtained by the morphological, structural and optical characterization of the produced single crystals are presented and discussed.

5.1 Laser floating zone (LFZ) technique

The growth of zirconia single crystals with high quality can be a hard task. This difficulty is related, on one hand, with the high melting temperature of this material, which makes difficult the growth of crystals from melting using the traditional processes, such as the well-known *Czochralski* method. In the other hand, the occurrence of martensitic t → m phase transformation, accompanied by a high volume expansion during cooling, prevents the production of zirconia single crystals grown from high temperatures [1]. This last issue can be overpassed by the addition of stabilizer cations to pure zirconia to avoid phase transformation during cooling and the cracking of the crystals, as discussed in the Chapter 3. The difficulty to grow zirconia single crystals from melt due to its high melting temperature, can be overcome by the replacement of the conventional heating elements, such as resistive elements, by other ones that allow to reach higher temperatures [2]. Laser floating zone (LFZ) technique, in which the material is heated by a high power focused laser, arises as an alternative technique with high potential to grow high quality single crystals of materials with high melting temperature, such is the case of zirconia [2].

The LFZ method, is similar to the laser heat pedestal growth (LHPG), being powerful techniques to produce single crystals or textured polycrystals fibres by directional solidification of the molten material [2,3]. In this type of technique only a small region of the precursor material is molten instead of being completely melted inside of a crucible, as occurs in other crystal growth techniques. For that, the starting material is previously shaped in a rod, called feed-rod, and then fixed to a vertical pedestal [2]. The material is melted using a high power infrared laser that is focused radially on the top of the precursor feed-rod. A gradual increase of the laser power promotes an increase of the material temperature and, after a certain laser power, the material melts and a liquid drop is formed on the top of the feed-rod [2]. A seed, which should also have a rod shape, called seed-rod, is slowly dipped into the molten drop in order to promote connection between the feed and the seed-rods by a molten zone. The growth is initialized by pulling the feed-rod at a constant rate. As the seed-rod is pulled, the melted material in its vicinity is dragged with it and cools down leading to its solidification at the liquid-solid interface [2]. A schematic representation of this process is depicted in Figure 5.1. The pulling rate defines the growth rate (R_s) of the crystal fibre. At the same time, the feed-rod needs to be pushed into the molten zone, also at constant rate (named the feeding rate (R_f)), in order to supply material to the molten zone as it is consumed during the crystal growth.
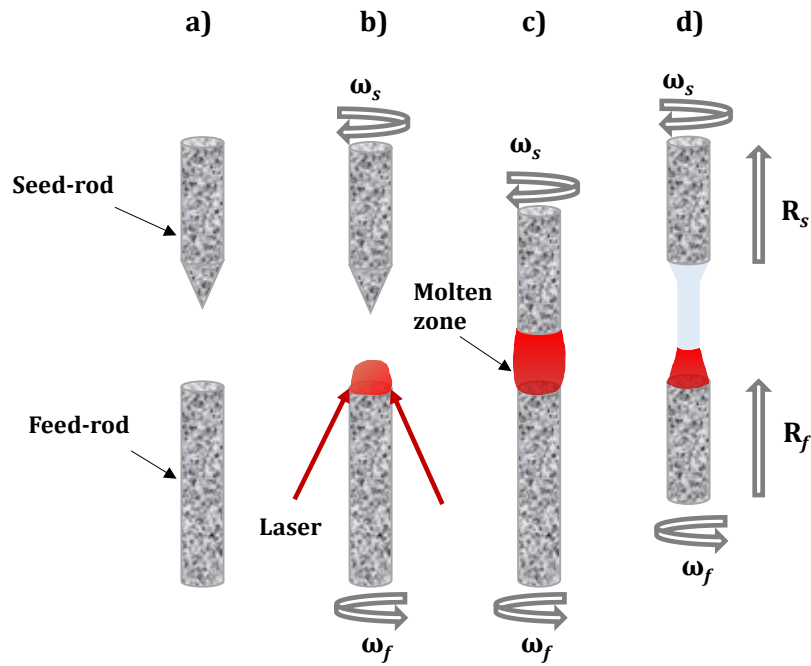
Figure 5.1. A schematic representation of LFZ crystal growth technique.

An important factor for the success of growth initialization and for its stabilization is the rotation of the precursor rods. In fact, the rotation of the feed-rod (ω_f) and the seed-rod (ω_s) promotes both temperature and composition homogenization within the molten zone [2].

The use of a laser as heating source and the absence of crucibles constitute two of the most important features of the LFZ process [3]. The use of a high power focused laser is advantageous comparatively to other heat sources, including halogen or mercury lamps or resistive elements, since higher temperatures can be reached and, by this way, materials with high melting temperatures can be grown [3]. Moreover, the use of this heat source allows a better control over the energy distribution by using conventional optical elements [3]. Being a container less technique, the LFZ allows the growth of crystals with high purity, due to the absence of reaction between the melt and the crucible [3]. This is particularly critical when the molten materials are oxides since they are extremely reactive at high temperatures. Crystal fibres grown by LFZ usually present a well-defined composition, high degree of crystalline orientation, uniform diameters, high density and homogeneity [2,3].

5.1.1 Growth stability and conditions for single crystal growth

The small volume of liquid phase needed to growth a crystal in the LFZ technique is the main responsible factor for the particular features of this technique [3]. In order to achieve a stable steady state growth and, by this way, high quality crystals with a constant diameter,

113

considerations about conservation of energy and mass, and shape stability of the molten zone should be taken into account in the LFZ process [3,4].

High crystalline quality crystals with stable dimensions can be grown by LFZ if the volume and length of the molten zone are kept constant and for this it is essential to guarantee that there is mass conservation during the solidification process. Considering that all the material from the precursor feed-rod crystallizes as a single crystal, the cross section areas of the precursor feed-rod and crystal fibre can be related with their pulling rates by *Eq.* 5.1 where ρ_s, r_s, R_s and ρ_f, r_f, R_f are the density, radius, and pulling rate of the crystal fibre and of the feed-rod, respectively [3].

$$\rho_s r_s^2 R_s = \rho_f r_f^2 R_f \qquad\qquad Eq.\,5.1$$

If the densities of the crystal fibre and the feed-rod are similar, then *Eq.* 5.1 can be simplified into *Eq.* 5.2:

$$r_s = r_f \cdot \sqrt{\frac{R_f}{R_s}} \qquad\qquad Eq.\,5.2$$

Therefore, if the pulling rates of the feed-rod and crystal fibre, and also the radius of the feed-rod are kept constant, the crystal fibre will be grown with a constant radius. In a real growth situation there are frequently fluctuations in the density and/or radius of the feed-rod, thus requiring to adjust the pulling rates to assure a constant crystal fibre radius.

Other important parameter that determines the stability of the growth process is the shape of the molten zone, characterized by the meniscus angle, φ_L, which is determined by the surface tension of the melt [4–6]. When the meniscus angle reaches an equilibrium value the growth process is stable and the diameter of the as-grown crystal remains uniform. On the other hand, a variation in this angle induces fluctuations in the diameter of the as-grown crystal. As shown in Figure 5.2, the shape of the molten zone depends on the growth direction.
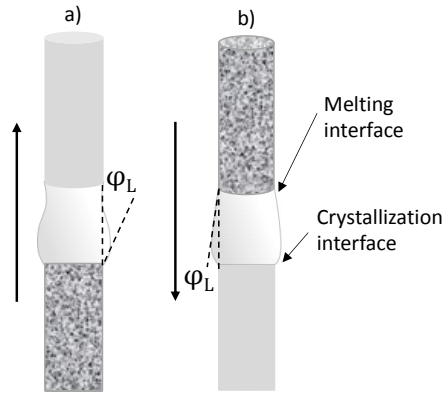
Figure 5.2. Equilibrium shape of molten zone if the crystallization occurs: a) upwards; b) downwards [6].

The morphology of the as-grown crystal depends on the solidification interface shape, which is determined by the growth rate, temperature gradient and composition. Thus, for a constant composition, one can have either planar, cellular, dendritic or equiaxed morphologies of the interface by changing the growth rate (R) and thermal gradients (G).

The growth of bulk single crystals from melt requires a planar growth front, i.e. the solid-liquid interface must advance into the melt as a planar surface [7]. One of the most important phenomena that affects the planar growth is the occurrence of constitutional supercooling (supercooling that results from local solute segregation in the melt at the advancing solid-liquid interface) which can lead to the disruption of the planar growth front [7]. Hence, in order to prevent constitutional supercooling the following condition should be satisfied [3]:

$$\frac{G}{R} \geq \frac{mC_s}{D_l} \cdot \left(\frac{1 - k_0}{k_0}\right) \qquad Eq.\,5.3$$

where G is the absolute value of the temperature gradient at the solid-liquid interface, R is the growth rate, m is the absolute value of the liquidus slope, C_s is the solute concentration, D_l the diffusion coefficient of the solute in the liquid, and k_0 is the equilibrium distribution coefficient (the ratio between solute concentration in the solid and liquid C_s/C_l) [3].

Consequently, in order to ensure the conditions of planar front growth (and hence, conditions favourable for single crystal growth), the G/R ratio should be high. Such can be reached by using slow growth rates (R) and/or high solid-liquid interface temperature gradients (G). It has been shown that the temperature gradient can be increased by decreasing the growth fibre radius, thus allowing higher growth rates without constitutional supercooling [3]. Additionally, using the LFZ technique, higher temperature gradients can be

achieved when compared with other crystal growth techniques. However, high temperature gradients are also responsible for a high level of stress in the as-grown crystal which is the main cause of many crystallographic defects. Figure 5.3 summarizes the effect of the temperature gradient (G) and the growth rate (R) on the solidification microstructure of the as-grown crystals. While the ratio G/R determines the mode of solidification, the size of the solidification structure is mainly determined by the product $G{\times}R$. Hence, for the growth of high quality single crystals, a smaller $G{\times}R$ product is required, which determines that low cooling rates are necessary [8].
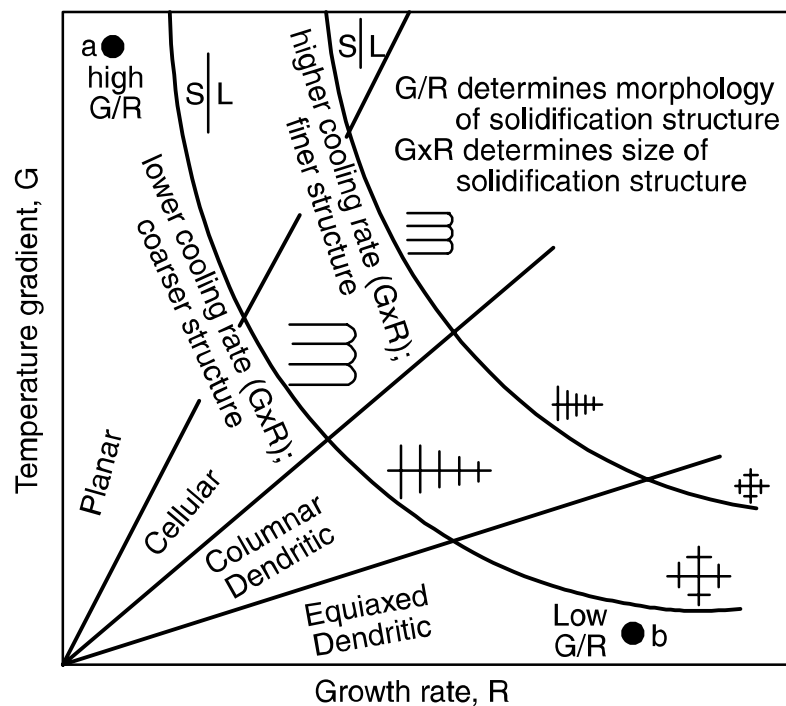
Figure 5.3. Effect of temperature gradient G and growth rate R on the morphology and size of solidification microstructure [8]

Based on the aforementioned conditions, it becomes clear that the growth stability and the quality of the crystals produced by LFZ method are affected by several parameters that need to be experimentally controlled [2,3]. A successful growth requires a very stable molten zone, which is strongly affected by the quality of the precursor rods and their alignment [3]. High quality, dense and straight precursor rods are indispensable. Before starting the growth it is important to make a correct alignment of the seed and feed-rods, in order to ensure that they are concentrically aligned [2]. This step can be a very time consuming and plaguy, mostly if the precursor bars are not straight. However, this step is crucial to achieve a stable growth. It is also important to ensure that the rods alignment is maintained during the rotation process and during the growth. A proper alignment of the laser beam and optic

components is also crucial, since they have a strong influence in the temperature distribution inside the molten zone [2]. Moreover, the characteristics of the seed-rod have an important effect on the quality of the as-grown crystal. The use of an oriented crystalline seed facilitates the beginning of crystallization and the control over crystal orientation [2].

As explained above, laser power, growth rate, growth direction, feeding rate, rotation direction and speed of the seed and feed-rods are parameters that can be adjusted in order to obtain high quality crystals with the required characteristics. When a material is grown for the first time by the LFZ technique, it is necessary to make a preliminary study to optimize these parameters. The pulling rate, which defines the growth rate, is the parameter that has a more direct effect in the crystalline quality of the as-grown material [9]. By changing the growth rate, depending on the material, single crystal fibres, polycrystalline fibres or even amorphous materials can be grown by the LFZ method [9]. The maximum laser power is related with the melting temperature of the material. The control of this parameter determines the temperature of molten zone and the temperature gradient at the solidification interface. Moreover, it also affects the size of the produced molten zone and the viscosity of the melt [9]. These parameters have a strong influence on the temperature at the crystallization front [9]. When the material is pulled at a high rate, the temperature in the crystallization front quickly decreases without giving enough time for diffusion to occur. As such, usually, high growth rates lead to the crystallization of texturized polycrystalline fibres or even amorphous fibres, while single crystals can be produced when low growth rates are used [9]. But, as mentioned above, this will be very dependent on the material nature and, in some cases, it is possible to grow single crystals at relatively high pulling rates comparatively to the rates used to grow the same material by other methods (typically 60× faster than the growth rates used in *Czochralski* method [3]).

The rotation rate is responsible for the creation of a pattern of forced convection flows within the molten zone that is favourable for the homogenization of temperature and composition [2,9]. The appropriated rotation speed strongly depends on the material to be grown and it is optimized experimentally for each material. In some cases, even though it is beneficial for temperature and composition homogenization, the rotation originates instability during the growth and the formation of defects in the as-grown crystal [2].

5.1.2 The LFZ System

The LFZ system used in this work was the one available at the Physics Department of University of Aveiro. This system is essentially constituted by a growth chamber, a laser (with respective alimentation source and cooling system), four motion motors (two motors

for longitudinal motions and another two for rotation), a computer with the software that controls all the system (see Figure 5.4-left) a video camera and a display monitor that allows to monitoring the growth.

Two different laser sources are available, a Nd: YAG laser (Quanta system, Qy-50) with 1064 nm wavelength and output power of 50 W and a CO_2 laser (Spectron SLC) with 10.6 μm wavelength and variable output power until 200 W. Both lasers are coupled to a water-cooled chiller for refrigeration. To grow the zirconia single crystals the high power CO_2 laser was used.

The laser beam enters into the growth chamber through a ZnSe window, which is transparent to the laser wavelength radiation. Inside the chamber an optical system and two concentric bars, the pedestals, where the rod precursors are fixed, constitute some of the elements necessary to the growth. The optical system, that is used to direct and converge the laser beam to the feed-rod top, is composed by a reflexicon, a flat and a parabolic gold-coated mirrors. The reflexicon is an indispensable optical component used to convert the cylindrical laser beam into a circular crown-like one (Figure 5.5). The planar mirror reflect the circular crown beam to the parabolic mirror that converges the beam at its focal plane. Both the planar and the parabolic mirrors have a centre hole that allows the seed and feed pedestals pass through. The pedestals are precisely concentrically aligned with the focal plane of the parabolic mirror.
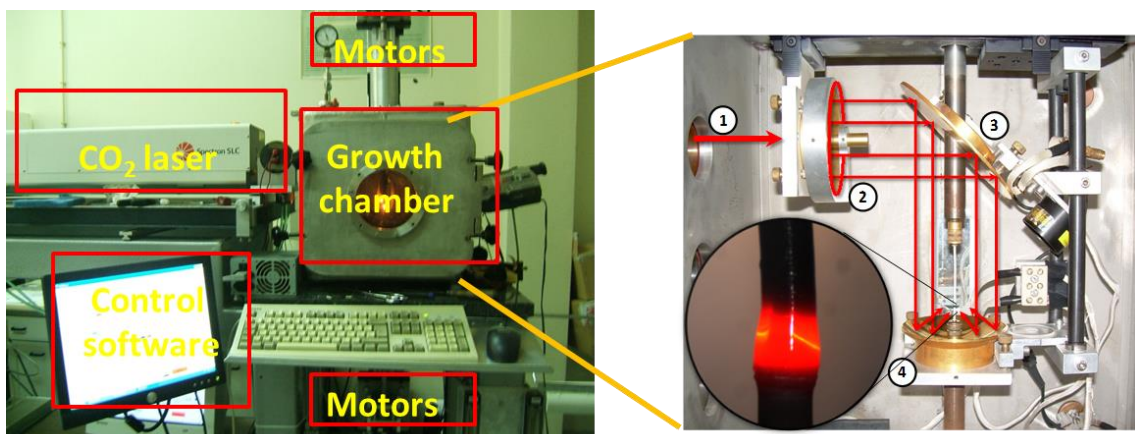
Figure 5.4. Left-photograph of the LFZ system used in this work. Right-photograph of the inside of the growth chamber (1-laser beam, 2-reflexicon, 3-planar miror, 4-parabolic mirror).

The pedestals are metallic cylindrical bars with screw systems on the top that allow to fix the precursors rods. Each one of the pedestals is connected to two motors, one that produce a longitudinal motion and the other one for rotation. The longitudinal motion can be either

upward or downward, allowing to select the growth direction. In the same way, the pedestals can rotate clock- or anticlockwise, either in the same direction or in opposite directions.

Laser power, growth and feeding rates and rotation velocities can be controlled independently using the software. The growth process can be visualized in two different ways. The first one is by a direct observation through a window placed in the door of the growth chamber, which has a set of polarizers that allow to control the intensity of the light that passes through. Alternatively, the process can also be visualized using a video camera placed in the opposite direction of the laser beam entrance. The image captured by the video camera is displayed in the computer monitor. The use of the video camera allows a closer visualization of the process by increasing the magnification of the growth region. Moreover, the visualization through the video camera is safer since it prevents any damage in the observer eyes by the light intensity.
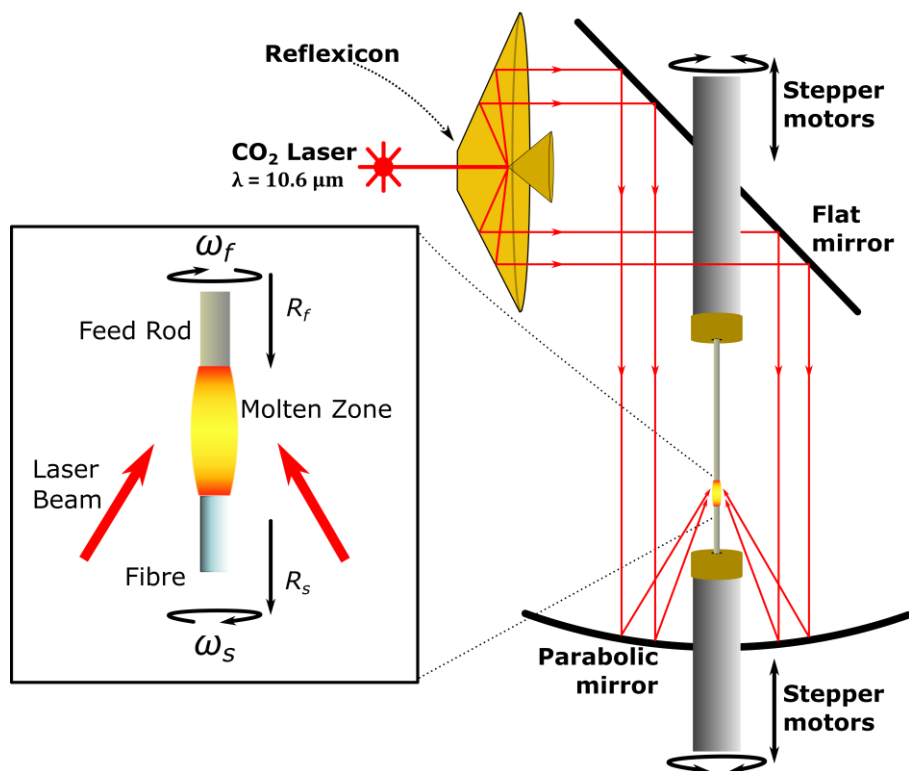
Figure 5.5. Schematic representation of the LFZ technique (adapted from [10]).

The growth camera is completely sealed from the exterior, and adapted to the growth in different gas atmospheres. Additionally, this LFZ system is adapted in order to introduce an electric current flow through the crystallization interface during the crystal growth. For that, a set of electrical contacts are available inside the growth chamber, which are

connected to an external electrical current source. The application of an electrical current flow has an important effect on the quality and microstructure of the as-grown crystals [11].

The preparation of the precursor rods is the first step in the growth of crystals by LFZ. There are different approaches that can be used for the preparation of the rods including, for example, piece of dense ceramics, cold extrusion, fusion and isostatic pressing [3].

The cold extrusion is the most advantageous due to its simplicity and the possibility to produce rods with a cylindrical shape that is the most appropriated form to achieve a homogeneous radial distribution of temperature by laser irradiation. The precursor rods used in this thesis work were prepared by a cold extrusion method. Stoichiometric amounts of precursor powders, in this case commercially available metal oxides (purity above 98 %), were mixed in a motor rotator, at 300 rpm by 1h. After, an organic ligand, a polyvinyl alcohol (PVA) in water, was added to the powder in order to obtain a conformable plastic mixture. This mixture is then extruded by pushing it through a cylindrical die, with 1.5 mm of diameter. The extruded cylindrical rods are placed in an appropriated holder, where they can dry at RT for 2-3 days without warp.

After the rods are dried they can be used as precursors in the LFZ growth system. For that, a long rod is used as feed-rod and a small piece is used as seed. The two rods are fixed to the pedestals and are carefully concentrically aligned. After the alignment, the rotation of the rods is initialized and the infrared CO_2 laser is turned on. The laser power is slowly increased until a molten drop is formed on the top of the feed-rod. At this point, the seed is dipped in the molten drop and the growth is initialized at a selected rate. Sometimes, during the first instants of the growth it is necessary to make slightly adjustments in some of the growth parameters, including laser power, rotation rates and feed rate, in order to achieve a stable growth. Figure 5.6 shows a simple diagram representing the different steps in the LFZ growth.

Stoichiometric amounts of metal oxide precursors
(ZrO_2, Y_2O_3 and Ln oxides)

Planetary ball mill
- 300 rpm
- 1 hour

Homogeneous mixture of precursor powders

Addition of PVA sol.

Conformable mixture of powders

Extrusion and drying of the rods
- RT
- 2-3 days

Dried precursor rods

LFZ crystal growth
- rods alignment
- parameters definition
- growth initialization

Grown crystal

Figure 5.6. Diagram of the precursor's rods preparation for crystal growth by LFZ.

In this thesis, different lanthanide doped YSZ crystals were grown by LFZ technique. These bulk crystals are good reference samples for the characterization of the luminescence features of Ln^{3+} in YSZ lattice and for comparison with the luminescent properties of the nanosized materials with the same composition. Before starting to grow doped single crystals, several growth parameters were adjusted experimentally in undoped yttrium stabilized zirconia composition. Two compositions of yttrium stabilized zirconia ($Zr_{0.92}Y_{0.08}O_2$) and ($Zr_{0.84}Y_{0.16}O_2$) were selected, based on the phase diagram of the ZrO_2-$YO_{1.5}$ system and in the literature, in order to prepare yttrium stabilized tetragonal (t'-YSZ) and yttrium stabilized cubic (c-YSZ) zirconia phases, respectively [1]. After experimental optimization, appropriated parameters were selected for the growth of doped YSZ crystals with Ln ions. It must be mentioned that in some cases, depending on the characteristics of the precursor rods, an adjustment of the experimental parameters from the predefined ones

was necessary. Table 5.1 displays the list of the produced LFZ crystals that were studied in this work and the principal parameters used in the growth. Additional information about the growth of each one of these crystals can be found in the respective discussion in the section 5.2.

Table 5.1. Identification of the crystals growth conditions used in the LFZ growth.

Sample identification	Dopant	Composition		Growth rate (mm/h)	Seed/feed rotation (rpm)	Laser power (W)
		mol.% $YO_{1.5}$	at.% Ln^{3+}			
t'-YSZ_20mm/h	undoped	8	-	-20	+5/-5	130-150
t'-YSZ_40mm/h		8	-	-40		
t'-YSZ_100mm/h		8	-	-100		
c-YSZ_20mm/h		16	-	-20		
c-YSZ_50mm/h		16	-	-50		
c-YSZ_100mm/h		16	-	-100		
t'-YSZ_3Eu_40mm/h	Eu^{3+}	8	3	-40	+5/-5	130-145
t'-YSZ_1Eu_40mm/h			1			
t'-YSZ_0.5Eu_40mm/h			0.5			
t'-YSZ_0.2Eu_40mm/h			0.2			
t'-YSZ_3Tb_40mm/h	Tb^{3+}	8	3	-40	+5/-5	130-140
t'-YSZ_1Tb_40mm/h			1			
t'-YSZ_0.5Tb_40mm/h			0.5			
t'-YSZ_0.2Tb_40mm/h			0.2			
t'-YSZ_0.05Dy_20mm/h	Dy^{3+}	8	0.05	20*	+5/-5	130-140
t'-YSZ_0.1Dy_20mm/h			0.1			
t'-YSZ_0.2Dy_20mm/h			0.2			
t'-YSZ_0.5Dy_20mm/h			0.5			
t'-YSZ_1Dy_20mm/h			1			
t'-YSZ_3Pr_40mm/h	Pr^{3+}	8	3	40*	+5/-5	120-130
t'-YSZ_3Sm_40mm/h	Sm^{3+}	8	3	40*	+5/-5	115-120
t'-YSZ_3Nd_40mm/h	Nd^{3+}	8	3	40*	+5/-5	100-120
t'-YSZ_0.3Tm_20mm/h	Tm^{3+}	8	0.3	-20	+5/-5	135
t'-YSZ_0.3Tm1Yb_20mm/h	Tm^{3+}/Yb^{3+}	8	0.3/1	-20	+5/-5	120-135
t'-YSZ_1Yb_20mm/h	Yb^{3+}	8	1	-20	+5/-5	135
t'-YSZ_1Er_40mm/h	Er^{3+}	8	1	-40	+5/-5	115-120
t'-YSZ_1Er1Yb_40mm/h	$Er3+/Yb^{3+}$	8	1/1	-40	+5/-5	115-120

* The precursor was firstly pulled at a high speed (100-150 mm/h) downward in order to densify and then the growth occur upward.

5.2 Results and discussion

5.2.1 Optimization of growth parameters in undoped YSZ

The starting point to the growth of any material by LFZ is the determination of the conditions in which the growth will be stable. Parameters like growth direction and rotation rates, as well as the optimum characteristics of the precursor rods, need to be optimized individually and experimentally for each material until stable growth conditions are achieved. In this work, these growth conditions were optimized experimentally for zirconia materials stabilized under two compositions: 8 mol.% $YO_{1.5}$ stabilized in the tetragonal crystalline structure (t'-YSZ) and 16 mol.% $YO_{1.5}$ stabilized in the cubic one (c-YSZ).

For both studied compositions, downward growth conditions proved to be advantageous over upward conditions leading to more stable growth processes. It was observed that the decomposition of the organic ligand (PVA) generates gases inside the molten zone. Since the gas bubbles, with a lower density, have a tendency to flow up, when the crystals were grown upward these gases inside the molten were retained in the as-grown crystals, creating defects, such as bubbles. In some cases, it was noticed that radial cracks are developed periodically in the upward growth crystals, at the same time that these gases were released from the melt. In contrast, for a downward growth the incorporation of this type of defects was strongly reduced and the stability of the process was increased.

Additionally, the movement of the gases inside the melt, due to convection currents, and their release to the atmosphere originates a wagging of the molten zone. In situations in which wagging was strong, the separation of the two rods, by the molten region, or even the break of the feed-rod occurred. This effect seems to be strictly related with the rods characteristics. Minimum amounts of PVA added to the precursor powders decrease the amount of produced gases and, as consequence, increased the process stability. Moreover, the quality of the precursor rods revealed to be an important factor that strongly determines the growth stability and crystal growth reproducibility. Slight warping of the cylindrical precursors or slight misalignment of the laser beam resulted in most cases in cracks inside the crystal during the growth process.

Regarding the optimization of the rotation rates, a higher stability of the growth was achieved for opposite rotation directions of the seed and feed-rods. On the other hand, the maximum limit of the speed rotation was found to be strongly dependent of the alignment of the rods during the process. In general, rotation velocities around 5 rpm revealed to be

enough for the homogenization of temperature and composition in the melt resulting on stable growths. In summary, downward growth, with rotation velocities around 5 rpm in opposite directions and precursor rods without warping and with low amount of PVA, in general leads to a stable growth of both t'-YSZ and c-YSZ crystals. Figure 5.7 shows some photos of the crystals grown at different rates for the two studied compositions, after optimization of experimental parameters. A visual inspection of the crystal shows that, while the ones stabilized with 8 mol.% $YO_{1.5}$ exhibit a more translucent aspect, the ones stabilized with 16 mol.% $YO_{1.5}$ are completely transparent, colourless, uniform and inclusions free.
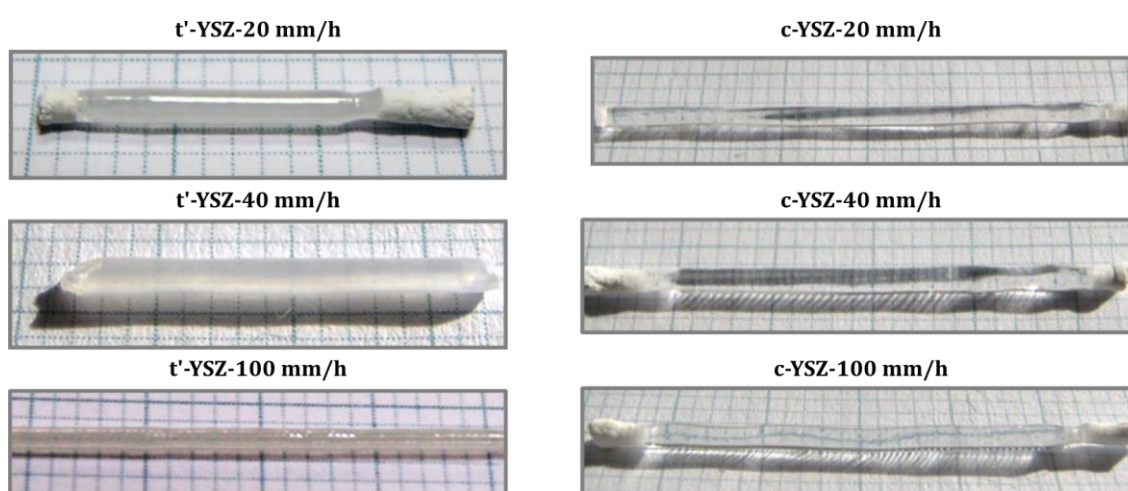
Figure 5.7. Photos of undoped YSZ crystals grown by LFZ at different growth rates. (t'-YSZ refers to compositions of 8 mol.% $YO_{1.5}$ and c-YSZ to 16 mol.% $YO_{1.5}$).

This high transparency suggests the crystallization and stabilization of cubic structure of zirconia, as expected by the analysis of the phase diagram of the ZrO_2-$YO_{1.5}$ system (Figure 3.7, section 3.3). Cubic zirconia is well known by their high transparency and high refractive index which provide an exceptional transparent ceramic [12].

The structure of the as-grown crystals was analysed by Raman spectroscopy. Figure 5.8 shows the Raman spectra of the as-grown crystals acquired in a backscattering configuration at RT and with 325 nm wavelength He-Cd laser line excitation. The addition of 8 mol.% $YO_{1.5}$ to zirconia promoted the stabilization of non-transformable tetragonal (t') phase at RT as evidenced by the Raman spectra shown in Figure 5.8 a). As referred in section 4.3, group theory analysis of tetragonal zirconia structure predicts that six Raman phonon modes are active in Raman with the symmetries A_{1g}+ $2B_{1g}$+ $3E_g$. Despite a non-observed peak near 146 cm^{-1} that falls out of the studied spectral range, the vibrational

frequencies found in the Raman spectra are in fair agreement with those assigned in other work to the tetragonal zirconia [13–16].
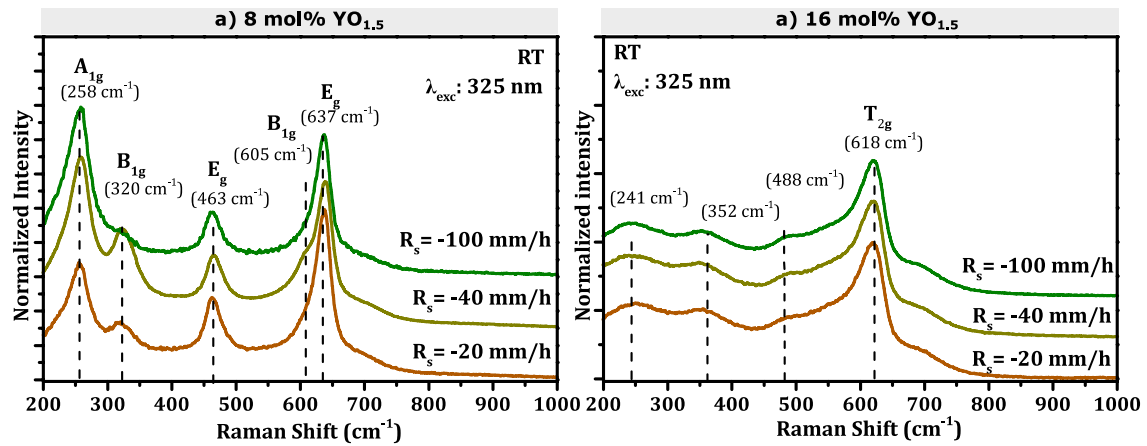
Figure 5.8. Raman spectra of undoped YSZ crystals stabilized 8 mol.% YO$_{1.5}$ (a) and 16mol.% YO$_{1.5}$ (b) grown at different rates. The spectra were acquired in a backscattering geometry at RT, under excitation of 325 nm wavelength of a He-Cd laser line.

In the case of zirconia crystals stabilized with 16 mol.% YO$_{1.5}$, Raman spectra evidences a predominant peak centred at ~618 cm^{-1} and a structured broad Raman band at lower wavenumbers. As already mentioned, for such composition the crystallization of cubic fluorite structure is expected and therefore only one Raman band with T$_{2g}$ symmetry in the 1st order Raman effect is expected [17]. It should be mentioned that, in stabilized zirconia Y^{3+} ions randomly replace some of the Zr^{4+} ions in the cubic structure, and consequently oxygen vacancies are formed to maintain charge neutrality. As a result, the cation positions of the lattice are randomly occupied by both Zr^{4+} and Y^{3+}, while anion positions are occupied both by oxygen ions and oxygen vacancies. Consequently, this disorder induced loss in translational symmetry of the crystal leads to a breakdown of the $\vec{q} = 0$ selection rule and to spectra that resembles the one-phonon density of states. In fact, Raman spectra similar to the ones obtained to the crystals stabilized with 16 mol.% YO$_{1.5}$ have been reported to the stabilized distorted cubic phase of zirconia [17,18].

The PL properties of the tetragonal and cubic undoped YSZ crystals were acquired at RT under UV excitation, using the 325 nm line of a cw He-Cd laser. Figure 5.9 shows the RT PL spectra acquired for the tetragonal crystal grown at 100 mm/h and for the cubic crystal grown at 20 mm/h. Under UV excitation, the undoped crystals exhibit an unstructured broad emission band with maxima around 550 nm (2.25 eV).
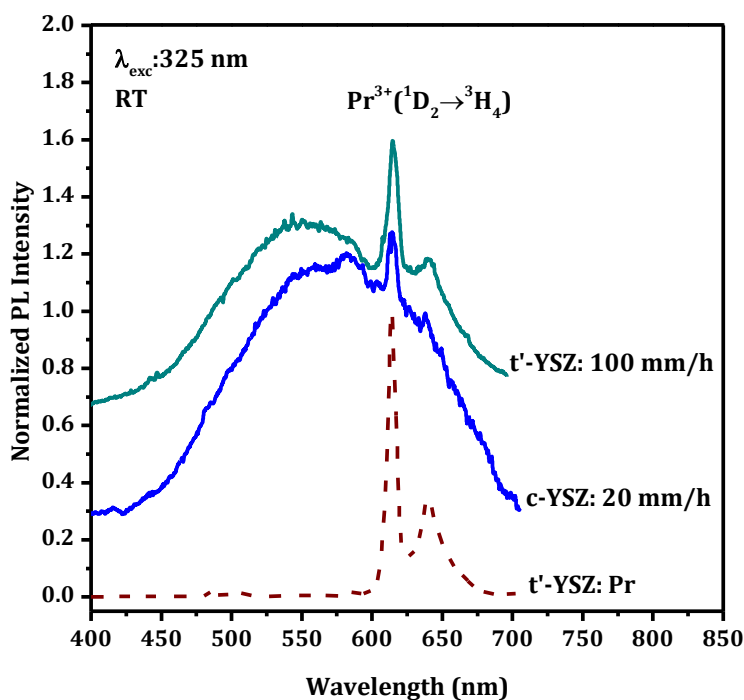
Figure 5.9. RT PL spectra of undoped YSZ cubic crystal grown at 20 mm/h and tetragonal YSZ crystal grown at 100 mm/h under 325 nm He–Cd laser line excitation. For comparison the RT PL spectrum of a praseodymium doped tetragonal YSZ crystal is also shown.

While for the cubic phase this broad emission band was observed in the crystal grown at lower pulling rates, in the tetragonal crystals the broad emission was only observed in the ones grown at higher growth rates. Broad unstructured deep level recombination in the yellow/orange spectral region have been observed in the different ZrO_2 polymorphs and assigned to F-type defects, involving the oxygen vacancy and their complexes [19–22]. Overlapped with the F-type emission band, the as-grown crystals show an additional emission in the red region with pronounced maxima at ~614 nm (2.02 eV) and 641 nm (1.93 eV). As the peak position and spectral shape of the observed lines match those of the transition between the $^1D_2$ and $^3H_4$ multiplets of the Pr^{3+} ion [23–26], it is likely that praseodymium ions could be present as precursor's contaminants in the as-grown crystals. Actually, praseodymium doped tetragonal YSZ were further produced and characterized, confirming the above assumption, as shown by the dashed line in Figure 5.9.

5.2.2 Ln-doped YSZ crystals

The experience and knowledge acquired during the growth of undoped YSZ crystals was applied in the growth of YSZ crystals doped with different Ln ions. Zirconia crystals stabilized with 8 mol.% $YO_{1.5}$ (t'-YSZ) and doped with several Ln ions were successfully grown by the LFZ process. As referred in section 5.1.2, the lanthanide ions were *in situ*

126

doped during the crystal growth, by adding the appropriate amount of the respective Ln oxide powder to the precursor rods.

Figure 5.10 displays some photos of the as-grown crystals of t'-YSZ (8 mol.% $YO_{1.5}$) doped with different lanthanide ions, including praseodymium (3 at.% Pr), europium (0.2-3 at.% Eu), erbium (1 at.% Er), cerium (3 at.% Ce), terbium (3 at.% Tb), thulium (0.3 at.% Tm), samarium (3 at.% Sm), dysprosium (0.1 at.% Dy) and ytterbium (1 at.% Yb). As can be observed, the incorporation of Pr, Tb, Ce and Er ions in 8 mol.% $YO_{1.5}$ stabilized zirconia crystals lead to a coloured crystal. In the case of Pr and Tb ions, the doping give rise to crystals with an orange colour, while in crystals doped with Nd and Er ions, a faint pink colour is observed. Tetragonal YSZ crystals co-doped with Er, Yb and Tm, Yb were also grown and studied.
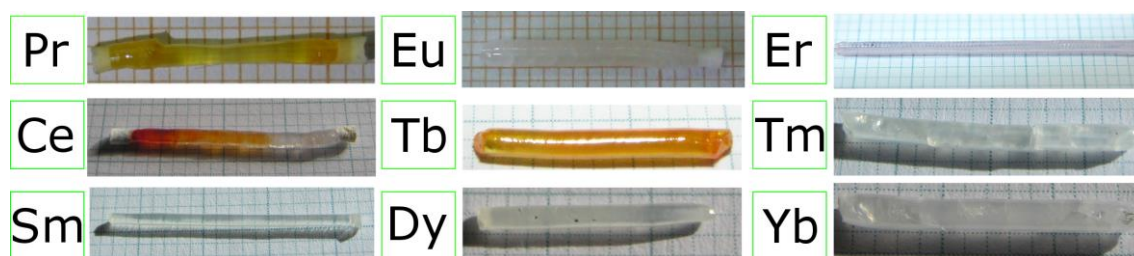
Figure 5.10. Photos of t'-YSZ crystals doped with different lanthanide ions.

In addition to the growth of Ln ions doped t'-YSZ crystals, the growth of c-YSZ doped with Ln ions was also explored. However, in this case, the growth of the crystals was a very hard task. It was observed that, after few millimetres of crystal grown, several cracks were developed along the crystal, resulting in their shattering and forcing to interrupt the growth.

As can be observed by the Raman spectra shown in Figure 5.11, performed in a small piece of one of these shattered crystals, the cubic phase is stabilized at RT. Such indicates that the occurred crystal cracking is not associated to the volume expansion resultant of the phase transition during cooling, as the cubic phase remains in the cracked crystals. A possible explanation could be the high crystal stress induced by the large concentration of the added stabilizer and dopant, together with a strong temperature gradient between the molten zone and the as-grown crystals characteristic of the LFZ process.
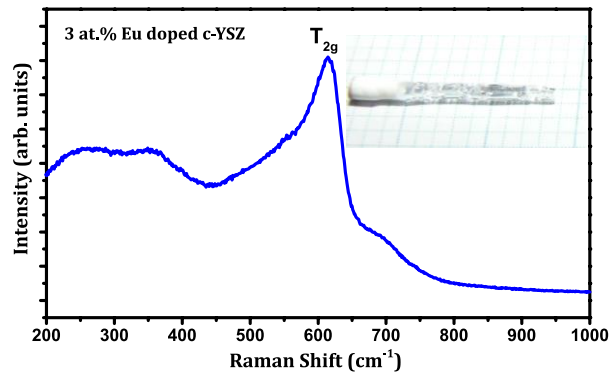
Figure 5.11. Raman spectrum of shattered crystals of cubic YSZ doped with 3 at.% Eu. The spectrum was acquired in a backscattering geometry at RT, under excitation of 325 nm wavelength of a He-Cd laser line. The inset in the figure shows a photo of a piece of the cubic YSZ crystal doped with europium with several cracks along it.

In an attempt to decrease cracks development, the total amount of dopant plus stabilizer was decreased to 16 mol.% (the same used for the undoped crystals). In addition, the precursor feed-rod was firstly pulled down at a high rate (150 mm/h) in order to increase their density and decrease the amount of gases released during the growth. The diameter of the precursor rod was also decreased. The dense rods, with several cracks along them, were used as precursor for the growth by pulling in the opposite direction. Several growth rates were tested within the rage of 5-100 mm/h. In the end, it was possible to grow crystals without any cracks. However, when the laser was turned off at the end of the growth process, instantaneously cracks appear and diffuse along all the crystals leading to their shattering. In an attempt to decrease this effect, the power of the laser (and consequently the temperature of the molten zone) was reduced very slowly. However, this effort was not enough to avoid the cracks propagation and crystal break. Such results hindered the production and study of intact cubic crystals doped with Ln ions. In the following, the properties of the tetragonal crystals doped with different lanthanide ions will be explored.

5.2.2.1 Eu^{3+} doped t'-YSZ crystals

Trivalent europium ion (Eu^{3+}), with a $4f^6$ valence configuration, is a very special ion within the trivalent lanthanide ions and its luminescence properties have been studied in several inorganic hosts due to their importance as a red emitter. Eu^{3+} are known to be spectroscopic probes in different hosts due to the simplest structure of its $^{2S+1}L_J$ multiplets with nondegenerate first excited and ground levels, $^5D_0$ and $^7F_0$, respectively [27]. In addition, the number of Stark components and intensity ratio of the $^5D_0 \rightarrow {}^7F_J$ transitions are typically used for acquiring information about the symmetry at the Eu^{3+} site. Usually, optically active Eu^{3+} inserted in inorganic hosts give rise to long lived orange/red emission due to $^5D_0 \rightarrow {}^7F_J$ transitions which are of interest for applications in different fields, including as bioprobes as

referred above. In order to study the luminescent properties of Eu^{3+}, crystals of zirconia stabilized with 8 mol.% $YO_{1.5}$ and doped with 0.2, 0.5, 1.0 and 3.0 at.% Eu were grown by LFZ, following the process described in section 5.1.2. Crystalline fibres, with diameter around 2 mm and 20 mm length were grown in the same conditions at 40 mm/h in air at atmospheric pressure.

The crystal microstructure was characterized by SEM with energy dispersive spectroscopy (EDS) on polished surface of the longitudinal crystals section. The structural characterization was accomplished by Raman spectroscopy in backscattering configuration by using a 325 nm line of a He-Cd laser.

Steady state PL measurements were carried out between 14 K and RT by excitation with the same He-Cd laser, a 457 nm laser line and a 1000 W Xe arc lamp coupled to a monochromator. The used excitation energies correspond to energies below the tetragonal zirconia gap which was predicted by theoretical models as 6.4 eV [28]. Besides the PL analysis, the samples were also studied by RT PLE with the emission monochromator set to the Eu^{3+} emission lines and the excitation wavelength scanned up to 240 nm.

Structural and microstructural characterization

The structural characterisation performed by Raman spectroscopy revealed that the as-grown material crystallized in the tetragonal structure (t') of zirconia, as shown in Figure 5.12 a) where only the typical bands assigned to the vibrational modes of tetragonal zirconia with symmetries $A_{1g} + 2B_{1g} + 2E_g$ were recognized. Tetragonal phase of zirconia was identified for all the produced crystals even for the ones with high concentration of Eu^{3+} dopant, which also acts as a stabilizer of the high temperature phases of zirconia at RT.

The morphological analysis of the longitudinal section of the grown crystals shows a uniform surface without grain boundaries or second phases, suggesting its monophasic and monocrystalline character, as shown in the SEM images in Figure 5.12 b) and c) for the crystal doped with 3 at.% Eu. In addition, no bubbles defects were observed. The EDS analysis shows a uniform distribution of both yttrium and europium along the crystal diameter and axis, Figure 5.12 d).
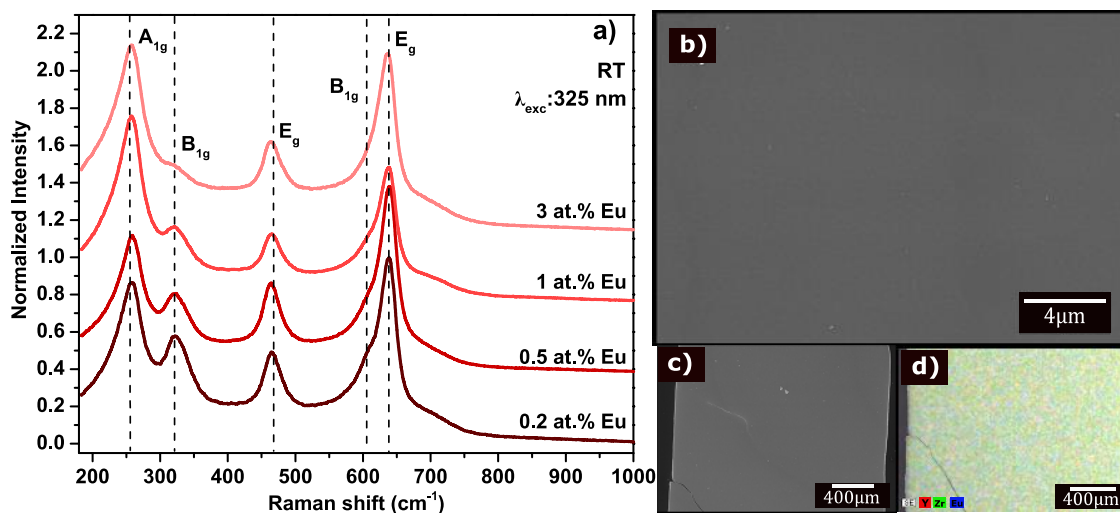
Figure 5.12. a) Raman spectra performed under backscattering configuration with 325 nm excitation, of the tetragonal YSZ crystals doped with different concentration of europium. SEM micrographs of longitudinal sections of the 3 at.% Eu doped crystal: b) general view; c) high magnification and d) EDS maps of Zr, Y and Eu distribution along the crystal diameter.

Luminescence characterization

The RT PL spectra of the t'-YSZ crystals doped with different amounts of Eu^{3+} are shown in Figure 5.13 a). The luminescence of europium doped t'-YSZ crystals under 266 nm wavelength excitation clearly evidences the fingerprints transitions between the $^5D_0$ and $^7F_{J(0-4)}$ multiplets of Eu^{3+} ions. The dominant emission line occurs in the red region at ~606 nm, corresponding to the forced electric dipole assisted $^5D_0 \rightarrow {}^7F_2$ transition. Given the absence of inversion symmetry, the spectra display additional lines, ascribed to the following transitions: ~579 nm, the strictly forbidden $^5D_0 \rightarrow {}^7F_0$; ~591 nm, the parity allowed magnetic dipole induced $^5D_0 \rightarrow {}^7F_1$; ~635 nm, a weak mixed character $^5D_0 \rightarrow {}^7F_3$; ~714 nm, the electric dipole assisted $^5D_0 \rightarrow {}^7F_4$. As result of the intense $^5D_0 \rightarrow {}^7F_J$ emission lines the Eu^{3+} doped crystals show a bright orange/red luminescence under UV excitation, observed by naked eye as shown in Figure 5.13 c) for the crystal doped with 3 at.% Eu^{3+}. Dexpert-Ghys *et al.* [29], in their work on yttria-doped zirconia ceramics, have shown the PL spectra of Eu^{3+} ions in samples with different monoclinic, tetragonal and cubic polymorphs. Our data shown in Figure 5.13 a) corroborate their results for the europium emission peak positions and intensity ratio of the $^5D_0 \rightarrow {}^7F_J$ transitions in t'-YSZ. One can see that no differences on spectral positions of the emission or in the relative emission intensities were observed in the crystals doped with different amounts of Eu^{3+} indicating that the emission comes from the same Eu^{3+} optical centres and that the increase in Eu^{3+} concentration does not affect the surrounding ambient of the emitting Eu ions.
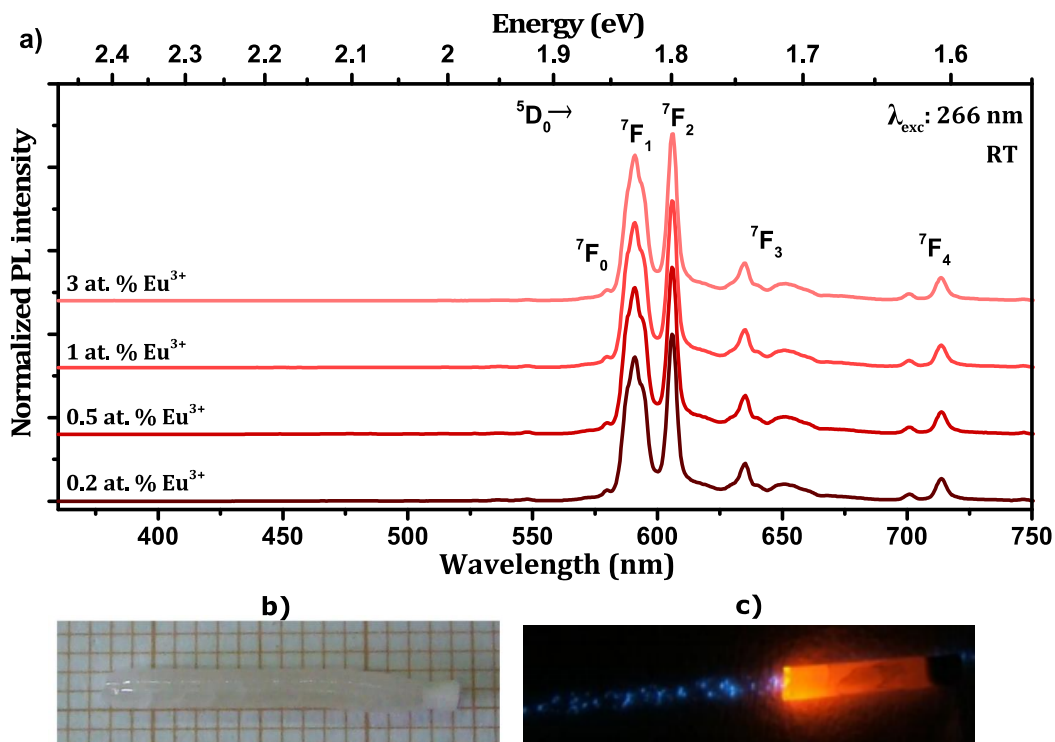
Figure 5.13. a) RT PL spectra of t'-YSZ crystals doped with different Eu³⁺ concentration under 325 nm He-Cd laser excitation. Photos of the crystal doped with 3 at.% Eu³⁺ without irradiation (b) and when irradiated with the UV light at RT (c).

Further analyses of the Eu^{3+} luminescence in the tetragonal YSZ crystals were performed in the crystal doped with 3 at.% Eu. Figure 5.14 shows a comparison between the 14 K and RT PL and PLE spectra of such sample. For both temperatures, under 325 nm excitation, the $^5D_J \longrightarrow {^7}F_J$ multiplets transitions occur at the same position, meaning that the emission comes only from the first excited state, $^5D_0$, even at RT. The number of transitions between the nondegenerate $^5D_0$ and $^7F_0$ multiplets is usually used to estimate the number of Eu^{3+} optically active centres in a crystalline lattice. For instance, this was the case observed for other oxide hosts crystals grown by the LFZ method [22,26]. The spectra shown in Figure 5.13 a) and Figure 5.14 a) evidence the presence of a $^5D_0 \longrightarrow {^7}F_0$ transition at ~579 nm. The appearance of this emission, together with a threefold Stark splitting of the $^5D_0 \longrightarrow {^7}F_1$, means that the emitting Eu^{3+} ions must lay at a lower symmetry than the expected tetragonal D_{4h} for the ion in a cation substitutional site. On the other hand, the full width at half maximum (FWHM) of the line (~5.3 meV) is rather large when compared with those of the $^5D_0 \longrightarrow {^7}F_0$ transitions in other oxides crystals grown by the same method. As an example, in Ta_2O_5 crystals, the FWHM is lower than < 1 meV [22,26]. The width of the $^5D_0 \longrightarrow {^7}F_0$ transition in ZrO_2 doped samples grown by different routes was also studied by others authors [29–31]. Particularly, site-selective spectroscopy measurements performed on the $^5D_0 \longrightarrow {^7}F_0$ transition [29,30] revealed different Eu^{3+}-centres in the samples.
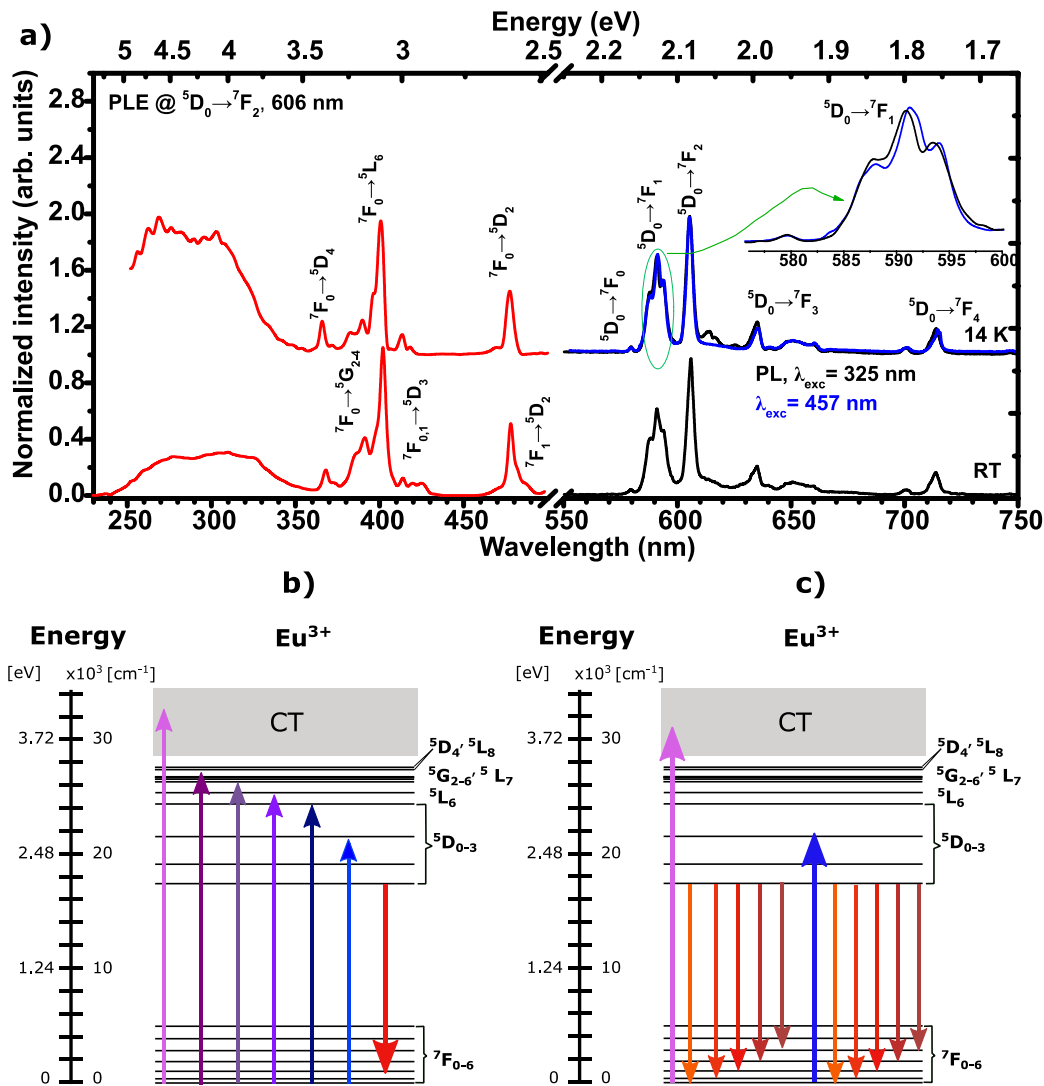
Figure 5.14. a) Comparison between the 14 K and RT PL and PLE spectra of 3 at.% Eu^{3+}doped t'-YSZ crystal. **b)** Representation of the absorption transitions that leads to the $^5D_0 \rightarrow {}^7F_2$ dominant Eu^{3+} emission, in accordance with the 14 K PLE spectra. **c)** Representation of observed intra-4f emission, under excitation in the CT/ 4f5d bands (325 nm) and resonantly in the $^5D_2$ levels of the intra-4f configuration (457 nm).

In order to investigate if the doped LFZ as-grown crystal exhibit multiple europium related optical centres, PLE and wavelength dependent excitation measurements were performed. The 14 K and RT PLE spectra monitored at the $^5D_0 \rightarrow {}^7F_2$ transition (606 nm) display the excitation paths for the observation of the Eu^{3+} luminescence, Figure 5.14 a) (red lines). The narrower lines are ascribed to several intra-4f^6 transitions between the ground state ^7F to the excited states ^5D, ^5L and ^5G multiplets. In addition to the sharper lines, the excitation spectra of Eu^{3+} luminescence shows two overlapping excitation broad bands with maxima at ~310 nm and ~270 nm. As referred in the section 2.1, in wide band gap hosts, apart the parity forbidden $f \rightarrow f$ transitions, the excitation spectra of Ln ions can exhibit broad absorption bands due to the parity allowed interconfigurational 4$f \rightarrow 4f\,5d$ and charge

transfer (CT) transitions [32,33]. The CT bands, also of interconfigurational nature, involve for instance the promotion of the ligand electrons to the metal ion and usually occur in the UV region [32–36]. In the particular case of Eu^{3+} in wide band gap oxide hosts, the promotion of an electron from the ground state configuration $4f^6$ to the lowest $4f^5 5d$ level occurs in the UV and vacuum UV spectral regions [32,33,35,36]. On the other hand, the CT transitions are known to occur at longer wavelengths than the $4f \rightarrow 4f^5 5d$ transitions and their peak positions are known to decrease in energy with larger average distance of the surrounding anions [35,36]. As the CT states are located at lower energies than those of the Eu^{3+} $4f^5 5d$ levels, the observed excitation bands with maxima at 310 and 270 nm could correspond to two different CT transitions, as also detected in other zircon based compounds [34]. These absorption transitions, which lead to the $^5D_0 \rightarrow {}^7F_2$ emission, are schematically represented in the diagram of energy level shown in Figure 5.14 b). Considering the relative integrated areas of the absorption bands in the PLE spectra, the Eu^{3+} luminescence from the $^5D_0$ level is preferentially populated by CT mechanisms rather than by light absorption into the intra-$4f^6$ Eu^{3+} excited levels. A comparison between the PL spectra obtained with excitation in the CT region and in the intra-$4f^6$ excited states (slightly above the $^5D_2$ level) can be observed in Figure 5.14 a) (blue and black lines). In both cases, the transitions intensity ratio are comparable but small shifts in the peak position of the $^5D_0 \rightarrow {}^7F_J$ transitions can be identified, as shown in the inset of Figure 5.14 a). Moreover, exciting the samples in the CT band and intraconfigurational absorption region leads to the appearance of additional lines in the $^5D_0 \rightarrow {}^7F_2$ spectral region, as highlighted in Figure 5.15, suggesting the presence of different Eu^{3+} optical centres in accordance with the observation by PLE.
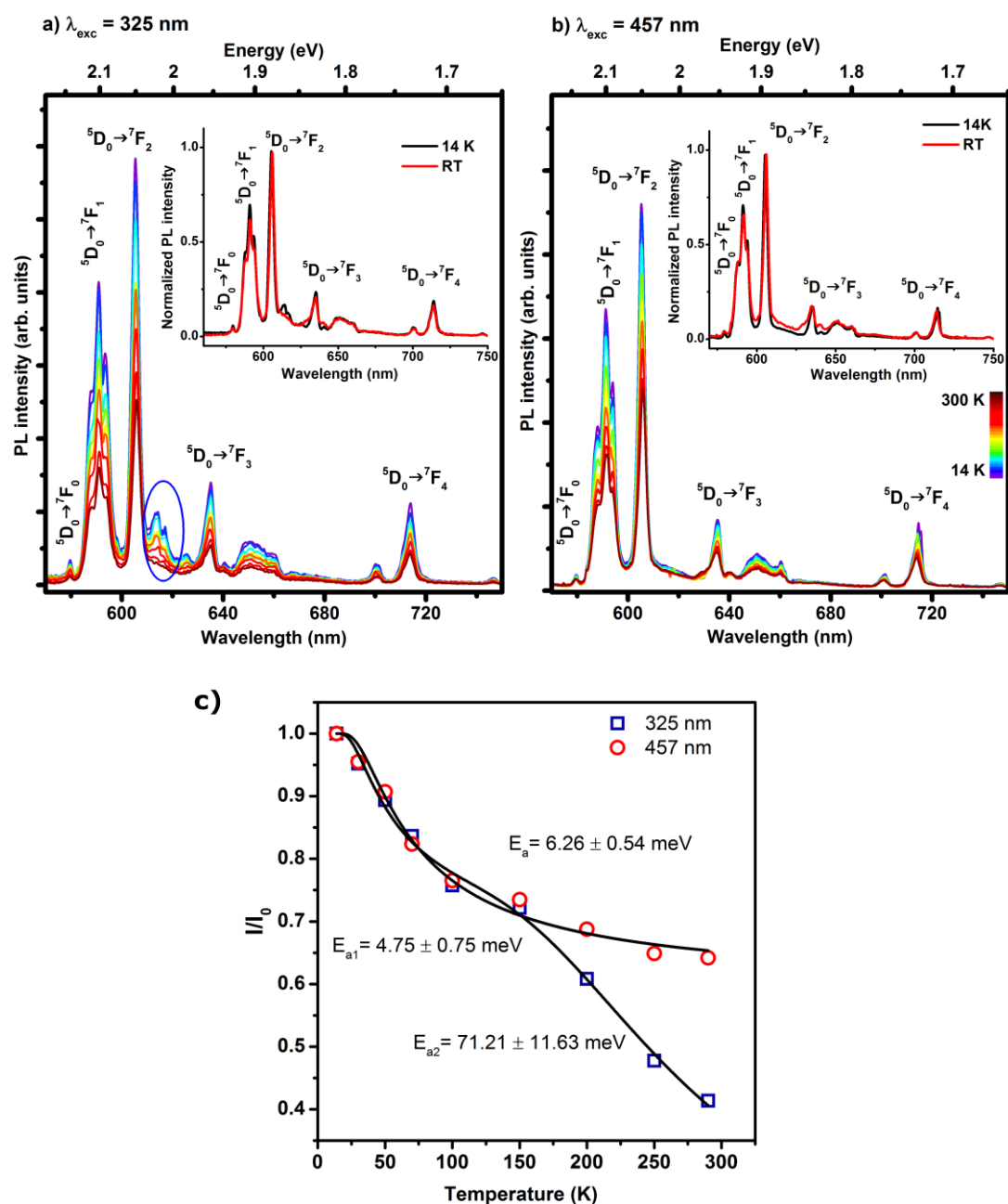
Figure 5.15. Temperature dependence of the Eu³⁺ luminescence, in the 3 at.% Eu³⁺ doped YSZ crystal, for two excitation wavelengths, 325 nm (a) and 457 nm (b). The insets depict the normalized PL intensity at 14 K and RT. c) Evolution of the integrated intensity of the overall luminescence with temperature.

The temperature dependence on the PL spectra of the 3 at.% Eu³⁺ doped YSZ crystal was studied for two excitation wavelengths, 325 nm and 457 nm, corresponding to the excitation via the CT band and $^5D_2$ energy level, respectively, Figure 5.15 a) and b). The temperature dependence of all the $^5D_0 \rightarrow {}^7F_{0-4}$ integrated intensity is shown in the Figure 5.15 c). The nonradiative deexcitation mechanisms of Eu³⁺-related centres are similar up to 150 K. However, for higher temperatures, a faster decrease in the PL intensity is observed when

the crystal is excited via the CT band indicating additional nonradiative deexcitation paths. Exciting the samples in the CT band, the RT PL intensity accounts for ~40% of the low temperature luminescence. With the excitation on the $^5D_2$ multiplet, a lower decrease in the integrated intensity is observed, ~60% of the low temperature intensity being still observed at RT. The activation energies involved in the thermal extinction process were determined by fitting the overall integrated intensity as a function of sample temperature, Figure 5.15 c), to the *Eq.* 4.15. Under intraconfigurational excitation (457 nm) the decrease of the emission intensity can be adjusted to a single thermal decay process with an activation energy (E_a) of ~6 meV. On the other hand, under excitation in CT band, two thermal decay processes were identified with activation energies E_{a1} and E_{a2} of ~5 meV and 70 meV.

Besides the analysis performed under steady state conditions, TR-PL spectra were measured for the 3 at.% Eu doped t'-YSZ crystal. The spectra were acquired under excitation with a pulsed (266 nm) laser at RT. The resultant time dependent emission spectra are shown in Figure 5.16 a). As can be observed, the Eu^{3+} emission corresponds to a slow luminescence that remains even 10 ms after the laser pulse. The inset in the Figure 5.16 a) displays a comparison between the emission spectra acquired at a time delay of ~0 and 11800 μs after the pulse excitation, revealing the same spectral dependence. As shown, all the emission bands follows the same decrease in intensity with time, and the relative intensity between the emission bands is the same at 11.80 ms after pulse and for t=0. In addition, luminescence decay curves of the emitting $^5D_0$ excited state were measured for a sample excitation in the CT band (325 nm) and resonantly in an intra-4f absorption levels of Eu^{3+} (402 nm). Figure 5.16 b) and c) display the two resultant decay curves. The curves can be well fitted into a single exponential decay with luminescence lifetimes, τ, around 2 ms as determined through the fit of the exponential depopulation decay expressed by *Eq.* 4.17. The obtained lifetime values are in the order of magnitude expected for the recombination between electronic states with different spin multiplicities, in line with the ones reported in literature for the $^5D_0$ emitting level of Eu^{3+} in tetragonal YSZ microtubes [37].
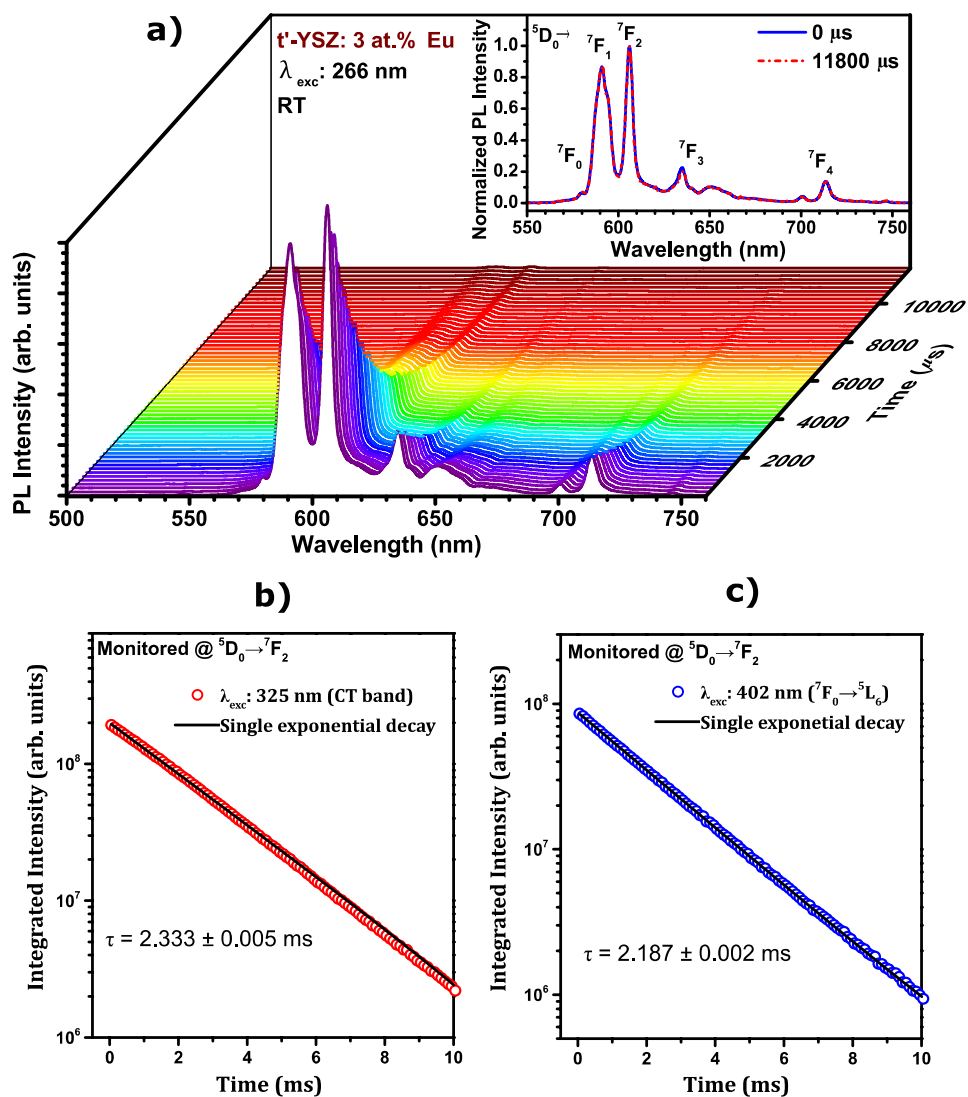
Figure 5.16. a) Time resolved photoluminescence spectra of the 3 at.% Eu^{3+} doped t'-YSZ crystal under 266 nm wavelength excitation. Luminescence lifetimes of the $^5D_0$ excited state upon excitation in the CT (b) and resonant in the intra-4f transitions.

Summary

Single crystalline fibres of tetragonal YSZ doped with different concentration of europium, with ~2 mm diameter and ~20 mm length were successfully grown by the LFZ technique at high pulling rates of 40 mm/h. The Eu^{3+} doped t'-YSZ as-grown crystals display an intense light guiding effect of the red emission at RT under UV excitation. Moreover, the crystals luminescence clearly evidence the fingerprint transition lines between the $^5D_0$ and $^7F_{J(0-4)}$ multiplets of the Eu^{3+}, being the main emission line in the red region at ~606 nm due to the forced electric dipole allowed $^5D_0 \rightarrow ^7F_2$ transition. No differences in the emission spectra of the crystals doped with different amounts of Eu^{3+} were observed indicating that the luminescence can be originated from Eu^{3+} in the same crystalline environments for all the studied concentrations. Additional studies were performed in the crystal doped with 3 at.%

Eu. PLE spectra show that Eu^{3+} ions are preferentially populated via high energy CT broad bands rather than via the intra-$4f^6$ configuration. Nevertheless, under the former excitation conditions, the detected $^5D_0 \rightarrow {}^7F_J$ luminescence at RT corresponds to 40% of its value at low temperature, while for an intraconfigurational excitation 60% of the intensity observed at low temperature is observed at RT, meaning that additional nonradiative paths occur under the CT excitation. The presence of different Eu^{3+} optical centres was discussed based on the observation of the two excitation CT bands and wavelength dependent PL spectra.

5.2.2.2 Tb^{3+} doped t'-YSZ crystals

Trivalent terbium (Tb^{3+}) is also a lanthanide ion with very interesting spectroscopic properties for green phosphors. This ion has a $4f^8$ electron configuration with a $^7F_6$ ground state level and a complex electronic excited states diagram [38]. When incorporated in wide band gap solid hosts, the visible emission of Tb^{3+} occurs predominantly in the green spectral region due to $^5D_4 \rightarrow {}^7F_J$ intra-$4f$ transitions. The green emission of Tb^{3+} is of particular interest for lighting application as it could be an alternative way to produce efficient green light. The luminescence properties of Tb^{3+} ions incorporated in stabilized tetragonal zirconia host were studied in this work. In such context, tetragonal zirconia crystals stabilized with 8 mol.% $YO_{1.5}$ and doped with 0.2, 0.5, 1.0 and 3.0 at.% terbium were grown by the LFZ process at 40 mm/h.

The crystalline structure was analysed by powder XRD and by RT Raman spectroscopy. For the PL measurements either a 325 nm laser line of a cw He–Cd laser or a Xe lamp coupled to a monochromator were used as excitation sources. For the PLE measurements the emission monochromator was set in the Tb^{3+} emission lines and the measurements were performed as described for the Eu doped crystals. Similarly, TR-PL spectra and decay times were studied.

Structural characterization

Figure 5.17 a) displays the RT Raman spectra performed with UV excitation of the as-grown crystals. As evidenced in the previous case, also the terbium doped crystals grown under the described experimental conditions were seen to be monophasic and exhibit a tetragonal crystalline structure. On one hand, the measured vibrational frequencies for these crystals corresponds exclusively to the ones expected for tetragonal structure [16,39]. On the other hand, and as observed in the Eu^{3+} doped crystals, the incorporation of a maximum of 3 at.% Tb in the YSZ host does not result in changes of the crystalline structure from tetragonal to cubic. The crystalline structure of the as grown crystals was further corroborated by XRD analysis. Figure 5.17 b) shows the XRD pattern after milling the crystal doped with 3 at.%

Tb. The XRD pattern matched well with the ICDD reference data of tetragonal structure of zirconia stabilized with yttrium belonging to the P4$_2$/*nmc* space group, with lattice parameters of *a*=*b*= 3.6309 Å, *c*= 5.1532 Å and α=β=γ = 90 ^{0} (assigned ICDD ref. 82-1243).
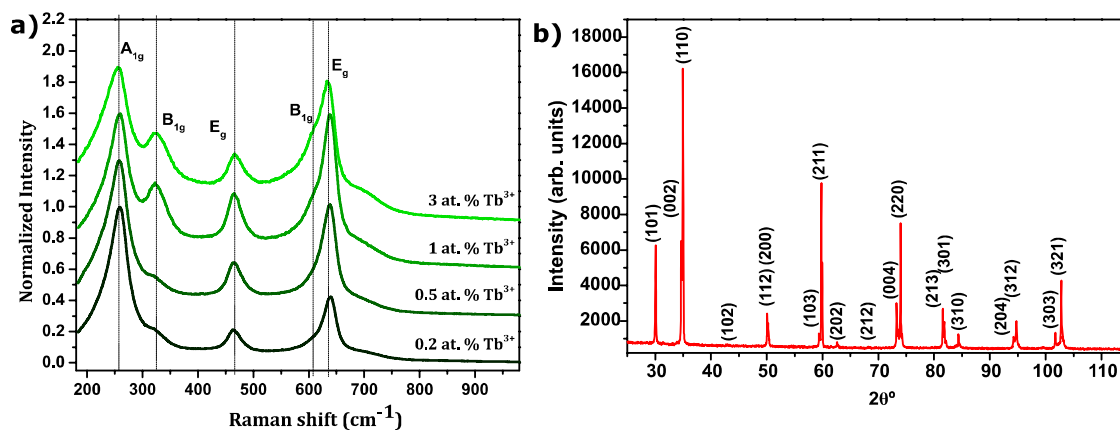

Figure 5.17. a) RT Raman spectra obtained in backscattering configuration with 325 nm He-Cd laser line of the crystals doped with different Tb concentrations. b) XRD pattern of the crystal doped with 3 at.% Tb³⁺ crystal after milling.

Luminescence characterization

The RT PL spectra of the t'-YSZ crystals doped with different amounts of Tb³⁺ are shown in Figure 5.18 a). The RT luminescence of terbium doped YSZ crystals under 325 nm wavelength excitation clearly evidences the fingerprints transitions between the ⁵D₄ and ⁷F$_{J(6-2)}$ multiplets of Tb³⁺ ions. The same Tb³⁺ intra-4*f* transitions have been also observed for other oxide hosts [40–47]. The strongest emission line occurs at 544 nm, assigned to the ⁵D₄→⁷F₅ transition, and is the responsible for the intense green emission at RT, observed by naked eye as shown in Figure 5.18 b) for the crystal doped with 3 at.% Tb³⁺. As happen for the crystals doped with different concentration of Eu³⁺, no differences on the spectral positions of the emission lines or in the relative emission intensity were observed in the crystals doped with different amounts of Tb³⁺ indicating that the emission comes from the same Tb³⁺ optically active centres and that the increase in Tb³⁺ concentration does not affect the surrounding ambient of the emitting Tb ions.
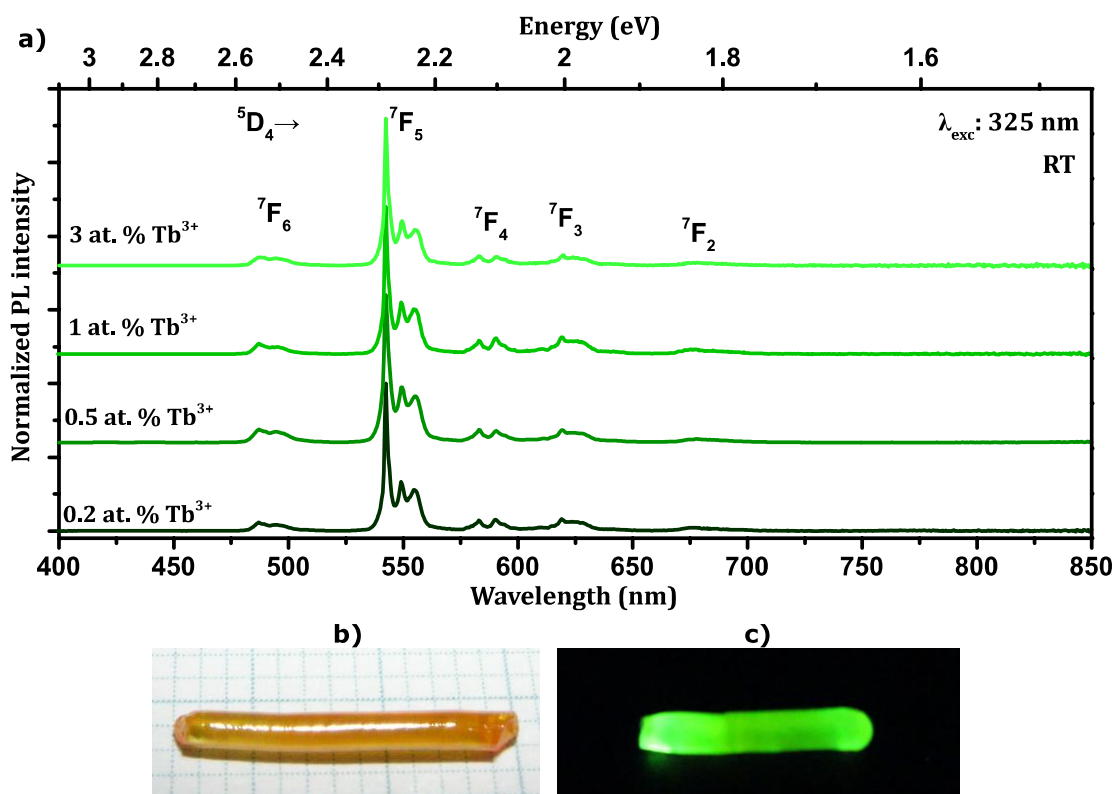
Figure 5.18. a) RT PL spectra of t'-YSZ crystals doped with different Tb³⁺ concentrations under 325 nm He-Cd laser excitation. Photography of the t'-YSZ:Tb³⁺ crystal without excitation (b) and under UV excitation (c).

Further analyses of the Tb^{3+} luminescence in the tetragonal YSZ crystals were performed in the crystal doped with 3 at.% Tb. The spectroscopic features of such t'-YSZ:Tb³⁺ crystal obtained under UV excitation (325 nm) at RT and 9 K are shown in Figure 5.19 a) and b), respectively. While at RT, the crystal luminescence (shown in logarithmic scale in Figure 5.19 a) is dominated by the transitions from the excited $^{5}D_4$ level to the lower lying $^{7}F_{J(6-2)}$ manifolds of the Tb^{3+} ions, at low temperature (9 K), besides the emission bands observed at RT, additional low intensity emission bands are observed in the high energy part of the spectrum. These lines correspond to the $^{5}D_3 \rightarrow ^{7}F_J$ transitions and their presence suggests that the minimum of the $4f^{7}5d^{1}$ potential energy is above to the one of the $^{5}D_3$ level, allowing the population of this excited state manifold [43,48]. Nevertheless, by increasing the temperature the $^{5}D_3 \rightarrow ^{7}F_J$ emissions intensities are greatly reduced, meaning that competitive nonradiative processes occur. In particular, cross-relaxation between the $^{5}D_3 \rightarrow ^{5}D_4$ and the $^{7}F_6 \rightarrow ^{7}F_0$ transitions and/or favourable nonradiative relaxation from the high energy feeding levels to the $^{5}D_4$ multiplet could be invoked to explain the higher average population of the $^{5}D_4$ level at RT, which leads to the observed predominant PL via this multiplet [43,48].
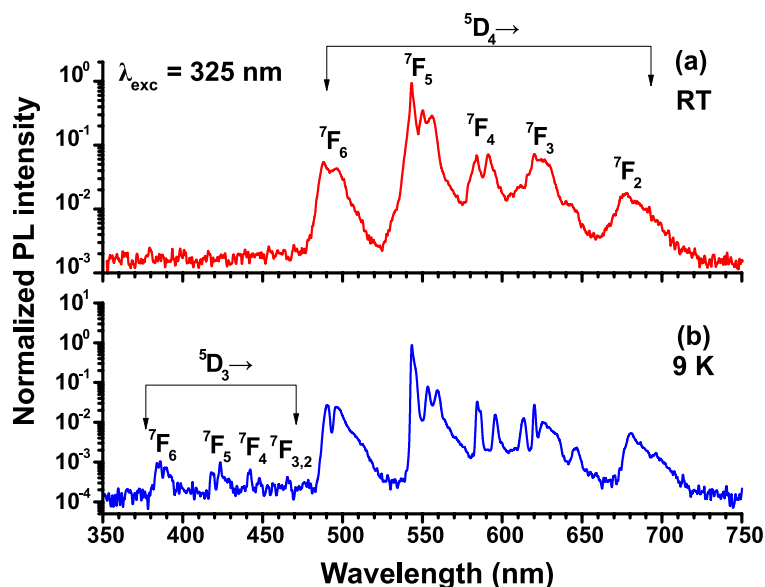
Figure 5.19. Normalized PL spectra at RT (a) and 9 K (b) acquired under 325 nm laser excitation.

The comparison between RT PL spectra under two different wavelength excitations (325 nm and 486 nm) and PLE spectra monitored at two different Tb^{3+} intra-$4f$ emission lines (544 nm and 623 nm) are displayed in Figure 5.20 a). The RT PLE spectra monitored in the emission at 544 nm, assigned to the $^5D_4\rightarrow^7F_5$ transition (blue line), reveal that the $^5D_4$ level can be populated resonantly via this state or by the higher excited states of the intra-$4f^8$ configuration such the $^5D_3$, $^5G_6$, $^5L_{10}$, $^5G_5$, $^5L_9$, $^5L_8$ and $^5L_7$, as labelled in the Figure 5.20 a). Additionally, at shorter wavelengths a very large and intense broad excitation band appears with maxima near ~300 nm. In a similar way to what was discussed for Eu^{3+}, this excitation band, from where the $^5D_4$ level is preferentially populated, is likely to be due to the spin allowed interconfigurational $4f^8\rightarrow4f^7\,5d^1$ transition of the Tb^{3+} ions or other CT mechanism [40,49,50]. As can be observed by the PL spectra shown in the Figure 5.20, no changes on the peak position in the emission spectra acquired under intraconfigurational (486 nm) and interconfigurational (325 nm) excitation conditions are observed. In addition PLE monitored in the $^5D_4\rightarrow^7F_3$ (623 nm) is very similar to the one monitored in the predominant $^5D_4\rightarrow^7F_5$ emission. Such evidences suggest that the emission arise from the same Tb^{3+}-related optical centres. However, if one looks more carefully to the PL spectra it is possible to observe slightly differences in the intensity ratio between the emission bands, under the two excitation wavelengths. This is more evident in the Stark splitted components of the $^5D_4\rightarrow^7F_4$ transition. Such suggests that different Tb^{3+} optical centres can exist in the sample.
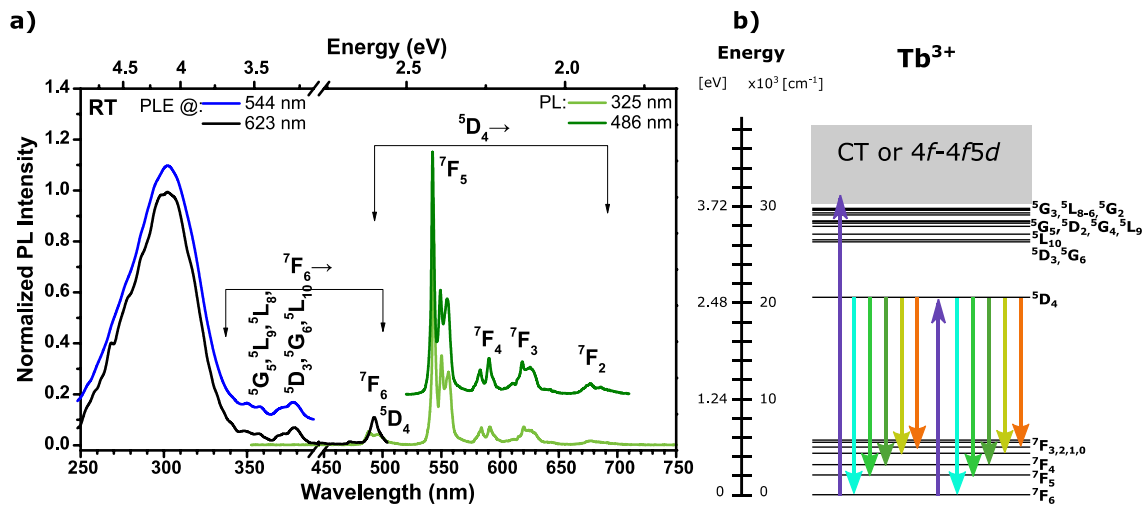
Figure 5.20. a) RT PL and PLE spectra of the t'-YSZ:Tb³⁺ crystal. b) Partial Tb³⁺ electronic energy level diagram.

The temperature dependence in the emission spectra of t'-YSZ:Tb³⁺ crystal under 325 nm wavelength excitation was also evaluated between 14 K and the RT. Figure 5.21 a) displays these PL spectra where one can see that the intensity of Tb³⁺ emission decrease with the increase in sample temperature. The comparison between the normalized PL intensity at 14 K and RT shown in Figure 5.21 b) clearly confirms the presence of different Tb³⁺ optical centres as different intensity ratios between lines from the same excited state ($^5D_4$) as well as between the unfolded Stark components of the same transition were identified (vertical lines in Figure 5.21 b). The integrated intensity of the overall $^5D_4{\rightarrow}^7F_J$ transitions as a function of temperature is displayed in Figure 5.21 c). A decrease of the intensity is observed in the studied interval range, with around 40% of the low temperature emission intensity being observed at RT. The data was fitted considering the classical model of nonradiative deexcitation expressed in *Eq*. 4.15 and described by an activation energy about 16 meV.
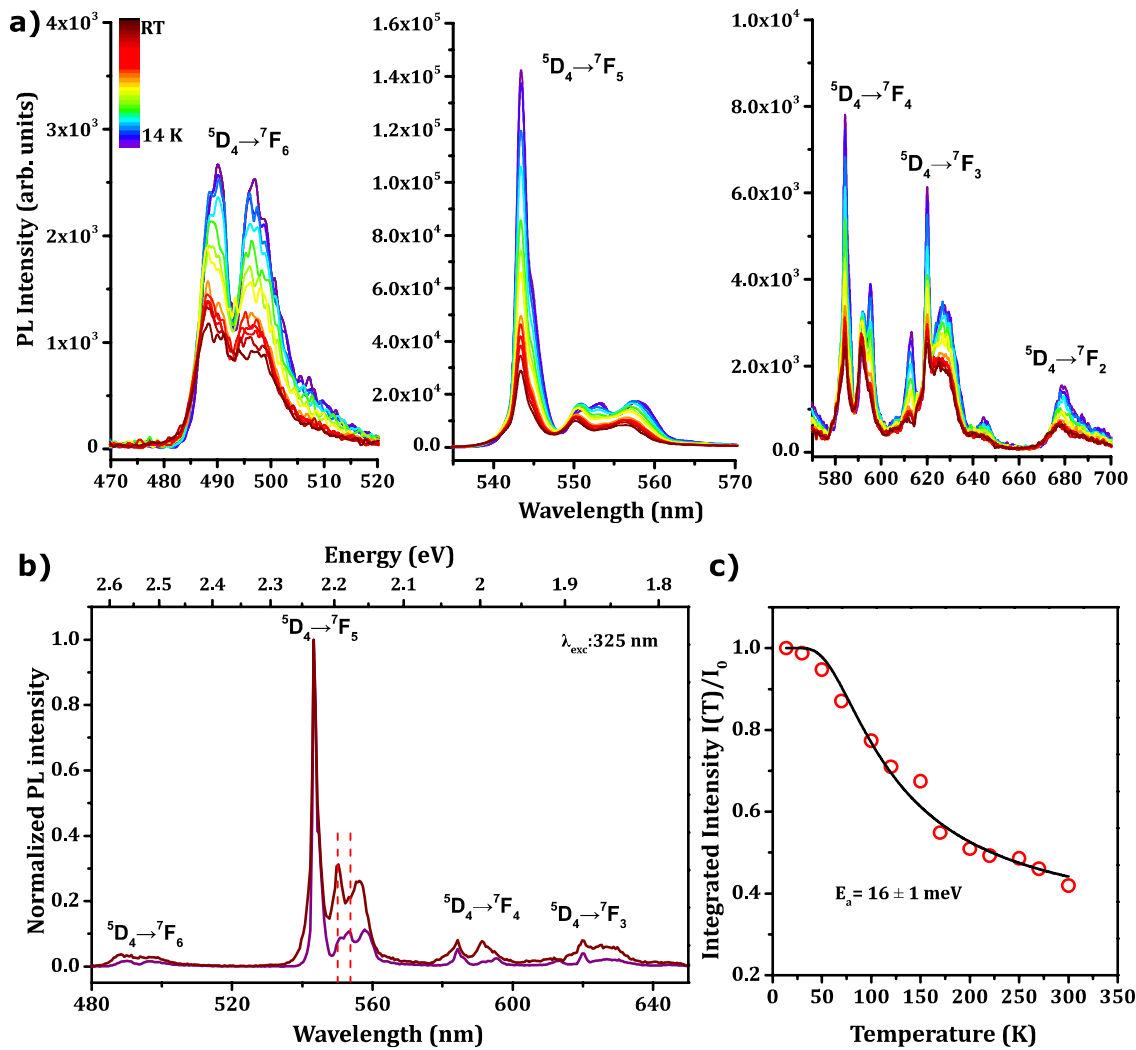
Figure 5.21. a) Temperature dependence of the PL spectra of the t'-YSZ:Tb³⁺ crystal under excitation in the broad UV band (325 nm). b) Comparison between the 14 K and RT PL spectra. c) Temperature dependence of the overall emission intensity (normalized to the emission intensity at T= 14K).

Additionally, in order to acquire information about the kinetics of the Tb³⁺ emitting level, TR-PL spectra, measured at RT under pulsed 266 nm laser line excitation (interconfigurational absorption), and time decay measurements were performed. Figure 5.22 a) displays the RT Tb³⁺ emission spectra acquired in the temporal range between 0 and 10 ms in which the same depopulation behaviour is observed for all the transitions from the $^5D_4$ emitting level. The time decay curve of the emitting $^5D_4$ level, (monitored in the $^5D_4 \rightarrow ^7F_5$ emission) shown in Figure 5.22 b) is well fitted to a single exponential decay with a time constant of ~2.7 ms.
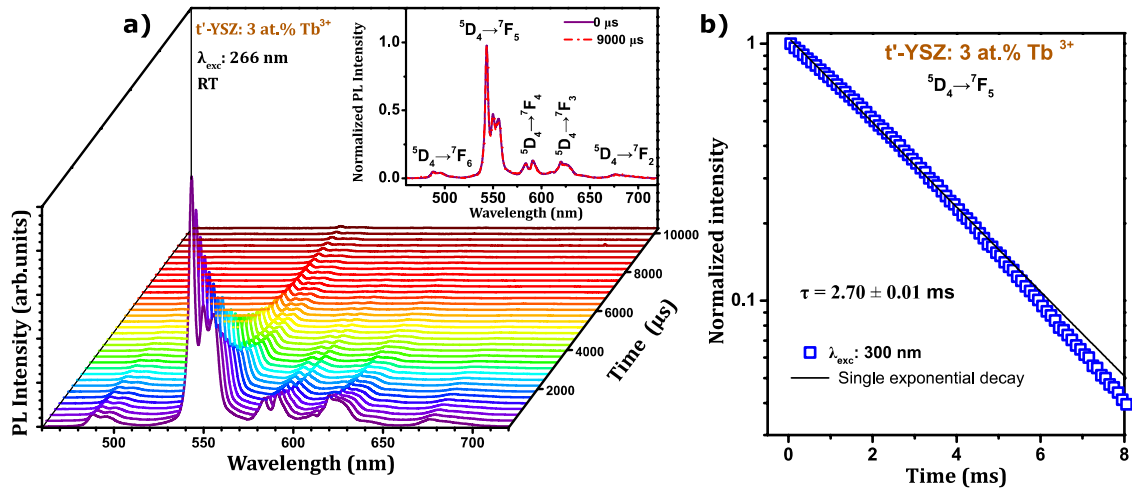
Figure 5.22. a) RT TR-PL spectra of t'-YSZ:Tb³⁺ crystal (3 at.%) under UV excitation. b) Luminescence decay curve of the emitting ⁵D₄ level under interconfigurational excitation.

Summary

Tb³⁺ ions doped YSZ crystals with a tetragonal crystalline structure were successfully grown by the laser floating zone method. The structural characterization confirms the single phase nature and the tetragonal crystalline structure. The optical features, evaluated by photoluminescence, show that at low temperatures, besides the high resolved emission from the $^5D_4$ level, lower intensity transitions from the $^5D_3$ level are observed suggesting that the minimum of the $4f^7 5d^1$ state is above to the one of the $^5D_3$ level. At RT the main emission is due to the $^5D_4 \rightarrow {}^7F_J$ transitions of the Tb³⁺ which are preferentially excited via an interconfigurational broad UV excitation band instead of the higher lying levels of the lanthanide ion. Under this excitation a bright green luminescence is observed by naked eye suggesting that t'-YSZ:Tb³⁺ could be considered as a promising candidate for applications in green solid state emitters for general illumination purposes. In addition, the long lifetime of the green emission, as expected from the spin degeneracies of the involved levels, is of high interest for biodetection.

5.2.2.3 Pr³⁺ doped t'-YSZ crystals

With a $4f^2$ electronic configuration, the free Pr³⁺ has a $^{2S+1}L_J$ scheme level corresponding to the $^3H_4$ ground state and $^3H_{5,6}$, $^3F_{2,3,4}$, $^1G_4$, $^1D_2$, $^3P_{0,1}$, $^1I_6$, $^3P_2$, $^1S_0$ excited states [38]. When optically activated in wide band gap oxide hosts the Pr³⁺ ions are known to be good candidates for a broad variety of optical applications that extends from the VUV to the infrared (IR) spectral region by making used of their interesting stimulated, downshifted and upconversion luminescence [51–55]. The proximity of the $^1S_0$ energy level to the $4f\,5d$ state confers to the Pr³⁺ the attractive property of photon cascade emission when the $^1S_0$ is

located below the $4f5d$ state [56,57]. Additionally, Pr^{3+} ion is known to be an upconverter in several hosts leading to blue emission (from the $^3P_0$ state) following red optical excitation in the $^1D_2$ state [52,58,59].

Typically, under UV and/or blue excitation, the visible emission in Pr^{3+}doped materials corresponds to the blue/green and red luminescence due to the $^3P_0{\rightarrow}^3H_4$ and $^1D_2{\rightarrow}^3H_4$ transitions, respectively [54,55]. Their intensity ratio is strongly dependent on the excitation energy, host lattice and activator concentration [54,55]. The intra-$4f^2$ transitions of praseodymium doped zirconia were previously observed and reported in samples with mixed crystalline phases (monoclinic, tetragonal and cubic) [60–62] as well as in presumable cubic YSZ single crystals [23,24,63,64]. In both cases, the dominant red luminescence arises from the $^1D_2$ state with the transitions from the ^1P_J states partially quenched, as also observed in other materials [54,55].

In order to study the luminescence features of Pr^{3+} incorporated in tetragonal zirconia, crystals of zirconia stabilized in the tetragonal phase (8 mol.% $YO_{1.5}$) and doped with 3 at.% Pr, were grown by the LFZ method at 40 mm/h. The growth was performed in air at atmospheric pressure.

As for the other cases, the crystalline nature of the as-grown crystalline fibre was analysed by RT Raman spectroscopy and XRD. The fibre microstructure was characterized by SEM and an elemental analysis was performed by micro Particle Induced X-ray Emission (µPIXE) at the 2.5 MV Van de Graaff accelerator installed at IST/CTN (Instituto Superior Técnico, Campus Tecnológico e Nuclear). Detailed description of the used setup may be found in the work of L.C. Alves *et al.* [65].

The PL properties of the doped crystal were studied in a similar approach used to Eu^{3+} and Tb^{3+} doped fibres. Besides the identification of the sample characteristics in the visible spectral region, the sample photoluminescence was also studied in the infrared region, using a Brucker 66V Fourier transform infrared spectrometer (FTIR). Additionally, ionoluminescence (IL) measurements in the range of 300 nm to 1000 nm were performed at RT in vacuum at the IST/CTN, where a microprobe beam line using a 2 MeV proton beam was used as excitation source (beam current of ~1 nA). Additional information about the setup used in the IL measurements can be found in the work of N. F. Santos *et al.* [66].

Structural and morphological characterization

A photo of the as-grown Pr^{3+} doped crystal is shown in Figure 5.23 a). The as-grown crystal has a diameter of about 1.2 mm and a length of few centimetres. The RT Raman spectrum

144

(Figure 5.23 b), performed in similar conditions to the other aforementioned doped crystals, evidence the nature of the tetragonal crystalline phase of the YSZ crystal, further confirmed by single crystal XRD (Figure 5.23 c). In the latter, the Laue diffraction pattern of the crystal is shown. The phase nature determination was performed using a XRD database to index the spots of the Laue pattern. Laue back reflection patterns confirm the single crystalline nature of the as-grown crystal with $a=b=$ 3.62 Å and $c=$ 5.16 Å lattice parameters of the tetragonal structure. The morphological analysis of longitudinal sections of the fibre reveals a uniform surface without grain boundaries or second phases, confirming its monophasic nature and single crystalline character, Figure 5.23 d).
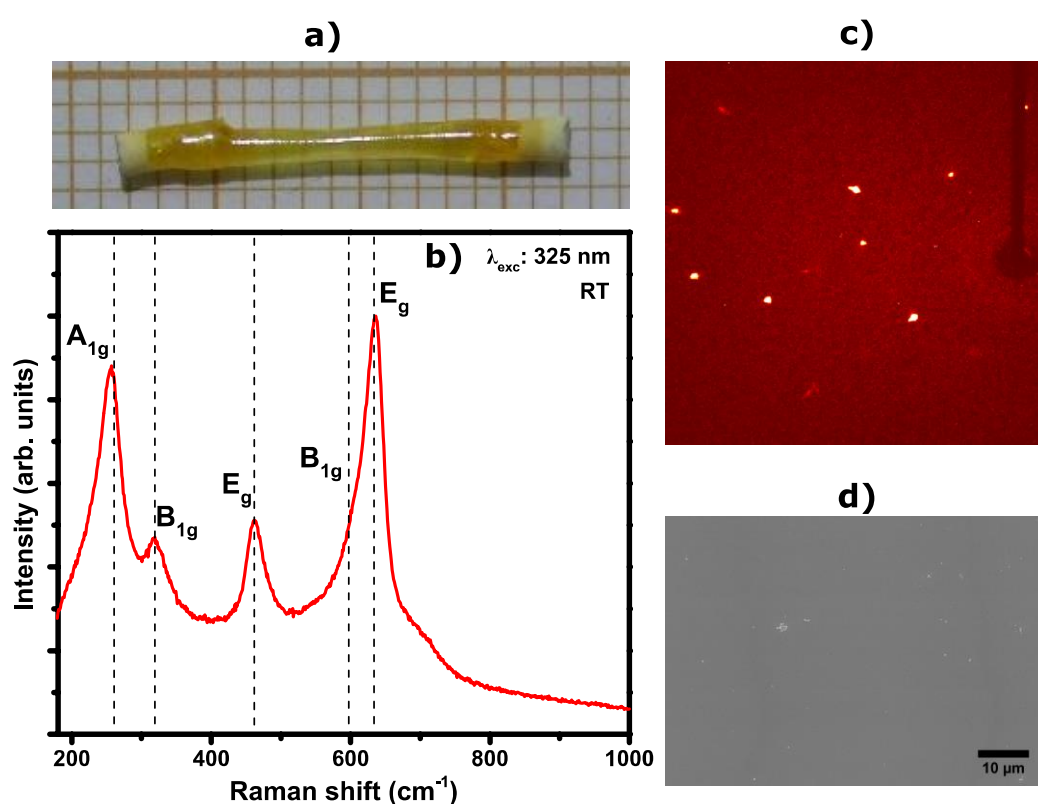
Figure 5.23. a) Photography of the t'-YSZ:Pr³⁺ as-grown crystal by LFZ. b) RT Raman spectrum collected in backscattering geometry with the 325 nm line of a cw He–Cd laser. c) Laue back reflection patterns. d) SEM micrography of polished transversal crystal section.

Microprobe elemental quantitative analysis using the μPIXE technique was performed in two different zones of the crystal, one of them close to the crystal seed and the other one close to the crystal end. On each of the probed zones a 2640 × 640 μm² initial scan was performed followed by a selected raster scan area at the central part of the crystal. The same Zr distribution maps, shown in Figure 5.24, evidence an apparent homogeneous crystal composition that was confirmed by comparing the spectra obtained from both

analysed regions and also shown in the same figure. In fact, the spectra revealed a very homogeneous composition for the major elements (Y, Zr) and for the dopant species (Pr), as well as for the detected impurities. Normalizing to the Zr content (Zr= 1) the mass ratio to the other elements was measured to be: Y= 0.08; Pr= 0.05; Hf= 0.02; Ca= 3×10^{-3}; Ti= 0.7×10^{-3}.
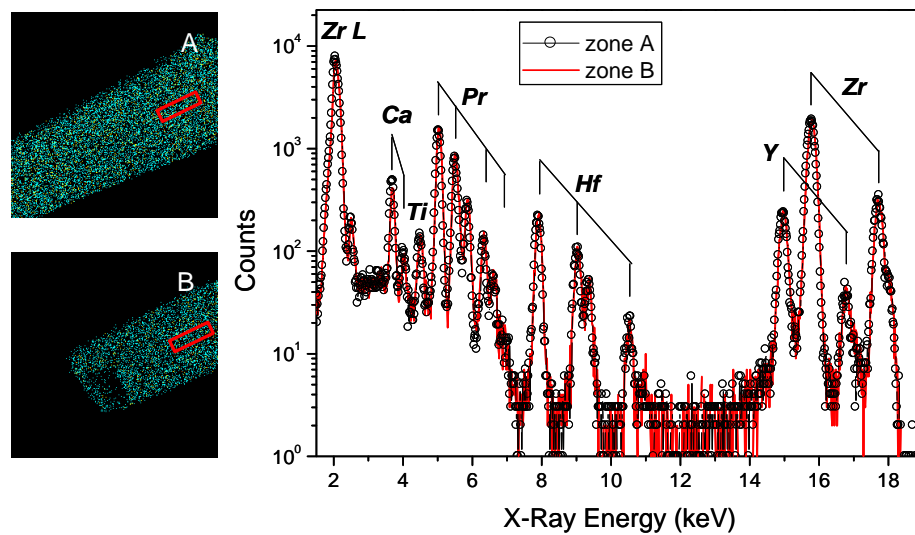

Figure 5.24. Zr distribution maps of two different crystal zones (close to the seed (top map) and close to the opposite end (bottom map)). Also indicated in the maps are the central areas chosen for obtaining data for PIXE quantitative analysis whose spectra are presented in the picture.

Luminescence characterization

Figure 5.25 a) displays the photography of the t'-YSZ:Pr[3+] as-grown crystal under irradiation with UV light (325 nm) at RT, where a very bright red emission is clearly observed by naked eye. The RT PL spectrum of the crystal under this excitation condition is shown in Figure 5.25 b) (pink line). A dominant emission with a maximum at ~615 nm assigned to the $^1D_2 \rightarrow {}^3H_4$ transition is observed. In addition, weaker luminescence lines from the $^1D_2$ and ^3P_J multiplets can be observed at longer and shorter wavelengths. Similar spectra were recently reported for YSZ:Pr[3+] nanopowders with the majority crystalline phase (82%) corresponding to the tetragonal one [62]. Additionally, zirconia single crystals stabilized with 6 wt% of Y_2O_3 and doped with Pr_2O_3 also show comparable luminescence spectra [23].

The RT PLE spectrum monitored at 615 nm, displayed in Figure 5.25 b) (green line), shows that the $^1D_2$ energy levels are populated via nonradiative relaxation between the intra-$4f^2$ $^3P_{0,1,2}(+^1I_6)$ levels as well as by two excitation bands with maxima at 308 nm and 254 nm. The pathways for the population of the $^1D_2$ emitting level are represented in the energy level

146

scheme in Figure 5.25 c) (right side). The same PLE spectra were obtained by monitoring the PL at 589 nm and 640 nm meaning that these lines are populated via the same processes. The two broad emission bands in the UV have been previously assigned to the $4f^2{\rightarrow}4f\,5d$ absorption for Pr^{3+} in different oxygen coordination [23,63]. Nevertheless, these bands could be associated to CT transitions, as pointed out by Ramos-Brito *et al*. [60], and are commonly observed in zirconia doped with other lanthanide ions [33]. A similar behaviour was found in this work for the tetragonal YSZ crystals doped with different lanthanide ions. Additionally, in this spectral region, the zirconia host absorption edge has been reported by others authors, although their energy values vary slightly from sample to sample and are somehow discrepant (~290 nm [61], ~250 nm [24,60,67], ~212 nm [62], ~450 nm [23]) meaning that more detailed studies on the band gap energy and its nature must be conducted for the different ZrO_2 polymorphs.
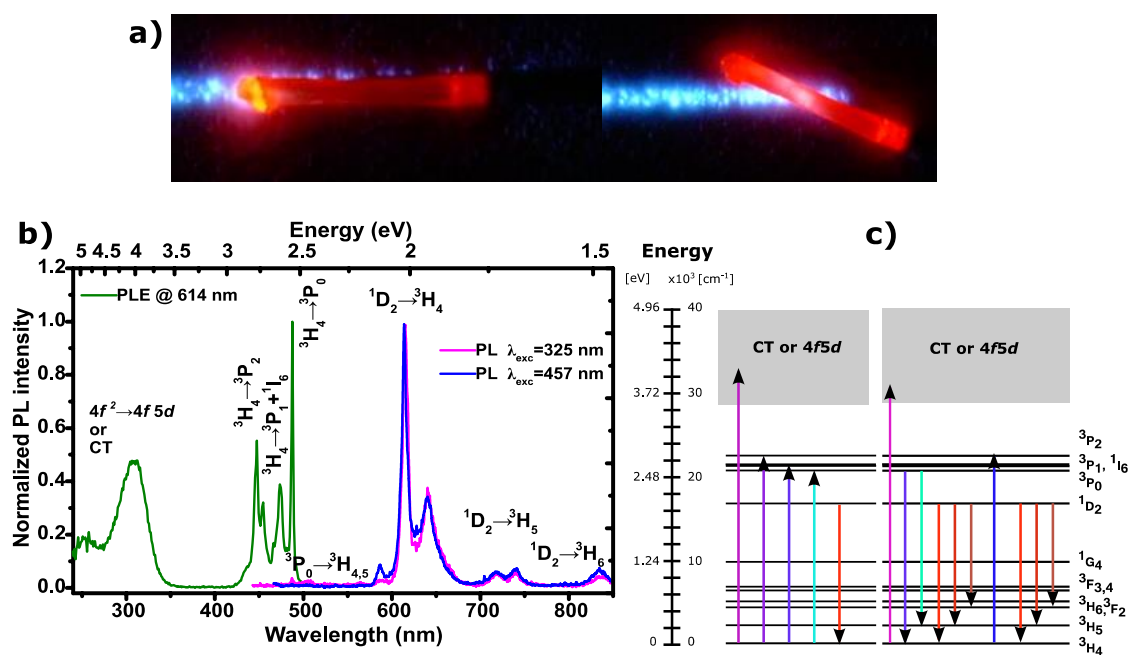
Figure 5.25. a) Photograph of t'-YSZ:Pr³⁺ emission under 325 nm laser excitation at RT. b) RT PL and PLE spectra of the t'-YSZ:Pr³⁺ crystal. c) Partial energy level scheme of Pr³⁺ ion in the oxide host, showing the excitation pathways for the ¹D₂→³H₄ red emission and the transitions corresponding to the visible emission observed at RT under inter- and intraconfigurational excitation.

Included in Figure 5.25 b) is also the PL spectrum obtained when pumping the sample in the ^3P_J ($+^1I_6$) intraconfigurational levels. Despite a small variation in the relative intensity of the transitions lines located between 470 and 600 nm, both PL spectra are similar meaning that the emission comes from the same electronic states for both excitation wavelengths used. The radiative transitions in the visible, observed at RT for the intra and interconfigurational

excitation are indicated in the energy diagram scheme shown in right side of the Figure 5.25 b).

Figure 5.26 shows a comparison between the low and high temperature PL of the tetragonal YSZ:Pr^{3+} crystal obtained with UV (325 nm) and blue (457 nm) excitation. The emission from the $^3P_0$ state is more pronounced at low temperature as also reported by Savoini *et al.* [23]. However, contrasting with the observed by these authors, the lines at 534 nm and 588 nm are seen even at low temperatures when the sample is excited at 457 nm wavelength photons (arrows in Figure 5.26 a) meaning that the transitions do not start in thermally populated levels. When the sample is excited at 325 nm none of the lines are seen at low temperature, suggesting that different Pr^{3+} optically active centres are present in the sample, likely due to different oxygen coordination [23,63]. Increasing the sample temperature promotes the thermal population of the 588 nm line (arrow in Figure 5.26 b). Similar RT spectra obtained with UV excitation was reported by De Vicente *et al.* [24]. The tetragonal YSZ:Pr^{3+} crystal also evidence RT upconversion from the $^1D_2$ level when the sample is pumped with 632.8 nm as shown in the inset of Figure 5.26 b).
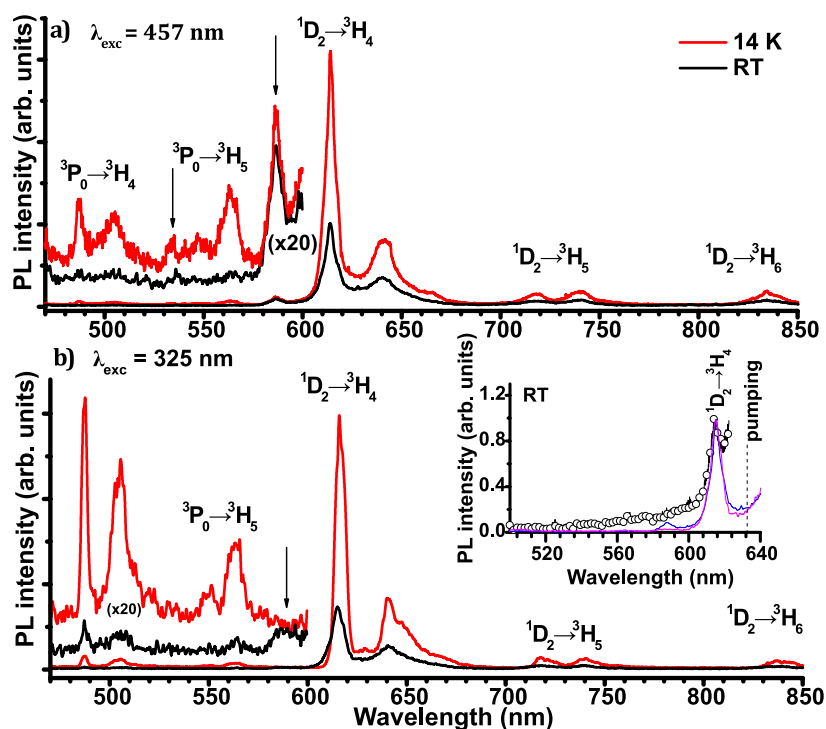

Figure 5.26. The 14 K and RT PL spectra for the t'-YSZ:Pr^{3+} LFZ crystal excited at 457 nm (a) and 325 nm (b). Inset of figure (b): RT upconversion luminescence from the $^1D_2$ level with 632.8 nm excitation (line and symbols) and normalized RT PL obtained with 325 nm (magenta line) and 457 nm (blue line) excitation.

148

In order to analyse the internal photoluminescence efficiency, the emission from Pr^{3+} was studied between 14 K and RT. The temperature dependence of the intraionic Pr^{3+} PL and its integrated intensity is shown in Figure 5.27 for two excitation wavelengths, 457 nm (a) and 325 nm (b). Increasing the temperature promotes nonradiative processes which compete with the radiative ones leading to the PL intensity quenching. For both excitation conditions, the overall decrease of the red luminescence of the Pr^{3+} ions can be well described by two activation energies of ca. 1 and 46 meV, for 325 nm excitation, and of ca. 1 and 25 meV for 457 nm excitation, in the low and high temperature ranges, respectively (inset in Figure 5.27). A faster decrease of the luminescence was found when the sample was excited in the UV (~46% of the 14 K PL intensity at RT) rather than in the intraconfigurational ^3P_J ($+^1I_6$) states (~75% of the 14 K PL intensity was found at RT), meaning that additional nonradiative pathways occur when the excitation is performed at the $4f^2 \rightarrow 4f\,5d$ or CT absorption bands.
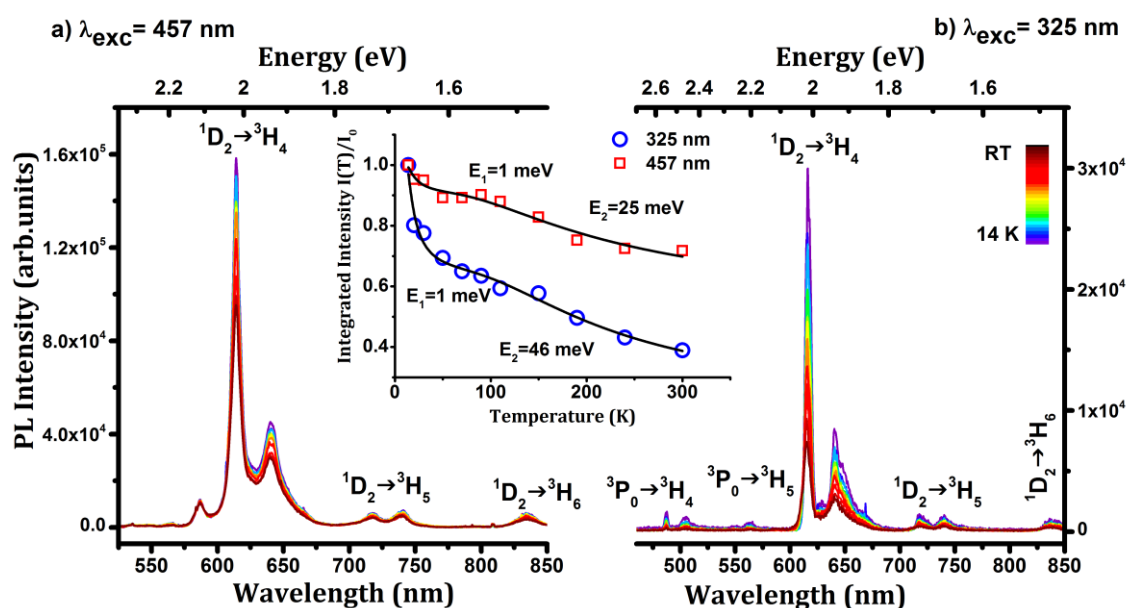

Figure 5.27. PL spectra acquired between 14 K and RT under 457 nm (a) and 325 nm (b) wavelength laser excitation. Inset: evolution of the red Pr^{3+} integrated PL with temperature for the two wavelength excitation.

Time resolved PL measurements were performed at RT under 266 nm pulsed laser excitation and the corresponding spectra are shown if Figure 5.28 a). As identified in the spectrum correspondent to t= 0s, under this excitation condition and in the studied spectral range, besides red emission arising from the $^1D_2$ excited level, the emission arising from the $^3P_0$ excited state is also observed (also seen in steady state conditions as shown in Figure 5.27 b). TR-PL spectra reveal that the intensity of the luminescence from the $^3P_0$ excited

149

state suffers a much faster decrease in time when compared with the intensity of the emission arising from the $^1D_2$ level. This rapid decay of the luminescence from the $^3P_0$ state can be very well observed through the analysis of the emission spectra acquired at t=0 s and t= 25 µs, shown in Figure 5.28 b) in which the intensity is plotted in a logarithmic scale. While for t= 25 µs the emission intensity from the $^1D_2$ state only suffered a slight decrease, for this short time after the pulse excitation, the emission from $^3P_0$ state is totally vanished. Such result means that the luminescence lifetime, τ, of the $^3P_0$ state is well below 25 µs. On the other hand, the luminescence lifetime of the emitting $^1D_2$ state is longer. Based on the TR-PL spectra shown in Figure 5.28 a), the decay curve of the $^1D_2$ emitting level was determined by the integration of the $^1D_2 \rightarrow {}^3H_4$ line intensity. The obtained decay curve is shown in Figure 5.28 c) (blue squares). In the same figure it is also represented the decay curve of the emission centred at 588 nm that was discussed above and associated with an additional Pr^{3+} optical centre. Both decay curves are well fitted to the classic model of excited state depopulation expressed by the exponential decay in the *Eq*. 4.17 (section 4.4.2). The calculated luminescence lifetimes from the two decay curves are very similar and around 130-140 µs. Such results confirm that the emission centred at 588 nm do not arise from the excited $^3P_0$ states, which has a much faster luminescence lifetime. This emission can come from the $^1D_2$ excited state of other Pr^{3+} optical centre, with similar $^1D_2$ luminescence lifetime.
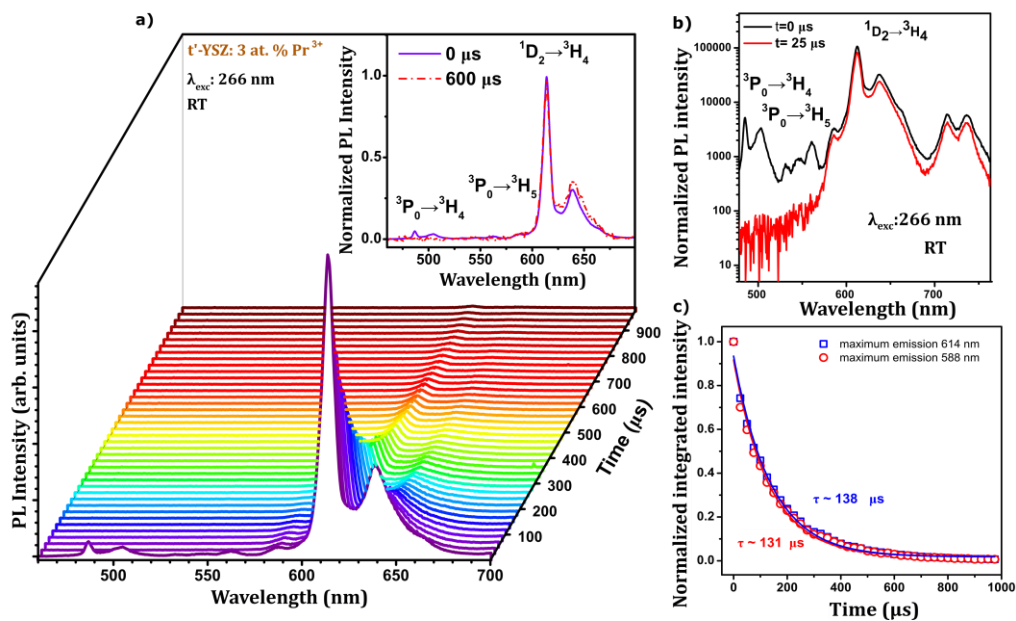

Figure 5.28. a) TR-PL spectra of the crystal under 266 nm wavelength excitation. Comparison between the PL spectra acquired at t= 0s and t= 600 µs after laser pulse (inset) and for t=0s and t=25 µs (b). c) Luminescence decay curves of the emission band with maxima at 615 nm and 588 nm.

Besides the visible PL, the spectroscopic properties of the Pr^{3+} ions in the tetragonal YSZ crystal were further analysed in the infrared spectral region. Figure 5.29 shows the wavelength dependent excitation PL spectra obtained at 90 K with optical pumping at the $^3P_{0,1}$ ($+^1I_6$) levels. A group of lines were found at ~1140 and 1560 nm. With excitation above the $^3P_0$ state (wavelengths shorter than 488 nm) the main transitions occur from the $^1D_2$ level as also observed for the visible counterpart spectrum. However, under the same spectral resolution, a broadening of the transition lines and changes in their relative intensity can be identified, confirming the presence of multiple Pr^3 optically activated centres. The most resolved spectrum was achieved with the excitation of 476.5 nm and the analysis of the temperature dependent PL spectra obtained with this excitation allows identifying an overall decrease of the luminescence intensity with ~20% of the 90 K PL intensity found at RT.
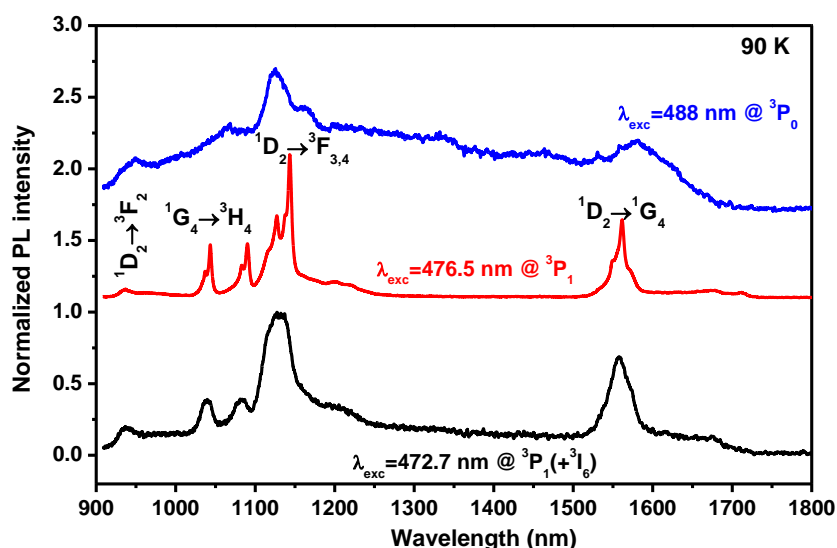

Figure 5.29. PL spectra of t'-YSZ:Pr^{3+} crystal in the IR region for different excitation wavelengths, acquired at 90 K.

Stability to high energy proton irradiation

For device and sensor applications a reliable analysis of the lattice and luminescence stability is crucial. In particular when assessing the potential of new materials for operation in harsh environments such as irradiation environments in nuclear reactors or space, the knowledge of the lattice and luminescence stability is a main request. Optical materials and in particular optical waveguides may be useful for information transmission when the lifetime of conventional electronics is limited by irradiation effects. However, crystal defects also hamper the performance of such devices since they affect the quantum efficiency as

well as the light transmission. Yttria stabilized zirconia is well-known due to its radiation hardness, being widely studied as transmutation matrix for the incineration of highly radioactive minor actinides from nuclear waste [68]. The optical response of this material to ionizing radiation remains, however, relatively unexplored. As such, in this work the stability of the t'-YSZ:Pr³⁺ crystal to high energy protons irradiation with a flux of ∼10¹³ p/s cm² was studied at RT. In this study, IL was used to assess the effect of high energy proton irradiation on the optical properties of the Pr³⁺ doped crystal.

Figure 5.30 a) shows the IL spectra of the t'-YSZ:Pr³⁺ crystal after different times of proton irradiation. The emission spectra acquired under proton irradiation is very similar to the one obtained under 3.8 eV photons (325 nm) irradiation. The spectral analogy suggests that either by using 3.8 eV photons or 2.0 MeV protons no rearrangement of the optical centres were found. In fact, independent of the probing depth (ca. 100 nm or up to ca. 30 μm, for PL and IL measurements, respectively) no modifications occur on the luminescence of the Pr³⁺ doped t'-YSZ crystal, indicating that the luminescence of the Pr³⁺ comes from the ions in the same local coordination. Photos of the crystal under proton irradiation are shown in Figure 5.30 b) where the red emission can be observed in the irradiated spot of the transparent crystal.
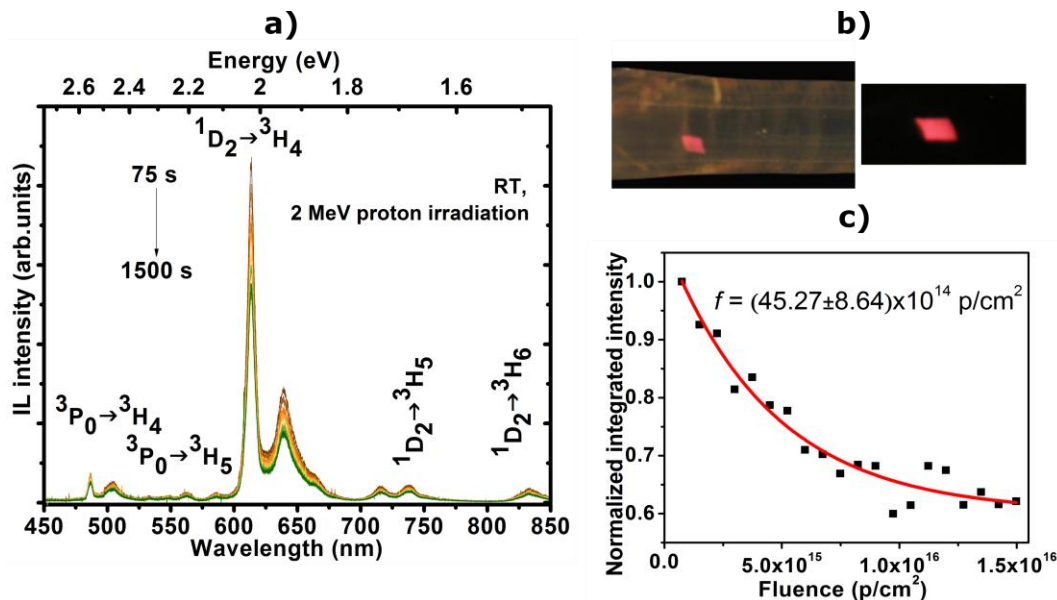

Figure 5.30. a) IL spectra obtained at RT for different proton irradiation (2 MeV) exposure times. b) RT emission of t'-YSZ:Pr³⁺ with proton irradiation (photograph was taken with background illumination). c) IL decay with increasing proton fluence.

As analysed above, with the 3.8 eV photon illumination the excitation occurs via the interconfigurational $4f^2 \rightarrow 4f\,5d$ absorption and/or CT bands, followed by nonradiative

relaxation to the $^3P_0$ and $^1D_2$ emitting levels giving rise to the observed PL. The light emission due to the penetration of the ion beam in the material is mainly due to electronic interactions leading, among other processes, to the generation of electron-hole pairs by above band gap excitation. Furthermore, direct impact excitation of the ions is also possible. Even under these distinct excitation conditions it is evident that the relative luminescence intensity from the $^3P_0$ state is lower than that arising from the $^1D_2$ state for both PL and IL. Quenching of the $^3P_0$ luminescence has been observed in several oxide hosts and explained by distinct deexcitation processes such as those related with intersystem crossing [55]. The spectral comparison among the PL and IL reveals, in both cases, the preferential population of the $^1D_2$ emitting level, rather than the ^3P_J levels suggesting that above band gap excitation provided by the proton irradiation leads to the same population mechanisms. Other possible paths for the population of the Pr^{3+} excited states under ion irradiation are related with the direct interaction of the beam with the Pr^{3+} ions [69–71]. In this process the irradiation could promote directly the ligand electrons to the rare earth metal ion, being therefore responsible for the CT excitation bands, or they can stimulate an electron from the ground state configuration $4f^2$ to the $4f5d$ configuration, similar to what is observed in the PL measurements.

The effect of 3.8 eV photons and 2.0 MeV protons irradiation time on the Pr^{3+} emission stability was studied. In the first case, no changes on the luminescence was observed after irradiating for several hours supporting the expected high stability of the host material upon photon excitation. On the other hand, the degradation of the red Pr^{3+} luminescence with increasing proton fluence is observed, Figure 5.30 c). In fact, for the used fluence range, the IL quenching is well described by an exponential decay with a decay constant of 4.5×10^{15} p/cm^2. Luminescence degradation is directly related with nonradiative paths which are induced by the proton irradiation process. In particular, phenomena like undesired sample heating [70] and point defect creation [69–71] must be considered as hypothesis to explain the observed IL intensity drop. In the first case, the collimated high energy proton beam is expected to increase the local sample temperature during the exposed irradiation time leading to the IL quenching due to competitive nonradiative pathways as observed using the temperature dependent PL measurements. Additionally, the accelerated ion beam creates defects (e.g. vacancies and aggregates) which could lead to changes in the Pr^{3+} environment decreasing the concentration of the optically active centres and the corresponding IL intensity. Furthermore, the introduced defects could act as nonradiative traps and/or killer centres responsible for the red IL quenching.

Summary

In summary, a millimetric single crystal fibre of Pr^{3+} doped tetragonal yttria stabilized zirconia was successfully grown by the laser floating zone technique. The spectroscopic characteristics of the fibres were studied. A very bright red luminescence was observed at RT by naked eye under UV excitation. The emission between the $^1D_2$ and $^3H_4$ multiplets is mainly populated via nonradiative relaxation from the interconfigurational ($4f^2 \rightarrow 4f\,5d$ or CT bands) and intraconfigurational ^3P_J levels, as measured by PLE. The 14 K luminescence observed with UV and blue excitations evidence different relative intensities of the transitions suggesting the presence of different Pr^{3+} emitting centres in the oxide host. This behaviour was also confirmed by the infrared PL measurements obtained with different wavelength photon excitation. In the infrared spectral region the main transitions were found at ~1140 and 1560 nm which are wavelengths of interest for optical communications. The Pr^{3+} luminescence was also studied under high energy proton irradiation (IL) in order to asses to the crystal stability to ionizing radiation. Pr^{3+} IL spectrum obtained under proton irradiation is very similar to PL spectrum acquired under 3.8 eV photon excitation. The similarity of the spectroscopic features measured by PL and IL suggest that independent of the different excitation mechanisms, by photons or protons, the same optically active centres were observed. The RT analysis of the IL fluence dependence indicates an intensity drop due to nonradiative effects which could be of different natures such as local heating, changes in the emitting Pr^{3+} environment or lattice defects produced by proton irradiation which act as killer centres. In order to provide Ln ions doped zirconia luminescence based devices to operate in harsh radiation environments, improvements on the luminescence stability should be further explored as identified by the luminescence behaviour observed under proton irradiation. Nevertheless, the fact that the Pr^{3+} IL saturates at non-zero value and that the spectral shape of the emission remains unchanged are promising results for the development of radiation hard optical materials.

5.2.2.4 Tm^{3+} doped t'-YSZ crystals

Trivalent thulium (Tm^{3+}) is other lanthanide ion with interesting properties commonly used as a blue luminescence optical activator in wide band gap hosts. With a $4f^{12}$ electronic configuration Tm^{3+} ions are known to have a complex $^{2S+1}L_J$ energy level scheme with a $^3H_6$ ground state and several excited states, allowing spanning the intraionic transitions from the UV to the infrared when the ions are incorporated in wide band gap hosts [72–74]. One of the most studied emissions of Tm^{3+} in inorganic hosts occurs around 2 µm, due to the $^3F_4 \rightarrow {}^3H_6$ transition, and is of special interest for applications in solid state laser technology [75]. Beyond the importance of the IR emission, Tm^{3+} provides luminescence in the visible

spectral range which is of great importance in other application areas. Particularly, the $^1D_2 \rightarrow {}^3F_4$ and $^1G_4 \rightarrow {}^3H_6$ transitions in the visible spectral range assume an important role in solid state lighting applications as, for instance, electroluminescent blue emitters [76]. In addition to the interesting UV, blue, red and IR downshifted emission of Tm^{3+} ions, the energy level scheme of Tm^{3+} ions is also suitable for upconversion emission under sensitization with Yb^{3+} ions, as it will be discussed in the Chapter 8 specially dedicated to upconversion phosphors.

In order to study the downshifted luminescence of Tm^{3+} ion in tetragonal zirconia host, a crystal of zirconia stabilized 8 mol.% $YO_{1.5}$ and doped with 0.3 at.% Tm was grown by the LFZ process at 20 mm/h, following the procedure described in section 5.1.2. The stabilization of the tetragonal phase in the as-grown crystal was confirmed by RT Raman spectroscopy. The luminescence properties of Tm^{3+} incorporated in the tetragonal YSZ crystal were analysed by PL and PLE spectroscopy performed in the visible and IR spectral regions, TR-PL and temperature dependent PL measurements.

Structural characterization

As in previous cases the structural characterization of the produced crystals was assessed by RT Raman spectroscopy. Figure 5.31 a) shows the Raman spectra of the Tm^{3+} doped and Tm^{3+}, Yb^{3+} co-doped crystals grown 20 mm/h. in both cases, the fibres crystallized in the tetragonal phase of zirconia. The corresponding photos of the two samples are depicted in Figure 5.31 b).
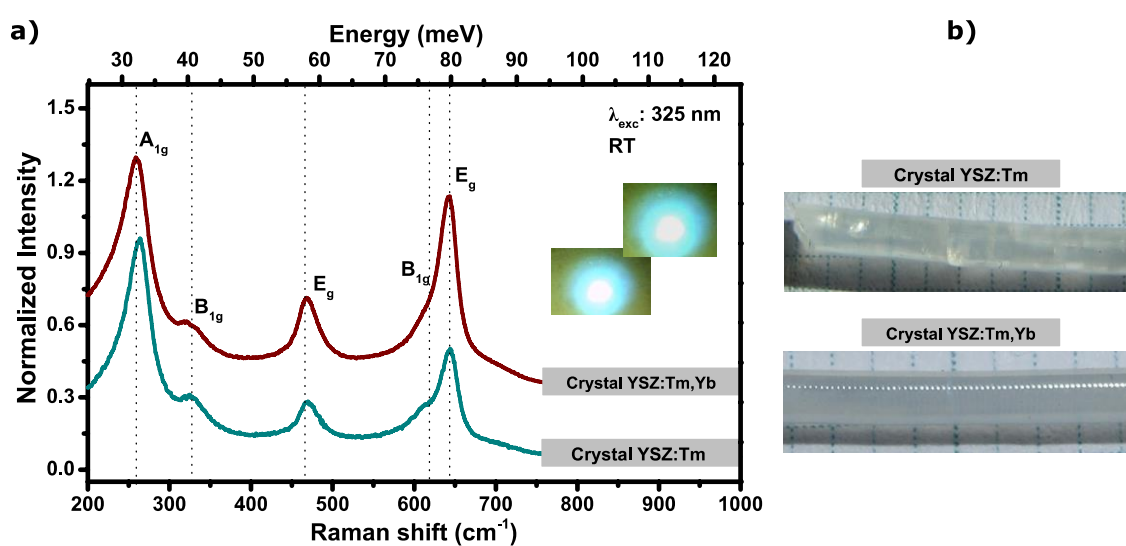

Figure 5.31. a) RT Raman spectra obtained in backscattering configuration with 325 nm He-Cd laser line. Inset: photos of the blue emission of the crystals when irradiated with UV light

155

Luminescence characterization

The PL and PLE spectra of both t'-YSZ:Tm^{3+} and t'-YSZ:Tm^{3+},Yb^{3+} crystals were investigated at RT as shown in Figure 5.32 a). Under excitation with UV light (358.5 nm), resonantly with the $^1D_2$ excited multiplet of the Tm^{3+} (Figure 5.32 b), the PL spectrum is composed of three groups of emitting lines in the blue/green, red and NIR spectral regions. The intraionic lines of the Tm^{3+} in the blue/green region are due to the $^1D_2{\rightarrow}^3F_4$, $^1G_4{\rightarrow}^3H_6$ and $^1D_2{\rightarrow}^3H_5$ transitions, while the red emission is assigned to the $^1G_4{\rightarrow}^3F_4$ transition, and the NIR luminescence to transitions between the $^1D_2{\rightarrow}^3F_2$, $^1G_4{\rightarrow}^3H_5$ and $^3H_4{\rightarrow}^3H_6$ multiplets. Under this excitation condition, the most intense emission occurs in the blue region (~459 nm) and is due to the $^1D_2{\rightarrow}^3F_4$ transition.
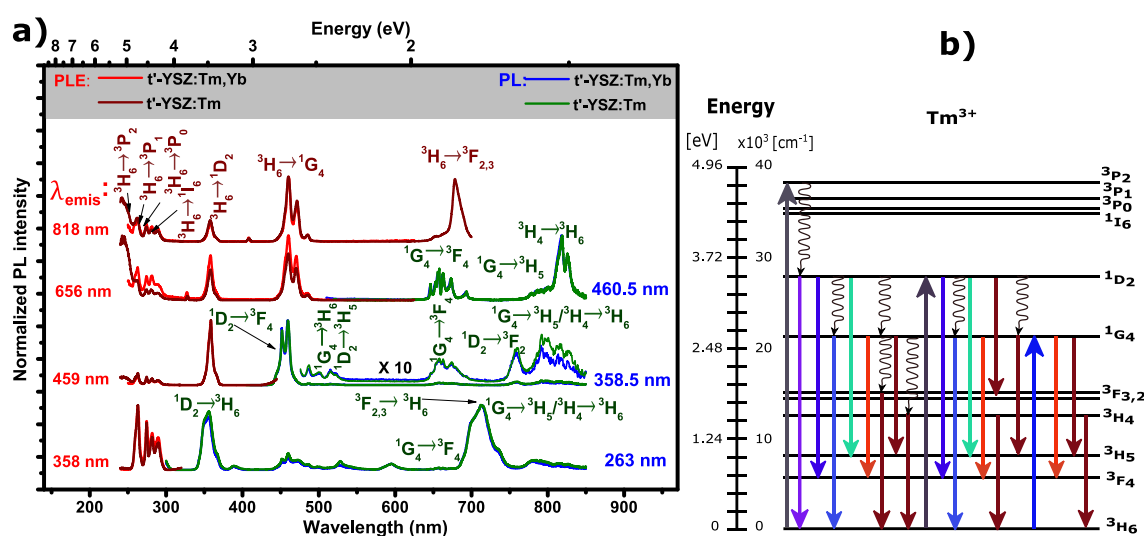

Figure 5.32. a) PL and PLE spectra of t'-YSZ:Tm^{3+} and t'-YSZ:Tm^{3+},Yb^{3+} crystals under resonant excitation into the Tm^{3+} excited multiplets. b) Partial energy level diagram of Tm^{3+} free ion with representation of the radiative transition observed in the PL spectra upon resonant excitation into the $^3P_2$, $^1D_2$ and $^1G_4$ excited multiplets.

The PLE monitored at 459 nm ($^1D_2{\rightarrow}^3F_4$) shows that, besides the resonant excitation into the $^1D_2$ multiplet, the ion luminescence can also be observed upon excitation into higher excited states of the Tm^{3+} ($^1I_6$ and $^3P_{2,1,0}$). By exciting the crystals into these ^3P_J higher energy multiplets (263 nm), dominant lines at 355 and 712 nm due to the $^1D_2{\rightarrow}^3H_6$ and $^3F_{2,3}{\rightarrow}^3H_6$ transitions are observed. The enlargement of the lines is due to the overlap of intraionic transitions from distinct multiplets occurring at similar energies. Figure 5.32 a) also displays the PL spectra under resonant excitation into the $^1G_4$ multiplet showing an

156

enhancement of the NIR transition arising between the $^1G_4{\rightarrow}^3H_5$ and $^3H_4{\rightarrow}^3H_6$ multiplets. The upper spectrum, corresponding to the PLE monitored at the $^3H_4{\rightarrow}^3H_6$ transition, indicates that this emission can also be directly excited through the $^3H_6{\rightarrow}^3F_{2,3}$ absorption. No significant differences were observed in the visible luminescence and PLE spectra for the Tm^{3+} doped and Tm^{3+}, Yb^{3+} co-doped YSZ single crystals.

The radiative internal quantum efficiency of the blue and red transitions was investigated by measuring the temperature dependent PL spectra of the Tm^{3+} doped t'-YSZ crystal with resonant excitation in the $^1D_2$ and $^1G_4$ excited levels, respectively (Figure 5.33). Figure 5.33 a) shows the evolution with temperature of the red luminescence observed under resonant excitation in the $^1G_4$ level. Although a slight decrease in the emission intensity of the strongest low temperature band is observed, increasing the sample temperature promotes the appearance of additional emitting lines in the high energy part of the spectrum. The comparison of the normalized RT and 14 K PL spectra, Figure 5.33 b), reveals different intensity ratios between the Stark splitted components which can be explained by a thermal population of higher energetic emitting levels from the same Tm^{3+} optically active centre. However, and as observed for the other studied ions, we cannot discard that Tm^{3+} in distinct sites/environments could exist in the YSZ lattice and therefore, the observed behaviour could be explained if a thermal population between two emitting centres slightly deviated in energy is considered. The overall integrated intensity of the red emission as a function of the sample temperature is displayed in the inset in Figure 5.33 a) and b) (red circles), where an almost constant emission intensity was observed between 14 K and RT. On the other hand, under resonant excitation in the $^1D_2$ energy level, a strong increase in the intensity of the Tm^{3+} blue emission is observed between 14 K and RT, Figure 5.33 b). The analysis of the integrated intensity of the overall $^1D_2{\rightarrow}^3F_4$ blue luminescence (inset in the Figure 5.33 a) and b) (blue squares)) shows that this duplicates between 14 K and the RT. With the used ultraviolet excitation, such behaviour clearly indicates an additional thermal activated feeding of the $^1D_2$ level (when compared with the thermal activation of the $^1G_4$ level when pumped with blue light) of a given Tm ion or, as mentioned above, the involvement of more than one optically activated Tm^{3+}. Cross-relaxation processes between nearest Tm ions cannot be excluded to justify the overall increase in intensity from the $^1D_2$ multiplet.
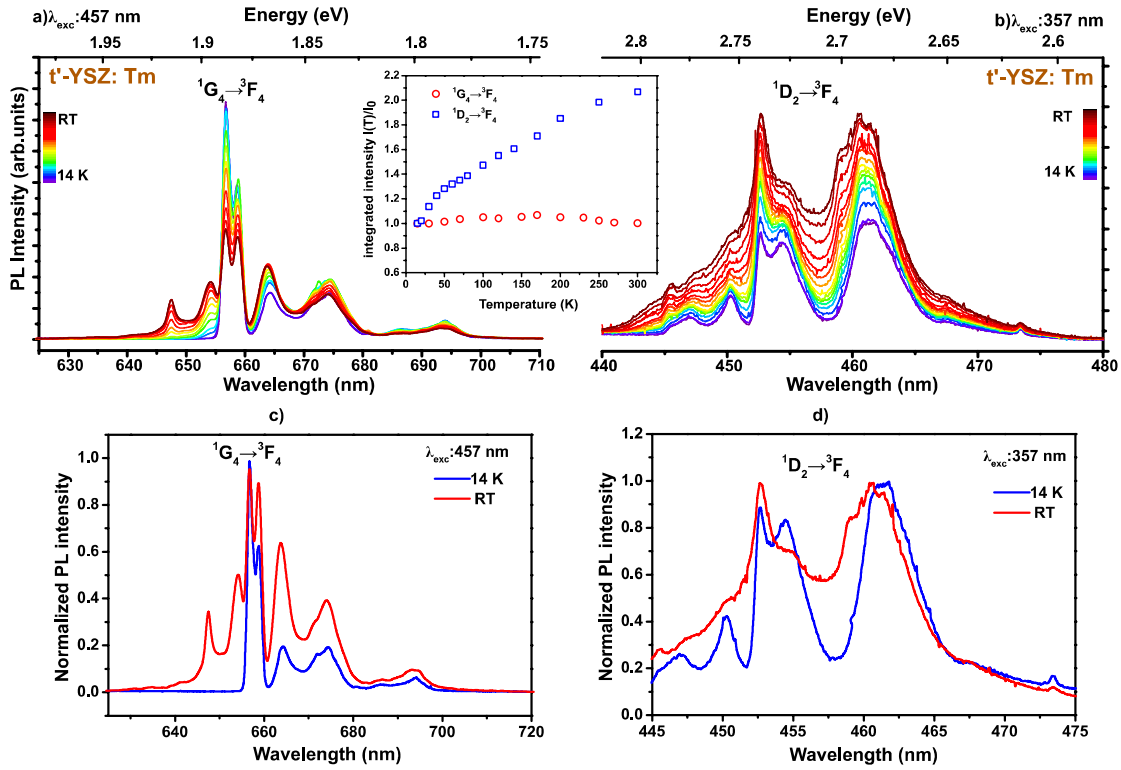
Figure 5.33. PL spectra measured between 14 K and the RT for t'-YSZ:Tm³⁺ crystal by pumping the sample in ¹G₄ (a) and ¹D₂ (b) manifold. The inset shows the temperature dependence of the ¹G₄→³F₄ and ¹D₂→³F₄ transitions. c), d) Comparison between the low and high temperature normalized ¹G₄→³F₄ and ¹D₂→³F₄ lines, respectively.

In order to get additional information of the luminescence kinetics of Tm³⁺ ¹D₂ and ¹G₄ emitting levels, TR-PL spectra of the t'-YSZ:Tm³⁺ crystal were acquired under 266 nm pulsed laser excitation at RT. Figure 5.34 a) shows the TR-PL spectra acquired in a time range after pulsed excitation between 0 and 650 μs. As identified in the figure, in the studied spectral range, there are several emission bands arising from both ¹D₂ and ¹G₄ excited states which show very distinct luminescence decays. For an easy analysis, some of the TR-PL spectra were normalized to the maxima intensity and are displayed Figure 5.34 b). With increasing times, the luminescence intensity from the ¹D₂ excited level undergoes a faster decrease comparatively to the luminescence from the excited ¹G₄ level. As observed in Figure 5.34 b), under the used excitation conditions and for t=0 s (which means steady state condition), in the spectral region between 430 and 520 nm there is a partial overlap between the emission bands assigned to the ¹D₂→³F₄ and ¹G₄→³H₆ electronic transitions. However, due to the faster decrease of the ¹D₂→³F₄ emission (shorter lifetime), for a time after pulse of 600 μs, only the ¹G₄→³H₆ is observed. Besides the information about the luminescence lifetime of the different emitting levels, the TR-PL spectra also helped to confirm the assigned emission lines. In addition to the identified emission band due to intra-4*f* emission of Tm³⁺, in the TR-PL spectra additional emission bands that were partially hidden in the steady state

158

spectra could be clearly identified. Such band, identified with an asterisk in Figure 5.34 b), could be attributed to the intra-4f emission of Tm^{3+} that exists as a contamination of the precursor commercial lanthanide oxide powders. The peak positions are in fair agreement with the one observed in the YSZ crystal doped with Tb^{3+}.
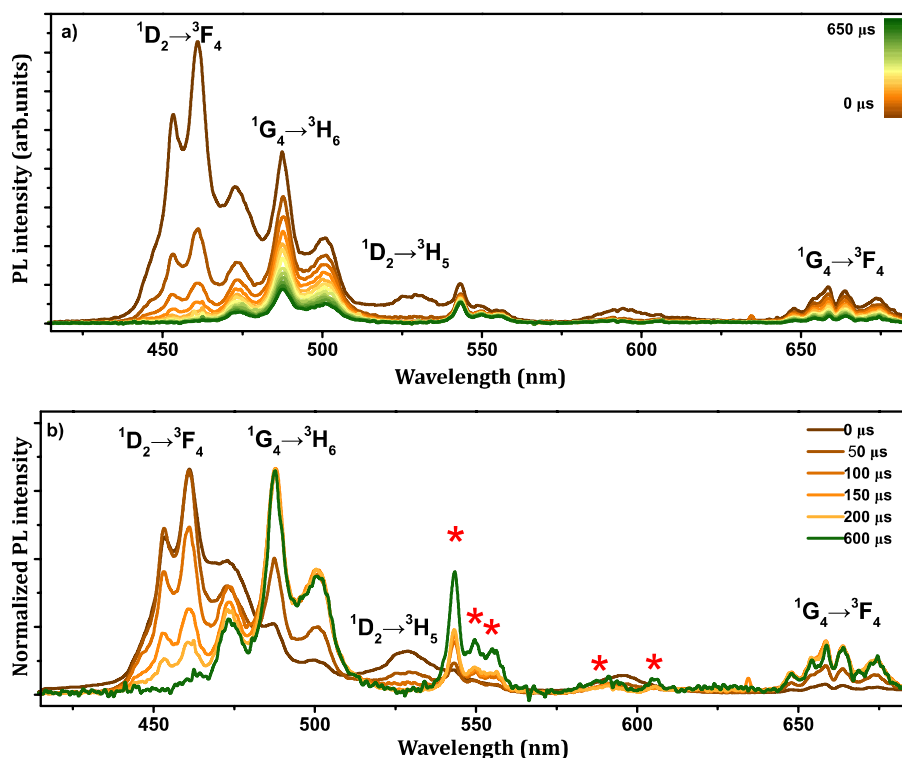

Figure 5.34. a) RT TR-PL spectra of the Tm^{3+} doped t'-YSZ crystal acquired under 266 nm pulsed laser excitation in a time range between 0 and 650 μs. b) Normalized TR-PL spectra for some of the time delays shown in a).The emission spectra were not corrected to the detector and optics.

In addition to the visible, the infrared downshifted emission of the Tm^{3+} doped and Tm^{3+}, Yb^{3+} co-doped t'-YSZ crystals was also studied. Figure 5.35 a) and b) displays the IR PL and the PLE spectra of both doped and co-doped crystals at 12 K and RT, respectively. The crystals exhibit strong IR photoluminescence in all the studied spectral range (from 900 to 1700 nm) due the intra-4f transitions of the trivalent Tm and Yb ions, when excited resonantly into different excited electronic states of Tm^{3+}. With resonant excitation in the $^1D_2$ (358.5 nm) multiplet of Tm^{3+}, the 12 K infrared PL spectra of the Tm^{3+} doped crystal (Figure 5.35 b) is dominated by three groups of emission bands with maxima around 1267 nm, 1464 nm and 1568 nm which were assigned to the $^1G_4{\rightarrow}^3H_6$, $^3F_2{\rightarrow}^3H_5$ and $^3H_4{\rightarrow}^3F_4$, and $^3F_3{\rightarrow}^3H_5$, respectively. With resonant excitation to the $^1G_4$ (460.5 nm) level the same emission bands were observed. However in this case the $^1G_4{\rightarrow}^3H_6$ radiative transition is

dominant. With resonant excitation in the $^3F_{2,3}$ (679 nm) Tm^{3+} multiplets the low energy transitions $^3F_2 \rightarrow {}^3H_5$, $^3H_4 \rightarrow {}^3F_4$, and $^3F_3 \rightarrow {}^3H_5$ were observed in the 12 K emission spectra of Tm^{3+} doped crystal. In the same Figure 5.35 b) (left side) is shown the 12 K PLE spectrum monitored in the $^1G_4 \rightarrow {}^3H_6$ and $^3F_3 \rightarrow {}^3H_5$ lines which reveal that besides resonant excitation in the respective emitting levels, these emission lines can be observed upon excitation into the high electronic energy levels of Tm^{3+}. In the co-doped crystal, besides the observed intra-4f emissions of Tm^{3+}, it is also identified an intense emission at between 950 and 1100 nm assigned to the electronic transition between the excited energy level ($^2F_{5/2}$) and the ground state ($^2F_{7/2}$) of Yb^{3+}. IR PL spectra acquired at RT with resonant excitation in the $^1D_2$, $^1G_4$ and $^3F_{2,3}$ multiplets shows the same emission observed at 12 K, however additional splitting of the emission band is identified.
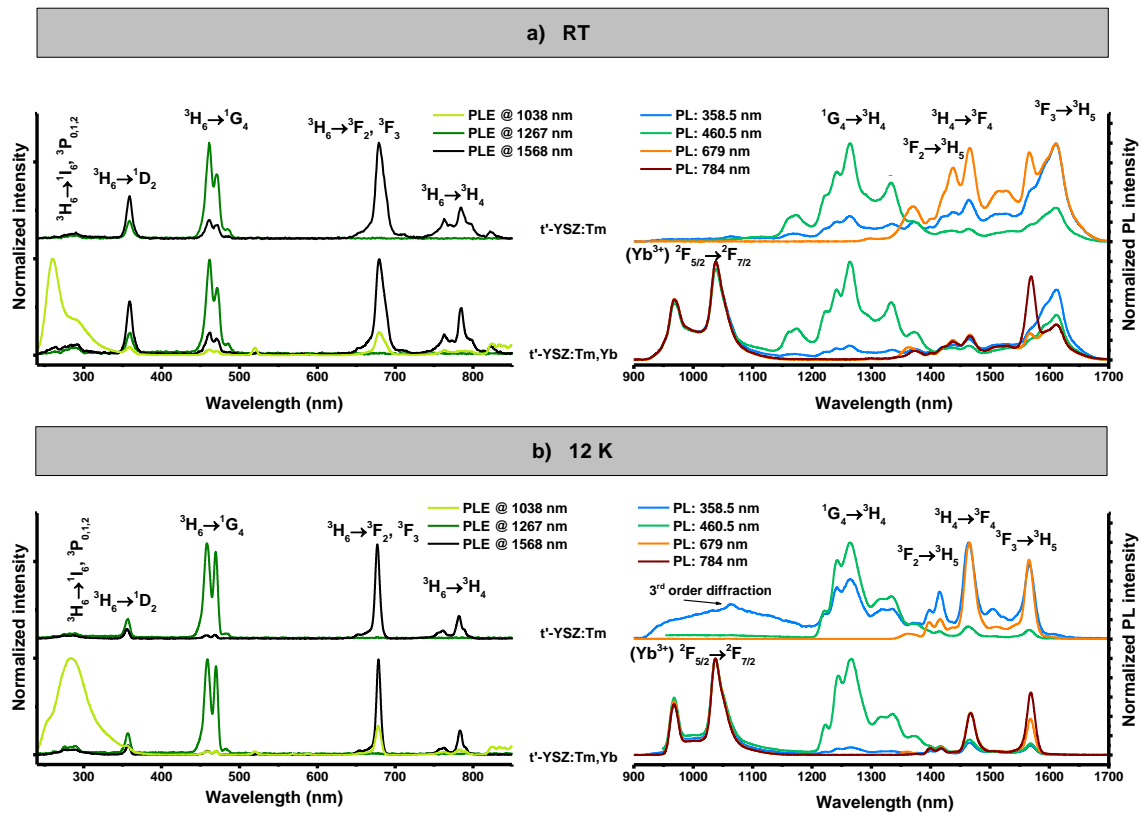

Figure 5.35. PLE and PL spectra of the infrared emissions of the Tm^{3+} doped and Tm^{3+}, Yb^{3+} co-doped t'-YSZ crystals at a) RT and b) 12 K.

The temperature dependent IR PL spectra of the Tm^{3+} doped and Tm^{3+}, Yb^{3+} co-doped crystals were studied between 12 K and RT. Figure 5.36 shows the acquired emission spectra with resonant excitation in the $^1D_2$ (a, d), $^1G_4$ (b, e) and $^3F_{2,3}$ (c, f) multiplets of Tm^{3+}. For the three studied excitation conditions, additional lines of the emission observed at low

temperature were identified corresponding to thermally populated states as identified for the visible PL. In particular, an emission with maximum around 1610 nm, weakly observed at low temperature, suffers a pronounced intensity increase with temperature as happens for the blue $^1D_2 \rightarrow {}^3F_4$. The mechanism behind this thermal population is not yet clearly understood and additional studies need to be performed to clarify this issue. Nevertheless, as the increase in intensity is clearly temperature dependent, nonradiative feeding of the emitting levels should be considered either by a direct thermal population and/or thermal activated cross-relaxation phenomena between neighbour ions.

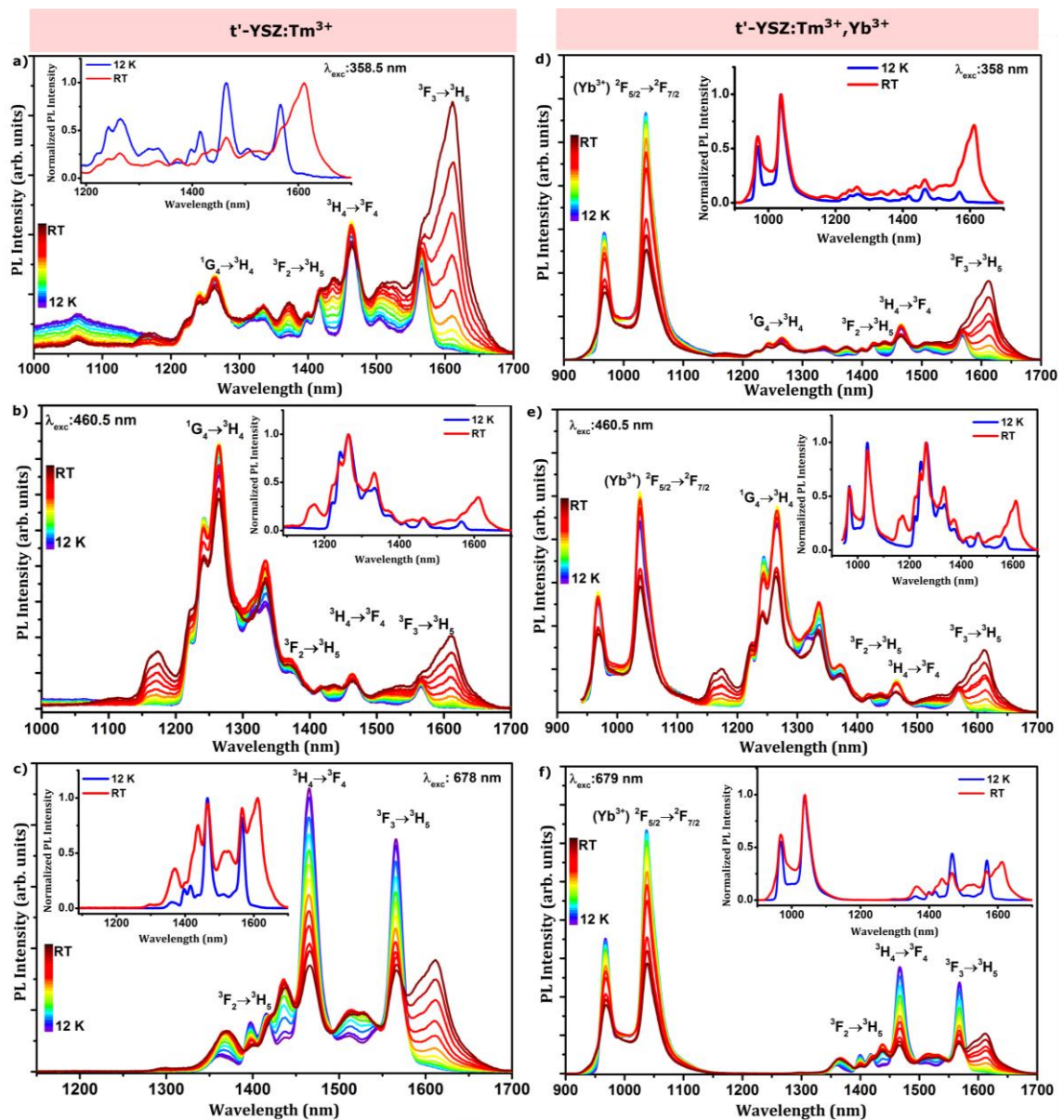

Figure 5.36. Temperature dependence IR PL spectra of the Tm³⁺ doped (a, b, and c) and Tm³⁺, Yb³⁺ co-doped (d, e and f) t'-YSZ crystals, with resonant excitation in the $^1D_2$ (a, d), $^1G_4$ (b, e) and $^3F_{2,3}$ (c, f) multiplets of Tm³⁺.

Summary

Tetragonal YSZ crystals doped with Tm^{3+} and co-doped with Tm^{3+} and Yb^{3+} were successfully grown by the LFZ technique at 20 mm/h. The visible and infrared luminescence of the doped and co-doped crystals was studied. Under UV excitation, resonant with the $^1D_2$ excited state of Tm^{3+}, emission bands in the blue/green, red and NIR spectral regions were observed and assigned to the intra-4f transition of Tm^{3+}. The dominant emission occurs in the blue region due to the $^1D_2 \rightarrow ^3F_4$ transition and is responsible for the blue emission observed at RT by naked eye. The intensity of this blue emission duplicates between 14 K and RT which could be associated with the thermal assisted feeding of the $^1D_2$ emitting level. A similar identification was found for the infrared band peaked at ~1600 nm. As expected Yb^{3+} does not play any role in the visible downshifted emission of Tm^{3+} and very similar PL and PLE spectra were observed for the two crystals. In the co-doped crystal additional emission bands assigned to the $^2F_{5/2} \rightarrow ^2F_{7/2}$ of Yb^{3+} were observed, indicating that energy transfer between the two ions occurs.

5.2.2.5 Er^{3+} doped t'-YSZ crystals

With a 4f^{11} electronic configuration Er^{3+} is known to have a complex schema of levels with a $^4I_{15/2}$ ground state multiplet and several excited states spanning in the wide band gap of the host. When optically active, Er^{3+} is well recognized for the transition between its first excited state $^4I_{13/2}$ and the ground state occurring near 1.54 μm, a wavelength of interest for telecommunications [27]. On the other hand the widespread of the Er^{3+} $^{2S+1}L_J$ multiplets in wide band gap hosts provides a useful opportunity to explore the visible intraionic transitions either in downshifted or upconversion luminescence.

In order to study the luminescence properties of Er^{3+} in the zirconia host, a crystal of tetragonal YSZ (stabilized with 8 mol.% YO$_{1.5}$) doped with 1 at.% Er (t'-YSZ:Er^{3+}) was grown by LFZ at 40 mm/h. In addition, a tetragonal YSZ crystal co-doped with 1 at.% Er and 1 at.% Yb (t'-YSZ:Er^{3+},Yb^{3+}) was grown in the same conditions in order to study the luminescence properties of Er^{3+} under sensitization of Yb^{3+}. The crystalline structure of the as-grown sample was confirmed by Raman spectroscopy. The downshifted luminescence of the crystals was analysed by RT PL and PLE spectroscopy in the visible and infrared spectral range.

Figure 5.37 shows the RT Raman spectra (a), performed with 325 nm laser line excitation, and the photos (b) of the Er^{3+} doped and Er^{3+}, Yb^{3+} co-doped crystals. Raman active modes of the grown crystals follow the expected behaviour for the tetragonal crystalline phase with identified resonances around 260, 324, 464, 606, and 637 cm^{-1} assigned to the A_{1g}, B_{1g}, E_g, B_{1g}, E_g symmetries, respectively.
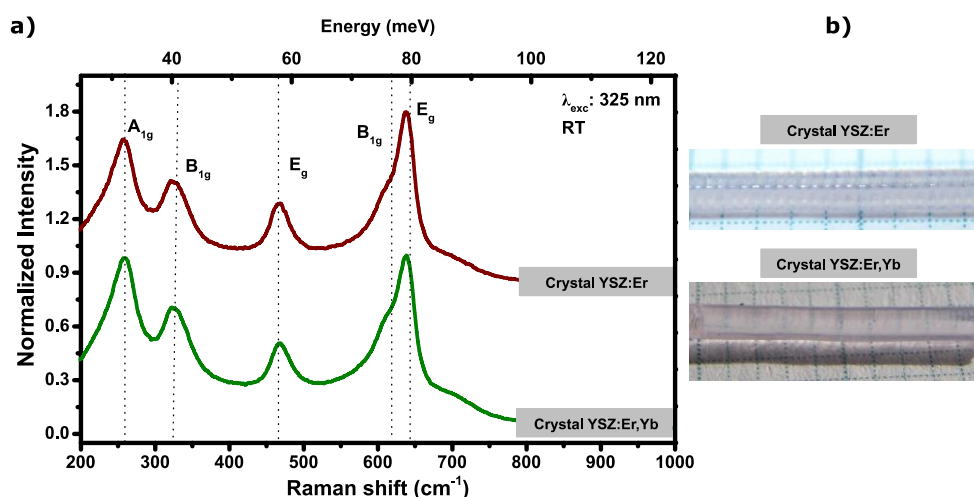

Figure 5.37. a) RT Raman spectra obtained in backscattering configuration with 325 nm He-Cd laser line. b) Photographs of tetragonal YSZ crystals doped with Er^{3+} and co-doped with Er^{3+} and Yb^{3+} ions.

Luminescence characterization

Figure 5.38 a) shows the RT PL spectra obtained with 376 nm wavelength excitation of the Er^{3+} doped and Er^{3+}, Yb^{3+} co-doped YSZ crystals. According with the partial electronic energy level diagram of Er^{3+} shown in Figure 5.38 b), the excitation condition corresponds to a resonant excitation into the $^4G_{11/2}$ excited state. In the studied spectral range, the dominant emission occurs in the green region due to the transition between the $^4S_{3/2}$ and the $^4I_{15/2}$ multiplets and is the responsible for the green emission of the crystals observed at RT. Additional lines are identified in the violet, green, red and NIR spectral regions due to $^2H_{9/2}{\rightarrow}^4I_{15/2}$, $^2H_{11/2}{\rightarrow}^4I_{15/2}$, $^4F_{9/2}{\rightarrow}^4I_{15/2}$, and $^2H_{11/2}{\rightarrow}^4I_{13/2}$, $^4I_{9/2}{\rightarrow}^4I_{15/2}$ and $^4S_{3/2}{\rightarrow}^4I_{13/2}$, respectively. Both crystals exhibit the same PL peak positions and spectral shape with no additional Stark splitting, suggesting that independent of the co-doping process, the optically active Er^{3+} in the tetragonal yttria stabilized zirconia crystals, have similar site symmetries/environments. PLE spectra, taken on the Er^{3+} emission maximum, in the green transition peaked at 562 nm, are displayed in Figure 5.38 a) (green lines). Besides the $^4G_{11/2}$

multiplet, the ion luminescence was found to be likely excited via other ion excited states. Well-defined intra-shell absorption lines from the $^4I_{15/2}$ multiplet to the higher lying Er^{3+} multiplet, $^4D_{7/2}$, can be identified up to ~255 nm (~4.86 eV; ~39217 cm^{-1}). The observation of such high energy absorption band of Er^{3+} incorporated in the tetragonal YSZ host constitutes a strong evidence that the tetragonal YSZ has a band gap energy higher than 5.0 eV, in agreement with the theoretical predicted value of 6.4 eV [28].

Figure 5.38. a) RT PL and PLE spectra of the Er^{3+} doped and Er^{3+}, Yb^{3+} co-doped t'-YSZ crystals. PL spectra were acquired under 376 nm wavelength excitation ($^4G_{11/2}$) and PLE spectra were performed by monitoring the $^4S_{3/2}\rightarrow^4I_{15/2}$ emission. b) Partial electronic energy level diagram of Er^{3+} in which the electronic transitions assigned to the absorption/emission bands observed in the PLE (left side)/PL (right side) spectra are identified.

The luminescence of the t'-YSZ:Er^{3+} and t'-YSZ:Er^{3+},Yb^{3+} crystals was also studied under excitation in the high energetic Er^{3+} multiplet $^4D_{7/2}$, peaked at 255 nm. The obtained spectra are shown in Figure 5.39 a). Under this excitation, additional violet, blue, red and NIR transitions arising from the $^2P_{3/2}$ and $^2G_{7/2}$, multiplets were identified for both doped and co-doped crystals. In fact, transitions between the $^2P_{3/2}$ and the lower lying energy levels are dominant under this excitation, which give rise to new emission bands over all the studied spectral range.

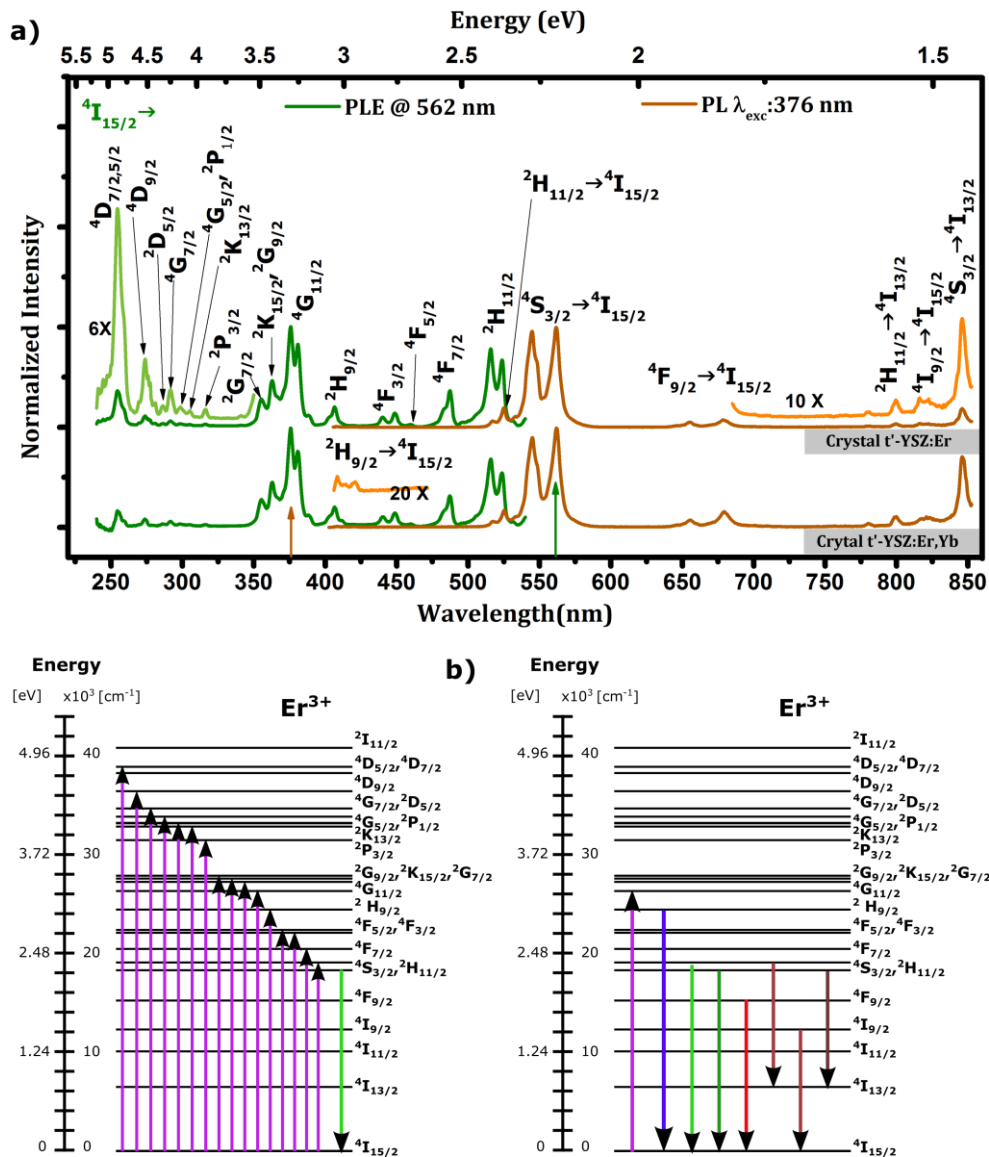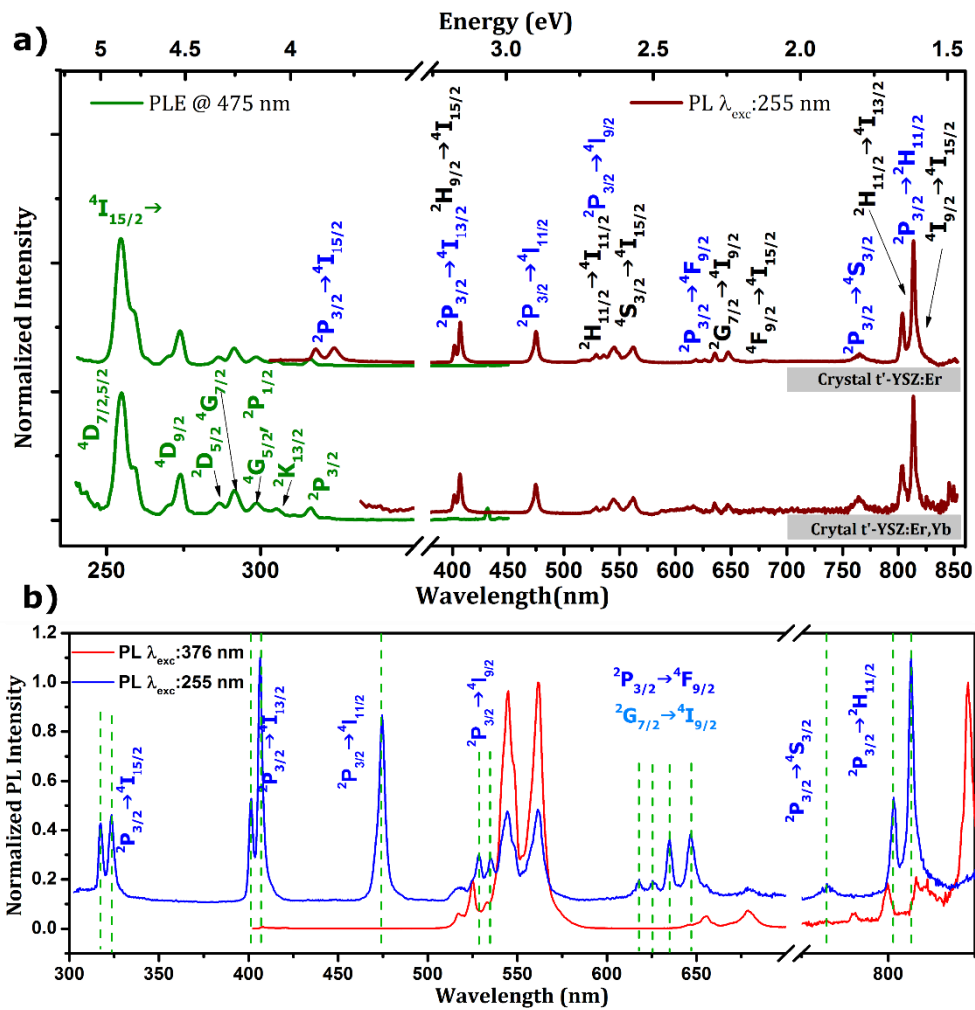**Figure 5.39. a)** RT PL and PLE spectra of the Er^{3+} doped and Er^{3+}, Yb^{3+} co-doped t'-YSZ crystals. PL spectra were acquired under 255 nm wavelength excitation ($^4D_{7/2}$) and PLE spectra were performed by monitoring the $^4P_{3/2}\rightarrow{}^4I_{11/2}$ emission. **b)** Comparison of the RT PL spectra of the t'-YSZ:Er^{3+} crystal under resonant excitation in the $^4D_{7/2}$ and $^4G_{11/2}$. The spectra were normalized to the maxima intensity in the visible and NIR spectral range.

The most intense emission occurs in the NIR which is due to the $^2P_{3/2}\rightarrow{}^2H_{11/2}$ transition overlapped with $^2H_{11/2}\rightarrow{}^4I_{13/2}$ and $^4I_{9/2}\rightarrow{}^4I_{15/2}$ transitions, also observed under excitation in the lower energy $^4G_{11/2}$ level. This excitation process revealed a strong suppression of the

Er^{3+} green $^4S_{3/2} \rightarrow \,^4I_{15/2}$, and red $^4F_{9/2} \rightarrow \,^4I_{15/2}$ light implying the absence of a preferential population of the $^4S_{3/2}$ and $^4F_{9/2}$ multiplets. This way, a change of the visible emission colour is possible in the single crystals by selecting different excitation energies. For an easier analysis of the emission bands observed under the two studied wavelength excitations, the normalized PL spectra under 376 and 255 nm excitation of the t'-YSZ:Er^{3+} crystal are shown in Figure 5.39 b). The spectra were normalized to the maxima intensity of luminescence in the visible and NIR spectral regions. The additional emission bands from the $^2P_{3/2}$ and $^2G_{7/2}$ are indicated (vertical green lines) and identified. PLE spectra monitored in the $^2P_{3/2} \rightarrow \,^4I_{11/2}$ blue emission, peaked at 475 nm, revealed that, in addition to the direct excitation in the $^2P_{3/2}$ level, this emission can be also stimulated by pumping in the higher energy multiplet, with preferential excitation in the $^4D_{7/2}$ level, Figure 5.39 a) (green lines). As previously observed for the Tm^{3+}, Yb^{3+} co-doped crystals, no significant differences in the PL and PLE spectra were observed in the doped and co-doped crystals, which means that Yb^{3+} do not play any role in the visible downshifted luminescence of the Er^{3+}.

In addition to the study of the visible and NIR emission of the Er^{3+} in the tetragonal YSZ host, preliminary studies of the IR emission were also performed. Figure 5.40 a) displays the RT PL spectra of the t'-YSZ:Er^{3+},Yb^{3+} crystals under 514 nm and 980 nm excitation in the spectral range from 900/1000 to 2000 nm.
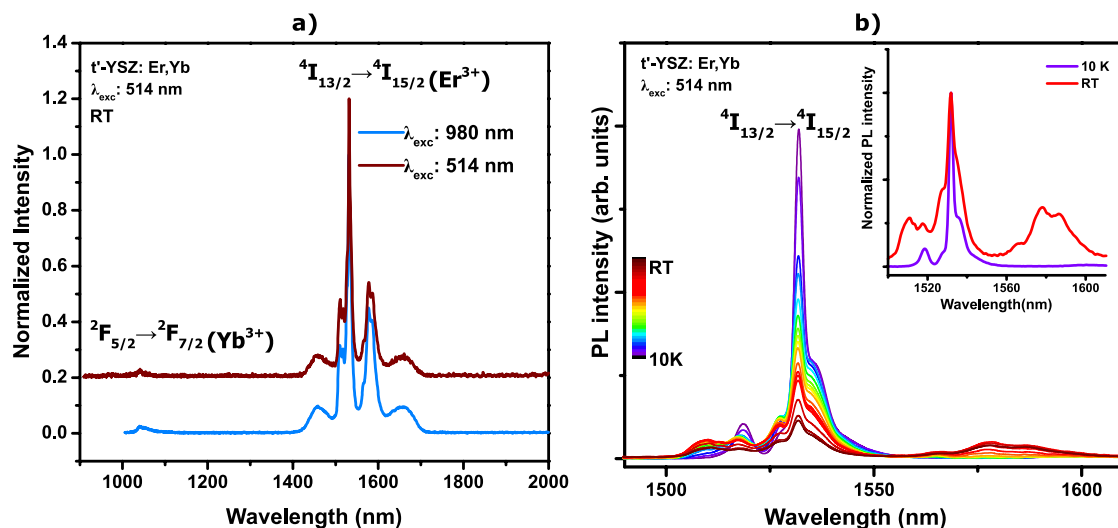
Figure 5.40. a) RT infrared emission of the t'-YSZ crystal co-doped with Er^{3+} and Yb^{3+} with 980 nm and 514 nm excitation. b) Temperature dependence of the infrared emission under 514 nm excitation. Inset in the figure compares the IR luminescence at 10 K and RT.

In the studied spectral range, and under these excitation conditions, a strong emission band with a maximum at ~1530 nm was observed for the two excitation wavelength. Such

emission band is assigned to the $^4I_{13/2}{\rightarrow}^4I_{15/2}$ transition of Er^{3+}. In addition, a band with very low intensity is observed at ~1040 nm due to the electronic transition between the excited state level ($^2F_{5/2}$) and the ground level ($^2F_{7/2}$) of the Yb^{3+}. Such results evidence that the lower energy excited levels of Er^{3+} are preferentially populated when compared with the Yb^{3+} excited level.

Temperature dependent PL spectra were acquired between 10 K and RT with 514 nm excitation, Figure 5.40 b). A decrease of the overall intensity was observed and only about 50% of the low temperature emission intensity is detected at RT. One can see that, while the intensity of the splitted emission band observed at 10 K decrease with temperature, additional high energy bands are observed as a result of thermally populated emitting levels. As mentioned above, this $^4I_{13/2}{\rightarrow}^4I_{15/2}$ IR emission of Er^{3+} is of particular interest for telecommunication.

Summary

Trivalent erbium was successfully incorporated and optically activated in the tetragonal YSZ host during the growth of crystals by LFZ. The study of the downshifted luminescence in both Er^{3+} doped and Er^{3+}, Yb^{3+} co-doped YSZ crystals revealed that no significant differences are induced in the PL and PLE spectra by the incorporation of the Yb ions, meaning that the environment of the emitting Er^{3+} is not affected. The RT visible downshifted emission of Er^{3+} has shown to be dependent on the wavelength excitation. Under resonant excitation in $^4G_{11/2}$ multiplet the dominant emission of Er^{3+} occurs in the green spectral region due to the $^4S_{3/2}{\rightarrow}^4I_{15/2}$ transition which results in the emission of green light at RT. Besides the excitation on the $^4G_{11/2}$ level, this green emission can be stimulated by resonant excitation in the other Er^{3+} levels with energy above of the $^4S_{3/2}$ emitting state. However, with resonant excitation in a higher excited state, $^4D_{7/2}$ (above the $^2P_{3/2}$ level) additional emission lines from $^2P_{3/2}$ level are observed over the PL spectra with dominant emission in the NIR region due to the $^2P_{3/2}{\rightarrow}^2H_{11/2}$ transition. Such emission tuning should be related with the parabolas crossover of the ion high energetic states, implying preferential feeding of the emitting multiplets. The doped crystal show also strong emission at 1530 nm assigned to the $^4I_{13/2}{\rightarrow}^4I_{15/2}$ transition. Additional analysis of the upconversion luminescence of these crystals will be discussed in Chapter 8.

5.2.2.6   Dy³⁺ doped t'-YSZ crystals

When incorporated in wide band gap hosts the visible emission from Dy^{3+} ions is mainly due to intra-4f^9 transitions between the crystal field splitted energy levels of the $^4F_{9/2}$ and $^6H_{J(15/2, 13/2)}$ manifolds which occur in the blue and yellow spectral regions. The visible emission from trivalent dysprosium ions have been studied in different inorganic wide band gap hosts, revealing a high potential for lighting applications, namely as a white emitter.

In this work, the luminescent properties of Dy^{3+} in tetragonal YSZ were studied. In such context, tetragonal YSZ (stabilized with 8 mol.% YO$_{1.5}$) crystals doped with Dy ions were grown by LFZ at 20 mm/h. The produced crystals were intentionally doped with distinct nominal Dy^{3+} concentrations, namely with 0.05, 0.1, 0.2, 0.5 and 1.0 at.%. Structural characterization of the as-grown crystals was accomplished by visible Raman spectroscopy and single crystal X-ray diffraction. The morphology and crystal quality was analysed by SEM and the homogeneity of elements distribution investigated by EDS. The Dy^{3+} luminescent properties were studied by steady state PL and PLE spectroscopy. PL spectra were acquired between 14K and RT under different wavelength excitation using a 1000 W Xe arc lamp coupled to a monochromator and a 325 nm line of a cw He-Cd laser. In addition TR-PL spectra were acquired under excitation with a 266 nm line of a pulsed laser.

Structural characterization

In line with previously LFZ grown YSZ crystals doped with different Ln ions, the translucent crystals fibres (~1.5 mm of diameter and ~15 mm of length) obtained after the dysprosium incorporation crystallized in the tetragonal form, as identified by the Raman spectra shown in Figure 5.41 a). The set of six fingerprint phonon modes of the YSZ host around 146, 260, 322, 462, 606 and 638 cm^{-1} were identified

The crystallinity and morphology of the t-YSZ doped with 0.1 mol.% Dy^{3+} was further analysed by single crystal XRD and SEM. Figure 5.41 b) shows the acquired Laue pattern that evidences the monocrystalline nature of the grown crystal. Corroborating the Raman spectra, the X-ray data was indexed to a tetragonal structure of zirconia, with lattice parameters: $a=b=$ 3.63 Å and $c=$ 5.19 Å. These are in fair agreement with the ones reported by Málek *at al.* [77]. The SEM analysis (Figure 5.41 c) and d) of the 0.1 mol.% doped t'-YSZ shows a good morphological homogeneity without any visible bubbles, cracks or grain boundaries, in agreement with the X-ray diffraction results that reveal the single crystal character of the fibre. In addition, the EDS analysis, Figure 5.41 e), f) and g), shows that the Zr, Y and Dy elements are homogeneously distributed along the crystal diameter and length.
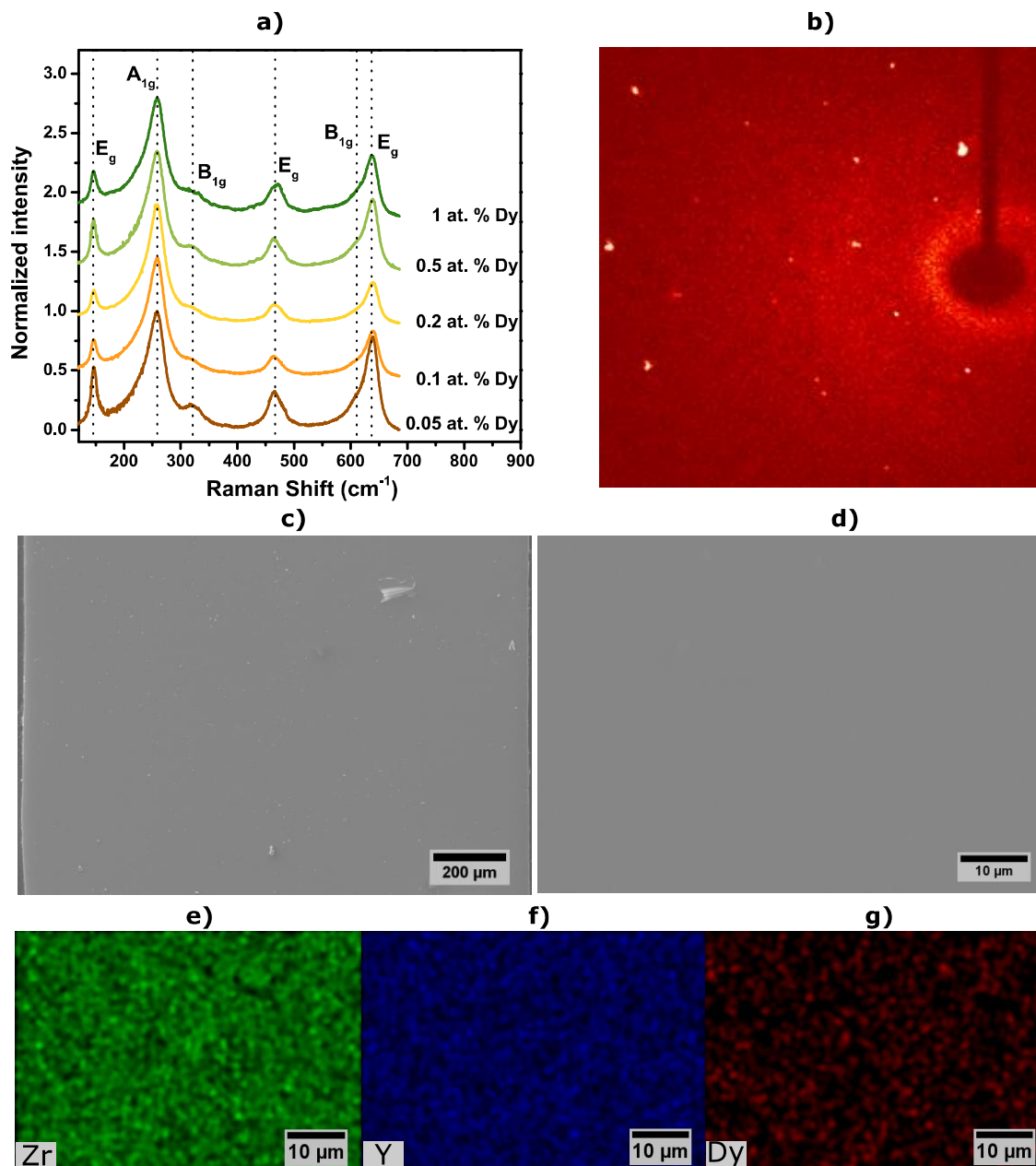
Figure 5.41. a) RT Raman spectra performed in backscattering geometry with visible excitation (532 nm laser line) of the YSZ crystals doped with different amounts of Dy^{3+}. **b)** Single crystal X-ray Laue patterns of the crystal doped with 0.1 at.% Dy^{3+}. Low **(c)** and high **(d)** magnification SEM image and EDS maps of Zr **(e)**, Y **(f)** and Dy **(g)** elemental distribution.

Luminescence characterization

The RT PL spectra of the doped crystals are shown in Figure 5.42 a). Under UV excitation (325 nm) all the crystals exhibit intraionic emission from the Dy^{3+} in the visible and NIR spectral regions due to transitions from the $^4F_{9/2}$ excited state to the $^6H_{15/2}$ ground state and $^6H_{13/2,11/2,9/2}$ levels. Embedded in the crystalline field the degeneracy of the Dy^{3+} free ion levels is lifted according to the symmetry of the local electric field, which allows the

admixture of the wave function of opposite parity, promoting the observation of transitions with electric dipole nature, otherwise parity forbidden. This is for instance the case of the yellow hypersensitive ($\Delta L = 2$; $\Delta J = 2$) $^4F_{9/2} \rightarrow {}^6H_{13/2}$ transition (at ~584.5 nm) which is strongly influenced by changes in the surrounding ions. Besides the yellow luminescence, blue light (~483 nm) is observed due to the magnetic dipole allowed $^4F_{9/2} \rightarrow {}^6H_{15/2}$ transition. Owing to the different characters of the above mentioned transitions the variations in their intensity ratio are particularly useful to identify changes in the surrounding of the Ln ions and the local symmetry.
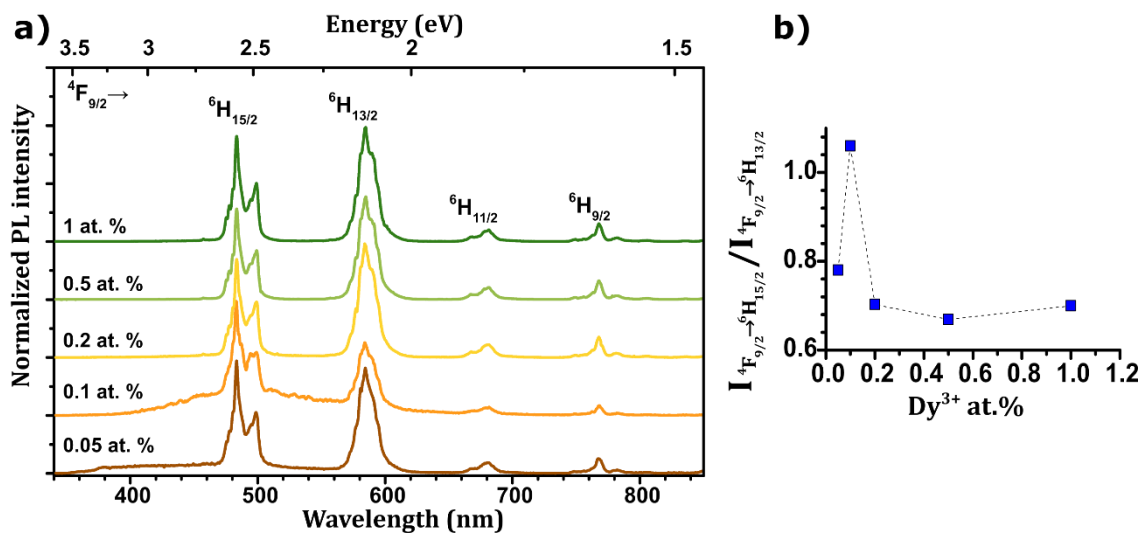
Figure 5.42. a) RT PL spectra of the as-grown crystals doped with different Dy^{3+} amounts, under 325 nm line of He–Cd laser excitation. b) Intensity ratio of the $^4F_{9/2} \rightarrow {}^6H_{15/2}$ and $^4F_{9/2} \rightarrow {}^6H_{13/2}$ transitions as a function of dopant concentration.

For dysprosium ions located at high symmetry sites a higher intensity of the blue emission has been reported when compared with the intensity of the yellow transition [32]. In Figure 5.42 b) the intensity ratio of the two transitions is shown for the crystal doped with different dysprosium contents. The intensity ratio was found to be dependent on the amount of the Ln ion, increasing up to an amount of 0.1 at.% followed by a decrease for heavily doped crystals. Besides the intraionic luminescence, the lightly doped crystals (with Dy^{3+} concentrations of 0.05 and 0.1 at.%) exhibit a broad green band peaked at ~500 nm which has been currently associated with the presence of native defects, as already mentioned for the undoped samples (section 5.2.1).

A suitable adjustment of the blue and yellow emission components of Dy^{3+} can be used to generate white light in materials doped only with this Ln ion (Dy^{3+}). The emission colour of the grown crystals was analysed based on their colour coordinates and correlated colour

temperature (CCT) in line with what was explained in Chapter 2. The results are shown in Figure 5.43 a) and b). Slight variations of the colour coordinates and of the CCT were identified in the crystals doped with different dysprosium amounts, which are due to the different intensity ratios of the blue and yellow Dy^{3+} emission bands, as well as to the background of the green broad band. To compare the different white emissions, the $W2=Y+800(x_R-x)+1700(y_R-y)$ whiteness parameter was calculated. Here, Y is a tristimulus value, (x, y) are the chromaticity coordinates in the CIE 1931 colour space and $(x_R,y_R)=$ (0.33,0.33) are the chromaticity coordinates of the perfect white emitter [78]. A perfect white gives a $W2=$ 100%. The calculated $W2$ for the Dy^{3+} doped crystals in Figure 5.43 b) show that the emission of the 0.1 at.% doped crystal is the most white ($W2=$88%) of the bunch. In this sample a proper intensity ratio between the intraionic blue and yellow emission, combined with the emission of the broad band results in the perceived white emission at RT, under excitation with 325nm. Furthermore, the intraionic luminescence was found to be stronger for lightly doped samples than for heavily doped ones, meaning that a further effect of the quenching of the luminescence due to concentration effects must be accounted.

mol %Dy	cieX	cieY	CCT	W2
0.05	0.36228	0.35869	4430.695	33.7305
0.1	0.29797	0.35727	7017.087	87.6023
0.2	0.41919	0.39712	3270.017	-77.1262
0.5	0.43121	0.39932	3060.931	-90.4792
1	0.42222	0.39426	3187.125	-74.6777
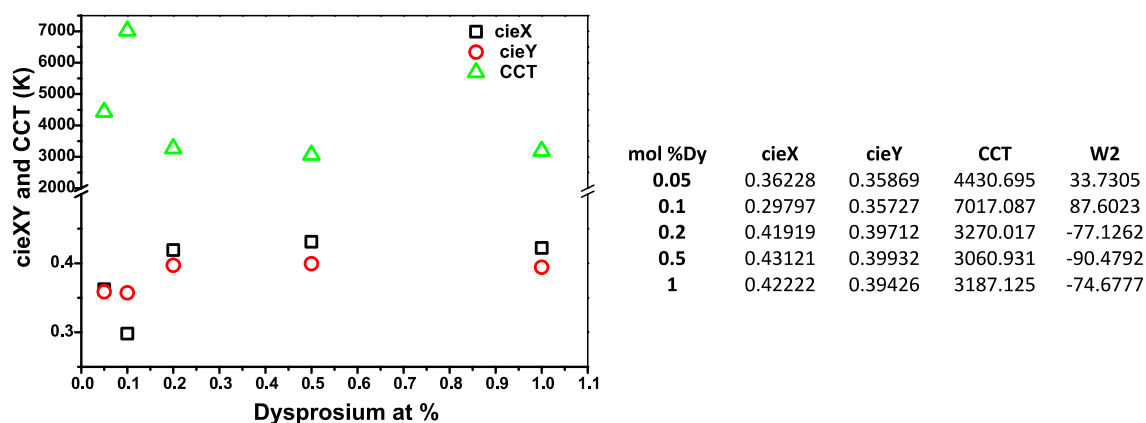
Figure 5.43. a) Variation of the colour coordinates and the CCT with the amount of Dy^{3+}. b) Values of cieX, cieY, CCT and $W2$ calculated for the different doped crystals.

Figure 5.44 shows the RT PL and PLE spectra for the strongest emitting sample (doped with 0.1 mol.%) where the broad green band can be clearly identified. In addition to the observation of the intra-$4f^9$ transitions observed with 325 nm excitation, the Dy^{3+} luminescence can be observed under distinct excitation paths, as shown in the PLE spectra (left side of Figure 5.44). When the excitation spectrum is monitored in the yellow (top spectrum) and blue (middle spectrum) transitions it can be observed that the emissions are preferentially excited via the higher excited states of the $4f^9$ configuration. The assignments of the dysprosium excited states were made in accordance with previous reported works on

wide band gap crystals [79,80]. Monitoring the excitation spectrum in the broad green band reveals that the defect from where the luminescence is originated is preferentially excited via a broad UV excitation band. However, and to less extent, the green luminescence can also be populated via some of the dysprosium excited states. Selected wavelength dependent PL spectra shown in Figure 5.44 (left side of the figure) show that when the excitation is performed with energies equal to or above the one corresponding to the $^3P_{3/2}$ state, both the broad band emission and the intraionic luminescence can be observed (see red and blue spectra in Figure 5.44). On the other hand, for a resonant excitation on the highest intensity excitation band of the dysprosium ions (located ~353 nm) only the intraionic emission is detected.
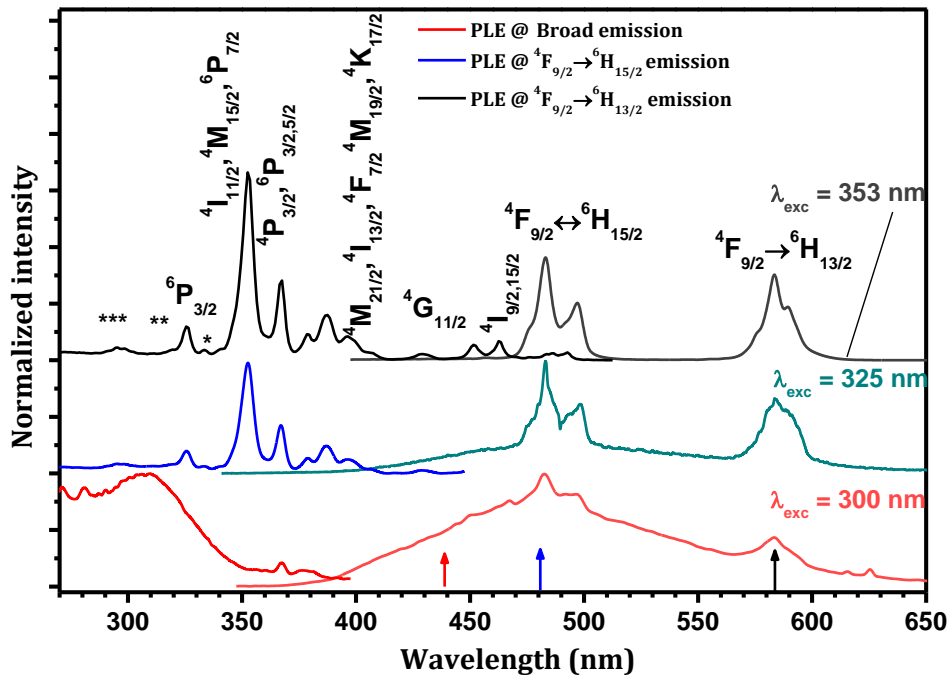
Figure 5.44. RT PL (right side) and PLE (left side) spectra of the t'-YSZ doped with 0.1 at.% Dy³⁺. PLE was monitored at the yellow $^4F_{9/2}{\rightarrow}^6H_{13/2}$ transition (top spectrum), blue $^4F_{9/2}{\rightarrow}^6H_{15/2}$ emission (middle spectrum) and in the broad green band (bottom spectrum). The arrows in the figure represent the wavelengths for which the excitation was monitored. The asterisks correspond to other Dy³⁺ excited states.

In order to evaluate the internal quantum efficiency of the luminescence in the crystal doped with 0.1 at.%, their emission spectrum was analysed in the temperature range of 14 K to RT and under two different excitation wavelengths (325 nm and 353 nm), as shown Figure 5.45. With 325 nm excitation the intensity of the intraionic recombination decreases with increasing temperature, Figure 5.45 a). The nonradiative processes follow almost the same trend as the broad band and only ~25% of the low temperature emission is detected

at RT, Figure 5.45 c). In contrast, nonradiative losses are practically absent when the sample is pumped with 353 nm excitation and about 90% of the overall emission intensity detected at low temperature remains at RT, Figure 5.45 b) and d). This means that efficient Dy^{3+} excitation in zirconia host could be achieved by UV light offering new potentialities for white-light based phosphors.
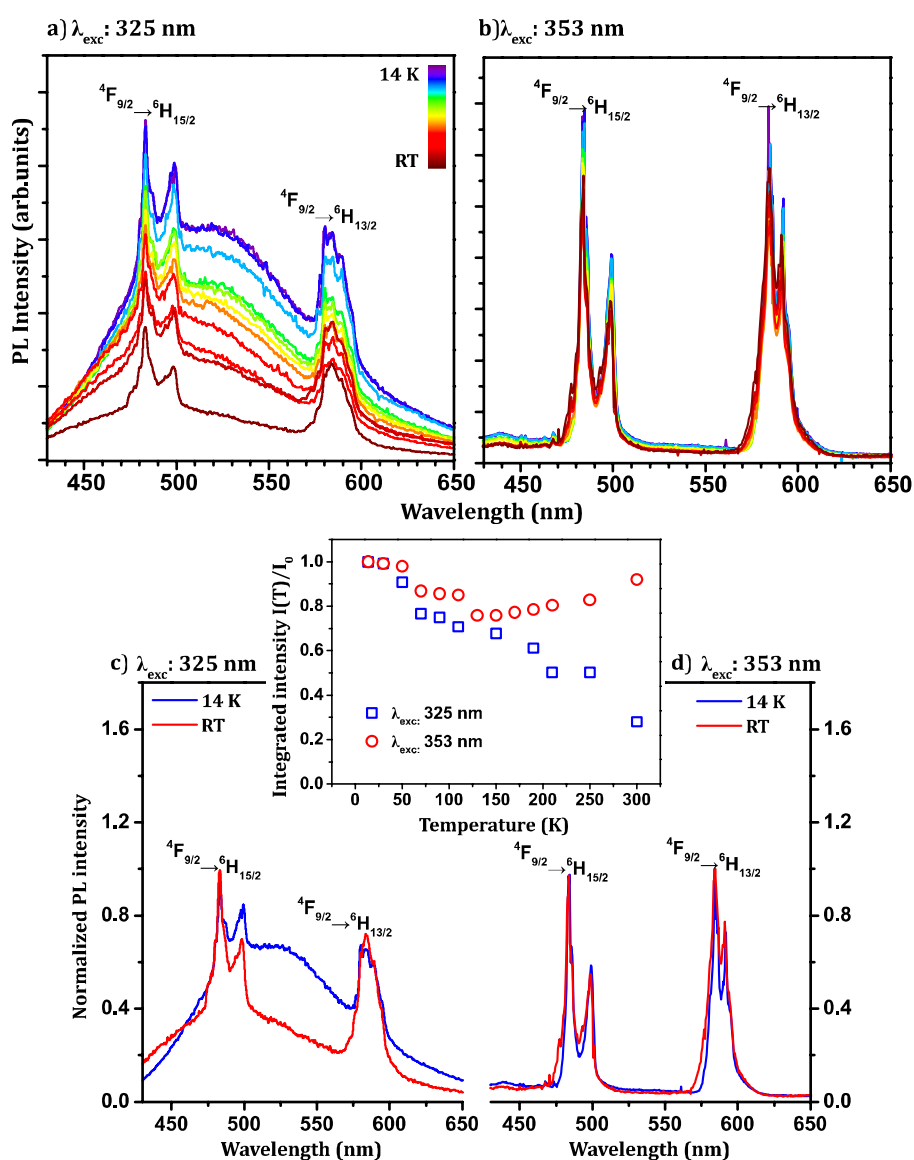
Figure 5.45. Temperature dependent PL spectra of the t'-YSZ crystal doped with 0.1 at.% Dy obtained with 325 nm (a) and 353 nm (b) excitation. Comparison of the spectra obtained at low and RT with 325 nm (c) and 353 nm (d) excitation. The inset shows the dependence of the overall integrated emission intensity with temperature for the two excitations.

The luminescence dynamics of the tetragonal YSZ crystal doped with 0.1 at.% Dy was studied by TR-PL spectroscopy under the excitation of a 266 nm line of a pulsed laser. Figure 5.46 a) displays the TR-PL spectra of this sample acquired for a time range after

pulse up to 2300 μs and time delay between spectra of 100 μs. For t= 0 s an overlap between the intraionic luminescence of Dy^{3+} and the broad emission band centred at 500 nm is observed in accordance with what is expected for the aforementioned steady state condition. As can be observed, the intensity of broad emission band suffers a faster decrease when compared with the emission from the $^4F_{9/2}$ excited state of Dy^{3+}. In fact, for a time delay after pulse of 100 μs the broad emission was no longer observed and the spectra is composed only by the emission band from the intraionic transitions. In order to analyse the time dependent behaviour of the broad emission band a TR-PL spectra were acquired for a shorter time range (0 to 1900 ns), Figure 5.46 b). Based on these spectra, and after removing the contribution of intraionic luminescence, a lifetime in the order of 340 ns was obtained for the decay of the broad emission. On the other hand, the luminescence lifetime of $^4F_{9/2}$ emitting state is significantly longer, in the order of 950 μs and 850 μs for 353 and 325 nm excitation, respectively, as shown in Figure 5.46 c).

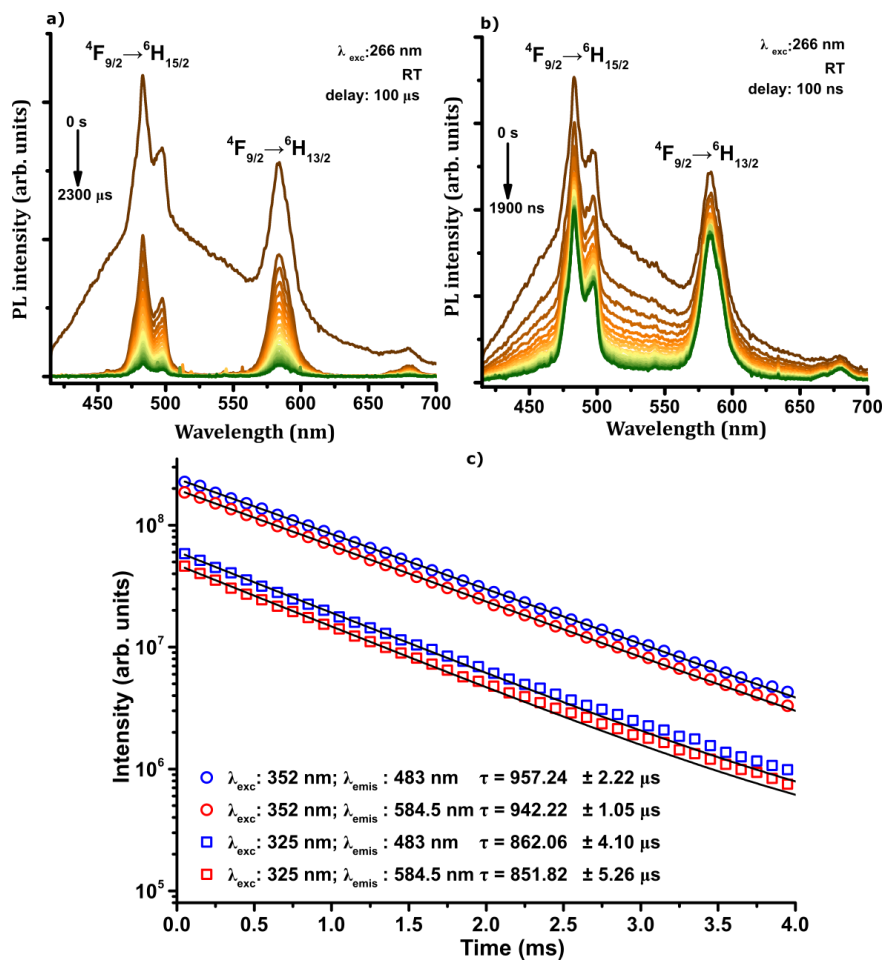**Figure 5.46. TR-PL spectra of the t'-YSZ crystal doped with 0.1 at.% Dy^{3+} under 266 nm pulsed laser excitation in a microseconds (a) and nanoseconds (b) time delay range. Luminescence decay curves for the intraionic emission of the 0.1 at.% Dy^{3+} doped YSZ crystal.**

Figure 5.47 a) and b) show the photographs of the RT emitted light from the crystal doped with 0.1 at.% Dy^{3+} under excitation with the 325 nm He–Cd laser line. A bright intense white light is perceived by naked eye. The white emitted light was characterized in terms of their (x,y) colour coordinates and CCT for three different wavelength excitations. Figure 5.47 c) shows the representation of the emitted colour for each wavelength excitation in the chromaticity coordinate diagram. The calculated values of (x,y) colour coordinates and CCT are displayed in Figure 5.47 d). As can be observed in Figure 5.47 c) and d), the white emitted light can be tuned from a cold to a warm light by change the excitation wavelength.

	a)		b)	

	CIE (1931) coordinates		
λ_{exc} (nm)	x	y	CCT(K)
330 nm (O)	0.221	0.293	16818
325 nm (□)	0.296	0.350	7205
353 nm (△)	0.364	0.366	4410
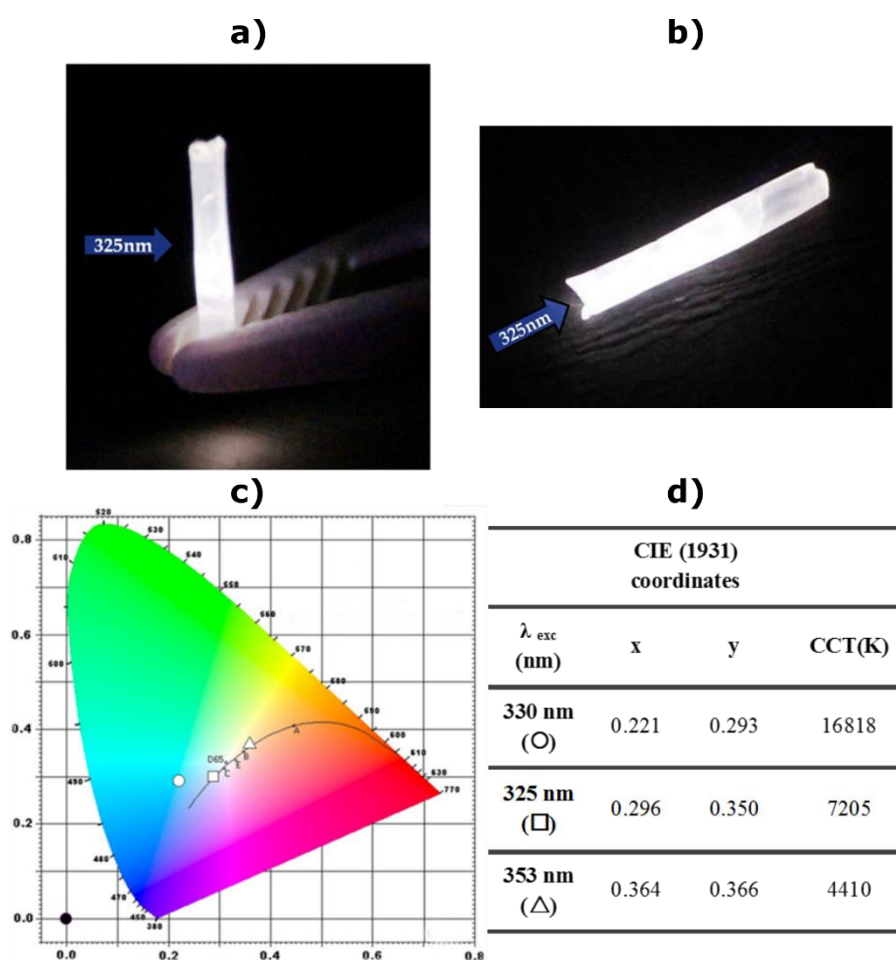
Figure 5.47. a) and b) Photos of the RT emitted light from the t'-YSZ crystal doped with 0.1 at.% Dy³⁺ when excited with the 325 nm line of a He–Cd laser. c) and d) Colour coordinates chromaticity diagram and the correlated colour temperature (CCT).

Summary

Tetragonal YSZ crystals doped with different amounts of dysprosium ions were grown by LFZ. The role of dysprosium concentration on the intensity ratio of the blue and yellow transitions of the YSZ crystals was discussed. For lightly doped samples, besides the

intraionic luminescence a broad green band related with native defects is also present. An intense and bright white light luminescence is perceived for the crystal doped with 0.1 mol.%. The excitation spectra monitored either on the intraionic emission or in the broad green band indicate different excitation pathways for the population of the Dy^{3+} emitting levels. When the excitation is performed at 325 nm, both the green luminescence and the Dy^{3+} are excited and the ion emission suffers nonradiative losses similar to the ones found for the green band. On the other hand, the excitation at 353 nm (resonantly with higher excited states of the Dy^{3+}) favours mainly the ion emission and practically no luminescence quenching was found between 14 K and the RT. This result indicates that efficient t'-YSZ:Dy^{3+} excitation could be achieved by UV light offering new potentialities for the production of white-light based phosphors.

5.2.2.7 Other Ln^{3+} doped t'-YSZ crystals

Tetragonal YSZ crystals doped with other Ln ions besides the ones explored above, including Sm or Ce were also grown by LFZ. Figure 5.48 a) display the Raman spectrum of the YSZ (8 mol.% $YO_{1.5}$) crystal doped with 3 at.% Sm grown at 40 mm/h following the same procedure earlier described. Figure 5.48 b) shows the photo of the as-grown crystal. As expected, and in line with the the other studied crystals, the addition of the 8 mol.% $YO_{1.5}$ to the zirconia precursor powders lead to the stabilization of the tetragonal phase at RT, confirmed by the Raman spectrum where the typical bands assigned to the vibrational modes of tetragonal zirconia were identified.
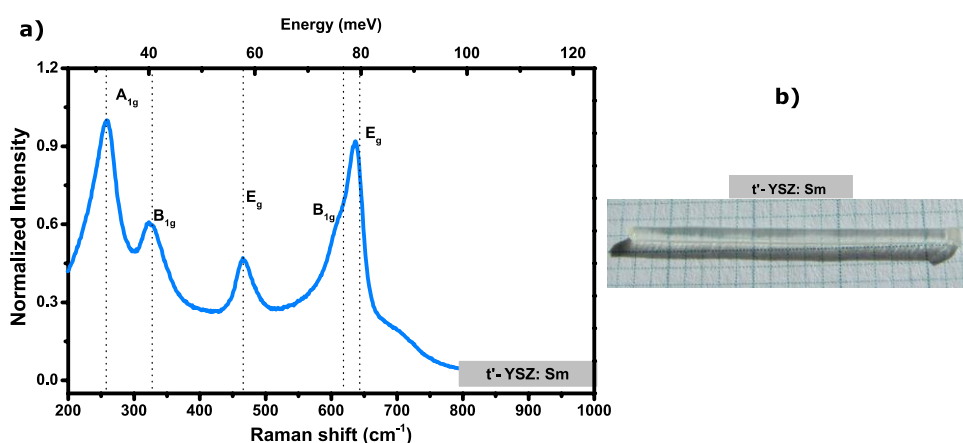

Figure 5.48. a) Raman spectrum and photo (b) of the t'-YSZ:Sm^{3+} crystal grown by LFZ.

The luminescence features of the tetragonal YSZ crystal doped with Sm^{3+} (t'-YSZ:Sm^{3+}) were analysed by PL and PLE spectroscopy. Trivalent samarium, with a $4f^5$ outer electronic configuration and a $^6H_{5/2}$ ground state, has a complex structure of excited energy levels. This

ion has been incorporated in several inorganic host to confer visible luminescence, namely in the red spectral region [81–85].

Figure 5.49 a) shows the PL and PLE spectra o the Sm^{3+} doped crystal. Under excitation with 405 nm, the most intense emission band occurs in the red spectral region, peaked at 622 nm, assigned to the $^5G_{5/2} \rightarrow ^6H_{7/2}$ intra-4f transition. Additional bands are observed at lower and higher energies assigned to the other $^5G_{5/2} \rightarrow ^6H_{J(5/2, 9/2, 11/2)}$ transitions, as identified in the PL spectra and represented in the partial energy level diagram of Sm^{3+} shown in Figure 5.49 b). Similar emission spectra were reported for the Sm^{3+} in tetragonal polycrystalline zirconia samples under identical excitation conditions [86]. The PLE spectra monitored in the dominant red emission peaked at 622 nm revealed that the $^5G_{5/2} \rightarrow ^6H_{7/2}$ emission can be observed by pumping the sample resonantly in the several Sm^{3+} excited multiplets or in a high energy CT broad excitation band. Excitation in the broad absorption band or resonantly in the excited levels of Sm^{3+} leads to similar emission spectra revealing that the emission comes from the same Sm^{3+} optical centres for both excitation conditions.
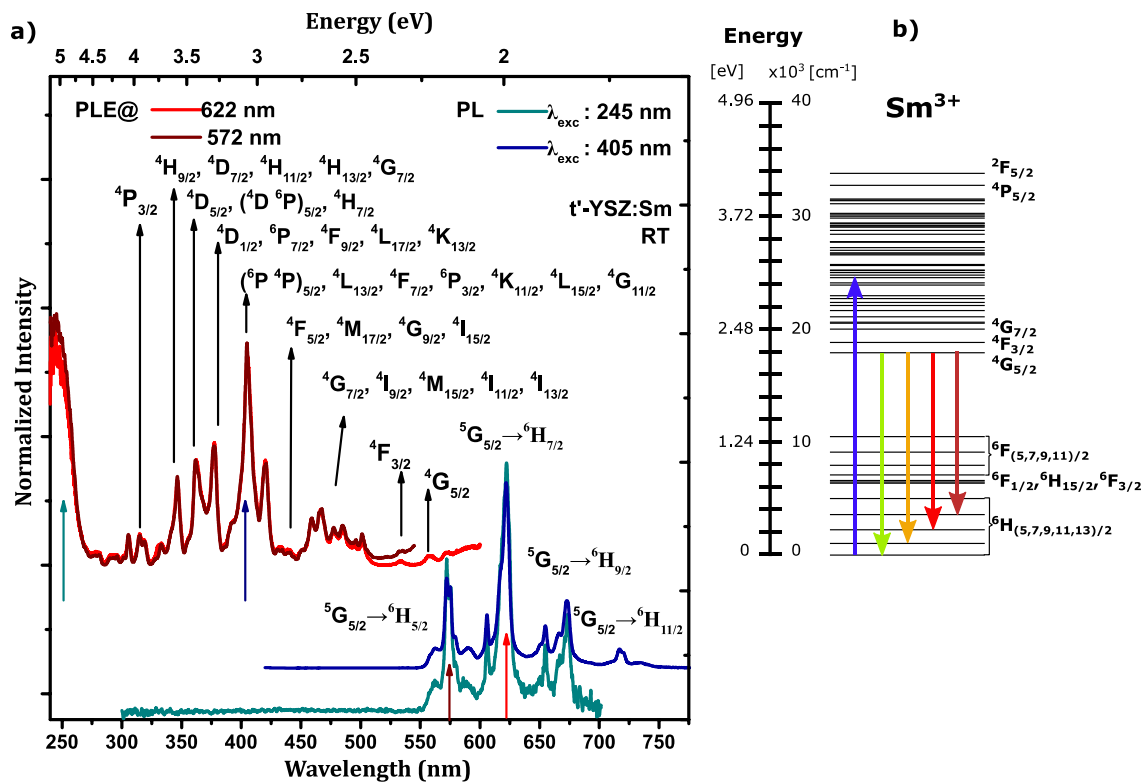

Figure 5.49. a) RT PL and PLE spectra of the t'-YSZ:Sm^{3+} crystal. PL spectra were acquired under resonant excitation in the intra-4f energy levels of Sm^{3+} and the high energy broad absorption band. PLE spectra were acquired by monitoring the $^5G_{5/2} \rightarrow ^6H_{5/2}$ and $^5G_{5/2} \rightarrow ^6H_{7/2}$ emission lines. b) Partial energy level diagram of Sm^{3+}.

PL spectra of the t'-YSZ:Sm³⁺ crystal obtained with 325 nm laser line excitation were acquired between 14 K and RT in order to analyse the internal quantum efficiency of the $^5G_{5/2}{\rightarrow}^6H_J$ emissions. Figure 5.50 a) and b) shows the temperature dependent PL spectra and the comparison of the emission spectra at 14 K and RT, respectively. The visible emission of Sm³⁺ in the tetragonal YSZ revealed to be very stable with temperature and despite a slightly variation in the peaks intensity and peaks broadening, due to thermal induced effects, the overall emission intensity remains almost constant within the studied range of temperature, as can be seen in the inset in Figure 5.50 a).
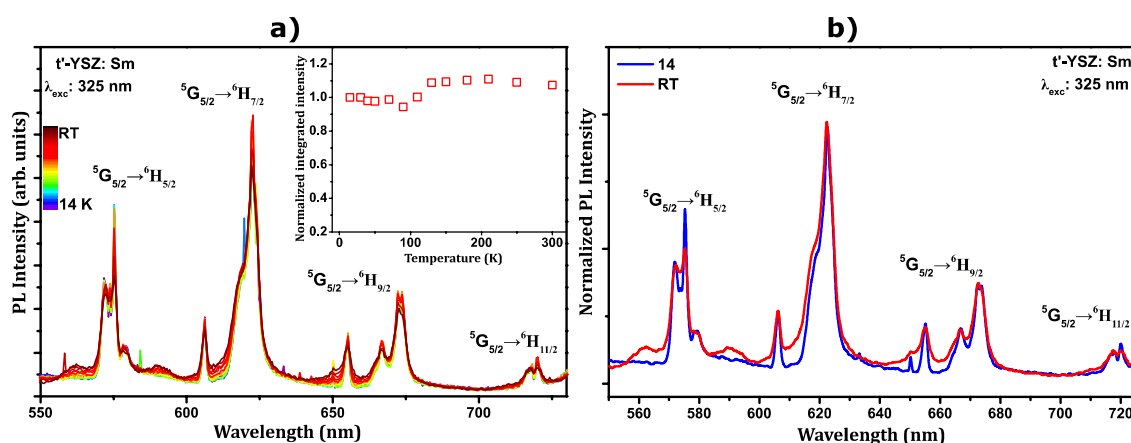
Figure 5.50. a) Temperature dependent PL spectra of the t'-YSZ:Sm³⁺ crystal under excitation with 325 nm laser line. The inset in the figure shows the dependence of the overall $^5G_{5/2}{\rightarrow}^6H_J$ integrated intensity with temperature. b) Comparison of the normalized PL spectra acquired at 14 K and RT.

For optical application purposes, another interesting dopant is Ce³⁺ that constitutes an exception within the trivalent lanthanides ions. In contrast with the other Ln³⁺ in which visible emission occurs due to electronic transition within the $4f$ configuration while $4f{\leftrightarrow}5d$ transitions typically occurs in the UV or VUV spectral region, visible emission of Ce³⁺ in a ligand field is based on the parity allowed $5d{\rightarrow}4f$. The excitation and emission energies are therefore strongly dependent on the ion chemical surroundings [87]. In particular, the $5d{\rightarrow}4f$ yellow emission of Ce³⁺ in YAG has been extensively used to produce yellow phosphors for lighting applications, including the currently used "white LEDs" as explained in Chapter 2. In the YSZ lattice cerium can be in a trivalent (Ce³⁺) or tetravalent (Ce⁴⁺) charge state depending on the processing conditions and the crystallized phases are highly affected by the ion valence [88,89].

A crystal of zirconia stabilized with 8 mol.% YO₁.₅ and doped with 3 at.% cerium was also grown by LFZ at 40 mm/h. In contrast with the other grown crystals, Ce doped YSZ crystal

shows a heterogeneous distribution of Ce evidenced by the colour gradient observed along the crystal fibre length. A photo of the as-grown crystal is shown in right side of Figure 5.51. The initial part of the as-grown crystal, the first grown millimetres, is completely transparent and colourless. This colourless zone is followed by a coloured transparent zone, with a colour gradient that changes from yellow to orange with the increase in the length of the grown crystal. Yellow-orange coloration in zirconia materials doped with cerium has been reported in literature [90]. A structural characterization was performed by Raman spectroscopy along the crystal length and the acquired spectra in three different zones in the crystals length are shown in the left side of Figure 5.51. Raman spectrum in the transparent and colourless zone evidences the Raman band assigned to the vibrational modes of cerium oxide [91], and no Raman bands assigned to the vibrational modes of zirconia phases were detected. However, the used nominal concentration of cerium dopant is low to grow a single crystal of cerium oxide with several millimetres length. Such result could be explained by the higher intensity of the Raman signal associated to the vibrational modes of cerium oxide that suppress the Raman signal associated to the vibrational modes of zirconia phases. On the other hand, in the opposite side of the crystal, corresponding to the final part of the growth, the Raman spectrum corresponds to the typical vibrational modes of tetragonal zirconia. The orange colour in this region indicates that cerium is introduced in the YSZ lattice. In order to understand the behaviour observed in the crystals doped with Ce further structural and elemental composition analysis need to be performed.
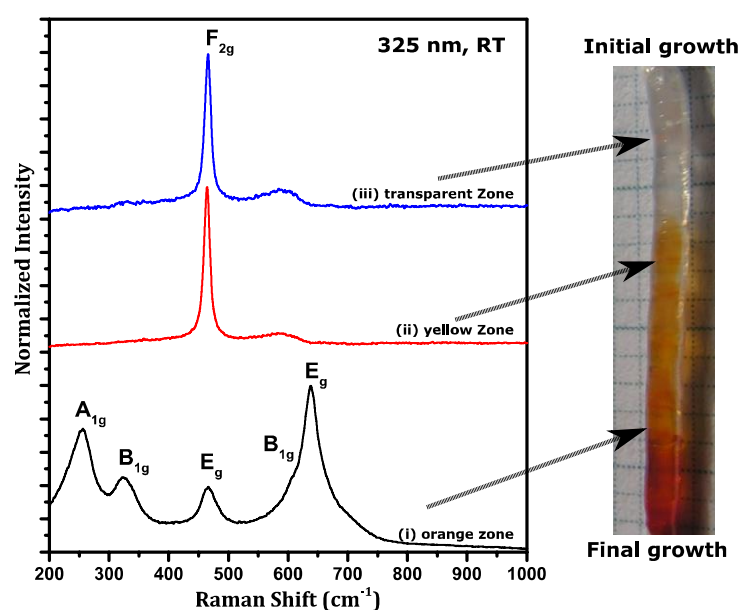
Figure 5.51. Raman spectra of the as-grown crystal doped with cerium with 325 nm laser line excitation. The spectra were acquired in differ regions of the crystal fibre as indicated in the figure.

Preliminary studies of the luminescence of the Ce doped YSZ crystal were performed by RT PL and PLE measurements, Figure 5.52. Under UV excitation (370 nm) the PL spectrum of the grown Ce doped YSZ crystal shows a broad emission band with two maxima at 416 and 438 nm, likely due to Ce^{3+} emitting centres, as happens in other oxide hosts [87,92]. Typically the luminescence is ascribed to the electric dipole allowed $5d{\rightarrow}4f$ transitions from the excited electron configuration to the spin-orbit splitted $^2F_{5/2}$ and $^2F_{7/2}$ multiplets of the fundamental electron configuration of the Ce^{3+} ions. The PLE spectra shown in Figure 5.52 (red lines), monitored in the two emission band maxima, revealed that the broad emission bands can be observed under excitation in the two excitation broad bands centred at 370 nm and 260 nm likely due to the $4f{\rightarrow}5d$ transitions.
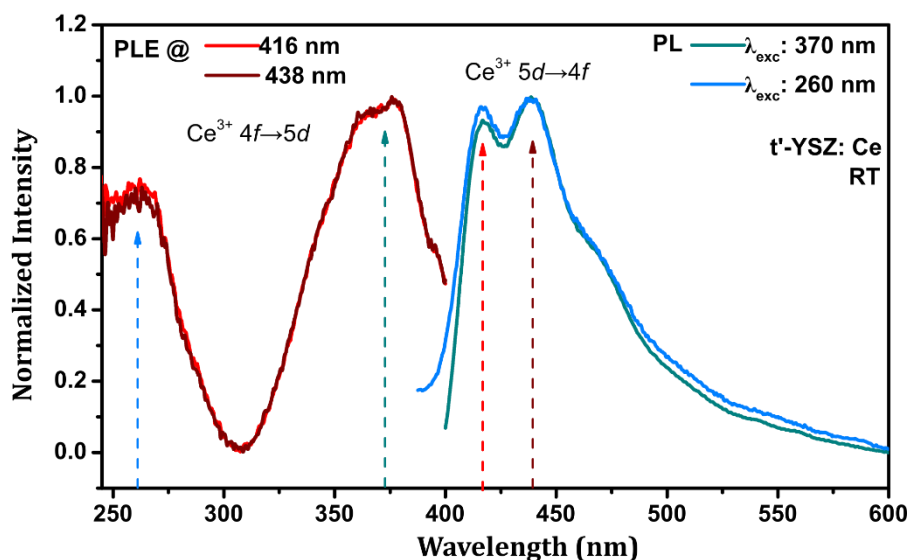
Figure 5.52. RT PL and PLE spectra of the crystal doped with cerium.

Comparatively to other trivalent Ln, the luminescence of Ce^{3+} ion in ZrO$_2$ hosts is reported to be relatively suppressed and their study limited to a few works [89,93]. L.Y. Zhu *et al.* [93] reported PL emission bands centred at 470 and 570 nm in Ce^{3+} doped tetragonal YSZ fibres produced by spinning method. On the other hand, Chih-Ming Lee *at al.* [89] reported a single emission band centred at 496 nm in Ce^{3+} doped zirconia phosphor produced by solid state reaction. A definitive assignment of the emission/excitation bands requires an in-depth study of the doped crystal, namely by using the time, energy and temperature dependence of the light emitted by the sample. Such doping and Ce^{3+} behaviour in the YSZ crystals could be of importance for the development of scintillators for medical imaging.

5.3 Conclusions

Laser Floating Zone, a directional solidification technique used in the growth of bulk crystals from the melt was explored for the growth of YSZ crystals. Due to the high melt temperature of zirconia based materials, the use of focused high power laser for melt the material is advantageous over other used heating sources. In this work, experimental parameters of the LFZ process, including rotation rates, growth direction, growth rate, precursor rods features and others, were studied and optimized in order to achieve the stable growth of YSZ crystals. LFZ method has revealed to be an effective method to the growth of both undoped tetragonal and cubic YSZ single crystals at high pulling rates. However, the as-grown cubic crystals showed a low mechanical stability, breaking very easy during handling. Such phenomena can be related with high crystal stress induced by a heavy additivation and high temperature gradients in the crystal during the growth process.

The knowledge and expertise acquired in the growth of undoped crystals was employed to the successful growth of tetragonal YSZ crystals doped with different lanthanide ions. Lanthanides in a trivalent charge state were easily incorporated and optically activated during the crystal growth without the need of any further thermal annealing for luminescence activation. The emission of Ln^{3+} doped YSZ is mainly due to electronic transitions between the energy levels within the $4f$ configuration of the dopant ion. Different downshifted emission colours could be achieved by a proper selection of Ln dopant ion and their concentration, under UV or visible excitation. Figure 5.53 displays the representation of the colour coordinates in the CIE diagram (left side) and the photos under UV light for some of the studied crystals.
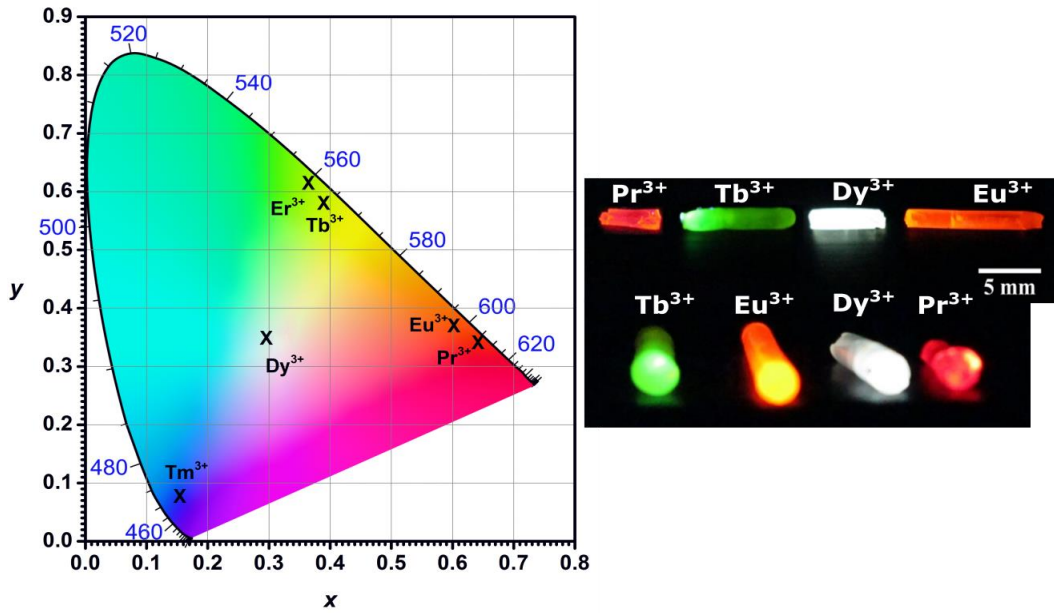
Figure 5.53. Representation of the colour coordinates in the CIE diagram of the emission of different Ln³⁺ doped YSZ crystal (left side). Photo of some of the studied crystals under UV excitation (right side).

In particular intense green, orange, red, blue and white light was observed in YSZ doped with Tb³⁺, Eu³⁺, Pr³⁺, Tm³⁺ and Dy³⁺, respectively. The intense emission observed at RT in Ln³⁺ doped crystals evidences the potential of zirconia as host for the production of efficient phosphors that can be used for practical light-based applications.

References

[1]   V. V. Osiko, M. A. Borik, E. E. Lomonova, In *Springer Handbook of Crystal Growth*; Dhanaraj, G.; Byrappa, K.; Prasad, V.; Dudley, M., Eds.; Springer Berlin Heidelberg, 2010; pp. 433–477.

[2]   H. A. Dabkowska, A. B. Dabkowski, In *Springer Handbook of Crystal Growth*; Dhanaraj, G.; Byrappa, K.; Prasad, V.; Dudley, M., Eds.; Springer Berlin Heidelberg, 2010; pp. 367–391.

[3]   M. R. B. Andreeta, A. C. Hernandes, In *Springer Handbook of Crystal Growth*; Dhanaraj, G.; Byrappa, K.; Prasad, V.; Dudley, M., Eds.; Springer Berlin Heidelberg, 2010; pp. 393–432.

[4]   T. Fukuda, P. Rudolph, S. Uda, *Fiber Crystal Growth from the Melt*; Springer Science & Business Media, 2004.

[5]   F. Agulló-López, *Insulating Materials for Optoelectronics: New Developments*; World Scientific, 1995.

[6]   H. Fredriksson, U. Akerlind, *Solidification and crystallization processing in metals and alloys*; Wiley: Chichester, 2012.

[7]   R. L. Ashbrook, *J. Am. Ceram. Soc.* **1977**, *60*, 428.

[8]   S. Kou, *Welding metallurgy*; 2nd ed.; Wiley-Interscience: Hoboken, N.J, 2003.

[9]   S. M. Koohpayeh, D. Fort, J. S. Abell, *Prog. Cryst. Growth Charact. Mater.* **2008**, *54*, 121.

[10]   C. Nico, Niobium oxides and niobates physical properties. Doutoramento em Nanociências e Nanotecnologia, Universidade de Aveiro: Aveiro, 2015.

[11]   M. F. Carrasco, M. R. Soares, V. S. Amaral, J. M. Vieira, R. F. Silva, F. M. Costa, *Supercond. Sci. Technol.* **2006**, *19*, 373.

[12]   L. B. Kong, Y. Z. Huang, W. X. Que, T. S. Zhang, S. Li, J. Zhang, Z. L. Dong, D. Y. Tang, *Transparent Ceramics*; Springer, 2015.

[13]   E. F. López, V. S. Escribano, M. Panizza, M. M. Carnasciali, G. Busca, *J. Mater. Chem.* **2001**, *11*, 1891.

[14]   M. Yashima, K. Ohtake, M. Kakihana, H. Arashi, M. Yoshimura, *J. Phys. Chem. Solids* **1996**, *57*, 17.

[15]   D. I. Torres, J. Llopis, *Superlattices Microstruct.* **2009**, *45*, 482.

[16]   T. Merle, R. Guinebretiere, A. Mirgorodsky, P. Quintard, *Phys. Rev. B* **2002**, *65*, 144302.

[17]   M. Ishigame, E. Yoshida, *Solid State Ion.* **1987**, *23*, 211.

[18]   K. Nogi, M. Naito, T. Yokoyama, *Nanoparticle Technology Handbook*; Elsevier, 2012.

[19]   E. D. Wachsman, N. Jiang, C. W. Frank, D. M. Mason, D. A. Stevenson, *Appl. Phys. Solids Surf.* **1990**, *50*, 545.

[20]   S. E. Paje, J. Llopis, *Appl. Phys. A* **1993**, *57*, 225.

[21]   N. G. Petrik, D. P. Taylor, T. M. Orlando, *J. Appl. Phys.* **1999**, *85*, 6770.

[22]   H. Nakajima, T. Mori, *J. Alloys Compd.* **2006**, *408-412*, 728.

[23]   B. Savoini, J. E. Muñoz Santiuste, R. González, *Phys. Rev. B* **1997**, *56*, 5856.

[24]   F. S. De Vicente, A. C. Hernandes, A. C. De Castro, M. F. De Souza, M. R. B. Andreeta, M. S. Li, *Radiat. Eff. Defects Solids Inc. Plasma Sci. Plasma Technol.* **1999**, *149*, 153.

[25]   F. Ramos-Brito, M. García-Hipólito, R. Martínez-Martínez, E. Martínez-Sánchez, C. Falcony, *J. Phys. Appl. Phys.* **2004**, *37*, L13.

[26]   J. D. Fidelus, S. Yatsunenko, M. Godlewski, W. Paszkowicz, E. Werner-Malento, W. Łojkowski, *Scr. Mater.* **2009**, *61*, 415.

[27]   G. Liu, B. Jacquier, *Spectroscopic Properties of Rare Earths in Optical Materials*; Springer, 2006.

[28]   B. Královič, E. K. Chang, S. G. Louie, *Phys. Rev. B* **1998**, *57*, 7027.

[29]   J. Dexpert-Ghys, M. Faucher, P. Caro, *J. Solid State Chem.* **1984**, *54*, 179.

[30] H. Yugami, A. Koike, M. Ishigame, T. Suemoto, *Phys. Rev. B* **1991**, *44*, 9214.
[31] L. Chen, Y. Liu, Y. Li, *J. Alloys Compd.* **2004**, *381*, 266.
[32] G. Blasse, B. C. Grabmaier, *Luminescent materials*; Springer-Verlag, Berlin, 1994.
[33] G. Blasse, *Handbook on the Physics and Chemistry of Rare Earths*; Elsevier Science, North-Holland Physics Publishing, 1979; Vol. 4.
[34] D. Van der Voort, G. Blasse, *Chem. Mater.* **1991**, *3*, 1041.
[35] H. E. Hoefdraad, *J. Solid State Chem.* **1975**, *15*, 175.
[36] P. Dorenbos, *J. Lumin.* **2005**, *111*, 89.
[37] K. Utt, M. Part, T. Tätte, V. Kiisk, M. G. Brik, A. A. Chaykin, I. Sildos, *J. Lumin.* **2014**, *152*, 125.
[38] G. H. Dieke, *Spectra and Energy Levels of Rare Earth Ions in Crystals*; Interscience Publishers: New York, 1968.
[39] D. Gazzoli, G. Mattei, M. Valigi, *J. Raman Spectrosc.* **2007**, *38*, 824.
[40] R. Reisfeld, M. Zelner, A. Patra, *J. Alloys Compd.* **2000**, *300–301*, 147.
[41] H. Amekura, A. Eckau, R. Carius, C. Buchal, *J. Appl. Phys.* **1998**, *84*, 3867.
[42] D. Jia, R. S. Meltzer, W. M. Yen, W. Jia, X. Wang, *Appl. Phys. Lett.* **2002**, *80*, 1535.
[43] M. Zawadzki, D. Hreniak, J. Wrzyszcz, W. Miśta, H. Grabowska, O. . Malta, W. Stręk, *Chem. Phys.* **2003**, *291*, 275.
[44] H. Nakajima, T. Mori, *J. Appl. Phys.* **2004**, *97*, 023503.
[45] J. M. Sun, W. Skorupa, T. Dekorsy, M. Helm, L. Rebohle, T. Gebel, *J. Appl. Phys.* **2005**, *97*, 123513.
[46] A. S. Pereira, M. Peres, M. J. Soares, E. Alves, A. Neves, T. Monteiro, T. Trindade, *Nanotechnology* **2006**, *17*, 834.
[47] J. B. Gruber, D. K. Sardar, K. L. Nash, U. V. Valiev, V. Y. Sokolov, S. A. Rakhimov, *J. Appl. Phys.* **2008**, *103*, 103103.
[48] N. Duhamel-Henry, J. L. Adam, B. Jacquier, C. Linarès, *Opt. Mater.* **1996**, *5*, 197.
[49] M. García-Hipólito, R. Martínez, O. Alvarez-Fregoso, E. Martínez, C. Falcony, *J. Lumin.* **2001**, *93*, 9.
[50] Y. Xie, Z. Ma, L. Liu, Y. Su, H. Zhao, Y. Liu, Z. Zhang, H. Duan, J. Li, E. Xie, *Appl. Phys. Lett.* **2010**, *97*, 141916.
[51] A. A. Kaminskii, K. Kurbanov, K. L. Ovanesyan, A. G. Petrosyan, *Phys. Status Solidi A* **1988**, *105*, K155.
[52] G. Özen, O. Forte, B. Di Bartolo, *J. Appl. Phys.* **2004**, *97*, 013510.
[53] A. Lorenzo, L. E. Bausá, J. García Solé, *Phys. Rev. B* **1995**, *51*, 16643.
[54] P. Boutinaud, R. Mahiou, E. Cavalli, M. Bettinelli, *J. Appl. Phys.* **2004**, *96*, 4923.
[55] P. Boutinaud, R. Mahiou, E. Cavalli, M. Bettinelli, *J. Lumin.* **2007**, *122–123*, 430.
[56] S. Kück, I. Sokólska, M. Henke, T. Scheffler, E. Osiac, *Phys. Rev. B* **2005**, *71*, 165112.
[57] F. You, S. Huang, C. Meng, D. Wang, J. Xu, Y. Huang, G. Zhang, *J. Lumin.* **2007**, *122–123*, 58.
[58] B. Di Bartolo, G. Özen, J. Collins, O. Forte, *J. Lumin.* **2007**, *122–123*, 447.
[59] Y. Huang, K. H. Jang, K. Jang, H. J. Seo, *J. Lumin.* **2007**, *122–123*, 47.
[60] F. Ramos-Brito, H. M. S, J. H. A, E. Camarillo, M. García-Hipólito, R. Martínez-Martínez, O. Álvarez-Fragoso, C. Falcony, *J. Phys. Appl. Phys.* **2006**, *39*, 2079.
[61] F. Ramos-Brito, C. Alejo-Armenta, M. García-Hipólito, E. Camarillo, J. Hernández A, H. Murrieta S, C. Falcony, *Opt. Mater.* **2008**, *30*, 1840.
[62] J. D. Fidelus, S. Yatsunenko, M. Godlewski, W. Paszkowicz, E. Werner-Malento, W. Lojkowski, *Scr. Mater.* **2009**, *61*, 415.
[63] J. E. Muñoz-Santiuste, B. Savoini, R. González, *J. Alloys Compd.* **2001**, *323-324*, 768.
[64] H. Nakajima, T. Mori, S. Itoh, M. Watanabe, *Solid State Commun.* **2004**, *129*, 421.
[65] L. C. Alves, M. B. H. Breese, E. Alves, A. Paúl, M. R. da Silva, M. F. da Silva, J. C. Soares, *Nucl. Instrum. Methods Phys. Res. Sect. B Beam Interact. Mater. At.* **2000**, *161–163*, 334.
[66] N. F. Santos, A. J. S. Fernandes, L. C. Alves, N. A. Sobolev, E. Alves, K. Lorenz, F. M. Costa, T. Monteiro, *Nucl. Instrum. Methods Phys. Res. B* **2013**, *306*, 195.

[67]   M. Godlewski, S. Yatsunenko, A. Nadolska, A. Opalińska, W. Łojkowski, K. Drozdowicz-Tomsia, E. M. Goldys, *Opt. Mater.* **2009**, *31*, 490.

[68]   A. Debelle, A. Declémy, L. Vincent, F. Garrido, L. Thomé, *J. Nucl. Mater.* **2010**, *396*, 240.

[69]   K. Schwartz, C. Trautmann, R. Neumann, *Nucl. Instrum. Methods Phys. Res. Sect. B Beam Interact. Mater. At.* **2003**, *209*, 73.

[70]   H. Calvo del Castillo, J. L. Ruvalcaba, T. Calderón, *Anal. Bioanal. Chem.* **2007**, *387*, 869.

[71]   P. D. Townsend, M. Khanlary, D. E. Hole, *Surf. Coat. Technol.* **2007**, *201*, 8160.

[72]   H. Dong, L.-D. Sun, C.-H. Yan, *Chem. Soc. Rev.* **2015**, *44*, 1608.

[73]   Y. Guyot, R. Moncorgé, L. D. Merkle, A. Pinto, B. McIntosh, H. Verdun, *Opt. Mater.* **1996**, *5*, 127.

[74]   I. Sokólska, W. Ryba-Romanowski, S. Gołąb, M. Baba, M. Świrkowicz, T. Łukasiewicz, *J. Phys. Chem. Solids* **2000**, *61*, 1573.

[75]   Z. Li, A. M. Heidt, J. M. O. Daniel, Y. Jung, S. U. Alam, D. J. Richardson, *Opt. Express* **2013**, *21*, 9289.

[76]   D. S. Lee, A. J. Steckl, *Appl. Phys. Lett.* **2002**, *81*, 2331.

[77]   J. Málek, L. Beneš, T. Mitsuhashi, *Powder Diffr.* **1997**, *12*, 96.

[78]   *CIE Colorimetry Technical Report, 3rd ed.*; 2004; Vol. 15.

[79]   G. Dominiak-Dzik, W. Ryba-Romanowski, M. N. Palatnikov, N. V. Sidorov, V. T. Kalinnikov, *J. Mol. Struct.* **2004**, *704*, 139.

[80]   G. Dominiak-Dzik, W. Ryba-Romanowski, L. Kovács, E. Beregi, *Radiat. Meas.* **2004**, *38*, 557.

[81]   C. Nico, M. P. F. Graça, M. Elisa, B. A. Sava, R. C. C. Monteiro, L. Rino, T. Monteiro, *Opt. Mater.* **2013**, *35*, 2382.

[82]   E. De la Rosa-Cruz, L. A. Diaz-Torres, P. Salas, R. A. Rodríguez, G. A. Kumar, M. A. Meneses, J. F. Mosiño, J. M. Hernández, O. Barbosa-García, *J. Appl. Phys.* **2003**, *94*, 3509.

[83]   S. Lange, I. Sildos, M. Hartmanova, J. Aarik, V. Kiisk, *J. Non-Cryst. Solids* **2008**, *354*, 4380.

[84]   C. A. Kodaira, R. Stefani, A. S. Maia, M. C. F. C. Felinto, H. F. Brito, *J. Lumin.* **2007**, *127*, 616.

[85]   S. Tsao, Y.-P. Fu, C.-T. Hu, *J. Alloys Compd.* **2006**, *419*, 197.

[86]   S. Lange, I. Sildos, M. Hartmanova, V. Kiisk, E. E. Lomonova, M. Kirm, *J. Phys. Conf. Ser.* **2010**, *249*, 012007.

[87]   L. V. Meyer, F. Schönfeld, A. Zurawski, M. Mai, C. Feldmann, K. Müller-Buschbaum, *Dalton Trans. Camb. Engl. 2003* **2015**, *44*, 4070.

[88]   H. Kinoshita, K. Kuramoto, M. Uno, T. Yanagi, S. Yamanaka, H. Mitamura, T. Banba, *J. Am. Ceram. Soc.* **2000**, *83*, 391.

[89]   C.-M. Lee, Y.-H. Pai, T.-P. Tang, C.-C. Kao, G.-R. Lin, F.-S. Shieu, *Mater. Chem. Phys.* **2010**, *119*, 15.

[90]   H. Y. Zhu, T. Hirata, *Solid State Commun.* **1992**, *84*, 527.

[91]   T. Taniguchi, T. Watanebe, S. Ichinohe, M. Yoshimura, K. Katsumata, K. Okada, N. Matsushita, *Nanoscale* **2010**, *2*, 1426.

[92]   J. Wu, L. Yin, L. Zhang, *RSC Adv.* **2013**, *3*, 7408.

[93]   L. Y. Zhu, X. Q. Wang, G. Yu, X. Q. Hou, G. H. Zhang, J. Sun, X. J. Liu, D. Xu, *Mater. Res. Bull.* **2008**, *43*, 1032.

Chapter 6.

Solution combustion synthesis (SCS)

In the first part of this chapter, the fundaments of the solution combustion synthesis are explained and the used experimental setup is described.

In the second part, the results obtained by the morphological, structural and optical characterization of the produced nanopowders are presented and discussed.

6.1 Production of nanophosphors by SCS

The production of oxide nanopowders by solution combustion synthesis (SCS), also known as self-propagating high temperature synthesis (SHS), explores a very quick and auto-sustained exothermic redox reaction between an organic fuel with relatively low ignition temperature (< 500 ^{0}C) and appropriated metallic salts in a aqueous solution [1–4]. The metallic salts, besides being sources of metallic cations for the final compound, act as oxidizers for the fuel in the combustion process. The fuel, which acts as a reducing agent in the redox reaction, can also acts as complexing agent for the metal cations [3]. Typical salts used in the SCS include carbonates, metal sulphates and nitrates. Within these, the nitrates are the most frequently used oxidizers due to its good solubility in water. The fuel are organic compounds such as amino acid, including urea or glycine [3,4]. In this method, once the ignition of the initial solution takes place, by means of an external thermal source (by heating the mixture above the ignition temperature (T_{ig})), an auto-sustained exothermic reaction occurs within a short period of time (from few seconds to few minutes) [3]. During this exothermic reaction, a certain amount of heat, expressed by a maximum temperature named combustion temperature, is released. During the combustion the temperature can reach values well above 1000 ^{0}C, which lead to the formation of crystalline oxide powders without involving any additional energy [3,5].

SCS has been increasingly explored as an effective alternative to the conventional methods used in the production of advanced ceramic oxides at nanoscale [3]. The high temperatures reached during the combustion promote the volatilization of any impurity present in the mixture, giving rise to products with high purity [2–5]. Furthermore, for a high number of materials, and depending on the used process conditions, the temperature reached in the combustion is enough to crystallize the required phases in the as-prepared powders, allowing to avoid additional steps of powder calcination or heat treatment [5]. Additionally, desirable dopants can be easy and uniformly incorporated in the crystalline lattice during the SCS in a single step [1]. Since the reaction occurs in aqueous solution, the reactants can be mixed at a molecular level, resulting in the formation of compounds with uniform and desired composition [5]. As it will be further explored, during the SCS a high volume of gaseous products are released. The production of a high amount of gases together with the short duration of the process inhibit the excessive particle growth, which favours the production of nanopowders with high specific surface area [5]. The high temperature gradients combined with rapid cooling rates allows the formation of unique microstructures and the stabilization of metastable phases [2,4].

In summary, SCS consists in a versatile, simple and quick strategy, which do not require specific sophisticated equipment, for the direct preparation of a wide variety of materials, with a strong energy and time saving comparatively with other techniques [1,3]. Its simplicity and cost effectiveness makes the SCS method a very interesting process for large scale industrial production. In general and as aforementioned, the powders produced by this method are characterized by high purity, high homogeneity, high degree of crystallinity and reduced grain size.

Due to the particular features of SCS and to the characteristics of the resultant powder, this method has been used for the preparation of a wide variety of materials for application in different areas, including pigments, catalysts or luminescent materials [1]. The control over particle size is possible by a proper selection of the fuel which affects the nature of the combustions. As it will be explored later, the characteristics of the combustion reaction, including the burning rate, exothermicity of the reaction, and the volume of gaseous products, which are all affected by the type of fuel used in the combustion, have a strong influence in the particle size of the produced powders. As such, a proper control over the combustion parameters allows the synthesis of powders at nanoscale [4].

Regarding the production of luminescent inorganic materials doped with Ln ions, the SCS has been increasingly explored for the preparation of nanosized powders [6]. During the combustion process, the required amounts of Ln dopants can be easily incorporated in the crystalline lattice due to the high temperature achieved during the exothermic redox reaction [6]. The use of lanthanide salts, such as lanthanide nitrates, dissolved in the precursor redox aqueous mixture promotes molecular mixtures of these ions in solution and, as a result a uniform distribution of the dopant in the crystalline lattice [5]. Moreover, in contrast with the majority of wet chemical techniques used to produce nanophosphors, for example the sol-gel process, in SCS there is no need of further calcination or thermal annealing to promote crystallization or optical activation of Ln ions [6].

Table 6.1 presents a summary of the inorganic nanophosphors doped with Ln ions produced by SCS reported in the literature. This method has been successfully used in the production and *in situ* doping, not only of simple oxides, such as Y_2O_3 or Gd_2O_3, but also of more complex materials including garnets, perovskites or different oxyorthosilicates. It should be pointed out that SCS is also an effective strategy for the co-doping of materials.

Table 6.1 - Some of the Ln-doped phosphors produced by SCS reported in literature.

| Phosphor	Fuel	Crystalline size (nm)	Ref.
Y_2O_3:Eu	Sucrose	30-50	[7]
$Gd_3Ga_5O_{12}$: (Pr, Tm)	Urea	30	[8]
$SrAl_2O_4$: (Eu, Dy, Tb)	Urea	50-80	[9]
$SrAl_2O_4$: (Eu,Dy)	Urea	80	[10]
Y_2SiO_5:Ce	Hexamine	20-80	[11]
Lu_2SiO_5:Ce	Hexamine	20-80	[11]
Gd_2SiO_5:Ce	Hexamine	20-80	[11]
$LaAlO_3$: Eu	Urea + ammonium nitrate	-	[12]
$YAlO_3$: Eu	Urea + ammonium nitrate	-	[12]
Gd_3PO_7:Eu	Glycine	300	[13]
$CaWO_4$:Eu	Citric acid	50-100	[14]
$SrAl_2O_4$: (Eu, Dy)	Urea	31	[15]
$BaAl_2O_4$: (Eu,Dy)	Urea	20	[15]
$CaAl_2O_4$: (Eu, Dy)	Urea	44	[15]
$SrAl_2O_4$:Eu	Urea	30-40	[16]
$SrAl_2O_4$:Dy	Urea	Tens of nm- few μm	[17]
$GdAlO_3$:Eu	Oxalyl dihydrazide	25-50	[18]
La_2O_3:(Pr,Yb)	Urea	20-50	[19]
La_2O_2S:(Er,Yb)	Thioacetamide	50-200	[20]
$YAlO_3$:Ho	Oxalyl dihydrazide	~30	[21]
$LaAlO_3$:Eu	Oxalyl dihydrazide	20-50	[22]
Y_2O_3: Eu	Glycine	8-70	[23]
Y_2O_3:Eu	Urea	10-20	[24]
$Y_3Al_5O_{12}$:Eu	Urea	60-90	[25]
Ga_2O_3:Er, (Er,Yb)	Urea	~20	[26]
$SrAl_2O_4$:(Eu,Dy)	Glycine	5-30	[27]

6.1.1 Combustion synthesis parameters

The properties of the SCS produced powders, including crystalline nature, crystallite size, purity, specific superficial area and nature of particles agglomeration can be strongly influenced by the characteristics of the exothermic reaction, such as the type of flame, maximum temperature or the volume of the released gases [3]. On the other hand, the characteristics of the exothermic reaction are affected by several parameters that can be optimized, including the type of fuel, the fuel/oxidant ratio, the ignition temperature or the amount of water in the initial solution [3]. In order to get a control over the powders properties it is essential to understand the effect of each one of these parameters in the SCS process.

The type of fuel plays a crucial rule in the combustion process and consequently in the properties of the final powders. An ideal fuel should fulfil some requirements including, be water soluble, have low ignition temperature, be compatible with the metallic nitrates (in order to produce a controllable combustion reaction), it should involve the generation of a high amount of non-toxic gases during the reaction and it should avoid the production of any by-products [4]. Fuels that are available or that are of easy preparation are also preferred [4]. Fuels are sources of C and H which form simple gaseous molecules such as CO_2 or H_2O in the combustion, contributing for the heat dissipation. In addition, the fuel dissociates into components from which they are formed. As a result of the decomposition of the components, combustible gases like HNCO, NH_3 which ignite with NOx are produced. Moreover, the fuel can form complexes with the metallic ions, which limits the precipitation of individual components of the precursors before the ignition allowing, by this way, an homogeneous distribution of the ion in the solution [3,4].

Depending on the fuel and the type of metallic ions involved, the combustion differs from flaming, nonflaming (smouldering) to explosive type [3,4]. The explosive reaction involves high pressure, high temperatures and high burning rates. The flaming combustion can endure for seconds or even minutes, while the smouldering combustion is extinguished in a few seconds [3]. Consequently, higher maximum temperatures are usually achieved in the flaming combustion. The occurrence of flaming reactions are attributed to the generation of some gaseous products such as nitrogen oxides, HNCO, CO_2 or NH_3, observed when fuels like urea are used [4]. On the other hand, the use of glycine as a fuel results in smouldering reactions. The effect of fuel in the type of flame generated in the combustion can be well visualized in Figure 6.1, reproduced from the work of Ianos *et al.* [28]. Figure 6.1 a) shows the evolution of combustion reaction in a mixture of $Ca(NO_3)_2$, $Al(NO_3)_3$ and β-alanine used to produce $CaAl_2O_6$ powders. As can be observed when β-alanine is used as fuel the combustion reaction occurs without flaming. However, when the fuel in the mixture is changed to urea, a flaming combustion, as the one observed in Figure 6.1 b), occurs. The type of flame developed in combustion has a strong effect in the particle size and purity of the as-produced powders.

a) evolution of SCS with *smouldering flame type*
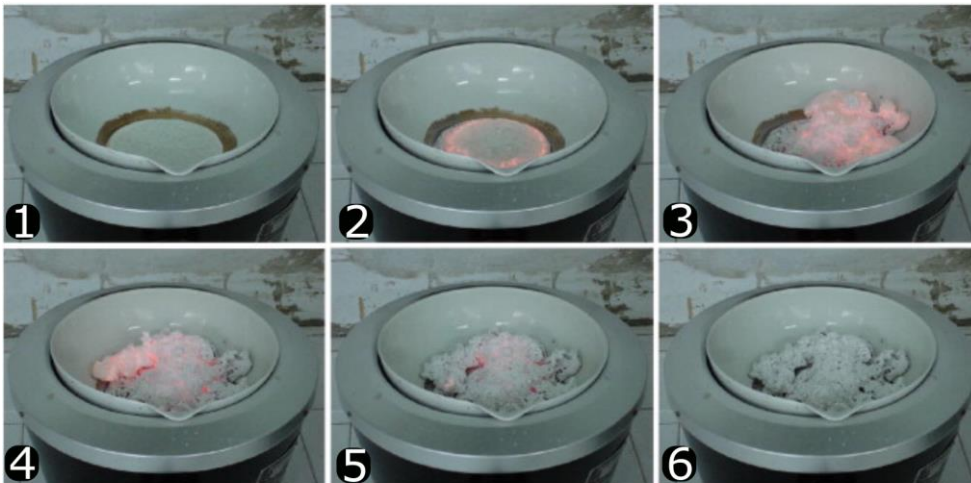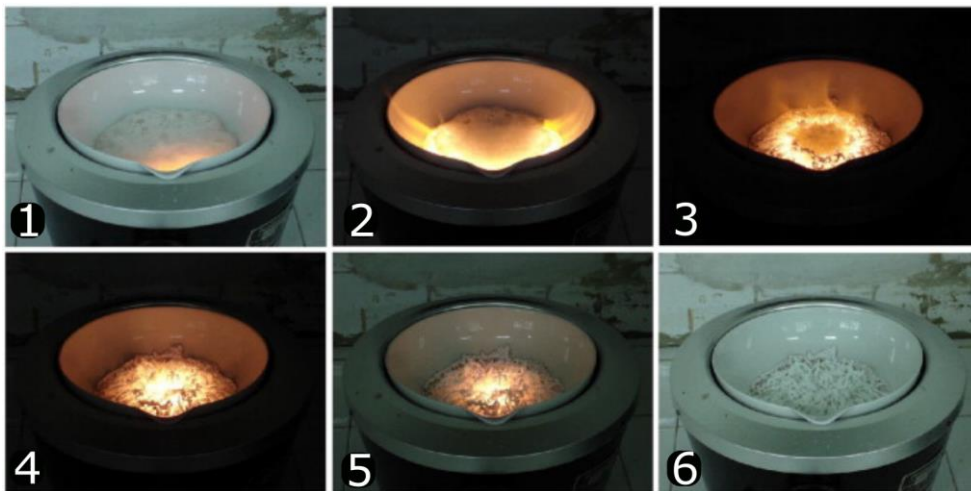
b) evolution of SCS with *flaming flame type*

Figure 6.1. Temporal evolution (1 to 6) of the combustion reaction in a mixture of Ca(NO$_3$)$_2$, Al(NO$_3$)$_3$ and β-alanine (a) and Ca(NO$_3$)$_2$, Al(NO$_3$)$_3$ and urea (b) [28].

In the synthesis of powders by SCS there are four temperatures that should be considered in the combustion reaction since they affect the characteristics of the final products. These are the initial temperature (T_{in}), the ignition temperature (T_{ig}), the adiabatic flame temperature (T_{ad}), and the maximum flame temperature or combustion temperature (T_{comb}) [3]. The T_{in} corresponds to the temperature of the solution before ignition, while the T_{ig} corresponds to the temperature for which the combustion reaction is dynamically activated without an additional supply of external heat. The T_{ad} is the maximum temperature achieved in adiabatic conditions. Since, in general the combustion synthesis is performed under non-adiabatic conditions, the maximum flame temperature is considered to specify the maximum temperature reached under these conditions. Due to the heat loss in non-adiabatic conditions, the maximum of combustion temperature is lower than the adiabatic one [3]. As can be expected, the combustion temperature strongly affects the

192

characteristics of the final powders, including the crystallinity, agglomeration and particle size. The combustion temperature is affected by seral factors, such the type of fuel and oxidizers and the fuel-oxidant ratio. This temperature can be increased by increasing the fuel-oxidant ratio [3].

The volume of gases released in the combustion strongly affects the particle size, the morphology and superficial area of the produced powders. A fast release of a large volume of gas in the combustion promotes the heat dissipation and limits the increase of the temperature [3]. By this way, excessive particle growth and premature sintering of the particles is reduced. Besides, the release of gases also helps to avoid contact between particles decreasing its agglomeration. In fact, the difference in particle size by using different fuels is related with the number of moles of gaseous products released during the combustion. This volume depends not only on the type of fuel but also on the fuel-oxidant ratio. An increase in the volume of the released gases is expected by increasing the fuel-oxidant ratio [3].

The fuel-oxidant ratio is one of the most important parameters in the combustion synthesis which determines the properties of the final products [3]. By proper adjust of fuel-oxidant ratio it is possible to get control over crystallites size, superficial area, morphology, phases and nature of the agglomerates in the produced powders. As referred above, this parameter determines the number of gaseous molecules generated in the combustion. The fuel-oxidant ratio used in the synthesis of oxide materials by combustion reaction is usually calculated based on the concepts of propellants chemistry [4,29]. Based in these concepts, maximum heat is produced when the equivalent ratio of the oxidizers and fuel mixture is unitary (Φ_e= oxidizer/fuel ratio= 1). The equivalent ratio is expressed in terms of the elemental stoichiometric coefficient and valence of oxidants and fuel (*Eq.* 6.1). When Φ_e=1 the mixture is stoichiometric, while $\Phi_e > 1$ corresponds to fuel lean mixtures and $\Phi_e < 1$ to fuel rich solutions. Stoichiometric mixtures produce maximum energy [4].

$$\Phi_e = \frac{\sum(coefficient\ of\ oxidizing\ elements\ in\ the\ specific\ formula)\times(valence)}{(-1)\sum(coefficient\ of\ reducing\ elements\ in\ the\ specific\ formula)\times(valence)} \qquad Eq.\,6.1$$

In the case of the solution combustion synthesis the valence of an oxidant or a fuel is calculated by the sum of the total oxidizing and reducing valences of the elements in the compound. The valence of the oxidizing elements is considered as negative, and the reducing elements as positive. As such, elemental valence of C and H is +4 and +1, respectively, and oxidizing valence of oxygen is −2, while the valence of nitrogen is considered to be zero [4]. The valence of metal cations is the same as the valence of the ion in

the respective oxides. The fuel-oxidant (F/O) molar ratio required for a stoichiometric mixture can be, by this way, easily obtained by summing the total oxidizing and reducing valences in the oxidizer compounds and dividing it by the sum of the total oxidizing and reducing valences in the fuel compounds [4]. More information about this subject can be found in the work of K. C. Patil [4].

6.1.2 Preparation of Zirconia based phosphors by SCS

Before the preparation of zirconia based nanophosphors by SCS, two different fuels were tested in the production of pure zirconia, the urea and glycine. It was observed, when glycine was used as fuel, that the as-produced powders show a dark colour associated with the existence of organic by-products of the reaction. On the other hand, the use of urea as a fuel allowed the production of pure white zirconia powders. Based on these preliminary results urea was selected as the fuel for the preparation of zirconia based nanophosphors by SCS. Additionally, metal nitrates were used as oxidizers and metal cation sources. Table 6.2 shows the commercial metal nitrates used for the preparation of the nanophosphors with different compositions. The reducing and oxidizing valence of the nitrates and fuel are also indicated.

Table 6.2. Valences of the commercial metal nitrates and fuel used in the production of zirconia based nanophosphors.

	Reactants	Chemical formula	Valence
	Fuel (Urea)	NH_2CONH_2	+6
Oxidizers	Zirconium oxynitrate hydrate	$ZrO(NO3)_2 \cdot xH_2O$	-10
	Yttrium nitrate hexahydrate	$Y(NO_3)_3 \cdot 6H_2O$	-15
	Europium nitrate pentahydrate	$Eu(NO_3)_3 \cdot 5H_2O$	-15
	Terbium nitrate pentahydrate	$Tb(NO_3)_3 \cdot 5H_2O$	-15
	Erbium nitrate pentahydrate	$Er(NO_3)_3 \cdot 5H_2O$	-15
	Praseodymium nitrate hexahydrate	$Pr(NO_3)_3 \cdot 6H_2O$	-15
	Thulium nitrate pentahydrate	$Tm(NO_3)_3 \cdot 5H_2O$	-15
	Ytterbium nitrate pentahydrate	$Yb(NO_3)_3 \cdot 5H_2O$	-15

The procedure used in the synthesis of the different zirconia based phosphors, was almost the same for all compositions. First, the stoichiometric amount of each metal nitrate was calculated for the desired final composition. The stoichiometric amount of urea added to the solution was calculated based on the concept of propellant chemistry, discussed before. A representative diagram of the process used in the preparation of zirconia nanophosphors by SCS is show in Figure 6.2.
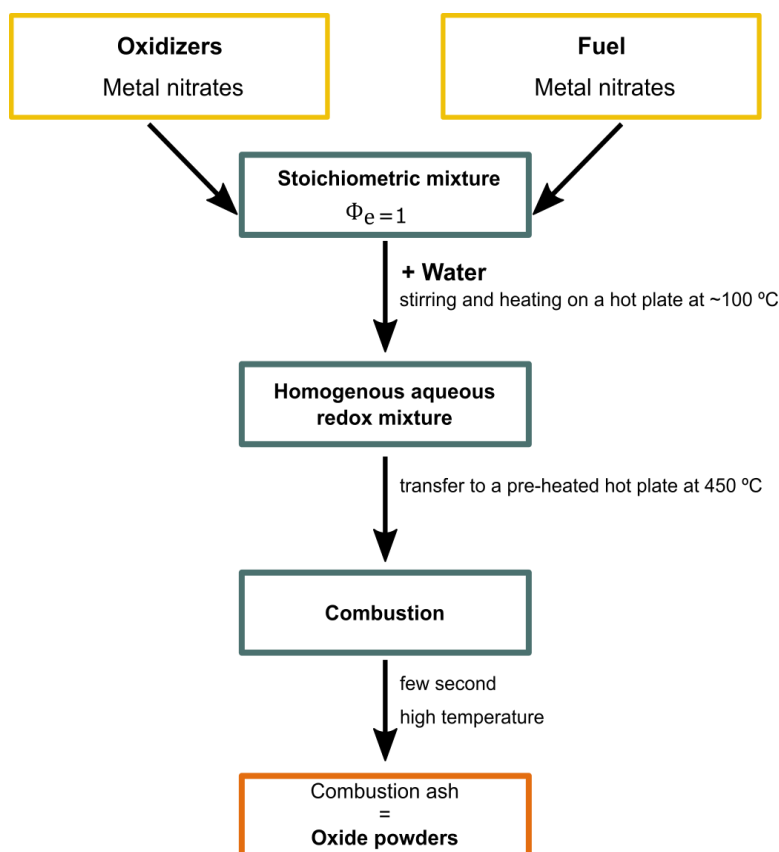
Figure 6.2. Diagram of the process used to produce zirconia nanophosphors by SCS.

After addition of stoichiometric amounts of urea to the metal nitrates, a minimum volume of distilled water, necessary to dissolve the nitrates and urea was added. The mixture was heated at ~100 ^{0}C, under continuous stirring in a hot plate, until a complete transparent solution is obtained. This step was essential to ensure that all the precursors are dissolved in the solution before the ignition. The redox solution was then transferred to other hot plate, pre-heated at 450 ^{0}C. After few minutes, the combustion reaction occurs and the powders are produced. Table 6.3 shows a list of the samples produced and studied by SCS in this thesis. In some cases, the as-produced samples were submitted to an additional thermal annealing process in air at atmospheric pressure in order to infer its effect on the phosphor luminescence. More information about the thermal annealing treatments will be given in the respective discussion section of each SCS produced powder.

Table 6.3. Identification and summary of the conditions used in the production of the powders by SCS.

Sample name	Dopant	Composition		
		at.% Ln^{3+}	mol.% Y^+	
SCS-ZrO_2-3Eu	Eu^{3+}	3	0	as-grown
SCS-t'-YSZ-3Tb	Tb^{3+}	3	0	as-grown
SCS-ZrO_2-0.1Pr		0.1	0	as-grown
SCS-ZrO_2-0.2Pr		0.2		
SCS-ZrO_2-0.5Pr	Pr^{3+}	0.5		
SCS-ZrO_2-1Pr		1	0	as-grown
SCS-ZrO_2-3Pr		3		
SCS-ZrO_2-0.1Pr-TT		0.1		
SCS-ZrO_2-0.2Pr-TT		0.2		
SCS-ZrO_2-0.5Pr-TT	Pr^{3+}	0.5	0	TT
SCS-ZrO_2-1Pr-TT		1		
SCS-ZrO_2-3Pr-TT		3		
SCS-ZrO_2-0.3Tm	Tm^{3+}	0.3		as-grown
SCS-t'-YSZ-0.3Tm	Tm^{3+}	0.3	8	as-grown
SCS-t'-YSZ-0.3Tm,1Yb	Tm^{3+}, Yb^{3+}	0.3/1	8	as-grown
SCS-ZrO_2-1Er		1		
SCS-ZrO_2-2Er		2		
SCS-ZrO_2-5Er	Er^{3+}	5	0	as-grown
SCS-ZrO_2-10Er		10		
SCS-ZrO_2-16Er		16		
SCS-ZrO_2-1Er,1Yb		1/1		
SCS-ZrO_2-1Er,2Yb	Er^{3+}/Yb^{3+}	1/5	0	as-grown
SCS-ZrO_2-1Er,5Yb		5/5		
SCS-t'-YSZ-1Er	Er^3	1	8	as-grown
SCS-t'-YSZ-1Er,1Yb	Er^{3+}, Yb^{3+}	1/1	8	as-grown

6.2 Results

In this section the most relevant results in Ln^{3+} doped ZrO_2 phosphors produced by SCS will be presented and discussed. A comparison between the spectroscopic properties of Ln ions in nanocrystalline zirconia powder prepared by SCS and in the Ln^{3+} doped crystals grown by LFZ will be made.

6.2.1 Eu^{3+} doped Zirconia nanopowders

ZrO_2 nanophosphors doped with europium were produced by SCS and characterized. Zirconyl nitrate ($ZrO(NO_3)_2 \cdot H_2O$) plus europium nitrate($Eu(NO_3)_3 \cdot 5H_2O$) oxidizers, and urea ($C_2H_5NO_2$) fuel, were used to produce 3 at.% Eu^{3+} doped ZrO_2 nanopowders by SCS following the procedure described above.

The structural characterization of the white powder obtained from the combustion synthesis was performed by powder XRD and RT Raman spectroscopy under backscattering geometry with 325 nm laser line excitation. The powders morphology and grain size were analysed by TEM. PL and PLE were performed under similar conditions as described in the last chapter.

Structural and morphological characterization

The XRD diffractogram of 3 at.% Eu^{3+} doped ZrO_2 ($ZrO_2:Eu^{3+}$) powders obtained by the SCS method is shown in Figure 6.3 a). The doped powders exhibit both tetragonal and monoclinic ZrO_2 crystalline phases with the lattice parameters a= 3.61 Å, b= 3.61 Å, c= 5.19 Å and $\alpha=\beta=\gamma= 90^0$ (assigned to ICDD ref. 04-005-4208) and a= 5.17 Å, b= 5.23 Å, c= 5.34 Å, α= 90°, β= 99.25° and γ= 90° (assigned to ICDD ref. 00-005-4252). In the case of the tetragonal lattice parameters the values are nearest to the ones found for the tetragonal crystalline fibres as shown in the last chapter. The coexistence of the two crystalline phases in the SCS powders is due to the reduced amount of stabilizer in the powder precursors. Trivalent lanthanide ions also act as stabilizers of the tetragonal and cubic phase of zirconia at RT, however an amount of 3 at.% Eu^{3+} reveals to be insufficient to completely stabilize the tetragonal phase in the produced powders. Even so, the intensity of the diffraction peaks associated to the monoclinic phase in the XRD pattern indicates a relatively low amount of monoclinic phase in these powders.
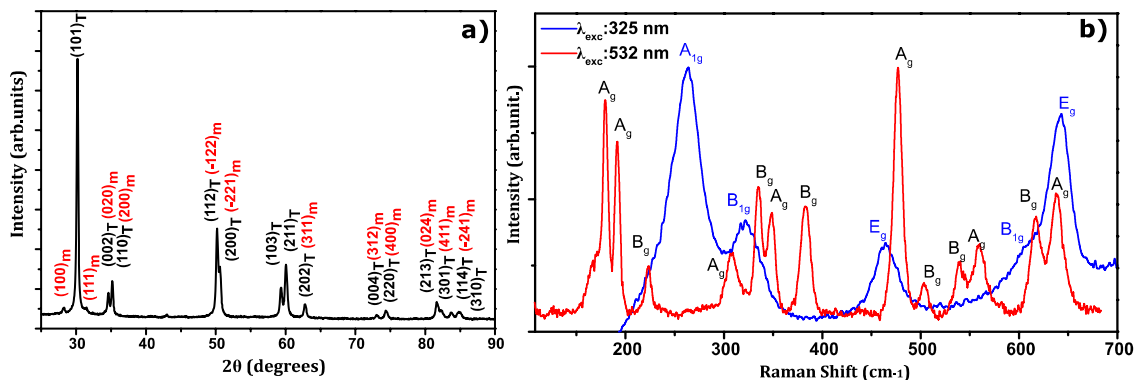
Figure 6.3. X-ray diffraction pattern (a) and Raman spectra performed in backscattering geometry under 325 nm and 532 nm laser lines excitation (b) of the 3 at.% Eu³⁺ doped ZrO₂ powders produced by SCS (blue and red lines correspond to the Raman spectra of the tetragonal and monoclinic phases of zirconia, respectively).

The structural characterization of the produced powders was further analysed by Raman spectroscopy, as shown in Figure 6.3 b). Raman spectra acquired in different regions of the powders reveal a predominant Raman spectra where the A_{1g}, B_{1g} and E_g symmetry vibrational modes of tetragonal zirconia are clearly observed (blue line) in line with the ones already discussed for the tetragonal YSZ crystal grown by LFZ. However, in some minority regions of the produced powders, sporadically, the vibrational modes assigned to the monoclinic zirconia are also observed (red), which confirms the presence of the monoclinic and tetragonal phases in the ZrO₂:Eu³⁺ produced powders.

TEM images of the doped powders are shown Figure 6.4. The SCS powders are characterized by a large particles size distribution with average grain size of ~50 nm and with a very irregular shape. The particles are highly aggregated as can be well seen in the right side image in Figure 6.4. This aggregation results from the high temperature achieved in the combustion synthesis that promotes some degree of coalescence between particles.
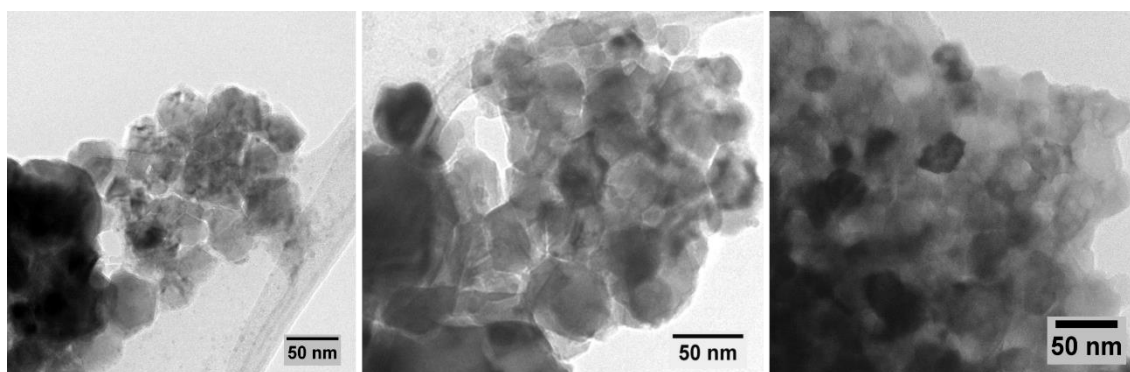

Figure 6.4. TEM image of the ZrO₂:Eu³⁺ nanopowders produced by SCS.

198

The RT PL spectrum of the white $ZrO_2:Eu^{3+}$ powders produced by SCS obtained with the 325 nm line of a cw He-Cd laser as excitation source, is shown in Figure 6.5 a). Besides the $^5D_0 \rightarrow ^7F_J$ luminescence of the Eu^{3+}, the spectrum also exhibits a broad emission band centred at ~490 nm. As referred above, broad emission bands are usually observed in zirconia polymorphs being assigned to native defects and their complexes [30,31]. For pure zirconia in monoclinic phase, a broad emission band with maximum at ~490 nm has been reported [32], being however the chemical nature of the intrinsic defect involved in the luminescence under debate. Therefore, it is reasonable to assume that the band identified in the studied SCS powders could come from native defects in grains with monoclinic crystalline structure. Concerning the intra-$4f^6$ emissions, and in line with the observed in the tetragonal YSZ crystals doped with Eu^{3+} discussed earlier (section 5.2.2.1), radiative transitions from the $^5D_0$ state to the $^7F_{J(0-4)}$ multiplets are observed, with the strongest emission at ~606 nm due to the $^5D_0 \rightarrow ^7F_2$ transition. As a result, an intense orange/red light is observed at RT in the powders irradiated with UV light, as one can see in Figure 6.5 c). The PLE spectrum monitored in the emission maximum of the Eu^{3+} shows that the intraionic luminescence could be achieved by excitation in a broad CT UV bands (with local maxima at about 270, 280 and 320 nm) and by exciting the samples in the ^5D, ^5L and ^5G excited states of the Eu^{3+} ions as shown in Figure 6.5 a) (blue line). The peak position and spectral shape of the detected transitions match well with those found for the tetragonal YSZ crystals doped with Eu^{3+} and grown by LFZ, indicating that the same Eu-centres are present in the SCS produced nanopowders.
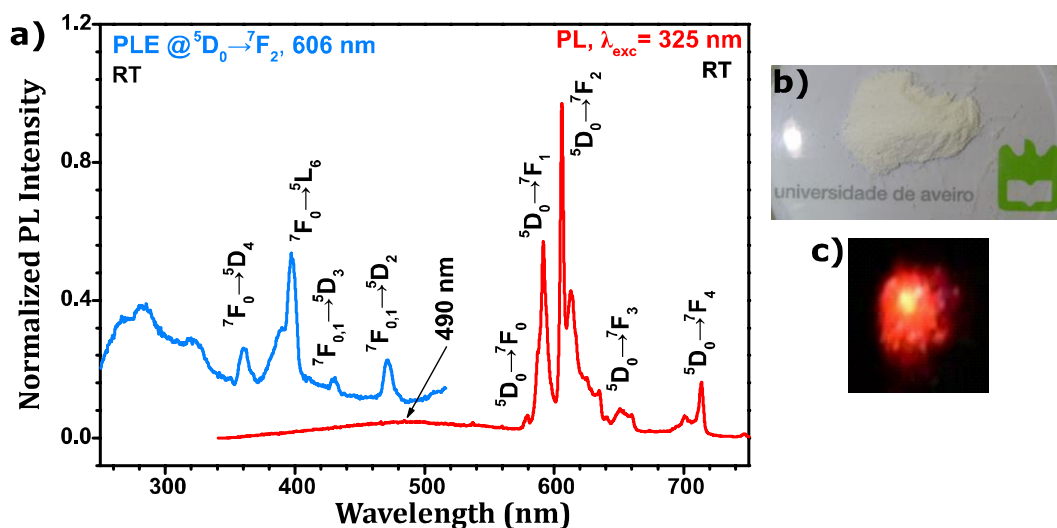
Figure 6.5. a) RT PL spectrum of the powders (red line) with UV excitation (325 nm) and PLE spectrum monitored in the $^5D_0 \rightarrow {}^7F_2$ emission (blue line) b) Photos of the produced white ZrO$_2$:Eu^{3+} nanopowders. c) Photo of the same powders under UV lamp irradiation.

Combined excitation–emission spectroscopy (CEES) has proven to be a powerful technique to identify different optical centres associated with the europium ions in a given host [33] and it was used for further characterization of the ZrO$_2$:Eu^{3+} powders. Figure 6.6 a) shows RT CEES contour plots for the ZrO$_2$:Eu^{3+} powders in the region of the highest intensity emission lines for excitation wavelengths between 250 and 500 nm. As aforementioned, the red RT Eu^{3+} luminescence can be obtained either by exciting the powders in the UV CT excitation bands as well as in the high energy multiplets of the lanthanide ion. In fact, exciting the samples between 250 and 325 nm gives rise to a dominant $^5D_0 \rightarrow {}^7F_2$ transition centred at 606 nm, previously identified in Figure 6.5 a) and well defined in CEES as seen in Figure 6.6 a). Moreover, this transition is the strongest one under excitation in the $^5L_6$ (~396 nm) and $^5D_2$ (~470 nm) multiplets, as shown in Figure 6.6 a). On the high wavelength side of the 606 nm transition, in the spectral region of the $^5D_0 \rightarrow {}^7F_2$ transitions, a peak at 612 nm is identified. This emission is always present when the excitation is performed on the CT bands, but in a lesser extent for shorter excitation wavelengths, as shown by the CEES plot. Slight variations on the excitation wavelength give rise to distinct relative intensity strengths of the $^5D_0 \rightarrow {}^7F_2$ Eu^{3+} transitions, meaning that different ion environments and/or site locations are responsible for the overall emission. Low temperature (14 K) PL spectra obtained with different excitation wavelengths are shown in Figure 6.6 b), where the differences in the relative intensity of the Eu^{3+} emission lines are highlighted indicating the presence of multiple Eu^{3+} optical centres in SCS powders. Changes on the relative intensity of the 606 nm $^5D_0 \rightarrow {}^7F_2$ emission band (and $^5D_0 \rightarrow {}^7F_4$) occur for non-resonant excitation pathways, as shown in the upper spectra in Figure 6.6 b). Additionally, as pointed out by the

200

CEES and the PLE spectrum, the detected CT excitation bands indicate the existence of different Eu–O distances [34,35]. As the europium ions usually substitute the Zr^{4+} with charge compensation provided by the generation of oxygen vacancies rather than multiple sites, it is likely to assume the ions in lower local site symmetry than the tetragonal one. The different Eu–O bond lengths are responsible for the distinct ion environments leading to the observed multiple optical centres.
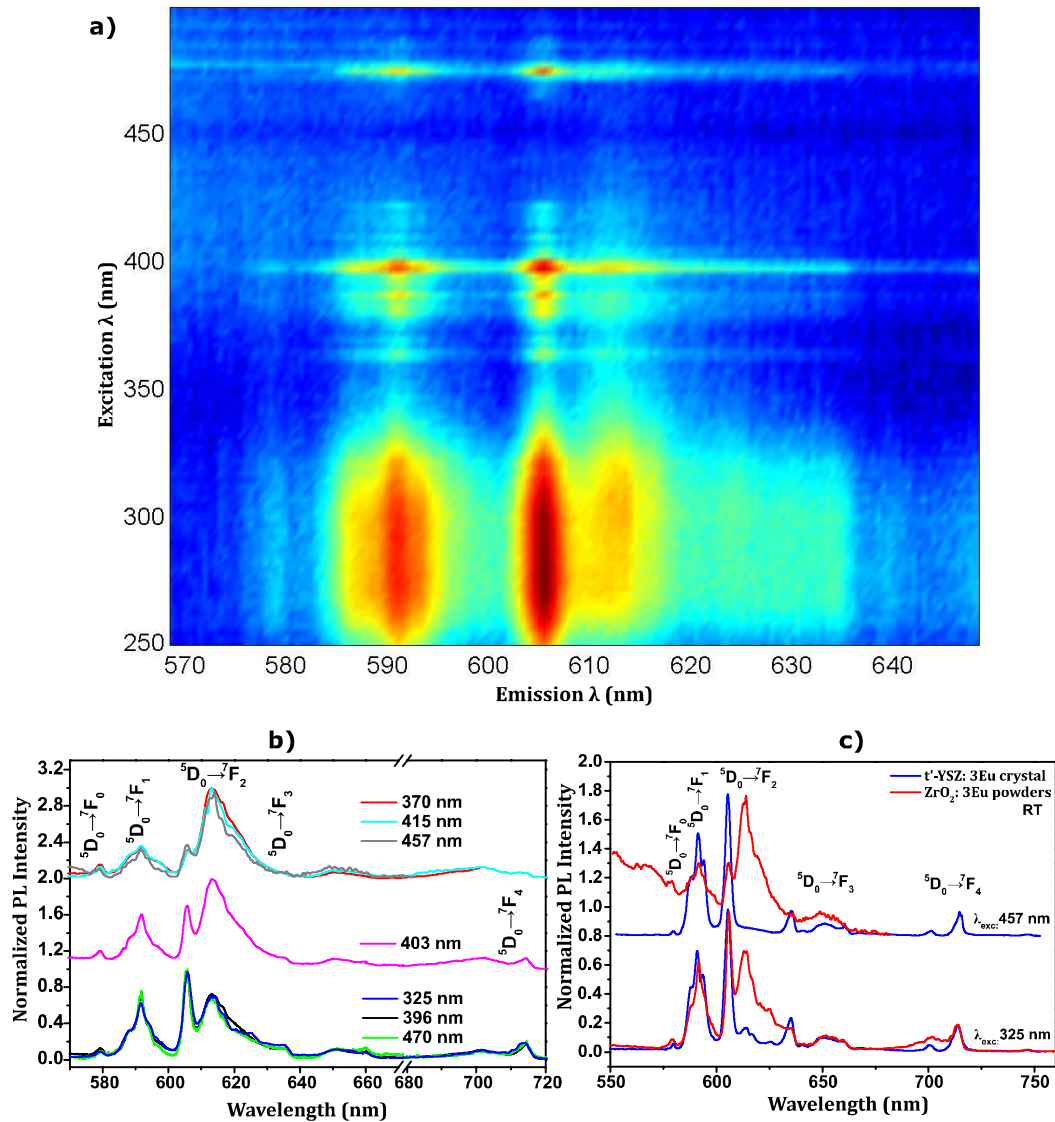
Figure 6.6. RT Combined excitation-emission spectroscopy contour plots for ZrO_2:Eu^{3+} powders produced by SCS. b) 14 K wavelength dependent normalized PL spectra. c) Comparison of the RT PL spectra of the Eu^{3+} doped powder produced by SCS with the RT PL of the Eu^{3+} doped crystal grown by LFZ.

As discussed in section 5.2.2.1, multiple optical centres were also identified in the tetragonal YSZ crystal doped with 3 at.% Eu^{3+} grown by LFZ. In the studied crystal, with 325 nm

201

excitation additional emission bands at energy just below the energy of the dominant $^5D_0{\rightarrow}^7F_2$ emission, peaked at 606 nm, were observed at RT. These emission lines were not observed under 457 nm wavelength excitation, and were associated to the emission of additional optical centres. In Figure 6.6 c) the RT PL spectra of the crystals and nanopowders doped with 3 at.% Eu³⁺ with 325 nm and 457 nm are compared. As one can see, the spectral position and shape of the emission peaks are very identical for both powders and crystals indicating that the emission came from the same Eu³⁺ optical centres. However, the emission from the optical centre that leads to additional $^5D_0{\rightarrow}^7F_2$ emission lines at ~612 nm is much stronger in the doped ZrO_2 nanopowders than the ones observed in the tetragonal YSZ crystal. This difference in the relative intensities of the emission lines indicates that the amount of the Eu³⁺ optically active centres with $^5D_0{\rightarrow}^7F_2$ emission lines at ~612 nm is increased in the nanopowders comparatively to the single crystal. Although no additional phases were detected in the tetragonal YSZ crystals, in the case of the SCS powders we cannot exclude that some of the additional emitting ions could come from the monoclinic phase resulting in an eventual enhancement of the europium emission in the ~612 nm region.

The luminescence of the Eu³⁺ doped ZrO_2 powders was further investigated as a function of temperature, between 14 K and the RT, by exciting the samples in the CT band (325 nm). The temperature dependent PL spectra acquired in these conditions are displayed in Figure 6.7 a). Despite the fact that a bright intraionic luminescence is observed at RT, a thermal quenching of the overall luminescence is seen when the temperature is increased from 14 K to RT. Indeed, at RT only about 40% of the overall intensity observed at 14 K is detected, indicating additional nonradiative processes competing with the intraionic emission with increase sample temperature. A similar behaviour was also detected for the intraionic luminescence in the LFZ grown 3 at.% Eu³⁺ doped crystal.
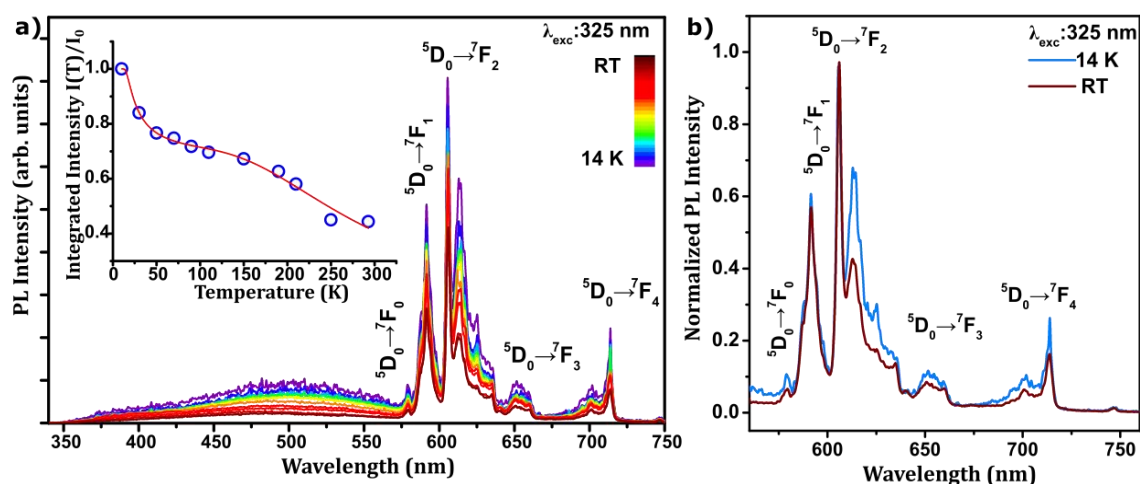
Figure 6.7. a) 14 K to RT PL spectra, obtained with 325 nm laser line excitation, of the ZrO₂:Eu³⁺ powders. Inset shows the dependence of the overall integrated $^5D_0{\rightarrow}^7F_J$ emission intensity with temperature. b) Normalized PL spectra acquired at 14 K and RT.

The decay kinetics of the $^5D_0{\rightarrow}^7F_J$ luminescence of the Eu³⁺ ions in ZrO₂ nanopowders was investigated by TR-PL spectroscopy. Figure 6.8 a) shows the RT TR-PL spectra obtained with 266 nm wavelength excitation, acquired for a temporal window after pulse between 0 and 7.8 ms. The normalization of the TR-PL spectra shown in Figure 6.8 a) to the maximum emission intensity with time after pulse, Figure 6.8 b) and c), clearly evidences a strong difference in the decay time of the $^5D_0$ emitting level in the two Eu³⁺ related optical centres. For example, considering the $^5D_0{\rightarrow}^7F_2$ emission with maxima intensity for a steady state PL spectra (t= 0) at ~606 nm and ~613 nm, associated to different optical centres, one can see that the emission at 613 nm undergoes a much faster decrease of the intensity when compared with the emission at 606 nm. In fact, for a time delay after pulse of 7.8 ms, only the emission from the optical active centre that leads to the maximum at 606 nm is observed. Based on these TR-PL spectra, the dependence of the overall integrated $^5D_0{\rightarrow}^7F_2$ emission intensity with time was obtained, Figure 6.8 d). The time depopulation of the $^5D_0$ excited state was fitted to two exponential decay processes described by decay constants around 330 μs and 1.3 ms, likely to be due to the luminescent decay time of the two distinct optical centres.
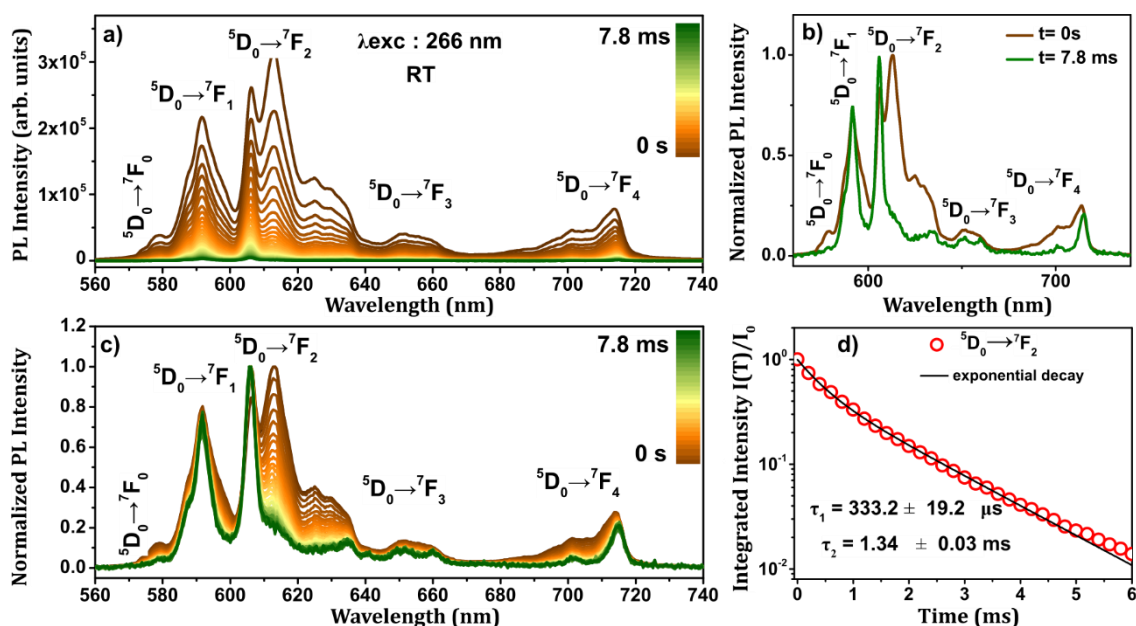
Figure 6.8. a) RT TR-PL spectra of the 3 at.% Eu^{3+} doped ZrO_2 nanopowders with 266 nm wavelength excitation and for a time window after pulse between 0 and 7.8 ms. **b)** Comparison of the normalized PL spectra acquired for delay time after pulse of 0 and 7.8 ms. **c)** RT TR-PL spectra normalized to the maximum emission intensity. **d)** Time dependent integrated intensity of the $^5D_0 \rightarrow {}^7F_2$ emission upon excitation in the CT (266 nm).

Summary

In summary, trivalent europium doped ZrO_2 nanopowders were successfully produced by SCS. The produced white powder, constituted by particles with irregular shape and average particle size around 50 nm, crystallized in the tetragonal phase with a minority amount of monoclinic phase. The incorporation and optical activation of Eu^{3+} was achieved during the synthesis due to high temperature reached in the process. The doped powder exhibit bright orange/red luminescence at RT, due to the Eu^{3+} intraionic transitions, which shown to be the same as the ones previously detected for the tetragonal YSZ:Eu^{3+} crystal grown by LFZ. Combined excitation–emission measurements revealed that the most intense transition of the Eu^{3+} ions is excited via a wide range of wavelengths which covers the CT excitation bands as well as the ion excited states. A slight variation of the excitation wavelength leads to distinct intensity ratios of the europium emitting lines, indicating the presence of distinct europium sites and/or environments in the zirconia host, in line with the previously observed for the Eu^{3+} doped YSZ crystals. The intense emitted red light together with their possible excitation not only in the UV CT bands but also in the bandwidth emission of commercial InGaN-based LEDs, is of utmost interest for the application of the produced powders in lighting.

6.2.2 Pr³⁺ doped Zirconia nanopowders

ZrO$_2$ powders doped with different concentrations of Pr^{3+}, from 0.1 to 3 at.%, were also prepared by the SCS process. For that, zirconyl nitrate (ZrO (NO$_3$)$_2$.H$_2$O) and praseodymium nitrate (Pr(NO$_3$)$_3$.6H2O) were used as oxidizers, and urea (C$_2$H$_5$NO$_2$) as fuel. Besides the as-synthesized samples, thermal annealing treatments at 1200 ^{0}C in air were carried out during 3 hours in order to analyse the role of heat treatment on the structural and optical properties of the praseodymium doped powders.

The samples morphology was investigated by TEM, while crystalline phase was analysed by RT Raman spectroscopy performed under backscattering geometry, with the 325 nm He-Cd laser line. The luminescence characteristics of the produced powders were studied by PL and PLE.

Structural and morphological characterization

Figure 6.9 a) and b) shows the photos and the RT Raman spectra of the as-synthesized zirconia nanopowders doped with different amounts of Pr^{3+} ions. As one can see, the incorporation of Pr^{3+} in zirconia lattice leads to a colouration of the produced powder, with colour changing from a light yellow, at low Pr^{3+} amounts, to a dark orange, for higher dopant amounts. Such colouration was also observed in the Pr^{3+} doped crystal grown by LFZ that has an orange colour (Figure 5.23 a). In Figure 6.9 b) several resonances are identified corresponding to the zirconia lattice vibrational modes. In particular, for the SCS samples synthesized in the presence of low dopant amount (Pr^{3+} concentration between 0.1 to 1 at.%) the nanopowders were found to exhibit a multiphase nature comprising the monoclinic and tetragonal zirconia polymorphs. Otherwise, the powders synthesized with the highest dopant amount, 3 at.%, only exhibit the vibrational modes of the tetragonal phase. The high degree of stabilization of the tetragonal phase of zirconia at RT is due to the introduction of high contents of Pr^{3+} in this lattice at the high temperatures achieved in the SCS method. The post-growth thermal annealing in air at 1200 ^{0}C leads to noticed changes in the vibrational spectra, as shown in Figure 6.9 c). The performed thermal annealing treatment seems to promote an increase in the monoclinic phase content. In fact, the annealed powders with lower doped content exhibit a monophasic phase with a monoclinic structure, while for 1 and 3 at.% of Pr^{3+} besides a predominant monoclinic phase, small amounts of tetragonal phase cannot be discarded. One possible explanation for this phase transformation can be attributed to the diffusion of Pr ion in the powders induced by the thermal annealing. Considering the situation in which initial Pr ions are not homogeneously

distributed in the powders, regions with high Pr amount are stabilized in tetragonal phase, while poor Pr^{3+} regions crystalize in the monoclinic phase. The annealing treatment can promote a homogenous distribution of the Pr ions, decreasing the Pr ion concentration in the tetragonal phase and consequently their destabilization at RT. Moreover, an additional effect of particle size in the stabilization of the tetragonal phase at RT in the as-produced powders cannot be discarded, and a particle size increase promoted by the thermal annealing can be also responsible for the tetragonal to monoclinic phase transformation [36,37].
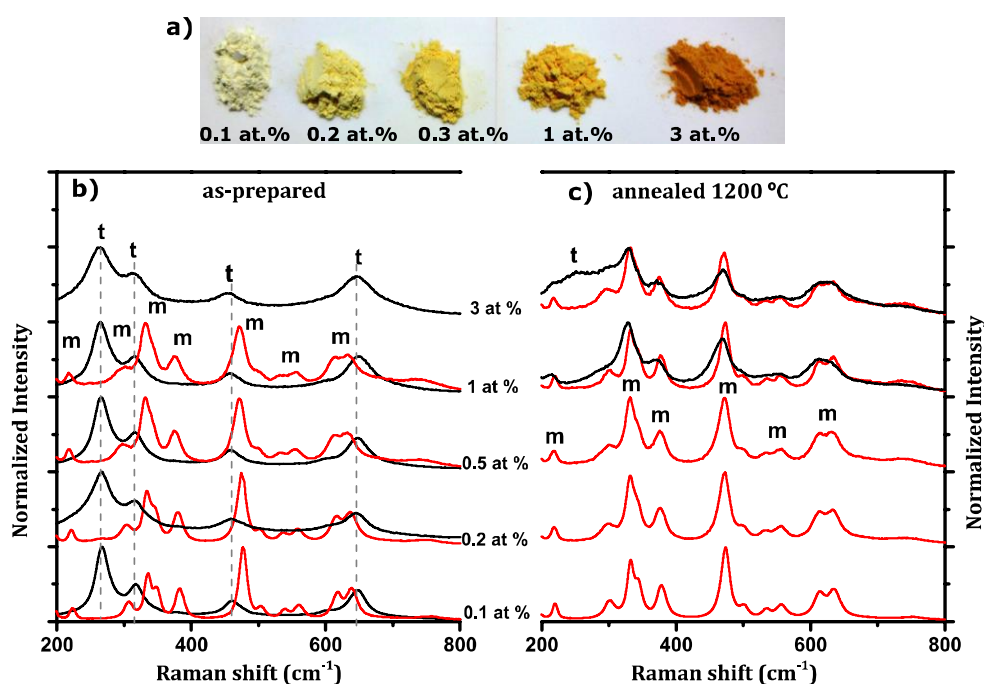
Figure 6.9. a) Photos of the as-produced ZrO₂ powders doped with different concentration of Pr^{3+}. RT Raman spectra in a backscattering configuration and with 325 nm laser line excitation of the as-produced (b) and thermal annealed (c) powders.

The morphology of the produced powders were analysed by TEM. The particles size and shape are very similar to the ones of the powders doped with Eu^{3+} meaning that the dopant ion does not play a significant role in the morphology of the zirconia powders produced by SCS. Moreover, no significant differences were observed in the particles size or shape with increased Pr^{3+} concentration, as can be observed in Figure 6.10 where the TEM images of the powders doped with 0.1 (a-c) and 3 (d-f) at.% Pr^{3+} are displayed. The as-produced powders are constituted by particles with an irregular shape and large sizes distribution. As identified for the Eu^{3+} doped powders, a high agglomeration and aggregation of the particles is observed, which is related to the high temperatures achieved in the combustion synthesis.

High resolution TEM images of the as-produced powders doped with 3 at.% Pr^{3+}, Figure 6.10 g) and h), reveals the crystallinity of the samples, which once again is related with the high temperature involved in the process that lead to material crystallization.
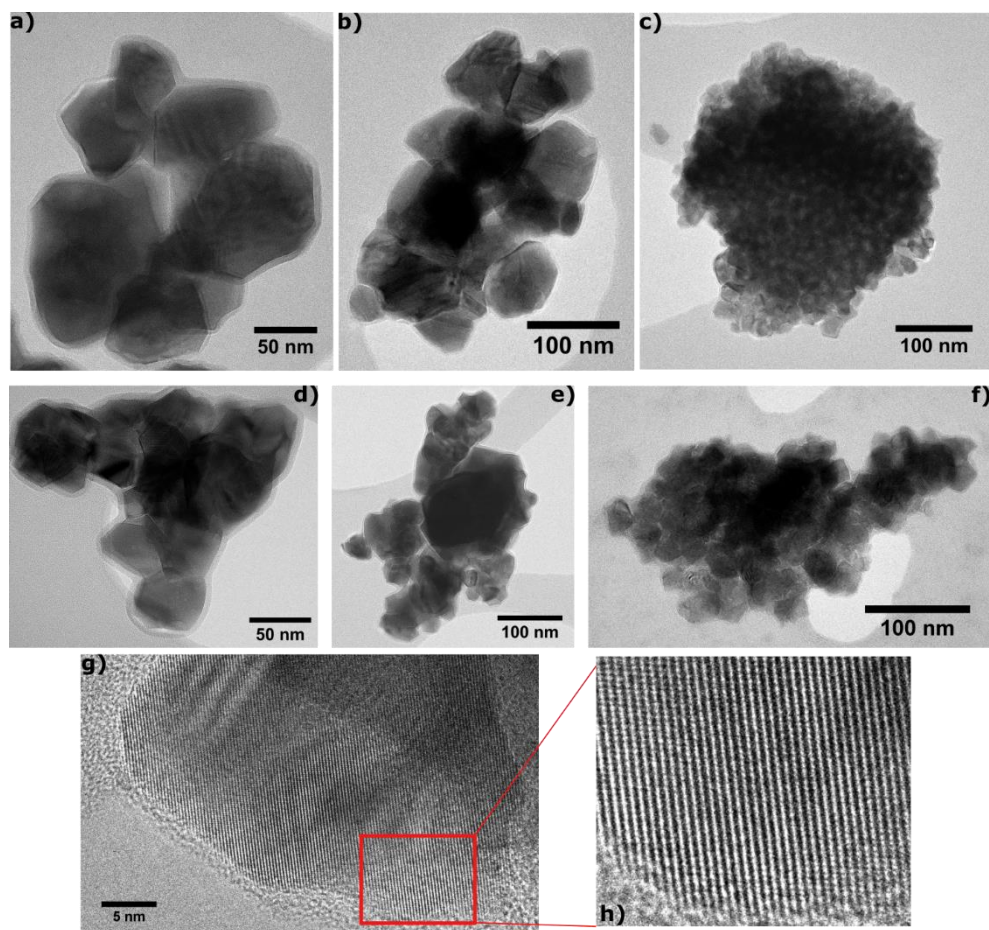
Figure 6.10. TEM images of the as-produced ZrO_2 powders doped with 0.1 at.% Pr^{3+} (a-c) and with 3 at.% Pr^{3+} (d-f). HRTEM image of the as-produced powders doped with 3 at.% Pr^{3+} (g, h).

Luminescence characterization

Figure 6.11 a) shows the RT PL spectra of the as-produced SCS powders doped with different concentration of Pr ions, obtained with UV excitation (325 nm). As identified, the PL is dominated by the transitions among the $^{2S+1}L_J$ multiplets of the $4f^2$ electron configuration. The main emission occurs in the red spectral region at ~614.5 nm, arising from the $^1D_2$ excited state to the $^3H_4$ ground state. Minor intensity lines from the $^1D_2$ to the $^3H_5$ and $^3H_6$ multiplets at ~720 nm and 833 nm are also observed. Furthermore, the intraionic emission arising from the high energetic $^3P_0$ excited multiplet is detected in the blue region. The same luminescence features were observed for all the doped powders though a quenching of the ion luminescence intensity is identified for higher amounts of Pr

ions. For a concentration of 3 at.% Pr^{3+}, the intensity of the detected light is very week, as indicated by the low signal to noise ratio in the PL spectrum. Photoluminescence quenching with concentration is a well-known phenomenon in Ln ions, including Pr^{3+}, incorporated in inorganic hosts, where the concentration threshold for luminescence concentration depends on both Ln ion and host nature [38]. According with the theory of resonant energy transfer, as a result of the dipole-dipole interaction between neighbour's ions, the intensity of the emission increases gradually with concentration until a maximum value, after which it decreases [38]. Two main energy transfer processes are suggested as the responsible for the occurrence of concentration quenching in Ln ions: CR processes and energy migration [38,39]. As aforementioned, CR process occurs between neighbour's ions and in system with equal (resonant CR) or similar (non-resonant CR, assisted by phonons) energy difference between electronic levels. On the other hand, energy migration occurs over Ln ion in the host and stops in quenching sites [38]. Usually, concentration quenching involving CR process starts at lower concentration comparatively to the ones where no CR occurs [38]. Concentration quenching of Pr^{3+} luminescence involving CR processes has been reported in literature for the ion in different inorganic host [40,41], including zirconia [42,43]. The analysis of the Pr^{3+} energy level diagram shows the existence of similar energy differences between multiplets which is favourable for the occurrence of CR processes at high ion concentrations. Figure 6.12 shows the partial energy level diagram of Pr^{3+} where different CR processes that lead to the relaxation of the $^3P_0$ and $^1D_2$ emitting levels are shown. In particular, the CR process described by $[^1D_2,^3H_4]\rightarrow[^1G_4,^3F_{3,4}]$ has been reported as an efficient channel for the nonradiative relaxation of the $^1D_2$ emitting level, responsible for the concentration quenching of the luminescence, due to the energy match between the involved levels [43].

Comparatively to studied single crystal doped with 3 at.% Pr^{3+} (section 5.2.2.3.), the emission intensity of the nanocrystals with the same Pr^{3+} doping concentration have shown to be much weaker. Similar results were reported in other Pr^{3+} doped hosts and it was suggested a dependence of the material size in the concentration quenching threshold [39]. As aforementioned in Chapter 2, crystal hosts with nanometric size creates special conditions for the luminescence dynamics of Ln ions [39,40]. Phonon assisted energy transfer processes, including CR, of Ln ions in a nanocrystalline material can be changed, comparatively to the bulk material, due to its discreteness of phonon density of states and the lack of low-energy acoustic phonons resultant of confinement effects [39,40,44].

High resolution PL spectra of the as-produced powders in the spectral region of $^1D_2\rightarrow^3H_4$ dominant emission shown in Figure 6.11 b) reveals that the transition can be further resolved in two emission lines with maxima at ~614.5 nm and ~615.5 nm in the powders

doped with 0.1 to 1 at.% Pr^{3+}. An increase of the intensity ratio between the lines peaked at 615.5 and 614.5 nm is found to occur with increasing Pr^{3+} concentration. Besides the intraionic emission of the lanthanide ion, PL spectra of the powders doped with low dopant concentrations show a low intensity broad emission band centred at 490 nm, as the one observed in the powders doped with Eu^{3+} and attributed to the emission from native defects of zirconia host.
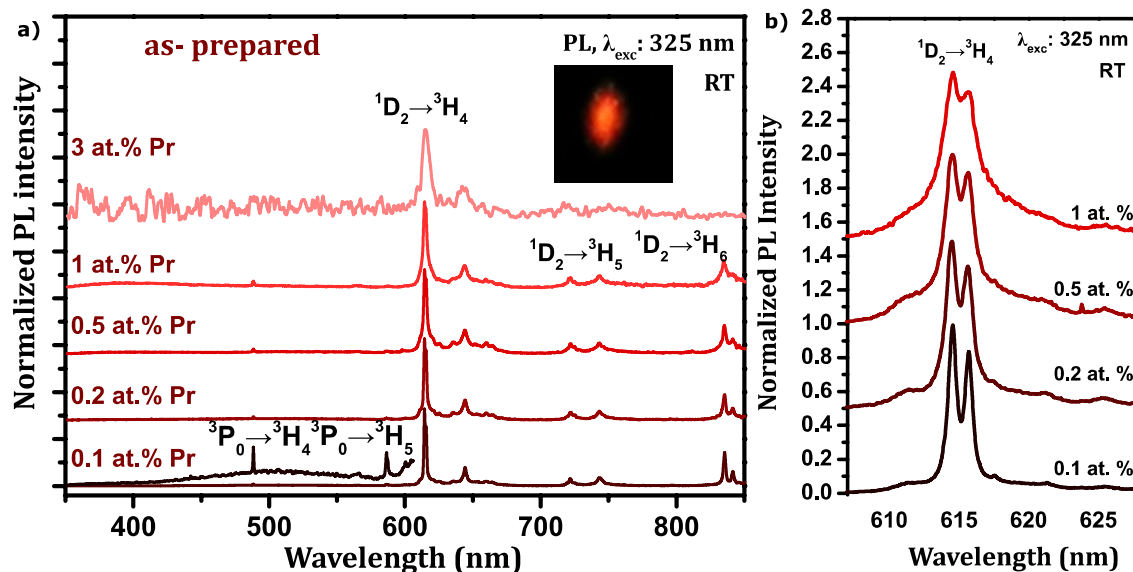

Figure 6.11. a) RT PL spectra of the as-synthesized SCS powders doped with different amounts of Pr ions, obtained with 325 nm laser line excitation. b) Normalized PL spectra in the spectral region of the $^5D_2{\longrightarrow}^3H_4$ emission.
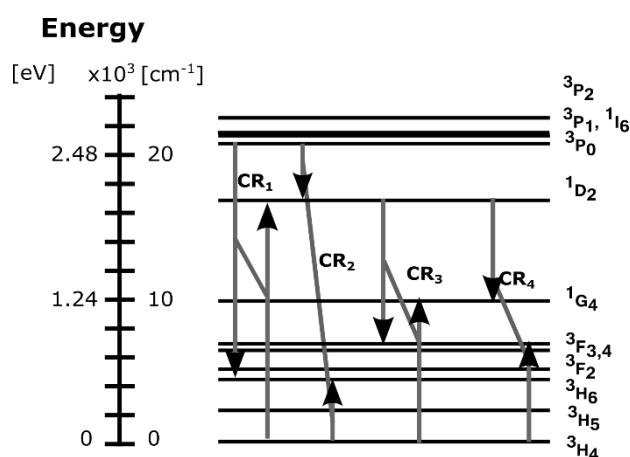

Figure 6.12. Partial energy level diagram of Pr^{3+} where possible CR processes are represented [38,45].

RT PLE spectra, as well as wavelength selective PL were performed in the powders doped with 0.1 at.% Pr^{3+}, the ones with the highest intensity of the intraionic luminescence, and that shows an intense red emission at RT (inserted photo in Figure 6.11 a). The PLE spectra shown in Figure 6.13 a) and monitored at 614.5 nm and 615.5 nm, in the most intense $^1D_2 \rightarrow ^3H_4$ emission lines, reveal that Pr^{3+} luminescence in the SCS powders can be excited via the ^3P_J excited states and preferentially via a CT band with maxima at 293 nm, which is shifted to shorter wavelengths when compared with the CT excitation band observed in the doped tetragonal crystal (peaked at 308 nm) grown by LFZ studied in section 5.2.2.3 (Figure 5.23 b). A comparison of the two PLE spectra is shown in Figure 6.13 a). As identified, slightly variations in the wavelength of the monitored $^5D_2 \rightarrow ^3H_4$ emission results in changes in the width and relative intensity ratio of the PLE excitation lines/band, suggesting the existence of multiple Pr^{3+} optical centres in the produced powders.

The existence of multiple Pr^{3+} optically active centres was further confirmed by wavelength selective luminescence. PL spectra of the 0.1 at.% Pr^{3+} doped powders, under different wavelength excitation are shown in the right side of Figure 6.13 a). As one can see, the spectra of the SCS multiphase powders doped with praseodymium exhibit satellite lines to the main ones. The lines intensity was found to be dependent on the photon wavelength excitation. In fact, while the excitation at the CT excitation band maximum (293 nm) and resonantly with the $^3P_0$ (487 nm) and $^3P_1 + {}^3I_6$ (474 nm) states lead to the ions recombination with additional satellite lines of minor intensity, using 325 nm photon excitation or resonant excitation in the $^3P_2$ (457 and 451 nm) increases the intensity of the satellite lines relatively to the main ones. This behaviour can be explained by the presence of multiple optically activated Pr^{3+} centres in the polyphasic powders, which could be related with the presence of monoclinic phase.

A comparison between the PL and PLE spectra of Pr^{3+} in the as-produced nanopowders and in the tetragonal YSZ crystal grown by LFZ is displayed in Figure 6.13 b). Despite the fact that the intraionic features occur in the same spectral region, as expected for the shielded intra-$4f^n$ electron configuration, the spectra reveal noticed changes. Besides the previously mentioned shift to lower energy of maximum of the CT band in the Pr^{3+} doped powders, additional intraionic excitation bands are observed in PLE. Furthermore, significant changes are observed in the PL spectra of the two types of samples, as one can see in the right side of Figure 6.13 b). Besides the already discussed satellite lines, the intraionic emission bands of the multiphase doped powders were found to be narrower than the ones of the Pr^{3+} in the tetragonal YSZ crystal. Such differences, clearly evidences the occurrence of additionally

activated praseodymium ions in the multiphase powders comparatively with the ones observed in the tetragonal YSZ crystal.
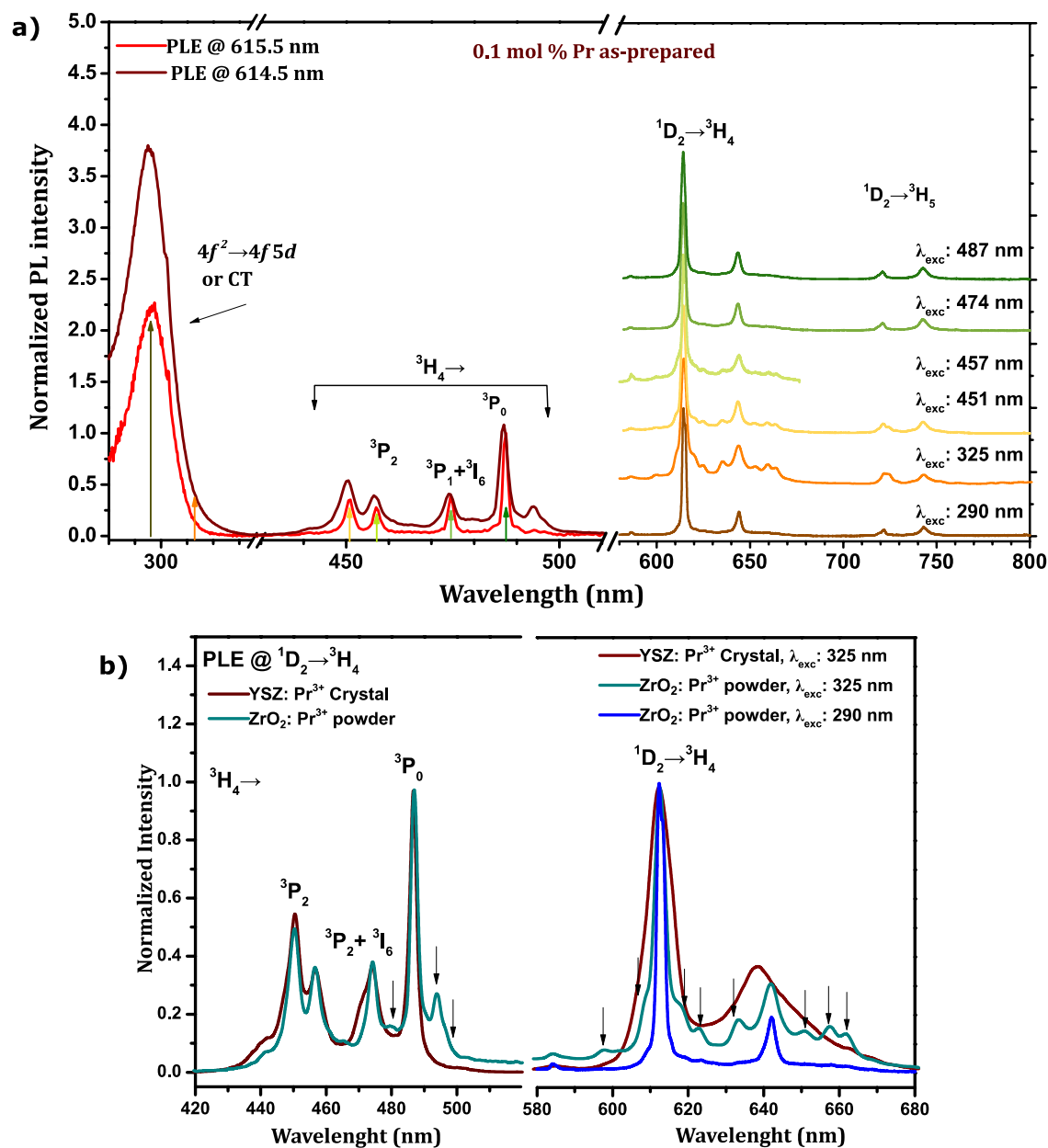
Figure 6.13. a) RT PL and PLE spectra for the as-prepared SCS sample doped with 0.1 at.% of Pr³⁺. b) Comparison of the emission and excitation spectra of Pr³⁺ in the as-produced nanopowders and in the tetragonal YSZ crystal grown by LFZ.

The luminescence of the thermal annealed powders, with a dominant monoclinic phase, was also investigated by RT PL and PLE spectroscopy in order to analyse the role of phase transformation in the luminescence features of the doped powders. Figure 6.14 a) shows the RT PL spectra of the thermal annealed powders doped with different concentration of Pr³⁺,

upon 325 nm wavelength excitation. As happens for the as-produced powders, a high quenching of the luminescence intensity is observed in the highly doped powders. The same intra-4f^2 luminescence lines of Pr^{3+} were observed before and after thermal annealing meaning that the heat treatment does not promotes new Pr^{3+} optical centres. However, the intensity ratio between the satellite lines and the main line peaked at ~614 nm increases with the thermal annealing treatment for all dopant concentrations as shown in Figure 6.14 b), suggesting a dominant recombination from the ions in the monoclinic phase.
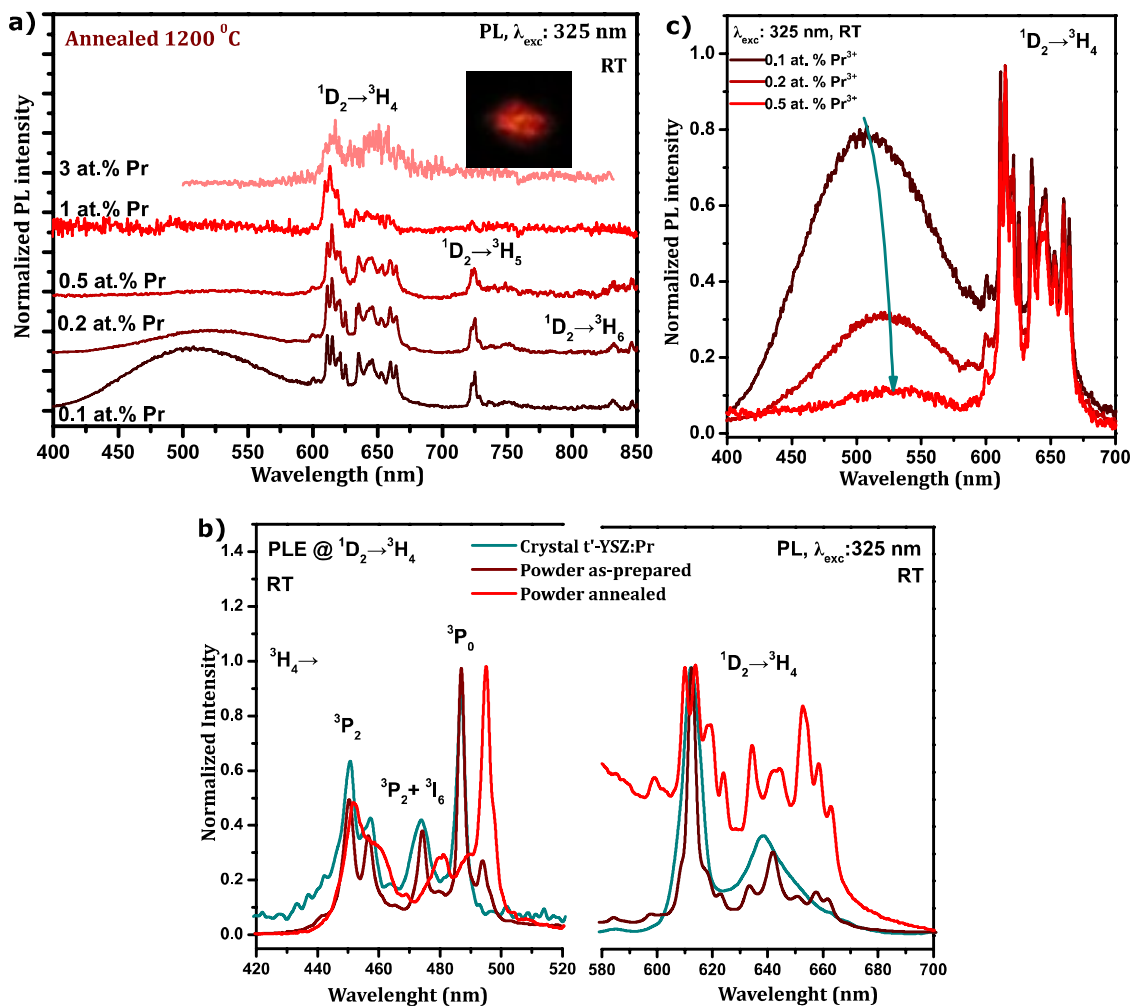
Figure 6.14. a) RT PL spectra of the thermal annealed powders doped with different Pr^{3+} concentrations, obtained with 325 nm excitation; b) Comparison of the normalized RT PL and PLE spectra of the as-produced and thermal annealed powders doped 0.1 at.% Pr^{3+} and the doped tetragonal YSZ crystal. Normalized RT PL spectra, obtained with 325 nm excitation, of the lightly doped and annealed powders.

Additionally to the intraionic emission, the intensity of the broad unstructured emission band increases with thermal annealing in air at 1200 °C for the lightly doped samples (0.1 to 0.5 at%) revealing the sensitivity of the native defects (such as oxygen vacancies) to the heat

treatment conditions. The maximum of the unstructured broad emission band in the green/orange spectral region was also found to be dependent on the dopant concentration. As can be observed in Figure 6.14 c), a shift of the main maxima from 512 nm to 524 nm and a decrease of the band intensity was observed with increasing dopant amount highlighting the role of the increasing ion concentration in the extinction of the broad host-related luminescence.

The presence of the different optically active sites/environments for the Pr^{3+} ions in the monoclinic lattice was further validated by the RT PLE spectra monitored in $^1D_2 \rightarrow {}^3H_4$ emission and PL spectra taken under selective wavelength excitation, shown in Figure 6.15 a).
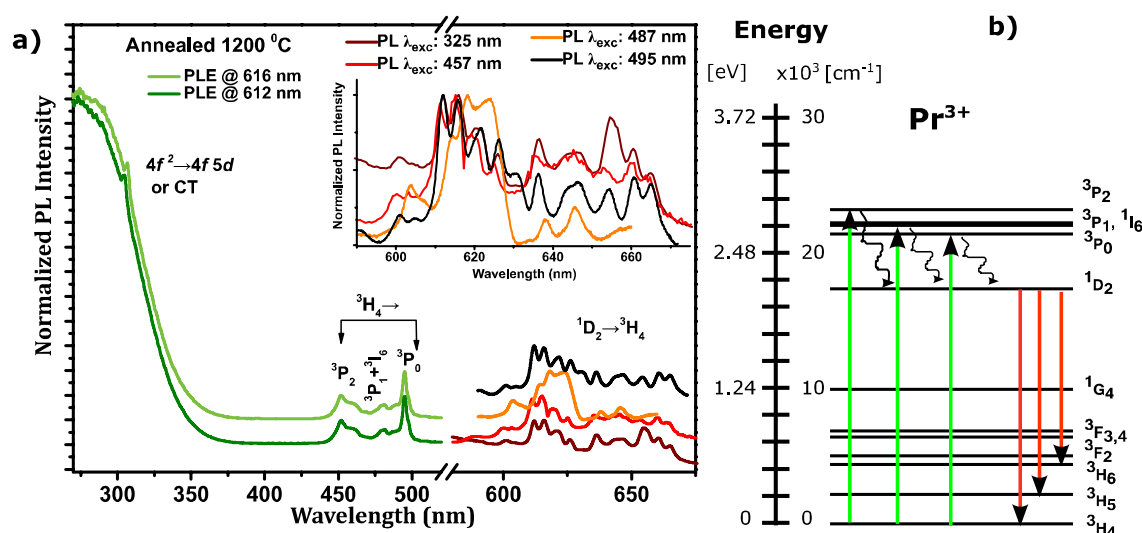
Figure 6.15. a) RT $^1D_2 \rightarrow {}^3H_4$ emission, under different wavelength excitation, and PLE spectra of the thermal annealed powders doped with 0.1 at.% Pr^{3+}. b) Partial energy level diagram of the Pr^{3+}.

PL spectra of the $^1D_2 \rightarrow {}^3H_4$ emission under different wavelength excitation clearly shows a variation of the relative intensities of the emission bands, which corroborates the presence of different optically active sites/environment for Pr^{3+} in the monoclinic powders. PLE spectra monitored in different lines of the $^1D_2 \rightarrow {}^3H_4$ transition shows that the Pr^{3+} luminescence in the monoclinic powders can be preferentially excited by the CT absorption band and also in the ^3P_J excited multiplets of Pr^{3+} as indicated in the left side of Figure 6.15 a). However, a comparison of the intraionic excitation bands in the PLE spectra of the as-produced and annealed powders, revealed noticed variations in the bands intensity ratio displayed in the Figure 6.14 b). While for the as-produced powders the dominant excitation of the Pr^{3+} luminescence occurs via absorption into the $^3P_0$ multiplet peaked at 487 nm, for

the annealed powders the preferential intraionic excitation is also via the same excited state ($^3P_0$) which is shifted to longer wavelengths (peaked at 495 nm). It should be emphasized that for a state with J= 0 only one line is expected if the excitation is made through one single optically centre. The $^3P_0$ excitation band at 495 nm observed in the annealed samples (also identified with lower intensity in the as-produced powders) is absent in the Pr^{3+} doped tetragonal YSZ crystal. Therefore, the measured data suggest that this line comes from the Pr^{3+} in the monoclinic crystalline lattice.

Summary

Zirconia powders doped with Pr^{3+} concentration between 0.1 and 3 at.% were produced by SCS using urea as a fuel. The as-produced powders show a colouration that changes from a light yellow to dark orange with increasing dopant concentration. For dopant concentrations below 3 at.% both monoclinic and tetragonal phases were identified in the as-produced powders by Raman spectroscopy, while for a 3 at.% concentration only the tetragonal was identified. A bright red light is observed in the lightly doped as-produced powders due to the predominant $^1D_2 \rightarrow {}^3H_4$ Pr^{3+} transition. In addition, lower intensity emission bands due to electron transitions from the $^3P_0$ excited state to the $^3H_{4,\,5}$ levels and from the $^1D_2$ to the $^3H_{5,\,6}$ levels are observed. The increase in the dopant concentration up to 3 at.% leads to a strong quenching on the RT emission intensity likely due to competitive nonradiative ion-ion transfer. Additional Pr^{3+} lines related with multi optically activated centres were identified in the multiphase as-produced powders, comparatively to the Pr^{3+} spectra in the tetragonal YSZ crystals grown by LFZ. Thermal annealing treatments of the doped powders at 1200 ⁰C in air leads to an increase in the amount of monoclinic phase, and consequently to an increase in the emission band from the Pr^{3+} in the monoclinic lattice.

6.2.3 Tm³⁺ doped Zirconia nanopowders

Solution combustion synthesis was also employed to produce zirconia and YSZ powders doped with trivalent thulium. Zirconyl nitrate ($ZrO\,(NO_3)_2.\,H_2O$) plus thulium nitrate ($Tm\,(NO_3)_3.\,5H_2O$) and urea ($C_2H_5NO_2$) fuel were used to produce 0.3 at.% Tm^{3+} doped ZrO_2 powders ($ZrO_2{:}Tm^{3+}$). For the preparation of 8 mol.% $YO_{1.5}$ stabilized zirconia (YSZ) doped with 0.3 at.% Tm^{3+} (YSZ:Tm^{3+}) powders, yttrium nitrate ($Y\,(NO_3)_3.\,6H_2O$) was added to the other precursor reagents. The powders were prepared following the procedure described in section 6.1.2.

As in the other cases, the crystalline phase identification was analysed by Raman spectroscopy, the morphology and grain size studied by TEM and the spectroscopic

characteristics by PL and PLE. The luminescent features of the produced zirconia and YSZ powders doped with 0.3 at.% Tm^{3+} were compared with the ones of the tetragonal YSZ single crystal grown by LFZ.

Structural and morphological characterization

Figure 6.16 a) shows the Raman spectra of the 0.3 at.% Tm^{3+} doped ZrO_2 and YSZ powders produced by SCS. In line with the crystalline fibres stabilized with 8 mol.% $YO_{1.5}$ (section 5.2.2.4), the peak position of the vibrational modes for the Tm^{3+} doped YSZ powders indicates their tetragonal single phase nature. Further resonances can be observed for the Tm^{3+} doped ZrO_2 powder, reflecting a multiphase composition corresponding to the tetragonal and monoclinic crystalline phases, similarly to the ones founded for Eu^{3+} and Pr^{3+} doped ZrO_2 powders produced by SCS.

Figure 6.16 b)-f) displays TEM images of the 0.3 at.% Tm^{3+} doped ZrO_2 powder. The powder is characterized by a large grain size distribution and irregular grain shape, in line with the observed for other powders produced by SCS in the same conditions. Figure 6.16 b) shows that the powders are constituted by particles with two very different medium grain sizes, one much below 100 nm and other about 100 nm. Also, as identified in the previous europium and praseodymium doped zirconia, a high degree of agglomeration occurs which is a common observation in powders produced by combustion synthesis technique due to the high temperatures achieved during the process (typically >1000 ^{0}C) [46]. The average grain size estimated from the TEM images is 87 nm. Figure 6.16 e) and f) shows bright (BF) and dark field (DF) images from one agglomerate. DF image confirms the crystalline nature of the particles and the presence of smaller particles agglomeration, since in the DF mode the image is formed from a diffracted beam and the contrast is mostly caused by the different orientations of the crystalline plans.
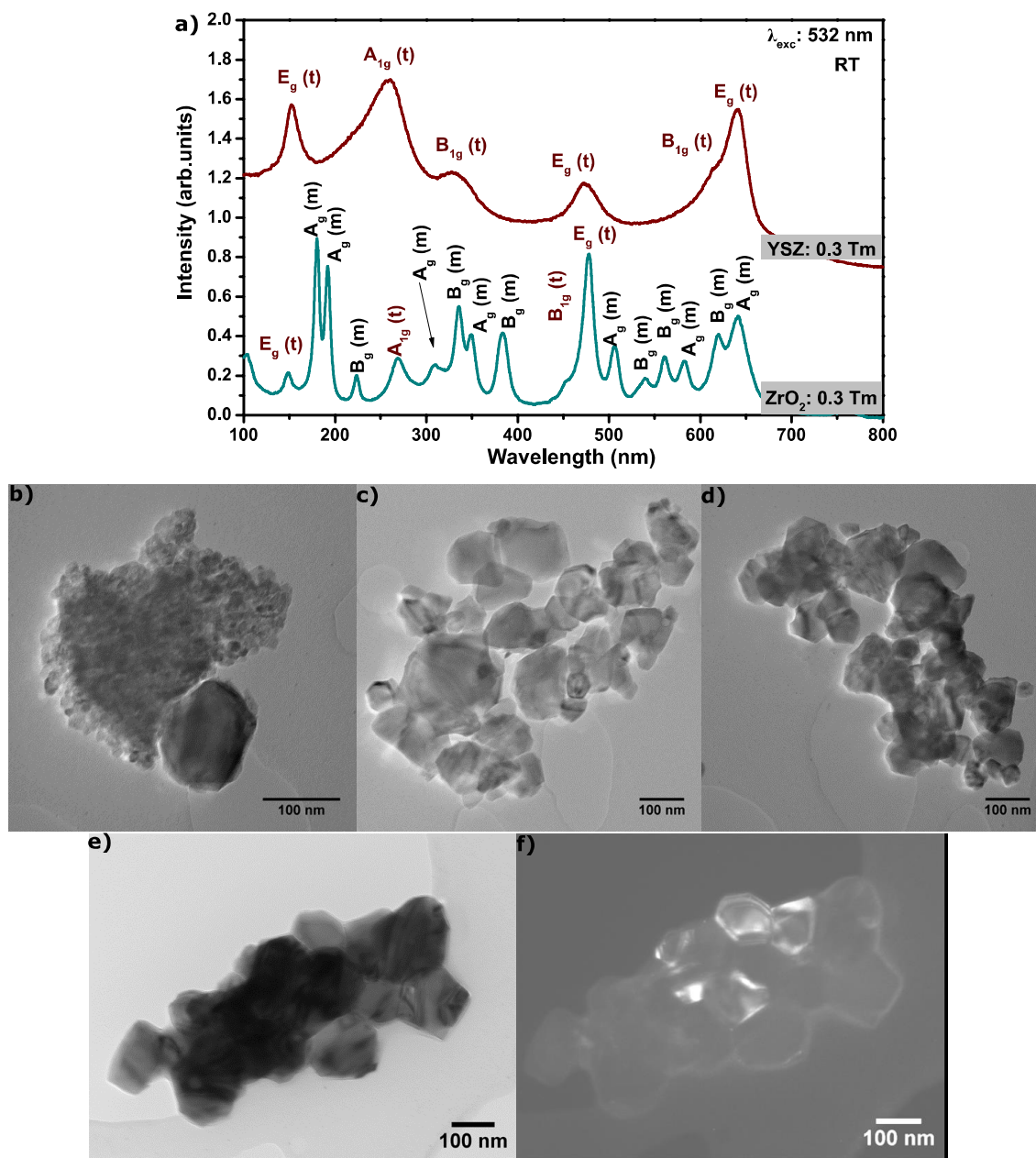
Figure 6.16. a) RT Raman spectra obtained with 532 nm excitation of the ZrO$_2$:Tm^{3+} and YSZ:Tm^{3+} powders produced by SCS. BF (b-e) and DF (f) TEM images of the ZrO$_2$:Tm^{3+} powders.

Luminescence characterization

Figure 6.17 a) and b) displays the RT PLE and visible PL spectra, respectively, of the Tm^{3+} doped ZrO$_2$ and YSZ nanopowders produced by SCS. The PL spectrum of the 0.3 at.% Tm^{3+} doped YSZ single crystal grown by LFZ is also shown for comparison. In line with the observed in the studied Tm^{3+} doped YSZ crystals, for the visible spectral range, under 355 nm excitation (resonant into the $^1D_2$ level of Tm^{3+}), the PL spectra of both doped powders, shows a dominant emission in the blue spectral range ($\sim$460 nm) assigned to the $^1D_2 \rightarrow {}^3F_4$

intra-4f^{12} transition of Tm^{3+}. Under the used excitation additional low intensity emission bands are observed in the blue and red spectral range due to the $^1G_4{\rightarrow}^3H_6$, $^1D_2{\rightarrow}^3H_5$ and $^1G_4{\rightarrow}^3F_4$ transitions, respectively. Additionally, intense red luminescence can be obtained under resonant excitation into the $^1G_4$ energy level of Tm^{3+}, as one can see in the PL spectra acquired under 461 nm wavelength excitation.

The PL spectrum of the ZrO$_2$:Tm^{3+} powders performed on the blue $^1D_2{\rightarrow}^3F_4$ transition reveals that the ions luminescence can be excited directly by pumping the sample resonantly into the $^1D_2$ excited state as well as via a broad UV excitation band, in a similar way to the ones observed in the Eu^{3+} or Pr^{3+} doped ZrO$_2$ powders produced by SCS, which has been assigned to CT excitation bands. The excitation of the ZrO$_2$:Tm^{3+} powders in the maximum intensity of this band (280 nm) leads to the observation of a broad unstructured emission band centred at ~470 nm, that was already discussed based on their association to optically active native defects, the so called F-type centres [47].

A close inspection of the $^1D_2{\rightarrow}^3F_4$ and $^1G_4{\rightarrow}^3F_4$ transitions revealed that the number of the emitting Stark components induced by the crystal-field splitting differs for the ZrO$_2$:Tm^{3+} and YSZ:Tm^{3+} powders, as shown in Figure 6.17 d). A higher number of lines are observed for the ZrO$_2$:Tm^{3+} powder indicating that the thulium ions occupy, in this case, different site locations and/or environments. In fact, some of the lines well fit the ones found for the single phase tetragonal YSZ:Tm^{3+} powders and t'-YSZ:Tm^{3+} crystal, suggesting that some of the ions occupy the same sites in the multiphase powders. In accordance with what was discussed above for the Eu^{3+} and Pr^{3+} multiphase ZrO$_2$ powders, the additional lines are likely to be due to the ions in the monoclinic crystalline phase.
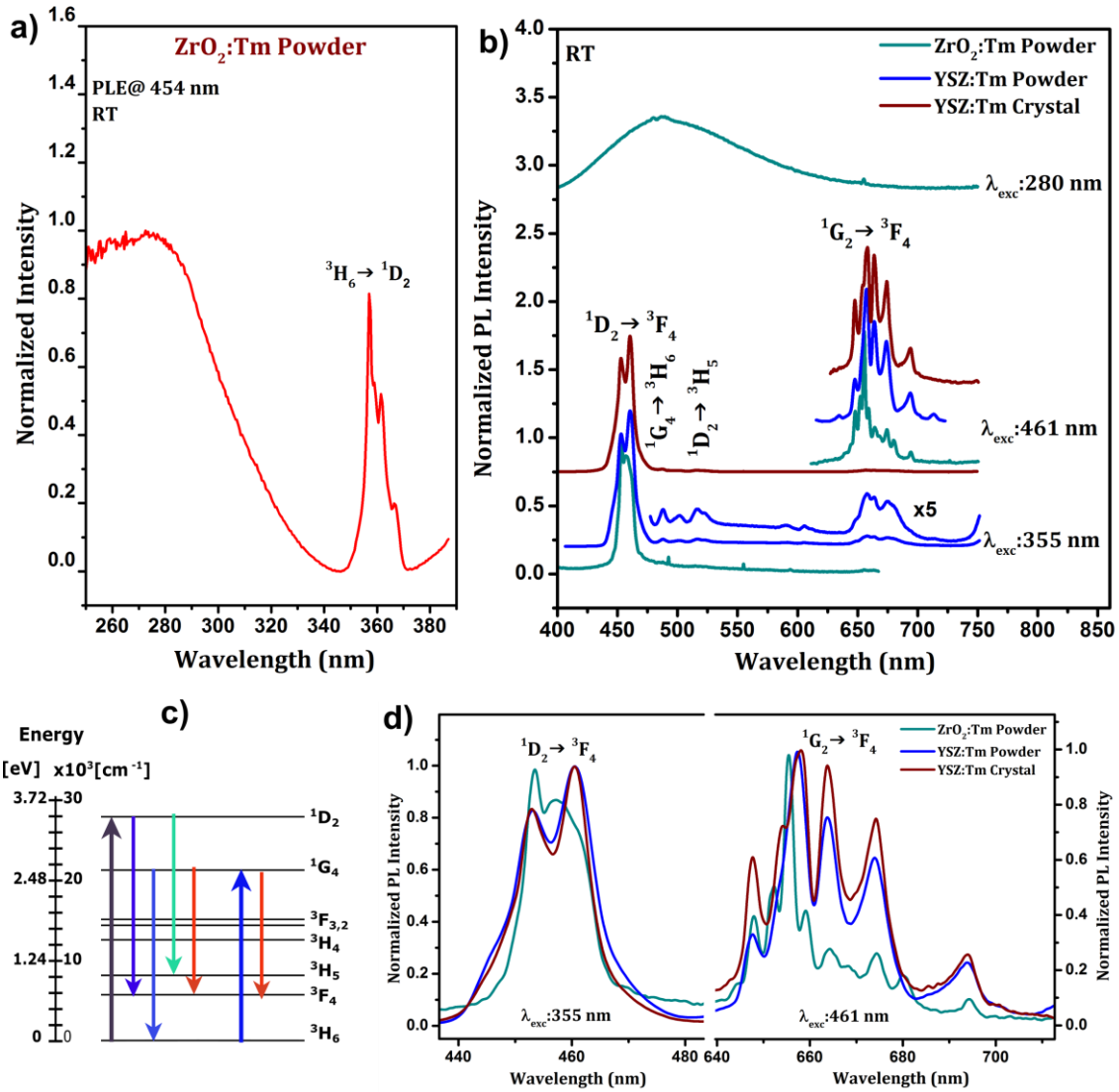
Figure 6.17. a) RT PLE spectra of the ZrO$_2$:Tm^{3+} powders, monitored in the ^{1}D$_2\rightarrow^3$F$_4$ blue emission. **b)** PL spectra of the ZrO$_2$:Tm^{3+} and YSZ:Tm^{3+} powders produced by SCS, with resonant excitation in the ^{1}D$_2$ and ^{1}G$_4$ multiplets as well as in the broad absorption CT band. PL spectra of the t'-YSZ:Tm^{3+} crystals are displayed for comparison. **c)** Partial energy level diagram of Tm^{3+} showing the visible radiative transitions under resonant excitation in the ^{1}D$_2$ and ^{1}G$_4$ multiplets. **d)** Comparison of the normalized blue and red emission of the two powders ad crystal.

The internal radiative quantum efficiency of the red transitions was investigated by measuring the temperature dependent PL spectra of the two powders with 457 nm excitation. Figure 6.18 a) and b) displays the temperature dependent PL spectra of the ZrO$_2$:Tm^{3+} and YSZ:Tm^{3+} powders, respectively. For the multiphase ZrO$_2$:Tm^{3+} powders, a decrease in the emission intensity is observed between 14K and RT and only around 40 % of the overall integrated emission intensity observed at low temperature remains at RT, as shown in Figure 6.18 a). On the other hand, and in line with the observed for the tetragonal YSZ:Tm^{3+} crystal, a higher luminescence stability was found to occur for the ions embedded

218

in the tetragonal crystal fibre, for which a nearly constant integrated intensity was observed between 14 K and RT. Such results, suggests that an enhanced luminescence stability of Ln^{3+} could be reached avoiding a mixed crystalline phase in the powder.
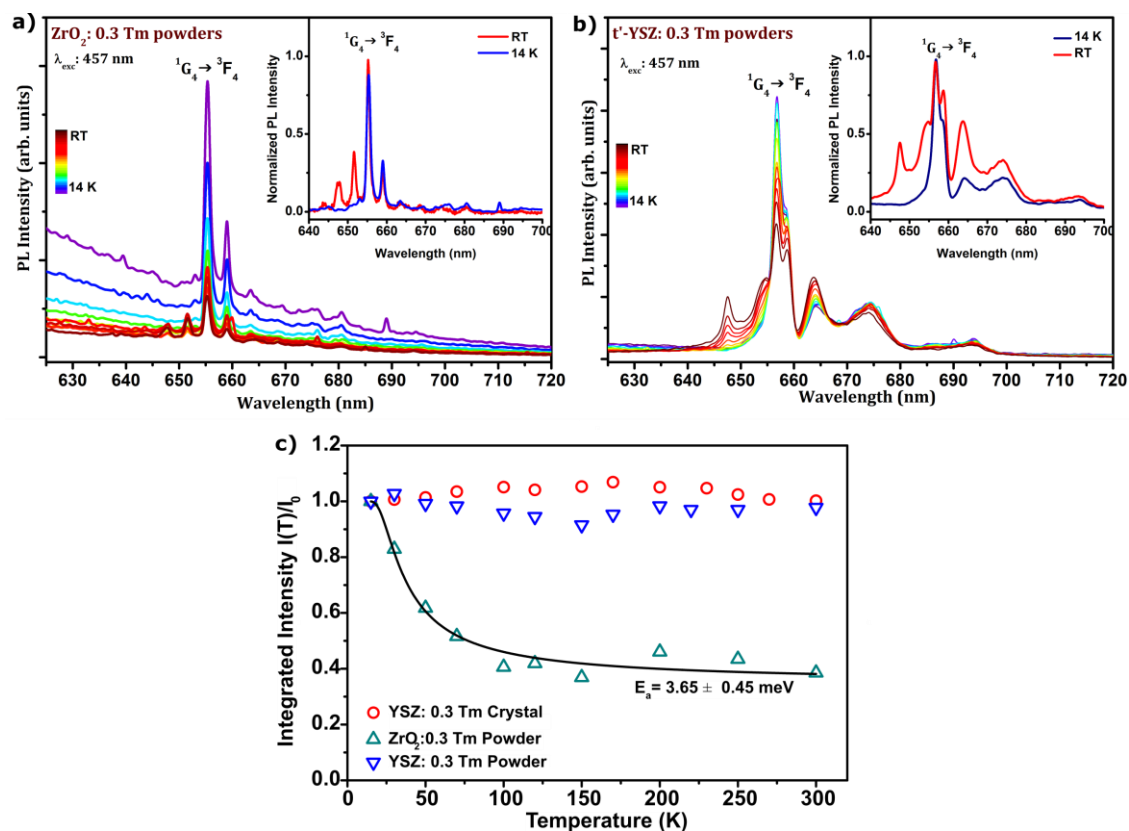
Figure 6.18. Temperature dependent PL spectra of the $ZrO_2:Tm^{3+}$ (a) and $YSZ:Tm^{3+}$ (b) powders. Insets: comparison between the normalized 14 K and RT PL spectra. c) Temperature dependent integrated intensity of the $ZrO_2:Tm^{3+}$ and $YSZ:Tm^{3+}$ powders. The results of t'-$YSZ:Tm^{3+}$ crystal is shown for comparison.

Summary

The luminescence of trivalent thulium in ZrO_2 powders, with a mixture of monoclinic and tetragonal phases, and in tetragonal YSZ powders produced by SCS were investigated and compared with the one previously studied fo the t'-$YSZ:Tm^{3+}$ crystal grown by LFZ. Tm^{3+} optical activation was found to occur for both doped powders and the intraionic transitions were assigned from the excitation and emission spectroscopic data. In the wavelength range studied, the ions luminescence arises mainly from the $^1D_2$ and $^1G_4$ and a detailed analysis of the blue $^1D_2 \rightarrow {}^3F_4$ and red $^1G_4 \rightarrow {}^3F_4$ transitions was performed under resonant excitation conditions. A comparison of the number of Stark transitions observed in the tetragonal YSZ and multiphase ZrO_2 powders indicates that additional Tm^{3+} sites/environments occur for the multiphase ZrO_2 doped powders, likely due to ions embedded in the monoclinic zirconia

structure. The intensity of the red emission between 14 K and RT shows a high stability for the tetragonal YSZ powders, in line with the results obtained in the tetragonal YSZ crystals, while for the polyphasic SCS powders nonradiative competitive paths strongly affect the red luminescence stability with temperature. Such results indicates that Ln^{3+} in the tetragonal zirconia phase rather than in the monoclinic one are desirable to achieve intense and stable luminescence at RT.

6.2.4 Other nanophosphors produced by SCS

Taking advantage of the simplicity of the SCS method together with the easy incorporation of the dopant Ln ions in the oxide host, this technique was used routinely to produce Ln doped zirconia and YSZ powders for further use in the production of ceramic targets for the pulsed laser ablation in liquids technique (PLAL). Before the use of the produced powders in preparation of ceramic targets, the crystalline structure was confirmed by Raman spectroscopy while preliminary studies of luminescence were carried out by PL at RT.

In particular, YSZ (8 mol.% $YO_{1.5}$) powders doped with 3 at.% Eu^{3+} and 1 at.% Tb^{3+} were prepared, following the procedure described above. Both powders were completely stabilized in a tetragonal zirconia phase through the incorporation of Y^{3+} in the zirconia lattice, as can be identified in the Raman spectra shown in Figure 6.19 RT PL spectra of the produced powders, under 325 nm irradiation, are displayed in Figure 6.19 b). In the case of YSZ powders doped with 3 at.% Eu^{3+} (red line), the emission spectra is very similar to the one acquired for the tetragonal YSZ crystals grown by LFZ, also doped with the same amount, which means that the Eu^{3+} ions occupy the same site symmetries/environments in the powders and crystal. Emissions in the red region due to electronic transitions from the $^5D_0$ excited state to the $^7F_{J(J=0-4)}$ multiplets of the $4f^6$ configuration are observed at RT in the doped powders, with a dominance of the $^5D_0 \rightarrow ^7F_2$ transition. As observed in the Eu^{3+} doped tetragonal crystals, with the same chemical composition (studied in section 5.2.2.1), a strong orange/red emission is observed when the powders are irradiated with UV light, as shown (inset of Figure 6.19 b). On the other hand, tetragonal YSZ powders doped with 1 at.% Tb^{3+} shows an intense green emission at RT under the same UV irradiation conditions, as can be identified in the same figure. The intense emission is due to the dominant green $^5D_4 \rightarrow ^7F_5$ transition of Tb^{3+} as was previously discussed for the terbium doped tetragonal crystals (studied in section 5.2.2.2).

Figure 6.19. RT Raman spectra performed in a backscattering geometry with 325 nm excitation (a) and RT PL spectra under 325 nm excitation of the YSZ powders doped with 1 at.% Tb and 3 at.% Eu ions. Inset in figure b) shows the photos of the doped powders upon irradiation with a UV lamp (254 nm).

Moreover, ZrO_2 powders doped with different Er ions concentration, from 1at.% to 16 at.% were successfully produced by SCS for subsequent targets preparation. Er^{3+} plays an important role in the stabilization of the high temperature tetragonal and cubic zirconia phases at RT, as clearly evidenced by Raman spectroscopy. The Raman spectra of the zirconia powders doped with different Er^{3+} concentration are shown in Figure 6.20 a). For the lowest dopant Er^{3+} concentration (1 at.%) only the vibrational modes of the monoclinic phase were identified, for a concentration of 2 at.% Er^{3+}, bands associated to the vibrational modes of the tetragonal phase appear overlapped with those corresponding to the monoclinic zirconia phase. This powder is constituted by a mixture of two phases: monoclinic and tetragonal. For a higher Er^{3+} concentration, 5 at.%, only the resonances associated to the vibrational modes of the tetragonal phase are observed and the powder is completely stabilized in the tetragonal zirconia phase. For an even higher dopant concentration of 16 at.% Er^{3+} a complete stabilization of the cubic phase of zirconia is achieved. At a dopant concentration of 10 at.%, even if the vibrational modes of tetragonal phase of zirconia can be identified, a broadening of the low energy peaks as well as a shift of the high energy band to lower energies, indicates some degree of distortion of the tetragonal cell into a cubic cell.
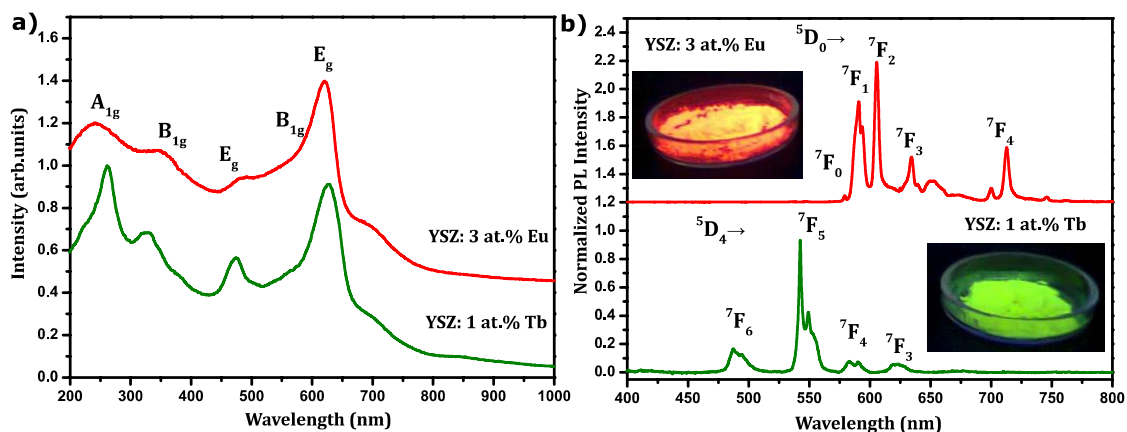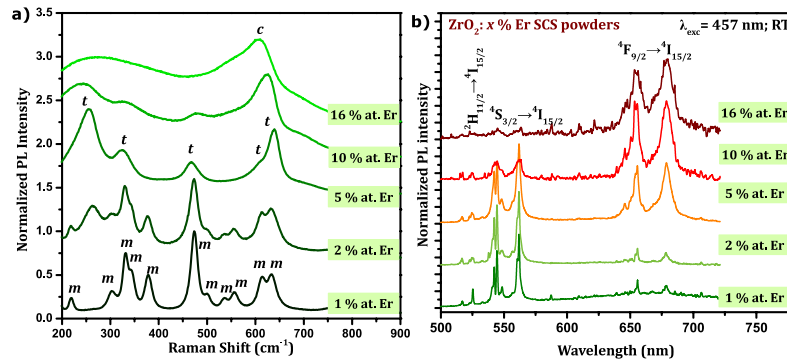
Figure 6.20. RT Raman spectra performed in a backscattering geometry obtained with 325 nm excitation (a) and RT PL spectra under 457 nm laser line excitation of the ZrO$_2$ powders doped with Er^{3+} concentration form 1 to 16 at.%.

RT PL spectra of the doped ZrO$_2$ powders obtained under 457 nm laser line excitation, resonant in the $^4F_{5/2}$ excited state of Er^{3+} is shown in Figure 6.20 b). Like it was observed and discussed in tetragonal YSZ crystals doped with 1 at.% Er^{3+} (analysed in section 5.2.2.5), visible emission in the green and red spectral regions is observed. As before, the green emission, assigned to the $^2H_{11/2} \rightarrow ^4H_{15/2}$ and $^4S_{3/2} \rightarrow ^4I_{15/2}$ electronic transitions, are shown to be the dominant ones for low erbium concentrations (1 and 2 at.% Er^3). Higher in Er^{3+} concentrations leads to an increase of the red emission assigned to the $^4F_{9/2} \rightarrow ^4I_{15/2}$ intraionic transition. For concentration higher than 10 at.% the red emission is the dominant one. Although this phenomenon is well known in several Er^{3+} doped inorganic materials, the limits of concentration in which it will occurs depends on material host . Moreover, materials size can also play a significant role [48]. The mechanism behind such effect will be discussed latter in section 7.2.2.3.

In addition, YSZ (8 mol.% YO$_{1.5}$) powders doped with Er^{3+} and co-doped with Er^{3+}, Yb^{3+} and with Tm^{3+}, Yb^{3+} were also produced by SCS and were subsequently employed in the preparation of ceramic targets to be used in the PLAL. As the aforementioned Er^{3+} doped ZrO$_2$ powders, the YSZ doped/co-doped with Er^{3+} and Tm^{3+} exhibit interesting upconversion luminesce properties for a wide range of applications, as it will be explored in Chapter 8.

6.3 Conclusions

Solution combustion synthesis (SCS) revealed to be a very effective technique to produce Ln^{3+} doped ZrO$_2$ nanophosphors in a simple and rapid way. The powders synthesized from metal nitrates and urea fuel (in stoichiometric conditions) are composed by crystals with nanometric dimensions. A large particle size distribution, as well as a high degree of

aggregation between particles, was found to occur in the as-prepared powders, due to the high temperature achieved during the combustion process. The high temperature is also responsible for the identified crystallinity in the zirconia powders produced by SCS, as well as by the easy incorporation and optically activation of the Ln ions in the host. Depending on the nature of the dopant ion and its concentration, intense emission can be observed at RT in the as-produced powders. The nature of monophasic and polyphasic material was assessed by Raman spectroscopy and the spectroscopic features of the ions in the powders were discussed based on a comparison with the single crystalline fibres grown by the LFZ technique. The ions luminescence stability is stronger in monophasic samples with the tetragonal structure.

References

[1]   S. T. Aruna, A. S. Mukasyan, *Curr. Opin. Solid State Mater. Sci.* **2008**, *12*, 44.
[2]   A. Varma, A. S. Mukasyan, *Korean J. Chem. Eng.* **2004**, *21*, 527.
[3]   A. K. Alves, C. P. Bergmann, F. A. Berutti, In *Novel Synthesis and Characterization of Nanostructured Materials*; Engineering Materials; Springer Berlin Heidelberg, 2013; pp. 11–22.
[4]   K. C. Patil, *Chemistry of nanocrystalline oxide materials: combustion synthesis, properties and applications*; World Scientific Pub Co Inc, 2008.
[5]   A. S. Mukasyan, P. Epstein, P. Dinka, *Proc. Combust. Inst.* **2007**, *31*, 1789.
[6]   S. Ekambaram, K. C. Patil, M. Maaza, *J. Alloys Compd.* **2005**, *393*, 81.
[7]   L. Xu, B. Wei, Z. Zhang, Z. Lü, H. Gao, Y. Zhang, *Nanotechnology* **2006**, *17*, 4327.
[8]   R. Krsmanović, V. A. Morozov, O. I. Lebedev, S. Polizzi, A. Speghini, M. Bettinelli, G. V. Tendeloo, *Nanotechnology* **2007**, *18*, 325604.
[9]   H. Song, D. Chen, *J. Biol. Chem. Lumin.* **2007**, *22*, 554.
[10]   Z. Qiu, Y. Zhou, M. Lü, A. Zhang, Q. Ma, *Solid State Sci.* **2008**, *10*, 629.
[11]   R. E. Muenchausen, E. A. McKigney, L. G. Jacobsohn, M. W. Blair, B. L. Bennett, D. W. Cooke, *IEEE Trans. Nucl. Sci.* **2008**, *55*, 1532.
[12]   S. Ekambaram, *J. Alloys Compd.* **2005**, *390*, L7.
[13]   Y. Jin, W. Qin, J. Zhang, X. Zhang, Y. Wang, C. Cao, *J. Solid State Chem.* **2008**, *181*, 724.
[14]   X. Lou, D. Chen, *Mater. Lett.* **2008**, *62*, 1681.
[15]   Z. Qiu, Y. Zhou, M. Lü, A. Zhang, Q. Ma, *Acta Mater.* **2007**, *55*, 2615.
[16]   R. Sharma, U. Sharma, *J. Alloys Compd.* **2015**, *649*, 440.
[17]   R. Sharma, D. P. Bisen, B. P. Chandra, *J. Lumin.* **2015**, *168*, 49.
[18]   P. K. Jisha, R. Naik, S. C. Prashantha, H. Nagabhushana, S. C. Sharma, H. P. Nagaswarupa, K. S. Anantharaju, B. D. Prasad, H. B. Premkumar, *J. Lumin.* **2015**, *163*, 47.
[19]   R. S. Yadav, R. K. Verma, A. Bahadur, S. B. Rai, *Spectrochim. Acta. A. Mol. Biomol. Spectrosc.* **2015**, *142*, 324.
[20]   N. Hakmeh, C. Chlique, O. Merdrignac-Conanec, B. Fan, F. Cheviré, X. Zhang, X. Fan, X. Qiao, *J. Solid State Chem.* **2015**, *226*, 255.
[21]   H. B. Premkumar, B. S. Ravikumar, D. V. Sunitha, H. Nagabhushana, S. C. Sharma, M. B. Savitha, S. Mohandas Bhat, B. M. Nagabhushana, R. P. S. Chakradhar, *Spectrochim. Acta. A. Mol. Biomol. Spectrosc.* **2013**, *115*, 234.
[22]   T. Manohar, R. Naik, S. C. Prashantha, H. Nagabhushana, S. C. Sharma, H. P. Nagaswarupa, K. S. Anantharaju, C. Pratapkumar, H. B. Premkumar, *Dyes Pigments* **2015**, *122*, 22.
[23]   T. Ye, Z. Guiwen, Z. Weiping, X. Shangda, *Mater. Res. Bull.* **1997**, *32*, 501.
[24]   N. Vu, T. Kim Anh, G.-C. Yi, W. Strek, *J. Lumin.* **2007**, *122-123*, 776.
[25]   S. Shikao, W. Jiye, *J. Alloys Compd.* **2001**, *327*, 82.
[26]   T. Biljan, A. Gajovic, Z. Meic, *J. Lumin.* **2008**, *128*, 377.
[27]   T. Peng, H. Yang, X. Pu, B. Hu, Z. Jiang, C. Yan, *Mater. Lett.* **2004**, *58*, 352.
[28]   R. Ianoş, I. Lazău, C. Păcurariu, P. Barvinschi, *Cem. Concr. Res.* **2009**, *39*, 566.
[29]   K. C. Patil, S. T. Aruna, S. Ekambaram, *Curr. Opin. Solid State Mater. Sci.* **1997**, *2*, 158.
[30]   S. E. Paje, J. Llopis, *Appl. Phys. A* **1993**, *57*, 225.
[31]   H. Nakajima, T. Mori, *J. Alloys Compd.* **2006**, *408-412*, 728.
[32]   E. De la Rosa-Cruz, L. A. Díaz-Torres, P. Salas, D. Mendoza, J. M. Hernández, Castaño, V. N., *Opt. Mater.* **2002**, *19*, 195.
[33]   N. Woodward, J. Poplawsky, B. Mitchell, A. Nishikawa, Y. Fujiwara, V. Dierolf, *Appl. Phys. Lett.* **2011**, *98*, 011102.
[34]   H. E. Hoefdraad, *J. Solid State Chem.* **1975**, *15*, 175.
[35]   P. Dorenbos, *J. Lumin.* **2005**, *111*, 89.

[36]   S. Shukla, S. Seal, *Rev. Adv. Mater. Sci.* **2003**, *4*, 123.

[37]   S. Shukla, S. Seal, R. Vij, S. Bandyopadhyay, Z. Rahman, *Nano Lett* **2002**, *2*, 989.

[38]   Y. Guan, T. Tsuboi, Y. Huang, W. Huang, *Dalton Trans.* **2014**, *43*, 3698.

[39]   A. Masalov, O. Viagin, I. Ganina, Y. Malyukin, *J. Lumin.* **2009**, *129*, 1695.

[40]   P. N. Zhmurin, N. V. Znamenskii, T. G. Yukina, Y. V. Malyukin, *Phys. Status Solidi B* **2007**, *244*, 3325.

[41]   V. V. Seminko, A. A. Masalov, Y. I. Boyko, Y. V. Malyukin, *J. Lumin.* **2012**, *132*, 2443.

[42]   F. Ramos-Brito, M. García-Hipólito, C. Alejo-Armenta, O. Alvarez-Fragoso, C. Falcony, *J. Phys. Appl. Phys.* **2007**, *40*, 6718.

[43]   B. Savoini, J. E. Muñoz Santiuste, R. González, *Phys. Rev. B* **1997**, *56*, 5856.

[44]   C. Wang, Q. Meng, *J. Nanosci. Nanotechnol.* **2014**, *14*, 3893.

[45]   N.-O. Hansen, A.-R. Bellancourt, U. Weichmann, G. Huber, *Appl. Opt.* **2010**, *49*, 3864.

[46]   A. S. Mukasyan, P. Dinka, *Int. J. Self-Propagating High-Temp. Synth.* **2007**, *16*, 23.

[47]   N. G. Petrik, D. P. Taylor, T. M. Orlando, *J. Appl. Phys.* **1999**, *85*, 6770.

[48]   J. A. Capobianco, F. Vetrone, J. C. Boyer, A. Speghini, M. Bettinelli, *J. Phys. Chem. B* **2002**, *106*, 1181.

Chapter 7.

Pulsed laser ablation in liquids (PLAL)

In the first part of this chapter, the fundaments of the pulsed laser ablation in liquid technique are explained and the used experimental setup is described.

In the second part, the results obtained by the morphological, structural and optical characterization of the produced nanoparticles are presented and discussed.

7.1 The PLAL process

In the last two decades, pulsed laser ablation in liquids (PLAL), also referred in literature as liquid-assisted pulsed laser ablation (LA-PLA), liquid-phase pulsed laser ablation (LP-PLA), pulsed laser ablation in aqueous medium (PLAAM) and others, emerged as a simple but effective alternative route to produce nanomaterials [1]. In a simple way, in this process NPs are generated by the ablation of a target immersed in a liquid through irradiation with a higher power pulsed laser [1].

Nanomaterials were firstly produced by PLAL in 1987 by Patil *et al*. using an iron solid target immersed in water to produce iron oxide NPs [2]. However, it was only recently that the booming in PLAL technique occurred. In the past decade the interest in PLAL technique increased exponentially motivated by the fast development in nanoscience and nanotechnology and by the demand for viable alternative methods to produce high performance nanomaterials [3]. PLAL consists in a simple and green technique that shows several advantages comparatively to the conventional chemical and physical methods used for nanomaterials formation [4]. First of all, the experimental setup is very simple and there is no need of expensive vacuum systems as the ones required in the laser ablation processes performed in vacuum or gas phase [4,5]. Since chemical precursors are not used in the PLAL process, the final product is free of any by-products and characterized by a high purity [3,4]. In addition, the collection of NPs in the liquid results, on one hand, in a low probability of the NPs to be inhaled and, by the other hand, in a process with high efficiency since there are no material losses [5]. PLAL is a very versatile method in which, by a proper combination of target and liquid media, it is possible to produce a wide range of nanomaterials with the required functions [4].

7.1.1 Fundamentals and mechanisms of PLAL

Depending on the target characteristics the PLAL process is usually divided in three classes: pulsed laser ablation of bulk solid targets, pulsed laser ablation of micro/NPs suspensions and pulsed laser ablation of meta salts or/and organic precursors [1,5]. The pulsed laser ablation of a bulk solid target is the most used PLAL approach to produce nanomaterials. In this process, the surface of a bulk solid target, immersed in an appropriated liquid, is ablated by irradiation with a focused pulsed laser at the solid-liquid interface, through the layer of the transparent liquid above the target. At the liquid-solid interface a laser-induced plasma is formed. This plasma is composed by atoms, ions, molecules or clusters ablated from the target. The high temperature of the laser-induced plasma heat and ionizes the liquid in its

vicinity and a plume is generated. This plasma-induced plume contains chemical species from the liquid. The chemical species in the two plasmas can mix and reacts, allowing the nucleation and growth of NPs [5]. The pulsed laser ablation of a solid bulk target immersed in liquid has been efficiently used to produce metal, metal alloys [6–8] and metal oxides nanoparticles [9–12]. In the literature, the production of nanostructures with higher complexity, as core-shell NPs, by the ablation of solid target is also reported [13,14].

Instead of a solid bulk target a suspension of micro/NPs can be irradiated by a focused pulsed laser to produce NPs with smaller size [1,5]. The particle size reduction can be caused by a thermal or a non-thermal process. In the first case, the laser irradiation induces the melt and/or vaporization of the particles of higher dimension, yielding to small melt drop or ions/atoms, respectively. The formation of smaller NPs occurs through the cooling and the condensation of the material. In the end, the resulting NPs can present different size, shape, phase and composition from the precursor ones [5]. In the non-thermal process the size reduction occurs through explosive fragmentation. In this case, the laser irradiation causes an injection of electrons from the surface of the particles leaving them positively charged. The positive charges induce a strong repulsion between different parts of the NPs, which can lead to its fragmentation [5]. The predominance of the thermal or the non-thermal mechanism depends on the experimental conditions, mostly on laser parameters. The melting/evaporation mechanism requires high laser irradiance in order to achieve temperatures above the boiling temperature of the material, and by that way, vaporize the atoms, ions or molecules at the surface. On the other hand, for the occurrence of the fragmentation mechanism, a matching of the laser wavelength with the work function of the target material is required in order induces photoelectrons ejection [1]. Moreover, the size of the resultant NPs also depends of the experimental parameters and it could be bigger or smaller than the initial particles size depending on the ablation time and the size of the precursor particles [5]. The pulsed laser irradiation of the micro/NPs in suspension can be used to irradiate a colloidal solution previously produced by ablation of a solid bulk target in order to reduce the particle size and particle size distribution [15,16]. As it will be discussed forward, due to the complexity and high number of parameters that can affect the particle size and size distribution, and due to the difficulty to have a narrow control over all these parameters in the PLAL process, in some cases, it is easier to perform a further laser irradiation of the produced colloidal solution in order to adjust particle size and size distributions [15–17].

As aforementioned, the production of NPs can be also achieved through the pulsed laser irradiation of a liquid target, i.e. a solution containing metal salt and/or organic precursors.

229

The laser irradiation promotes the dissociation of the metal salt or organic precursors in neutral atoms which can form clusters that can grow resulting in NPs [1,5].

Depending on the characteristics of the target and liquid medium the generation of nanomaterials by PLAL can occur through a reactive or non-reactive process [1]. In the reactive process the chemical species from the target will reacts with the chemical species from the liquid, and the final products will present a different chemical composition from the precursor target. This is the case, for example, of the metal oxide NPs produced by the ablation of a metallic target in an oxidant liquid medium, for example water [18–20]. On the other hand, if the process is non-reactive, the produced NPs will have the same chemical composition as the precursor target. One example is the production of metallic NPs by ablation of a metallic target in a non-reactive liquid medium [21].

The chemical and physical phenomena involved in the particles generation by pulsed laser ablation at the liquid-solid interface are more complex than the ones involved in vacuum or gas phase, and are not completed understood nowadays [3,5]. This is due to the high density and, in some cases, to the high reactivity of the liquid medium and to the complexity of possible interactions between the laser beam, target, liquid and products. The plasma plume in the PLAL is under high confinement due to the high density of the liquid, which results in a high temperature, high pressure and high density of the plasma [5]. These conditions are highly favourable to the formation of metastable phases that cannot be produced under normal conditions [5]. A high effort has been applied for an in-depth understanding of the physical and chemical phenomena involved in PLAL. Time-resolved shadow-graph technique has been used to study the PLAL process [3,5,22,23]. Different particular phenomena, occurring in a short time scale after the laser-matter interaction, were successfully identified by this technique. For example, Tsuji *et al.* reported the nanosecond time-resolved observation of pulsed laser ablation of a silver target in water [22] and in a polyvinylpyrrolidone solutions [24]. Time-resolved shadowgraph images of the laser ablation process at different delay times from laser irradiation of silver target in polyvinylpyrrolidone solutions are shown in Figure 7.1. Several phenomena were identified with time after the pulse laser irradiation. First, a shock wave is generated, followed by the formation of cavitation bubble with the plasma plume inside. After that, cavitation bubble collapses and the material is released to the liquid, with the emission of a second shock wave. The same type of phenomenon has been observed for other target materials and liquids. More information about the dynamics of the PLAL process can be found in the revision works of Singh and Yang [5,17].
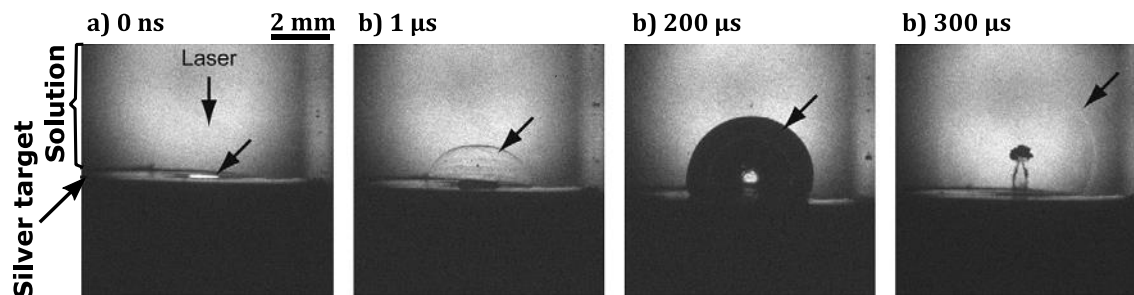
Figure 7.1. 10 ns resolved shadowgraph images of laser ablation phenomena observed for a silver target polyvinylpyrrolidone solutions, where some remarkable effects are observed: a) optical emission, (b) shockwave, (c) cavitation bubble and (d) secondary shockwave generated at the bubble collapse. [24].

As aforementioned, during PLAL process, the laser pulse, liquid medium, target and products can interact with each other, in a short time after the laser pulse. As such, the characteristics of the produced NPs, such as shape, average particle size, particle size distribution, crystalline phases and composition, will be strongly dependent on each ones of these components [4,25,26]. Several laser parameters can be adjusted in order to control the NPs characteristics and the process efficiency, including laser wavelength, pulse width, pulse repetition rate, pulse energy and fluency [4,26]. The liquid properties, such as the reactivity, the presence of surfactants, pH, absorption wavelengths and refraction index, and the target characteristics, including target composition, density, and surface roughness, also play an important role in the properties of the NPs produced by PLAL [4]. Some of these parameters are not independent one of each other, and sometime an appropriated compromise between them is necessary.

Several experimental studies were performed in order to understand the effect of these parameters in the NPs size and efficiency of NPs generation [15,26–32]. Two of the most studied parameters are the laser wavelength and the laser energy density (J/cm^2, hereafter denoted as laser fluence), since they are critical in the PLAL process. The results obtained by different research groups, show that the wavelength dependence in the NPs size and process efficiency is changed by the irradiation conditions [17]. As an example, studies performed during the laser ablation of silver targets, with different irradiation conditions (under focused and unfocused laser beam) showed that the dependence of laser wavelength in the NPs size and process efficiency has two behaviours: for a low fluence regime (< 1 J/cm^2), under unfocused condition, both NPs size and process efficiency increase with decreasing of the laser wavelength; on the other hand, when a high laser fluence (>1 J/cm^2) is used (focused conditions), both the NPs size and process efficiency increase with increasing in the laser wavelength [17]. These differences in the wavelength dependence at low and high laser fluences, were attributed to the possible absorption of the incident laser

energy by the NPs produced by PLAL. During the PLAL process the produced NPs may stay in the path of the incident laser beam due to their low mobility in the liquid. Consequently, part of the laser beam can be absorbed by the NPs. The absorption of the laser light by the formed NPs increases with increase in laser fluence, since for high laser fluences a higher number of NPs are produced. As a result, the intensity of the laser light that reaches the target surface is lower. Moreover, the size of the NPs that absorb part of the incident light can be decreased due to fragmentation [17]. The strong effect of laser fluence in NPs size and process efficiency leads to the need of a narrow control of this parameter during PLAL synthesis. However, several factors can affect the laser fluence at the surface of the solid target, such as the thickness of the liquid layer, the distance of the target surface to the focusing lens, the amount of produced NPs in the path of the laser beam, etc [17].

The control over these experimental conditions is not an easy task since they can change along the laser ablation process. For example, the liquid level above the target can be reduced by evaporation, the distance between focusing lens and target can increase due to the reduction in the target thickness at the irradiated spot. These changes will consequently affect the ablation conditions along the process, which can limit the efficiency and change the characteristics of the produced NPs [5].

Several PLAL experimental configurations have been subjected to detailed research in order to improve the control over the ablation process and, by this way, achieve a strict control and reproducibility over the NPs characteristics. Even though there are several modifications of the experimental setups used in PLAL technique, the principal elements remain the same. Basically, the main constituents are a pulsed laser, optical components (mirrors and lens) and a cell to keep the target and liquid [3,5]. The most traditional experimental arrangement for the ablation of a solid target in a liquid medium is shown in Figure 7.2. a). Here, the laser beam is focused vertically and perpendicularly to the surface of the solid target placed horizontally on the bottom of a cell. The stirring of the liquid is important to homogeneously distribute the NPs in the liquid and, by this way, remove a large amount of produced NPs from the laser beam path. The motion of the laser spot on the surface of the target, even by moving the laser beam, using an optical scanner, or by rotation of the solid target, is important to avoid a deep ablation crater and ensure that the fluence is maintained constant along the process [5]. One of the main problems of this experimental setup is the high interaction of the produced NPs with the laser beam, since the plasma plume is formed perpendicularly to the target. Once again, this interaction induces changes in the ablation conditions. For example, the laser beam that reaches the surface of the target is attenuated. Moreover, the interaction of the laser beam with the produced NPs in the

solution can change the size of the NPs, as mentioned above. Depending on the conditions, the size of the NPs can be reduced by fragmentation or increased due to the merger of closer NPs, which in the end can originate a broadening of the particles size distribution [5].
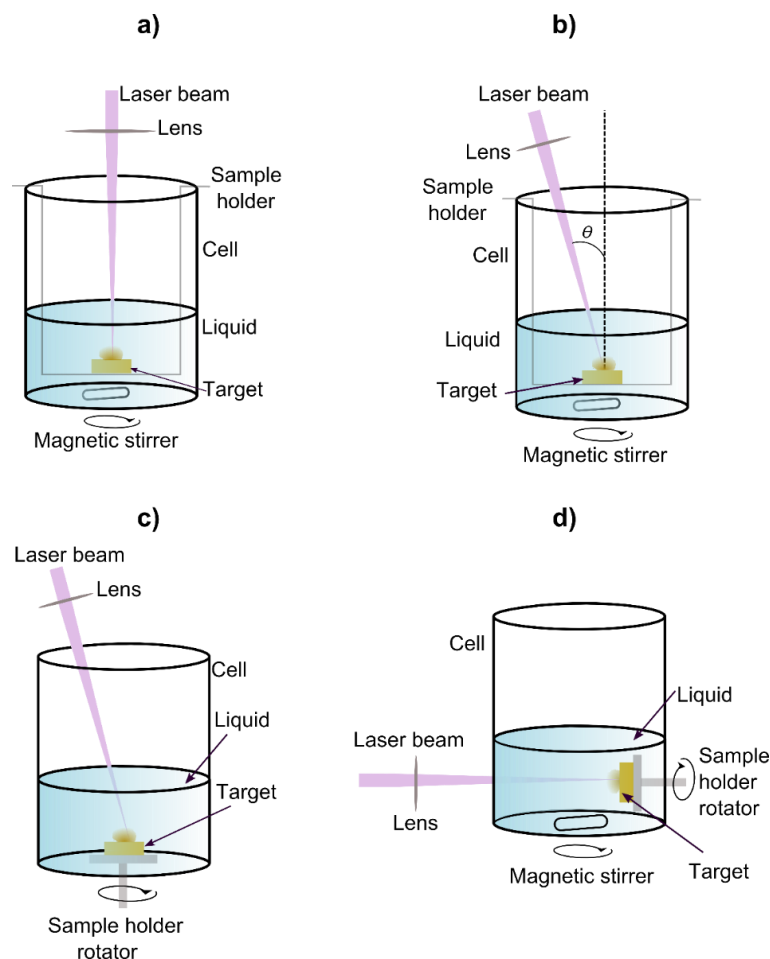
Figure 7.2. Different modifications of the experimental setup used in PLAL (adapted from [5]).

It was reported that the interaction of the laser beam with the generated particles in the solution can be considerable reduced by adopting an experimental setup as the one shown in Figure 7.2 b) [5]. The only difference between the first setup and this one is the position of the laser beam relatively to the surface of the target. In the latter case the laser beam is not completely vertically and perpendicular to the target promoting a way to reduce the interaction between the laser beam and the plasma plume. The same effect can be obtained by tilting the target, instead of the laser beam. However, in this case the target should not be rotated, otherwise the laser fluence will not be constant due to the variation in the spot dimensions [5]. In a situations that the rotation of the target is needed, the tilt of the laser beam is desirable (Figure 7.2 c). Other alternative setup is presented in Figure 7.2. d). In this configuration, the solid target instead of being placed in the bottom of the cell is fixed

perpendicularly to it, which allows to avoid any change in the thickness of liquid level above the target due to evaporation of the liquid [5]. In this case, the thickness is defined by the distance of the target to the wall of the cell. In addition, with this setup it is easier to promote a simultaneous rotation of the target and the stirring of the solution magnetically. However, the used cell should be completely transparent to the laser beam in order to avoid laser attenuation and the damage of the cell. Other PLAL setup configurations, not presented here, have been reported both for the ablation of solid bulk targets and particles targets in liquids [5]. In some of them only simple changes are made while in other ones the modifications in the configuration is more significant. For example in some works, it was reported the use of a liquid flux that promotes a continuous renewal of the liquid solvent around the target [33,34]. In this case there is no random interaction of the pulse laser with the produced particles in solution. All of the suggested experimental configurations evidence the effort that has been made in order to get a higher control and reproducibility over laser ablation process in liquids.

Pulsed laser ablation in liquids has been used for the synthesis of a wide variety of nanomaterials with different functionalities for innumerable application fields. A key point of laser ablation in liquids is the possibility to directly produce stable colloidal solutions [5]. Typically, the surface of PLAL produced NPs is highly charged, providing a high stability of the NPs in the solutions, even in water, without addition of any surfactant for the stabilization [5]. Since no chemical precursors are needed in the process, the colloids are highly pure and the surface of the NPs free of any chemical contamination [5]. Even so, if necessary, surfactants can be added to the liquid medium to control particle growth, increase the dispersion of NPs or other complementary functions [1,5]. Additionally, it was reported that the surface of the NPs generated by PLAL is highly reactive, resulting in a very good affinity to ligands [5]. For example, it was reported that the number of biomolecules that can be conjugated to the surface of NPs produced by PLAL are 3 to 5 times higher than the number that is usually achieved in the NPs produced by chemical routes [5]. Moreover, *in situ* [35–38] and *ex*-situ [34] conjugation of biomolecules is also a possibility.

Colloidal solutions of NPs are used in a wide range of areas from energy to biomedicine. Usually, they are produced by complex chemical routes that lead to colloids with low purity implying the use of further processes of purification [17]. The interest in the PLAL technique by the academic and industrial communities suffers a marked growth in the recent years. The first is expressed by the increasing number of scientific articles, doctoral thesis and published books in this subject, where not only the preparation of different nanomaterials by this technique is reported but also the mechanism beyond the process and the effects of

several growth parameters in the properties of the produced materials are studied [17,39,40]. In addition, commercial PLAL products are already available on the market. Particular® GmbH, a Germany company founded in 2009, was the first worldwide company dedicated to the industrial production of colloidal solutions by pulsed laser ablation in liquids [41]. Highly pure NPs from different materials and of different sizes, dispersed in various solvents and produced by PLAL, are now available on the market. Figure 7.3 shows some of Particular® GmbH commercial products produced by this technique, including metal (Au, Pt, Ag) and ceramic (ZrO_2) colloids.

| Au NPs in Water | Pt NPs in Water | Ag NPs in Water | ZrO_2 NPs in Water |
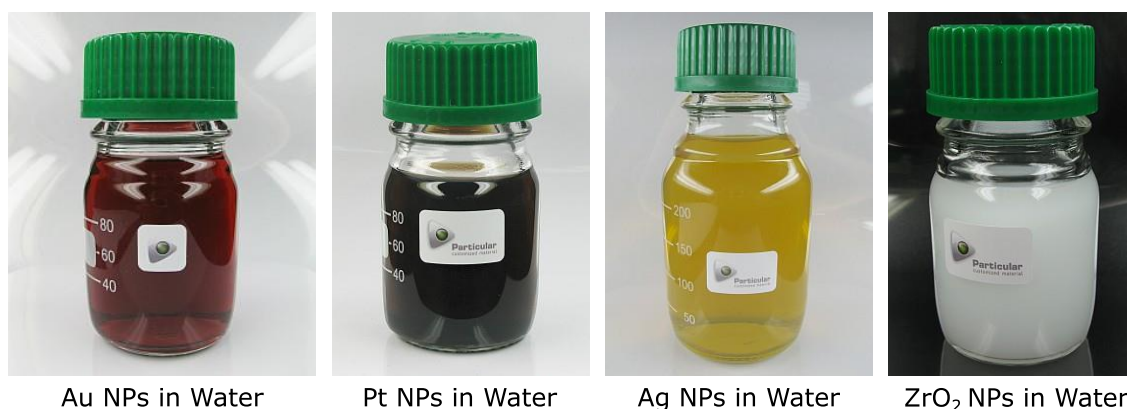
Figure 7.3. Some of the metal (Au, Pt, Ag) and ceramic (ZrO_2) colloids commercial products produced by Particular GmbH using the PLAL technique [41].

Recently, the potential of PLAL technique for the preparation of inorganic luminescent NPs doped with Ln ions has been a matter of interest by the worldwide scientific community. A summary of these NPs is presented in Table 7.1. Different types of inorganic NPs including nitrides, fluorides, but mostly oxides have been used to produce luminescent NPs by this technique. The produced NPs, are usually crystalline in nature exhibiting intense luminescence at RT [42–44]. The possibility to produce these luminescent NPs directly in biocompatible solutions, together with the high purity and crystallinity of produced NPs, has aroused the interest of PLAL produced NPs as luminescent bioprobes [42–44].

Table 7.1. Summary of Ln^{3+} doped inorganic NPs produced by PLAL, reported in literature

Ref	Phosphor	Liquid medium	Particle size
G. Ledoux *et al.* [45]	Lu$_3$TaO$_7$:(Gd^{3+}, Tb^{3+})	deionized water	6.2 nm
	Y$_2$O$_3$:Eu^{3+}		7.0 nm
	Gd$_2$SiO$_5$:Ce^{3+}		8.9 nm
	Lu$_2$O$_2$S:Eu^{3+}		Not specified
T.Nunokawa *et al.* [46]	Y$_2$O$_3$:(Er^{3+}, Yb^{3+})	deionized water	100-1000 nm
R. Zamiri *et al.* [47]	YO$_3$:Er^{3+}	distilled water	5.8 nm
	Bi$_2$O$_3$:Er^{3+}		32.1 nm
	Sb$_2$O$_3$:Er^{3+}		151.7 nm
S. A. Al-Mamun *et al.* [48]	Y$_2$O$_3$:Eu^{3+}	distilled water	6.8 nm, 20.4 nm and 9.7 nm (different target characteristics)
		H$_2$O$_2$ aqueous solution	12.2 nm and 12.3 nm (different target characteristics)
K. Hasna *et al.* [43]	Eu^{3+}:Ca$_{10}$(PO$_4$)$_6$(OH)$_2$	water	15 nm (for 1 h of ablation time)
			60 nm (for 4 h of ablation time)
K. M. Kim *et al.* [42]	Y$_3$Al$_5$O$_{12}$:Ce^{3+}	deionized water	8.7 nm
		LDA* aqueous solution	4.5 nm
Y. Onodera *et al.* [49]	Y$_2$O$_3$:(Er^{3+}, Yb^{3+})	deionized water	11.1 nm to 21.5 nm (laser energy from 1.6 to 15.6 mJ/pulse)
S.K. Singh *et al.* [50]	Gd$_2$O$_3$:(Er^{3+}, Yb^{3+})	distilled water	8–26 nm
G. Qin *et al.* [51]	(Zn$_{0.3}$Al$_{0.25}$Pb$_{0.3}$ Li$_{0.098}$Yb$_{0.1}$Tm$_{0.002}$F$_{2.354}$)	ethanol	1–10 μm
T. Maldiney *et al.* [44]	Ca$_2$Si$_5$N$_8$:(Eu^{2+},Tm^{3+})	deionized water	3-5 nm
D. Amans *et al.* [52]	Y$_2$O$_3$:Eu^{3+}	aqueous solution of MEEAA**	1.9 nm to 4.7 nm (Depending on experimental conditions)
	Gd$_2$O$_3$:Eu^{3+}		
	Y$_3$Al$_5$O$_{12}$:Ce^{3+}		
F. Yoshimura *et al.* [53]	Sr$_2$MgSi$_2$O$_7$:(Eu^{2+},Dy^{3+})	deionized water	76 to 710 nm (Depending on experimental conditions)
		ethanol	
D. Katsuki *et al.* [54]	ZnO:Eu^{3+}	aqueous solution with SDS ***	15 nm
		Solution of LiOH	
Mhin *et al.* [55]	Tb$_3$Al$_5$O$_{12}$:Ce^{3+}	deionized water	11.64 nm
		LDA aqueous solution	6.47 nm
Park *et al.* [56]	Y$_3$Al$_5$O$_{12}$:Ce^{3+}	deionized water	10.4 nm

* LDA- lithium diisopropylamide; ** MEEAA - 2-[2(2-methoxyethoxy)ethoxy]acetic acid; *** SDS- Sodium dodecyl sulfate

Regarding the production of zirconia NPs by PLAL, few works can be found in literature [57–59], which are limited to the production of undoped zirconia. The high potential of PLAL to produced luminescent NPs shown in other inorganic hosts, together with the excellent properties of zirconia as a host for the incorporation of Ln ions, strongly motivated the use of PLAL to produce Ln-doped zirconia NPs in this thesis work.

7.1.2 Production of Zirconia NPs by PLAL

Figure 7.4 shows the experimental setup used to produce the undoped and Ln^{3+} doped ZrO$_2$ and YSZ NPs by PLAL. This simple setup is manly composed by a pulsed laser, optical components, and a glass cell. A nanosecond (7 ns pulse width) Q-switched Nd:YAG laser, from Continuum®, with 1064 nm wavelength and working at a maximum pulse repetition rate of 10 Hz was used. Under unfocused conditions, the laser beam has a diameter spot of 7 mm and maximum pulse energy of 685 mJ. Both pulse frequency and pulse energy can be controlled, the latter one by change the Q-switch delay. The laser beam was focused into the surface of the target, placed in a sample holder within the glass cell and parallel to their bottom, by a flat mirror. The glass cell was filled with distillated water and the height of water column above the target was controlled. The sample holder allows to support the target at a certain distance from the bottom of the cell and thus the magnetic agitation of the liquid. During the ablation, the water was kept under continuum magnetic agitation in order to homogenize the generated NPs in the solution. The glass cell was also manually rotated several times during the ablation process in order to change the ablation spot thus avoiding a deep wear down of the target.
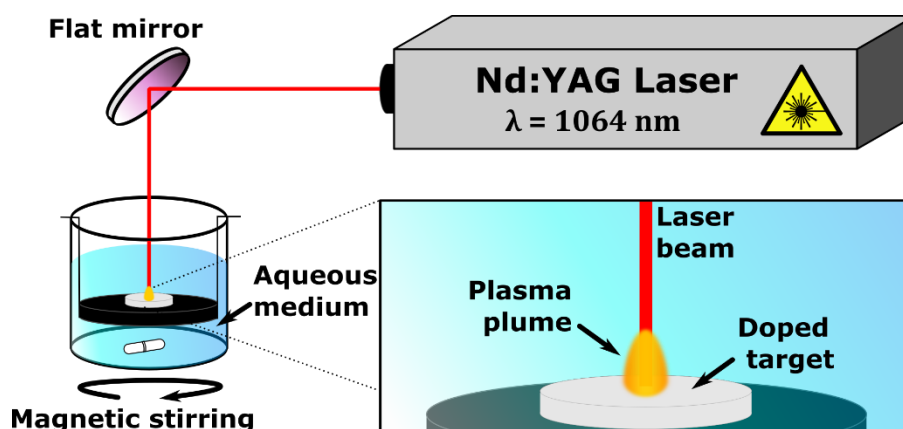
Figure 7.4 Schematic representation of the experimental setup used in PLAL to produce NPs.

The ceramic targets used in the ablation were prepared through the uniaxial pressing and densification of precursor powders. In a first study, the effect of several ablation parameters in the characteristics of the produced NPs were analysed through the ablation of undoped zirconia ceramic targets. In this case, the precursors were commercial zirconia powders (with > 99 % purity), which were uniaxial pressed into pellets with a diameter of ~13 mm and densified at 1000 ^{0}C for 72 hours. In the case of doped targets, the precursors were the powders produced by SCS, by making use of the simple incorporation and homogeneous

distribution of the dopant in the powders produced by this process. The powders were also pressed into pellets with a diameter of ~13 mm and were further densified at 1350 ^{0}C for 72 hours. Table 7.2 presents a summary of the samples produced by PLAL studied in this work. Special importance was dedicated to the production of NPs doped with Ln ions that can exhibit intense long lived downshifted luminescence or intense upconversion luminescence (see Chapter 8) due to the high potential of such NPs as bioprobes.

Table 7.2. Samples produced by PLAL and ablation parameters.

Sample name	Dopant (at.%)	Target Composition	PLAL parameters			
			Fluence (J/cm^2)	Pulse freq.(Hz)	L$_{solvent}$ (mm)	Irradiation time (min)
ZrO$_2$ NPs1	undoped	Ceramic pellets: ZrO$_2$ -SSR	15	10	20	15
ZrO$_2$ NPs2			10	10	20	15
ZrO$_2$ NPs3			5	10	20	15
ZrO$_2$ NPs3			1.8	10	20	15
ZrO$_2$ NPs4			5	5	15	15
ZrO$_2$ NPs5			5	2.5	15	15
ZrO$_2$ NPs6			5	10	15	15
ZrO$_2$ NPs7			5	10	10	15
ZrO$_2$ NPs8			5	10	25	15
t'-YSZ:3Eu NPs	3at.% Eu	Ceramic pellets: (SCS –t'-YSZ:3Eu)	1.8	10	15	30
t'-YSZ:3Eu NPs	3at.%	Single crystal: t'-YSZ:3Eu-40mm/h	1.8	10	15	60
t'-YSZ:1Tb NPs	1 at.% Tb	SCS –ZrO$_2$:Tb	1.8	10	15	30
ZrO$_2$:1Er NPs	1 at.% Er	SCS –ZrO$_2$:1Er	1.8	10	15	30
ZrO$_2$:2Er NPs	2 at.% Er	SCS –ZrO$_2$:2Er	1.8	10	15	30
ZrO$_2$:5Er NPs	5 at.% Er	SCS –ZrO$_2$:5Er	1.8	10	15	30
ZrO$_2$:10Er NPs	10 at.% Er	SCS –ZrO$_2$:10Er	1.8	10	15	30
ZrO$_2$:16Er NPs	16 at.% Er	SCS –ZrO$_2$:16Er	1.8	10	15	30
tYSZ-1Er NPs	1 at.% Er	SCS-tYSZ-1Er	1.8	10	15	30
t'-YSZ-1Er1Yb NPs	1 at.% Er, 1 at.% Yb	SCS-tYSZ-1Er1Yb	1.8	10	15	30
t'-YSZ-0.3Tm NPs	0.3 at.% Tm	SCS-tYSZ-0.3Er	1.8	10	15	30
t'-YSZ-0.3Tm1Yb NPs	0.3 at.% Tm, 1 at.% Yb	SCS-tYSZ-1Er1Yb	1.8	10	15	30

7.2 Results

7.2.1 Study of ablation parameters in the generation of ZrO$_2$ NPs

The effect of different ablation parameters, including laser fluence, pulse frequency and height of water layer above the target, in the characteristics of the produced ZrO$_2$ NPs, as well as in the yield of the process, was studied. For this study, an experimental setup based

in the one shown previously in Figure 7.14 but with slight modification, was used. The setup adjustments include the use of a converging lens, which allows focusing the 7 mm spot of the laser beam on the target surface and, by this way, increasing the range of the studied laser fluence. On the other hand, in order to avoid a constant wearing of the target surface in the same region, the glass cell was placed on the top of a spinning plate in order to promote the rotation of the target during the ablation. The rotation ($\sim$40 rpm) allowed a more uniform wearing of the target and consequently a lower influence of this parameter in the laser fluence variation along the process.

The ablation was carried out in distillated water, using the nanosecond pulsed Nd: YAG laser, with 1064 nm wavelength, described above. The height of water layer above the target surface was changed between 10 and 25 mm. On the other hand, pulse frequencies in the range of 2.5 to 10 Hz were studied, while the laser fluence was varied, by adjusting the Q-switch delay, until a maximum value of 15 J/cm^2. The target was irradiated by 30 min. The morphology and size of the generated NPs were evaluated by TEM. Based on TEM images, the diameter of more than 1000 particles were manually measured for each sample in the *ImageJ* software in order to construct the histograms of particle size distribution and determine the average particle size.

The generation of ZrO_2 particles during the ablation process was identified by the progressive milky of the water with the ablation time, which revealed to be dependent on the experimental parameters, indicating their effect in the process yield. Figure 7.5 displays the TEM images and the histograms of particle size distribution of ZrO_2 NPs produced by PLAL at different laser fluences of 1.8, 5.0, 10.0 and 15.0 J/cm^2. A constant height of 20 mm of the water layer (L_{sol}) above the target and a pulse frequency of 10 Hz were kept constant in these experiments. As can be observed by the TEM images, the pulse laser ablation of the ZrO_2 ceramic target in water leads to the generation of almost spherical NPs. Within the studied laser fluence range, NPs with two main average sizes are formed, one with diameters around 100 nm and the other one with a much lower average diameter around 10 nm. The bigger NPs exist in a lower quantity comparatively to the lower sized ones. In general, a large average particles size distribution was observed for the three studied fluences and no significant differences were identified in the NPs morphology and sizes. It should be mentioned that for the highest laser fluences (10 and 15 J/cm^2) some water was evaporated during the process due to the heating of the solution. Moreover for laser fluences higher than 15 J/cm^2, and in the same experimental conditions, the generated shock wave is so strong that induces the cracking of the ceramic target and the split out of the water from the glass cell. In these conditions the process needed to be stopped.

The effect of pulse frequency in the characteristics of the produced NPs was also analysed. In this case, a 15 mm layer of water and laser fluence of 5 J/cm^2 were maintained constant while the pulse frequency was changed. Figure 7.6 shows the TEM images and the histograms of particle size distribution of ZrO_2 NPs produced at different pulse frequencies of 2.5, 5.0 and 10.0 Hz. Once again, NPs with a spherical shape are produced for the three studied pulse frequencies. The spherical shape of the produce NPs, indicates the dominance of a mechanism of nucleation and growth rather than fragmentation, in the formation of NPs. As shown in the histograms of particle size distribution, a slight decrease of average particle size, as well in the particle size distribution (expressed by the normal standard deviation) is observed with increasing laser fluence to 10 Hz.
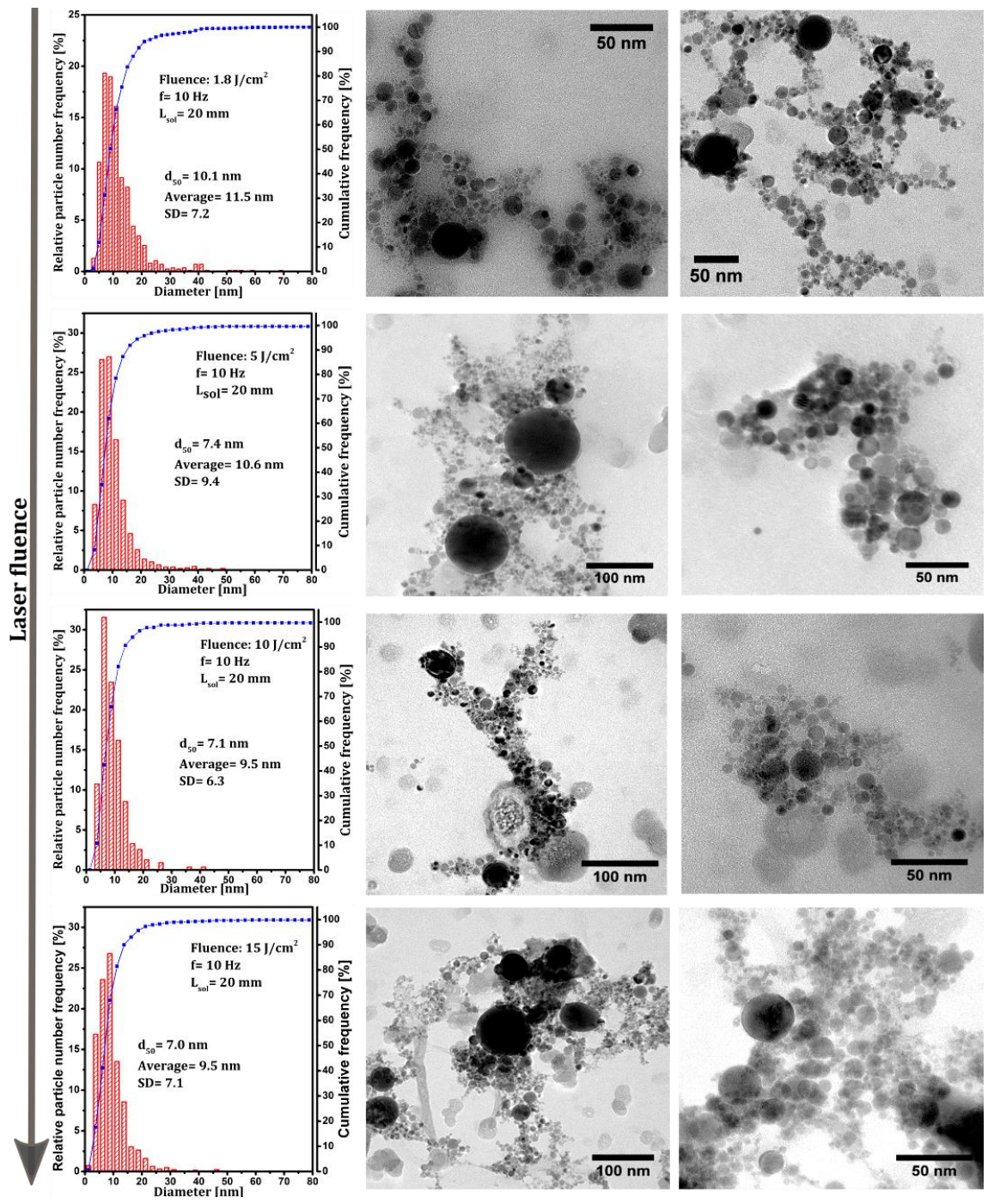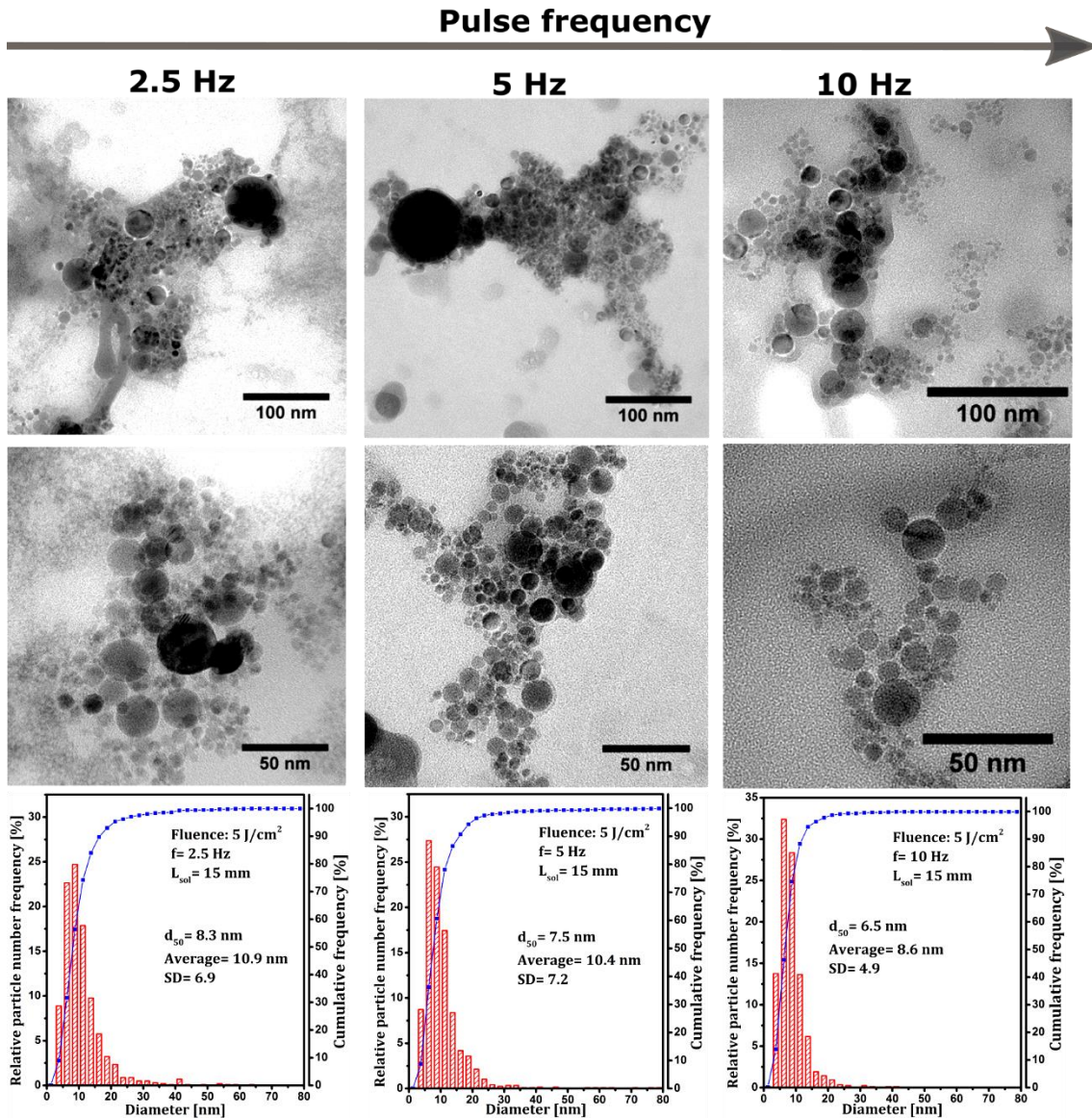
Figure 7.5 .TEM images and histograms of particle size distribution of ZrO₂ NPs produced by PLAL with increasing laser fluence (1.8, 5, 10 and 15 J/cm²) from top to bottom rows).

241

Figure 7.6. TEM images and histogram of particle size distribution of ZrO₂ NPs produced by PLAL under different pulse frequencies: 2.5 Hz (left column), 5 Hz (middle column) and 10 Hz (right column).

Figure 7.7 displays the TEM images and respective histograms of particle size distribution of the NPs produced with different height of water layer, L_{sol}, above the target surface. L_{sol} = 10, 15, 20 and 25 mm were explored. In these experiments the laser fluence and pulse frequency were maintained constant at 5 J/cm² and 10 Hz, respectively. Under the studied experimental conditions, the height of water layer revealed to be a crucial parameter that determines not only the stability and yield of the process but also the characteristics of the produced particles. For a 10 mm layer of water, in addition to the spherical small NP, bigger particles with irregular shape are observed in the TEM images, as shown in top images in Figure 7.7. These big particles are likely to result from the target fragmentation due to the high energy that reaches the surface of the target. The same effect of target fragmentation

242

for liquid layers below a certain value was previously reported by Al-Mamun *et al.* [31] for the ablation of a alumina target. In their work, the optimum value of water layer height divides the water-level domain into two regions, one dominated by fragmentation process (low L_{sol}) and the other one dominated by melting and/or vaporizing (high L_{sol}). Such results revealed that the attenuation of the power of the incident laser by the water medium is significant. For a lower layer of water, this attenuation is low and the laser power that reaches the target is higher, resulting in a significant heating of the material leading to thermal induced stress that can causes the material fragmentation. With increase in water layer height, the attenuation of the laser powder increases and the laser fluence that reaches the target surface is reduced. For the latter condition, for layer of 15, 20 and 25 mm, the produced particles have spherical shape with similar particle average size and size distributions. However, it should be mentioned that high layer of water are also disadvantageous as it reduce significantly the yield process due to the strong attenuation of the laser power. The ideal value of water layer must be higher than the ones that induce fragmentation but, on the other hand, should not be very high in order to avoid significant laser power attenuation. This value is dependent on the other process parameters, mostly on the used laser fluence. A good compromise between these parameters must be reached in order to improve particles characteristics and process yield. Within the range of the studied parameters, the best conditions for the generation of ZrO_2 NPs includes a low laser fluence of (1.8 to 5 J/cm^2), a pulse frequency of 10 Hz and a height of water layer of 15 mm.

The crystalline structure of the ZrO_2 NPs produced by PLAL, was analysed by Raman spectroscopy with a 325 nm laser line excitation. The Raman spectra of the different NPs are shown in Figure 7.8 and, for comparison the Raman spectrum of the precursor target is also displayed. For all the produced NPs, Raman bands assigned to the vibrational modes of the monoclinic zirconia were detected. In addition, a band with low intensity centred at ~263 cm^{-1}, coincident with the intense A_{1g} vibrational mode of tetragonal zirconia, is observed in the Raman spectra (identified with an asterisk). These results suggest that the NPs produced by PLAL maintain the same crystalline structure of the precursor target. However, some stabilization of high temperature tetragonal zirconia phase can be achieved in the pure zirconia as a result of size effect.
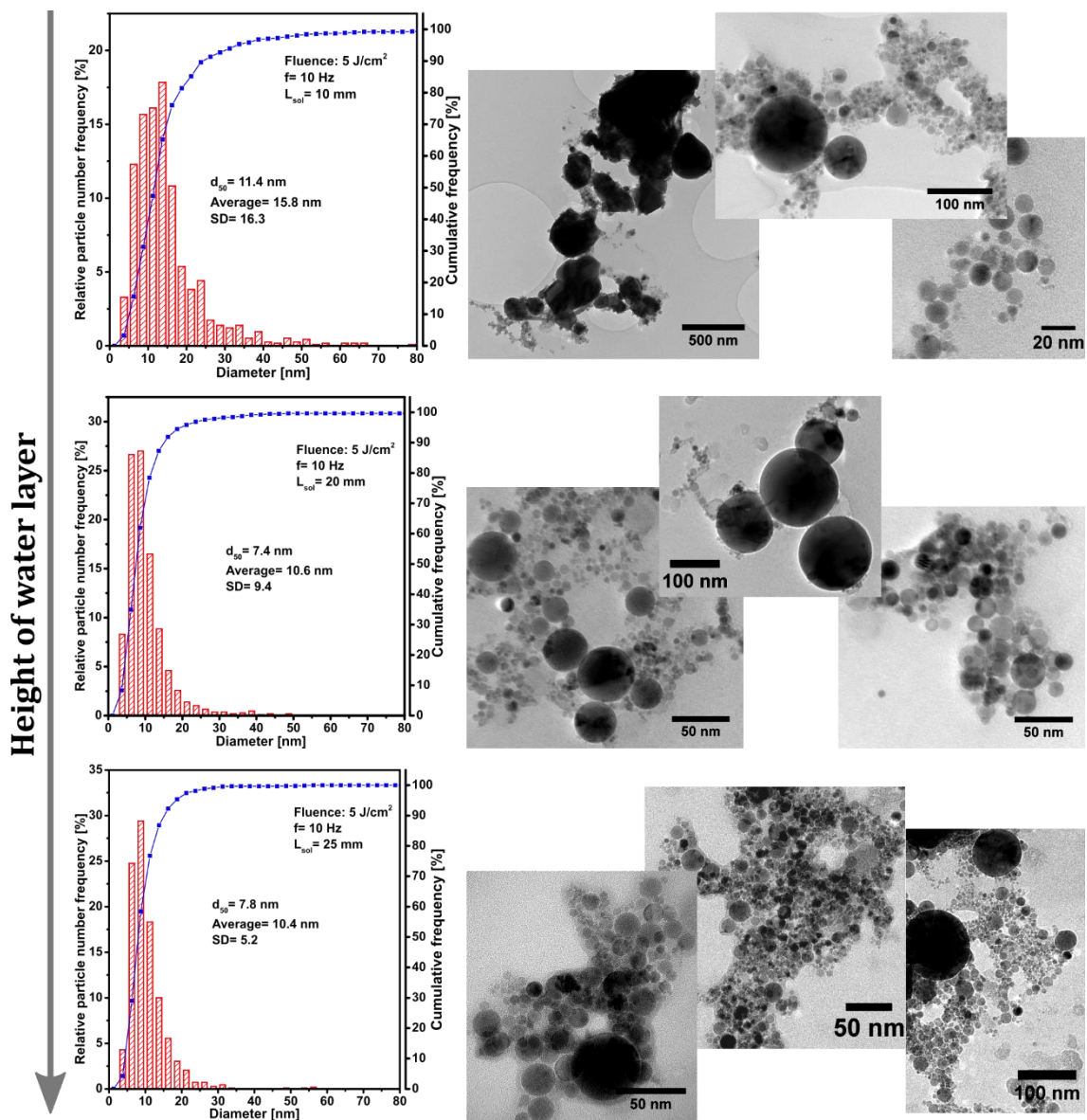
Figure 7.7. TEM images and histogram of particle size distribution of ZrO₂ NPs produced by PLAL under different height of water layer above the target: 10 mm (top), 20 mm (middle) and 25 mm (bottom).
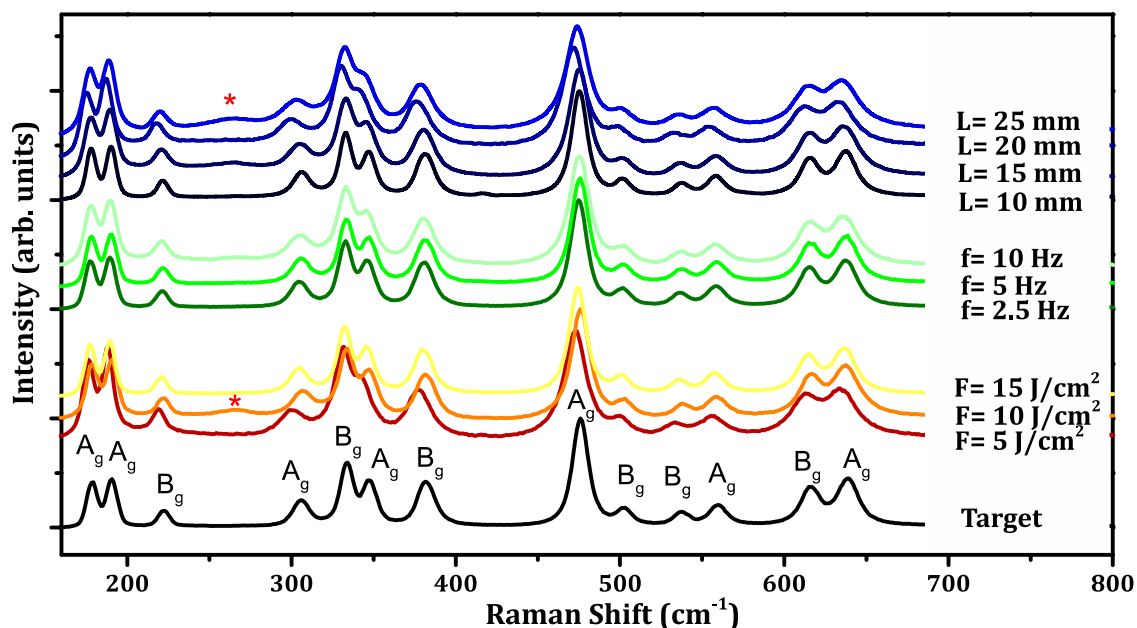
Figure 7.8. Raman spectra, performed in backscattering configuration with 325 nm excitation, of the produced ZrO$_2$ NPs by PLAL under different experimental conditions.

7.2.2 Ln-doped NPs produced by PLAL

In addition to undoped ZrO$_2$ NPs, PLAL technique was explored in the production of luminescent zirconia or YSZ NPs, doped with different trivalent Ln ions. Regarding the high potential of the luminescent NPs produced by laser ablation in water or other biocompatible solvents as luminescent bioprobes, specific Ln^{3+} ions were selected. Based on their long lived downshifted luminescence, both Eu^{3+} and Tb^{3+} ions were chosen as dopants for the NPs produced by PLAL. As referred in section 2.2.1, the long lived DS luminescence of these ions can be used, for example, *in vitro* TR-FRET assays. On the other hand, Ln ions with efficient upconversion luminescence were also selected, namely the Er^{3+} and Tm^{3+}, that can show visible and/or NIR emission under NIR excitation. As point out in Chapter 2, NIR excitation is very beneficial for *in vivo* assays. The optical properties of the produced doped NPs will be discussed in the following subsections and compared with the ones of their bulk counterparts.

7.2.2.1 Eu^{3+} doped YSZ NPs produced by PLAL

Pulsed laser ablation in liquid was used to produce NPs of tetragonal YSZ doped with europium ions in order to study their luminescence properties to explore them for further bioapplications. Both single crystals and polycrystalline pellets were used as targets in the PLAL process. While t'-YSZ (8 mol.% YO$_{1.5}$) single crystals doped with 3 at.% Eu^{3+} were grown by LFZ (section 5.2.2.1), ceramic polycrystalline pellets were prepared through the

245

pressing and densification of tetragonal YSZ (8 mol.% $YO_{1.5}$) powders doped with 3 at.% Eu^{3+} produced by SCS. As before, the SCS powders were uniaxial pressed into pellets with 13 mm diameter and were further submitted to thermal annealing treatments in air at 1350 ^{0}C for 3 days to promote densification. In order to use the single crystal fibres as targets in the PLAL process two parallel longitudinal surfaces were polished. Due to the low diameter of the crystals, which is lower than the spot size of the unfocused used laser beam, several polished crystals were placed side by side.

For the ablation, each type of the t'-YSZ:Eu^{3+} targets were placed within the glass cell, supported by the sample holder, as was described above. The ablation was performed in distilled water and a 15 mm thickness of water column above the surface of the target was maintained constant for all the experiments. As already described the ablation was performed under irradiation with the 1064 nm line of a Nd:YAG laser. The experiments were carried out under unfocused laser beam conditions, with a laser spot diameter of 7 mm and a pulse energy of 685 mJ (laser fluence of 1.8 J/cm^2) at a repetition rate of 10 Hz. For the ceramic target, the time of ablation was 30 min, while in the crystal targets was of 1 hour.

The crystalline structure and spectroscopic characteristics of the produced NPs were measured with the same experimental setups already pointed out: Raman, SEM (in scanning and transmission modes), PL, PLE, TR-PL and decay times. The luminescence features of the NPs were compared with the ones of the precursor ceramic and crystal targets.

Structural and morphological characterization

As for the undoped zirconia NPs, the formation of YSZ NPs doped with Eu^{3+} is identified by the milky of the solution after some time of laser irradiation. The yield of the process was shown to be higher by using a ceramic target rather than for the ablation of crystal targets. While for the ceramic target the solution is completely milky after 30 min of laser irradiation, for the ablation of the crystal targets, and after the same period of time, the solution is almost transparent. As identified in the pictures shown in Figure 7.9 a) and b), the amount of NPs in solution produced from the ablation of the crystal target (Figure 7.9 b), during an irradiation time of 60 min, seems to be less than the amount of NPs in solution ablated from the ceramic target by 30 min. Raman spectra of the produced NPs from the ablated ceramic and crystal targets are shown in Figure 7.9 c) and d), respectively. For comparison, the Raman spectra of the respective targets are displayed in the same figure. In both cases, the tetragonal structure of the precursor targets is preserved after ablation, as

indicated by the Raman spectra in which the vibrational frequencies related to the tetragonal crystalline phase of zirconia were identified.

Scanning and transmission microscopy images of the produced NPs are shown in Figure 7.10 a)-e). The laser ablation of the Eu^{3+} doped targets leads to the formation of NPs with a spherical shape in which two main medium average sizes, one around 100 nm and the other well below, can be well identified. Comparatively to the larger NPs, the number of NPs with lower average particle size is much higher. EDS analysis, Figure 7.10 f) and g), shows a uniform distribution of the Zr and Eu elements in the NPs ablated from the ceramic target. In contrast with what it was observed regarding the process yield, no significant differences in particle size or morphology were observed in NPs produced by the ablation of targets with different densities.
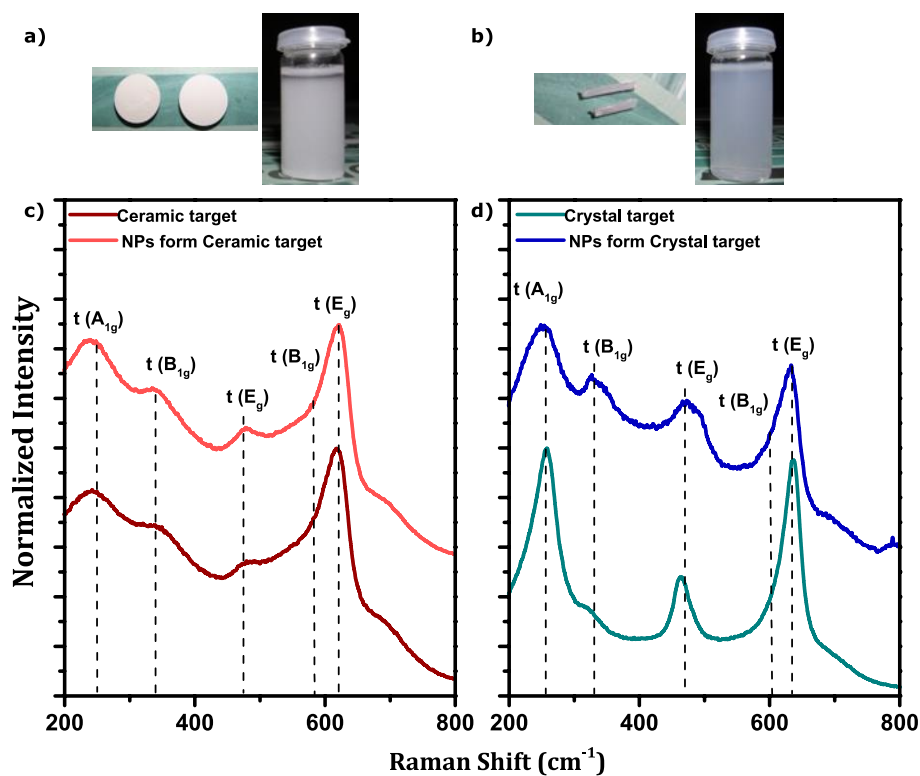

Figure 7.9. a) Pictures of the ceramic (a) and crystal (b) targets used in the ablation and respective produced NPs solution after 30 min and 60 min laser irradiation, respectively. Raman spectra of the ceramic target and the respective NPs (c) and crystals target and respective NPs (d), performed in a backscattering configuration with 325 nm excitation.
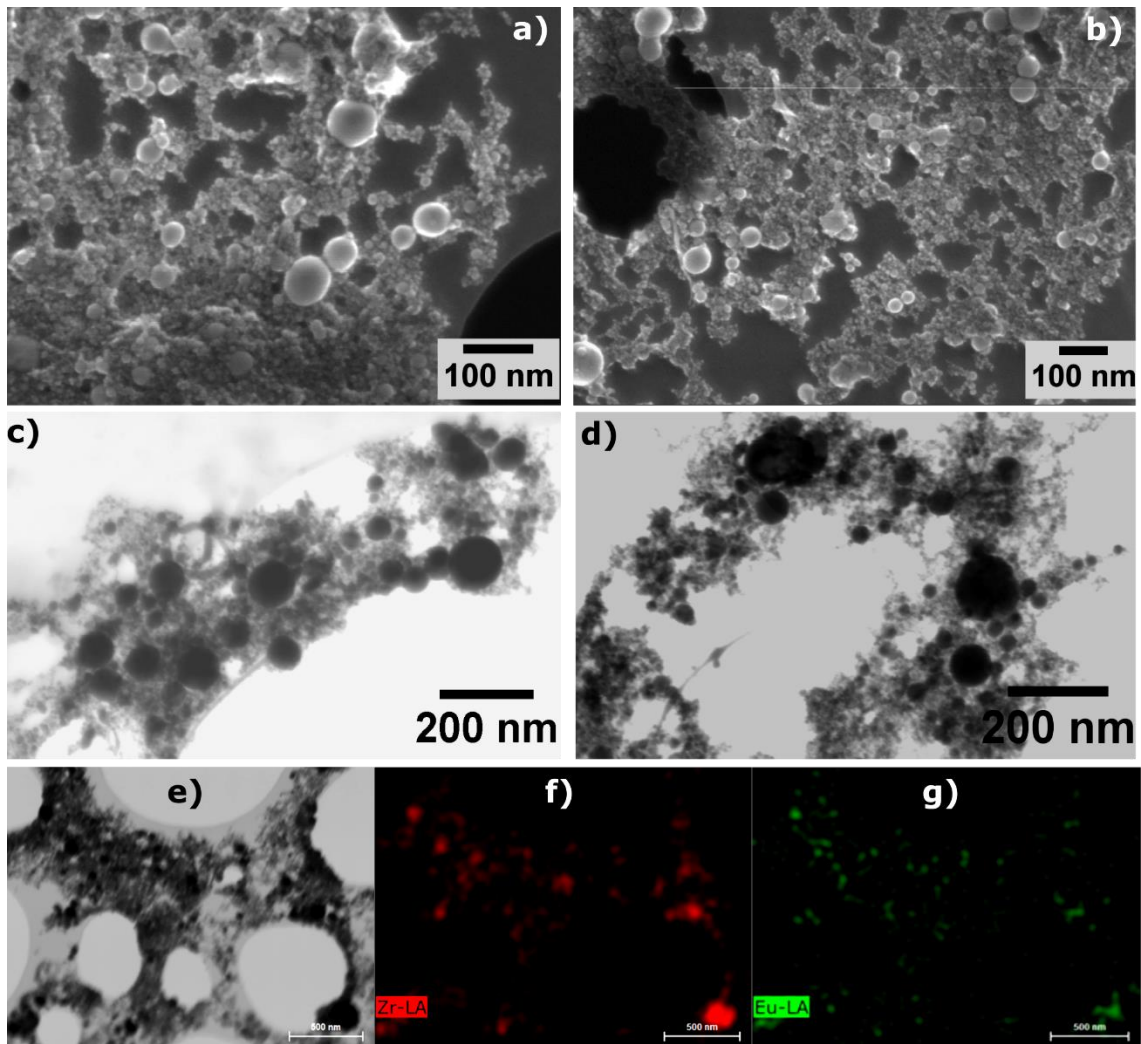
Figure 7.10. SEM and TEM images of the YSZ:Eu³⁺ NPs ablated form the ceramic target (a, c) and from the crystal targets (b,d). Zr and Eu elemental distribution maps for the NPs produced from the ceramic target.

Luminescence characterization

Figure 7.11 a) shows the RT PL spectra of the YSZ:Eu^{3+} NPs produced from both ceramic and crystal targets. For comparison, the PL spectra of the respective targets are also shown in the same figure. As observed in the tetragonal Eu^{3+} doped targets, the NPs produced by PLAL show an intense orange/red luminescence at RT under UV excitation, as seen in Figure 7.11 b) where the photos of ceramic and crystals targets and of the Eu^{3+} doped YSZ NPs after dried on the top of a quartz substrate are displayed. The visible emission spectra consist in a set of emission bands assigned to $^5D_0{\rightarrow}^7F_{J(0-5)}$ intraionic transition of Eu^{3+}, with the dominant emission occurring at $\sim$606 nm due to the $^5D_0{\rightarrow}^7F_2$ electronic transition. The peak position and shape of the emission bands are similar to the ones observed in the PL spectra of Eu^{3+} in the tetragonal YSZ crystals, discussed in section 5.2.2.1, and used as targets in this study. As one can see in the PLE spectrum, also displayed in Figure 7.11 a)

248

(green line), monitored in the emission band at 606 nm of the NPs ablated from the ceramic target, besides the resonant excitation into several excited energy states of the Eu^{3+} ion (including $^5D_4$, $^5G_{2-4}$, $^5L_5$, $^5D_3$ and $^5D_2$) the ion luminescence is preferentially stimulated by excitation in the high energy excitation CT excitation band. Comparatively to the CT band observed in the tetragonal YSZ crystals doped with Eu^{3+}, the one observed in the PLE spectrum of the NPs is shifted to lower energies and the ratio of the intensities between the CT bands and the absorption bands of the Eu ion is much higher. As observed in the Eu^{3+} doped crystals, also in the case of the PLAL NPs, more than one Eu^{3+} optical active centre can be identified by the analysis of the PL spectra acquired with different excitation conditions. Comparing the RT emission of the NPs and correspondent targets, an enhancement of the emission from the additional Eu^{3+} optical centre, identified before in the tetragonal crystals (peaked at ~614 nm), is promoted in the NPs.

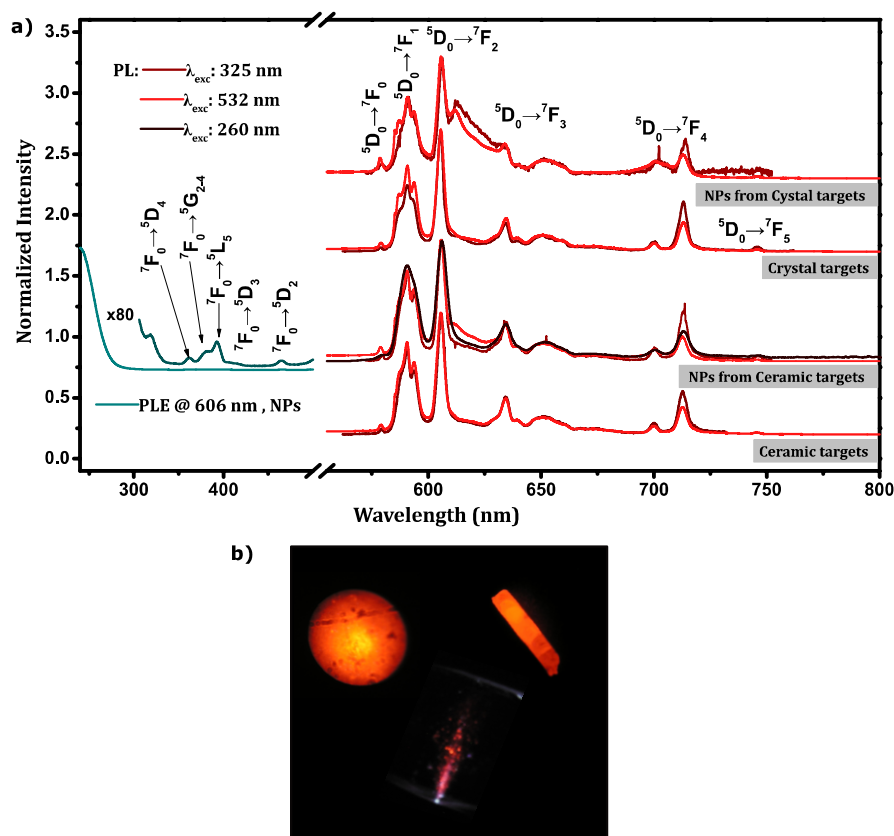**Figure 7.11. a) RT PLE spectra monitored in the $^5D_0{\rightarrow}^7F_2$ emission of Eu^{3+} in the YSZ NPs produced from the ceramic target and RT PL spectra obtained with different wavelength excitations. b) Photos of the RT luminescence observed for the single crystal and ceramic targets and of the PLAL NPs after dried in a sapphire subtract, under excitation with a 325 nm laser line.**

The kinetic of Eu^{3+} luminescence in the PLAL NPs was further studied by TR-PL spectroscopy. Figure 7.12 a) displays the RT TR-PL spectra of the YSZ:Eu^{3+} NPs produced by the ablation of the ceramic target, with 266 nm pulsed excitation. A similar decrease of luminescence intensity with time after pulse is observed for all the emission bands, as can be observed in the inset of the figure, where the normalized PL spectra for a t= 0 and 6 ms are compared. In addition, luminescence time-decay curves of the emitting $^5D_0$ excited state were measured in the PLAL NPs under excitation in the CT band (260 nm). Figure 7.12 b) displays the obtained decay-curve. The curve can be well fitted into a single exponential decay with a luminescence lifetime around 2.5 ms as determined through the fit of the exponential depopulation decay according with *Eq*. 4.17. Comparatively to the reference singe crystal, the emission lifetime of Eu^{3+} is not affected by the size reduction. Regarding the potential applications of these doped NPs as bioprobes, their long lived luminescence is advantageous. In addition, the intensity of the luminescent bioprobes should not decrease when NPs are added into an aqueous medium. As seen in the photo displayed in Figure 7.12 c), the YSZ:Eu^{3+} NPs colloids produced by PLAL show an intense luminescence at RT when pumped in the UV.
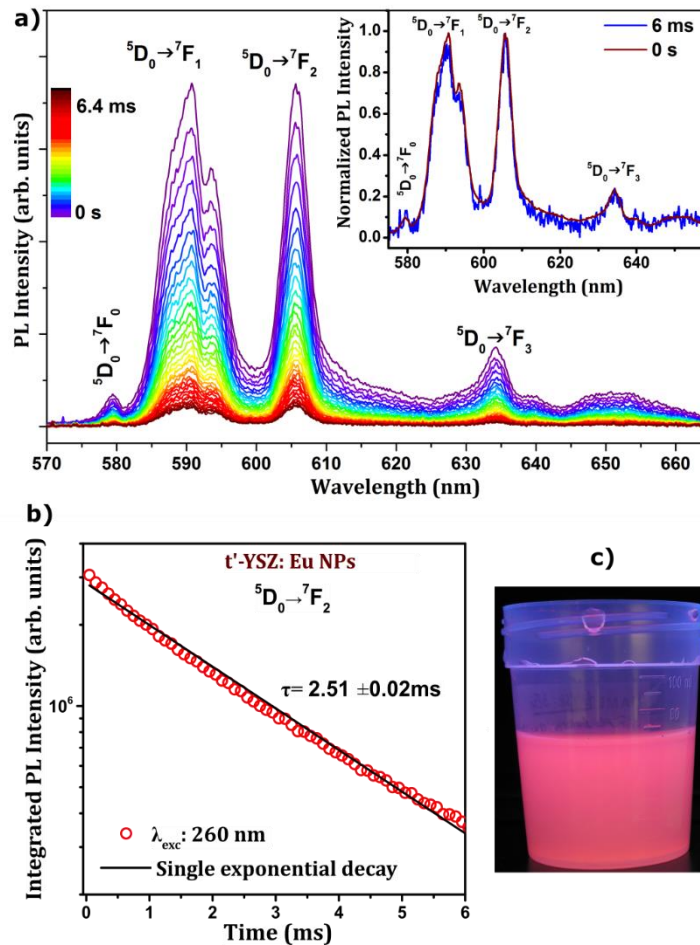
Figure 7.12. a) RT TR-PL spectra, acquired between 0 and 6.4 ms after 266 nm pulsed laser excitation, of the NPs ablated from the ceramic target. The emission spectra were not corrected to the detector and optics. Inset shows the comparison between normalized spectra acquired at 0 and 6 ms after pulse. b) RT luminescence decay curve with 260 nm excitation. c) Photo of the solution of YSZ:Eu^{3+} NPs under 254 nm lamp irradiation.

PL spectra of the YSZ:Eu^{3+} NPs produced through the ablation of the ceramic target, were also studied between 14 K and RT, with excitation in the CT absorption band (325 nm), in order to identify the ion internal emission efficiency. The temperature dependent PL spectra are displayed in Figure 7.13 a). Under the used excitation conditions, the emission at ~614 nm, associated to an additional Eu^{3+} optical active centre, is clearly observed at 14 K. Comparatively to the other emission bands, this emission undergoes a stronger quenching in its intensity and is totally extinguished at RT. These results constitute an additional confirmation of the presence of different Eu^{3+} related optical active centres in the produced samples. In general, the overall visible luminescence from the $^5D_0$ Eu^{3+} excited state is maintained almost constant until up to 175 K, with further luminescence quenching until the RT, as can be observed in Figure 7.13 b) where the temperature dependence of the overall $^5D_0 \rightarrow {}^7F_J$ emission of PLAL NPs is shown. More than 75 % of the 14 K emission

251

intensity is still detected at RT. Comparatively to the other Eu^{3+} doped samples studied in this work, including the tetragonal YSZ crystals grown by LFZ and ZrO$_2$ nanopowders produced by SCS, the stability of the Eu^{3+} luminesce is significantly improved in the NPs produced by PLAL. The temperature dependence of the overall $^5D_0 \rightarrow ^7F_J$ emission of Eu^{3+} doped YSZ crystal and SCS nanopowders is also shown in Figure 7.13 b) for comparison. In these two samples only around 40 % of the low temperature luminescence intensity was detected at RT.
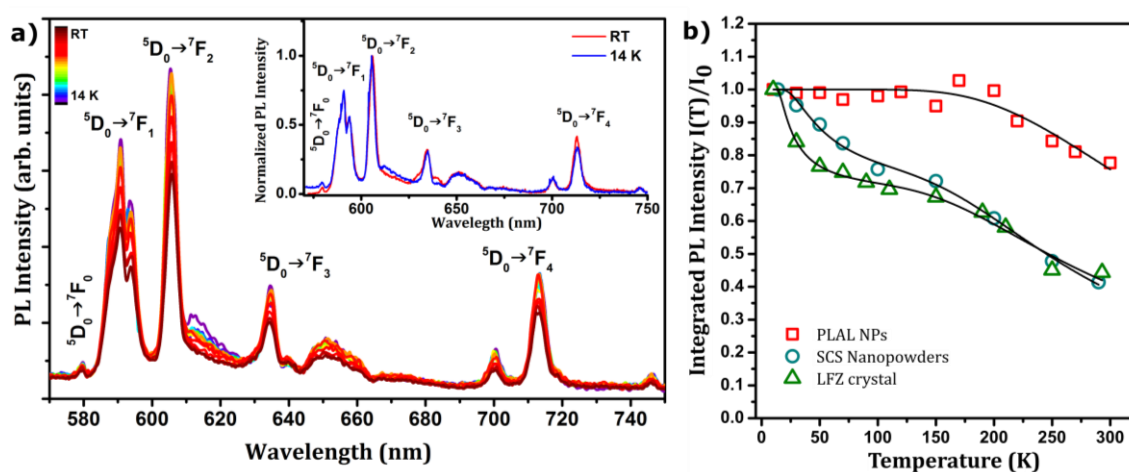

Figure 7.13. a) Temperature dependent PL spectra of the Eu^{3+} doped NPs produced from the ceramic target, with 325 nm laser line excitation. The inset shows a comparison between RT and 14 K normalized spectra. b) Temperature dependence of the overall $^5D_0 \rightarrow ^7F_J$ emission for the doped PLAL NPs, SCS nanopowders and LFZ crystal.

Summary

Eu^{3+} doped tetragonal YSZ NPs were successfully produced through the ablation of doped ceramic and crystal targets. The produced NPs have a spherical shape and a large size distribution, with two main average particle sizes, one around 100 nm and the other around one order of magnitude lower. No differences in the average particle size and size distribution or even in the morphology were observed in the particles produced from the two types of targets with different densities. The Eu^{3+} was easily incorporated and optically activated in the YSZ NPs during the ablation. The spectroscopic features of the doped NPs are similar to the ones of Eu^{3+} in the tetragonal YSZ reference crystals, indicating the presence of the same Eu^{3+} related optical centres in the two types of samples. The produced NPs show an intense long lived orange/red emission at RT also recognizable in the colloidal solutions. An higher intraionic luminescence stability was found to occur for the PLAL produced NPs. Such results are very promising for bioapplications.

As previously pointed out, Tb^{3+} ions, with a long lived emission are also interesting luminescence activators in bioprobes. The PLAL technique was used to produce NPs of YSZ doped with Tb^{3+} in order to study their luminescent properties. Polycrystalline YSZ:Tb^{3+} pellets were used as targets in the PLAL process. These targets were prepared through the pressing and densification of tetragonal YSZ (8 mol.% $YO_{1.5}$) powders doped with 1 at.% Tb^{3+} produced by SCS at 1350 ^{0}C during 3 days in air, to promote densification. The ablation was performed in distilled water (L_{sol}= 15 mm) and under the same laser irradiation conditions described above for the Eu^{3+} case.

The crystalline structure, morphology and spectroscopic characteristics of the Tb^{3+} doped NPs were analysed by Raman spectroscopy, TEM, PL, PLE TR-PL and lifetimes. The luminescence features of the NPs were compared with the ones of the precursor ceramic and reference crystals grown by LFZ.

Structural and morphological characterization

The Raman spectrum of the PLAL produced Tb^{3+} doped YSZ NPs is shown in Figure 7.14 a). For comparison, the Raman spectrum of the precursor target is also shown in the same figure. In accordance with the results of the other NPs produced by PLAL, the tetragonal structure of the polycrystalline target is preserved in the generated NPs, as indicated by the observed Raman bands assigned to the vibrational modes of the tetragonal zirconia. However, a broadening of the low energy emission bands together with a slight shift of the high energy band to lower energy indicate an additional distortion of the tetragonal cell, as was also observed in other samples produced by SCS.

Figure 7.14 b) shows the histogram of particle size distribution, constructed based on the diameters of more than 1000 particles, manually measured in the *ImageJ* software, using TEM images as the ones depicted in Figure 7.14 c). The spherical produced particles, with an average size of 9.6 nm, were found to be crystalline, as evidenced in the HR-TEM images displayed in Figure 7.14 c), where well-defined inter-planar distances can be observed.
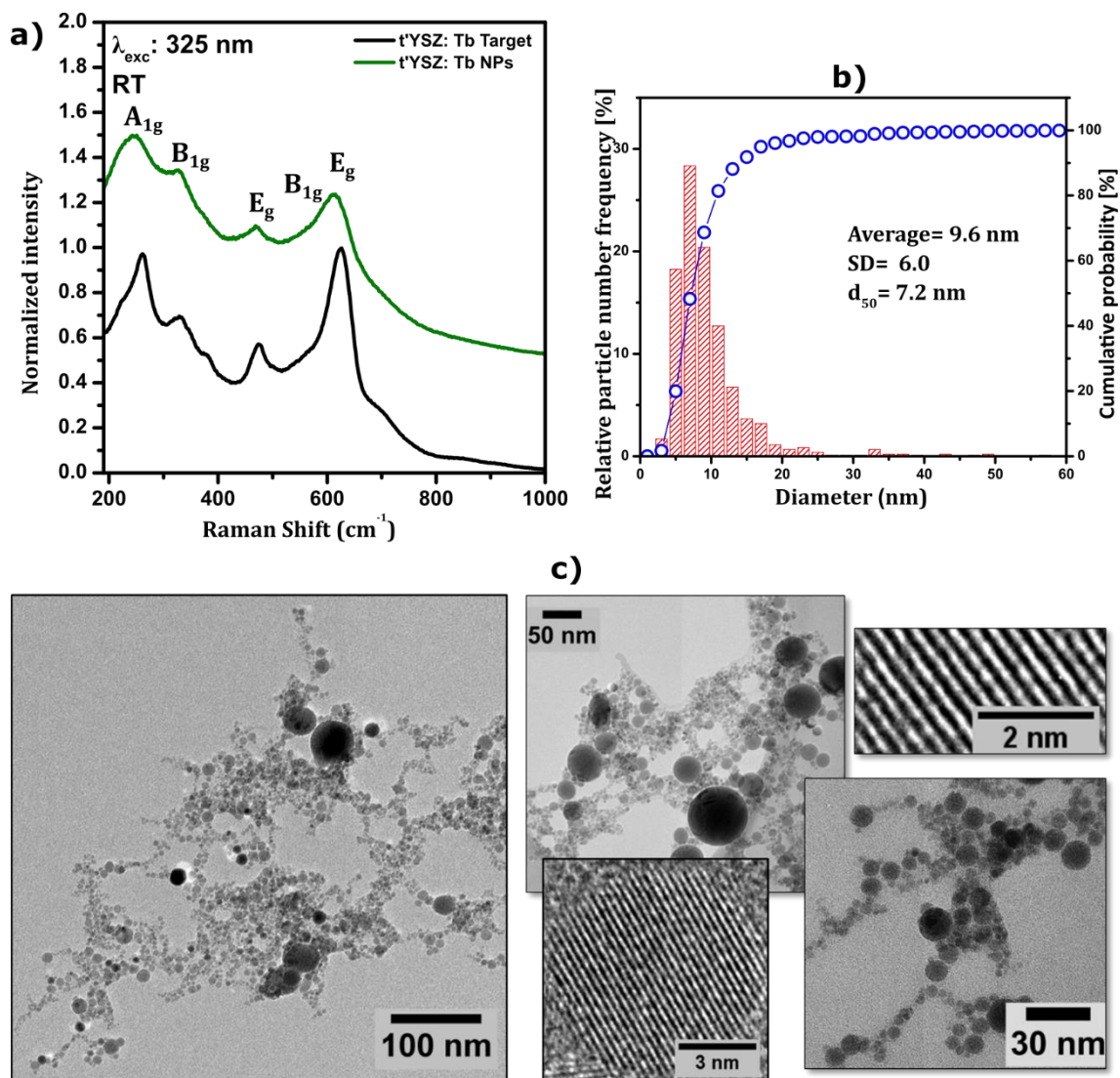
Figure 7.14. a) Raman spectra performed in backscattering geometry with 325 nm excitation of the Tb[3+] doped NPs and respective target. b) Histogram of particle size distribution. c) TEM images of the produced NPs.

Luminescence characterization

The RT PL and PLE spectra of the tetragonal YSZ NPs doped with 1 at.% Tb[3+] are shown in Figure 7.15 a). The RT PL and PLE spectra of the precursor target are also shown in the same figure for comparison. The RT luminescence of Tb[3+] incorporated in the YSZ NPs under 277 nm wavelength excitation clearly evidences the fingerprint transitions between the $^5D_4$ and $^7F_{J(6-2)}$ multiplets of Tb[3+] ions, with a dominant emission peaked at 544 nm, assigned to the $^5D_4 \rightarrow {}^7F_5$ intraconfigurational transition. The spectral position, number of Stark splitted components and shape of the emission band are similar to the ones previously studied in the tetragonal YSZ crystals doped with Tb[3+] (section 5.2.2.2) and to the PL spectrum of the tetragonal YSZ precursor target. Such results indicate that the same Tb[3+] related optical

active centres are responsible for the RT Tb^{3+} emission in the three types of tetragonal samples. PLE spectra of the precursor targets and NPs monitored in the most intense emission, peaked at 544 nm, show that the $^5D_4$ level can be populated resonantly via this state or by the higher excited states of the intra-$4f^8$ configuration as labelled in the Figure 7.15 a). As previously discussed for the LFZ grown $YSZ:Tb^{3+}$ crystals, the emitting level is preferential populated via excitation in a high energy broad band, likely to be due to the spin allowed interconfigurational $4f^8 \rightarrow 4f^7 5d^1$ transition of the Tb^{3+} ions or other CT mechanism. As observed in the europium doped NPs, a shift of the broad excitation band to higher energies is observed in the Tb^{3+} doped NPs and precursor target (277 nm), relatively to the position of the band in the Tb^{3+} doped YSZ crystal ($\sim$300 nm). Tb^{3+} doped NPs dispersed in water shows an intense green emission at RT under UV excitation, as seen in the photo displayed in Figure 7.15 b).
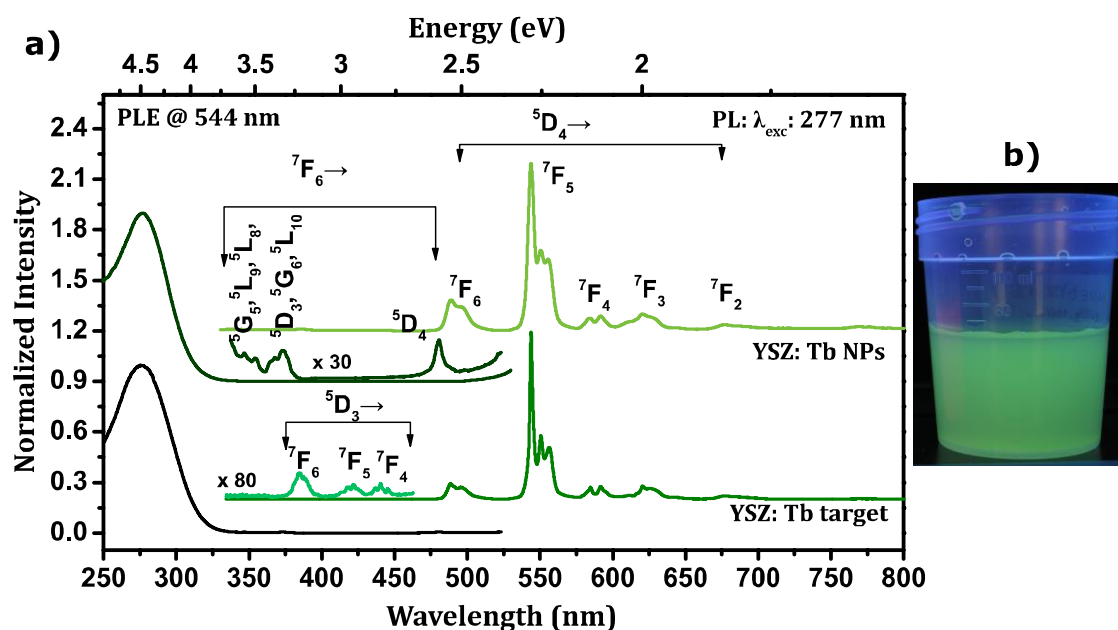
Figure 7.15. a) RT PLE spectra, monitored in the $^5D_4 \rightarrow ^7F_5$ emission of Tb^{3+} and RT PL spectra under 277 nm excitation of the Tb^{3+} doped YSZ produced NPs and target. b) Photo of the colloidal NPs solution under a UV (254 nm) lamp irradiation.

PL spectra acquired between 14 K and RT, under 325 nm wavelength excitation, are shown in Figure 7.16 a). A decrease in the ions emission intensity is observed between the low and high temperature. The integrated intensity of the overall $^5D_4 \rightarrow ^7F_J$ transitions as a function of temperature is displayed in inset of this figure. As identified, only around 50% of the emission intensity observed at 14 K is detected at RT. Comparatively to the emission of the tetragonal $YSZ:Tb^{3+}$ crystal, in which around 40% of the low temperature emission intensity was detected at RT, a slight increase on the emission stability with temperature was

achieved in the doped NPs. The data could not be fitted considering the classical model of nonradiative deexcitation expressed in *Eq.* 4.15, indicating additional mechanisms of thermal quenching of the luminescence as seen by the fast quenching for temperatures above 200 K. In contrast with the doped YSZ:Tb^{3+} crystals, in which the presence of different Tb^{3+} optical centres were clearly confirmed by the different intensity ratios between lines from the same excited state ($^5D_4$) as well as between the unfolded Stark components of the same transition, in the doped NPs the same was not observed. In fact, the comparison between the normalized RT and 14 K spectra shown in Figure 7.16 b) reveals only a very slight variation in the intensity ratio between the different transitions.
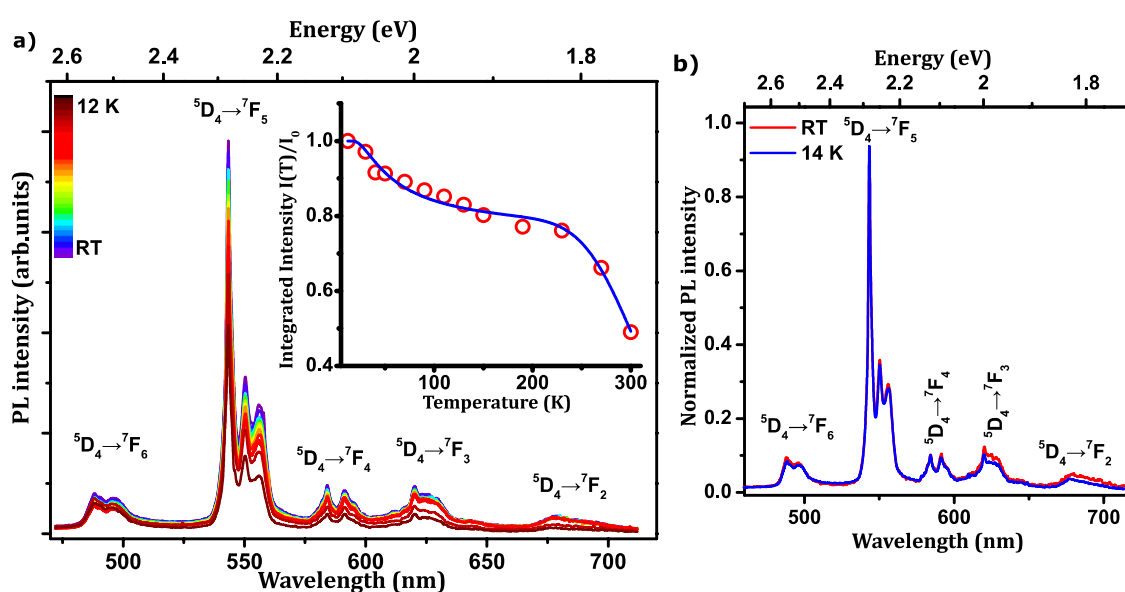
Figure 7.16. a) Temperature dependent PL spectra of the Tb^{3+} doped NPs produced by PLAL, with 325 nm laser line excitation. The inset shows the temperature dependence of the integrated intensity of overall $^5D_4{\rightarrow}^7F_J$ emission. b) Comparison between RT and 14 K normalized spectra.

Additional information about the kinetics of the Tb^{3+} emitting level was obtained by TR-PL spectra, acquired at RT under pulsed 266 nm laser line excitation (interconfigurational absorption), and time decay measurements. Figure 7.17 a) shows the RT PL spectra of the Tb^{3+} doped NPs acquired in the temporal range between 0 and 8 ms. An identical depopulation behaviour is observed for all the transitions from the $^5D_4$ emitting level. In addition, the time decay curve of the emitting $^5D_4$ level, monitored in the $^5D_4{\rightarrow}^7F_5$ emission is shown in Figure 7.17 b). The curve is well fitted to a single exponential decay with a time constant of ~2.4 ms. Comparatively to the tetragonal YSZ:Tb^{3+} single crystal (and in line with the observed for the Eu^{3+} doped NPs), the emission lifetime of Tb^{3+} is not significantly affected by the size reduction.

Figure 7.17. a) RT TR-PL spectra, acquired between 0.5 and 8 ms after 277 nm pulsed excitation. Inset shows a comparison between the normalized spectra acquired at 0.05 and 8 ms after pulse. b) Time decay curve of the emitting $^5D_4$ level, monitored in the $^5D_4 \rightarrow ^7F_5$ emission.

Summary

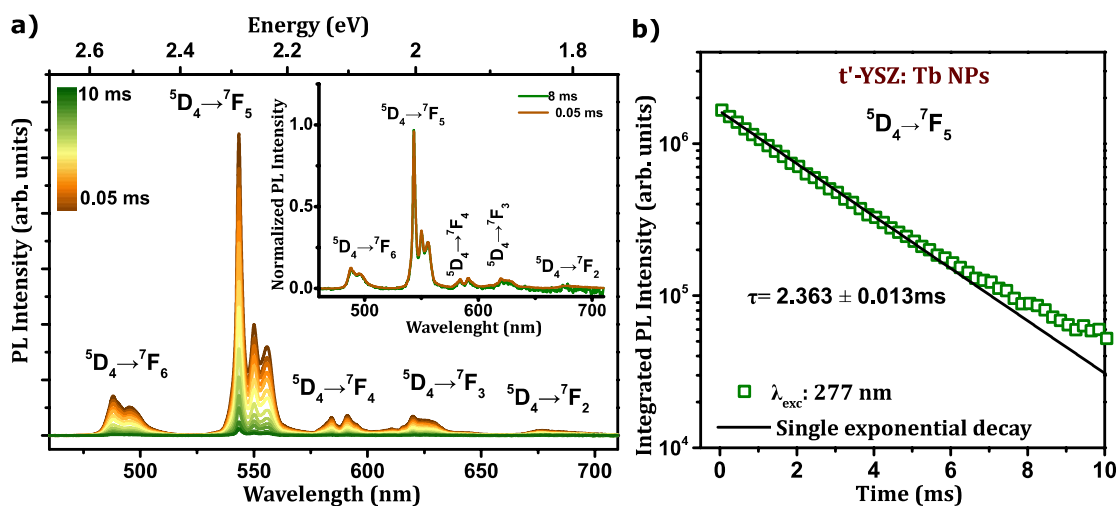Luminescent tetragonal YSZ NPs doped with Tb^3 were produced by laser ablation in water. The produced NPs have a spherical shape, with an average particle size around 10 nm and their crystallinity was evidenced by well-defined lattice planes seen in TEM. The RT PL spectra of the doped NPs, under UV light excitation, reveals the fingerprint transitions between the $^5D_4$ and $^7F_{J(6-2)}$ multiplets of Tb^{3+} ions. The dominant emission is peaked at 544 nm, assigned to the $^5D_4 \rightarrow ^7F_5$ intraconfigurational transition, and is the responsible for the intense green emitted light observed at RT under the used excitation conditions. The intense and long lived luminesce of Tb^{3+} doped NPs dispersed in water are of potential application as bioprobes.

7.2.2.3 Er^{3+} doped ZrO_2 NPs produced by PLAL: effect of erbium concentration

Zirconia NPs doped with different erbium nominal concentrations, from 1 to 16 at.% were produced by PLAL and their structural, morphological and luminescent properties were analysed. Laser ablation was performed under irradiation with the Nd: YAG laser (with 1064 nm wavelength) described before, working at a pulse frequency of 10 Hz and a pulse energy of 685 mJ focused in an area of 0.38 cm^2 (laser fluence: 1.8 J/cm^2). The height of water layer above the target was kept constant at 15 mm. The targets used in the ablation were ceramic pellets produced by uniaxial pressing and thermal densification (1350 ^0C by 3 days) of ZrO_2 powders doped with different concentration of Er^{3+}, previously produced by SCS. The ceramic targets were taken as reference samples for the measured optical properties.

For the crystalline phase identification, the targets and NPs were analysed by RT Raman spectroscopy, the samples morphology was evaluated by SEM/STEM and EDS analysis was performed in the SEM, for chemical elemental identification. The samples luminescence was assessed at RT using UV and visible light as excitation, enabling the analysis of the downshifted intraionic emission. Moreover, the identification of the preferential ion luminescence excitation pathways was assessed by RT PLE.

Structural and morphological characterization

Photos of the precursor targets used in the ablation are shown in Figure 7.18 a). The incorporation of the Er^{3+} in the lattice leads to a light pink colouration, becoming darker with increasing erbium concentration. The same colouration was also observed in the tetragonal crystals doped with Er^{3+}, grown by LFZ. Figure 7.18 b) and c) displays the Raman spectra of the ceramic targets and the PLAL produced ZrO_2 NPs doped with different nominal erbium concentrations. As expected, the number of Raman active modes decreases with the rise of dopant content due to increase of the zirconia crystal symmetry with the phase transformation from monoclinic to tetragonal and to cubic. As evidenced in the Raman spectra shown in Figure 7.18 b), the ceramic target doped with the lower Er^{3+} concentration (1 at.%) crystallized in the monoclinic phase of zirconia. Increasing erbium concentration favours the stabilization of the high temperature phases at RT. A mixture of monoclinic and tetragonal phases was found for the intermediate contents (2–5 at.% of Er^{3+}), and for nominal concentrations of 10 and 16 at.% Er^{3+} the Raman spectra evidence that zirconia doped targets crystallize in tetragonal and cubic phases, respectively. The main phases identified in the NPs perfectly matches those of the reference targets for the high dopant concentrations, where only the high temperature phases are present. In the case of lower dopant concentrations, additionally to the monoclinic phase identified in the targets, NPs crystallized in the tetragonal phase were also present. This mismatch in the crystalline phases in the targets and NPs can be explained based in the existence of additional pathways to stabilize the high temperature metastable zirconia phases in the NPs. As already discussed, these phases can be stabilized in pure zirconia by reducing the particle size below a critical value [60,61], in line with the results obtained for the pure zirconia NPs produced by PLAL. No secondary crystalline phases, such as Er_2O_3 or other Er based oxides were detected, even for the nominal high dopant concentrations, meaning that the PLAL process allows an efficient incorporation of the Er^{3+} in the zirconia lattice.
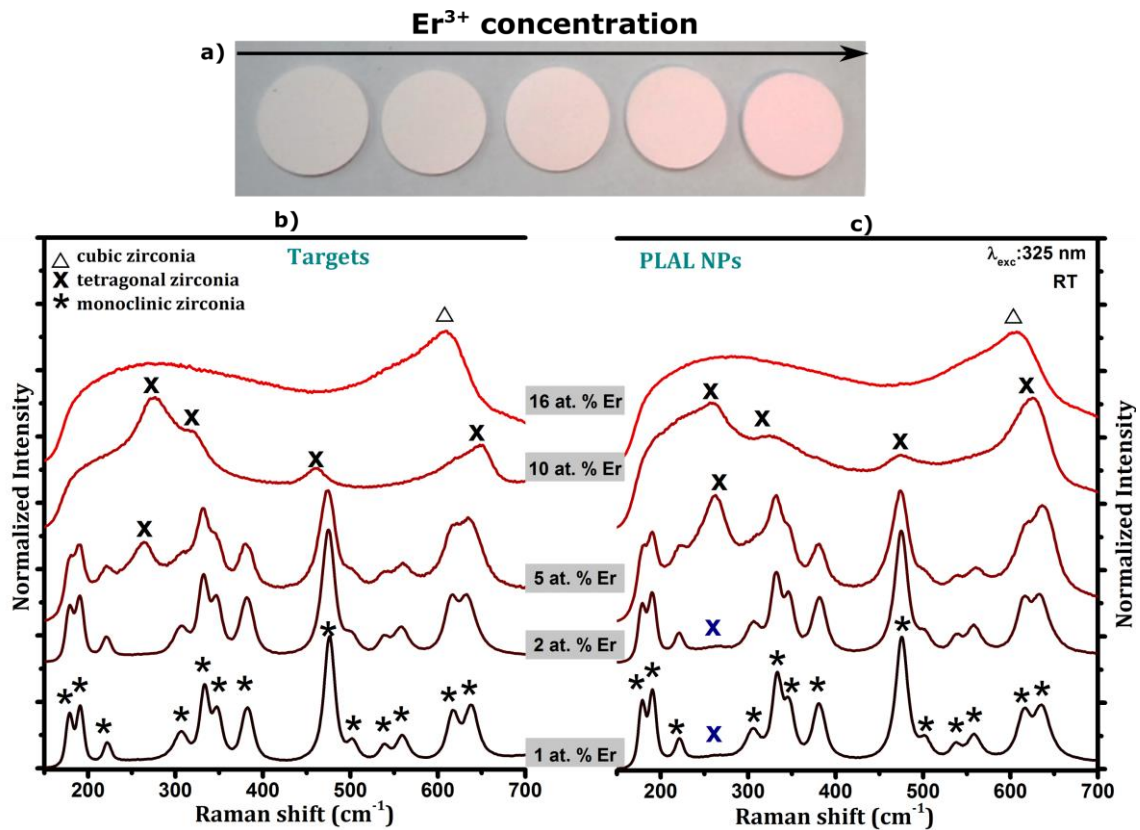
Figure 7.18. a) Photos of the zirconia targets doped with different concentration of Er ions. Raman spectra of the targets (b) and PLAL produced NPs(c) by using 325 nm wavelength excitation in backscattering geometry.

The morphology and grain size of the doped zirconia NPs are shown in Figure 7.19 a) –f). The STEM images reveal that the PLAL produced ZrO_2 NPs have spherical shape with reduced dimensions as expected for a very fast process far from equilibrium due to the narrow quenching times. However, as can be observed in the STEM images, the formed NPs have a large size distribution and a high degree of agglomeration, particularly in the smaller ones. This behaviour is a typical characteristic in NPs produced by PLAL [62,63] and is in line with what was observed in the previously studied NPs. Concerning the morphology, no differences were observed with the increase of dopant amount. The EDS analysis, shown in Figure 7.19 f) –h), reveals a uniform distribution of the erbium ions in the produced zirconia NPs, meaning that the high pressure and high temperature environment conditions created by the laser ablation in water is fast enough to preserve the erbium inside the zirconia network.
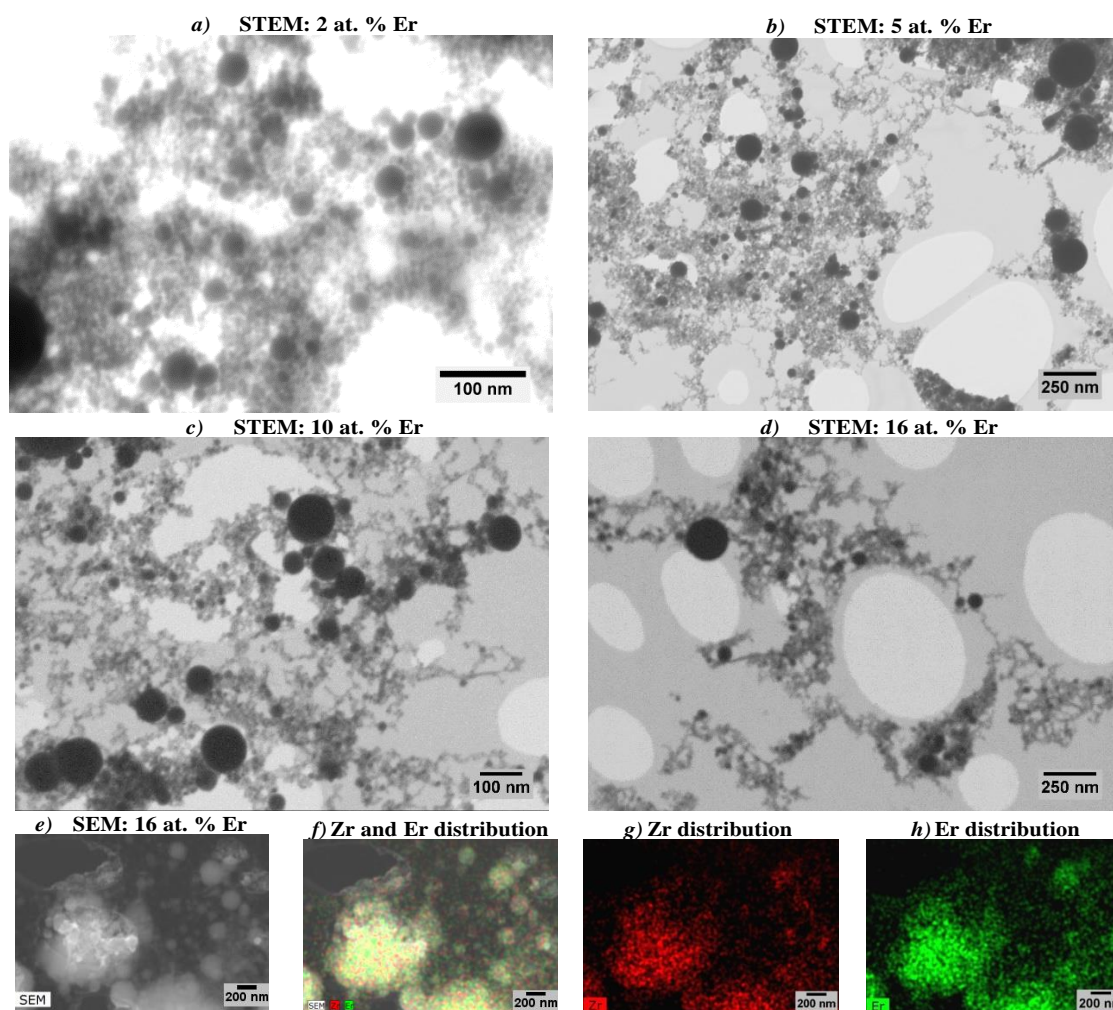
Figure 7.19. (a–e): STEM/SEM images of the NPs with different erbium dopant concentrations. (f–h) EDS map of the NPs doped with 16 mol.% Er.

Luminescence characterization

Figure 7.20 displays the PL and PLE spectra of ZrO$_2$ targets doped with different concentration of Er^{3+}. In all the doped samples, intraionic Er^{3+} emission is observed meaning that independently of the incorporated erbium amount and zirconia crystalline phase, Er^{3+} optically activation is achieved. However, significant differences are observed in the PL and PLE spectra of the samples doped with different Er^{3+} concentrations. In addition and in line with the results discussed for the Er^{3+} doped tetragonal YSZ crystal (section 5.2.2.5), substantial differences in the PL spectra were observed under different wavelength excitations.
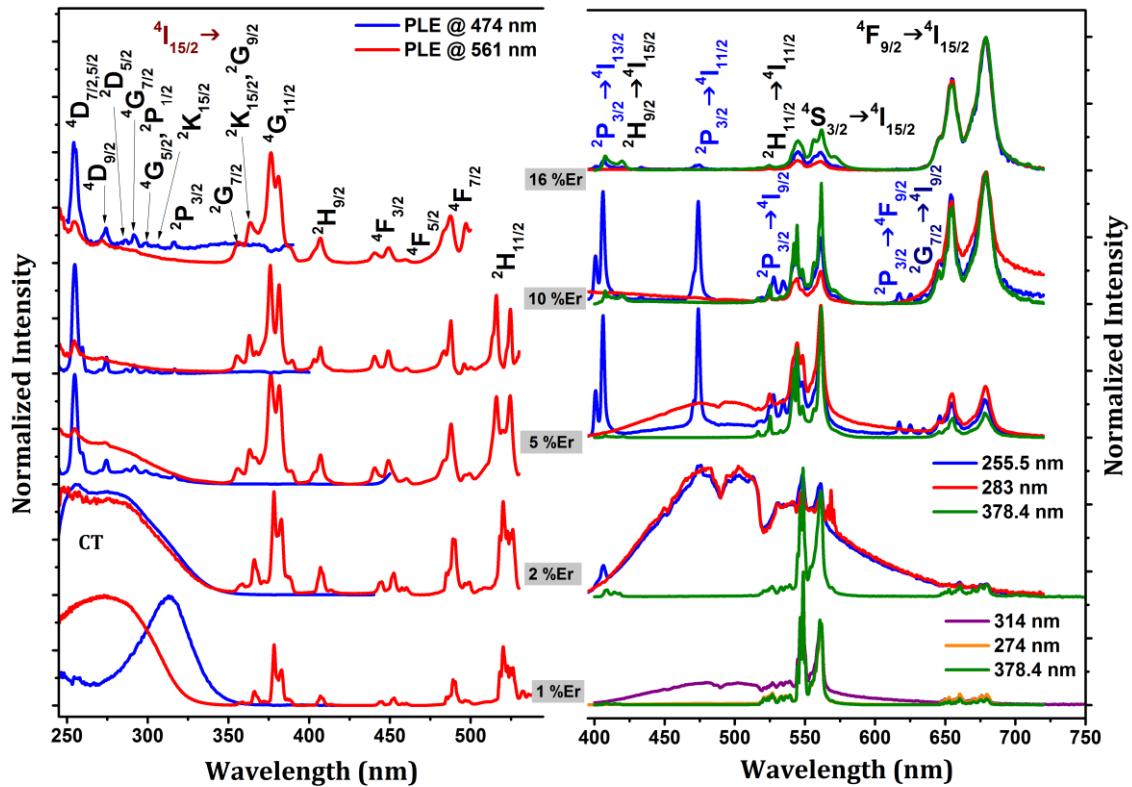
Figure 7.20. PLE (left side) and PL (right side) spectra of the erbium doped ZrO_2 targets. The PLE spectra were monitored at the green ($^4S_{3/2} \rightarrow {}^4I_{15/2}$ Er^{3+} transition) and blue (broad band at 474 nm and $^2P_{3/2} \rightarrow {}^4I_{11/2}$ Er^{3+} transition) spectral regions. The PL was recorded by pumping the samples into the CT excitation band (CT), $^4D_{7/2}$ and $^4G_{11/2}$ Er^{3+} multiplets.

In order to identify the preferential pathways for the ions luminescence, the PLE spectra were monitored in the blue and green spectral regions, in accordance with the previous results of the tetragonal YSZ crystals doped with Er^{3+}. The latter corresponds to the $^4S_{3/2} \rightarrow {}^4I_{15/2}$ transition of the Er^{3+} ions. In the case of the blue luminescence, depending on the ion content (and thus on the zirconia crystalline phase), the PLE was monitored or at the maximum of the intrinsic broad PL band (for lower erbium contents) or on the maximum of the $^2P_{3/2} \rightarrow {}^4I_{11/2}$ Er^{3+} transition (for samples with higher erbium amounts). The PLE data taken from the green $^4S_{3/2} \rightarrow {}^4I_{15/2}$ transition, with maxima at 561 nm, indicates that the population paths of the Er^{3+} luminescence occur both via a broad violet CT excitation band and under resonant excitation conditions via the Er^{3+} excited multiplets. For samples in the monoclinic phase, with lower erbium amounts, the intraionic Er^{3+} luminescence is preferentially populated via the CT band peaked between 270–280 nm. Similarly, the broad host-related PL band due to native defects is also excited by broad excitation bands with their peak position dependent on the ion content. For higher erbium concentrations, and in the studied spectral region, a general trend is observed: the decrease of the intensity of the CT excitation band results in changes in the preferential population of the Er^{3+} ion

261

luminescence. For the high lattice symmetry of the tetragonal and cubic zirconia polymorphs, the resonant excitation into the ion excited multiplets dominates the excitation pathways of the Er^{3+} luminescence, in line with the results obtained in the LFZ crystal doped with Er^{3+}. The measured PLE spectra also corroborate the increase in the band gap energy of the zirconia host with the crystalline phase transformation from monoclinic to tetragonal and cubic.

The samples luminescence obtained with excitation in the UV CT band and resonantly into the Er^{3+}, $^4G_{11/2}$ and $^4D_{7/2}$ excited multiplets, is depicted in the right side of Figure 7.20. The PL response is sensitive either to the excitation energy and erbium content. For a resonant excitation into the $^4G_{11/2}$ multiplet (378 nm) the PL spectra are only constituted by three groups of intraionic emission lines: the violet, green and red transitions arising from the $^2H_{9/2}$, $^2H_{11/2}$, $^4S_{3/2}$ and $^4F_{9/2}$ excited states to the $^4I_{15/2}$ ground state, respectively. On the other hand, with excitation into the CT band, the PL spectra of the samples doped with lower erbium content (1 and 2 at .% Er) correspond to an overlap of the broad emission band from native defects with the sharper intraionic emission lines of Er^{3+}. Additionally, intraionic photon re-absorption was identified. The intensity of the broad PL band decreases with increasing erbium concentration, as observed for samples doped with higher erbium amounts. In these samples (5, 10 and 16 at.% Er^{3+}), resonant excitation in the highest energetic Er^{3+} multiplet peaked at 255 nm ($^4D_{7/2}$) leads to additional emission bands comparatively to the ones observed under resonant excitation in the lower energy $^4G_{11/2}$ multiplet. The same behaviour was previously observed in the YSZ crystals doped with Er^{3+}, also with a tetragonal crystalline structure. These additional emission lines are due to the electronic transitions arising from the $^2P_{3/2}$ and $^4G_{7/2}$ excited multiplets and are observed in the violet ($^2P_{3/2}\rightarrow^4I_{13/2}$), blue ($^2P_{3/2}\rightarrow^4I_{11/2}$), green ($^2P_{3/2}\rightarrow^4I_{9/2}$) and red ($^2G_{7/2}\rightarrow^4I_{9/2}$; $^2P_{3/2}\rightarrow^4F_{9/2}$) spectral regions.

The downshifted luminescence intensity of the Er^{3+} incorporated in ZrO$_2$ target and NPs was found to be dependent on the ion amount and consequently on the crystalline phase nature, in line with the one observed in the SCS powders with the same compositions and crystalline phases. For lower erbium concentrations, where the monoclinic zirconia phase dominates, the radiative recombination in the visible range mainly occurs between the $^4S_{3/2}$ level and the ground state, resulting in a green visual appearance in the reference targets and NPs, as shown in PL the spectra in Figure 7.21 a) and b), respectively. The change in the crystalline phase due to higher erbium concentration is accompanied by a relative increase of the red light due to the $^4F_{9/2}\rightarrow^4I_{15/2}$ transition. Since the number of the observed Stark levels is known to be dependent on the ion site location symmetry it should be emphasized

that a reduction of the number of lines for the $^4S_{3/2} \rightarrow {}^4I_{15/2}$ and $^4F_{9/2} \rightarrow {}^4I_{15/2}$ transitions is identified consistently with the higher symmetry of the host by changing the crystal phase from monoclinic to cubic with increasing dopant amount, as can be observed Figure 7.21 c) and d). As one can see in Figure 7.21 e), the intensity ratio between the red and green emission strongly increases with Er^{3+} dopant concentration from 1 to 16 at.%, which results in a tuning of the downshifted emission colour from green to red.
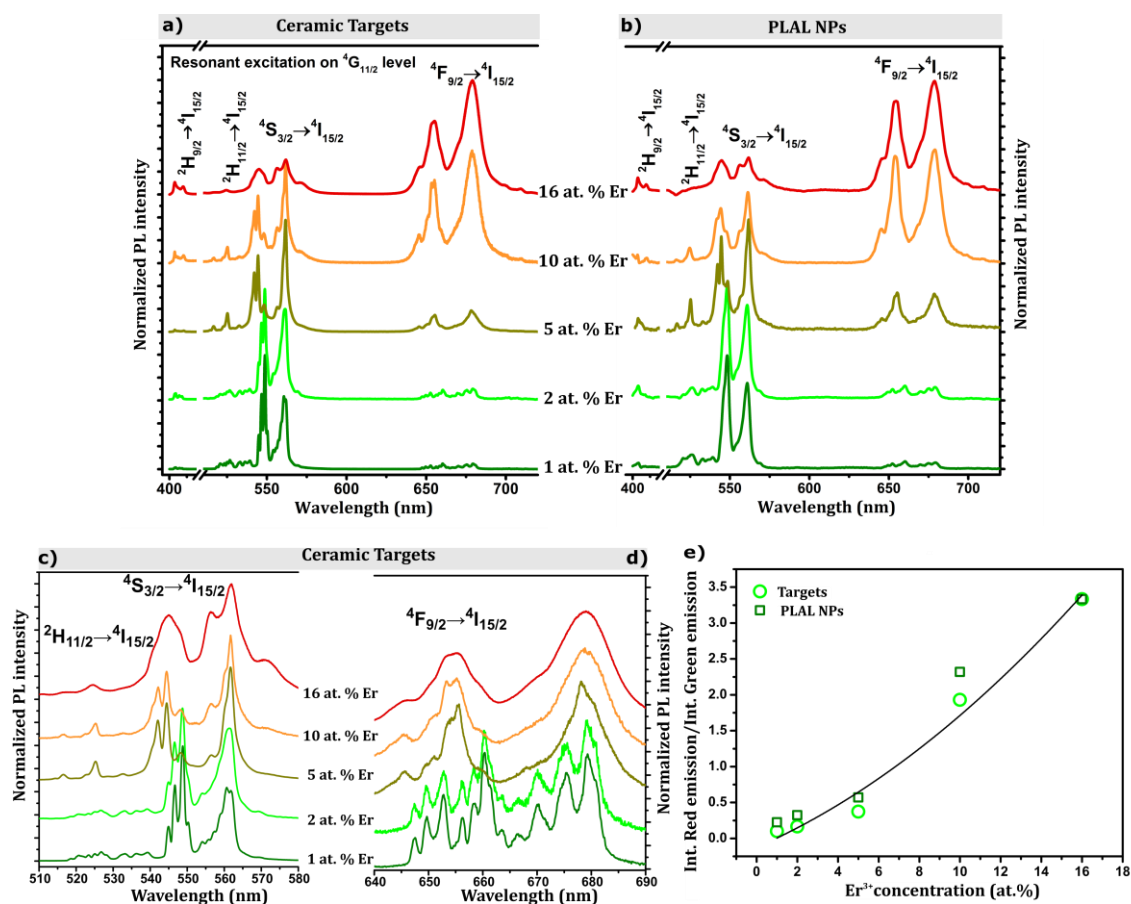
Figure 7.21. PL spectra of the targets (a) and PLAL produced NPs (b) obtained with resonant excitation into the $^4G_{11/2}$ level. Closer view of the Stark splitting of the green (c) and red (d) emission of the Er^{3+} doped targets. e) Ratio between the integrated red and green emission intensities of targets and NPs with increase in Er^{3+} concentration.

A likely explanation to the increase of the intensity ratio between the red and green emission is related with the promotion of ion–ion interactions favoured for higher dopant concentrations, potentiating energy transfer processes among the interacting defects [64–69]. Particularly, nonradiative energy transfer processes, such as resonant phonon assisted transfer and cross-relaxation mechanisms among the nearby ions are commonly observed in lanthanide doped wide band gap hosts leading, in some cases, to self-luminescence quenching when the interaction occurs among ions from the same chemical specie [64,66–69].

For instance, the depletion of $^2H_{11/2}$,$^4S_{3/2}$ states to the $^4F_{9/2}$ level by multiphonon deexcitation and cross-relaxation processes such those involving the population of the $^4I_{13/2}$ and $^4I_{11/2}$ long lived intermediate levels which in turn repopulates the $^4F_{9/2}$ by energy transfer encompassing ground state absorption (GSA) from a near neighbouring ion, justifies the decrease in the intensity of the green light [64,66–69].

Summary

Luminescent zirconia NPs doped with erbium ions, with tuneable downshifted emission colour (from green to red), depending on dopant concentration, were produced in water by PLAL. Different polymorphs (monoclinic to tetragonal to cubic crystalline phases) of ZrO_2 were promoted increasing the amount of Er^{3+}. No other crystalline oxides were found even for high nominal erbium contents proving that a uniform incorporation of the Er^{3+} ions into the ZrO_2 lattice was achieved, as observed by elemental EDS analysis. ZrO_2:Er^{3+} NPs have a spherical shape and particle sizes up to 200 nm. No differences in NPs morphology were observed with the change in the crystalline structure of the zirconia as a result of erbium incorporation. The studies of the downshifted Er^{3+} luminescence showed that the dominant visible emission of the Er^{3+} ions in zirconia NPs occurs in the green and red regions due to transitions from the $^4S_{3/2}$ and $^4F_{9/2}$ multiplets to the $^4I_{15/2}$ ground state, respectively. The number of the Stark levels in the green transition was found to decrease with increasing erbium amount as expected for ions placed in high symmetry sites following the crystalline host phase transformation. Additionally, the green to red luminescence intensity ratio was found to be dependent of the erbium amount, accompanying the increase in the lattice symmetry. The suppression of the green transition for higher concentrations was discussed based on nonradiative competitive mechanisms such as cross-relaxation processes between near neighbouring ions as expected for higher dopant contents.

7.2.2.4 Er^{3+} doped and Er^{3+}, Yb^{3+} co-doped YSZ NPs produced by PLAL

In addition to the ZrO_2 NPs doped with different erbium concentration, 1 at.% Er doped and 1 at.% Er and 1 at.% Yb co-doped YSZ NPs were also produced PLAL in order to investigate their luminescent properties. The NPs were produced by laser ablation in water of a ceramic target, prepared by uniaxial pressing and densification (1350 ^{0}C for 3 days) from powders prepared by SCS method. The targets were irradiated with a laser fluence of 1.8 J/cm^2 and with a pulse frequency of 10 Hz. The height of water above the target was 15 mm and the liquid was continuously stirring during the ablation to allow the produced NPs to spread uniformly in the liquid medium.

As before, the spectroscopic properties of the produced NPs were compared with the properties of single crystals grown by LFZ by measuring RT Raman spectra, PL, PLE and lifetimes. The samples morphology and particles size were evaluated by TEM.

**Structural and morphological characterization**

Figure 7.22 shows the RT Raman spectra performed with 325 nm laser line excitation of the doped and co-doped NPs and respective precursor targets. The observed vibrational modes, corresponding to the tetragonal crystalline phase of the zirconia, reveal that PLAL produce NPs preserved the same crystalline structure of the precursor target and no additional crystalline phases were detected, indicating a successful incorporation of the dopant ions into the YSZ lattice.

The morphology, average particle size and size distribution of the NPs were studied by TEM. As can be observed by the TEM images in Figure 7.23 a)-f) the PLAL process leads to the formation of particles with spherical morphology. High resolution TEM images of single crystalline particles, presented in the same figure, confirm the crystallinity of the particles. No significant differences were observed in the NPs morphology for the different compositions, meaning that the NPs morphology is not affect by the type of dopant ions.
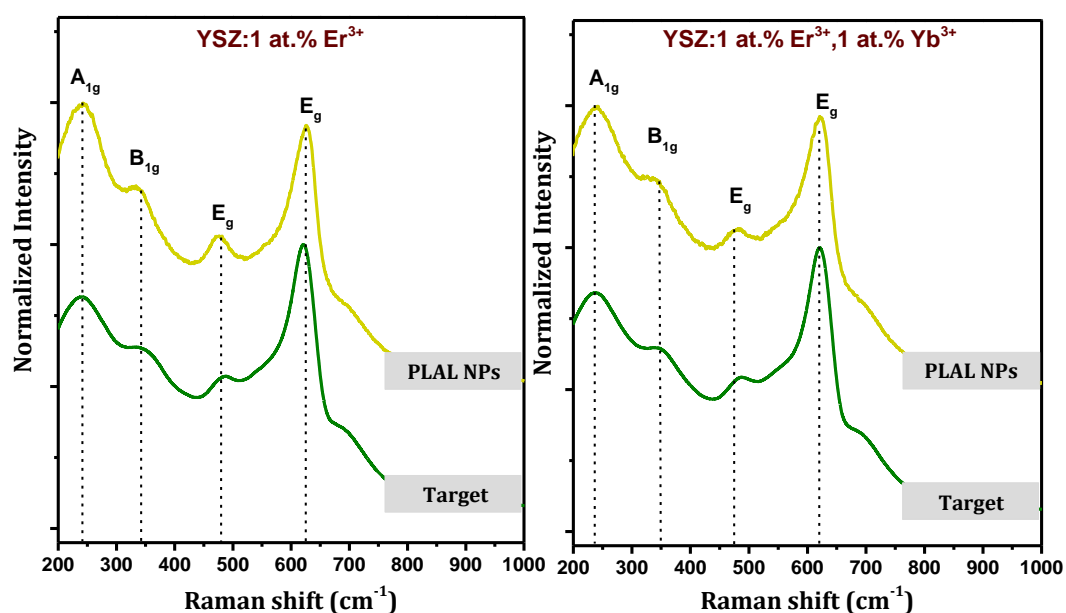
Figure 7.22. Raman spectra of the precursor targets and NPs doped with 1 at.% Er^{3+} (left side) and co-doped with 1 at.% of Er^{3+} and 1 at.% Yb^{3+} (right side). The spectra were acquired at RT in a backscattering configuration, with 325 nm laser line excitation.
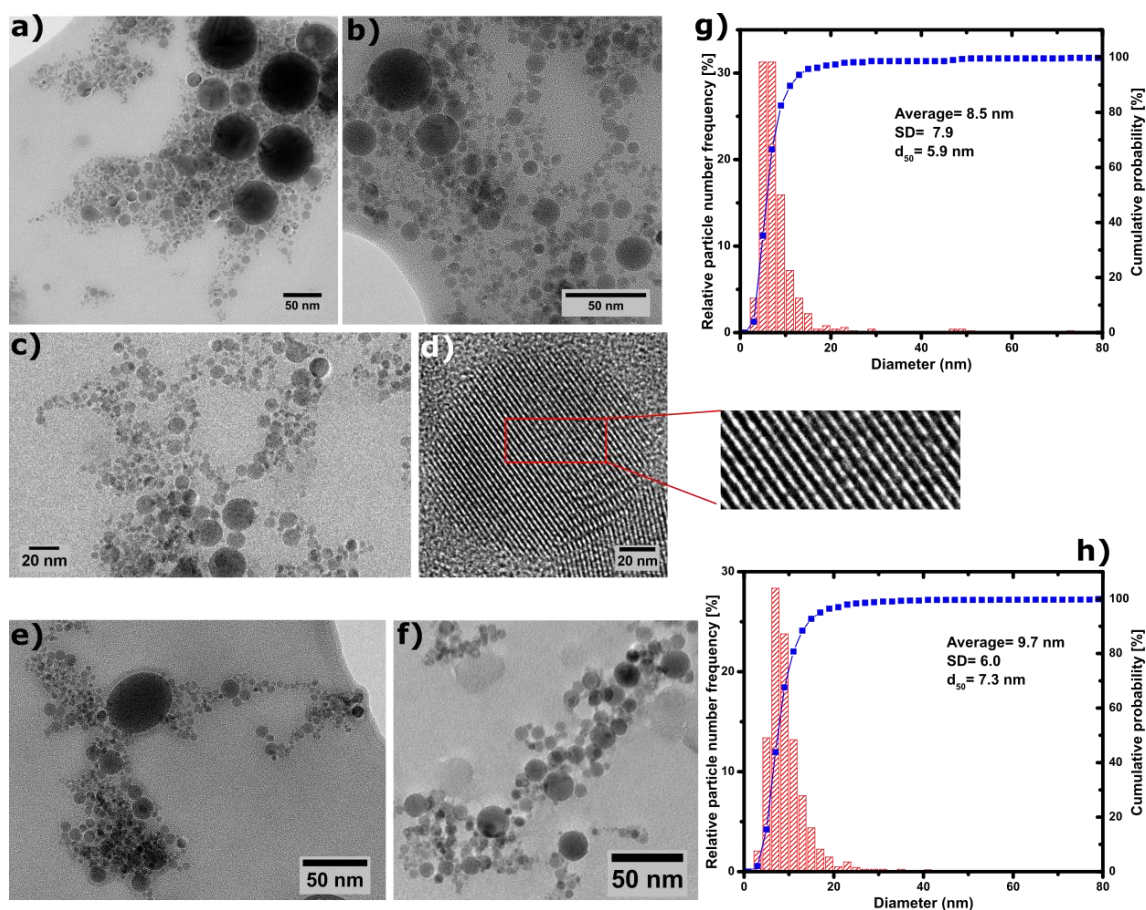
Figure 7.23. TEM images of the YSZ:Er³⁺ (a-d) and of the YSZ:Er³⁺,Yb³⁺ NPs produced by PLAL, and respective histograms of particles size distribution (g and h).

Statistical information on the NPs average size and size distribution was obtained through the analysis of the TEM images in *ImageJ* software. For this analysis, the diameters of more than 500 particles were measured for each sample. Figure 7.23 g) and h) show the histogram of the particle size distribution and the respective cumulative probability for the YSZ:Er³⁺ and YSZ:Er³⁺,Yb³⁺ NPs, respectively. Most of produced NPs have diameters ranging from 2 and 30 nm. Particles with bigger diameters (near 100 nm) are also observed, however the number of these bigger NPs is comparatively lower. As can be observed by the curve of cumulative probability, in Figure 7.23 g) and h), ~99 % of the analysed NPs have a diameter below 30 nm in both samples. The calculated average particles diameters was 9.7 and 8.5 nm for the YSZ:Er³⁺ and YSZ:Er³⁺,Yb³⁺ NPs, respectively.

Luminescence characterization

Figure 7.24 shows the RT PL spectra of the Er³⁺ doped and Er³⁺, Yb³⁺ co-doped NPs under UV excitation (325 nm). For comparison the PL spectra of the precursor targets are shown in the same figure. In accordance with the luminescence of the tetragonal YSZ crystals

studied in the section 5.2.2.5, doped with the same amount of activator and sensitizer ions, and of the ZrO_2 NPs doped with low Er^{3+} concentrations, studied above, the visible emission spectra of the produced NPs are dominated by emission bands in the green spectral region, due to the $^2H_{11/2}{\rightarrow}^4I_{11/2}$ and $^4S_{3/2}{\rightarrow}^4I_{15/2}$ transitions. Under the used excitation conditions, in addition to the dominant green emission, emission bands in the red spectral region, due to the $^4F_{9/2}{\rightarrow}^4I_{15/2}$ transition are also observed. The peak positions and spectral shape of the emission band are very similar in both doped and co-doped NPs. Additionally, they are also similar to the ones observed in the tetragonal YSZ crystals and targets with the same composition. Such results show that optically activated Er^{3+} were successfully incorporated in the tetragonal YSZ host of the NPs during the ablation in water.

RT PLE spectra monitored in the green emission of Er^{3+}, with maxima at 562 nm are shown in Figure 7.25 a) and b) for the doped and co-doped samples, respectively. Like it was previously observed in the Er^{3+} doped crystals, the ion luminescence was found to be excited via several Er^{3+} excited states as labelled in the figure. It should be noticed that in the shorter wavelength region a distinct behaviour was observed in the PLE of the doped and co-doped NPs (and in the precursor targets), comparatively to the doped and co-doped crystals studied before. Despite the fact that in the crystal well-defined intraconfigurational excitation lines to the higher-lying Er^{3+} multiplet, $^4D_{7/2}$, were identified up to $\sim$255 nm ($\sim$4.86 eV; $\sim$39217 cm^{-1}), in the case of the NPs (and respective targets), a broad UV CT excitation band was found, overlapped with the intraionic transitions $^4I_{15/2}{\rightarrow}^4D_{7/2}$, $^2H_{9/2}$, $^4G_{5/2}$, $^2P_{1/2}$, $^2K_{13/2}$, $^2P_{3/2}$ of Er^{3+}, indicating an additional excitation pathway to the ion luminescence. Similar PLE spectra were observed in the tetragonal ZrO_2 target doped with 5 at.% Er.
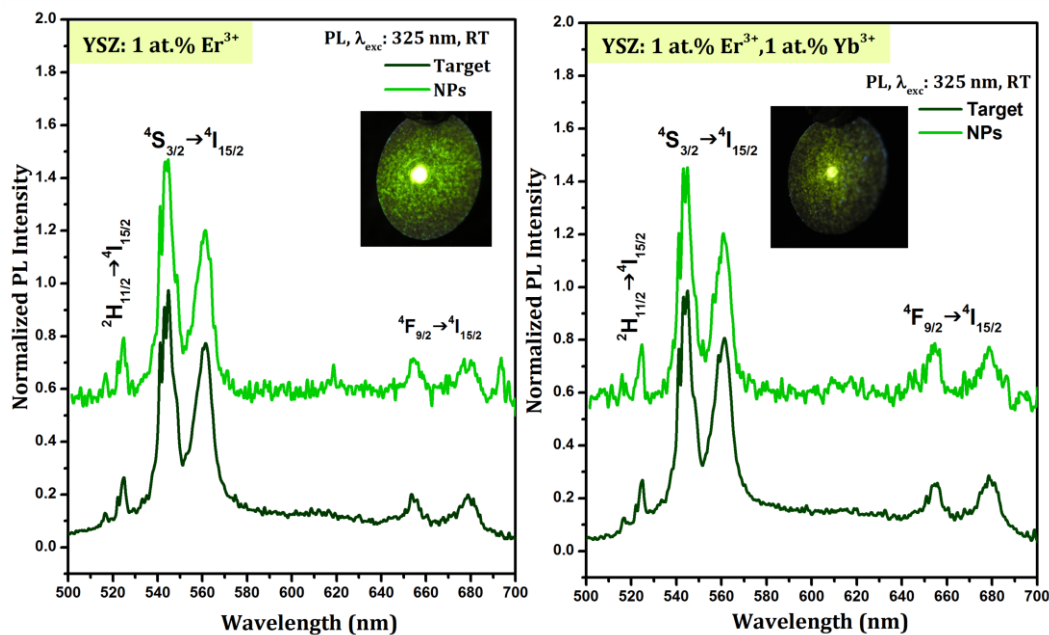
Figure 7.24. RT PL spectra of the YSZ:Er³⁺ and YSZ: Er³,Yb³⁺ NPs produced by PLAL and respective targets, under 325 nm wavelength excitation.

RT PL spectra of the studied NPs and targets obtained by excitation in the high energy $^4D_{7/2}$ multiplet of Er³⁺, peaked at 255 nm and overlapped with the CT band, and in the $^4G_{11/2}$ multiplet (376 nm) are shown in Figure 7.25 a) and b), for the doped and co-doped samples, respectively. Under excitation in the $^4G_{11/2}$ multiplet, emission bands in the green ($^2H_{11/2}{\rightarrow}^4I_{15/2}$ and $^4S_{3/2}{\rightarrow}^4I_{15/2}$), red ($^4F_{9/2}{\rightarrow}^4I_{15/2}$) and NIR ($^2H_{11/2}{\rightarrow}^4I_{13/2}$, $^4I_{9/2}{\rightarrow}^4I_{11/2}$ and $^4S_{3/2}{\rightarrow}^4I_{13/2}$) spectral regions were observed. As observed with 325 nm excitation, the most intense emission occurs in the green spectral region due to the $^4S_{3/2}{\rightarrow}^4I_{15/2}$. In a similar way to what was found for the tetragonal YSZ:Er³⁺ and YSZ:Er³⁺,Yb³⁺ crystals, under excitation in the $^4D_{7/2}$ multiplet, additional violet, blue and red transitions arising from the $^2P_{3/2}$ and $^2G_{7/2}$, multiplets were identified. However, in contrast to the luminescence of tetragonal crystals, in which a strong suppression of the green and red emissions was observed, in the case of the NPs and targets, the same suppression was not observed. This behaviour could be related with the existence of multiple excitation paths found for the green and red bands. As aforementioned, in this case the emission is simultaneously excited via the CT broad band and resonantly into the absorption of the high energetic multiplets of the Er³⁺ ions. The unsuppressed green and red lines suggest that the CT band has an important role in the feeding of the $^4S_{3/2}$ and $^4F_{9/2}$ excited states from where the green and red band originates, in the NPs and targets. No significant differences were observed in the downshifted luminescence of doped and co-doped NPs.

Figure 7.25. RT PL, under resonant excitation in the ⁴G₁₁/₂ and ⁴D₇/₂ multiplets, and PLE monitored in the green (562 nm) and blue (475 nm) emission, of the Er³⁺ doped (a) and Er³⁺,Yb³⁺ co-doped (b) NPs and respective targets.

Summary

Er^{3+} doped and Er^{3+}, Yb^{3+} co-doped tetragonal YSZ NPs were successful produced by PLAL. The produced NPs crystallized in the tetragonal zirconia phase. Beside some particles with diameters up to ~100 nm, it was found that ~99 % of the analysed spherical NPs have a diameter below 30 nm in both doped and co-doped samples. The RT visible downshifted luminescence of the produced NPs evidence the fingerprints of the electronic transitions of Er^{3+} ions, confirming the successful incorporation and optical activation of the dopant into the YSZ lattice of the as-produced NPs. Resonant excitation in the Er^{3+} $^4G_{11/2}$ (376 nm) and $^4D_{7/2}$ (255 nm) multiplets lead to a distinct visible emissions, in line with what was previously observed for the other studied samples doped with Er^{3+}. Under excitation in the $^4G_{11/2}$ multiplet the emission bands in the green, red and NIR, were observed, with a dominant green emission with maxima at 561 nm. Additional emission bands in the violet, blue and NIR spectral regions from the $^2P_{3/2}$ and $^2G_{7/2}$, multiplets were identified under resonant excitation in the $^4D_{7/2}$ multiplet. In contrast with the Er^{3+} doped crystals, the intensity of the green and red emission of the NPs is not suppressed with the used excitation condition. Besides their downshifted luminescence Er^{3+} can show interesting upconversion luminescence, as will be explored in the next chapter.

7.2.2.5   Tm^{3+}, Yb^{3+} co-doped YSZ NPs produced by PLAL

The production of Tm^{3+}, Yb^{3+} co-doped YSZ (YSZ:Tm^{3+},Yb^{3+}) NPs by PLAL was explored. The target used in the ablation was produced by uniaxial pressing and densification (T= 1350 °C, 3 days) of the 0.3 at.% Tm and 1 at.% Yb co-doped YSZ (8 mol.% YO$_{1.5}$) powders produced by SCS. The ablation was performed in distilled water under irradiation with the 1064 nm wavelength pulsed Nd: YAG laser, in the same conditions described for the previously doped NPs. The crystalline phases of the produced samples were investigated at RT by Raman spectroscopy, performed in backscattering geometry with a 325 nm laser line excitation, while the morphology and NP size distribution were evaluated by TEM. Preliminary studies of the downshifted luminescence were performed by steady state PL and PLE.

Structural and morphological characterization

Figure 7.26 a) shows the Raman spectra of the Tm^{3+}, Yb^{3+} co-doped YSZ NPs and of the precursor target. Five bands centred at~264, ~323, ~467, ~612 and ~643 cm^{-1} were identified in the studied spectral region for the co-doped NPs and target, corresponding to the already discussed tetragonal crystalline phase, indicating that the tetragonal structure of the precursor targets was preserved in the Tm^{3+}, Yb^{3+} co-doped NPs produced by PLAL.

The morphology of the NPs was analysed by TEM and HRTEM. Based on TEM images, the diameter of more than 1000 particles were measured, using *ImageJ software*, for statistical data analysis. The histogram of particle size distribution and respective cumulative probability is shown in Figure 7.26 b), while representative TEM images are shown in Figure 7.26 c)-e). As before, the PLAL produced NPs show a spherical shape and are crystalline, as confirmed by the HR-TEM image shown in Figure 7.26 e), were the crystallographic planes of a single crystal particle with diameter around 12 nm, are clearly observed. The produced NPs have an average particle size of 8.4 nm and 98% of the NPs have diameters lower than 23 nm.
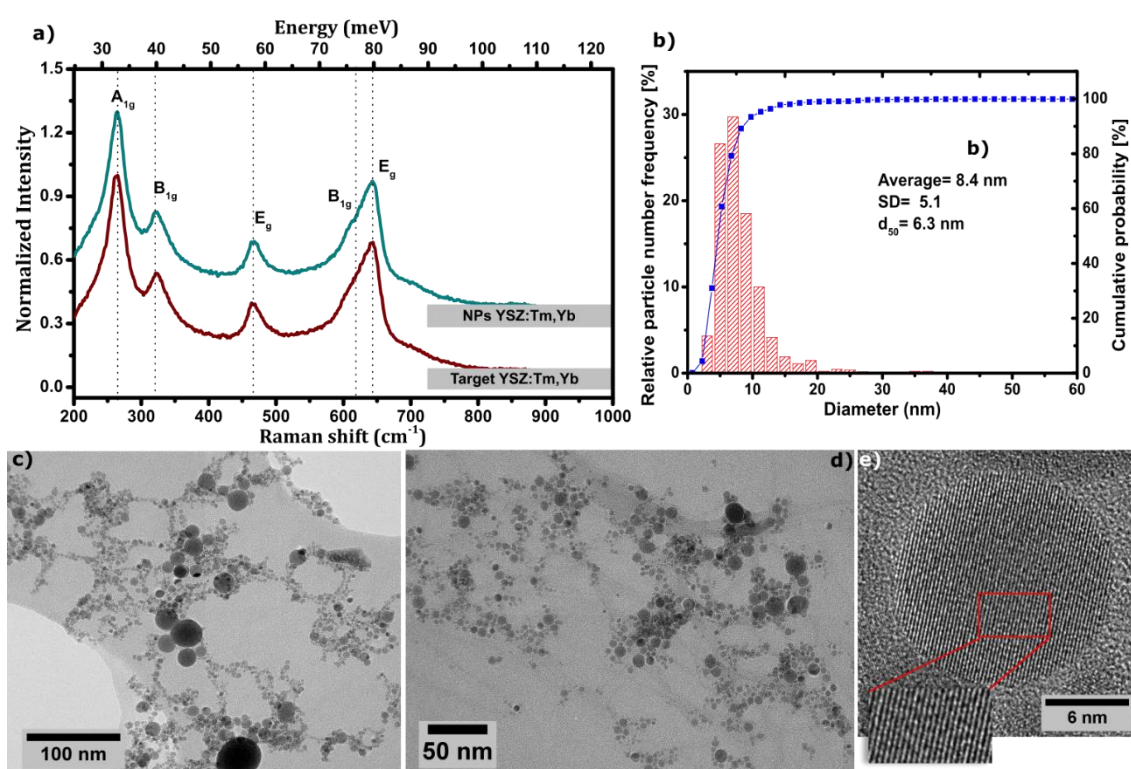
Figure 7.26. a) Raman spectra, under 325 nm excitation, of the YSZ:Tm^{3+},Yb^{3+} NPs and of the precursor target. Histogram of particle size distribution and TEM images of the YSZ:Tm^{3+},Yb^{3+} NPs produced by PLAL.

Luminescence characterization

PL and PLE of the YSZ:Tm^{3+},Yb^{3+} NPs under excitation into the Tm^{3+} excited multiplets are shown in Figure 7.27. RT PL and PLE spectra of the precursor target and of the tetragonal YSZ:Tm^{3+},Yb^{3+} crystal grown by LFZ (section 5.2.2.4) are displayed in the same figure for comparison. Under resonant excitation into the $^1D_2$ and $^1G_4$ multiplets (358.5 and 460.5 nm,

respectively) the emission spectra of the co-doped NPs produced by PLAL exhibit the same intraionic features as the reference co-doped crystals and of the precursor target.
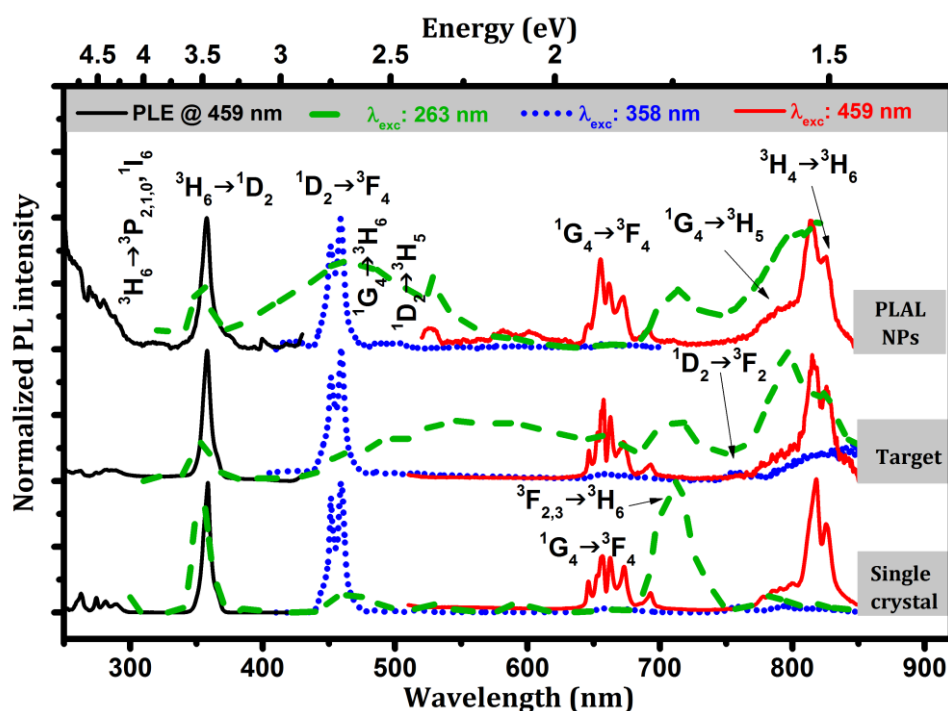
Figure 7.27. RT PL and PLE spectra of the YSZ:Tm^{3+},Yb^{3+} NPs under resonant excitation into the Tm^{3+} excited multiplets. For comparison, the RT spectra of the precursor target and of the tetragonal YSZ:Tm^{3+},Yb^{3+} crystal grown by LFZ are shown.

With resonant excitation in the $^1D_2$ multiplet, a dominant emission in the blue spectral region was observed, which is due to the $^1D_2 \rightarrow ^3F_4$ electronic transition of Tm^{3+}. Additional lines in the red and NIR spectral regions were observed and assigned to the, $^1G_4 \rightarrow ^3F_4$, and $^1G_4 \rightarrow ^3H_5$ and $^3H_4 \rightarrow ^3H_6$ transitions of Tm^{3+}, respectively. On the other hand, resonant excitation in the $^1G_4$ multiplet lead to a dominant red emission in the visible spectral region and a relative increase in the intensity of the NIR emission from the $^3H_4 \rightarrow ^3H_6$ transition, in line with the discussed in the YSZ:Tm^{3+},Yb^{3+} crystals. However, for the excitation at shorter wavelengths, besides the intraionic luminescence observed in the crystal, native defects luminescence, peaked in the blue ($\sim$465 nm) and orange ($\sim$570 nm) regions were observed for the PLAL NPs and targets, respectively. These results show that the luminescent native defects of the host are strongly dependent, not only on the crystalline zirconia phases, but also on the synthesis conditions. For the NPs, the RT PLE monitored at 459 nm, in the blue region, assesses both the preferential pathways to populate the ion emission as well as the host defect luminescence. At shorter wavelengths, in the spectral region where the $^3H_6 \rightarrow ^3P_{2,1,0}$, $^1I_6$ absorption transitions occurs, the identified broad excitation band is likely to

be responsible for the population of the intrinsic defect luminescence. Taking into account the interesting upconversion luminescence properties of Tm^{3+} for bioapplications, further studies of visible luminescence of these co-doped NPs, under NIR excitation will be discussed in the following chapter.

7.3 Conclusions

Pulsed laser ablation in water was explored in the preparation of zirconia based NPs under irradiation of solid targets with a nanosecond pulsed Nd:YAG laser, with 1064 nm wavelength. The study of the processing parameters, such as laser fluence, pulse frequency and height of water layer above the target surface, revealed that, for the range of studied parameters, an appropriated balance between laser power and height of water layer must be achieved in order to avoid the production of big particles by fragmentation and to improve the yield of the process. The height water layer was found to have a strong influence in the process, as it can strongly attenuate the power of the laser beam that reaches the target. Under experimental conditions in which fragmentation is avoided, the change of the different experimental parameters do not reveals any significant impact in the characteristics of the produced NPs. In general, the NPs produced by PLAL exhibit spherical shape, evidence a high crystallinity and have an average particle size in the order of 10 nm. The incorporation and optical activation of different Ln ions, such as Eu^{3+}, Tb^{3+}, Tm^{3+} and Er^{3+} in the zirconia and YSZ lattices, was successfully achieved during the synthesis of the NPs by PLAL. In particular, the intense green and orange/red long lived luminescence at RT of the YSZ NPs doped with Tb^{3+} and Eu^{3+} dispersed in water is of upmost interest for TR-FRET assays. On the other hand, the downshifted luminescence of the NPs doped with Er^{3+} and Tm^{3+} are not so important for such assays, yet the knowledge of their properties is of upmost interest for further studies. As it will explored in the next chapter, the NPs doped with these ions can show interesting visible and/or NIR upconversion luminescence that are also of special importance for bioapplications.

References

[1]   H. Zeng, X.-W. Du, S. C. Singh, S. A. Kulinich, S. Yang, J. He, W. Cai, *Adv. Funct. Mater.* **2012**, *22*, 1333.

[2]   P. P. Patil, D. M. Phase, S. A. Kulkarni, S. V. Ghaisas, S. K. Kulkarni, S. M. Kanetkar, S. B. Ogale, V. G. Bhide, *Phys. Rev. Lett.* **1987**, *58*, 238.

[3]   Z. Yan, D. B. Chrisey, *J. Photochem. Photobiol. C Photochem. Rev.* **2012**, *13*, 204.

[4]   N. G. Semaltianos, *Crit. Rev. Solid State Mater. Sci.* **2010**, *35*, 105.

[5]   S. C. Singh, H. B. Zeng, C. Guo, W. Cai, *Nanomaterials: Processing and Characterization with Lasers*; John Wiley & Sons, 2012.

[6]   Y. Vitta, V. Piscitelli, A. Fernandez, F. Gonzalez-Jimenez, J. Castillo, *Chem. Phys. Lett.* **2011**, *512*, 96.

[7]   X. P. Zhu, T. Suzuki, T. Nakayama, H. Suematsu, W. Jiang, K. Niihara, *Chem. Phys. Lett.* **2006**, *427*, 127.

[8]   Y.-H. Chen, C.-S. Yeh, *Colloids Surf. Physicochem. Eng. Asp.* **2002**, *197*, 133.

[9]   L. Pei-sheng, C. Wei-ping, W. Li-xi, S. M. Ming-da, L. Xiang-dong, L. Wei-ping, *Trans. Nonferrous Met. Soc. China* **2009**, *19*, s743.

[10]   M. K. Singh, M. C. Mathpal, A. Agarwal, *Chem. Phys. Lett.* **2012**, *536*, 87.

[11]   H. Usui, Y. Shimizu, T. Sasaki, N. Koshizaki, *J. Phys. Chem. B* **2005**, *109*, 120.

[12]   V. Caratto, M. Ferretti, L. Setti, *Appl. Surf. Sci.* **2012**, *258*, 2393.

[13]   Z. Yan, R. Bao, D. B. Chrisey, *Phys. Chem. Chem. Phys.* **2013**, *15*, 3052.

[14]   H. Zeng, Z. Li, W. Cai, B. Cao, P. Liu, S. Yang, *J. Phys. Chem. B* **2007**, *111*, 14311.

[15]   V. Amendola, M. Meneghetti, *Phys. Chem. Chem. Phys.* **2009**, *11*, 3805.

[16]   S. I. Alnassar, E. Akman, B. G. Oztoprak, E. Kacar, O. Gundogdu, A. Khaleel, A. Demir, *Opt. Laser Technol.* **2013**, *51*, 17.

[17]   G. Yang, *Laser Ablation in Liquids: Principles and Applications in the Preparation of Nanomaterials*; CRC Press, 2012.

[18]   S. C. Singh, R. K. Swarnkar, R. Gopal, *J. Nanosci. Nanotechnol.* **2009**, *9*, 5367.

[19]   N. G. Semaltianos, S. Logothetidis, N. Frangis, I. Tsiaoussis, W. Perrie, G. Dearden, K. G. Watkins, *Chem. Phys. Lett.* **2010**, *496*, 113.

[20]   E. Fazio, M. Santoro, G. Lentini, D. Franco, S. P. P. Guglielmino, F. Neri, *Colloids Surf. Physicochem. Eng. Asp.* **2016**, *490*, 98.

[21]   V. Amendola, S. Polizzi, M. Meneghetti, *Langmuir* **2007**, *23*, 6766.

[22]   T. Tsuji, Y. Okazaki, Y. Tsuboi, M. Tsuji, *Jpn. J. Appl. Phys.* **2007**, *46*, 1533.

[23]   W. Soliman, N. Takada, K. Sasaki, *Appl. Phys. Express* **2010**, *3*, 035201.

[24]   T. Tsuji, D.-H. Thang, Y. Okazaki, M. Nakanishi, Y. Tsuboi, M. Tsuji, *Appl. Surf. Sci.* **2008**, *254*, 5224.

[25]   T. E. Itina, *J. Phys. Chem. C* **2011**, *115*, 5044.

[26]   V. Amendola, M. Meneghetti, *Phys. Chem. Chem. Phys.* **2013**, *15*, 3027.

[27]   D. Riabinina, J. Zhang, M. Chaker, J. Margot, D. Ma, *Int. Sch. Res. Not.* **2012**, *2012*, e297863.

[28]   R. Matsutani, K. Inoue, N. Wada, K. Kojima, *Chem. Commun.* **2011**, *47*, 5840.

[29]   A. Schwenke, P. Wagener, S. Nolte, S. Barcikowski, *Appl. Phys. A* **2011**, *104*, 77.

[30]   G. Marzun, J. Nakamura, X. Zhang, S. Barcikowski, P. Wagener, *Appl. Surf. Sci.* **2015**, *348*, 75.

[31]   S. A. Al-Mamun, R. Nakajima, T. Ishigaki, *Thin Solid Films* **2012**, *523*, 46.

[32]   S. A. Al-Mamun, R. Nakajima, T. Ishigaki, *J. Colloid Interface Sci.* **2013**, *392*, 172.

[33]   S. Barcikowski, A. Menéndez-Manjón, B. Chichkov, M. Brikas, G. Račiukaitis, *Appl. Phys. Lett.* **2007**, *91*, 083113.

[34]   C. L. Sajti, A. Barchanski, P. Wagener, S. Klein, S. Barcikowski, *J. Phys. Chem. C* **2011**, *115*, 5094.

[35]   S. Petersen, S. Barcikowski, *Adv. Funct. Mater.* **2009**, *19*, 1167.

[36] S. Petersen, A. Barchanski, U. Taylor, S. Klein, D. Rath, S. Barcikowski, *J. Phys. Chem. C* **2011**, *115*, 5152.

[37] S. Petersen, S. Barcikowski, *J. Phys. Chem. C* **2009**, *113*, 19830.

[38] S. H. Stelzig, C. Menneking, M. S. Hoffmann, K. Eisele, S. Barcikowski, M. Klapper, K. Müllen, *Eur. Polym. J.* **2011**, *47*, 662.

[39] T. Salminen, Production of Nanomaterials by Pulsed Laser Ablation. Doctoral dissertation, Tampere University of Technology: Tampere, Finland, 2013.

[40] W. M. A. Soliman, Fundamental studies on the synthesis dynamics of nanoparticles by laser ablation in pressurized water. Doctoral dissertation, Nagoya University: Nagoya, Japan, 2011.

[41] Particular GmbH-nanoparticles. http://particular.eu/nanoparticles.html (acessed: September 2, 2015).

[42] K. M. Kim, J. H. Ryu, *J. Alloys Compd.* **2013**, *576*, 195.

[43] K. Hasna, S. S. Kumar, M. Komath, M. R. Varma, M. K. Jayaraj, K. R. Kumar, *Phys. Chem. Chem. Phys.* **2013**, *15*, 8106.

[44] T. Maldiney, G. Sraiki, B. Viana, D. Gourier, C. Richard, D. Scherman, M. Bessodes, K. Van den Eeckhout, D. Poelman, P. F. Smet, *Opt. Mater. Express* **2012**, *2*, 261.

[45] G. Ledoux, D. Amans, C. Dujardin, K. Masenelli-Varlot, *Nanotechnology* **2009**, *20*, 445605.

[46] T. Nunokawa, Y. Onodera, M. Hara, Y. Kitamoto, O. Odawara, H. Wada, *Appl. Surf. Sci.* **2012**, *261*, 118.

[47] R. Zamiri, H.-R. Bahari-Poor, A. Zakaria, R. Jorfi, G. Zamiri, A. Rebelo, A. A. Omar, *Chin. Phys. Lett.* **2013**, *30*, 118103.

[48] S. A. Al-Mamun, T. Ishigaki, *J. Am. Ceram. Soc.* **2014**, 1.

[49] Y. Onodera, T. Nunokawa, O. Odawara, H. Wada, *J. Lumin.* **2013**, *137*, 220.

[50] S. K. Singh, K. Kumar, S. B. Rai, *Mater. Sci. Eng. B* **2010**, *166*, 180.

[51] G. S. Qin, W. P. Qin, C. F. Wu, S. H. Huang, D. Zhao, J. S. Zhang, S. Z. Lu, *Opt. Commun.* **2004**, *242*, 215.

[52] D. Amans, C. Malaterre, M. Diouf, C. Mancini, F. Chaput, G. Ledoux, G. Breton, Y. Guillin, C. Dujardin, K. Masenelli-Varlot, P. Perriat, *J. Phys. Chem. C* **2011**, *115*, 5131.

[53] F. Yoshimura, K. Nakamura, F. Wakai, M. Hara, M. Yoshimoto, O. Odawara, H. Wada, *Appl. Surf. Sci.* **2011**, *257*, 2170.

[54] D. Katsuki, T. Sato, R. Suzuki, Y. Nanai, S. Kimura, T. Okuno, *Appl. Phys. A* **2012**, *108*, 321.

[55] S. W. Mhin, J. H. Ryu, K. M. Kim, G. S. Park, H. W. Ryu, K. B. Shim, T. Sasaki, N. Koshizaki, *Nanoscale Res. Lett.* **2009**, *4*, 888.

[56] G. S. Park, K. M. Kim, S. W. Mhin, J. W. Eun, K. B. Shim, J. H. Ryu, N. Koshizaki, *Electrochem. Solid-State Lett.* **2008**, *11*, J23.

[57] D. Tan, Y. Teng, Y. Liu, Y. Zhuang, J. Qiu, *Chem. Lett.* **2009**, *38*, 1102.

[58] A. K. Mahmoud, *Adv. Mater. Res.* **2013**, *871*, 194.

[59] D. Tan, G. Lin, Y. Liu, Y. Teng, Y. Zhuang, B. Zhu, Q. Zhao, J. Qiu, *J. Nanoparticle Res.* **2011**, *13*, 1183.

[60] S. Shukla, S. Seal, R. Vij, S. Bandyopadhyay, Z. Rahman, *Nano Lett* **2002**, *2*, 989.

[61] S. Shukla, S. Seal, *Rev. Adv. Mater. Sci.* **2003**, *4*, 123.

[62] C. Liu, X. L. Mao, S. S. Mao, X. Zeng, R. Greif, R. E. Russo, *Anal. Chem.* **2004**, *76*, 379.

[63] S. Alves, M. Kalberer, R. Zenobi, *Rapid Commun. Mass Spectrom.* **2003**, *17*, 2034.

[64] J. F. Suijver, In *Luminescence*; Ronda, C., Ed.; Wiley-VCH Verlag GmbH & Co. KGaA, 2007; pp. 133–177.

[65] B.G. Wybourne, *Spectroscopic Properties of Rare Earths*; Interscience Publishers, New York.; 1965; Vol. 148.

[66] F. E. Auzel, *Proc. IEEE* **1973**, *61*, 758.

[67] F. Auzel, *Chem. Rev.* **2004**, *104*, 139.

[68] G. Liu, B. Jacquier, *Spectroscopic Properties of Rare Earths in Optical Materials*; Springer, 2006.

[69]   J. C. Wright, In *Radiationless Processes in Molecules and Condensed Phases*; Topics in Applied Physics; Springer Berlin Heidelberg, 1976; pp. 239–295.

Chapter 8.

Upconversion phosphors

This chapter is focused in the upconversion luminescence of the Ln ions. In the first part of this section, fundaments and mechanisms behind the upconversion luminescence are revised. After, the upconversion luminescence of bulk crystal, nanocrystalline powders and nanoparticles are detailed and explored

In addition to the Stokes emission, such as the downshifted luminescence explored in the previous chapters, in which photons with lower energy than the excitation energy are emitted, anti-Stokes emission, involving the emission of photons with higher energy then the absorbed ones, can occurs. Basically, anti-Stokes emission can arise via three different mechanisms: simultaneous two photon absorption (STPA), second harmonic generation (SHG) and upconversion (UC) [1]. Within these processes, UC is the most efficient and does not require coherent (as in the SHG) or high excitation power.

Upconversion is a nonlinear optical process that involves the sequential absorption of two or more low energy photons, via long lived intermediate energy states, with a subsequent emission of radiation with high energy. The most efficient mechanisms of upconversion occur in solid state materials doped with lanthanide ions such as Er^{3+}, Tm^{3+} and Ho^{3+} [1,2]. As already pointed out, these ions have a ladder-like free-ion energy level scheme with similar gaps between the fundamental and intermediate states and from the latter to high energy excited multiplets. Hence, and considering the long lifetime of the intermediate excited states, it is possible for an already excited ion to absorb a second photon, thus reaching a high energy level from which the radiative deexcitation results in UV, visible emission and/or NIR emission, using low energy photons as excitation (usually NIR). However, since the intra-4f transitions of trivalent Ln ions are parity forbidden by the Laporte rule, the low absorption probability of light is a limitation when these ions are used to produce efficient UC phosphors. Nevertheless, the upconverted light from these ions can be strongly improved through the co-doping with appropriated sensitizer ions with high cross section absorption of the excitation radiation which in turn efficiently transfer the absorbed energy to the activators. The most frequently used sensitizer ion for the UC luminescence purposes involving Er^{3+}, Tm^{3+} or Ho^{3+} as activators, is the trivalent Yb ion [1]. In addition to the high absorption cross section in the NIR, the energy of the excited level of Yb^{3+}, near 980 nm allows the excitation of ytterbium doped materials by using commercial available laser diodes [1].

Since the discovery of UC phenomena in the 1960s in an independent way by Auzel [3] and Ovsyankin, and Feofilov [4], a strong and increasing research has been dedicated to the study of the UC mechanisms for a high number of UC luminescent materials. Nowadays, the most promising UC materials are those based on Ln^{3+} doped fluorides, including cubic $NaYF_4$: Er, Yb [1,5,6], for which the highest value of UC quantum efficiency was reported. The low phonon energies of fluoride lattices reduces the probability of phonon assisted nonradiative transitions that, associated with the longer lifetimes of the intermediated Ln^{3+} electronic excited states, yields to very efficient upconversion processes. Even so, and as stated in

Chapter 2, fluoride materials have limited chemical and thermal stability that can hamper their practical applications [7]. Moreover, the complex and expensive processes used in the synthesis of these materials associated with the toxicity of some of its precursors are also limitative. In other hand, wide band gap metal oxide hosts, including Y_2O_3 [8–10], $Y_3Al_5O_{12}$ [11], Lu_2O_3 [12], $Lu_3Ga_5O_{12}$ [13,14] and ZrO_2 [15–18], despite less efficient than fluoride materials, can have high chemical, thermal and photo stability and can be produced by simple and low cost routes, being also interesting hosts for exploring UC phenomena.

Nowadays, UC luminescent materials can found application in compact solid state lasers, infrared quantum counters and temperature sensors [1]. In addition, these materials show a high potential for other important technological applications including displays, energy conversion in photovoltaics and bioapplications, including bioimaging, drug delivery, biosensors and photodynamic therapy [19]. An intensive worldwide research in UC materials for bioapplications emerged in the last decades stimulated by the developments in nanoscience and nanotechnology that pave the way to the production of upconversion NPs. As discussed in Chapter 2, the use of UC luminescent nanoprobes that can be excited under NIR light is advantageous as it reduces the autofluorescence background from the biological tissues and photo-damage [20–22].

8.1 Mechanisms of upconversion luminescence

UC luminescence is a complex process that can be mediated by distinct mechanisms, such as excited state absorption (ESA), energy transfer upconversion (ETU), cooperative sensitization upconversion (CSU), cross-relaxation (CR), energy migration mediated UC (EMU) and photon avalanche (PA), as well-documented in the specialized literature [1,21,23–25] and schematically illustrated in Figure 8.1. The UC luminescence efficiency of a given lanthanide doped material will be dependent on the energy transfer processes involved in the ion luminescence [25]. For the materials studied in this work, ESA, ETU and CR are the most important ones and will be discussed below.

Excited state absorption (ESA) is the UC process in which two or more excitation photons are sequentially absorbed by the same ion with an energy level scheme of at least three electronic states. As shown in Figure 8.1 a), in this mechanism an electron of the activator ion is promoted from their ground state to an intermediated excited state by the absorption of an excitation photon (ground state absorption, GSA). Due to the long-lived nature of the intermediate energy level, a second photon can be absorbed before deexcitation, leading the

electron in a higher excited energy state. From this level the electron can relax radiatively with the emission of light with higher energy than the excitation photons. In order to ESA occur a resonant excitation in both intermediate state and higher excited state is needed. With monochromatic excitation, this means that the energy difference between the ground and intermediate states and from the latter to the higher energy level should be the equal [1,21,25]. This process is favoured by a high pump power density and a large ion absorption cross section and usually occurs in materials doped with lower activator concentration, as for high activator concentrations processes as CR could be dominant [25]. Other important UC process that also consists in the sequential absorption of two photons is the one involving the participation of two different ions, a sensitizer and an activator assisted by ETU. As illustrated in Figure 8.1 b), the excitation energy is mainly absorbed by the sensitizer ion, which has higher cross section absorption and the absorbed energy is subsequently transferred nonradiatively to the activator ion. ETU process is favoured in Ln ions with multiple excited states and comparatively to the ESA mechanism, ETU is more efficient [25]. Moreover, the efficiency of the ETU process is strongly influenced by the dopant concentration as it determines the distance between the neighbouring ions that can be of the same or different species [1]. The occurrence of CR is also strongly dependent on dopant concentration. As illustrated in Figure 8.1 f), this process occurs by the ion-ion interaction, in which an ion A transfer part of its absorbed energy to an ion B by a process described according to: E_2 (ion A) + G (ion B)$\rightarrow E_1$(ion A) + E_1 (ion B). In some cases the process can occur with ion 2 in an excited state. For ions A and B of the same specie the occurrence of CR results in a concentration quenching mechanisms for the luminescence originated from the high excited states. However it could be useful for achieve upconversion colour tuning materials.
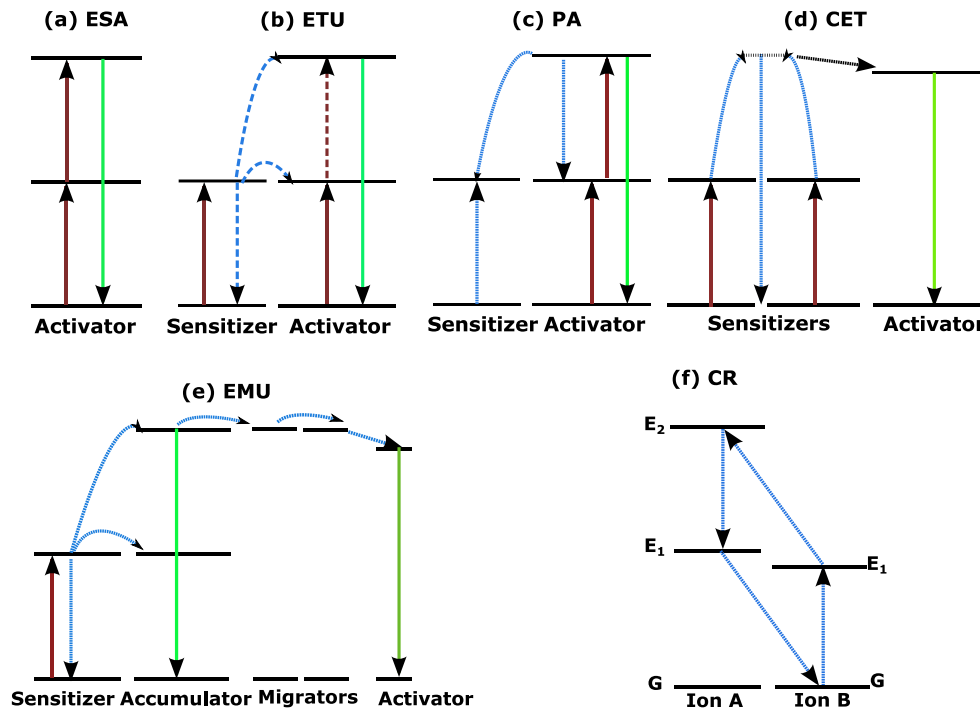
Figure 8.1. Schematic representation of different UC processes: a) excited state absorption (ESA), b) energy transfer upconversion (ETU), c) photon avalanche (PA), d) cooperative sensitization upconversion (CSU), e) energy migration mediated upconversion (EMU) and f) cross-relaxation (CR) (adapted from [1,25]).

The excitation mechanisms for the UC luminescence that usually occurs in systems with several metastable excited states are very complex. Besides the different excitation (GSA, ESA and/or ETU) and depletion (radiative or multiphonon relaxation) mechanisms, additional processes including CR and other energy transfer mechanisms can occur in such complex systems which influence in a nonlinear way the excitation and relaxation of the excited states [26]. The dominant excitation and depletion mechanisms involved in the UC luminescence of an emitting system are frequently investigated by the analysis of the dependence of the pump power, P_{exc}, in the UC luminescence intensity, I_{ems}. It is frequently assumed that $I_{ems} \propto P_{exc}{}^{n}$, in which n is the order of the UC process, i.e. the number of excitation photons needed to populate an emitting level, and can be obtained by the slope value of the double logarithmic representation of the I_{ems} versus P_{exc}. Considering the example of the activator ion with three energy levels shown in Figure 8.1 a), two excitation photons are need to populate the higher excited state and a slope value of two is expected. However, experimental values of slopes lower than the number of photons needed to populate a certain emitting level are frequently reported in literature [26]. Pollnau *et al.* [26] developed a simple theoretical model that explains the dependence of the absorbed pump power in the UC luminescence intensity. This model, obtained from the solution of simple rate equations, allows to distinguish between different excitation and decay mechanisms

involved in the UC luminescence, by the analysis of the measured experimental slopes [26]. In such model, it is considered that the decrease in the experimental slope with the pump power is determined by the competition between the linear decay and UC processes (ETU/ESA) involved in the depletion of the intervenient intermediate states. As such, important information about the dominant excitation mechanisms involved in the UC induced luminescence can be extracted from the experimental slope values. This model was used in this thesis to explain the experimental slope values and to analyse the mechanism involved in the UC luminescence. Following, a brief explanation of the used model will be given where a simplest UC system (i.e. one constituted by a three energy levels ion) is considered as displayed in Figure 8.2.
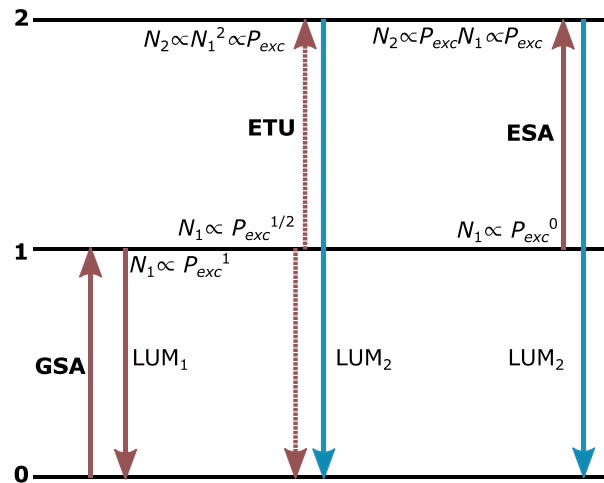

Figure 8.2. Simple three-level upconversion scheme. Solid and dashed arrows indicate the radiative and nonradiative population and depopulation mechanisms for each level, respectively. The dependence of the population density N_1 on pump power for the corresponding depletion pathways, and the dependence of N_2 on N_1 are indicated for the different cases of ETU and ESA [26].

According with the model proposed by Pollnau *et al.* the rate equations for the excited state population density N_i, of each excited energy level $i=$ 1,　n=2, depends on the dominant mechanisms involved in the UC luminescence [26]. For simplification, in this model it is assumed that: the ground state population density is constant ($N_0 \approx const.$); the system is excited continuously by GSA; both ETU and ESA occurs between subsequent excited states; and an excited state i decay with a rate constant $A_i = \tau_i^{-1}$ (τ_i is the lifetime) either to the next lower lying state, with a predominant occurrence of multiphonon relaxation (branching ratio $\beta i= 1$) or directly to the ground state, by predominant radiative processes (branching ratio $\beta i= 0$). Moreover, it is also assumed that for small absorptions, the pump rate (R_i) at the transition from a state i, is independent of the absorption at transitions from

other states and that the pump rate is given by *Eq. 8.1*, where λ_p is the pump wavelength, w_p the pump radius, h the Planck's constant, c the vacuum speed of light, l the sample absorption length, P the incident pump power, α the absorption coefficient at the pump wavelength for a system with n excited levels, σ_i and N_i the absorption cross section and the population density of a state i and ρ_p the pump constant given by *Eq. 8.2* [26].

$$R_i = \frac{\lambda_p}{hcl\pi w_p^2} P\{1 - e^{[-l\alpha]}\}\frac{\sigma_i N_i}{\alpha} \approx \frac{\lambda_p}{hc\pi w_p^2} P\sigma_i N_i = \rho_p \sigma_i N_i \qquad Eq.\,8.1$$

$$\rho_p = \frac{\lambda_p}{hc\pi w_p^2} P \qquad Eq.\,8.2$$

Taking into account these simplifications, and considering the simplest UC system represented in Figure 8.2, for upconversion steps achieved by ETU, with a parameter W_1, the rate equation for the excited state population density are given by *Eq. 8.3* and *Eq. 8.4*.

$$\frac{dN_1}{dt} = \rho_p \sigma_0 N_0 - 2W_1 N_1 N_1 - A_1 N_1 \qquad Eq.\,8.3$$

$$\frac{dN_2}{dt} = W_1 N_1 N_1 - A_2 N_2 \qquad Eq.\,8.4$$

As such, in steady state excitation conditions, the relations in Eq. 8.5 and Eq.8.6 are achieved.

$$W_1 N_1 N_1 = A_2 N_2 \qquad Eq.\,8.5$$

$$\rho_p \sigma_0 N_0 = 2W_1 N_1 N_1 + A_1 N_1 \qquad Eq.\,8.6$$

Form Eq. 8.5, one can see that

$$N_2 \propto N_1^2 \qquad Eq.\,8.7$$

Assuming that the dominant mechanism for the depletion of the level 1 in Figure 8.2 is the linear decay (illustrated by the LUM$_1$) in such way that the upconversion mechanism can be neglected (i.e. the term $2W_1 N_1 N_1$ in the *Eq. 8.6* can be ignored), then, by *Eq. 8.6* and 8.2, one can see that $N_1 \propto P$ and consequently (by *Eq. 8.7*) $N_2 \propto N_1^2 \propto P^2$. On the other hand, if the depletion of the level 1 occurs predominantly by ETU mechanisms, i.e. the term of linear decay in *Eq. 8.6* can be neglected, then $N_1 \propto P^{1/2}$ and consequently $N_2 \propto N_1^2 \propto P$. These two situations are limit conditions, the first one for dominant depletion by linear decay and the second one for dominant ETU processes. However, for pump powers between these two

limit conditions, a competition between the linear decay and ETU processes occurs and the experimental slopes for the UC luminescence are between these two limits [26].

If instead of ETU, the UC mechanism occurs by ESA, then the rate equations for this simplest case are given by *Eq.* 8.8 and *Eq.* 8.9.

$$\frac{dN_1}{dt} = \rho_p \sigma_0 N_0 - \rho_p \sigma_1 N_1 - A_1 N_1 \qquad\qquad Eq.\,8.8$$

$$\frac{dN_2}{dt} = \rho_p \sigma_1 N_1 - A_2 N_2 \qquad\qquad Eq.\,8.9$$

Once again, considering steady state excitation conditions, by *Eq.* 8.9 and *Eq.* 8.2, one can see that

$$N_2 \propto N_1 P. \qquad\qquad Eq.\,8.10$$

Assuming a limit condition in which the depletion of the level 1 occurs only by linear decay, then $N_1 \propto P$ and consequently $N_2 \propto N_1 P \propto P^2$. On the other hand, if the depletion of the level 1 occurs dominantly by ESA then N_1 is independent of P and consequently $N_2 \propto N_1 P \propto P$ [26].

The obtained dependences for these limit conditions in the studied simplest UC system revealed that, in a general way, an intensity versus power dependence of P^n occurs for the cases in which upconversion rates are negligible, while for considerable rates of upconversion this dependence is less then P^n. In fact, in a situation in which upconversion mechanisms dominate over linear decay in the depletion of the intermediate state, the slope of the luminescence from the upper emitting level is almost linear [26]. These limit conditions are indicated in the Figure 8.2 for the different predominant processes.

Pollnau *et. al.* applied the same model to more complex UC systems with n excited states [26]. The generalized steady state rate equations for the excited state population density, for a situation in which the UC is achieved only by ETU are shown in *Eq.* 8.11 (for small upconversion and $\beta_i=0$ or $\beta_i=1$) and in *Eq.* 8.12 and *Eq.* 8.13 for large upconversion and for $\beta_i=1$ and $\beta_i=0$, respectively.

$$N_i = A_1^{-1} \prod_{j=2,\ldots,i} \left[W_{j-1} A_j^{-1}\right] \left(\rho_p \sigma_0 N_0\right)^i, \quad i = 1, \ldots, n. \qquad Eq.\,8.11$$

$$N_i = \prod_{j=2,\ldots,i} \left[W_{j-1} A_j^{-1}\right] \prod_{k=2,\ldots,n-1} \left[A_k^{i/n}\right] \prod_{l=1,\ldots,n-1} \left[W_l^{-i/n}\right] \left(\rho_p \sigma_0 N_0\right)^{i/n}, \quad i = 1, \ldots, n \qquad Eq.\,8.12$$

$$N_i = 0.5 \, W_1^{0.5} \, W_i^{-1} \left(\rho_p \sigma_0 N_0 \right)^{0.5}, \quad i = 1, \dots, n-1 \qquad Eq.\,8.13$$

$$and \; N_n = 0.25 \, A_n^{-1} \rho_p \sigma_0 N_0$$

On the other hand, the generalized steady state rate equations for the excited state population density, for a situation in which the UC is achieved only by ESA are shown in *Eq.* 8.14 (for small upconversion and βi=0 or βi=1 and for large upconversion and βi=1) and in *Eq.* 8.15 for large upconversion and βi=0.

$$N_i = \prod_{j=1,\dots,i} [A_j^{-1}] \rho_p{}^i \prod_{j=1,\dots,i} [\sigma_{j-1}] N_0, \quad i = 1, \dots, n \qquad Eq.\,8.14$$

$$N_i = (\sigma_0/\sigma_i) N_0, \quad i = 1, \dots, n-1 \qquad Eq.\,8.15$$

$$and \; N_n = A_n^{-1} \rho_p \sigma_0 N_0$$

A summary of the dependence of the UC luminescence intensity with the pump powder for these limit conditions is shown in Table 8.1.

Table 8.1. Characteristic slopes of the steady-state excited-state population densities N_i of levels i=1,..., n and luminescence from these states for n-photon excitation obtained from the model developed by Pollnau *et al*. [26]. The investigated limits are: (1) small upconversion or (2) large upconversion by (A) ETU or (B) ESA, decay predominantly (i) into the next lower-lying state or (ii) by luminescence to the ground state, and (a) a small or (b) a large fraction of pump power absorbed in the material [26].

Influence of UC	UC mechanism	Predominant decay route	Fraction of absorbed pump powder	Powder dependence	From level
(1) Small	ETU or ESA	next lower state or ground state	small or large	$N_i \sim P_{exc}{}^i$	i= 1,..., n
(2) Large	(A) ETU	(i) next lower state	small or large	$N_i \sim P_{exc}{}^{i/n}$	i= 1,..., n
		(ii) ground state	small or large	$N_i \sim P_{exc}{}^{1/2}$	i= 1,..., n-1
				$N_i \sim P_{exc}{}^1$	i= n
	(B) ESA	(i) next lower state	(a) small	$N_i \sim P_{exc}{}^i$	i= 1,..., n
			(b) large	$N_i \sim P_{exc}{}^{i/n}$	i= 1,..., n
		(ii) ground state	small or large	$N_i \sim P_{exc}{}^0$	i= 1,..., n-1
				$N_i \sim P_{exc}{}^1$	i= n

According with the considered model, the dependence of the pump power on the UC luminescence, excited by the sequential absorption of n photons, range from P^n to P^1 for the upper excited state and less than P^1 for the intermediate states, depending on the dominant excitation and depletion mechanisms. Even if, for a real system the population mechanisms are more complex than the situation considered in this simple model, these dependences

could be very useful to discuss the excitation and depletion process involved in the UC luminescence through the analysis of the experimental slopes [26].

8.2 Results

In addition to the downshifted luminescence discussed in the Chapters 5, 6 and 7, the samples doped and co-doped with Er^{3+} and Tm^{3+}, produced by the different synthesis techniques explored above, also show interesting upconversion luminescence properties when irradiated with NIR light. The upconversion luminescence of zirconia and YSZ samples doped with Er^{3+} and Tm^{3+} was studied under excitation with a diode laser with 980 nm wavelength and adjustable power output with a maximum power of 1 W.

8.2.1 UC luminescence of Er^{3+} doped ZrO_2

Besides the direct intraionic emission, Er^{3+} doped hosts evidence an adequate schema of levels for the observation of NIR to visible upconversion emission as shown in earlier reported studies [1,23,26,27]. The UC luminescence of the ZrO_2 NPs doped with different Er^{3+} concentrations and produced by PLAL (section 7.2.2.3), and of the ceramic pellets used as targets in ablation and produced by the densification of SCS nanopowders (section 6.2.4) will be discussed. A resume of the composition of these samples, preparation method and crystalline phases is shown in Table 8.2.

Table 8.2. Summary of the synthesis conditions and crystalline phases of the studied samples.

Sample name	Nominal dopant concentration	Preparation	Detected Phases
Target ZrO_2:1Er	1 at.% Er		Monoclinic
Target ZrO_2:2Er	2 at.% Er	Ceramic pellets produced by sintering of SCS powders	Monoclinic
Target ZrO_2:5Er	5 at.% Er		Monoclinic and tetragonal
Target ZrO_2:10Er	10 at.% Er		Tetragonal
Target ZrO_2:16Er	16 at.% Er		Cubic
NPs ZrO_2:1Er	1 at.% Er		Monoclinic and tetragonal
NPs ZrO_2:2Er	2 at.% Er		Monoclinic and tetragonal
NPs ZrO_2:5Er	5 at.% Er	NPs produced by pulsed laser ablation in water	Monoclinic and tetragonal
NPs ZrO_2:10Er	10 at.% Er		Tetragonal
NPs ZrO_2:16Er	16 at.% Er		Cubic

Figure 8.3 a) and b) shows the RT PL spectra of the ZrO_2 ceramic targets and NPs doped with different concentration of Er^{3+}, under excitation with low energy photons (980 nm).

This excitation energy is resonant with the $^4H_{11/2}$ energy level of Er^{3+}, as indicated in the partial energy level diagram of Er^{3+} (brown arrows) shown in Figure 8.3 c). In the studied spectral range, emissions bands in the green and red regions are observed assigned to the $^2H_{11/2} \rightarrow {}^4I_{15/2}$ and $^4S_{3/2} \rightarrow {}^4I_{15/2}$ and to the $^4F_{9/2} \rightarrow {}^4I_{15/2}$ transitions of Er^{3+}, respectively, like the ones observed in downshifted luminescence studies. The UC emission of the different samples is observed by naked eye at RT and, as for the downshifted luminescence, the upconversion phenomenon allows the identification of a tuneable green to red luminescence by increasing the Er^{3+} content. Figure 8.3 d) shows the CIE colour diagram where the colour coordinates of the emission of the samples doped with different Er^{3+} concentrations are represented, and in which the colour tuning from green to red with increase in Er^{3+} concentration can be well identified. In addition, photos of the samples obtained with 980 nm wavelength excitation are displayed in Figure 8.3 e) and f).

Under 980 nm wavelength excitation, assuming GSA, the Er^{3+} ions are excited into an intermediate state, the $^4I_{11/2}$ multiplet, which is known to have a long decay time, in the ms range [28]. Therefore, when a second photon is absorbed the $^4I_{11/2}$ level is still populated and, considering a model of a sequential absorption of two 980 nm photons involving GSA and ESA, the $^4I_{15/2} \rightarrow {}^4I_{11/2} \rightarrow {}^4F_{7/2}$ transitions are favoured [24]. Moreover, upconversion processes are also mediated by ETU [23,27,29]. From the $^4F_{7/2}$ multiplet nonradiative multiphonon relaxation to the $^4S_{3/2}$ and $^4F_{9/2}$ excited states occur with further green and red radiative deexcitation to the ground state. A second route to the population of the $^4F_{9/2}$ excited state can be considered. After the $^4I_{15/2} \rightarrow {}^4I_{11/2}$ absorption, sequential nonradiative relaxation from the $^4I_{11/2}$ to the $^4I_{13/2}$ multiplet can occur, followed by ESA and/or ETU to the higher energetic multiplet from where the red emission originates. These possible pathways for UC luminescence are represented in the partial energy level diagram of Er^{3+} shown in Figure 8.3 c).
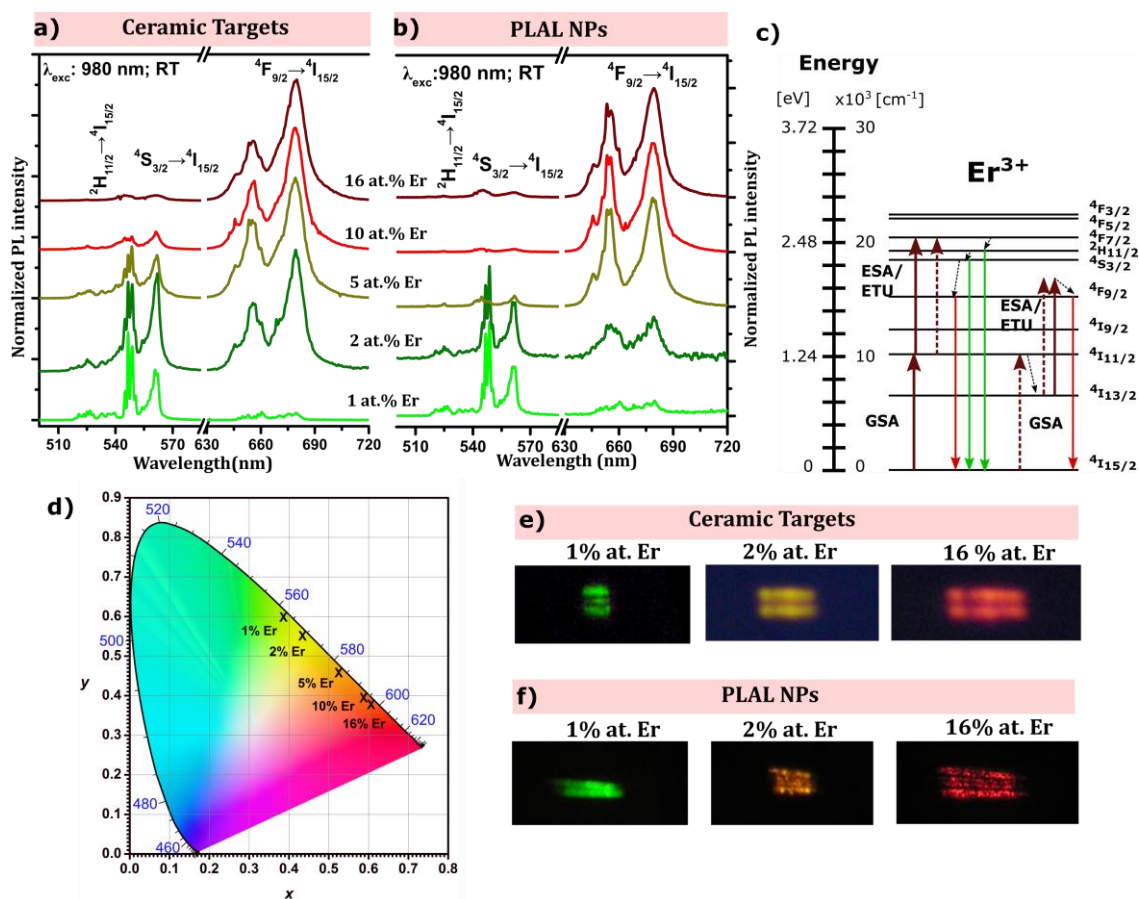
Figure 8.3. PL spectra of the targets (a) and the PLAL produced NPs (b) obtained with 980 nm wavelength excitation photons. (c) Schematic partial energy level diagram for Er³⁺ ions illustrating the upconverted luminescence. (d) Colour diagram coordinates with the representation of the overall upconversion emission for the different erbium amounts. Photographs of the RT upconversion luminescence of ceramic targets (e) and NPs (f), after dried on the top of a quartz substrate, obtained with 980 nm excitation.

To investigate the upconversion luminescence mechanisms, the excitation power dependence of the green and red upconversion PL spectra were carried out. The excitation power dependence of the integrated green and red light of the ceramic targets and NPs produced by PLAL are shown in the log–log plots of Figure 8.4 a) and b), respectively. As already mentioned, it is well established [23,24,26,27,30,31] that the upconverted emission intensity scales with a power law, $I_{ems} \propto P_{exc}{}^n$, where P_{exc} corresponds to the excitation power and n is the number of photons involved in the process, as defined before. For the analysed ZrO$_2$:Er³⁺ samples n ranges between $1 < n < 2$, agreeing well with the rate equations model of Pollnau *et al.* [26]. As discussed above, according with this model, the intensity of the emitting state follows a P^n law for systems where the upconversion (ETU/ESA) mechanisms could be neglected in the intermediate states and adopt a P^1 law in systems where the same upconversion processes dominates [26]. As such, a unitary slope of the luminescence intensity is expected to occur with increasing power excitation. Besides

these two limit situations, real cases can be located in an intermediate regime, where a competition between the linear decay and upconversion processes for the depletion of an intermediate state arises, leading to slopes among the two mentioned values [23,24,26,30]. As aforementioned, additional processes (e.g. CR mechanisms) also influence the intensity of the upconverted luminescence, as earlier reported by Auzel [23,27,31] and Pollnau *et al.* [26].
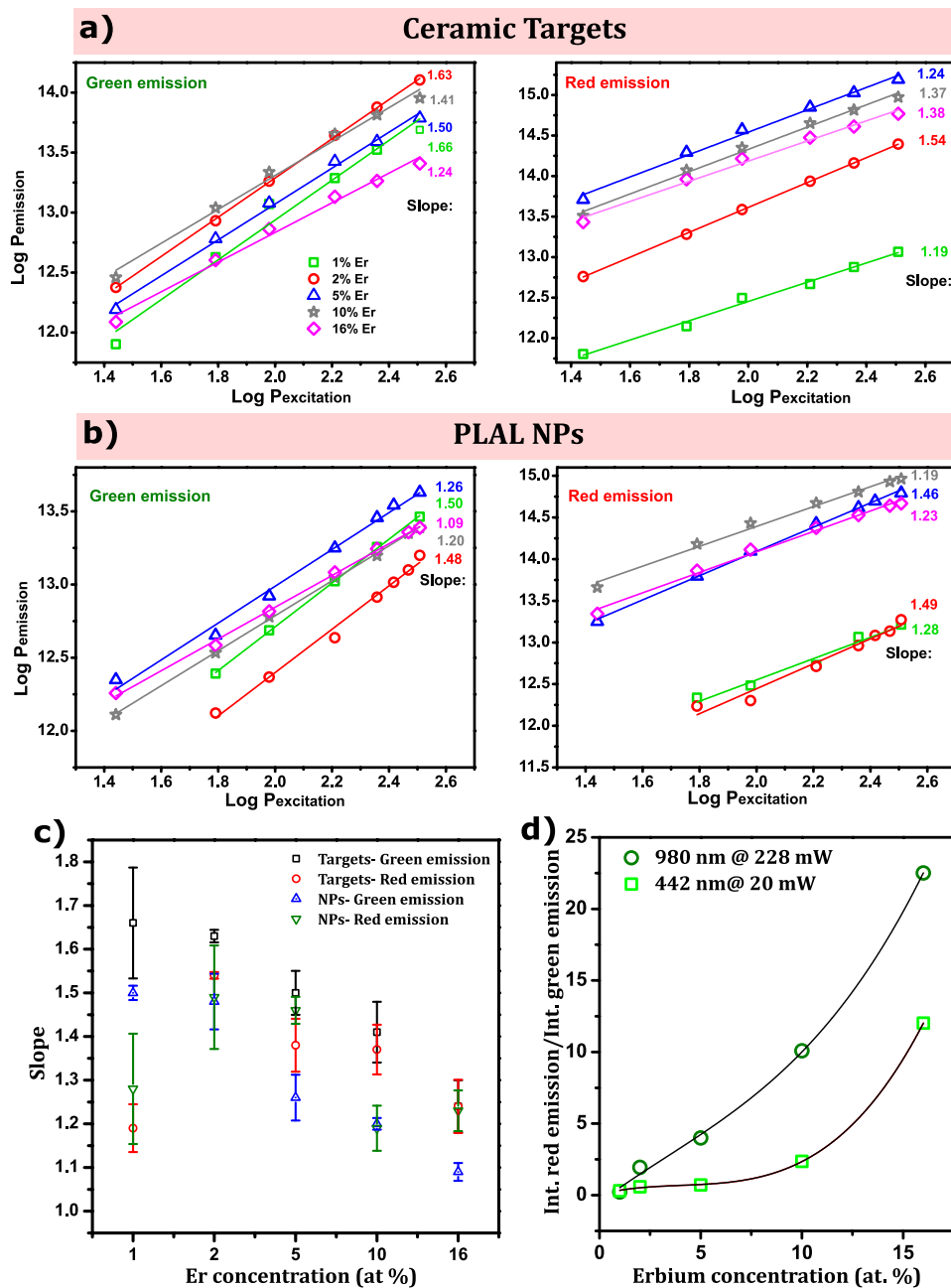

Figure 8.4. Excitation power dependence of the integrated green and red RT upconversion luminescence for different Er^{3+} concentrations doped ZrO_2 targets (a) and NPs (b). The excitation was performed with 980 nm wavelength photons corresponding to the GSA $^4I_{15/2} \rightarrow ^4I_{11/2}$. c) Er concentration dependence of the slope of the green and red upconverted light. d) Red/green intensity ratio for the prompt (378 nm excitation) and upconversion Er^{3+} emission (980 nm excitation at 228 mW).

The data shown in Figure 8.4 allows further investigation about the dominating processes involved in the upconversion mechanims for the ZrO_2:Er^{3+} samples. As a starting point, it should be emphasized that either for the green or red luminescence none of the measured slopes corresponds to $n=2$. This corresponds to the case where a linear decay from the intermediate levels is expected and the upconversion processes are insignificant. However, the higher slope tendency observed for the green $^4S_{3/2} \rightarrow ^4I_{15/2}$ multiplet transition in samples with lower erbium concentration, suggests that the radiative decay is the dominant process involved on the depopulation of intermediate levels, instead of the competitive UC processes. As such, the values close to $n=2$ reflect the photon excitation steps for the population of the $^4S_{3/2}$ level. On the other hand, the measured slope for the red luminescence originated in the $^4F_{9/2}$ multiplet for the same set of samples (lower amount of erbium ions) is slightly lower than those of the green emission. As above mentioned the tendency for a lower n value, means that a higher competition occurs among the radiative depletion of the intermediate states and the upconversion processes. For instance, besides the $^4I_{15/2} \rightarrow ^4I_{11/2} \rightarrow ^4F_{7/2}$ path (involved on the population of the $^4S_{3/2}$ and $^4F_{9/2}$ multiplets) a likely mechanism for the population of the $^4F_{9/2}$ state corresponds to the two step excitation following the $^4I_{15/2} \rightarrow ^4I_{11/2} \rightarrow ^4I_{13/2} \rightarrow ^4F_{9/2}$ route, with nonradiative relaxation among the $^4I_{11/2}$ and $^4I_{13/2}$ states. As both processes own for different probability rates a different slope for the red emission intensity is expected when compared with the green one, suggesting a higher competition among the upconversion mechanisms and the radiative decay of the intermediate level to the ground state. Figure 8.4 c) shows the concentration dependence of the slope of the green and red upconverted light, while the red/green luminescence intensity ratio for the downshifted and upconversion luminescence of Er^{3+} is shown Figure 8.4 d). A linear decrease slope tendency of the green and the red upconverted light emission is observed. In addition, a stronger increase of the red/green intensity ratio with erbium concentration is observed for the UC luminescence comparatively to the downshifted luminescence. The slope tendency, with a value close to the unity for the highest doped samples, leads to the assumption that large upconversion rates arise for these samples, reflecting the role of the increase in the lattice symmetry (from monoclinic $\rightarrow$ monoclinic + tetragonal $\rightarrow$ tetragonal $\rightarrow$ cubic) and ion site location on the transition probability rates of the observed emission. On the other hand, and for samples with higher erbium amounts, a promotion of the red $^4F_{9/2} \rightarrow ^4I_{15/2}$ transition was found, either in downshifted as in the UC luminescence. As aforementioned for the DS luminescence, this behaviour leads us to consider that the suppression of the green emission could involve additional nonradiative pathways for the depopulation of the $^4S_{3/2}$. On the other hand, considering the excitation

with low energy 980 nm photons the increase in the population of the $^4I_{11/2, 13/2}$ results in enhanced red emission intensity as observed in other sesquioxides such as Y_2O_3 [32].

__Summary__

The UC luminescence of ZrO_2 NPs produced by PLAL, and ceramic targets doped with different concentration of Er ions, were studied with 980 nm photon excitation. UC emission in green and red regions was identified due to Er^{3+} transitions from the $^4S_{3/2}$ and $^4F_{9/2}$ multiplets to the $^4I_{15/2}$ ground state, respectively. As observed previously in the downshifted luminescence of these Er^{3+} doped samples, the green to red luminescence intensity ratio was found to be dependent of the erbium amount, accompanying the increase in the lattice symmetry. The suppression of the green transition for higher concentrations was discussed based on nonradiative competitive mechanisms such as cross-relaxation processes between near neighbouring ions, as expected for higher dopant contents. The power dependence of the visible Er^{3+} upconversion emission reveals slopes between 1 and 2 meaning that competition occurs among the radiative depletion of the intermediate states and the upconversion mechanisms. The lowest doped samples, showing a dominant green light, evidence higher slope suggesting small upconversion rates. On the opposite side, the highest doped samples (those where the red emission prevails) exhibit a slope near the unity. In both cases, the visual appearance of the green and red upconverted light is clearly observed at RT with naked eye.

8.2.2 UC luminescence in Er^{3+}doped and Er^{3+}, Yb^{3+} co-doped YSZ

The UC luminescence of the Er^{3+} doped and Er^{3+} and Yb^{3+} co-doped YSZ ceramic targets, crystals and NPs, produced by the different techniques discussed earlier and identified in Table 8.3, was also studied under NIR excitation. The effect of Yb^{3+} sensitizer in the Er^{3+} UC luminescence was analysed.

Table 8.3 Samples identification and respective chemical composition.

Sample name	Lattice	Activator dopant	Sensitizer dopant	Synthesis process
Target YSZ:Er	8 mol.% $YO_{1.5}$ stabilized zirconia		-	Pressing and densification of SCS powder
Target YSZ:Er, Yb			1 at.% Yb	
NPs YSZ:Er	8 mol.% $YO_{1.5}$ stabilized zirconia	1 at.% Er	-	PLAL
NPs YSZ:Er, Yb			1 at.% Yb	
Single crystal YSZ:Er	8 mol.% $YO_{1.5}$ stabilized zirconia		-	LFZ
Single crystal YSZ:Er, Yb			1 at.% Yb	

Figure 8.5 a) and b) depicts RT PL spectra of the different doped and co-doped samples, respectively, under excitation with 980 nm laser line. As already mentioned, such excitation energy is resonant with $^4I_{15/2}\rightarrow^4I_{11/2}$ absorption transition of the Er^{3+} (in the doped samples) and additionally to the $^2F_{7/2}\rightarrow^2F_{5/2}$ absorption of the Yb^{3+} ions (in the co-doped samples). With this excitation, and for the studied spectral range, the $^2H_{11/2}\rightarrow^4I_{15/2}$ and $^4S_{3/2}\rightarrow^4I_{15/2}$ green and the $^4F_{9/2}\rightarrow^4I_{15/2}$ red emissions were identified, as also observed in downshifted PL. With the 980 nm photon wavelength excitation conditions the doped and co-doped YSZ appear as an efficient media to produce green light as identified by the visual appearance of the RT upconverted luminescence shown in Figure 8.5 c) and d). In the case of the single crystals the ion luminescence is guided along its millimetric length which is of interest for waveguide applications.
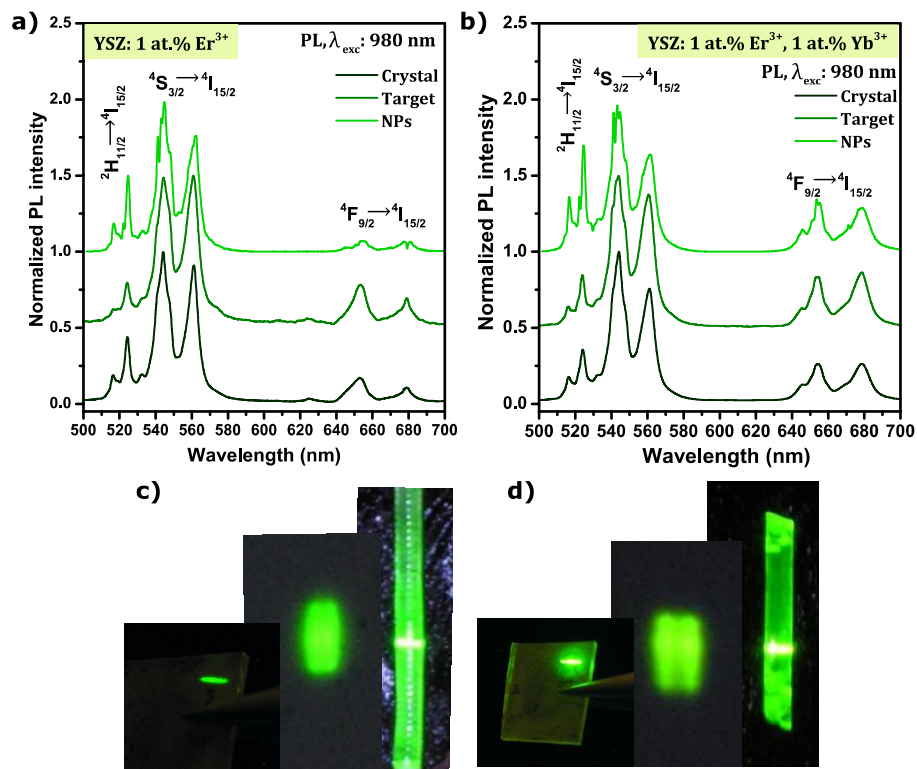

Figure 8.5. PL spectra of the YSZ ceramic targets, NPs and crystals doped with Er³⁺ (a) and co-doped with Er³⁺ and Yb³⁺ under 980 nm laser excitation. Photos of the doped (c) and co-doped (d) samples under 980 nm excitation.

The intensity of the overall UC luminescence was found to be dependent on the presence of the Yb^{3+} sensitizer, as revealed by the PL spectra measured in the same excitation and detection conditions of the ceramic targets shown in Figure 8.6 a), where an increase in the overall intensity of the UC emission, by a factor of ~3, was observed in the co-doped sample. This result is expected due to the higher absorption cross section of Yb^{3+} to the 980 nm

radiation [1] and to the efficient energy transfer to the Er^{3+} activators. In addition, a comparison of the integrated intensity ratio of the red and green luminescence in the doped and co-doped samples revealed a slight increase in the relative intensity of the red emission in all the co-doped samples, as shown in Figure 8.6 b). This behaviour is similar to the one observed for samples doped with higher concentration of Er^{3+}.
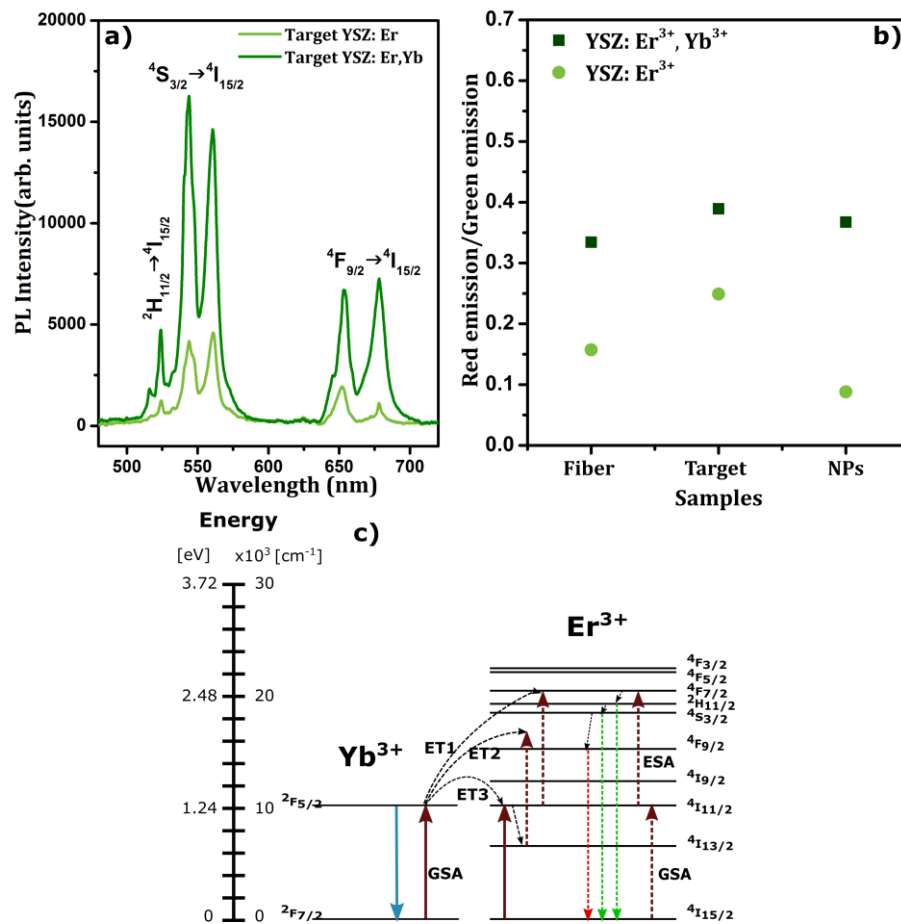

Figure 8.6. a) Comparison of the UC luminescence intensity in the doped and co-doped ceramic targets excited with 980 nm photons. b) Comparison of the ratio between the red and green intensity in the doped and co-doped samples. c) Partial energy diagram of the Er,Yb system.

In order to understand the increase in the relative intensity of the red emission for the co-doped samples, the UC luminescence of ZrO_2 powders co-doped with 1 at.% Er^{3+} and with different concentrations of Yb^{3+}, produced by SCS, was investigated. Figure 8.7 a) shows the RT PL spectra under 980 nm excitation of the ZrO_2 powders co-doped with different Yb^{3+} concentration. As observed in the ZrO_2 samples doped with different Er^{3+} concentrations, a strong increase in the relative intensity of the red emission occurs with increasing concentration of Yb^{3+} sensitizer, Figure 8.7 b), and a tuneable visible emission, from green (at low Yb^{3+} concentrations) to red (at high sensitizer concentrations) is achieved. Such

results confirm that the increase in the relative intensity of the red emission is promoted by the interaction between neighbour ions due to their higher proximity in highly doped samples. These interactions seems to favour the occurrence of energy transfer processes between neighbour Er and Yb ions, such as CR, that increase the population of the $^4F_{9/2}$ red emitting level.
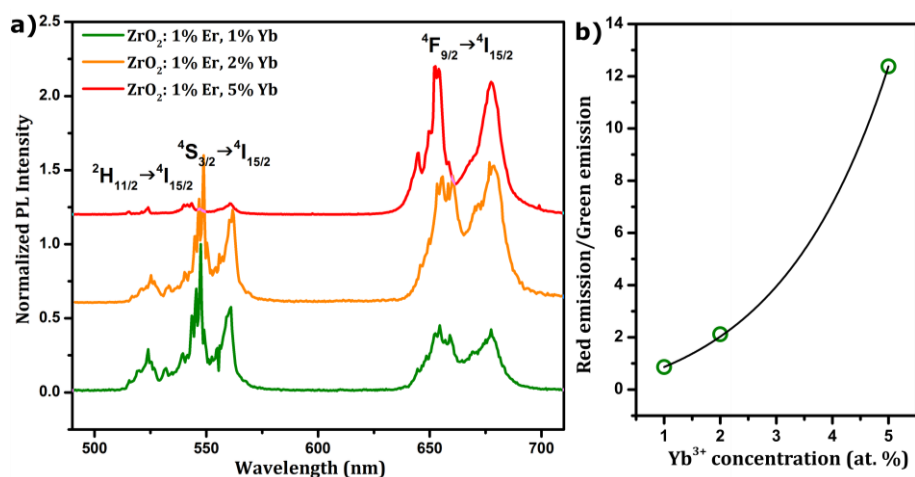

Figure 8.7. a) RT PL spectra of the ZrO$_2$ powders produced by SCS co-doped with 1 at.% Er^{3+} and with different concentration of Yb^{3+}. The samples were excited with 980 nm photon. b) Integrated intensity ratio between the red and green emission for the sample co-doped with different Yb^{3+} amounts.

As illustrated in the partial energy diagram of Er^{3+} and Yb^{3+} system, shown in Figure 8.6 c), and assuming the Er^{3+} ions in the ground state, in the case of the Er^{3+} doped samples, the mechanism involved in the population of the green and red emitting levels are the same as the ones discussed above for the ZrO$_2$ samples doped with different Er^{3+} concentrations. The Er^{3+} ion is raised to the $^4I_{11/2}$ excited multiplet under the GSA of a 980 nm wavelength photon. The sequential absorption of a second photon, before the decay of the intermediate state, involving ESA promotes the population of the $^4F_{7/2}$ multiplet, with an excitation pathway for the green and red upconversion luminescence described by $^4I_{15/2} \rightarrow ^4I_{11/2} \rightarrow ^4F_{7/2}$. From the $^4F_{7/2}$ multiplet further nonradiative multiphonon relaxations to the $^2H_{11/2}$, $^4S_{3/2}$ and $^4F_{9/2}$ excited states occur, with the radiative return from these states to the ground one, responsible for the green and red emissions. An alternative way to the population of the $^4F_{7/2}$ multiplet resides in the ETU process related with the interaction of two Er^{3+} ions in the $^4I_{11/2}$ excited state where one of the ions relaxes to the $^4I_{15/2}$ ground state and the other one is raised to the $^4F_{7/2}$ ($^4I_{11/2} + ^4I_{11/2} \rightarrow ^4I_{15/2} + ^4F_{7/2}$). An additional comment should be done concerning the population of the $^4F_{9/2}$ state via nonradiative relaxation from the $^4S_{3/2}$ multiplet. The energy difference between these two multiplets is around 3200 cm^{-1}

which means that at least five lattice phonons should be involved to bridge the energy gap. This leads to a low nonradiative rate for the multiphonon relaxation process likely explaining the low intensity of the red light, in sample doped with low erbium concentration, in which additional process involving the interaction between neighbour ions are negligible.

In the case of the Er^{3+}, Yb^{3+} co-doped samples the majority of the 980 nm wavelength photons will be absorbed by the Yb^{3+} ions, which has larger absorption cross section. The absorption of the excitation energy promotes the Yb^{3+} from the ground state ($^2F_{7/2}$) to the excited one ($^2F_{5/2}$) and further energy transfer to the $^4I_{11/2}$, $^4F_{9/2}$, $^4F_{7/2}$ excited states of the Er^{3+} are expected to occur in order to observe visible upconverted light. In the case of the $^4I_{11/2}$ state a sequential absorption of a second photon from the same or a neighbour Yb^{3+} raises the Er^{3+} to the $^4F_{7/2}$ multiplet as mentioned before. On the other hand, as an higher integrated intensity of the red/green upconverted emission was found in the co-doped samples, an alternative route to increase the $^4F_{9/2}$ population consists in consider a nonradiative depletion from the $^4I_{11/2}$ intermediate state to the $^4I_{13/2}$ multiplet followed by $^4I_{13/2} \rightarrow ^4F_{9/2}$ ESA/ETU.

The pumping mechanisms of the upconverted visible luminescence for the crystals, targets and PLAL NPs were analysed based on the dependence of the green ($^2H_{11/2}$, $^4S_{3/2} \rightarrow ^4I_{15/2}$) and red ($^4F_{9/2} \rightarrow ^4I_{15/2}$) luminescence intensity, I_{ems}, with the pump power, P_{exc}, as depicted in Figure 8.8. An expected increase of the overall UC luminescence with the excitation powder was observed for all samples. Slight variation on the relative intensity between the emissions bands were observed in the normalized PL spectra acquired at low and high power excitation. The slopes of the green and red upconverted intensity light in a double logarithmic scale are shown in Figure 8.9 for the different studied samples. Again, values of n between $1 < n < 2$ were obtained by the slope of the represented curves, which are similar to the ones obtained for the ZrO_2 samples doped with different Er^{3+} concentration. For the erbium doped samples a higher slope to the intensity of the green band versus the pump power was found meaning that, according with Pollnau *et al.* model [26], negligible upconversion rates are involved in the excitation of the green emitting levels. An almost linear slop was found for the red transition meaning that higher upconversion rates are involved in such emission.
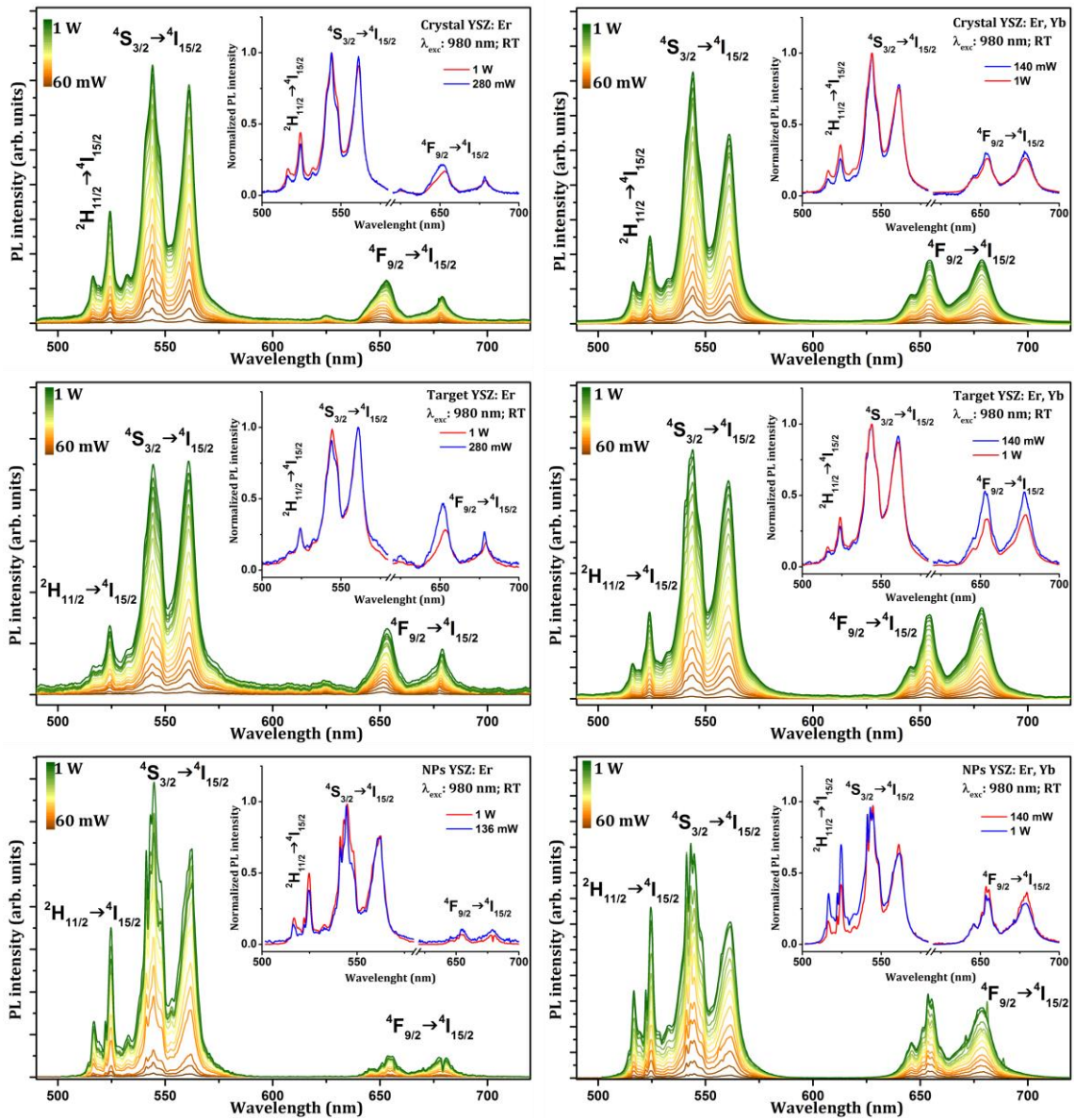
Figure 8.8. Power excitation dependence in UC emission spectra of the doped and co-doped samples, with 980 nm excitation. Insets show a comparison of the normalized PL spectra acquired at low and high power excitations.
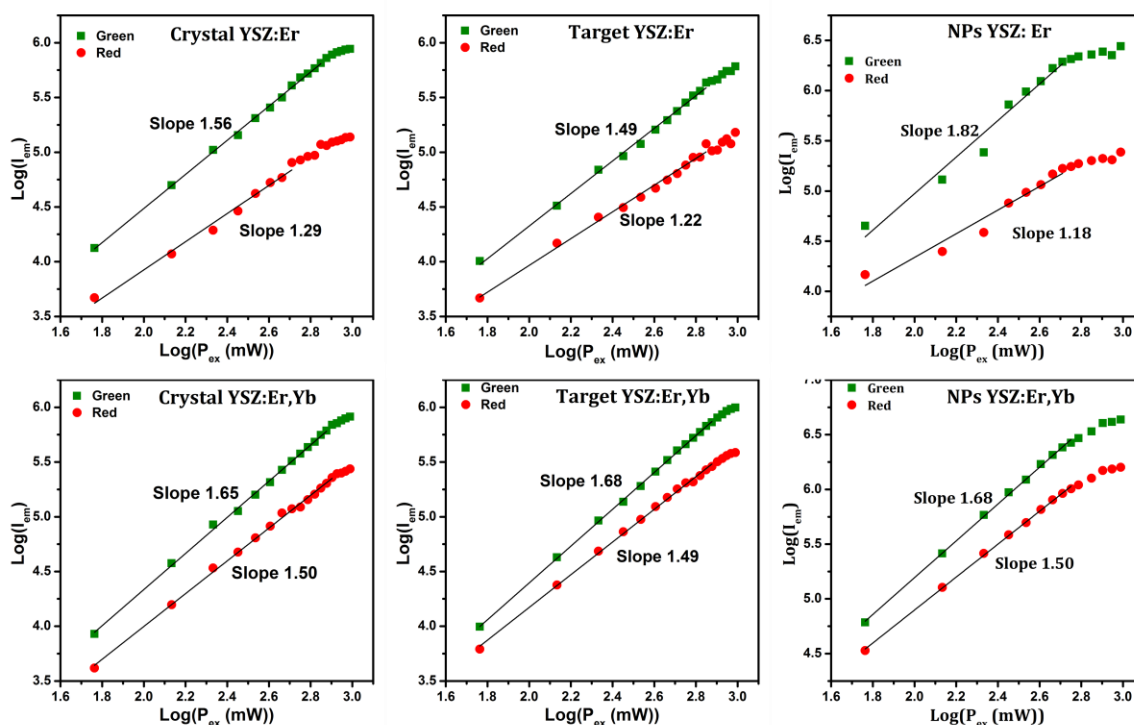
Figure 8.9. Excitation power dependence of the integrated green and red RT upconversion luminescence for the doped and co-doped samples.

A similar trend to the one observed in the doped samples was identified in the case of the Er^{3+}, Yb^{3+} co-doped samples while in general the slope of the red light increases when compared with the single doped samples. Additionally, a decreasing slope was observed with increasing pump power, in a more pronounced way to the NPs, revealing that the upconversion rates are dominating for higher excitation densities although other saturation effects could not be discarded.

Summary

Green and red visible upconversion was observed with 980 nm wavelength photon excitation in Er^{3+} doped and Er^{3+} and Yb^{3+} co-doped YSZ samples. A higher intensity of the green and red Er^{3+} luminescence was found in the presence of the Yb^{3+} sensitizer. Moreover, an increase in the red/green intensity ratio was identified for the co-doped samples. The pumping mechanisms of the upconverted emission were analysed based on the dependence of the luminescence intensity as a function of the power pump and the slope of the upconverted green and red light was found to be $1 < n < 2$. The doped and co-doped tetragonal YSZ NPs show to be promising valuable systems for bioimaging sensing with NIR excitation.

8.2.3 UC luminescence in Tm^{3+}, Yb^{3+} co-doped YSZ

The UC luminescence of the YSZ sample co-doped with Tm^{3+} and Yb^{3+} produced by LFZ, densification of SCS powders and PLAL (see Table 8.4), were studied under NIR radiation.

Table 8.4. Identification of the studied Tm^{3+}, Yb^{3+} co-doped samples

Sample name	Lattice	Activator dopant	Sensitizer dopant	Synthesis process
Target YSZ:Tm, Yb				Pressing and densification of SCS powders
Single crystal YSZ:Er, Yb	8 mol.% $YO_{1.5}$ stabilized zirconia	0.3 at.% Tm	1 at.% Yb	LFZ
NPs YSZ:Tm, Yb				PLAL

As mentioned before, the corresponding photon excitation energy is nearly resonant with the absorption between the ground and excited state of the Yb^{3+} sensitizer. Figure 8.10 a) displays the UC luminescence spectra of the YSZ:Tm^{3+},Yb^{3+} single crystal, ceramic target and NPs upon the NIR excitation. The spectra are composed of four groups of emission lines in the UV, blue/green, red and NIR spectral regions, corresponding to the $^1D_2{\rightarrow}^3H_6$, $^1D_2{\rightarrow}^3F_4/^1G_4{\rightarrow}^3H_6$, $^1G_4{\rightarrow}^3F_4$ and $^1G_4{\rightarrow}^3H_5/^3H_4{\rightarrow}^3H_6$ transitions of the 3+ charged thulium ions. Comparing the Stokes shifted luminescence discussed in the sections 5.2.2.4 and 7.2.2.6, using high energy photons in the excitation (pumping directly the $^1D_2$ multiplet), with the samples luminescence observed by the excitation with 980 nm photons, the intensity ratio of the (blue + red)/NIR emission is much higher in the former case than in the upconversion process, revealing that the NIR UC luminescence is enhanced by energy transfer from the $^2F_{7/2}{\rightarrow}^2F_{5/2}$ photon absorption of the Yb^{3+} ions. These findings agree well with the model described by Ostermayer *et al.* [33] and Pandozzi *et al.* [34] where the population of the excited energy levels of the Tm^{3+} ions is realized via nonradiative energy transfer and multiphonon decay. After the non-resonant energy transfer $^2F_{7/2}, ^3H_6{\rightarrow}^2F_{5/2}, ^3H_5$ (where the excess in energy, $\sim$1650 cm^{-1}, is assisted by absorption of the YSZ lattice phonons) multiphonon relaxation into the $^3F_4$ multiplet of the Tm^{3+} occurs. This process is followed by a second energy transfer (or via ESA) to the $^3F_2$ state with subsequent multiphonon relaxation into the $^3H_4$ from where the NIR $^3H_4{\rightarrow}^3H_6$ emission arises. This route has a high probability of occurring due to the low energy difference between the $^3F_2$ and $^3F_3$ levels ($\sim$640 cm^{-1}) which can be easily covered by an YSZ host phonon. On the other hand, the subsequent nonradiative relaxation to the $^3H_4$ (displaced from the $^3F_3$ by $\sim$1800 cm^{-1}) requires the assistance of a low number of host phonons [33,34]. Therefore, the intensity of the $^3H_4{\rightarrow}^3H_6$ transition is higher under the excitation with the

low energy photons than when observed by visible or UV excitation. In the latter case a preferential radiative depopulation of the higher energetic levels (separated from the lower lying levels by a high energetic gap) is expected to occur, as also reported by Pandozzi *et al* [34]. From the UC luminescence spectra it is seen that, at RT, a fourth non-resonant energy transfer occurs in the Tm^{3+} ions involving the population of the $^1D_2$ level since the blue $^1D_2{\rightarrow}^3F_4$ and the UV $^1D_2{\rightarrow}^3H_6$ transitions were identified.
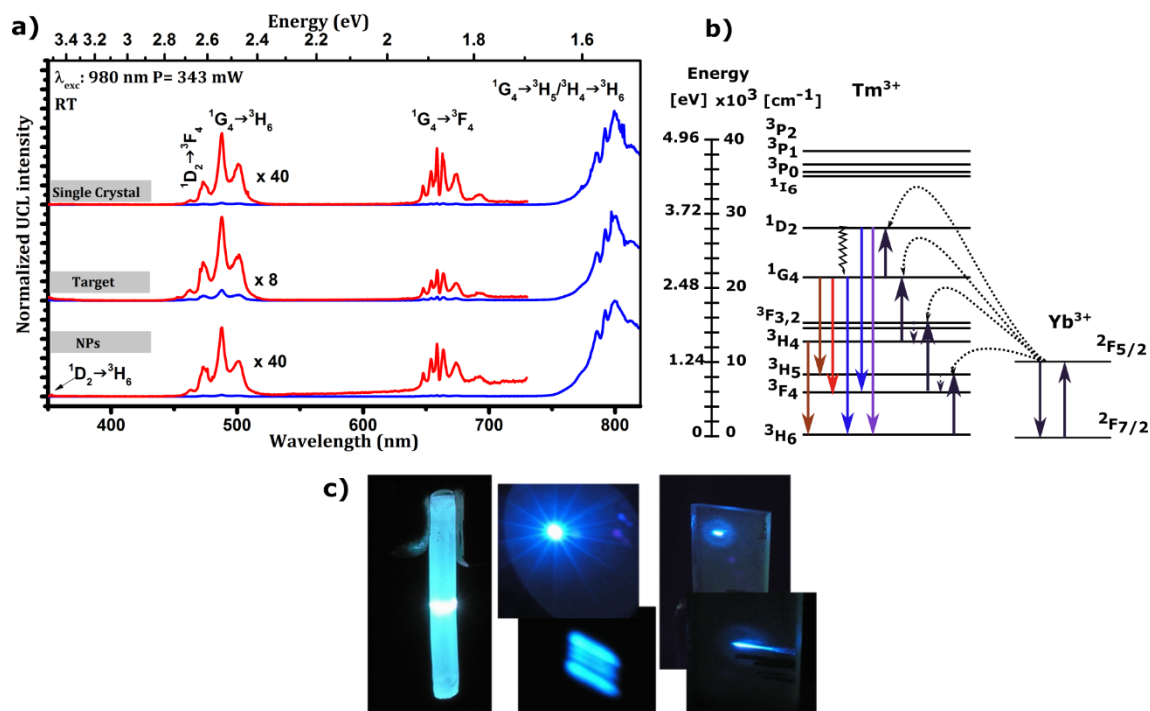

Figure 8.10. a) RT PL spectra of the YSZ:Tm^{3+},Yb^{3+} samples in air upon 980 nm photon excitation. c) Partial energy level diagram of Tm^{3+} and Yb^{3+} with excitation and emission process after 980 nm photon excitation. c) Photos of the single crystal (left), target (middle) and PLAL produced NPs deposited in a sapphire substrate (right) under 980 nm excitation at RT.

Particularly, for bioimaging purposes, the intense $^1G_4{\rightarrow}^3H_5$/$^3H_4{\rightarrow}^3H_6$ transitions of Tm^{3+}, located ~800 nm, well within the biological window, is of upmost importance [35]. As mentioned in Chapter 2, NIR wavelength leads to a deeper light penetration in the biological tissues and a high image contrast due to the absence of the tissue autofluorescence background and reduced light scattering [35]. Although in the studied spectral region the infrared emission is the strongest one, in the visible spectral region the blue emission is the most intense and is responsible for the blue appearance of the samples observed with the unaided eye at RT, when pumped with 980 nm light (Figure 8.10 c).

An in-depth comprehension of the UCL mechanisms for the YSZ:Tm³⁺,Yb³⁺ samples was obtained through the investigation of the power excitation dependence of the UC luminescence intensity as shown in Figure 8.11 a), b) and c) for the single crystal, the ceramic target and NPs, respectively.
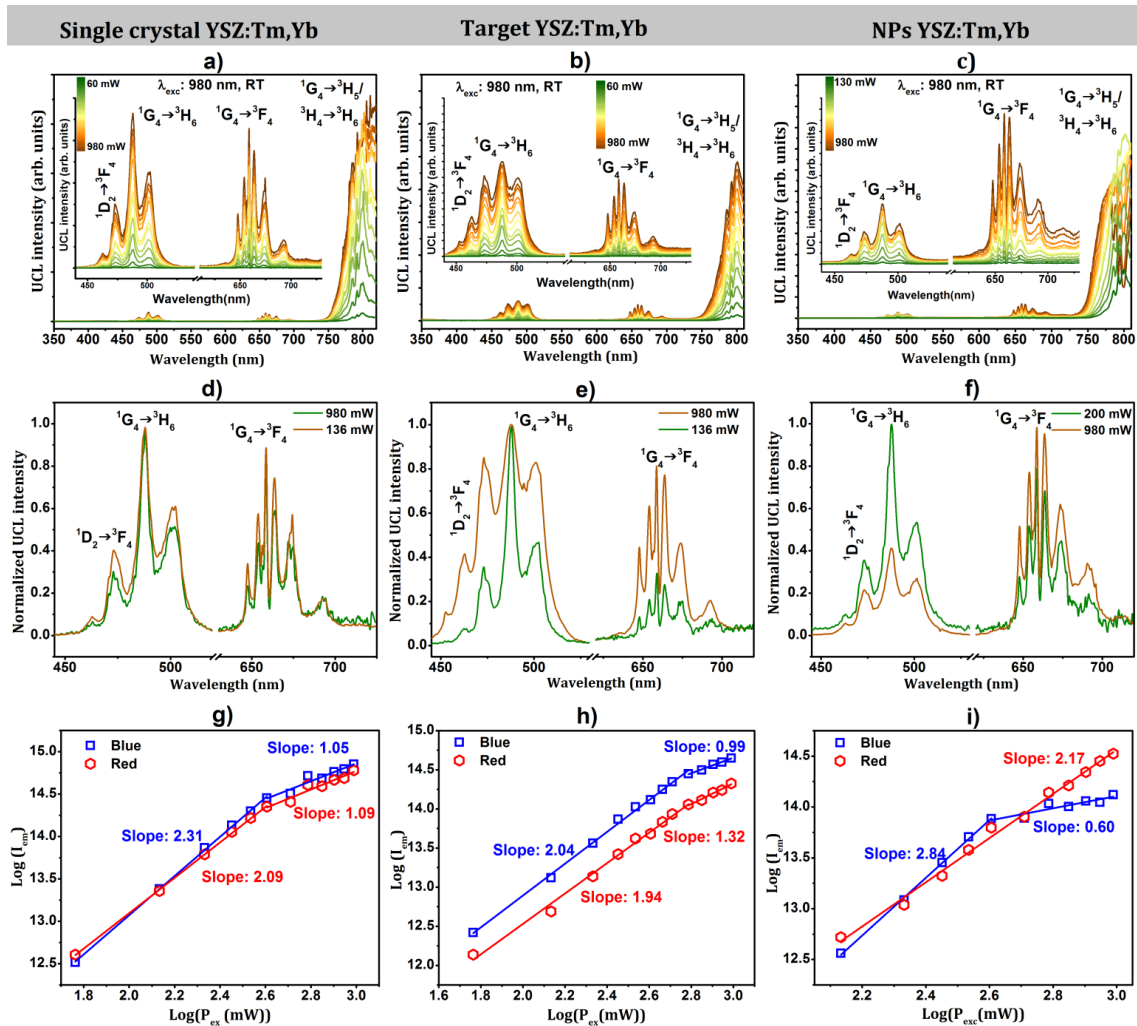
Figure 8.11. Dependence of the UC luminescence intensity with the excitation power in the YSZ:Tm³⁺,Yb³⁺ single crystal (a), target (b) and NPs (c). d), e) and f) comparison of the visible luminescence upon lower and high power excitation and g), h) and i) linear dependence in a log-log representation of the UC luminescence intensity with the excitation power and respective slopes. The measurements were realized with the samples at the atmospheric pressure

As can be identified, within the incident light power range studied, the overall UC luminescence intensity was found to increase with the pump power. However, as one can see in Figure 8.11 d), e) and f), where the normalized PL spectra under lower and higher power excitations are compared, such increase in the visible UC luminescence intensity follows distinct trends for single crystals, targets and NPs. For the single crystal, the

normalized spectra under lower and higher power excitations are almost overlapped, in all the visible spectral range. This means that the increase in the power pumping results in an almost equal increase in the intensity of the blue and red upconverted light. However, it is possible to observe that for the higher power excitation the ratio between the red and blue luminescence slightly increases when compared to the lower power excitation. Moreover, looking at the blue emission, a slight change in the intensity ratio between the emissions arising from the different energy levels is also observed with the increase in power excitation. This effect is much more pronounced for the ceramic target and NPs due to heating effects as discussed later on. In the ceramic target, the increase in power excitation leads to a strong increase of the intensity ratio between the red and blue luminescence, compared to the lower power excitation. Additionally, a broadening of the blue emission is also observed for the higher power excitation due to the changes in the relative intensities of the $^1D_2 \rightarrow ^3F_4$, and $^1G_4 \rightarrow ^3H_6$ transitions. In the case of the NPs, the increase in the power excitation originates a reversed change in the dominant emission, as seen by the change in the intensity ratio between the red and blue light. An n value of 3 and 4 is expected for the population of the $^1G_4$ and $^1D_2$ multiplets by excitation with 980 nm photons, as shown in the energy diagram in Figure 8.10 b). The log–log plots of the blue and red integrated UC luminescence as a function of the excitation power for the YSZ:Tm^{3+},Yb^{3+} single crystal, target and NP samples presented in Figure 8.11 g)-i) show two main regimes. In the first regime, with a lower power excitation, both the blue and red light show a pronounced increase. A slope of ~2 was found for the single crystals and targets for both transitions indicating saturation effects in the feeding levels. In the case of the heated NPs, a slope of ~3 reflects the increase in the population of the $^1D_2$ multiplet being, however, accompanied by saturation. The experimental slopes are lower than the expected number of absorbed photons, as also documented in the literature for different host lattices, [36,37] including co-doped ZrO$_2$ nanocrystals [15]. After a certain power threshold, a second regime is observed. In this higher excitation power regime, the increase of the integrated UC luminescence intensity with the excited power saturates, as evidenced by the calculated slope value (near 1). In the single crystal both blue and red emission follow almost the same trend in both regimes, and no significant changes are observed in the relative emission intensities. In the ceramic target the blue and red intensity follows different trends after the power threshold, evidencing a higher saturation effect for the blue light, explaining the increase in the intensity ratio between the red and blue transitions for higher power excitation. The effect of the saturation of blue light is enhanced in the case of NPs as shown by a slope of ~0.6, explaining the change in the dominant emission colour for the PLAL NPs. Due to the nonlinear effect of the upconversion, for higher power excitation conditions

(when the upconversion rates are large) saturation effects are expected, explaining the deviation of the measured *n* values when compared with the predicted ones [23,26,27,31,38]. Additionally, the nanosized YSZ particles exhibit a higher heating than larger materials resulting in a pronounced saturation effect for higher excitation powers.

The temperature dependence of the upconverted emission for the YSZ:Tm[3+],Yb[3+] single crystal and target was investigated with the samples in an evacuated cryostat in the temperature range between 12 K and 300 K, as shown in Figure 8.12. The case of the NPs will be discussed later on. With the used incident light power, the overall intensity was found to increase with temperature for both samples, which can be explained by an additional feeding of the emitting levels. Particularly, a notable rise of the intensity of the high energy transitions arising from the $^1G_4$ and $^1D_2$ multiplets is clearly identified with the increase of temperature, as can be well identified in the 14 K and RT normalized PL spectra shown in Figure 8.13. The temperature dependence of the UC luminescence intensity is well accounted for by a thermal population law described by a classical Boltzmann distribution defined by *Eq.* 8.16 [39], where *T* is the absolute temperature, *I(T)* and I_0 stand for the UC luminescence integrated intensity at a given temperature *T* and 10 K, respectively (assuming negligible nonradiative processes at low temperatures), *C* corresponds to the ratio of the electronic levels and the effective degeneracies, k_B is the Boltzmann constant and E_a is the activation energy for the thermal population.

$$\frac{I(T)}{I_0} = 1 + C \cdot e^{-\frac{E_a}{k_B(T-T_0)}} \qquad Eq.\,8.16$$

Figure 8.12 b) and d) display the dependence of the blue and red integrated intensity with the temperature, with the full lines corresponding to the theoretical fits according to *Eq.* 8.16, for the single crystal and the target, respectively. Activation energies of ca. ~10 meV and 30 meV were obtained for the thermal population of the blue and red emitting states for the single crystal and the target, respectively, likely due to phonon absorption/emission energy compensation mechanisms as discussed by Auzel [23,27,31]. The estimated values match well with the low energy phonons of the YSZ host, found in the Raman spectra, responsible for the material thermal conductivity. For these large sized materials (single crystal and targets) the thermal dissipation process is realized via multiphonon nonradiative processes.

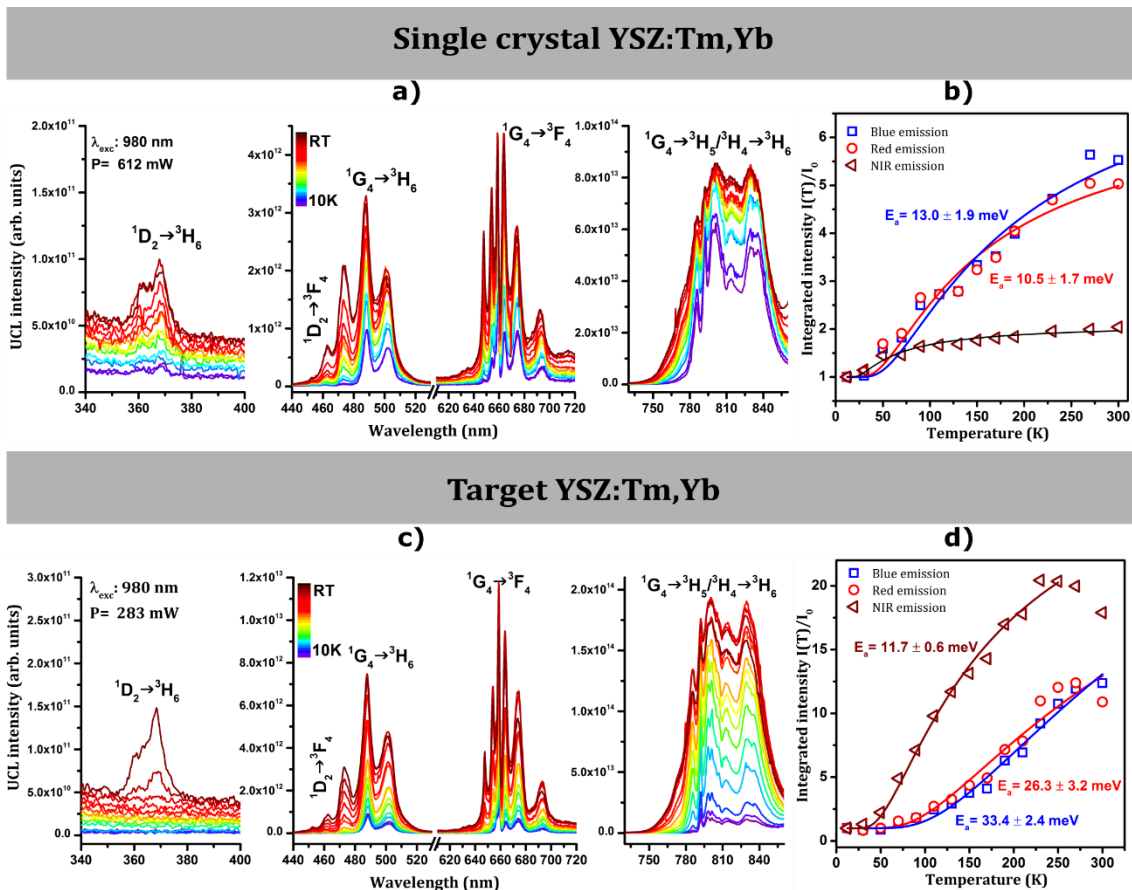**Figure 8.12.** a) and c) Temperature dependence of the PL spectra, with 980 nm excitation, of the single crystal and target, respectively. b) and d) Temperature dependence of the integrated intensity of the red, and NIR green emission for the single crystal and target, respectively.
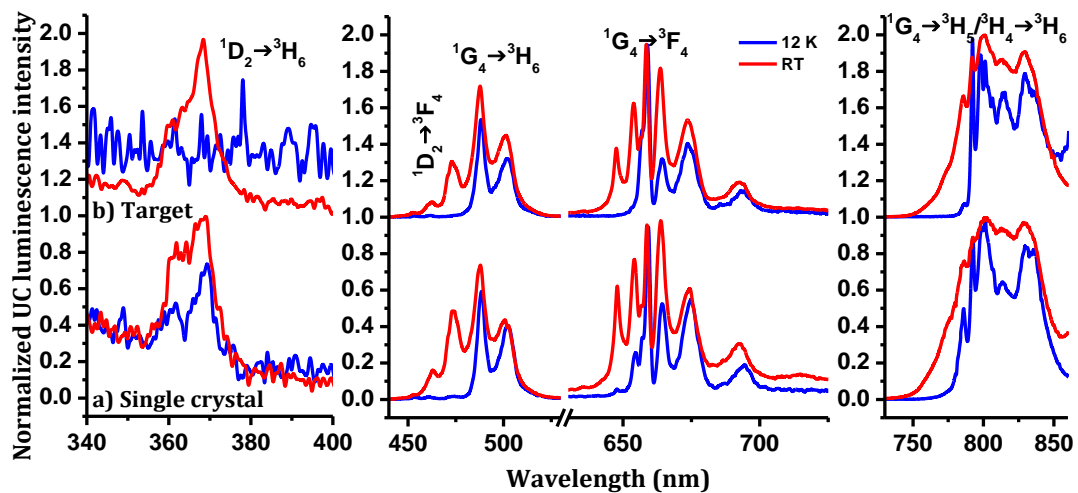

Figure 8.13. Comparison between the normalized PL spectra at 12 K and RT of the single crystals (a) and targets (b).

Anti-Stokes Blackbody radiation

Unlike that observed in the single crystal and in the target, the RT UC luminescence of the NPs was found to be strongly sensitive to the samples environment pressure conditions (air and vacuum, ~10^{-3} mbar) and incident power excitation as shown in Figure 8.14.
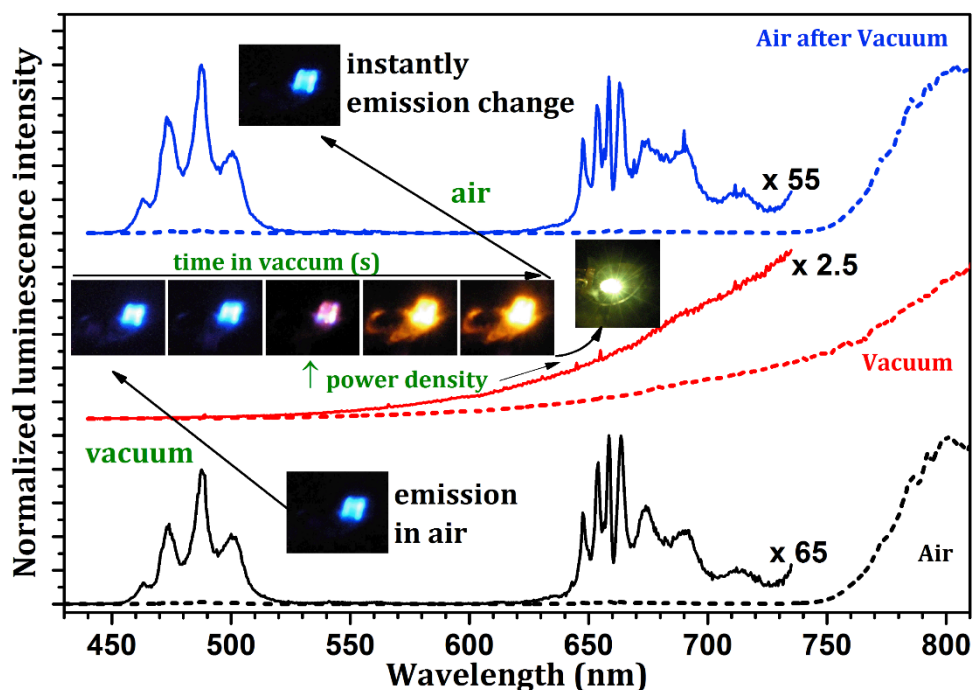

Figure 8.14. RT PL spectra of the NPs upon 980 nm excitation performed in air (black lines), in vacuum (red lines) at 10^{-3} mbar and in air after vacuum (blue lines). The dashed lines are the PL spectra in the spectral range between range 440 and 810 nm and the solid lines are magnifications of the same PL spectra in the visible region. Inserted in the figure are photos of the sample when pumped with 980 nm photons in the different atmospheric condition.

In air, the blue and red NPs upconversion luminescence (black lines in Figure 8.14) exhibits the same behaviour of the single crystal and the target. Independently of the used incident excitation power the blue light is the dominant colour as observed by the naked eye. Under vacuum, in few seconds, a gradual colour change from blue to yellow/orange is observed for the NPs upconverted emission (photos in Figure 8.14). This effect is totally reversible, with further air replenishments in the cryostat, with a prompt change of the UC luminescence to blue light (upper spectrum in Figure 8.14) showing a non-contact colour-pressure sensor behaviour. In contrast to the line spectra measured for the Tm^{3+} intraionic emission, the NPs anti-Stokes radiation measured after a few seconds of keeping the samples under vacuum, corresponds to an almost unstructured continuous broad band. The ratio of these two broad band/intraionic anti-Stokes processes was found to be dependent on the used power

excitation conditions and material dimensions as shown in Figure 8.15, being enhanced for the NPs. Particularly, in this case, an increase of the broad band intensity was observed with increasing excitation power. The same effect was observed to a minor extent in the ablated area of the targets, whereas no difference was detected for the UC luminescence in single crystals under air and vacuum atmospheres.
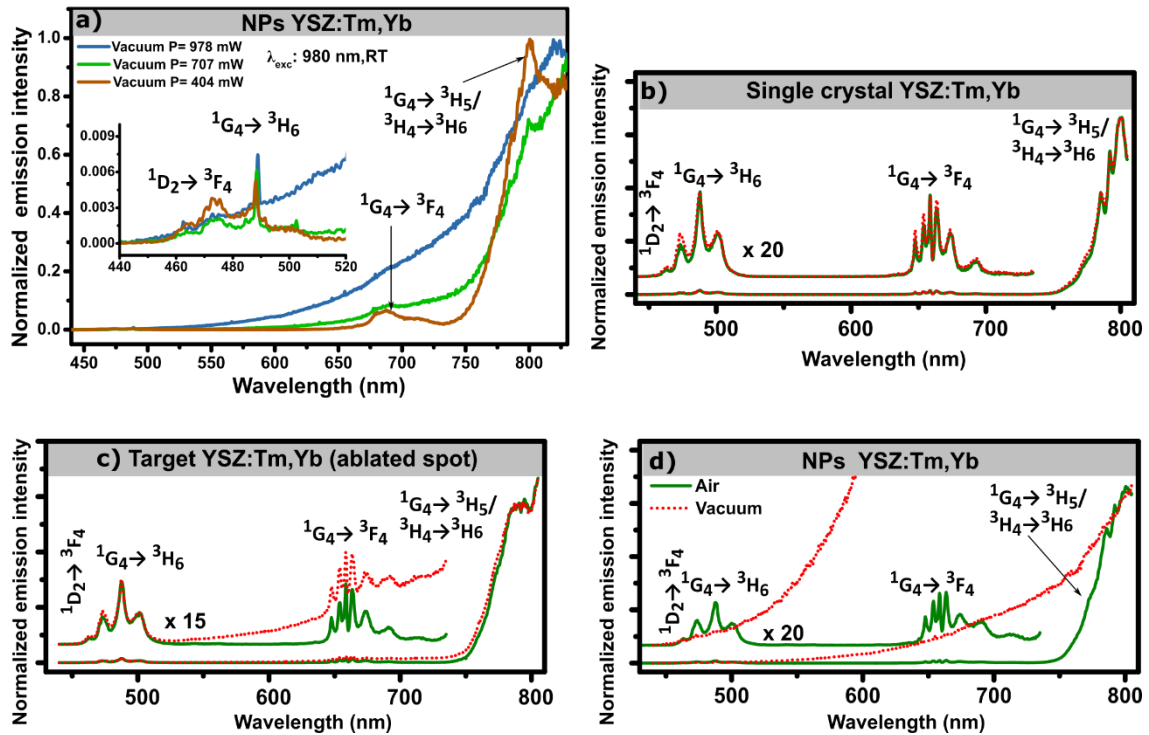

Figure 8.15. a) RT PL spectra of NPs, obtained with 980 nm photon excitation, performed in vacuum (10^{-3} mbar) at different power excitation showing the changes in the intensity ratio of the UCL broad band/Tm^{3+} luminescence. Comparison of the UCL acquired at atmospheric pressure in air and vacuum, for the single crystal (b), target (c) and NPs (d).

These results suggest that the phenomenon is related to material size reduction, namely with the way the heat is dissipated on the NPs. It is well established that reducing the material size implies a strong modification of the material physical properties. Particularly, a discrete phonon density of states is expected for the nanocrystals as well as a cut-off of the acoustic phonons [40]. Recently, in distinct classes of undoped and doped nanomaterials with reduced thermal conductivity (YSZ is a thermal barrier coating with typical values of 0.02–0.03 W cm^{-1} K for thermal conductivity [41]), anti-Stokes broad unstructured bands have been reported in different spectral regions [42–55], when the samples are excited with NIR photons. The anti-Stokes broad band has been discussed based on two main models: blackbody radiation [42–48] and the photon avalanche mechanism [49–54]. Typically, the emission is enhanced under vacuum conditions. Under such reduced pressure conditions,

the samples can only dissipate absorbed energy from the incident laser as radiation. On the other hand, for higher pressures, alternative mechanisms of heat dissipation such as gas collisions result in the quenching of the broad band emission. Accordingly, the emission intensity is expected to decrease exponentially with increasing pressure as reported in literature [44,46,47,50–52]. Low pressures and strong excitations were found to promote the observation of the broad band [42] as identified in the studied NPs. In order to gain insights into the nature of the anti-Stokes broad band, additional measurements were performed on nominally undoped YSZ and YSZ:Er^{3+},Yb^{3+} NPs with identical dimensions, as shown in Figure 8.16. As one can see, the observation of the broad band is independent of the presence of lanthanide ions (Figure 8.16 a)-c), suggesting that the observed anti-Stokes band is due to thermal radiation of the NPs. The broad emissions observed in the Tm,Yb and Er,Yb co-doped YSZ NPs and in the undoped YSZ produced by PLAL, acquired upon different 980 nm laser power excitation (depicted in Figure 8.16 a), b) and c), respectively) were well described by the Planck's law of blackbody radiation defined by *Eq*. 8.17 (black dot curves in the figures), where *I* is the spectral radiance that is proportional to the intensity of the radiation, λ the wavelength, *c* the vacuum speed of light, *h* and k_B the Planck's and Boltzmann's constants, respectively, and *T* the absolute temperature [45].

$$I(\lambda, T) = \frac{2\pi hc^2}{\lambda^5 \left(\exp\left(\frac{hc}{\lambda k_B T}\right) - 1\right)} \qquad Eq.\,8.17$$

The absolute temperature of the blackbody radiation revealed to be very dependent on laser powder excitation and focusing conditions and increases with powers excitation. These results confirm the blackbody radiation nature of the anti-Stokes broad emission observed in the NPs produced by PLAL.

It was also observed that for a fixed incident power the intensity of the unstructured band intensity increases monotonically with increasing wavelength and the band maxima of the emission (limited by the detector cut-off) exhibits a shift to high energies with increasing incident laser power (Figure 8.16 d), as expected for a blackbody radiation behaviour. A supralinear dependence of the band intensity on the incident power excitation is in fair agreement with other recently published studies [44,46]. On the other hand, this model was also supported by the excitation and deexcitation transients of the emitted radiation (Figure 8.16 e). As expected for a blackbody radiation the excitation transients evidence a long rise time when compared with the decay lifetime [44]. Figure 8.16 f) gives additional support for the blackbody radiation model of the anti-Stokes broad band. A near constant intensity of the emission when the cryostat temperature is cooled down from RT to 10 K was observed.

As expected, such behaviour indicates that the emitted radiation is nearly insensitive to the measured cryostat temperature. Similar findings were reported by Strek *et al*. [51]. However, in this case the authors assign the broad emission to a CT-lanthanide model supported by photoconductivity data, in analogy with other cases [55].
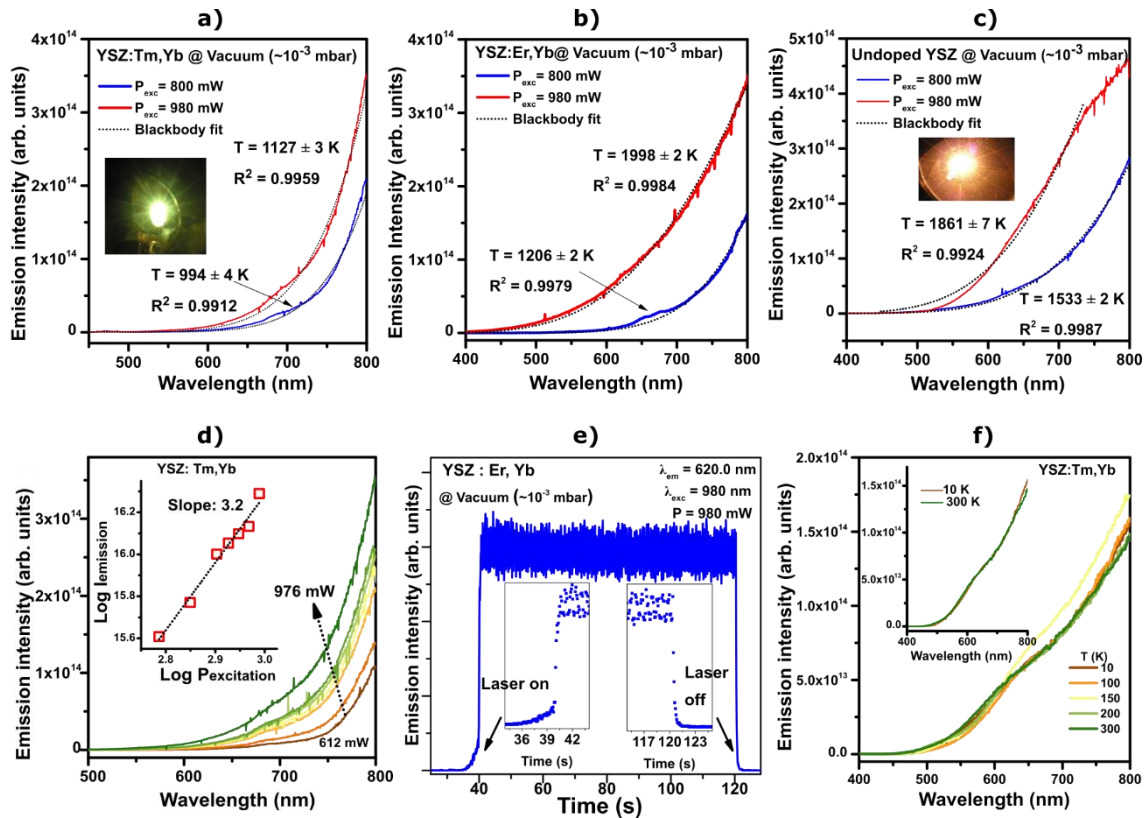

Figure 8.16. a), b) and c) Broad emission band acquired under two different infrared laser powers excitation in YSZ:Tm³⁺,Yb³⁺, YSZ:Er³⁺,Yb³⁺ and YSZ NPs, respectively, produced by PLAL. Black dot curves in the figures represent the fit of the broad emission to the Planck's law of blackbody radiation. The calculated temperatures are indicated in the figures. d) Power excitation dependence of the broad emission in the YSZ:Tm³⁺,Yb³⁺ NPs. Inset in the figure shows the excitation power dependence of the integrated broad emission. e) Excitation and deexcitation transients of the emitted radiation in the YSZ:Er³⁺,Yb³⁺ NPs. f) Temperature dependence of the broad emission band in YSZ:Tm³⁺,Yb³⁺ NPs. Inset in the figure shows a comparison between the emission spectra acquired at 10 K and 300 K.

The high potentialities of the anti-Stokes blackbody radiation appear to be unquestionable. For instance, intense white emission was observed under IR laser excitation in some oxide hosts paving the way for an alternative approach to efficiently generate white light [46,47], displays and IR detection. Additionally, in an ytterbium doped ZrO_2 host, the conversion of low-energy solar photons into high energetic ones through thermal radiation with power efficiencies of 16% was recently reported by Wang *et al.* [42] opening the way for the use of such radiation in photovoltaic developments. Moreover, and as evidenced in this work, the

pressure dependence colour-tuning is of upmost interest for the development of non-contact pressure sensors.

Summary

Intense NIR emission and visible blue light was observed upon infrared excitation in Tm^{3+}, Yb^{3+} co-doped crystals, ceramic target and NPs, produced by LFZ, sintering of SCS powders and PLAL, respectively. UC emission was investigated as a function of the incident power excitation. Two regimes were found for the blue and red light for single crystals and targets with slopes of ~ 2 and 1, respectively. The saturation effects were found to be more pronounced for the blue light of the YSZ:Tm^{3+},Yb^{3+} NPs. The temperature dependence of the UC luminescence was investigated for single crystals and targets. An overall increase of the integrated intensity was found on account of the thermal activated processes described by activation energies of 10 meV and 30 meV for the single crystal and the target, respectively. The estimated energy values are well within the expected values for the low energy phonons in the YSZ host, responsible for the thermal conductivity in large dimension materials. In the case of the NPs, the upconverted luminescence undergoes a change of colour from blue to orange in seconds when the samples are placed under vacuum, and to white for high power IR excitation. Simultaneously, the spectral shape of the emitted radiation under vacuum corresponds to an unstructured wide band starting in the visible and extending to the infrared region. The anti-Stokes blackbody radiation was found to be dependent on the incident photon energy power level, pressure and material size dimensions. The effect is enhanced for the nanosized particles as in such case the thermal conduction can be neglected in favour of the thermal radiation. A reversible effect, with a dominant blue light occurs when the NPs are again exposed to air ambience. As shown in the present work, the UC luminescence of lanthanide co-doped YSZ NPs evidence high potentialities for luminescence based sensors aiming biomedical applications. Additionally, the new findings on the continuous upconversion emission are of high importance as alternative approaches for lighting, photovoltaic and pressure-based sensors applications.

8.3 Conclusions

ZrO_2 and YSZ hosts doped with Er ions and co-doped with Tm, Yb and Er, Yb trivalent ions, produced by simple, fast and one-step procedures, were found to exhibit interesting UC luminescence, under excitation within the biological optical window (980 nm). The optical activation of different concentration of Er^{3+} ions in zirconia samples, leads to tuneable UC

emission colour, from green to red with increasing dopant concentration. This behaviour was explained based on the interactions enhancement between close neighbours ions in highly doped samples that promote energy transfer processes between then, such as cross-relaxation mechanism, which favours the population of the red emitting level. The same effect was observed in Er^{3+}, Yb^{3+} co-doped ZrO_2 powders produced by SCS, in which Yb^{3+} concentration was increased. Such results evidence that the interaction between close neighbour's ions that leads to the preferential population of the red emitting level occurs not only between Er^{3+} ions, but also via Yb^{3+} ions. The study of the UC luminescence in Er lightly doped and Er^{3+}, Yb^{3+} co-doped samples (crystal, target and NPs), with visual green emission at RT, shows that the sensitized luminescence of Er^{3+} via Yb^{3+}, in the YSZ host can be increased by ~3 times (for an activator: sensitizer atomic ratio of 1:1) when compared to the emission of the doped samples. This increase is promoted by the high cross section absorption of Yb^{3+} to 980 nm radiation, and evidence an efficient energy transfer process between Yb^{3+} and Er^{3+} ions in the YSZ crystal, ceramic targets and NPs. Intense blue and NIR UC luminescence in Tm^{3+}, Yb^{3+} co-doped YSZ crystals, ceramic targets and NPs, was achieved at RT under 980 nm photon irradiation. In particular, the observed intense NIR to NIR emission in the PLAL NPs, well within the biological optical window, is of upmost interest for *in vivo* biodetection and bioimaging. In the single crystal and ceramic targets an overall increase in the visible and NIR emission was observed between 12 K and RT. On the other hand, an intense yellow/white anti-Stokes blackbody radiation was found in the co-doped NPs when these are submitted to vacuum conditions, with 980 nm photon excitation. The same phenomena was observed in undoped YSZ and Er^{3+}, Yb^{3+} co-doped YSZ NPs, and was explained based on a strong increase of the temperature in the nanostructured YSZ material in the absence of a thermal dissipation medium. The anti-Stokes blackbody radiation shown to be dependent on the incident photon energy power level, pressure and material size dimensions, and could result in alternative approach for lighting technologies, photovoltaic and pressure-based sensors applications.

References

[1] F. Zhang, *Photon Upconversion Nanomaterials*; Springer: Ottawa, Ontario, Canada, 2015.

[2] M. Bettinelli, L. Carlos, X. Liu, *Phys. Today* **2015**, *68*, 38.

[3] F. Auzel, *CR Acad Sci B Paris* **1966**, *262*, 1016.

[4] V. V. Ovsyankin, P. P. Feofilov, *Sov. J. Exp. Theor. Phys. Lett.* **1966**, *3*, 322.

[5] M. Haase, H. Schäfer, *Angew. Chem. Int. Ed.* **2011**, *50*, 5808.

[6] F. Vetrone, J. A. Capobianco, *Int. J. Nanotechnol.* **2008**, *5*, 1306.

[7] F. Gonell, M. Haro, R. S. Sánchez, P. Negro, I. Mora-Seró, J. Bisquert, B. Julián-López, S. Gimenez, *J. Phys. Chem. C* **2014**, *118*, 11279.

[8] J. A. Capobianco, F. Vetrone, J. C. Boyer, A. Speghini, M. Bettinelli, *J. Phys. Chem. B* **2002**, *106*, 1181.

[9] F. Vetrone, J.-C. Boyer, J. A. Capobianco, A. Speghini, M. Bettinelli, *J. Appl. Phys.* **2004**, *96*, 661.

[10] J. A. Capobianco, F. Vetrone, T. D'Alesio, G. Tessari, A. Speghini, M. Bettinelli, *Phys. Chem. Chem. Phys.* **2000**, *2*, 3203.

[11] M. Liu, S. W. Wang, J. Zhang, L. Q. An, L. D. Chen, *Opt. Mater.* **2007**, *29*, 1352.

[12] F. Vetrone, J. C. Boyer, J. A. Capobianco, A. Speghini, M. Bettinelli, *J. Phys. Chem. B* **2002**, *106*, 5622.

[13] V. Venkatramu, D. Falcomer, A. Speghini, M. Bettinelli, C. K. Jayasankar, *J. Lumin.* **2008**, *128*, 811.

[14] V. Mahalingam, F. Mangiarini, F. Vetrone, V. Venkatramu, M. Bettinelli, A. Speghini, J. A. Capobianco, *J. Phys. Chem. C* **2008**, *112*, 17745.

[15] A. Patra, S. Saha, M. A. R. C. Alencar, N. Rakov, G. S. Maciel, *Chem. Phys. Lett.* **2005**, *407*, 477.

[16] A. Patra, C. S. Friend, R. Kapoor, P. N. Prasad, *J. Phys. Chem. B* **2002**, *106*, 1909.

[17] Luis A. Gómez, L. de S. Menezes, C. B. de Araújo, R. R. Gonçalves, S. J. L. Ribeiro, Y. Messaddeq, *J. Appl. Phys.* **2010**, *107*, 113508.

[18] D. Solis, E. D. la Rosa, O. Meza, L. A. Diaz-Torres, P. Salas, C. Angeles-Chavez, *J. Appl. Phys.* **2010**, *108*, 023103.

[19] J. Chen, J. X. Zhao, *Sensors* **2012**, *12*, 2414.

[20] D. Tu, W. Zheng, Y. Liu, H. Zhu, X. Chen, *Coord. Chem. Rev.* **2014**, *273–274*, 13.

[21] M. V. DaCosta, S. Doughan, Y. Han, U. J. Krull, *Anal. Chim. Acta* **2014**, *832*, 1.

[22] W. Zheng, P. Huang, D. Tu, E. Ma, H. Zhu, X. Chen, *Chem. Soc. Rev.* **2014**.

[23] F. Auzel, *Chem. Rev.* **2004**, *104*, 139.

[24] J. F. Suijver, In *Luminescence*; Ronda, C., Ed.; Wiley-VCH Verlag GmbH & Co. KGaA, 2007; pp. 133–177.

[25] H. Dong, L.-D. Sun, C.-H. Yan, *Chem. Soc. Rev.* **2015**, *44*, 1608.

[26] M. Pollnau, D. R. Gamelin, S. R. Lüthi, H. U. Güdel, M. P. Hehlen, *Phys. Rev. B* **2000**, *61*, 3337.

[27] F. E. Auzel, *Proc. IEEE* **1973**, *61*, 758.

[28] F. Vetrone, J.-C. Boyer, J. A. Capobianco, A. Speghini, M. Bettinelli, *Appl. Phys. Lett.* **2002**, *80*, 1752.

[29] J. C. Wright, In *Radiationless Processes in Molecules and Condensed Phases*; Topics in Applied Physics; Springer Berlin Heidelberg, 1976; pp. 239–295.

[30] G. Liu, B. Jacquier, *Spectroscopic Properties of Rare Earths in Optical Materials*; Springer, 2006.

[31] F. Auzel, P. A. Santa-Cruz, G. F. de Sá, *Rev. Phys. Appliquée* **1985**, *20*, 273.

[32] H. Lu, W. P. Gillin, I. Hernández, *Phys. Chem. Chem. Phys. PCCP* **2014**, *16*, 20957.

[33] F. W. Ostermayer, J. P. van der Ziel, H. M. Marcos, L. G. Van Uitert, J. E. Geusic, *Phys. Rev. B* **1971**, *3*, 2698.

[34]   F. Pandozzi, F. Vetrone, J.-C. Boyer, R. Naccache, J. A. Capobianco, A. Speghini, M. Bettinelli, *J. Phys. Chem. B* **2005**, *109*, 17400.

[35]   N.-N. Dong, M. Pedroni, F. Piccinelli, G. Conti, A. Sbarbati, J. E. Ramírez-Hernández, L. M. Maestro, M. C. Iglesias-de la Cruz, F. Sanz-Rodriguez, A. Juarranz, F. Chen, F. Vetrone, J. A. Capobianco, J. G. Solé, M. Bettinelli, D. Jaque, A. Speghini, *ACS Nano* **2011**, *5*, 8665.

[36]   S. Xu, W. Xu, Y. Wang, S. Zhang, Y. Zhu, L. Tao, L. Xia, P. Zhou, H. Song, *Nanoscale* **2014**, *6*, 5859.

[37]   L. An, J. Zhang, M. Liu, S. Wang, *J. Alloys Compd.* **2008**, *451*, 538.

[38]   H. U. Gudel, M. Pollnau, *J. Alloys Compd.* **2000**, *303*, 307.

[39]   C. Nico, R. Fernandes, M. P. F. Graça, M. Elisa, B. A. Sava, R. C. C. Monteiro, L. Rino, T. Monteiro, *J. Lumin.* **2014**, *145*, 582.

[40]   G. Liu, X. Chen, In *Handbook on the Physics and Chemistry of Rare Earths*; Karl A. Gschneidner, J.-C. B. and V. K. P., Ed.; Elsevier, 2007; Vol. 37, pp. 99–169.

[41]   A. M. Limarga, S. Shian, M. Baram, D. R. Clarke, *Acta Mater.* **2012**, *60*, 5417.

[42]   J. Wang, T. Ming, Z. Jin, J. Wang, L.-D. Sun, C.-H. Yan, *Nat. Commun.* **2014**, *5*, 5669.

[43]   S. Redmond, S. C. Rand, X. L. Ruan, M. Kaviany, *J. Appl. Phys.* **2004**, *95*, 4069.

[44]   P. Roura, J. Costa, M. López-de Miguel, B. Garrido, J. Fort, J. R. Morante, E. Bertran, *J. Lumin.* **1998**, *80*, 519.

[45]   M. L. Debasu, D. Ananias, I. Pastoriza-Santos, L. M. Liz-Marzán, J. Rocha, L. D. Carlos, *Adv. Mater.* **2013**, *25*, 4817.

[46]   G. Bilir, B. Di Bartolo, *Opt. Mater.* **2014**, *36*, 1357.

[47]   G. Bilir, G. Ozen, J. Collins, M. Cesaria, B. Di Bartolo, *IEEE Photonics J.* **2014**, *6*, 1.

[48]   W. Chen, Y. Shi, Z. Chen, X. Sang, S. Zheng, X. Liu, J. Qiu, *J. Phys. Chem. C* **2015**, *119*, 20571.

[49]   J.-F. Bisson, D. Kouznetsov, K.-I. Ueda, S. T. Fredrich-Thornton, K. Petermann, G. Huber, *Appl. Phys. Lett.* **2007**, *90*, 201901.

[50]   J. Wang, P. A. Tanner, *J. Am. Chem. Soc.* **2010**, *132*, 947.

[51]   W. Strek, L. Marciniak, A. Bednarkiewicz, A. Lukowiak, R. Wiglusz, D. Hreniak, *Opt. Express* **2011**, *19*, 14083.

[52]   L. Marciniak, W. Strek, A. Bednarkiewicz, D. Hreniak, M. C. Pujol, F. Diaz, *J. Lumin.* **2013**, *133*, 57.

[53]   W. Strek, L. Marciniak, P. Gluchowski, D. Hreniak, *Opt. Mater.* **2013**, *35*, 2013.

[54]   W. Strek, L. Marciniak, D. Hreniak, A. Lukowiak, *J. Appl. Phys.* **2012**, *111*, 024305.

[55]   C. Brandt, S. T. Fredrich-Thornton, K. Petermann, G. Huber, *Appl. Phys. B* **2011**, *102*, 765.

Chapter 9.

Perspectives of applications

In this chapter the perspectives of applications of the produced luminescent materials are envisaged.

ZrO$_2$ and YSZ materials doped with different trivalent lanthanides, displaying intense and tuneable emission colours depending on dopant nature and dopant concentration were successfully produced by simple, fast and easy to scale up techniques. Even if additional characterization, including the measurements of the quantum yield of the produced luminescent materials, are required before further application, the characteristics of the produced materials evidence their potential for several optical-based applications, including for lighting, sensor and bioapplications.

Regarding lighting and displays applications, the intense emission of the produced phosphors, in particular the ones doped with Eu^{3+}, Tb^{3+}, Pr^{3+}, or Dy^{3+} could be very attractive for further consideration for phosphor converted LED or other lighting technologies based on luminescent materials. In particular, these materials could be of particular interest for applications in aggressive work environments, taking advantage of the chemical, thermal and mechanical stability of the selected host. However, additional measurements, for example regarding the stability of the Ln^{3+} in the zirconia hosts at high temperatures should be performed. The most promising result regarding lighting application is, undoubtedly, the one obtained in Dy^{3+} doped crystals. The strong white emission achieved in this crystal under UV excitation could consist in an alternative strategy for white light generation. Once again, information of quantum yield is fundamental for further practical applications. White light generated by a single phosphor, could be advantageous since it does not requires any adjust of phosphors concentration in order to get a white light, allowing a better reproducibility of colour in different pc-LEDs. Moreover, problems associated to differential variations of the different colour components in a multicolour-based device due to, for example, changes in temperature, could be avoided by using a single white phosphor. In addition, in the YSZ:Dy^{3+} phosphor the white light can be adjusted from a more cold to a more warm by selecting the appropriated excitation wavelength. As referred in the second chapter of this work, usually phosphors are applied in the pc-LED in a powder form, embedded in an epoxy or silicon resin. Several problems are associated to this type of pc-LEDs configuration, in particular in the high power LEDs. The encapsulating resin highly limits the work conditions of the LEDs, as it requires high chemical, photo and thermal stability, in order to prevent aging effects. The aging of the resin affects not only the intensity of the emitted light by the device but also the colour characteristics of the emitted radiation, including the CRI and CCT. Nowadays, an intense research in the development and improvements of LEDs is dedicated to find ways to surpass the limitation associated with the use of encapsulating resins. An interesting strategy to surpass these problems consists in the use of a thin slice of a single crystal on the surface of the chip LED instead of the

powders embedded in a resin. Besides the improved physical and chemical stability of the single crystals, higher quantum efficiency can be achieved due to the absence of grains boundaries losses in the single crystal comparatively to the powders. This concept was firstly proposed in 2013 by the group of K. Shimamura [1,2], which used a yellow emitting single crystal of YAG: Ce, Gd on the top of a 455 nm commercial LED to produce white light. The same strategy could be explored to produce white light using the YSZ:Dy^{3+} single crystal on the top of a UV LED, as schematically represented in Figure 9.1.
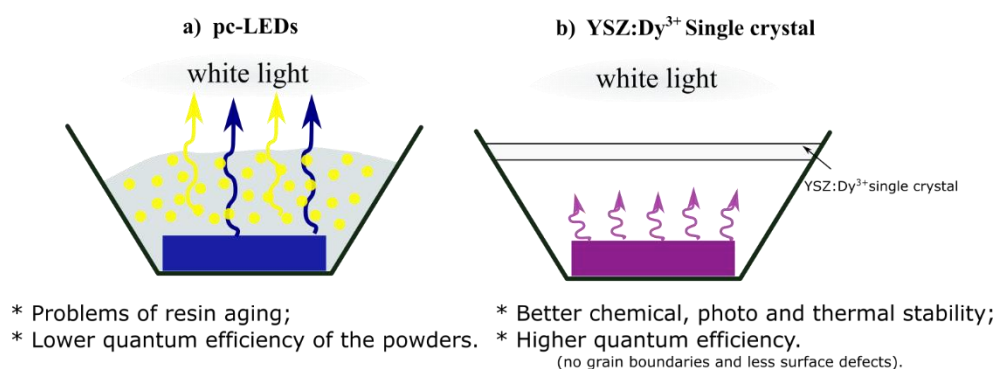
Figure 9.1. Schematic representation of the pc-LED configuration using a powder phosphor (a) and an YSZ:Dy^{3+} single crystal layer (b).

In addition, the NPs produced by PLAL show a high potential to be used as bioprobes for both *in vivo* and *in vitro* assays. In particular, downshifted luminescent YSZ NPs doped with Tb^{3+} and Eu^{3+} exhibiting intense long lived emission in aqueous medium could be very attractive for TR-FRET assays, avoiding the autofluorescence background. In this case, due to the required UV excitation the NPs should be applied for *in vitro* tests. On the other hand, YSZ NPs co-doped with Tm^{3+}, Yb^{3+} and Er^{3+}, Yb^{3+}, with intense upconversion luminescence upon NIR excitation have a strong potential for *in vivo* biodetection and bioimaging. In particular the strong NIR to NIR UC luminescence is of upmost importance for application in bioimaging as both excitation and detected radiation are within the biological window. Moreover, with NIR excitation, the photo-damage of the tissues are minimized comparatively to UV and visible radiation, the penetration depth of excitation light is higher, allowing the analysis of more deep tissues, and autofluorescence is not stimulated, resulting in higher acquired signal to noise ratio. An illustration of the possible applications of the downshifted and UC luminescent YSZ NPs is shown in Figure 9.2.
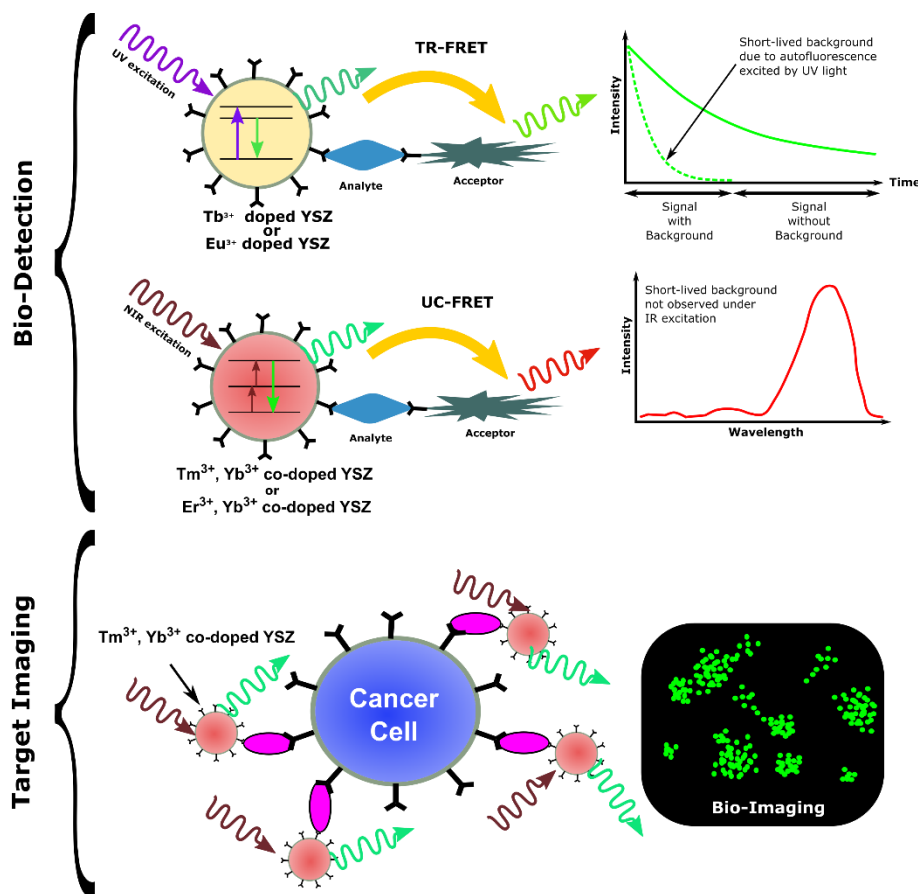
Figure 9.2. Schematic representation of the possible applications of downshifted and UC luminescent YSZ NPs doped with lanthanides for biodetection and target imaging.

Despite the high perspectives of application of the PLAL produced NPs, there is still a long way to go until their practical use in bioapplications. As referred above, zirconia is a bio inert material that found other practical biomedical applications. Even so, since material size and chemical surface play an important role in this field, the toxicity of the doped NPs produced by PLAL are now under analysis, in order to ensure their non-toxicity. In addition, particle size distribution of the NPs produced by PLAL needs to be narrowed in order to be used as bioprobes. Besides the advantageous of the PLAL process in the production of the luminescent crystalline NPs (due to its simplicity, NPs and easily incorporation of lanthanide activators), the control over particle size distribution without the use of surfactant is a crucial issue that need to be solved. The complex interaction between the laser beam, plasma plume, produced NPs, target and liquid medium makes difficult to get NPs with a strict control over their size distribution. As such, alternative ways should be explored in order to narrow the particle size distribution, without jeopardize the other advantageous characteristics of the colloidal solutions produced by PLAL. A strategy that should be explored is a second laser irradiation of the colloidal solution. Other important step for the applications of the produced NPs as luminescent bioprobes is the NPs surface

functionalization and further bioconjugation. As shown in Figure 9.3 an appropriated overlap between the emissions of YSZ:Tb^{3+} and, in special of the YSZ:Tm^{3+},Yb^{3+} with the excitation spectra of a FITC dye (an organic dye extensively used in TR-FRET for detection of avidin [3]) occurs evidencing the potential of these NPs in TR-FRET assays in combination with FITC dye. Based on this knowledge, a first attempt for the functionalization of the NPs surface with amine group, and posterior conjugation with biotin molecules for further detection of avidin was performed. However this preliminary experiment was not successfully achieved. Alternative approaches for the YSZ NPs surface functionalization should be further explored. Strategies based on *in situ* functionalization during the ablation process could be an interesting approach for further exploitations in this field.

Other potential applications of the YSZ NPs produced by PLAL of upmost interest are those related with pressure based luminescent sensors and white light generation, as discussed in Chapter 8 based on the blackbody radiation phenomena observed in vacuum conditions. The dependence of the blackbody radiation *versus* upconverted emission in co-doped YSZ leads to changes in the samples colour emission depending on the pressure conditions that can be further explored to be used in pressure based sensors. On the other hand, the strong white blackbody radiation observed under NIR excitation could consist in a new and efficient alternative for lighting. Based on these ideas, two patents were already submitted to the National Institute of Industrial Property.
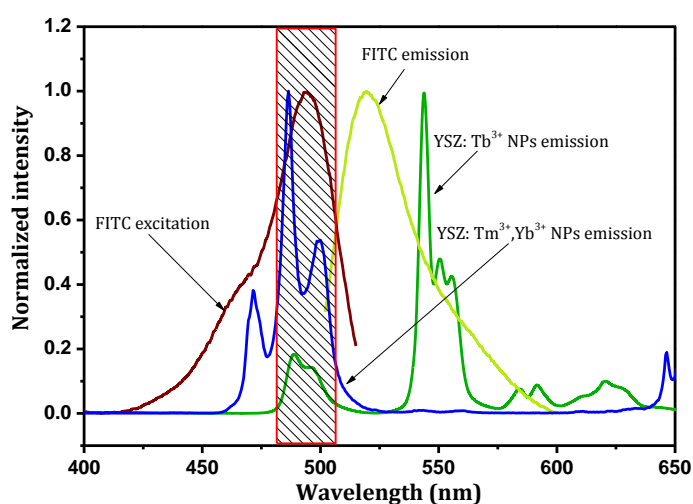
Figure 9.3. Comparison between emission spectra of YSZ:Tb^{3+} NPs under, UV excitation, and of the YSZ:Tm^{3+},Yb^{3+}, under NIR excitation, with the excitation spectra of the FITC dye.

References

[1]   A. Latynina, M. Watanabe, D. Inomata, K. Aoki, Y. Sugahara, E. García Víllora, K. Shimamura, *J. Alloys Compd.* **2013**, *553*, 89.

[2]   E. G. Víllora, S. Arjoca, K. Shimamura, D. Inomata, K. Aoki, *Proc SPIE* **2014**, *8987*, 89871U.

[3]   Y. Liu, S. Zhou, D. Tu, Z. Chen, M. Huang, H. Zhu, E. Ma, X. Chen, *J. Am. Chem. Soc.* **2012**, *134*, 15083.

Chapter 10.

Overview and final Conclusions

An overview of the work undertaken in this thesis and final conclusions, followed with new ideas for further developments are presented in this chapter.

Luminescent materials based on zirconia doped with different trivalent lanthanide ions were produced and their properties analysed taking into account their potential luminescence-based applications. Three processing methods, LFZ, SCS and PLAL, were studied for the preparation of zirconia single crystals, nanopowders and NPs, respectively.

LFZ revealed to be an effective technique to produce both undoped and Ln^{3+} doped tetragonal YSZ single crystals at relatively high growth rates (20-40 mm/h). The production of undoped cubic YSZ crystal was also successfully achieved by this process, but the produced crystal show a poor mechanical stability and easily breaks under small mechanical impact. On the other hand, the Ln^{3+} doped intact cubic YSZ crystal could not be produced, as the crystal completely shatters during the growth or in the cooling process, when the power of the laser is decreased. Such behaviour was associated to the high stress in the grown crystal induced by large amount of dopant and stabilizer ions and high temperature gradient between the molten zone and the grown crystal. Regarding the growth of Ln doped tetragonal YSZ single crystal, different lanthanide ions in the trivalent charge state, were successfully incorporated in the YSZ host during the growth process. The ion optical activation was successfully achieved, without the need of any additional thermal annealing. In general, intense emission at RT was observed in the YSZ doped crystals due to the electronic transitions between the energy levels within the $4f$ configuration of the dopant Ln ions in the trivalent charge state. As the energy multiplets of such Ln^{3+} spread along all the visible spectra, different emission colour were obtained by a proper selection of the Ln ion, ion concentration and excitation energy: intense green light in Tb^{3+} doped YSZ, orange/red light in Eu^{3+} doped YSZ, blue light in Tm^{3+} doped YSZ, green emission in Er^{3+} doped YSZ, red light in Pr^{3+} doped YSZ, or even white light in Dy^{3+} doped YSZ crystals fibres. The intense emission observed at RT in Ln^{3+} doped YSZ LFZ grown crystals evidence the potential of zirconia host for the production of luminescent materials with potential for practical applications. In particular, the white emission obtained in the tetragonal YSZ:Dy^{3+} crystal fibres under UV excitation, is of special importance for lighting applications as it could consist in an alternative strategy for white light generation. Such fibres also can be used as light guides as was observed from the Ln^{3+} emission propagation through the fibres.

In a high number of phosphor applications, for example in lighting and displays, phosphors are needed in a powder form. Simple and economic processes are required for large scale production of phosphor materials with improved performance characteristics. Solution combustion synthesis was effectively used to produce crystalline zirconia nanopowders doped with lanthanide ions. The powders produced from metal nitrates and urea fuel (in stoichiometric conditions), are composed by crystals with nanometric dimensions. The high

temperature achieved in the process allows, on one hand to produce high crystalline powders and, in the other hand, an easy incorporation and optically activation of different Ln ions in the zirconia host. A comparison between the luminescence of Ln ions in the tetragonal YSZ and in the monoclinic YSZ revealed that, in general, an increase in the luminescence from additional Ln^{3+} optical centres is observed in the doped samples where the monoclinic phase is present. In addition, the results obtained in $ZrO_2:Tm^{3+}$ and tetragonal $YSZ:Tm^{3+}$ powders show that the luminescence of Tm^{3+} ions in a tetragonal YSZ host has higher stability with temperature, following the same tendency as the one observed in the tetragonal $YSZ:Tm^{3+}$ single crystal.

Pulsed laser ablation in water was explored for the preparation of colloidal solution of ZrO_2 and YSZ NPs doped with different lanthanides, envisaging manly their potential application as bioprobes. An initial study of the effect of the different processing parameters on the characteristics of the ZrO_2 NPs and on the process yield was performed. The results revealed that, within the studied range of parameters, an appropriated compromise between laser power and height of water layer must be achieved in order to avoid the production of big particles by fragmentation and improve the yield of the process. For the range of studied parameters highly crystalline NPs with a spherical shape and average particle size in the order of 10 nm were produced by the ablation of the solid target. Similar characteristics were found in ZrO_2 and YSZ NPs doped with different Ln ions, including Eu^{3+}, Tb^{3+}, Tm^{3+} and Er^{3+} produced by the same process. The RT luminescence observed in the as-produced doped NPs evidence the easy and successful incorporation of the optically activated ions in the zirconia and YSZ lattices. In particular, YSZ NPs doped with Tb^{3+} and Eu^{3+} show intense long lived luminescence at RT and when dispersed in water, exhibiting higher potential to be further used in TR-FRET assays.

Besides the downshifted luminescence of the trivalent Ln ions in zirconia lattices, with high potential for optoelectronic applications (e.g. lighting and displays) the produced samples doped with Tm^{3+} and Er^{3+} also show interesting upconversion luminescence. In particular Er^{3+} doped and Er^{3+}, Yb^{3+} and Tm^{3+}, Yb^{3+} co-doped samples show intense upconverted visible light at RT, when excited with 980 nm photons, well inside the biological optical window. Besides the intense visible emission of the co-doped NPs, the intense NIR to NIR upconversion emission in the Tm, Yb co-doped NPs produced by PLAL is of upmost importance for *in vivo* biodetection and bioimaging as both excitation and detection are within the biological optical window. Moreover, an intense yellow/white anti-Stokes blackbody radiation was found in these co-doped NPs which are of superior importance

paving the way to the development of non-contact luminescence-based pressure sensors as well as new strategies for white light generation.

Besides the need of additional characterization, mostly regarding to the quantum efficiency measurements for the produced ZrO_2 based phosphors, and functionalization/bioconjugation for the already discussed bioapplications, the results here presented evidence the high potential of these materials and laser processing routes for the *in situ* doped hosts, herein assumed with high potential for practical applications in lighting technologies, sensors, and bioprobes.